# Regulation of Epithelial–Mesenchymal Plasticity Through Lamin A/C and EZH2 Phosphorylation

विद्या वाचस्पति की
उपाधि की अपेक्षाओं की आंशिक पूर्ति में प्रस्तुत शोध प्रबंध

A thesis submitted in partial fulfillment of the requirements of the degree of
Doctor of Philosophy


बालाजी अ क

पंजीकरण सं.: 20203782

Balaji A K

Registration No.: 20203782


शोध प्रबंध पर्यवेक्षक / Thesis Supervisor:

प्रो कुंदन सेनगुप्ता / Prof. Kundan Sengupta



भारतीय विज्ञान शिक्षा एवं अनुसंधान संस्थान पुणे
INDIAN INSTITUTE OF SCIENCE EDUCATION AND RESEARCH PUNE


2026

# CERTIFICATE

Certified that the work incorporated in the thesis entitled "Regulation of Epithelial-Mesenchymal Plasticity through Lamin A/C and EZH2 phosphorylation" submitted by Balaji A K was carried out by the candidate, under my supervision. The work presented here or any part of it has not been included in any other thesis submitted previously for the award of any degree or diploma from any other University or institution.

डॉ. कुंदन सेनगुप्ता/Dr. Kundan Sengupta
(Supervisor)
प्राध्यापक, जीवशास्त्र विभाग/Professor, Biology Department
भारतीय विज्ञान शिक्षा एवं अनुसंधान संस्थान
Indian Institute of Science Education & Research
पुणे / Pune- 411 008, भारत / India

Date:13-01-2026

**Declaration by Student**

Name of Student: Balaji A K

Reg. No.: 20203782

Thesis Supervisor: Prof. Kundan Sengupta

Department: Biology

Date of joining program: 01-September-2020

Date of Pre-Synopsis Seminar: 01-September-2025

Title of Thesis: Regulation of Epithelial-Mesenchymal Plasticity through Lamin A/C and EZH2 phosphorylation

I declare that this written submission represents my idea in my own words and where others' ideas have been included; I have adequately cited and referenced the original sources. I declare that I have acknowledged collaborative work and discussions wherever such work has been included. I also declare that I have adhered to all principles of academic honesty and integrity and have not misrepresented or fabricated or falsified any idea/data/fact/source in my submission. I understand that violation of the above will be cause for disciplinary action by the Institute and can also evoke penal action from the sources which have thus not been properly cited or from whom proper permission has not been taken when needed.

The work reported in this thesis is the original work done by me under the guidance of

Prof. Kundan Sengupta

Date:13-01-2026

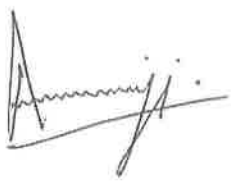

Signature of the student

# Table of Contents

# Acknowledgements

I would like to express my sincere gratitude to all those who contributed, directly and indirectly, to the successful completion of my doctoral research.

First and foremost, I 'm deeply indebted to my parents and friends – Santam, Arnav, Priyam, Tanmoy, Anish and Kshitij for their unwavering support, patience, and encouragement throughout my PhD journey. Their constant belief in me, along with the emotional and academic support they provided during both challenging and rewarding phases of this work, has been invaluable. I also extend my heartfelt thanks to my friends and peers for their companionship, constructive discussions, and moral support, which greatly enriched my experience during these years. I acknowledge Santam Saha for his support in the cloning process.

I acknowledge my PhD advisor, Prof. Kundan Sengupta, for providing me with the freedom and independence to pursue my research questions, while offering timely guidance and critical insights whenever required. This autonomy played a crucial role in shaping my scientific thinking and fostering my growth as an independent researcher.

I sincerely acknowledge the support of the non-teaching staff of the Department of Biology and the Bio-office at IISER Pune for their efficient administrative assistance. I am thankful to the facility teams at IISER Pune, including the FACS facility, Mass Spectrometry facility, and Microscopy facility, for their technical expertise, training, and continuous support. I also acknowledge all the biology laboratories at IISER Pune for providing a collaborative and intellectually stimulating research environment.

I extend my gratitude to the Animal Facility at IISER Pune, with special thanks to Dr. Krishnaveni and Mr. Omkar Atole, for their assistance with animal experiments and for maintaining high standards of animal care. I also thank AG Diagnostics, Pune, and RV Diagnostics, Bangalore, for their support with H&E sample processing. I am grateful to MedGenome, Bangalore, for processing the samples for RNA sequencing and for their professional and timely services.

I would like to acknowledge Ellora Sen for generously sharing the PRMT1 antibody, Prof. Ruby Huang for providing the GRHL2 constructs, and Prof. Sorab Dalal (ACTREC) for

sharing the CDK1 construct. These contributions were instrumental to the successful execution of several key experiments in this thesis.

Finally, I would like to thank everyone who, in ways both big and small, contributed to my scientific training and personal growth during my PhD. I would like to thank all members of chromosome biology lab, IISER Pune for constructive criticism that were given during presentations that helped me in moving this work forward. I would like to acknowledge the use of ChatGPT and Grammarly AI tool mainly for polishing the sentences and grammar but not used for generating any data. This work would not have been possible without the collective support, collaboration, and encouragement of this extended academic community.

**Abbreviations**

EMT: Epithelial to mesenchymal transition

MET: Mesenchymal to epithelial transition

EMT-TFs: Epithelial-to-mesenchymal transition promoting transcription factors

EMP: Epithelial-to-Mesenchymal Plasticity

PRC2: Polycomb repressive complex

EZH2: Enhancer of Zeste Homolog 2

CDK1: Cyclin Dependent Kinase 1

NOD-SCID: Non-Obese Diabetic Severe Combined Immunodeficiency

CTC: circulating tumor cell clusters

scRNA-seq: single-cell RNA sequencing

CSC: cancer stem cell

WHO: World Health Organization

TGF-β: Transforming Growth Factor-Beta

GRHL2: Grainyhead-like 2

OVOL2: Ovo-like 2

HDACs: Histone deacetylases

PTMs: Post-translational modifications

TNBCs: triple-negative breast cancers

ChIP-PCR: Chromatin Immunoprecipitation-Polymerase chain reaction

CoIP-MS: Co-immunoprecipitation mass spectroscopy

RT-qPCR: Real Time- quantitative Polymerase Chain Reaction

LINC complex: Linker of Nucleoskeleton and Cytoskeleton

LADs: Lamina Associated Domains

PVDF: Polyvinylidene Fluoride membrane

shRNA: short-hairpin RNA

CHX: Cycloheximide

PCA: Principal Component Analysis

RO3306: Roscovintine

AR: Aspect Ratio

**Abstract**

Epithelial-to-Mesenchymal Transition (EMT) and its reverse, Mesenchymal-to-Epithelial Transition (MET), underlie essential physiological processes, such as development and wound healing, while also driving pathological conditions, including cancer metastasis. While the role of chromatin regulators in EMT is well established, the contribution of nuclear structural components, particularly nuclear lamins, remains poorly understood.

In this study, we demonstrate that Lamin A/C plays a pivotal role in regulating epithelial–mesenchymal (E-M) plasticity through its interaction with EZH2, a key component of the Polycomb Repressive Complex 2 (PRC2). We show that overexpression of Lamin A maintains epithelial identity, whereas its depletion facilitates a mesenchymal phenotype, establishing Lamin A/C as a gatekeeper of epithelial homeostasis. Mechanistically, the phosphorylation of Lamin A/C at Ser22 and EZH2 at Thr345 by CDK1 disrupts their interaction, leading to the destabilization of EZH2. This leads to a marked reduction in H3K27me3 enrichment at the promoters of canonical EMT transcription factors, such as SNAI1, TWIST1, and ZEB1, thereby promoting mesenchymal gene expression.

Conversely, expression of phospho-deficient mutants Lamin A/C (S22A) and EZH2 (T345A) stabilizes their interaction and restores epithelial features, even in EMT-inducing conditions. In vivo xenograft assays further reveal that tumorigenic potential correlates with the phosphorylation status and interaction dynamics of Lamin A/C and EZH2.

Together, our findings uncover a novel nuclear structural-chromatin regulatory axis—Lamin A/C–EZH2—that governs transcriptional plasticity during EMT. This axis not only integrates the structural and epigenetic regulation of cell state transitions but also presents a potential therapeutic target for restricting metastasis in breast cancer.

**Synopsis**

## 1. Introduction and Background

Epithelial-to-Mesenchymal Transition (EMT) and its reverse, Mesenchymal-to-Epithelial Transition (MET), are highly dynamic and reversible biological processes that govern a wide array of physiological and pathological phenomena (Nieto et al., 2016). EMT enables stationary epithelial cells to acquire a mesenchymal phenotype characterized by enhanced motility, invasiveness, and resistance to apoptosis, which is indispensable during early

developmental processes such as gastrulation, neural crest cell migration, and somite segmentation. MET, on the other hand, facilitates the re-establishment of epithelial traits and is essential during organogenesis, epithelial tissue regeneration, and the reconstitution of epithelial layers following injury (Acloque et al., 2009; Lim and Thiery, 2012).

These transitions involve profound alterations at the molecular, cellular, and tissue levels, including a switch from apical-basal polarity to front-rear polarity, remodeling of the cytoskeleton, dissolution of intercellular junctions, and reprogramming of gene expression (Acloque et al., 2009; Lim and Thiery, 2012). Epithelial cells undergoing EMT downregulate key adhesion molecules such as E-cadherin and upregulate mesenchymal markers like N-cadherin, vimentin, and fibronectin. These changes are tightly regulated by specific transcription factors—SNAI1, SNAI2, ZEB1, ZEB2, and TWIST1—collectively known as EMT-TFs. In contrast, during MET, cells regain their epithelial characteristics through the re-expression of epithelial markers and attenuation of EMT-TFs (Lamouille et al., 2014). This bidirectional plasticity allows cells to adapt to changing microenvironmental cues and is tightly regulated by signaling pathways (e.g., TGF-β, Wnt, Notch), extracellular matrix interactions, and epigenetic mechanisms (Brabletz et al., 2018; Pastushenko and Blanpain, 2019).

Importantly, the reversibility of EMT and MET endows cells with the ability to oscillate between epithelial and mesenchymal states—a phenomenon referred to as epithelial-mesenchymal plasticity (EMP) (Pastushenko et al., 2018). This plasticity is crucial not only for physiological development but also for pathological processes such as cancer metastasis, where tumor cells exploit EMT for dissemination and MET for metastatic colonization (Pastushenko et al., 2021). Despite advances in our understanding of the signaling and transcriptional drivers of EMP, the influence of nuclear structural elements, particularly the nuclear lamina, on EMP dynamics remains an underexplored and compelling frontier in cell and cancer biology.

In pathological contexts, EMT and MET play critical roles in cancer progression, particularly in invasion, dissemination, and colonization of tumor cells. EMT imparts cancer cells with invasive and migratory capacities, whereas MET facilitates metastatic colonization at distant sites (Dongre and Weinberg, 2019; Nieto et al., 2016). The dynamic and reversible nature of these transitions, termed EMP, enables tumor heterogeneity, metastatic seeding, and resistance to therapy (Aiello and Kang, 2019).

EMP is orchestrated by a complex network of signaling pathways, EMT-inducing transcription factors (EMT-TFs), and epigenetic regulators. Among these, transcription factors such as SNAI1, ZEB1, and TWIST1 are well-characterized repressors of epithelial markers and inducers of mesenchymal gene expression (Puisieux et al., 2014). Epigenetic mechanisms, including histone methylation, acetylation, and chromatin remodeling, have emerged as crucial layers of EMP regulation. However, the role of nuclear architecture—particularly the nuclear lamina and its interaction with chromatin modifiers—in EMP regulation remains poorly understood.

The nuclear lamina, primarily composed of type V intermediate filament proteins Lamin A/C and B-type lamins, lines the inner nuclear membrane and provides essential structural support to the nucleus. Beyond its architectural role, Lamin A/C is a multifunctional protein involved in mechanotransduction, genome organization, and transcriptional regulation (Dechat et al., 2008; Swift and Discher, 2013). One of its critical functions is anchoring chromatin to the nuclear periphery, which restricts chromatin accessibility and helps maintain the transcriptional repression of lineage-inappropriate genes, thereby influencing cellular differentiation and plasticity (Buxboim et al., 2014). Loss of Lamin A/C has been associated with increased nuclear deformability, disruption of peripheral heterochromatin, and aberrant activation of developmental and stress response programs. However, the specific role of Lamin A/C in modulating epithelial–mesenchymal transition (EMT) and mesenchymal–epithelial transition (MET)—two key axes of cellular plasticity in development and cancer—remains incompletely understood.

Given the capacity of Lamin A/C to shape the spatial organization of the genome, it is likely to intersect with epigenetic mechanisms that enforce transcriptional repression. Among these, the Polycomb Repressive Complex 2 (PRC2) is a central regulator of chromatin-mediated gene silencing, primarily through catalyzing the trimethylation of histone H3 at lysine 27 (H3K27me3). EZH2, the catalytic subunit of PRC2, plays a pivotal role in maintaining repressive chromatin states during development, stem cell maintenance, and cancer progression. Despite extensive research on PRC2 function, the upstream cues that regulate EZH2 activity and stability—particularly in the context of higher-order nuclear architecture and Lamin A/C-dependent chromatin organization—remain poorly defined.

## 2. Hypothesis

We hypothesize that Lamin A/C contributes to the regulation of epithelial–mesenchymal plasticity in breast cancer through its interactions with chromatin-associated factors and modulation of gene expression programs.

Based on this hypothesis, I have divided the thesis into four main objectives as stated below:

## 3. Objectives

1. To determine the role of Lamin A/C in regulating EMT and MET transitions in breast cancer models.

2. To investigate the molecular interaction between Lamin A/C and EZH2 and its impact on epigenetic regulation of EMT transcription factors.

3. To assess how post-translational modifications (specifically CDK1-mediated phosphorylation) affect Lamin A/C–EZH2 interaction and function.

4. To examine the consequences of modulating Lamin A/C–EZH2 interaction on tumor progression and metastasis in vivo.

### AIM 3.1: To determine the role of Lamin A/C in regulating EMT and MET transitions in breast cancer models.

Emerging evidence underscores the dynamic and reversible nature of EMT and MET during breast cancer progression. While transcription factors and signaling cascades have been extensively studied, the influence of nuclear lamins, particularly Lamin A/C, remains under-investigated. Given its integral role in chromatin tethering and nuclear rigidity, Lamin A/C could provide novel insights into how the structural environment of the nucleus influences cellular plasticity (Lamouille et al. 2014; Wang et al. 2019). Exploring this avenue may reveal additional layers of EMT regulation critical for understanding metastasis.

To address this, in vitro EMT and MET models were established using breast epithelial (MCF10A) and carcinoma cell lines (MCF7 and MDA-MB-231). Lamin A/C expression was

modulated through the use of overexpression constructs and siRNA/shRNA-mediated knockdown. EMT and MET progression were tracked by examining marker expression (E-cadherin, N-cadherin, Vimentin) using qPCR, immunoblotting, and immunofluorescence, while morphological shifts were quantified through wound healing and transwell migration assays. Lamin A/C overexpression preserved epithelial features and suppressed mesenchymal traits, while its knockdown induced a mesenchymal phenotype, indicating its suppressive role in EMT. Time-course experiments linked dynamic Lamin A/C expression with EMT and MET transitions, and functional assays corroborated its role in curbing cell migration and invasion.

**AIM 3.2: To investigate the molecular interaction between Lamin A/C and EZH2 and its impact on epigenetic regulation of EMT transcription factors.**

While Lamin A/C is known to associate with chromatin modifiers, its functional interaction with key epigenetic regulators of EMT remains unexplored. EZH2, the catalytic component of the PRC2 complex, silences genes through the trimethylation of H3K27, emerged as a special interactor exclusively in epithelial cells with Lamin A/C. Determining whether Lamin A/C anchors EZH2 at chromatin sites could help clarify how nuclear structure integrates with epigenetic signaling to regulate EMT-TF activity.

We utilized co-immunoprecipitation and proximity ligation assays to examine Lamin A/C–EZH2 interactions, discovering that these proteins physically associate in epithelial-like cells. Upon Lamin A/C depletion, EZH2 exhibited diminished nuclear retention and stability, suggesting that Lamin A/C plays a role in regulating its localization. ChIP-PCR demonstrated decreased H3K27me3 occupancy at SNAI1, ZEB1, and TWIST1 promoters in Lamin A/C-depleted cells, suggesting impaired EZH2 recruitment. These epigenetic changes corresponded with upregulation of mesenchymal transcription factors, reinforcing Lamin A/C's role as an upstream regulator of chromatin-mediated EMT repression.

**AIM 3.3: To assess how post-translational modifications (specifically CDK1-mediated phosphorylation) affect Lamin A/C–EZH2 interaction and function.**

The functional integrity of nuclear lamins and their interacting partners is frequently modulated by post-translational modifications, with phosphorylation being a principal mechanism. CDK1, active during cell cycle progression and stress responses, is known to phosphorylate both

Lamin A/C and chromatin modifiers. We hypothesized that CDK1-mediated phosphorylation of Lamin A/C and EZH2 regulates their interaction, impacting EMT plasticity.

To test this, phosphorylation sites on Lamin A/C and EZH2 were identified by an unbiased domain deletion approach and LC-MS/MS data. Mutants mimicking (phospho-mimetic) (e.g., Lamin A/C (S22D), EZH2 (T345D)) or preventing (phospho-deficient) phosphorylation were generated (e.g., Lamin A/C (S22A), EZH2 (T345A)). Co-immunoprecipitation and immunofluorescence studies showed that phosphorylation hindered Lamin A/C–EZH2 binding and altered their subnuclear localization. Cells expressing phospho-deficient mutants maintained epithelial morphology and resisted EMT upon TGF-β stimulation, while phospho-mimetic variants facilitated EMT-associated phenotypes, indicating that CDK1-driven phosphorylation dynamically governs this protein interaction during phenotypic switching.

**AIM 3.4: To examine the consequences of modulating Lamin A/C–EZH2 interaction on tumor progression and metastasis in vivo.**

Although in vitro studies provide mechanistic insights, validating these findings in vivo is crucial for determining their pathophysiological relevance. Breast cancer progression involves not only cellular plasticity but also tumor microenvironmental cues that influence metastasis. Therefore, studying how Lamin A/C–EZH2 interactions affect tumor growth and metastatic behavior in animal models can strengthen their candidacy as potential therapeutic targets.

We developed stable MDA-MB-231 cell lines expressing wild-type or phospho-mutant Lamin A/C and EZH2. These were orthotopically implanted into the mammary fat pads of NOD/SCID mice. Tumor growth was monitored using vernier calliper measurements every 72 hours, while histopathological analyses were conducted to evaluate invasiveness and metastatic spread. Tumors derived from cells with phosphorylated Lamin A/C and EZH2 exhibited increased tumor burden, a higher metastatic score, increased invasiveness, and mesenchymal characteristics. In contrast, tumors expressing phospho-deficient constructs remained epithelial-like, with limited growth and lower metastatic scores. Immunofluorescence analyses validated in vivo the correlation between interaction status and tumor phenotype, demonstrating that this nuclear structural–epigenetic axis plays a crucial role in modulating breast cancer aggressiveness.

**4. Rationale and Significance**

Given the dual roles of Lamin A/C in nuclear architecture and gene regulation, and EZH2 in chromatin-mediated transcriptional repression, exploring their crosstalk provides a unique perspective to decipher the mechanisms of cancer plasticity. By understanding how structural nuclear components, such as Lamin A/C, interface with chromatin modifiers like EZH2, we aim to uncover novel targets for mitigating metastatic progression in breast cancers. This work bridges nuclear mechanics with transcriptional control, offering insight into the layered regulation of cell identity transitions.

## 5. Conclusion

The findings presented in this thesis provide novel insights into the interplay between nuclear architecture and chromatin-mediated transcriptional regulation in governing epithelial–mesenchymal plasticity, a key hallmark of breast cancer progression. By systematically dissecting the role of Lamin A/C, we establish it as a pivotal suppressor of EMT, not only by preserving nuclear structure and epithelial identity but also by functioning as a chromatin tether for the epigenetic repressor EZH2. This interaction influences the transcriptional repression of core EMT transcription factors, such as SNAI1, ZEB1, and TWIST1, by maintaining H3K27me3 occupancy at their promoter regions.

Importantly, our findings elucidate how CDK1-mediated phosphorylation of Lamin A/C and EZH2 dynamically modulates this interaction, thereby altering the chromatin localization of EZH2 and reprogramming the epigenetic landscape during EMT and MET transitions. This regulatory axis is further validated in in vivo xenograft models, where tumors with disrupted Lamin A/C–EZH2 interaction show enhanced growth, invasiveness, and mesenchymal traits. Conversely, phospho-deficient mutants that stabilize this interaction maintain epithelial identity and restrain tumour growth and metastatic potential.

Collectively, this work reveals a previously unrecognized nuclear lamina–chromatin interface that plays a crucial role in regulating cell fate transitions. By identifying the Lamin A/C–EZH2 interaction as a regulatory node responsive to phosphorylation, we provide a mechanistic framework that links the structural and epigenetic control of EMT. These insights have broad implications for understanding cancer metastasis and open new avenues for targeting epithelial–mesenchymal plasticity in breast cancer therapeutics.

Future investigations should explore whether similar mechanisms operate in other tumor types and how microenvironmental signals converge on the Lamin A/C–EZH2 axis. Additionally,

pharmacological strategies to modulate this interaction or its phosphorylation status may offer promising leads for therapeutic intervention against metastatic cancers.

## References


Acloque, H., Adams, M. S., Fishwick, K., Bronner-Fraser, M., and Nieto, M. A. (2009). Epithelial-mesenchymal transitions: the importance of changing cell state in development and disease. J. Clin. Invest. 119, 1438–1449.

Aiello, N. M. and Kang, Y. (2019). Context-dependent EMT programs in cancer metastasis. J. Exp. Med. 216, 1016–1026.

Brabletz, T., Kalluri, R., Nieto, M. A. and Weinberg, R. A. (2018). EMT in cancer. Nat. Rev. Cancer 18, 128–134.

Buxboim, A., Swift, J., Irianto, J., Spinler, K. R., Dingal, P. C. D. P., Athirasala, A., Kao, Y.-R. C., Cho, S., Harada, T., Shin, J.-W., et al. (2014). Matrix elasticity regulates lamin-A/C phosphorylation and turnover with feedback to actomyosin. Curr. Biol. 24, 1909–1917.

Dechat, T., Pfleghaar, K., Sengupta, K., Shimi, T., Shumaker, D. K., Solimando, L. and Goldman, R. D. (2008). Nuclear lamins: major factors in the structural organization and function of the nucleus and chromatin. Genes Dev. 22, 832–853.

Dongre, A. and Weinberg, R. A. (2019). New insights into the mechanisms of epithelial-mesenchymal transition and implications for cancer. Nat. Rev. Mol. Cell Biol. 20, 69–84.

Lamouille, S., Xu, J. and Derynck, R. (2014). Molecular mechanisms of epithelial-mesenchymal transition. Nat. Rev. Mol. Cell Biol. 15, 178–196.

Lim, J. and Thiery, J. P. (2012). Epithelial-mesenchymal transitions: insights from development. Development 139, 3471–3486.

Nieto, M. A., Huang, R. Y.-J., Jackson, R. A. and Thiery, J. P. (2016). EMT: 2016. Cell 166, 21–45.

Pastushenko, I. and Blanpain, C. (2019). EMT Transition States during Tumor Progression and Metastasis. Trends Cell Biol. 29, 212–226.

Pastushenko, I., Brisebarre, A., Sifrim, A., Fioramonti, M., Revenco, T., Boumahdi, S., Van Keymeulen, A., Brown, D., Moers, V., Lemaire, S., et al. (2018). Identification of the tumour transition states occurring during EMT. Nature 556, 463–468.

Pastushenko, I., Mauri, F., Song, Y., de Cock, F., Meeusen, B., Swedlund, B., Impens, F., Van Haver, D., Opitz, M., Thery, M., et al. (2021). Fat1 deletion promotes hybrid EMT state, tumour stemness and metastasis. Nature 589, 448–455.

Puisieux, A., Brabletz, T. and Caramel, J. (2014). Oncogenic roles of EMT-inducing transcription factors. Nat. Cell Biol. 16, 488–494.

Swift, J. and Enhances (2013). Nuclear Lamin-A Scales with Tissue Stiffness and Enhances Matrix-Directed Differentiation. Science.

# Chapter 1: Review of Literature

## 1.1 Introduction

Cancer remains one of the most significant global health challenges, accounting for millions of deaths annually. While advances in early detection and treatment have improved outcomes in some cancers, metastatic disease continues to be the primary cause of cancer-related mortality, responsible for over 90% of cancer deaths (WHO). Metastasis is a highly complex, multistep process involving detachment of tumor cells from the primary site, invasion into surrounding tissue, intravasation into the bloodstream or lymphatics, survival in circulation, extravasation, and colonization of distant organs (Fares et al. 2020). Central to this metastatic cascade is a dynamic cellular process known as the epithelial–mesenchymal transition (EMT). EMT is a highly conserved biological program through which epithelial cells lose their junctional contacts and apico-basal polarity and acquire mesenchymal traits such as motility, invasiveness, and resistance to apoptosis (Lambert et al. 2017; Aiello and Kang 2019).

Although initially characterized during embryonic development, where it regulates processes such as gastrulation and neural crest migration, EMT has since been implicated in various adult physiological and pathological contexts (Nakaya and Sheng, 2008; Acloque et al., 2009; Lim and Thiery, 2012). In wound healing and tissue regeneration, EMT facilitates cell mobilization and tissue remodeling. In pathological states, particularly in cancer progression, EMT is hijacked by tumor cells to gain invasive and metastatic abilities. Importantly, EMT in cancer is not a uniform or complete transformation. Recent studies have shown that cells often undergo partial or incomplete EMT, leading to the emergence of hybrid epithelial/mesenchymal (E/M) phenotypes. These intermediate states allow cells to simultaneously express both epithelial markers like E-cadherin and mesenchymal markers like Vimentin, contributing to cellular plasticity and adaptive responses during metastasis (Jolly et al. 2015).

This concept of epithelial–mesenchymal plasticity (EMP) has redefined our understanding of EMT, positioning it as a spectrum rather than a binary switch. Hybrid E/M states confer multiple advantages: they allow for collective migration of tumor cell clusters, enhance resistance to environmental stress and therapy, and support the acquisition of stem-like features that contribute to tumor heterogeneity (Pastushenko et al. 2018; Jolly et al. 2019; Sahoo et al. 2021). EMP enables tumor cells to dynamically adapt to their microenvironment, aiding in survival during the metastatic journey and in colonization at distant sites. Moreover, the reversibility of EMT, facilitated through the mesenchymal-to-epithelial transition (MET), is

essential for the successful establishment of secondary tumors. The capacity for reversible state switching underscores the significance of EMP in tumor progression and therapy resistance.

The regulation of EMT is orchestrated by an intricate network of intracellular and extracellular cues. Canonical signaling pathways such as transforming growth factor-beta (TGF-β), Wnt, Notch, and Hedgehog converge on transcriptional regulators including SNAI1, SNAI2, ZEB1, ZEB2, and TWIST1/2. These EMT-inducing transcription factors (EMT-TFs) repress epithelial gene programs while activating mesenchymal gene expression. The coordination of these programs requires epigenetic modifications, chromatin remodeling, and post-transcriptional regulation. Epigenetic changes, including histone methylation and acetylation, are mediated by complexes such as the Polycomb Repressive Complex 2 (PRC2), while DNA methylation silences key epithelial genes. Post-transcriptional regulators, including microRNAs (e.g., the miR-200 family) and long non-coding RNAs (e.g., HOTAIR, MALAT1), further fine-tune gene expression by targeting mRNA stability or by recruiting chromatin modifiers to specific loci (Peng et al. 2020; Deshmukh et al. 2021).

In recent years, the role of nuclear architecture in modulating EMT and EMP has garnered increasing attention. Historically considered a static barrier, the nuclear envelope is now recognized as a mechanosensitive and transcriptionally active interface that links extracellular signals to genome function. The inner nuclear membrane is supported by the nuclear lamina, a fibrous meshwork composed primarily of type V intermediate filament proteins, including Lamin A/C and B-type Lamins. Lamin A/C, encoded by the LMNA gene, is a critical structural protein that regulates nuclear stiffness, chromatin organization, and gene expression. It interacts with a wide array of transcription factors, chromatin modifiers, and structural proteins, and is essential for the maintenance of nuclear shape and integrity (Shimi et al. 2008; Swift et al. 2013).

Perturbations in Lamin A/C expression and function are frequently observed in aggressive cancers (Wang et al. 2019). Reduced Lamin A/C levels have been associated with increased nuclear deformability, enhanced metastatic potential, and elevated transcriptional plasticity (Bell et al. 2022). Moreover, Lamin A/C participates in chromatin tethering and gene silencing by interacting with PRC2 and other repressive complexes (Kubben et al. 2010). The spatial organization of chromatin within the nucleus is modulated through these interactions, impacting access to key regulatory elements. In cancer cells, aberrations in Lamin A/C phosphorylation, particularly at Ser22, alter its localization and interaction with chromatin-

binding proteins such as EZH2, the enzymatic core of PRC2. This work highlights that phosphorylation by kinases, such as CDK1, has been shown to modulate the Lamin A/C–EZH2 interaction, affecting EZH2 stability and its ability to deposit H3K27me3 marks on epithelial gene promoters. Loss of this repression facilitates the upregulation of EMT-TFs and promotes mesenchymal gene expression.

The nuclear lamina is further connected to the cytoskeleton through the LINC (Linker of Nucleoskeleton and Cytoskeleton) complex, which spans the nuclear envelope and mechanically couples the nuclear interior to the actin cytoskeleton and the extracellular matrix (Buxboim et al. 2014). This physical linkage enables cells to sense and respond to mechanical stress, modulating chromatin organization and gene expression in a force-dependent manner. The transmission of mechanical cues through the LINC complex and nuclear envelope has been implicated in stem cell differentiation, lineage commitment, and now, increasingly, in the regulation of EMT.

Taken together, these insights position Lamin A/C and the nuclear envelope as crucial regulators of phenotypic plasticity during cancer progression. The ability of Lamin A/C to scaffold chromatin regulators, respond to phosphorylation events, and transmit mechanical cues places it at the intersection of nuclear mechanics and transcriptional regulation. This intersection is particularly relevant in the context of EMT, where dynamic reprogramming of the transcriptome and changes in nuclear deformability co-occur.

Here, I aim to provide a comprehensive examination of the molecular and structural basis of EMT, with a particular focus on the nuclear envelope and its role in modulating chromatin accessibility and transcriptional dynamics. We begin by redefining EMT as a continuum of phenotypic states and exploring the functional implications of this plasticity. We then elaborate on the hallmarks of EMT-driven cancer progression and dissect the molecular networks that govern this transition. Special attention is given to the structural elements of the nucleus—including Lamin A/C, the LINC complex, and associated chromatin regulators—which collectively influence the nuclear landscape during EMT. By highlighting the crosstalk between nuclear architecture and gene regulatory mechanisms, this review provides new insights into the structural underpinnings of cellular plasticity and identifies potential therapeutic avenues for targeting EMT in cancer.

### 1.2 EMT as a Continuum, not a Binary Switch

The epithelial–mesenchymal transition (EMT) has historically been portrayed as a binary process; whereby epithelial cells transform completely into mesenchymal cells. This traditional model served as a foundational concept in developmental biology and oncology for decades. However, accumulating evidence from transcriptomic profiling, lineage tracing, and single-cell sequencing has fundamentally reshaped this perspective. EMT is now widely recognized as a spectrum of intermediate cellular states, in which cells do not necessarily fully relinquish their epithelial traits, nor do they fully commit to a mesenchymal phenotype (Figure 1.1). This nuanced understanding of EMT has led to the concept of epithelial–mesenchymal plasticity (EMP), a flexible program enabling cancer cells to acquire dynamic, context-dependent phenotypes along the epithelial–mesenchymal axis (Pastushenko and Blanpain 2019).

Cells in partial EMT states exhibit a blend of epithelial and mesenchymal markers. For instance, it is now well established that tumor cells coexpressing E-cadherin and Vimentin, or N-cadherin, represent a distinct hybrid E/M population with enhanced adaptability. These cells often exhibit collective migration, wherein clusters of partially transitioned cells invade as a cohesive group, retaining cell–cell adhesions while acquiring migratory capabilities. Such hybrid states are not rare anomalies but are widely detected in various human cancers, including breast, lung, pancreatic, and colorectal tumors (Lu and Lu 2021). Importantly, these intermediate states are functionally relevant: they are associated with increased tumor-initiating capacity, resistance to therapy, and higher metastatic efficiency compared to fully mesenchymal cells (Aiello 1.3et al. 2018).

One of the hallmarks of partial EMT is collective migration—a phenomenon where cells retain partial epithelial characteristics, such as E-cadherin-mediated junctions, while exhibiting front–rear polarity, cytoskeletal rearrangements, and protease secretion. Leader cells in these migratory clusters often express higher levels of EMT transcription factors (e.g., ZEB1, SNAI2), while follower cells maintain epithelial features. This allows for coordinated invasion through the extracellular matrix while preserving the ability to re-epithelialize at secondary sites, a crucial step in metastatic colonization that often necessitates a mesenchymal-to-epithelial transition (MET).

Recent advances in single-cell RNA sequencing (scRNA-seq) and spatial transcriptomics have confirmed the prevalence and stability of hybrid E/M states in tumors. For example, studies in breast cancer have revealed distinct subpopulations occupying stable intermediate EMT states with unique transcriptional profiles and functional phenotypes (Pastushenko et al., 2018;

Karacosta et al., 2019). These hybrid cells resist anoikis, survive in circulation as circulating tumor cell (CTC) clusters, and contribute to minimal residual disease following therapy. Moreover, the presence of CTC clusters has been correlated with poor prognosis, underscoring their clinical relevance (Aceto et al., 2014).

The maintenance of hybrid EMT states is regulated by a balance of transcriptional activators and repressors. Phenotypic stability factors (PSFs), such as GRHL2, OVOL1/2, and ΔNp63α, have been shown to prevent complete mesenchymal transition by antagonizing EMT-TFs like ZEB1 and SNAI1 (Werner et al. 2013). These PSFs not only inhibit the expression of mesenchymal genes but also sustain epithelial traits, thereby locking cells in a metastable hybrid state. Significantly, the expression and function of these factors are modulated by external cues from the tumor microenvironment (TME), including cytokines (TGF-β, IL-6, TNF-α), ECM stiffness, and hypoxic conditions (Le et al. 2018).

TGF-β signaling plays a pivotal role in driving partial EMT under various pathophysiological contexts. Short-term or low-dose TGF-β exposure induces incomplete EMT, characterized by partial loss of epithelial traits and transient gain of mesenchymal features (Zhang et al. 2014). This state is reversible upon withdrawal of the stimulus. In contrast, sustained or high-dose TGF-β leads to more permanent EMT changes, including chromatin remodeling and stable repression of epithelial gene loci. These outcomes are mediated by context-dependent Smad and non-Smad signaling axes that converge on EMT-related gene networks (Qiao et al. 2020).

From a mechanical standpoint, the physical properties of cells undergoing EMT change progressively along the spectrum of EMT. Partial EMT cells often display nuclear and cytoskeletal stiffness intermediate between that of epithelial and mesenchymal cells (Aiello and Kang 2019). This mechanical plasticity allows them to squeeze through confined spaces during invasion while maintaining nuclear integrity and genomic stability—traits essential for surviving the metastatic cascade.

The epigenetic regulation of EMT also supports the concept of a continuum model. Histone modifications such as H3K27me3, deposited by EZH2, contribute to the repression of epithelial genes, while chromatin relaxes at mesenchymal loci marked by H3K4me3 or H3K27ac. These bivalent chromatin states, where both activating and repressive marks coexist, create a poised transcriptional landscape that can be rapidly shifted in response to signaling inputs. Chromatin

accessibility analyses (e.g., ATAC-seq) have revealed gradual, rather than abrupt, remodeling of the chromatin landscape during EMT progression (Cardenas et al. 2016).

MicroRNAs and long non-coding RNAs (lncRNAs) further buffer the epithelial–mesenchymal equilibrium. For example, the miR-200 family maintains epithelial identity by targeting ZEB1/2, while miR-21 and miR-10b promote EMT through suppression of PTEN and HOXD10, respectively (Tian et al. 2021; Rajagopal et al. 2020). The interplay between miRNAs and EMT-TFs constitutes robust feedback loops that stabilize hybrid phenotypes. LncRNAs such as HOTAIR and MALAT1 act as scaffolds for chromatin modifiers and influence EMT gene expression by regulating histone modifications at promoter regions (Dongre and Weinberg 2019).

In the context of therapeutic resistance, partial EMT states confer significant survival advantages. Hybrid E/M cells have been shown to resist chemotherapy, radiation, and targeted therapies more effectively than fully epithelial or mesenchymal populations. This resistance stems from reduced proliferation, activation of DNA repair pathways, and expression of anti-apoptotic genes (Guo et al. 2021). Furthermore, partial EMT enhances immune evasion by modulating antigen presentation, downregulating MHC molecules, and upregulating immune checkpoint proteins such as PD-L1 (Gaponova et al. 2020).

In summary, EMT is best conceptualized not as a binary switch but as a spectrum of stable and dynamic states regulated by intricate networks of transcriptional, epigenetic, and mechanical inputs. The ability of cancer cells to exist in hybrid epithelial/mesenchymal states provides them with remarkable adaptability, allowing them to survive therapeutic challenges, evade immune responses, and efficiently colonize distant organs. Future therapeutic strategies must account for this phenotypic plasticity and aim to disrupt the regulatory circuits that sustain partial EMT, either by enforcing complete MET or by rendering hybrid states metabolically or immunologically vulnerable.

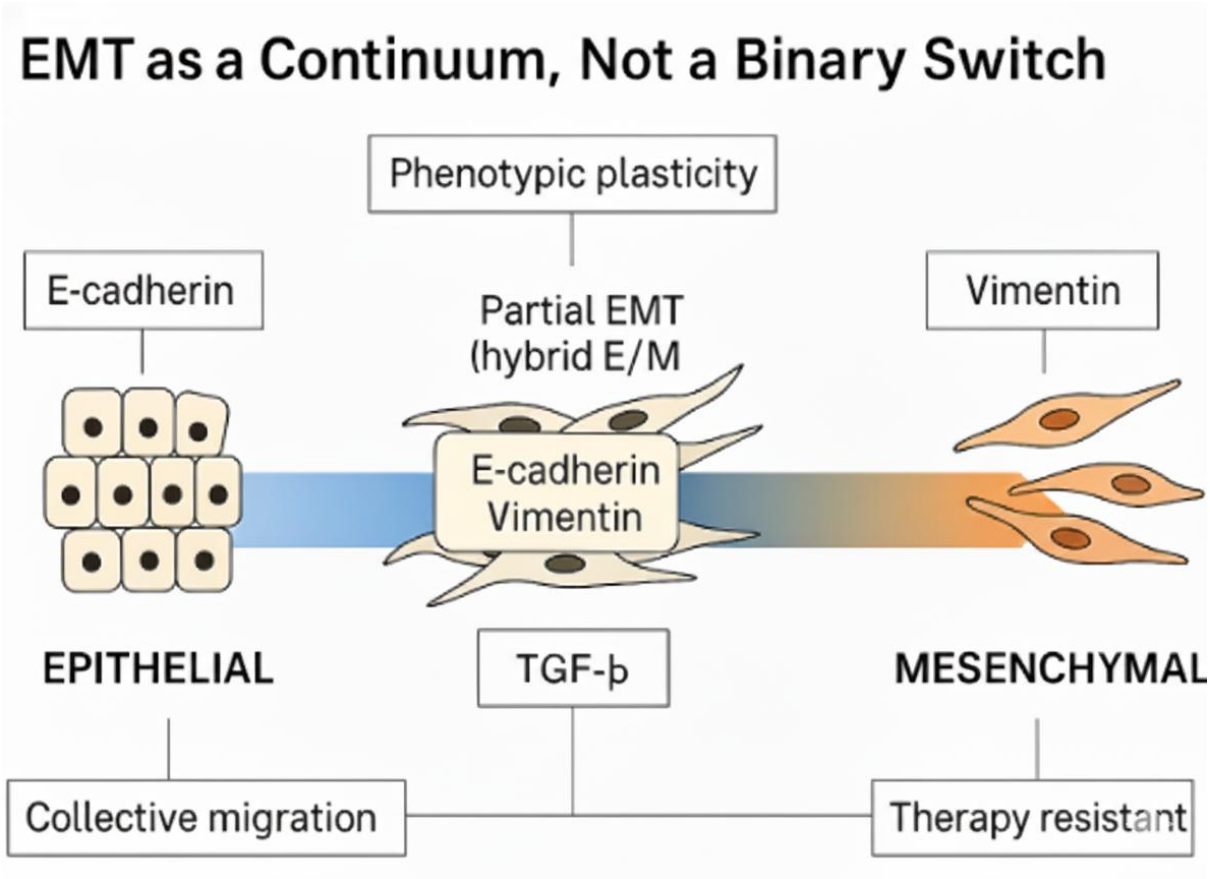


***Figure 1.1. EMT exists as a continuum rather than a binary epithelial–mesenchymal switch.***

*Schematic representation of epithelial–mesenchymal transition (EMT) showing that cells do not transition directly from a fully epithelial to a fully mesenchymal state. Instead, cells occupy intermediate "partial EMT" or hybrid E/M states characterized by co-expression of epithelial markers (e.g., E-cadherin) and mesenchymal markers (e.g., vimentin). Epithelial cells maintain strong cell–cell adhesion and support collective migration, whereas mesenchymal cells exhibit high vimentin expression and contribute to therapy resistance. Phenotypic plasticity enables cells to shift along the EMT spectrum in response to cues such as TGF-β. This continuum underlies functional heterogeneity and dynamic state transitions during development, tissue repair, and cancer progression.*

## 1.3 Hallmarks of EMT-Driven Cancer Progression

The epithelial–mesenchymal transition (EMT) is not merely a transcriptional program but a multifaceted cellular reprogramming event that drives profound functional transformations in cancer cells. By enabling epithelial cells to acquire mesenchymal-like traits, EMT facilitates tumor progression at multiple levels—from invasion and dissemination to resistance and relapse (Figure 1.2) (Zheng et al. 2015). Below, we dissect the major hallmarks of EMT-driven cancer progression, elaborating on the molecular and phenotypic shifts that empower cancer cells to thrive under therapeutic and environmental challenges.

### 1.3.1 Acquisition of Stemness and Tumor-Initiating Capacity

A defining hallmark of EMT is its strong association with cancer stem cell (CSC) phenotypes. EMT programs, particularly those in partial EMT states, confer stem-like features, including self-renewal, differentiation plasticity, and tumor-initiating potential. Pioneering studies by (Mani et al. 2008) demonstrated that EMT induction via TWIST or SNAIL overexpression in mammary epithelial cells led to the emergence of a CD44^high/CD24^low population—a classical marker of breast cancer stem cells (Chen et al. 2021). Hybrid epithelial/mesenchymal (E/M) cells are often enriched for such markers and are highly tumorigenic in xenograft models. Moreover, the expression of core pluripotency factors such as NANOG, OCT4, and SOX2 is often elevated in cells that have undergone partial EMT (Wilson et al. 2020).

Mechanistically, EMT transcription factors (EMT-TFs) like ZEB1 not only repress epithelial markers but also promote stemness by activating Wnt, Notch, and Hedgehog signaling pathways. For example, ZEB1 represses miR-200 family members, which in turn derepresses BMI1, a stemness-associated polycomb group protein. These interconnected networks form bistable circuits that reinforce the CSC phenotype during EMT (Kim et al. 2012).

More recently, integrative transcriptomic and epigenomic analyses have shown that EMT-TFs establish permissive chromatin landscapes at pluripotency loci while repressing differentiation-associated genes (Wilson et al. 2020). Partial EMT stabilizes this balance, allowing cells to exhibit both epithelial adherence and stemness-associated plasticity. These hybrid cells show enhanced organoid-forming ability, resistance to differentiation cues, and the capacity to regenerate tumors after therapy (Chen et al. 2021).

Clinical implications of EMT-induced stemness are profound. Tumors enriched in EMT signatures often exhibit higher intratumoral heterogeneity, increased metastasis, and poor response to treatment (Adams et al. 2015). EMT-induced CSCs survive chemotherapy and radiotherapy due to their slow-cycling nature, enhanced drug efflux, and superior DNA repair capacity. These cells can lie dormant and repopulate the tumor bed post-therapy, contributing to recurrence (Chen et al. 2021). Notably, inhibitors targeting EMT-TFs, epigenetic readers (e.g., BRD4), or TGF-β signaling have demonstrated preclinical efficacy in reversing EMT-induced stemness and reducing tumorigenicity (Yu et al. 2023).

### 1.3.2 Enhanced Invasion and Migration

EMT enables cells to detach from epithelial sheets, invade through basement membranes, and migrate through stromal environments—hallmarks of metastatic dissemination (Lim and Thiery 2012; Lamouille et al. 2014). A major molecular hallmark of EMT is the loss of E-cadherin, which destabilizes adherens junctions and promotes cell dissociation (Lamouille et al. 2014; Nieto et al. 2016). Simultaneously, the upregulation of mesenchymal markers, such as N-cadherin (a phenomenon known as cadherin switching), Vimentin, and Fibronectin, allows for the dynamic reorganization of the cytoskeleton, integrin engagement, and mechanical responsiveness (Mani et al. 2008; Nieto et al. 2016).

During EMT, cells gain motility through actin cytoskeleton remodeling mediated by Rho GTPases, Rac1, and CDC42 (Parri and Chiarugi 2010). These changes support the formation of lamellipodia, filopodia, and invadopodia—actin-rich protrusions involved in matrix degradation and invasion (Leong et al. 2014). These structures are stabilized by interactions with integrins and focal adhesion complexes that regulate traction forces necessary for forward movement (Huttenlocher and Horwitz 2011).

EMT also enhances secretion and activation of matrix metalloproteinases (MMPs), particularly MMP2 and MMP9, which cleave components of the extracellular matrix (ECM), facilitating invasion (Kessenbrock et al. 2010; Gialeli et al. 2011). MMP activity is often spatially localized to the leading edge of migrating cells and is tightly regulated by tissue inhibitors of metalloproteinases (TIMPs) (Sternlicht and Werb 2001). EMT-TFs such as TWIST1 and SNAI1 directly induce the transcription of MMPs, while suppressing ECM components like laminins and collagens that anchor epithelial cells (Peinado et al. 2017; Dongre and Weinberg 2019).

Importantly, invasion is not limited to single-cell migration. Hybrid E/M cells often migrate collectively, where leader cells with partial EMT phenotypes pull trailing cells through ECM

conduits (Pastushenko et al. 2018). These clusters retain intercellular adhesion via desmosomes or low-level E-cadherin expression and demonstrate higher resistance to mechanical stress and apoptosis (Kröger et al. 2019). Collective migration also enables cooperative navigation through chemotactic gradients, thereby enhancing directional motility (Friedl and Gilmour 2009).

Recent imaging studies and intravital microscopy have shown that EMT-driven invasion can occur in waves, with cells switching dynamically between epithelial, hybrid, and mesenchymal states depending on microenvironmental cues such as hypoxia, stiffness, and cytokine exposure (Nieto et al. 2016; Aiello and Kang 2019). This plasticity enables tumor cells to adapt their migration modes—namely, amoeboid, mesenchymal, or collective—as they encounter varying tissue architectures (Friedl and Gilmour 2009).

At the metastatic site, the reversion to an epithelial phenotype via MET is often essential for colonization and proliferation (Tsai and Yang 2013). Thus, EMT not only facilitates initial dissemination but also primes cells for the eventual invasion-migration axis, a central feature in metastatic colonization (Lambert et al. 2017).

### 1.3.3 Resistance to Apoptosis and Anoikis

Apoptosis, or programmed cell death, is a critical safeguard mechanism that eliminates damaged or unanchored cells, especially during detachment from the extracellular matrix—a form of cell death known as anoikis (Frisch & Francis, 1994; Paoli et al., 2013). Resistance to apoptosis, particularly anoikis, is a fundamental feature acquired during EMT. This resistance enables cancer cells to survive as they detach from the primary tumor and disseminate through the bloodstream or lymphatic system (Chaffer and Weinberg 2011; Diepenbruck and Christofori 2016).

During EMT, epithelial cells lose integrin-mediated contacts with the basement membrane and shift to a mesenchymal program that includes the upregulation of pro-survival signaling cascades (Lamouille et al. 2014). One of the central pathways activated during EMT is the PI3K/Akt pathway, which promotes survival through phosphorylation and inactivation of pro-apoptotic factors such as BAD and the forkhead family of transcription factors (Datta et al. 1999; Testa and Tsichlis 2005). Simultaneously, EMT leads to the upregulation of anti-apoptotic proteins, including BCL-2, BCL-XL, Survivin, and XIAP, thereby tipping the balance toward cell survival even under conditions of detachment or genotoxic stress (Youle and Strasser 2008; Zhao et al. 2012).

Transcription factors such as SNAI1, TWIST1, and ZEB1 actively repress p53-mediated apoptotic responses (Chen et al. 2012; Zhang et al. 2014). SNAI1, for example, suppresses PTEN—a negative regulator of PI3K/Akt—and p53 itself, thereby preventing apoptosis (Vega et al. 2004). TWIST1 can inhibit the expression of pro-apoptotic genes like BIM and PUMA(Kwok et al. 2007; Puisieux et al. 2014). These factors also promote mitochondrial membrane stabilization and modulate mitochondrial dynamics to resist apoptotic signals (Tait and Green 2010).

Moreover, EMT cells exhibit increased autophagy, a catabolic survival mechanism that recycles intracellular components and provides energy under nutrient stress (Yang et al. 2013). TWIST1 and SNAI1 are known to induce autophagy-related genes such as Beclin1 and ATG5 (Gugnoni et al. 2016; Dower et al. 2018). This autophagic activity helps cells cope with metabolic stress, chemotherapy, and oxidative damage, thereby contributing to cellular fitness in hostile microenvironments (White 2012; Strohecker and White 2014).

Another mechanism by which EMT protects cells from anoikis is through changes in focal adhesion and cytoskeletal dynamics (Yang et al. 2013). Mesenchymal cells generate new integrin-based contacts with the ECM via FAK and Src activation (Mitra et al. 2005; Sulzmaier et al. 2014). These focal adhesion kinases (FAKs) transmit survival signals that prevent caspase activation even in the absence of canonical epithelial integrins (Streuli 2009; Huttenlocher and Horwitz 2011). Additionally, activation of YAP/TAZ—a mechanotransduction pathway responsive to cell spreading and matrix stiffness—has been implicated in supporting EMT-induced resistance to anoikis (Zanconato et al. 2016; Kim and Jho 2018).

From a clinical standpoint, EMT-induced apoptosis resistance facilitates survival of circulating tumor cells (CTCs), contributing to the establishment of metastatic lesions (Comaills et al. 2016). CTCs must survive not only detachment but also shear stress and immune surveillance in circulation (Fidler 2003; Massagué and Obenauf 2016). EMT traits such as elevated BCL-XL expression and reduced Fas receptor availability enhance this survival (Mehlen and Puisieux 2006; Shi et al. 2019). Therapeutically, combining EMT-inhibitors with BH3 mimetics (which neutralize BCL-2 family proteins) has shown promise in preclinical models to sensitize EMT-positive cells to apoptosis (Lopez and Tait 2015; Debnath et al. 2022).

### 1.3.4 Chemoresistance and Therapy Resistance

One of the most clinically relevant consequences of EMT is its profound association with resistance to a broad range of cancer therapies (Nieto et al. 2016). EMT induces a transcriptional reprogramming that endows cells with properties enabling them to escape

apoptosis, evade immune responses, and adapt to metabolic and oxidative stress induced by treatment (Bouwman et al., 2010; Wang et al., 2009). These adaptations contribute to both intrinsic resistance, where cells are unresponsive to therapy from the outset, and acquired resistance, which arises during or after treatment (Gesson et al., 2016; Sati et al., 2020).

Mechanistically, EMT leads to reduced intracellular accumulation of chemotherapeutic agents due to increased expression of ATP-binding cassette (ABC) transporters such as ABCB1 (P-glycoprotein), ABCC1 (MRP1), and ABCG2 (BCRP) (Goldberg et al., 2010; Santi et al., 2020). These transporters actively efflux drugs such as doxorubicin, paclitaxel, and cisplatin, thereby reducing their cytotoxic impact (Chin et al., 2006). In parallel, EMT-induced epigenetic changes result in a more repressive chromatin environment that limits drug access to DNA and reduces transcription of pro-apoptotic genes (Mahen et al., 2013; Aiello and Kang, 2019)

EMT also promotes cell cycle arrest in the G0/G1 phase, a characteristic of cancer stem-like cells (Coschi et al., 2014). These slow-cycling or dormant cells evade the cytotoxic effects of therapies that target rapidly dividing populations (Vallette et al., 2019). TWIST1, ZEB1, and SNAIL have been shown to induce quiescence-associated pathways while repressing genes involved in mitotic progression, DNA replication, and cell division (Bohl et al., 2014; Meyer-Schaller et al., 2019).

Furthermore, EMT enhances the DNA damage response (DDR) and repair capacity (Almeida et al., 2017; Khot et al., 2020). For instance, ZEB1 promotes the expression of CHK1 and BRCA1, facilitating homologous recombination and allowing cells to survive genotoxic stress (Crompton et al., 2014; Santi et al., 2020). EMT is also associated with upregulation of antioxidant programs, including NRF2 and glutathione metabolism, which neutralize reactive oxygen species (ROS) generated by radiation or chemotherapy (Barnhart et al., 2011; Crompton et al., 2014).

Emerging evidence also shows that EMT modulates autophagy—a lysosome-dependent degradation process that sustains metabolic homeostasis and cell survival under therapy-induced stress (Ano Bom et al., 2012; Crompton et al., 2014). SNAIL and TWIST1 transcriptionally activate autophagy-related genes (e.g., ATG5, Beclin1), enabling cancer cells to recycle damaged organelles and evade cell death (Gesson et al., 2016; Baugh et al., 2018).

Clinically, tumors enriched in EMT signatures often exhibit a poor response to chemotherapy and targeted agents (Friedl and Gilmour, 2009; Fischer et al., 2015). For example, triple-negative breast cancers (TNBCs), which often exhibit mesenchymal and stem-like features, are resistant to conventional chemotherapy (Hanahan and Weinberg, 2011). In lung

adenocarcinoma, EGFR-TKI resistance has been linked to EMT progression and the development of a mesenchymal phenotype (Chen et al., 2012; Chang et al., 2015).

Therapeutic strategies aimed at overcoming EMT-mediated resistance include combining chemotherapeutics with EMT-inhibiting agents, such as TGF-β inhibitors, HDAC inhibitors, or microRNA mimics (e.g., miR-200 family) (Zhang et al., 2016; Kröger et al., 2019). Several preclinical studies have demonstrated that reversing EMT can restore sensitivity to drugs and prevent tumor relapse (Wilson and Foisner, 2010; Lovisa et al., 2015).

### 1.3.5 Immune Evasion

Epithelial–mesenchymal transition (EMT) profoundly impacts the tumor immune microenvironment by facilitating immune escape mechanisms (Dongre & Weinberg, 2019; Terry et al., 2017). As cells transition to a mesenchymal-like state, they not only evade physical barriers and therapy-induced stress but also develop the capacity to suppress or avoid immune recognition (Nieto et al., 2016). EMT drives immuno-evasive traits through molecular reprogramming that affects antigen presentation, cytokine secretion, and immune checkpoint regulation (Wong et al., 2009; Nieto et al., 2016).

One key immune evasion mechanism during EMT is the downregulation of primary histocompatibility complex class I (MHC-I) molecules, which impairs antigen presentation to cytotoxic CD8+ T cells (Xu et al., 2017). The reduction in MHC-I expression is driven by transcriptional repression of antigen processing components, such as TAP1/2 and β2-microglobulin, as well as inhibition of key regulators like NLRC5 (Mehta et al., 2018). EMT-TFs such as SNAI1, ZEB1, and TWIST1 have been implicated in silencing these components, effectively masking tumor cells from immune surveillance (Wong et al., 2009; Yin et al., 2017).

Moreover, EMT leads to an increased secretion of immunosuppressive cytokines, including TGF-β, IL-10, and VEGF (Dechat et al., 2010; X. Kang et al., 2019). These factors not only dampen effector T-cell activity but also recruit regulatory T cells (Tregs) and myeloid-derived suppressor cells (MDSCs), which further suppress antitumor immunity (Redwood et al., 2011; Pastushenko et al., 2018). Tumor cells undergoing EMT also express chemokines, such as CCL2 and CXCL5, that enhance the infiltration of immunosuppressive immune cell subsets, thereby shifting the tumor microenvironment (TME) from a pro-inflammatory to an immunosuppressive state (Shimi et al., 2008; Tait and Green, 2010).

Another central axis of EMT-induced immune evasion is the upregulation of immune checkpoint molecules, especially PD-L1 (programmed death ligand-1) (Panier and Boulton, 2014). ZEB1 has been shown to directly induce PD-L1 expression by repressing miR-200

family members, which normally inhibit PD-L1 transcription (Ye et al., 2018). Increased PD-L1 expression attenuates cytotoxic T cell responses by engaging PD-1 on T cells, leading to T cell exhaustion and apoptosis (White, 2012). Furthermore, EMT enhances the expression of CD47, a "do not eat me" signal that protects cancer cells from phagocytosis by macrophages (Zeitlin et al., 2009).

EMT also intersects with innate immunity. For instance, EMT-like states suppress the expression of ligands for activating receptors on natural killer (NK) cells, including NKG2D ligands, which results in reduced NK cell-mediated cytotoxicity (Guerra et al., 2008). EMT-TFs can modulate the expression of these ligands via chromatin remodeling and interaction with epigenetic repressors (Reis-Sobreiro et al., 2018).

Clinical observations support the notion that EMT promotes resistance to immunotherapy. Tumors exhibiting EMT signatures show lower infiltration of CD8+ T cells and reduced expression of IFN-γ–related genes, correlating with poor response to checkpoint inhibitors (Ogiyama et al., 2018). This has led to the exploration of combination therapies targeting EMT and immune checkpoints simultaneously (Yang et al., 2018). Preclinical studies using TGF-β inhibitors in conjunction with PD-1 or PD-L1 blockade have shown promising results in overcoming EMT-associated immune resistance (Taylor et al., 2018).

Thus, EMT not only contributes to physical dissemination and therapy resistance but also actively remodels the immune landscape to favor tumor progression (Dongre and Weinberg, 2019). Targeting EMT-driven immune evasion mechanisms holds significant potential for enhancing the efficacy of immunotherapy, particularly in tumors with a mesenchymal or hybrid phenotype (Antony et al., 2020).

### 1.3.6 Metabolic Reprogramming

Metabolic reprogramming is a key hallmark of cancer, enabling cells to adapt their energy production, biosynthesis, and redox homeostasis to meet the demands of uncontrolled proliferation and survival under stress (Solomon et al., 2011). During epithelial–mesenchymal transition (EMT), cells undergo profound metabolic shifts that support the functional and phenotypic changes associated with mesenchymal identity (Gesson et al., 2016). These metabolic adaptations enable EMT-primed cells to survive in hostile microenvironments, resist apoptosis, and facilitate invasion and metastasis (Yin et al., 2017).

One of the most striking features of EMT-associated metabolic reprogramming is the shift from oxidative phosphorylation (OXPHOS) to aerobic glycolysis, also known as the Warburg effect (Zeitlin et al., 2009). EMT-inducing transcription factors, such as SNAIL and TWIST1,

directly upregulate glycolytic enzymes, including hexokinase 2 (HK2), phosphofructokinase-1 (PFK1), and pyruvate kinase M2 (PKM2), thereby increasing glucose uptake and lactate production (Wandke and Kutay, 2013; Xu et al., 2017). This glycolytic shift supports ATP generation and produces intermediates for nucleotide, amino acid, and lipid biosynthesis, fueling rapid growth and remodeling (Wei et al., 2011).

In parallel, EMT cells exhibit increased activity of the pentose phosphate pathway (PPP), which generates NADPH and ribose-5-phosphate (Leong et al., 2014). NADPH is crucial for maintaining redox balance and supporting fatty acid synthesis, while ribose-5-phosphate contributes to nucleotide biosynthesis (Leong et al., 2014). TWIST1 and ZEB1 have been shown to regulate PPP enzymes such as glucose-6-phosphate dehydrogenase (G6PD), reinforcing this metabolic shift (Lukášová et al., 2017).

Lipid metabolism also undergoes substantial reconfiguration during EMT (Bjerke et al., 2013). EMT-positive cells often rely on enhanced fatty acid oxidation (FAO) for ATP production, especially under conditions of glucose limitation (Yin et al., 2017). ZEB1 and SNAIL promote the expression of key FAO regulators such as CPT1A, the rate-limiting enzyme for mitochondrial fatty acid import (Gesson et al., 2016). FAO not only provides energy but also limits the accumulation of reactive oxygen species (ROS), thereby reducing oxidative stress and supporting cell survival (Ray-Gallet et al., 2011).

In addition, EMT reprograms glutamine metabolism to support redox homeostasis (Moly et al., 2016). Glutaminase (GLS), which converts glutamine to glutamate, is upregulated in EMT-driven tumors (Almeida et al., 2017). Glutamate feeds into the tricarboxylic acid (TCA) cycle as α-ketoglutarate, sustaining biosynthetic flux and balancing NAD+/NADH ratios (Wilson and Foisner, 2010). This process supports chromatin-modifying enzymes such as TETs and JmjC-domain histone demethylases, directly linking metabolic reprogramming to epigenetic regulation of EMT genes (Lupiáñez et al., 2015).

Significantly, the metabolic plasticity of EMT cells extends to hypoxic adaptation (Little and McMahon, 2012). Hypoxia-inducible factors (HIF-1α and HIF-2α), stabilized under low oxygen conditions, work in concert with EMT-TFs to reprogram gene expression and metabolism (Malashicheva et al., 2015). HIF-1α cooperates with SNAIL to repress epithelial genes and activate glycolytic and angiogenic pathways, thereby facilitating metastasis (Shimi et al., 2008).

Recent studies have also uncovered the role of mitochondrial dynamics and metabolism in EMT (Nelson et al., 2016). EMT induces mitochondrial fission, a process associated with enhanced migratory capacity and stress resistance (Lopez and Tait, 2015). Proteins such as

DRP1, which are activated during EMT, modulate mitochondrial shape and function, thereby optimizing energy output for invasion and migration (Almeida et al., 2017).

Therapeutically, targeting EMT-associated metabolic pathways has emerged as a promising approach (Shi et al., 2017). Inhibitors of glycolysis (e.g., 2-deoxyglucose), FAO (e.g., etomoxir), and glutaminolysis (e.g., CB-839) have demonstrated efficacy in preclinical models by sensitizing EMT-primed cells to conventional therapies (Ano Bom et al., 2012). Moreover, metabolic inhibitors can modulate the epigenetic landscape and suppress EMT-TFs, reversing mesenchymal traits (Mattioli et al., 2018).

Overall, EMT-induced metabolic reprogramming is a multifaceted and dynamic process that supports the survival, invasion, and therapy resistance of cancer cells (Marullo et al., 2016). Understanding the metabolic dependencies of EMT states can provide novel targets for intervention and aid in the development of combination therapies to combat metastatic disease (Antony et al., 2020).

### 1.3.7 Genomic Instability and Replicative Stress

EMT introduces genomic instability through several mechanisms (Ano Bom et al., 2012). First, partial EMT states are often associated with weakened cell cycle checkpoints, allowing cells to bypass DNA damage-induced arrest (Redwood et al., 2011). Second, changes in chromatin architecture during EMT impair the fidelity of DNA replication and repair (Turinetto et al., 2012). Third, cytoskeletal remodeling and nuclear deformation during invasion cause nuclear envelope rupture, chromatin fragmentation, and DNA double-strand breaks (Labade et al., 2016; Moly et al., 2016).

Moreover, EMT-TFs, such as ZEB1, suppress the expression of DNA damage response (DDR) genes, including ATM and ATR (Laberge et al., 2015). This compromises homologous recombination (HR) repair, leading to the accumulation of mutations (Lukášová et al., 2017). Such genomic instability fuels tumor heterogeneity and accelerates clonal evolution, contributing to therapy resistance and disease progression (Yin et al., 2017).

Taken together, these seven hallmarks highlight the multifaceted role of EMT in cancer progression (Nieto et al., 2016). EMT not only drives physical transformation of cells but also rewires their transcriptional, epigenetic, metabolic, and immunological programs (Dongre and Weinberg, 2019). Understanding these hallmarks in a context-specific manner is critical for developing interventions that can halt or reverse EMT-mediated malignancy (Scheller et al., 2020).

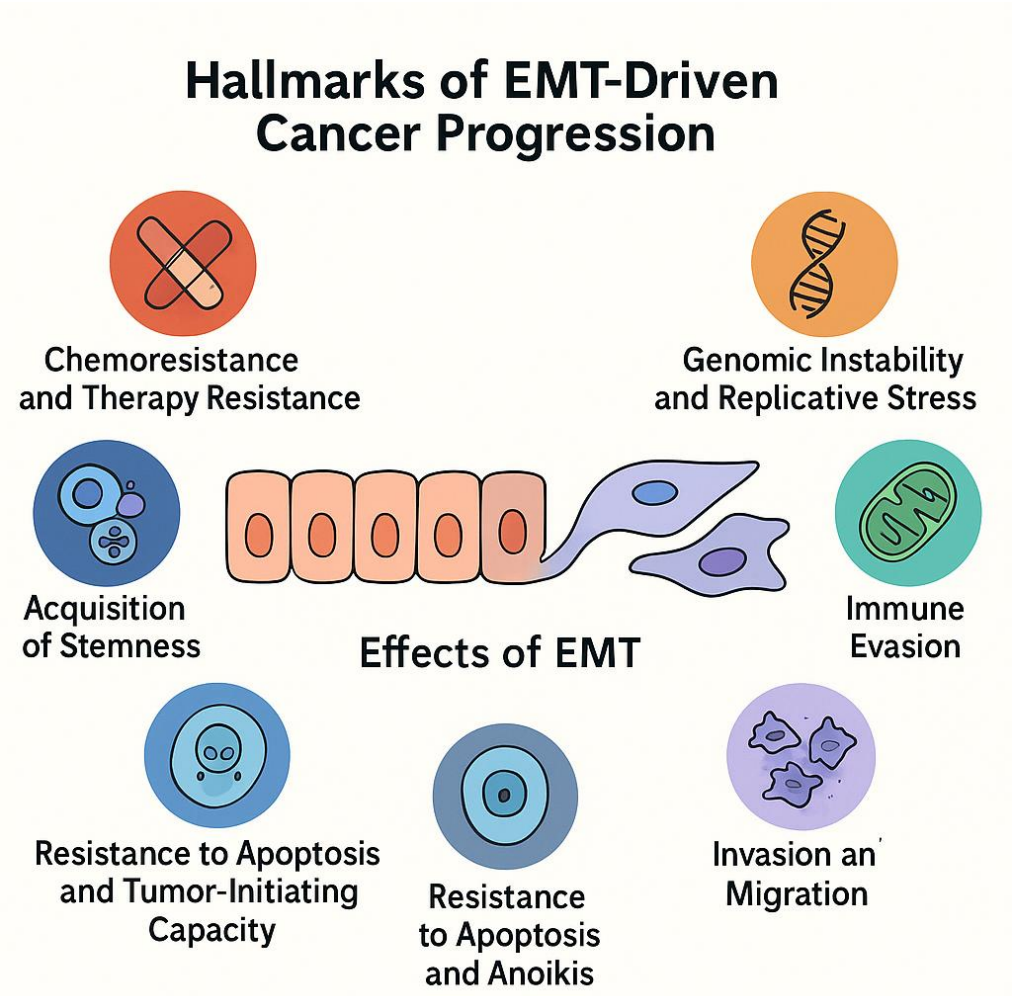


***Figure 1.2. Hallmarks of EMT-driven cancer progression.***

*Epithelial–mesenchymal transition (EMT) equips carcinoma cells with multiple traits that promote tumor progression, metastasis, and therapy failure. As epithelial cells transition toward mesenchymal states, they acquire stemness properties, enhanced invasive and migratory capacity, and increased resistance to apoptosis and anoikis. EMT also confers tumor-initiating potential, chemoresistance, and broader therapy resistance. Additionally, EMT contributes to immune evasion and promotes genomic instability and replicative stress, thereby driving the evolution of cancer. Collectively, these EMT-associated phenotypes enable tumor cells to survive hostile microenvironments, disseminate, and seed metastases.*

### 1.4 Molecular Regulation of Epithelial-Mesenchymal Transition (EMT)

The epithelial-mesenchymal transition (EMT) represents a fundamental biological process characterized by the phenotypic conversion of immotile, polarized epithelial cells into migratory, invasive mesenchymal cells (Bustin et al., 2009). This complex cellular reprogramming is orchestrated by a multifaceted network of regulatory mechanisms operating at transcriptional, post-transcriptional, epigenetic, and post-translational levels (Nieto et al., 2016). Far from being a rigid or unidirectional program, EMT is exquisitely context-dependent and dynamically shaped by an intricate interplay of intercellular signaling pathways, intrinsic chromatin accessibility landscapes, and extrinsic microenvironmental cues (Pastushenko et al., 2018). This inherent complexity in its regulation allows cells to traverse a continuum of states, enabling transitions not only between fully epithelial and fully mesenchymal phenotypes but also facilitating the emergence and persistence of hybrid epithelial/mesenchymal (E/M) states (Yamazaki et al., 2018). These hybrid states are increasingly recognized for their crucial role in endowing cells with enhanced plasticity and adaptability, and for contributing significantly to tumor heterogeneity and therapeutic resistance in cancer progression (Baugh et al., 2018). A comprehensive understanding of these intricate molecular regulatory mechanisms is therefore paramount, offering critical insights for the development of targeted therapeutic strategies against EMT-driven pathologies, particularly in the context of cancer metastasis and drug resistance (Crompton et al., 2014).

#### 1.4.1 EMT-Inducing Transcription Factors (EMT-TFs)

At the apex of the EMT regulatory hierarchy resides a core group of master transcription factors (TFs), collectively known as EMT-TFs (Scheller et al., 2020). This highly conserved family comprises prominent members, including SNAI1 (Snail), SNAI2 (Slug), ZEB1, ZEB2, TWIST1, and TWIST2, as well as other context-dependent factors (Leong et al., 2014). Their collective and coordinated action is pivotal in initiating and sustaining the EMT program primarily through the direct transcriptional repression of epithelial marker genes, most notably E-cadherin (encoded by CDH1), while concomitantly activating the expression of mesenchymal signature genes (e.g., Vimentin (VIM), Fibronectin (FN1), N-cadherin (CDH2)) and genes associated with cell motility and invasion (Rossi et al., 2007). The functional attributes of these EMT-TFs often display significant cooperativity, redundancy, and context-specificity, underscoring the robustness and adaptability of the EMT process (Solomon et al., 2011).

SNAI1 and SNAI2, both members of the Snail family, are characterized by a conserved C-terminal zinc finger domain that mediates direct binding to E-box consensus sequences (CANNTG) found within the promoter regions of epithelial genes such as CDH1 and various Claudins (CLDNs) (Moir et al., 2000). Their repressive function is not solely through direct DNA binding but is extensively mediated by the recruitment of diverse corepressor complexes. These include the SIN3A complex, histone deacetylases (HDACs), and components of the Polycomb Repressive Complex 2 (PRC2), all of which contribute to the establishment of repressive chromatin states at epithelial gene promoters, thereby silencing their transcription (Rajagopalan and Lengauer, 2004).

Similarly, ZEB1 and ZEB2 are zinc finger homeobox proteins that execute their transcriptional repression of epithelial genes and concomitant promotion of mesenchymal and stemness programs through interactions with co-factors such as C-terminal Binding Protein (CtBP) and Lysine Specific Demethylase 1 (LSD1) (Narita et al., 2003). The recruitment of CtBP by ZEB proteins facilitates the recruitment of HDACs, leading to histone deacetylation and chromatin condensation (Favreau et al., 2003). LSD1, a histone demethylase, removes repressive histone marks, such as H3K4me2, thereby contributing to gene silencing (Lee et al., 2010). This concerted action by ZEB proteins not only downregulates epithelial markers but also upregulates genes associated with cellular plasticity, stemness, and invasive capabilities (Friedl and Gilmour, 2009).

TWIST1, a foundational member of the basic helix-loop-helix (bHLH) protein family, functions as a transcriptional regulator primarily through dimerization with ubiquitously expressed E proteins (e.g., E12, E47) (Fukagawa et al., 2004). This heterodimerization allows TWIST1 to bind to specific DNA sequences (E-boxes) and initiate broad mesodermal and invasive gene expression programs. Key targets include matrix metalloproteinases (MMPs), which facilitate the degradation of the extracellular matrix, and components of the platelet-derived growth factor (PDGF) signaling pathway, which regulate cell proliferation, migration, and angiogenesis (Redwood et al., 2011). TWIST1's role extends beyond simple repression of epithelial genes; it actively promotes a pro-migratory and invasive phenotype by activating genes critical for mesenchymal structure and function (González-Romero et al., 2008).

The intricate regulation of these EMT-TFs themselves is a hallmark of EMT complexity. They are activated by a diverse array of upstream extracellular signals, including canonical pathways such as Transforming Growth Factor-beta (TGF-β), Wnt/β-catenin, Notch, and various receptor tyrosine kinases (RTKs) like EGFR and FGFR (Zeitlin et al., 2009). These upstream signals often converge to induce EMT-TF expression or enhance their activity and stability

(Lamouille et al., 2014). Furthermore, EMT-TFs frequently operate within intricate feedback loops, both positive and negative, which serve to sustain or stabilize the acquired mesenchymal phenotype (Xu et al., 2011). For instance, activated EMT-TFs can upregulate the expression of their own activators or repress their repressors, solidifying the mesenchymal state (Xu et al., 2011). Cross-regulation among different EMT-TFs is also common, exemplified by TWIST1's ability to activate ZEB1 expression, creating an amplification cascade (Ray-Gallet et al., 2011). Conversely, their activities are finely tuned by reciprocal repression from epithelial regulators such as Grainyhead-like 2 (GRHL2) and Ovo-like 2 (OVOL2), which directly or indirectly antagonize EMT-TF function, highlighting the dynamic balance between epithelial and mesenchymal states (McCord et al., 2013).

### 1.4.2 Epigenetic Regulation

Epigenetic mechanisms represent a critical layer of gene regulation in EMT progression, enabling stable, long-term transcriptional reprogramming without altering the underlying DNA sequence (Wang et al., 2007; Landt et al., 2012). These modifications dynamically regulate the accessibility of EMT-TFs to their target loci, thereby dictating the transcriptional landscape that underpins the epithelial-mesenchymal transition (Flavahan et al., 2016). The primary epigenetic modalities involved include histone modifications, DNA methylation, and ATP-dependent chromatin remodeling (Kwok et al., 2007; Moly et al., 2016).

The Polycomb Repressive Complex 2 (PRC2), with its catalytic subunit Enhancer of Zeste Homolog 2 (EZH2), plays a prominent role in establishing and maintaining gene silencing during EMT (Rajagopalan and Lengauer, 2004; Kind et al., 2013). EZH2 mediates the tri-methylation of histone H3 at lysine 27 (H3K27me3), a well-established repressive epigenetic mark (Kind et al., 2013). This mark, by creating a compacted chromatin structure, hinders the binding of RNA polymerase and general transcription factors, thus silencing gene expression (Guo et al., 2013). During EMT, EZH2 significantly contributes to the repression of epithelial genes and concurrently promotes mesenchymal reprogramming (Geigl et al., 2008; Solomon et al., 2011). Compelling studies have demonstrated that EMT-TFs such as SNAI1 and TWIST1 can directly recruit EZH2 to the promoter regions of epithelial genes, most notably CDH1, to actively silence E-cadherin expression (Yusufzai et al., 2004; Nakaya and Sheng, 2008). Conversely, experimental depletion or pharmacological inhibition of EZH2 has been shown to reverse EMT phenotypes, leading to the re-expression of epithelial markers and a

reduction in cellular invasiveness, underscoring its functional significance in EMT stability and progression (Ogiyama et al., 2018).

Beyond PRC2, other enzymes involved in histone modifications are crucial (Holaska and Wilson, 2007). Histone deacetylases (HDACs), particularly HDAC1 and HDAC2, contribute to chromatin compaction by removing acetyl groups from histone tails, which promotes tighter DNA-histone interactions and gene repression (Wang et al., 2007). For example, SNAI1 is known to recruit HDAC1 to the CDH1 promoter, contributing to E-cadherin silencing (Peinado et al., 2004). Similarly, histone demethylases, such as Lysine Specific Demethylase 1 (LSD1), also play a role (Yang et al., 2010). ZEB1, for instance, can interact with CtBP and LSD1 to repress the expression of miR-200 family members, which are crucial microRNAs for maintaining epithelial integrity (Tait and Green, 2010).

DNA methylation, specifically the methylation of cytosine residues within CpG dinucleotides, constitutes another robust epigenetic mechanism that stabilizes EMT transitions (Jones, 2012; Yang et al., 2014). This modification, particularly when occurring in promoter regions, leads to gene silencing (Lim and Thiery, 2012). DNA methyltransferases (DNMTs), including DNMT1 (responsible for maintenance methylation during replication) and de novo methyltransferases DNMT3A and DNMT3B, are key players (Jha and Strahl, 2014). During EMT, the promoter regions of epithelial genes, such as CDH1, undergo hypermethylation, leading to their sustained silencing (Kong et al., 2012). This DNA methylation often acts synergistically with repressive histone marks to establish a profoundly silenced epigenetic state, making the mesenchymal phenotype more stable and resistant to reversal (Vassilev et al., 2006).

Finally, ATP-dependent chromatin remodelers play a dynamic role in EMT by physically altering nucleosome positions and accessibility (Solomon et al., 2011; Shi et al., 2017). Complexes such as SWI/SNF and NuRD (Nucleosome Remodeling and Deacetylase) are recruited to specific genomic loci to either open or close chromatin, thereby allowing or restricting the access of transcriptional machinery or silencing complexes to their target sites (Almeida et al., 2017). For instance, BRG1 (Brahma-related gene 1), a core catalytic subunit of the SWI/SNF complex, has been implicated in regulating EMT mediated by TWIST1 and FOXC2 in various cancers, including breast and pancreatic malignancies (Solomon et al., 2011). By remodeling chromatin, these complexes can facilitate the binding of EMT-TFs to mesenchymal gene promoters while simultaneously contributing to the silencing of epithelial genes (Solomon et al., 2011; Lukášová et al., 2017).

### 1.4.3 Non-Coding RNAs (miRNAs and lncRNAs)

Non-coding RNAs (ncRNAs), particularly microRNAs (miRNAs) and long non-coding RNAs (lncRNAs), represent an additional, highly sophisticated layer of post-transcriptional and epigenetic regulation in EMT (Figure 1.3) (Xu et al., 2011; Taylor et al., 2018). These molecules exert their effects by fine-tuning gene expression without encoding proteins, offering dynamic and reversible control over cellular transitions (Ogiyama et al., 2018).

The miR-200 family (comprising miR-200a, miR-200b, miR-200c, miR-141, and miR-429) stands out as the most extensively characterized miRNA family involved in EMT regulation (Margueron et al., 2008). Their primary mechanism of action involves directly targeting the messenger RNAs (mRNAs) of EMT-TFs, specifically ZEB1 and ZEB2, leading to the degradation of their mRNA or inhibition of their translation (Redwood et al., 2011). By suppressing ZEB1/2, the miR-200 family effectively maintains epithelial identity, promotes E-cadherin expression, and inhibits the development of mesenchymal characteristics (Nakaya and Sheng, 2008). During the initiation of EMT, a hallmark event is the significant downregulation of miR-200 levels (Geigl et al., 2008). This downregulation can be triggered by various mechanisms, including direct transcriptional repression by ZEB1 itself (creating a negative feedback loop) (Bracken et al., 2008) or through epigenetic silencing of miR-200 promoter regions (Towbin et al., 2012). This reciprocal negative feedback loop between miR-200 and ZEB1/2 is critically important; their mutual inhibition can generate bistable or even tristable states, allowing cells to stably exist in a fully epithelial, fully mesenchymal, or a dynamic hybrid epithelial/mesenchymal phenotype, providing crucial phenotypic plasticity (Ogiyama et al., 2018; Bjerke et al., 2013; Redwood et al., 2011).

Beyond the miR-200 family, numerous other miRNAs actively participate in the EMT network (Pencheva & Tavazoie, 2013):

- **miR-34 family:** This family (miR-34a, miR-34b, miR-34c), often transcriptionally activated by the tumor suppressor p53, acts as a crucial EMT suppressor by directly targeting the mRNAs of key EMT-TFs like SNAI1 and the Notch signaling effector NOTCH1 (Solomon et al., 2011). Their downregulation is frequently observed in aggressive cancers, contributing to enhanced EMT and metastasis (Lee et al., 2010).
- **miR-203:** This miRNA is known to inhibit both stemness characteristics and the expression of various EMT-TFs, reinforcing an epithelial phenotype and suppressing migratory capabilities (Wong et al., 2009).

- **EMT-promoting miRNAs:** Conversely, miRNAs like miR-9 and miR-10b actively promote EMT and cellular invasion (Tait and Green, 2010). miR-9, for instance, targets E-cadherin (Lim and Thiery, 2012), while miR-10b can promote metastasis by indirectly affecting pro-invasive genes or directly regulating factors involved in cell migration and invasion (Kwok et al., 2007).

Long non-coding RNAs (lncRNAs), defined as RNA molecules greater than 200 nucleotides in length that do not encode proteins, contribute to EMT regulation through highly diverse and often intricate mechanisms (Landt et al., 2012; Maishman et al., 2016). Their functions can include:

- **miRNA sponging:** Certain lncRNAs contain multiple binding sites for specific miRNAs, effectively acting as "sponges" to sequester and inactivate these miRNAs (Crompton et al., 2014). For example, some lncRNAs can sponge the miR-200 family, thereby derepressing ZEB1 and ZEB2 and promoting EMT (Leong et al., 2014).
- **Chromatin modification:** Many lncRNAs interact directly with chromatin-modifying complexes (e.g., PRC2, HDACs, DNMTs) to recruit them to specific genomic loci, thereby influencing the epigenetic state and transcriptional activity of target genes (Wei et al., 2011). For instance, MALAT1 (Metastasis Associated Lung Adenocarcinoma Transcript 1) has been shown to interact with EZH2 and PRC2, leading to the repression of E-cadherin and other epithelial genes (Aird and Zhang, 2013). Similarly, HOTAIR (HOX Antisense Intergenic RNA) actively promotes EMT by recruiting chromatin remodeling complexes to silence epithelial gene loci (Dechat et al., 2010).
- **Scaffolding regulatory complexes:** LncRNAs can act as molecular scaffolds, bringing together multiple proteins to form functional regulatory complexes that influence gene expression or protein stability (McCord et al., 2013).
- **mRNA stabilization:** Some lncRNAs can directly bind to and stabilize the mRNA of key EMT-related proteins, preventing their degradation (Larson et al., 2019). An example is ZEB2-AS1 (ZEB2 Antisense RNA 1), which stabilizes ZEB2 mRNA, thereby sustaining ZEB2 expression and promoting the mesenchymal state (Nakaya and Sheng, 2008).

The dynamic and often reversible regulation afforded by non-coding RNAs, particularly in feedback loops with EMT-TFs, allows for rapid and finely controlled shifts in gene expression during EMT and its reversal (MET, mesenchymal-epithelial transition) (Kröger et al., 2019).

This crucial role makes ncRNAs increasingly recognized as promising diagnostic biomarkers and novel therapeutic targets for a range of diseases, particularly in overcoming cancer metastasis and drug resistance (Reis-Sobreiro et al., 2018; Aiello and Kang, 2019).

### 1.4.4 Post-Translational Modifications

Post-translational modifications (PTMs) represent a rapid and highly dynamic layer of molecular regulation that profoundly influences the activity, stability, subcellular localization, and protein-protein interaction networks of EMT-related proteins, including EMT-TFs and their coregulators (Rajagopalan and Lengauer, 2004; Dechat et al., 2007). These modifications act as molecular switches, allowing for swift cellular responses to extracellular stimuli without requiring de novo protein synthesis (Narita et al., 2003).

Phosphorylation, the addition of a phosphate group, is one of the most prevalent and critical PTMs (Cronshaw et al., 2002). For instance, the stability and activity of SNAI1 are exquisitely regulated by phosphorylation (Vega et al., 2004). Glycogen Synthase Kinase 3 beta (GSK3β) phosphorylates SNAI1 at specific serine residues, typically targeting it for proteasomal degradation via the ubiquitin-proteasome system (Zheng et al., 2004; Chin et al., 2006). Conversely, specific kinases (e.g., AKT, MAPK) can phosphorylate SNAI1 at different sites, stabilizing it and promoting its nuclear localization and activity (Wang et al., 2007; Panier and Boulton, 2014). This dynamic phosphorylation state determines the half-life and functional output of SNAI1, thus profoundly impacting the initiation and maintenance of EMT (Favreau et al., 2003). Phosphorylation of co-factors and other EMT-related proteins, such as nuclear lamins (e.g., Lamin A/C), has also been implicated in altering chromatin accessibility and global gene expression patterns that contribute to EMT progression (Shimi et al., 2008). For example, phosphorylation of Lamin A/C can affect nuclear stiffness and chromatin organization, influencing the binding of transcription factors (Kind et al., 2013). Additionally, CDK1-mediated phosphorylation, particularly during the G2/M phase of the cell cycle, has been shown to modify chromatin-bound regulators and epigenetic enzymes (Kuga et al., 2014). This can influence EMT epigenetics by disrupting existing protein-protein interactions or creating new binding sites, thereby fine-tuning gene expression during critical cellular transitions (Wood et al., 2014).

Ubiquitination, the covalent attachment of ubiquitin molecules to a target protein, typically flags proteins for degradation by the 26S proteasome (ubiquitin-proteasome system) (Datta et al., 1999). As mentioned, the ubiquitin ligase β-TrCP targets phosphorylated SNAI1 for

proteasomal degradation (Zheng et al., 2004). However, ubiquitination can also have non-proteolytic roles, such as regulating protein localization, activity, or interactions (Wang et al., 2007). The balance between ubiquitination and deubiquitination, catalyzed by deubiquitinases (DUBs), is crucial for maintaining steady-state levels of EMT-TFs (Wang et al., 2009). For example, specific DUBs can stabilize ZEB1, thereby promoting its transcriptional activity and sustaining EMT (Leiserson et al., 2015).

Acetylation, the addition of an acetyl group, primarily to lysine residues, is another vital PTM, particularly for histone proteins and transcription factors (Hartman et al., 2005). Histone acetylation typically leads to chromatin relaxation and transcriptional activation (Kwok et al., 2007). However, non-histone protein acetylation is also crucial (Friedl and Gilmour, 2009). For example, TWIST1 stability and transcriptional activity are significantly influenced by acetylation, predominantly mediated by histone acetyltransferases (HATs) such as p300/CBP. Acetylation of TWIST1 can enhance its dimerization, DNA binding, and resistance to degradation, thereby amplifying its pro-EMT effects (Kasper et al., 1999). Conversely, deacetylation by specific HDACs can reduce TWIST1 activity or promote its degradation (Harada et al., 2014).

Other PTMs, such as SUMOylation (Small Ubiquitin-like Modifier conjugation), also play significant roles (Mitra et al., 2005). For instance, sumoylation has been shown to stabilize ZEB1 and enhance its transcriptional activity, further contributing to its role in promoting mesenchymal gene programs (Gonzalo, 2014). These diverse PTMs rarely act in isolation; instead, they often occur in concert, forming a complex 'PTM code' that precisely regulates the spatiotemporal activity of EMT proteins, dictating the precise kinetics and outcomes of the epithelial-mesenchymal transition (Iwabuchi et al., 2006). The intricate interplay of these modifications underscores the adaptability and robustness of the EMT program, providing multiple checkpoints for its regulation and offering diverse avenues for therapeutic intervention (Dechat et al., 2010).

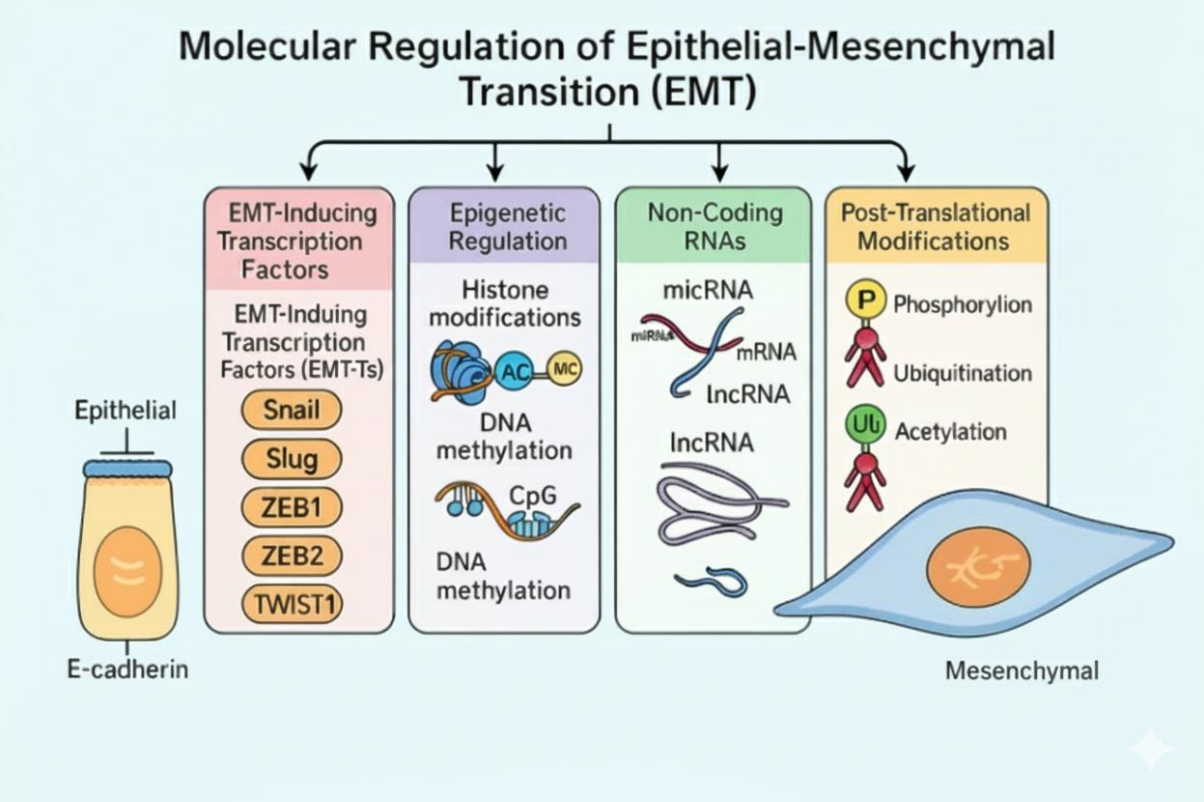


***Figure 1.3: Molecular Mechanisms Regulating EMT***

*This diagram illustrates the Epithelial-Mesenchymal Transition (EMT), a process whereby epithelial cells (left, characterized by E-cadherin) transform into motile mesenchymal cells (right). Four primary regulatory pathways drive the transition. Firstly, EMT-inducing transcription factors (EMT-TFs), such as Snail, Slug, ZEB1/2, and TWIST1, act to repress epithelial gene expression. Secondly, Epigenetic Regulation, including Histone modifications (acetylation/methylation) and DNA methylation, modulates gene accessibility. Thirdly, various non-coding RNAs, like miRNA and lncRNA, fine-tune gene expression post-transcriptionally. Finally, Post-Translational Modifications of proteins, such as Phosphorylation, Ubiquitination, and Acetylation, influence protein function and stability.*

### 1.5 Nuclear Envelope and Chromatin Reorganization in EMT

Beyond the well-established transcriptional and epigenetic levels of control, the epithelial-mesenchymal transition (EMT) is increasingly recognized as a process profoundly regulated by the intrinsic architecture and mechanics of the cell nucleus (Shimi et al., 2008; Bjerke et al., 2013). Changes in nuclear shape, deformability (often referred to as stiffness or pliability), and the spatial organization of chromatin within the nucleus, predominantly driven by the structural elements of the nuclear envelope, exert a profound influence on the precise orchestration of gene regulatory networks underlying EMT (Wood et al., 2014). This section elucidates how alterations in the nuclear envelope, particularly through the dynamics of Lamin A/C and the mechanosensitive LINC complex, coupled with global chromatin reorganization, contribute to the acquisition and stabilization of the mesenchymal phenotype (Towbin et al., 2012; McLaughlin-Drubin et al., 2013).

#### 1.5.1 Lamin A/C as a Structural and Regulatory Node

Lamin A/C, encoded by the LMNA gene, represents a type V intermediate filament protein and is a principal constituent of the nuclear lamina (Nakaya and Sheng, 2008). The nuclear lamina is a dense fibrillar meshwork situated immediately beneath the inner nuclear membrane, providing essential mechanical support to the nucleus, maintaining its characteristic morphology, and serving as a crucial anchoring platform for heterochromatin at the nuclear periphery (Mitra et al., 2005). Beyond its established structural roles, accumulating evidence highlights Lamin A/C as a critical regulatory node, mediating the interplay between nuclear mechanics, chromatin organization, and gene expression (Ibarra et al., 2016). This dual functionality stems from its direct interactions with various chromatin regulatory proteins, including components of the Polycomb Repressive Complex 2 (PRC2), histone deacetylases (HDACs), histone methyltransferases, and other epigenetic modulators (Ha et al., 2014). These interactions suggest that Lamin A/C is not merely a passive scaffold but an active participant in determining chromatin states and gene accessibility (Demmerle et al., 2012).

A recurrent observation during EMT, particularly in various cancer contexts, is the downregulation or significant reorganization of Lamin A/C expression (Rossi et al., 2007). This alteration in Lamin A/C levels or its architectural integrity precipitates a cascade of events at the nuclear level, fundamentally impacting cellular behavior (Ha et al., 2014).

Increased Nuclear Deformability: A reduction in Lamin A/C expression directly compromises the mechanical integrity of the nuclear lamina, leading to a noticeable increase in nuclear pliability and deformability (Taddei et al., 2006). This diminished nuclear stiffness is hypothesized to facilitate the passage of cells through constricted interstitial spaces within

tissues, a critical requirement for mesenchymal cell migration and invasion during processes like embryogenesis, wound healing, and cancer metastasis (Gesson et al., 2016). The physical compliance of the nucleus becomes a rate-limiting factor in cellular transmigration, and the loss of Lamin A/C directly addresses this mechanical bottleneck (McCord et al., 2013).

Reduced Tethering of Heterochromatin to the Lamina: The nuclear lamina, mainly through interactions with Lamin A/C and other lamina-associated proteins, serves as a binding platform for lamina-associated domains (LADs), which are typically heterochromatic regions of the genome (Shimi et al., 2008). Downregulation or disruption of Lamin A/C results in the release or reduced tethering of these LADs from the nuclear periphery into the nuclear interior (Lin et al., 2013). This spatial redistribution of chromatin can alter gene expression profiles by changing the local environment of genes from a repressive peripheral zone to a more permissive internal compartment, or vice versa for genes moving towards the periphery (Zhou and Panté, 2010).

Redistribution of Transcriptionally Repressive Histone Marks: The spatial relationship between chromatin and the nuclear lamina is intimately linked to the distribution of epigenetic marks (Puisieux et al., 2014). The loss of Lamin A/C can lead to a global redistribution of transcriptionally repressive histone marks, such as H3K27me3 (associated with PRC2 activity) and H3K9me3 (associated with constitutive heterochromatin) (Dechat et al., 2008). This redistribution can result in the displacement of these marks from specific gene loci or their re-patterning within the nucleus, influencing the accessibility of these regions to transcription factors and RNA polymerase machinery (Mahen et al., 2013).

Collectively, studies have consistently shown that the loss or depletion of Lamin A/C facilitates the access of EMT-TFs to previously inaccessible or silenced chromatin regions by increasing nuclear pliability and fundamentally altering the local chromatin environment, making it more amenable to transcriptional reprogramming (Yusufzai et al., 2004). In the context of breast cancer cells, a strong correlation has been observed between Lamin A/C depletion and an increase in cellular invasion, alongside enhanced expression of mesenchymal markers (Kuga et al., 2014). The provided research further substantiates this by demonstrating a direct interaction between Lamin A/C and EZH2, the catalytic subunit of PRC2 (Margueron et al., 2008). Crucially, this interaction is shown to be disrupted during EMT, which in turn alters the precise deposition of H3K27me3 at the promoters of key transcription factors involved in maintaining epithelial identity or promoting mesenchymal transition (Dittmer et al., 2014). This suggests a direct molecular mechanism by which nuclear architectural changes,

specifically through Lamin A/C, directly impact epigenetic landscapes and gene expression during EMT (Marullo et al., 2016).

### 1.5.2 LINC Complex and Mechanotransduction

The Linker of Nucleoskeleton and Cytoskeleton (LINC) complex serves as a crucial molecular bridge that physically connects the nuclear lamina to the extensive cellular cytoskeleton (actin, intermediate filaments, and microtubules) (Taddei et al., 2006; Liu et al., 2013). This intricate complex is assembled from SUN (Sad1 and UNC-84) domain proteins located in the inner nuclear membrane, which interact with Lamin A/C, and KASH (Klarsicht, ANC-1, Syne Homology) domain proteins (e.g., Nesprins) that span the outer nuclear membrane and link to cytoskeletal elements (Tait and Green, 2010). The paramount function of the LINC complex is to transduce mechanical forces generated from the extracellular matrix (ECM) and within the cytoplasm directly to the nucleus, thereby regulating nuclear stiffness, morphology, and profoundly influencing chromatin organization and gene expression (Xu et al., 2011; Puisieux et al., 2014).

Mechanical cues from the cellular microenvironment are increasingly recognized as potent regulators of cell fate and function, including EMT (Xu et al., 2011; Aird and Zhang, 2013). Factors such as increased matrix stiffness, altered tissue tension, and fluidic shear stress, all of which are known to promote EMT, are efficiently transmitted across the nuclear envelope via the LINC complex (Cucco et al., 2018). This mechanical input can induce significant nuclear deformations, including nuclear flattening and changes in nuclear volume, and drive widespread heterochromatin remodeling, as well as nuclear rotation (Kong et al., 2012; Fudenberg et al., 2016). The mechanosensitive nature of the LINC complex allows cells to "feel" their physical environment and translate these physical signals into biochemical cues that regulate gene expression (Kojic et al., 2018). This regulation occurs through several proposed mechanisms, including modulating the accessibility of nuclear pores (thereby affecting nucleocytoplasmic transport) and altering the overall mobility and spatial positioning of chromatin within the nucleus. For instance, increased mechanical tension can lead to the unfolding of chromatin, making previously inaccessible genes available for transcription (Wang et al., 2017).

In the context of cancer progression, alterations in the expression or integrity of LINC complex components (e.g., SUN1, Nesprin-2) have been directly linked to altered nuclear mechanics and a subsequent facilitation of EMT-driven invasion (Peric-Hupkes et al., 2010; Labade et al.,

2016). These disruptions can enhance nuclear deformability, enabling tumor cells to navigate through dense stromal environments more effectively (Fudenberg et al., 2016). Furthermore, a key signaling pathway that interfaces intimately with LINC-mediated mechanotransduction is the tension-driven activation of YAP (Yes-associated protein) and TAZ (transcriptional coactivator with PDZ-binding motif) (Hanahan and Weinberg, 2011; Mohammad and Helin, 2017). YAP/TAZ are well-established mechanosensors that translocate to the nucleus and activate gene expression programs in response to increased matrix stiffness and cell spreading (Solomon et al., 2011). The LINC complex plays a critical role in transmitting these mechanical cues to the nucleus, influencing the nuclear localization and activity of YAP/TAZ (Elosegui-Artola et al., 2017). Activated YAP/TAZ then directly or indirectly interacts with EMT-TFs or their co-regulators, leading to the enhanced expression of EMT-associated genes, thus creating a powerful feed-forward loop that integrates mechanical signals with the genetic reprogramming of EMT (Malashicheva et al., 2015; Maishman et al., 2016).

### 1.5.3 Chromatin Reorganization During EMT Nuclear Envelope and Chromatin Architecture: The Spatial Control Layer

Beyond localized changes in histone modifications and DNA methylation discussed previously, EMT involves a global and highly coordinated reorganization of chromatin structure and nuclear positioning (X. Kang et al., 2019; Scheller et al., 2020). This architectural remodeling is not merely a consequence of EMT but an active participant in establishing and stabilizing the mesenchymal gene expression program (Sati et al., 2020). Key aspects of this large-scale chromatin reorganization include:

Relocation of LADs (Lamina-Associated Domains): As alluded to earlier, during EMT, there is a distinct tendency for traditionally lamina-associated domains (LADs), which are typically transcriptionally silent and tethered to the nuclear periphery, to detach and relocate from the nuclear periphery towards the nuclear interior (Figure 1.4) (Holwerda and de Laat, 2013; Crompton et al., 2014). This relocation can lead to the derepression of genes within these domains that were previously silenced by their peripheral location, providing access for transcription factors (Nakaya and Sheng, 2008). Conversely, some active gene regions might move towards the periphery or become sequestered, leading to their repression (Peric-Hupkes et al., 2010).

Loss of H3K27me3-Rich Repressive Zones and Increased Euchromatin Formation: EMT is characterized by a dynamic shift in the landscape of repressive histone marks (Zhao et al.,

2017). While H3K27me3 is crucial for silencing epithelial genes, its overall distribution can be reconfigured (Karoutas et al., 2019). Studies indicate a general trend towards the decondensation of specific chromatin regions and a reduction in the density of H3K27me3-rich repressive zones at specific loci, particularly at mesenchymal gene promoters (Nava et al., 2020). This shift is accompanied by an increased formation of euchromatin (transcriptionally active, open chromatin) at mesenchymal gene loci (Sciacovelli and Frezza, 2017). This architectural opening makes these genes readily accessible to EMT-TFs and the transcriptional machinery, facilitating their activation (X. Kang et al., 2019).

The overarching consequence of such profound chromatin reorganization is to create a nuclear environment that enables mesenchymal transcription factors to readily access previously silenced or inaccessible chromatin regions, thereby driving the expression of genes associated with the mesenchymal phenotype (Wilson et al., 2020). Furthermore, the altered positioning of genes within the intricate 3D nuclear space has significant ramifications for various aspects of gene regulation (Leiserson et al., 2015).

**Transcriptional Bursts:** Changes in chromatin compaction and gene positioning can influence the frequency and amplitude of transcriptional bursts, affecting the kinetics of gene expression (Kim et al., 2019).

**Enhancer-Promoter Looping:** The spatial proximity between enhancers and their cognate promoters, crucial for robust gene activation, can be dramatically altered during EMT (Hanssen et al., 2017). Chromatin reorganization can bring mesenchymal gene enhancers and promoters into closer contact while disrupting epithelial gene looping, contributing to the switch in gene expression (Karoutas et al., 2019).

**Phase-Separated Transcriptional Condensates:** Emerging evidence suggests that transcription occurs within dynamic, membrane-less organelles formed through liquid-liquid phase separation (Boija et al., 2018). Alterations in chromatin organization and nuclear mechanics can influence the formation, stability, and composition of these transcriptional condensates, thereby impacting the efficiency and specificity of gene expression (Taylor et al., 2018).

Advanced genomic technologies, such as single-cell ATAC-seq (Assay for Transposase-Accessible Chromatin using sequencing) and Hi-C (High-throughput Chromosome Conformation Capture), have provided unprecedented insights into these architectural changes (Dittmer et al., 2014; Jolly et al., 2015). Single-cell ATAC-seq data have unequivocally demonstrated that EMT transitions are accompanied by a marked increase in chromatin accessibility at the promoter regions of mesenchymal genes, while simultaneously revealing

reduced accessibility at the enhancers of epithelial genes (X. Kang et al., 2019). Hi-C data, which maps genome-wide chromatin interactions, further corroborates these findings by showing large-scale reorganization of topologically associating domains (TADs) and chromatin loops during EMT (Jolly et al., 2019). Importantly, these specific changes in chromatin accessibility and 3D organization are not isolated events but are actively reinforced by simultaneous disruptions in nuclear architecture, including the observed loss of Lamin A/C expression and a broader reorganization of the nuclear lamina (Crompton et al., 2014). This intricate interplay between nuclear structural components, chromatin architecture, and gene regulatory factors underscores a sophisticated, multi-layered control mechanism that governs the dynamic and reversible nature of EMT (Nava et al., 2020).

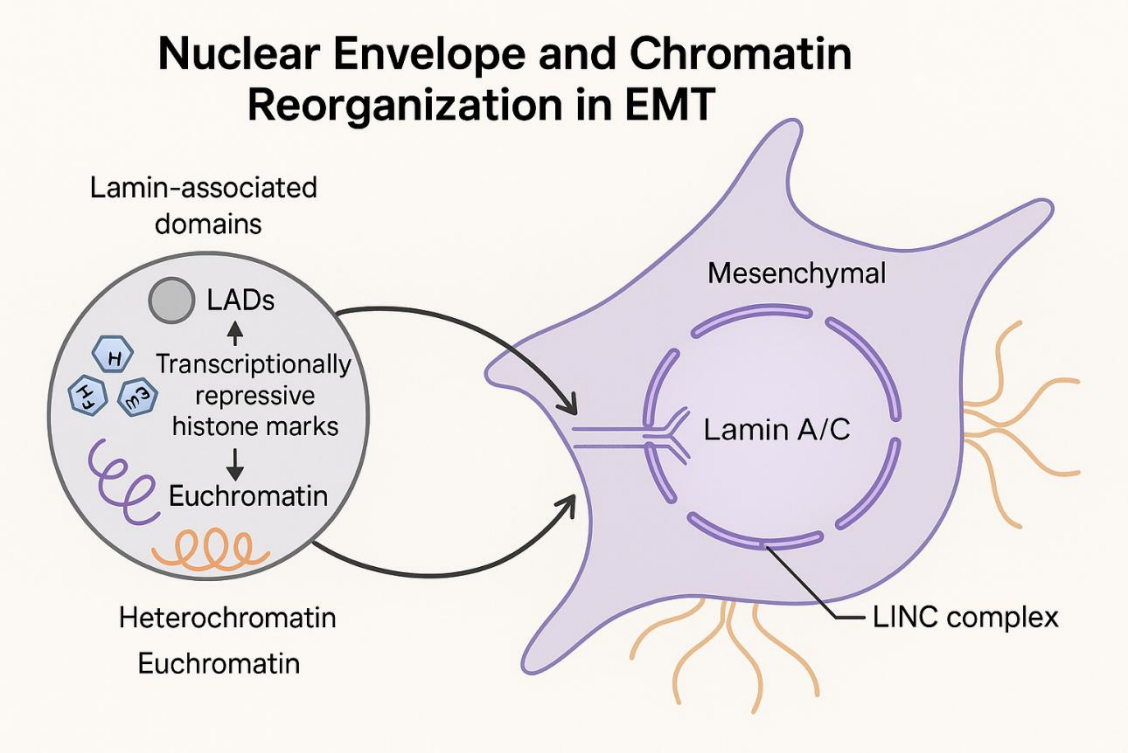


***Figure 1.4: Nuclear and Chromatin Reorganization in EMT***

*Illustration showing how the cell's nucleus and DNA structure change during EMT. The transition to the Mesenchymal state involves the reorganization of Heterochromatin and Euchromatin, the formation of Lamin-associated domains (LADs) tethered to the nuclear envelope (comprising lamin A/C), and connections mediated by the LINC complex.*

## 1.6 Conclusion and Discussion

Epithelial–mesenchymal transition (EMT) is no longer viewed as a linear or binary switch but as a highly plastic and context-sensitive cellular process governed by intricate layers of regulatory mechanisms (Flavahan et al., 2016; Antony et al., 2020). The current chapter provides a comprehensive overview of these mechanisms, ranging from master transcriptional regulators to the contributions of nuclear architecture and chromatin topology (Gonzalo, 2014). Here, we synthesize these findings and reflect on their implications for cancer biology, particularly in the context of metastasis, therapy resistance, and epigenetic reprogramming (Larson et al., 2019).

### 1.6.1 Integration of Multilayered EMT Regulation

At the core of EMT regulation lies a conserved set of transcription factors (EMT-TFs), including SNAI1, SNAI2, ZEB1/2, and TWIST1/2, which repress epithelial identity and activate mesenchymal gene expression (Zhang et al., 2014). However, their function is neither isolated nor self-sufficient. Instead, it is deeply embedded within a web of epigenetic cues, chromatin accessibility states, and post-transcriptional feedback loops (McLaughlin-Drubin et al., 2013; Mattioli et al., 2018).

The interplay between EMT-TFs and chromatin remodelers such as PRC2, HDACs, and SWI/SNF complexes enables context-dependent reprogramming of gene expression (Tzur et al., 2006; Lukášová et al., 2017). This regulatory relationship is reinforced by non-coding RNAs, particularly the miR-200 family and long non-coding RNAs (lncRNAs) such as MALAT1 and HOTAIR, which form feedback loops to buffer EMT fluctuations (Nakaya and Sheng, 2008; McCord et al., 2013). These findings illustrate that EMT is not solely a transcriptional phenomenon—it is fundamentally an epigenetically stabilized, dynamically reversible phenotype that integrates diverse regulatory modalities (Figure 1.5) (Ebrahimi et al., 2018).

Moreover, the role of post-translational modifications—especially phosphorylation, acetylation, ubiquitination, and sumoylation—adds temporal resolution to this process (Fukagawa et al., 2004; Gonzalo, 2014). These modifications finely tune the activity, stability, and localization of EMT-related proteins, including Lamin A/C and EMT-TFs, thus acting as "molecular switches" to rapidly adapt to extracellular signals like TGF-β, hypoxia, or matrix stiffness (Harada et al., 2014; Shi et al., 2017).

### 1.6.2 Nuclear Envelope and Chromatin Architecture: The Spatial Control Layer

A distinctive feature of this chapter is the integration of nuclear architecture and chromatin spatial organization into the paradigm of EMT regulation (Shimi et al., 2008; Aird and Zhang, 2013). Lamin A/C, traditionally viewed as a mechanical scaffold, has emerged as a critical modulator of gene expression through its tethering of heterochromatin at the nuclear periphery (Nakaya and Sheng, 2008; Diepenbruck and Christofori, 2016). Its depletion during EMT facilitates increased nuclear deformability and relaxation of chromatin, promoting the expression of mesenchymal genes (Coschi et al., 2014).

The LINC complex, acting as a conduit between cytoskeletal tension and nuclear organization, further bridges mechanical cues with gene regulation (Tzur et al., 2006; Nacev et al., 2020). Mechanotransduction via SUN–Nesprin complexes alters chromatin conformation and nuclear shape, influencing the accessibility of transcription factors and the nuclear localization of mechano-responsive proteins, such as YAP/TAZ (Redwood et al., 2011; Mattioli et al., 2018). These findings underscore that EMT cannot be fully understood without considering biophysical regulation—cell mechanics are not merely passive consequences but active regulators of transcriptional reprogramming (Brabletz et al., 2018).

Additionally, large-scale chromatin reorganization, including the relocation of LADs and topologically associating domains (TADs), dramatically reshapes the transcriptional landscape (Cho et al., 2019; Ikegami et al., 2020). This reorganization is not random but orchestrated—epithelial gene silencing coincides with their peripheral migration and PRC2 recruitment, while mesenchymal gene loci become more euchromatic and accessible (Kim et al., 2017; Jolly et al., 2019). These spatial transitions offer mechanistic explanations for the long-term stabilization of mesenchymal identity or hybrid states, even in the absence of sustained EMT stimuli (Wilson et al., 2020).

### 1.6.3 Functional Implications and Therapeutic Opportunities

Understanding the depth of EMT regulation has far-reaching implications (Strohecker and White, 2014). Hybrid epithelial/mesenchymal (E/M) states are characterized by high plasticity, collective invasion, resistance to apoptosis, and the initiation of metastasis (Mattioli et al., 2018). These cells also evade immune surveillance and persist after treatment, contributing to recurrence (Lambert et al., 2017). From a clinical standpoint, targeting EMT plasticity—rather than blocking EMT entirely—may be a more viable therapeutic strategy (Dongre and Weinberg, 2019).

Moreover, because EMT also affects antigen presentation and immune checkpoint expression (e.g., PD-L1), combining EMT-targeting agents with immunotherapy holds promise (Dittmer et al., 2014). As EMT states may be reversible, therapeutic strategies that enforce MET (mesenchymal-to-epithelial transition) could sensitize tumors to both chemotherapy and immune recognition (Chan et al., 2013).

### 1.7 Future Directions

Several open questions remain (Kadota et al., 2020). How do cells select for or stabilize hybrid E/M states? Are there distinct chromatin topologies or nuclear architectures unique to these states? How do Lamin A/C and the LINC complex influence enhancer–promoter looping or transcriptional condensates? (Cucco et al., 2018).

Future studies employing integrative approaches—such as single-cell RNA-seq, ATAC-seq, spatial transcriptomics, and super-resolution imaging—will be instrumental in answering these questions (Puisieux et al., 2014; Malashicheva et al., 2015). Importantly, identifying phenotypic stability factors (PSFs) and dissecting their crosstalk with mechanical and epigenetic regulators will help map the EMT–MET landscape with greater resolution (Boija et al., 2018).

This chapter highlights that EMT is a multi-dimensional, spatially and temporally orchestrated process, where transcriptional and epigenetic regulators interact with the nuclear envelope, chromatin topology, and post-transcriptional feedback loops (Santi et al., 2020). Lamin A/C emerges not only as a nuclear scaffold but also as a gatekeeper of chromatin accessibility, working in concert with EZH2 and other epigenetic regulators to modulate EMT transitions (González-Romero et al., 2008; Diepenbrück and Christofori, 2016).

By positioning the nucleus as both a sensor and effector of EMT, this integrated view bridges structural biology, gene regulation, and cell signaling into a cohesive model of cellular plasticity (Kojic et al., 2018). The therapeutic implications are substantial, offering new routes to disrupt metastatic progression by targeting not only signaling cascades but also nuclear and chromatin organization (Dongre and Weinberg, 2019).

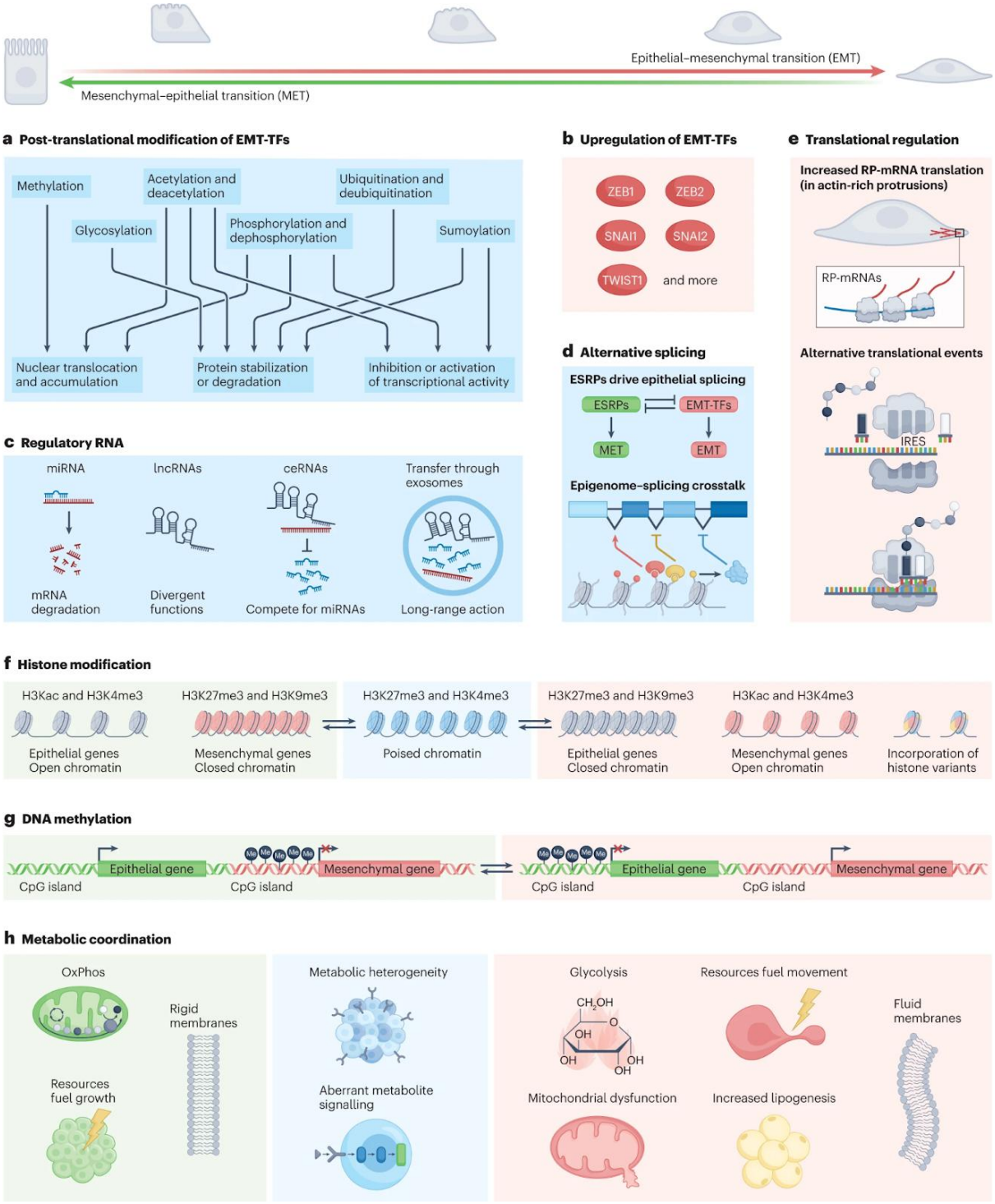


***Figure 1.5: Regulatory Mechanisms Governing Epithelial-Mesenchymal Transition (EMT) and Mesenchymal-Epithelial Transition (MET)***

*This comprehensive diagram illustrates the multi-level molecular control governing the reversible transition between epithelial and mesenchymal cell states (EMT and MET, as shown at the top). The figure details various regulatory layers: (a) post-translational modifications (PTMs), such as*

*Methylation, Acetylation, Phosphorylation, Ubiquitination, Glycosylation, and Sumoylation, which control the stability, activity, and localization of EMT-Transcription Factors (EMT-TFs). (b) Upregulation of EMT-TFs, highlighting core factors like ZEB1, ZEB2, SNAI1, SNAI2, and TWIST1. (c) Regulatory RNA, showing the roles of miRNAs (leading to mRNA degradation), lncRNAs (with divergent functions), circRNAs (competing for miRNAs), and the transfer of these RNAs through exosomes for long-range action. (d) Alternative splicing, driven by Epithelial Splicing Regulatory Proteins (ESRPs), and the crucial Epigenome-splicing crosstalk. (e) Translational regulation, demonstrating increased 5'UTR-based mRNA translation and alternative translational events involving internal ribosome entry sites (IRES). (f) Histone modification, depicting the reversible changes in histone marks (e.g., H3K4me3, H3K27me3) that switch genes between open, closed, or poised chromatin states. (g) DNA methylation, which involves the methylation/demethylation of CpG islands, serves as a means to switch gene expression between the epithelial and mesenchymal programs. Finally, (h) Metabolic coordination illustrates the shift towards metabolic heterogeneity, including increased Glycolysis and Lipogenesis, which supports the mesenchymal phenotype over the OxPhos-driven epithelial state (illustration taken from* (Lamouille et al., 2014).

# Chapter 2: Materials and Methods

## 2.1 Common to all Chapters

### Cell Culture

The human breast cancer cell line MCF7 (HTB-22) was obtained from ATCC and cultured in DMEM (gifted by Dr. Dimple Notani, NCBS Bengaluru, India), supplemented with 10% Fetal Bovine Serum, 10% (v/v) L-Glutamine, penicillin (100 U/mL), and streptomycin (100 µg/mL). The MCF10A (CRL-10317) cell line was procured initially from ATCC (provided by Dr. Madhura Kulkarni, IISER Pune) and maintained in Dulbecco's modified Eagle's medium/F12 (1:1) (Invitrogen #11330-032) supplemented with 5% horse serum (Horse serum has lower levels of undefined growth-promoting factors than FBS) (Invitrogen #16050-122), 10% (v/v) L-Glutamine, human Epidermal Growth Factor (Peprotech #AF-100-15; 20 ng/mL), hydrocortisone (Sigma # H-0888; 0.5 mg/mL), cholera toxin (Sigma #C-8052; 0.1 mg/mL), insulin (Sigma # I-1882; 10 mg/mL), penicillin (100 U/mL), and streptomycin (100 µg/mL). The MDA-MB-231 cell line (HTB-26) was also obtained from ATCC and maintained in RPMI medium supplemented with 10% Fetal Bovine Serum, L-glutamine (10% v/v), penicillin (100 U/mL), and streptomycin (100 µg/mL). All cell lines were incubated at 37°C in a 5% $CO_2$-supplemented environment. Cell lines were authenticated by brightfield imaging and karyotyping. Mycoplasma contamination was periodically assessed using DAPI staining to check for any extraneous staining outside the nucleus.

### EMT Induction in MCF7 By Twist1 Overexpression

MCF7 cells (~0.35 million) were seeded in six-well plates and allowed to adhere for ~10–12 hours to attain a confluency of ~50%. Cells were independently transfected with 2µg of pEGFPN1 (Empty vector) or TWIST1 in Opti-MEM using PolyEthyleneImine (PEI) (Sigma#408727-100ML) at a ratio of 1:3 plasmid: branched PEI. After ~6 hours post-transfection, Opti-MEM was replaced with DMEM containing 10% FBS. Transfected cells were selected with G418 (890 µg/mL, Roche #4727878001) for 24 hours. Cells were harvested for RT-PCR, immunofluorescence assay, or immunoblotting at ~48 hours post-transfection to assess for expression of E & M marks, respectively.

### TGF-β Mediated EMT Induction

MCF10A cells (~0.15 million) were seeded at a confluency of (~30–40%) in six-well plates and allowed to adhere overnight (~16 hours). MCF10A cells were treated with recombinant

human TGF-β1 (10 ng/mL, PeproTech, #100-21) to induce Epithelial-to-Mesenchymal Transition (EMT) in a complete growth medium. Media containing fresh TGF-β1 was replenished every ~48 hours for a total duration of 7 days. Control cells were maintained in complete media without TGF-β.

**GRHL2 overexpression for the induction of Mesenchymal to Epithelial Transitions (MET)**

MET induction was performed by stable overexpression of the transcription factor GRHL2 with the lentiviral expression vector pLVX-TetOn-Puro-GRHL2 (kindly provided by Dr. Ruby Yun-Ju Huang, National Taiwan University, Taiwan). Lentiviral particles were produced by transfecting ~8 µg of GRHL2 with PEI (DNA: PEI; 1:3 ratio) in HEK293T cells (~1 million cells). Viral supernatants were collected at ~48 and ~72 hours post-transfection, filtered through a 0.45µm filter, and added to MDA-MB-231 cells (~1 million cells) in the presence of 8 µg/mL polybrene. Cells were subjected to selection with puromycin (2 µg/mL) for ~2 days to generate stable GRHL2-overexpressing MDA-MB-231 cell lines. Overexpression of GRHL2 was validated by quantitative RT-PCR (qRT-PCR) and Western blotting.

**Aspect Ratio Analysis**

Cell morphology was quantified by calculating the aspect ratio, defined as the ratio of the major axis length to the minor axis length of individual cells. Brightfield or phase-contrast images were acquired, and cell boundaries were segmented using ImageJ (NIH, USA).

For each cell, an ellipse was fitted to the segmented cell outline using the "Fit Ellipse" function, and the major (longest) and minor (shortest) axe**s** were extracted. The aspect ratio was calculated as:

$$Aspect\ Ratio\ (AR) = \frac{Major\ Axis\ length}{Minor\ Axis\ length}$$

An aspect ratio of **~1** indicates a rounded morphology, whereas higher values indicate increased elongation.

**siRNA Transfection**

MCF7, MCF10A, and MDA-MB-231 cells (~0.35 million) were seeded in six-well plates or 35 mm dishes ~24 hours prior to transfection. Cells were cultured in Opti-MEM and transfected with 50 nM siRNA using 4 µL of RNAiMAX (Invitrogen#13778150). After ~6 hours, Opti-MEM was replaced with DMEM with 10% FBS for a total duration of ~48 hours. Cells were harvested for immunofluorescence assay, RT-PCR, or immunoblotting post-transfection. Sequences of siRNA are provided in Appendix 1

**Retroviral Transduction**

HEK293T cells (~1million) were transfected with ~8 µg of the retroviral plasmid of interest, 4 µg of packaging plasmid Gag-Pol (Plasmid #14887), and VSV-G (2 µg, Plasmid #14888) using PolyEthyleneImine (PEI ~42µL), in the ratio of DNA: PEI - 1:3 (w/v). Viral supernatant (~8mL) was collected ~48 hours post-transfection from HEK293T cells and added to ~0.35 million cells (~1.5mL) (seeded at ~0.35 million cells per well in a 6-well plate). Polybrene (10 µg/mL ~10µL Sigma#H9268) was added to facilitate viral attachment and entry. This procedure was repeated at ~72 hours post-transfection. Cells were selected using puromycin (2 µg/mL, Gibco#A1113802) (for pBabe-Puro constructs) for ~48 hours or hygromycin (50 µg/mL, Gibco#10687010) (for MSCV-F-Hygro constructs) for ~24 hours (Details of plasmids used in Appendix 2).

**Lentiviral Transduction**

Lentiviral transduction was performed by transfecting HEK293T cells simultaneously with the transfer vector (~8 µg), packaging plasmid psPAX2 (4 µg, Addgene #12260), and pMD2G (2 µg, Addgene #12259) using PEI (42µL), in the ratio of DNA: PEI - 1:3 (w/v). Viral particles were collected from HEK293T cells ~48 hours post-transfection and applied to target cells (seeded at ~0.35 million cells per well in a 6-well plate), with the addition of polybrene (10 µg/mL). This process was repeated ~72 hours post-transfection. Cells were selected using 2 µg/mL of puromycin for two days (Figure 2.1) (Details of plasmids used in Appendix 2).

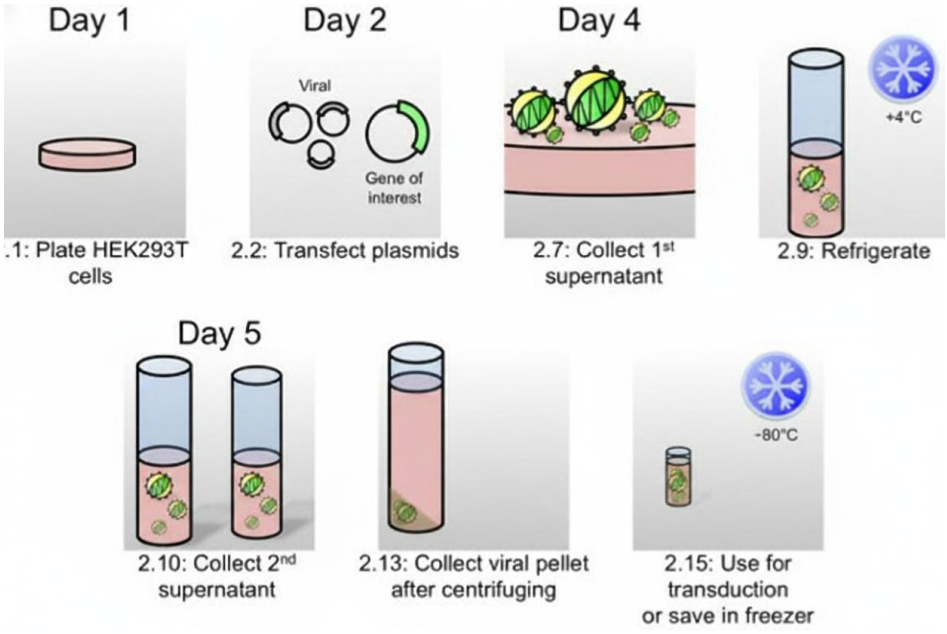


***Figure 2.1: Protocol for Lentiviral Transduction***

*This figure outlines the five-day protocol for producing a viral supernatant containing the gene of interest for use in cell transduction. Day 1 (2.1) involves plating HEK293T cells. Day 2 (2.2) involves transfecting the cells with viral plasmids (containing the viral components and the gene of interest). On Day 4 (2.7), the first batch of viral supernatant is collected, followed by a refrigeration step (2.9). On Day 5 (2.10), the second batch of supernatant is collected, which is then processed to collect the viral pellet after centrifuging (2.13). The final viral stock (2.15) can then be used immediately for transduction or saved long-term in a freezer(image credits: Jove Video: A Protocol for Lentiviral Transduction and Downstream Analysis of Intestinal Organoids).*

**Immunofluorescence**

Cells (~0.35 million) were seeded on coverslips (22 mm × 22 mm) for knockdown or overexpression. Cells were washed twice with 1× Phosphate-Buffered Saline (PBS, pH 7.4) for 5 min each and fixed with 4% paraformaldehyde (pH=7.4 PFA; Sigma, 158127) in 1× PBS (pH=7.5) for 15 minutes at RT. Cells were washed thrice using 1X PBS (pH=7.5). Permeabilization was performed using 0.5% Triton X-100 prepared in 1× PBS (~1mL for a 22 mm × 22 mm coverslip) for 10 minutes. Cells were washed thrice using 1X PBS (~1mL for a 22 mm × 22 mm coverslip) (pH=7.5). Next, cells were blocked with 1% Bovine Serum Albumin (BSA; Sigma, A2153) in 1× PBS for 30 minutes at RT. Cells were washed thrice using 1X PBS (pH=7.5). Primary antibodies were diluted in 1xPBST (0.1% Tween-20) (anti-mouse E-Cadherin(#ab1416), 1:1000; anti-rabbit Vimentin (#ab188499), 1:1000; anti-rabbit Lamin A/C(#ab108595), 1:1000; anti-mouse Lamin A/C(Jol2), #ab40567, -1:50; anti-rabbit EZH2 (D2C9) XP Rabbit mAb CST #5246 - 1:1000) and incubated for 90 minutes at RT, followed by three washes in 1X PBST and stained by fluorophore-conjugated secondary antibodies (Alexa Fluor 488- Goat-anti-Rabbit (#A11034), 1:1000; Alexa Fluor 568- Goat-anti-Mouse (#A11004, 1:1000; Alexa Fluor 568- Goat-anti-Rabbit (#A11011, -1:1000; Alexa Fluor 488- Goat-anti-Mouse (#A11001, - 1:1000) for 60 minutes at RT, followed by three washes of 1X PBST. Cells were counterstained using 0.05µg/mL 4′,6-diamidino-2-phenylindole (DAPI) for two minutes at RT, followed by a thorough wash in 1× PBS (pH=7.5) for 5 mins. Cells in coverslips were mounted using SlowFade Gold Antifade Reagent (Invitrogen, S36937) and stored at 4°C until imaging (Details and dilutions of antibodies used in Appendix 3).

**Imaging and acquisition parameters**

Confocal microscopy was performed using a Zeiss LSM 710 microscope (Carl Zeiss, Thornwood, NJ, USA) equipped with a 63× Plan-Apochromat 1.4 NA oil immersion objective and an AxioCam MRm Rev.3 charge-coupled device camera (Zeiss). Images were acquired at a zoom of 1.0 as Z-stacks at a resolution of 512 × 512 pixels per frame with an 8-bit pixel depth per channel. Voxel size was set to 0.105 µm × 0.105 µm × 0.34 µm, and line averaging = 4.0 in sequential three-channel mode. Samples were mounted in SlowFade Gold Antifade (Thermo Fisher Scientific), and fluorescence signals were detected appropriately with filters for DAPI, Alexa Fluor-488, and Alexa Fluor-568. Image processing and analysis were performed using ImageJ software.

**Immunoblotting**

Protein lysates were prepared by lysing cells for 10 min at 4°C in 1X RIPA buffer (50 mM Tris-HCl (pH 7.4–8.0), 150 mM NaCl, 1% NP-40 (or Triton X-100), 0.1% SDS, 0.5% sodium deoxycholate, and 1 mM EDTA) supplemented with (1x) protease and 1µM phosphatase inhibitors (Roche). Protein concentration was estimated using the BCA assay. Protein samples were resolved in a 12.5% SDS-PAGE gel and transferred onto 0.45 µm PVDF membranes (Millipore # IPVH00010) using a wet transblot system at 100 V for 2h at 4°C in transfer buffer (25 mM Tris, 192 mM glycine, 20% (v/v) methanol). PVDF membranes were blocked in 5% non-fat dry milk or 5% BSA in 1X-TBST (20 mM Tris-HCl (pH 7.5), 150 mM NaCl, 0.1% (v/v) Tween-20) for 1 h at RT and incubated overnight at 4°C with primary antibodies (anti-mouse-E-Cadherin-1:1000; anti-rabbit-Vimentin-1:1000; anti-rabbit-Zeb1-1:1000; anti-rabbit-EZH2-1:1000; anti-rabbit-pEZH2(Thr345)-1:1000; anti-rabbit-Lamin A/C-1:1000; anti-rabbit-pLamin A/C(ser22)-1:100; anti-rabbit-pSmad3-1:1000; anti-rabbit-Smad3-1:1000; anti-rabbit-SUV39H1-1:1000; anti-rabbit-Lamin B1-1:1000; anti-rabbit-Lamin B2-1:1000; anti-rabbit-CyclinB1-1:1000; anti-rabbit-Snail1-1:1000; anti-rabbit-GRHL2-1:1000; anti-mouse-pCDK1-1:1000; anti-rabbit-Twist1-1:1000; anti-rabbit-H3K27me3-1:1000; anti-rabbit-H3K9me3-1:1000; anti-rabbit-H3-1:3000) diluted in blocking buffer. After washing with 1XTBST, membranes were incubated with HRP-conjugated secondary antibodies for 1h at RT (Goat-anti-rabbit-HRP (#111-035-003)- 1:10000; and Sheep anti-mouse-HRP (#515-035-003)- 1:10000 Jackson Labs). Protein bands were visualized using enhanced chemiluminescence (ECL) substrate (Biorad clarity substrate (cat#1705061)) and imaged with a LAS4000 (GE). Densitometric analysis was performed using ImageJ software (Details and dilutions of antibodies used in Appendix 4).

**RT-qPCR**

**RNA Isolation**

Cells (~$0.3\times10^6$) were seeded in a 6-well plate. Cells were washed thrice with 1X PBS (pH=7.5) for 5 mins each. Subsequently, 1mL of TRIzol reagent (Invitrogen, 15596018) was added to the cells. Samples were vortexed briefly for 10 s, and 100 µL of chloroform was added per 500 µL of TRIzol. The mixture was vortexed for 10 s and incubated for 10 min at RT. Phase separation was achieved by centrifugation at 12,000 × g for 15 min at 4°C. The aqueous phase was carefully transferred to fresh 1.5 mL microfuge tubes, and an equal volume of isopropanol

was added. Samples were vortexed for 15 s, incubated at RT for 15 min, and centrifuged again at 12,000 × g for 15 min at 4°C. The RNA pellet was washed with 70% ethanol, air-dried at 37°C for 5–10 min, and resuspended in nuclease-free water. The RNA solution was incubated at 37°C for 5 minutes. RNA samples were stored at −80°C until further use. RNA concentration and purity were assessed using a NanoDrop spectrophotometer.

**cDNA Synthesis and Quantitative Real-Time PCR (RT-qPCR)**

cDNA was synthesized from 1 µg of total RNA using Oligo (dT) primers (5 µM) and a Takara cDNA synthesis kit (Cat#6110B). RNA (1 µg), dNTPs (40 mM), and Random hexamers (5 µM) were mixed, heated at 65°C for 5 min, and chilled on ice. 5X PrimeScript Buffer (4µL) and 1 µL of PrimeScript RTase (200 U/µL) were added, and the mixture was incubated at 42°C for 30–60 min, heat-inactivated at 70°C for 15 min. Quantitative real-time PCR (qRT-PCR) was performed using the TB Green qPCR Master Mix (2×) (TAKARA#RR82WR) and gene-specific forward and reverse primers (2µM). RT-PCR amplifications were carried out on a Bio-Rad CFX96 Real-Time PCR Detection System (PCR conditions: initial denaturation at 95°C for 30 seconds, followed by 40 cycles of denaturation at 95°C for 5 seconds and combined annealing and extension at 60°C for 30 seconds). After amplification, a melt curve analysis was performed by heating from 60°C to 95°C with a ramp rate of 0.3°C per second and continuous fluorescence acquisition to confirm the specificity of amplification. Relative transcript levels were calculated using the $2^{-\Delta\Delta Ct}$ method, with GAPDH as the internal control and untreated samples as the reference (Details of primer sequences used are given in Appendix 5).

## 2.2 Specific to Chapter 3

**Cycloheximide (CHX) Chase Assay**

To examine the stability of Lamin A/C protein during epithelial–mesenchymal transition (EMT), a cycloheximide (CHX) chase assay was performed in MCF7 cells undergoing TWIST1-induced EMT. MCF7 cells were seeded to achieve ~70–80% confluency at the time of treatment. EMT was induced by transient overexpression of TWIST1, while cells transfected with empty vectors served as controls.

After 48 hours of TWIST1 expression, cycloheximide (CHX, 10 µg/mL) was added to inhibit de novo protein synthesis. Cells were harvested at the indicated time points (0, 2, 4, 8, 12, and

24 hours) following CHX addition. For each time point, cells were washed twice with ice-cold PBS (pH=7.4) and lysed directly in 8 M urea lysis buffer (8 M urea, 50 mM Tris-HCl, pH 7.5, 150 mM NaCl, 1 mM EDTA, 1 mM DTT) supplemented with protease and phosphatase inhibitor cocktails (Roche). The lysates were incubated on ice for 30 minutes with intermittent vortexing and clarified by centrifugation (14,000 × g, 15 minutes, 4 °C). Protein concentration was determined using the BCA assay (Thermo Fisher Scientific).

Equal amounts of protein (30µg) were resolved by SDS–PAGE and transferred onto PVDF membranes (Millipore). Immunoblotting was carried out using antibodies against Lamin A/C (Cell Signaling Technology), TWIST1, and β-actin. β-actin served as a loading control. Blots were developed using enhanced chemiluminescence (ECL, Bio-Rad), and images were acquired using the LAS4000 (GE). Band intensities were quantified using ImageJ software, and the relative Lamin A/C signal at each time point was normalized to β-actin.

To assess whether Lamin A/C degradation was proteasome-dependent, parallel cultures were treated with CHX (10 µg/mL) in the presence or absence of the proteasome inhibitor MG132 (1 µM). The relative Lamin A/C stability was plotted as a function of chase time.

**RNA Sequencing (RNA-Seq)**

MCF10A cells (~0.35 million) were plated in six-well plates or 35 mm dishes around 24 hours before transfection. The cells were maintained in Opti-MEM and transfected with 50 nM siRNA using 4 µL of RNAiMAX (Invitrogen #13778150). ~6 hours after transfection, the Opti-MEM medium was replaced with DMEM supplemented with 10% FBS, and the cells were incubated for approximately 48 hours. Following transfection, cells were collected for immunofluorescence analysis, RT-PCR, or immunoblotting. Post-transfection (~48h), MCF10A cells were collected in 1mL TRIzol, and RNA sequencing was outsourced to Medgenome, Bangalore. Quality control checks for the two independent biological replicates were confirmed through RIN number analysis (RIN = 10, for all samples) (Figure 2.2).

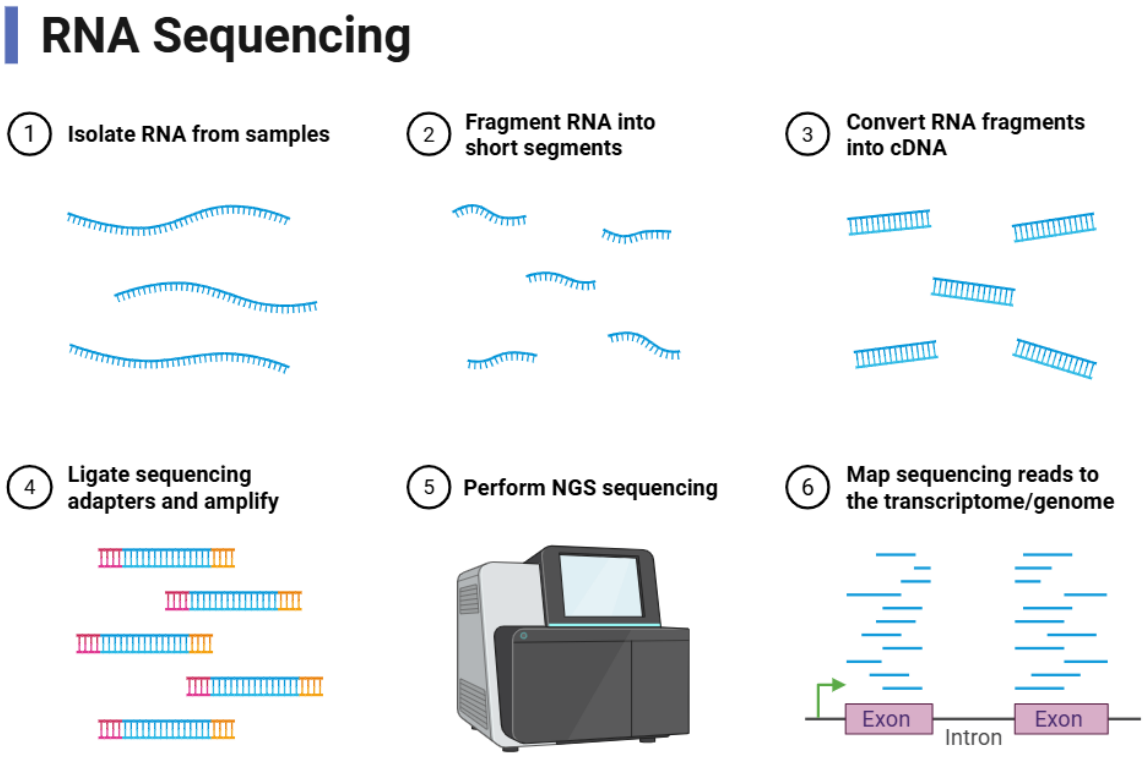


***Figure 2.2: Overview of the RNA Sequencing Protocol***

*This diagram illustrates the six sequential steps used for RNA Sequencing (RNA-Seq), a high-throughput method for transcript analysis. The process begins with (1) isolation of RNA from biological samples, followed by (2) fragmentation of the RNA into short segments. The fragments are then (3) converted into complementary DNA (cDNA). Next, (4) sequencing adapters are ligated, and the fragments are amplified to construct the sequencing library. This library is then loaded into a machine to (5) perform Next-Generation Sequencing (NGS), which generates millions of short sequence reads. Finally, these reads are (6) mapped to the known transcriptome or genome to quantify gene expression and identify novel transcripts (image from biorender).*

**RNA Sequencing and Data Analysis**

RNA sequencing libraries were prepared from total RNA using a poly(A) selection strategy to enrich for mRNA transcripts, with concurrent depletion of ribosomal RNA. Libraries were sequenced on the Illumina NextSeq 500 platform using a paired-end sequencing format (2 × 75 bp reads).

On average, ~30–50 million reads per sample were generated. Raw sequencing reads were processed for quality control and adapter trimming using fastp (v0.20.1). High-quality reads were subsequently aligned to the GRCh38 reference genome using the splice-aware aligner HISAT2 (v2.2.1), achieving an average alignment rate of ~85–95% across samples.

Aligned reads were assembled into transcripts using StringTie (v2.1.5), and gene-level read counts were computed. Expression values were normalized using the fragments per kilobase of transcript per million mapped reads (FPKM) method.

Differential gene expression analysis was performed using the DESeq2 R package, with raw read counts as input. Genes with a $p$-value < 0.05 were considered significantly differentially expressed. A threshold of $\log_2$ fold change > 1 was applied to classify genes as upregulated, while a $\log_2$ fold change < −1 was used to classify genes as downregulated in Lamin A/C knockdown compared to control samples in MCF10A cells.

The RNA sequencing data generated in this study have been deposited in the Gene Expression Omnibus (GEO) under accession number GSE289750.

**Functional Enrichment Analysis**

Functional enrichment analysis, including Gene Ontology (GO) and pathway enrichment, was conducted using the DAVID Functional Annotation Tool (v6.8). GO plots were generated using the WEGO software. Gene Set Enrichment Analysis (GSEA) was performed using the WEB-based Gene Set Enrichment Analysis Toolkit (WEB-GESTALT). Enriched gene sets were visualized using bubble plots, with the Gene Ratio representing the normalized enrichment score (NES) from GSEA. A false discovery rate (FDR) threshold of ≤ 0.05 was applied to identify significantly enriched terms.

**2.3 Specific to Chapter 4**

**Co-Immunoprecipitation**

Cells (~$110^7$) were scraped and lysed using Co-IP buffer (50 mM Tris–HCl (pH 8.0), 300 mM NaCl, 0.5% NP-40, and a 1× protease inhibitor cocktail, Roche#5892970001). The lysates were incubated on ice for 15 min and centrifuged at 14,000 rpm for 15 min at 4°C. The total protein concentration in the supernatant was quantified using the Bicinchoninic Acid (BCA) assay. For each immunoprecipitation, 2 µg of specific primary antibody (as mentioned below) or normal rabbit IgG as a control was pre-bound (~4 hours) to protein A sepharose beads (Roche#P3391) in the Co-IP buffer. The following antibodies were used for immunoprecipitation: Rabbit anti-Lamin A/C (ab108595; Abcam), Rabbit anti-EZH2 (D2C9; #5246; Cell Signaling Technology), and normal rabbit IgG (Invitrogen#10500C). Equal amounts of lysate (500 µg of total protein) were added to the antibody-coated beads, and the mixture was incubated overnight at 4°C on a rotary shaker operating at ~6–7 rpm. After incubation, the beads were washed 5–6 times with a chilled Co-IP buffer, with each wash performed for 10 min at 4°C on a rotary shaker set to 12–13 rpm. The immune complexes were eluted by heating in 2× Laemmli buffer at 95°C for 10 min. The eluted proteins were resolved by SDS-PAGE and analyzed via immunoblotting.

**Co-immunoprecipitation (Co-IP) and Mass Spectrometry Analysis**

To analyze endogenous protein-protein interactions, an optimized co-immunoprecipitation (Co-IP) protocol followed by liquid chromatography-tandem mass spectrometry (LC-MS/MS) was employed (Figure 2.3). **Cell Culture and Lysis:** MCF7-(Empty Vector (EV)), MCF7+TWIST1 were cultured in DMEM (supplemented with 10% FBS), and MDA-MB-231-Dox (-GRHL2), MDA-MB-231+Dox (+GRHL2) cells (~$2.5\times10^6$) were cultured in RPMI (supplemented with 10% FBS), until reaching ~80% confluence (~$1\times10^7$ cells). The cells were washed with ice-cold 1X phosphate-buffered saline (PBS; pH=7.5) and lysed in a Co-IP lysis buffer (50 mM Tris–HCl (pH 7.5), 150 mM NaCl, 1% Nonidet P-40 (NP-40)), and a 1x protease inhibitor cocktail. The lysates were incubated on ice for 30 minutes with occasional mixing and clarified by centrifugation at 14,000 × g for 15 minutes at 4°C. **Immunoprecipitation:** The protein A (SureBeads Protein A Magnetic Beads #161-4013) (transfer 100 µl (1 mg at 10 mg/ml)) magnetic beads used for immunoprecipitation are washed thrice with ~1mL of 1x PBS-T (pH=7.5) and equilibrated in Co-IP lysis buffer. Primary antibodies (2 µg) specific to Lamin A/C (ab#108595) or isotype control normal anti-rabbit IgG (Invitrogen#10500C) were conjugated to protein A magnetic beads. The antibody-conjugated

beads were incubated with 1 mg of cell lysates overnight at 4°C with gentle rotation at 7-12 rpm to facilitate antigen-antibody binding. **Washing and Elution:** The beads were washed thrice for 5 minutes each with a lysis buffer (pH=7.5) to remove non-specifically bound proteins. Bound proteins were eluted by heating the beads with a 2× Laemmli buffer at 95°C for 10 minutes.

**Sample Preparation for Mass Spectrometry**

The eluants were resolved in a 12.5% SDS-PAGE gel for ~2 inches, stained with Coomassie dye, and excised into ~1 $mm^3$ pieces. The gel pieces were washed with 50 mM ammonium bicarbonate (pH=8.0). Proteins were reduced with 10 mM dithiothreitol (DTT) at 56°C for 30 minutes and alkylated with 55 mM iodoacetamide (pH=8.0) at RT in the dark for 30 minutes. The samples were digested overnight at 37°C with sequencing-grade trypsin (Promega: V5111) (100µg/mL of trypsin was diluted in 40 mM ammonium bicarbonate buffer (pH=8.0) at a 1: 50 enzyme-to-substrate ratio). Tryptic digests were eluted in 2% (v/v) formic acid in acetonitrile by sequentially increasing the acetonitrile concentration from 10% (v/v) to 100% (v/v). **LC-MS/MS Analysis:** Peptide mixtures were resuspended in 0.1% (v/v) trifluoroacetic acid in acetonitrile and desalted by passing them through C18 disc columns and analyzed using a Sciex TripleTOF6600 mass spectrometer interfaced with an Eksigent nano-LC 425. **Data Analysis:** Raw data files were processed using ProteinPilot (version 2.0.1, Sciex) software for protein identification and quantification. Database searches were performed against a human protein database.

The mass spectrometry proteomics data are available via the PRIDE repository with the dataset identifier PXD060831.

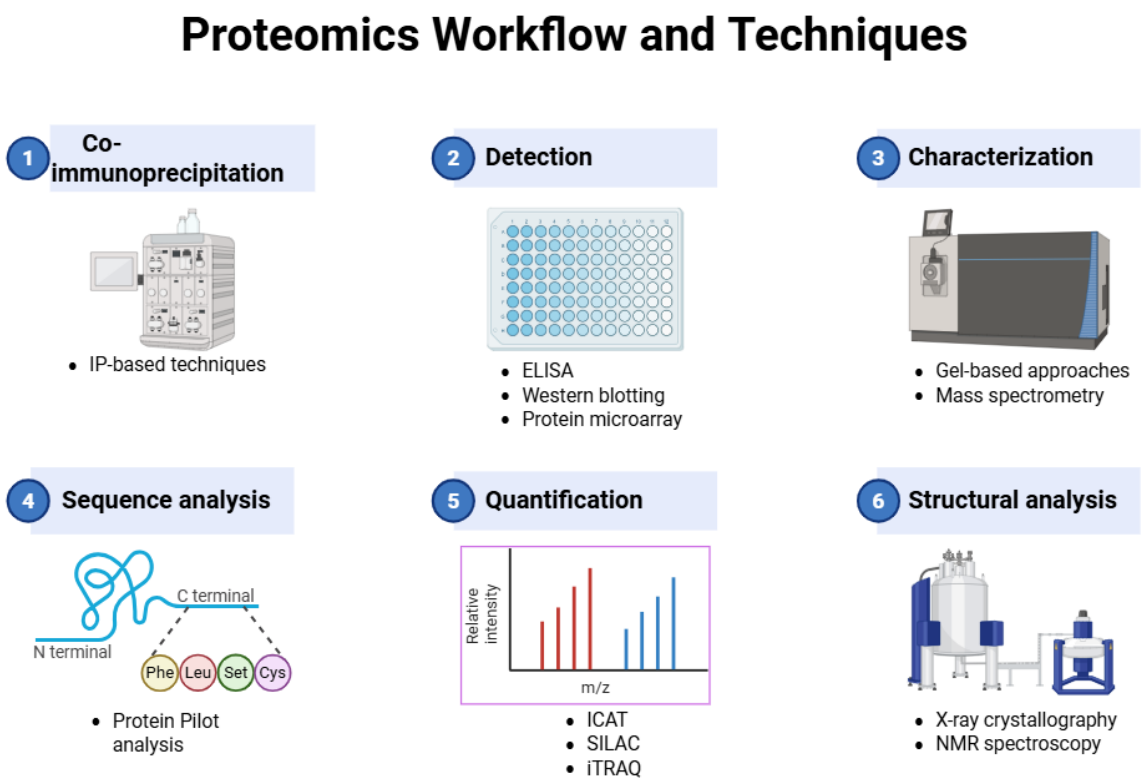


***Figure 2.3: Proteomics Workflow and Techniques***

*This figure outlines the six main stages of a typical proteomics workflow, used to study the entire complement of proteins expressed by a cell, tissue, or organism. The workflow begins with (1) Co-immunoprecipitation, which includes IP-based techniques used to isolate target proteins and their interaction partners. This is followed by (2) Detection methods like ELISA, Western blotting, and protein microarray to verify the presence and quantity of specific proteins. Next, (3) Characterization is performed using Gel-based approaches and Mass spectrometry to identify the proteins. The sequence of the protein is determined in (4) Sequence analysis via Protein Pilot analysis. (5) Quantification is achieved using techniques like iCAT, SILAC, and iTRAQ, which measure relative protein abundance. Finally, (6) Structural analysis employs methods like X-ray crystallography and NMR spectroscopy to determine the three-dimensional structure of the identified proteins (image from biorender).*

**Proximity Ligation Assay (PLA)**

Chilled CSK buffer (10 mM Pipes (pH 6.8), 100 mM NaCl, 300 mM Sucrose, 3 mM $MgCl_2$, 1 mM EGTA) was used to digest the cytoplasm for ~4 minutes at RT. The nuclei were fixed in 4% PFA for 12 minutes. The cells were washed using 1X PBS (pH=7.4), permeabilized using 0.5% Triton X-100 for 10 minutes, and blocked using ~40µl of Duolink Blocking solution 1X at RT for 30 minutes. Following three washes in 1x PBS (pH=7.4), nuclei were incubated with primary antibodies diluted in Duolink antibody diluent, including Mouse anti-Lamin A/C (Jol2 ab40567, 1:50), Rabbit anti-EZH2 (D2C9; #5246; Cell Signaling Technology, 1:1000), and Rabbit anti-Phospho-cdc2 (Thr161) (#9114; Cell Signaling Technology, 1:500) and incubated at 4°C overnight. Subsequently, PLA probes - anti-mouse PLUS and anti-rabbit MINUS were diluted in antibody diluent (1:5) and were incubated with the cells for 1 hour at 37°C. After washing with 1X PBS (pH=7.4), the PLUS and MINUS strand DNAs were ligated by Duolink ligase (1U/µl) diluted in ligation buffer (1:40), and the ligated concatemers were amplified using polymerase (10U/µl) diluted in amplification buffer (1:80) (Sigma Duolink detection kit #DUO92008) according to the manufacturer's instructions. Finally, the cells were washed in 1 ml of 1x PBS (pH=7.5) and mounted using Duolink® In Situ Mounting Medium with DAPI (#DUO82040) (Figure 2.4).

**Imaging and acquisition parameters**

Confocal microscopy for PLA was performed using a Zeiss anisotropy microscope (Carl Zeiss, Thornwood, NJ, USA) equipped with a 63× Plan-Apochromat 1.4 NA oil immersion objective and an AxioCam MRm Rev.3 charge-coupled device camera (Zeiss). Images were acquired with ZEN software, employing a scan zoom of 1.0. Images were acquired as Z-stacks at a resolution of 512 × 512 pixels per frame with an 8-bit pixel depth per channel. Voxel size was set to 0.105 µm × 0.105 µm × 0.34 µm, and line averaging was 4.0 in sequential two-channel mode. Samples were mounted in SlowFade Gold Antifade (Thermo Fisher Scientific), and fluorescence signals were detected using DAPI and Alexa Fluor-568. Image processing and analysis were performed using ImageJ software.

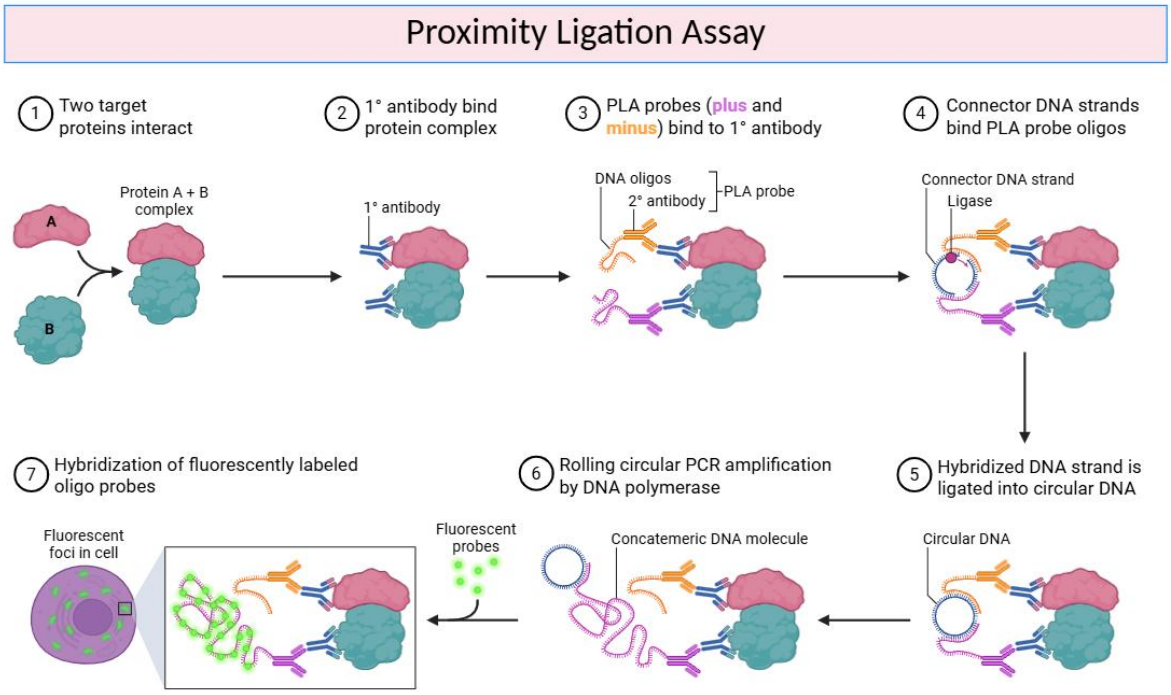


***Figure 2.4: Proximity Ligation Assay (PLA) Workflow***

*This diagram illustrates the seven sequential steps of the Proximity Ligation Assay (PLA), a sensitive technique used to detect and visualize the interaction of two target proteins (Protein A and Protein B) inside a fixed cell. The process begins with (1) the interaction of two target proteins to form a complex. Next, (2) a primary antibody binds to this protein complex. This is followed by the binding of (3) PLA probes (consisting of a 1 antibody and a DNA oligo) to the primary antibody. (4) Connector DNA strands bind the two PLA probes, and a ligase closes the gap, resulting in (5) a circular DNA molecule. This circular DNA then serves as a template for (6) Rolling Circular PCR amplification by DNA polymerase, which creates a long, single-stranded DNA molecule. Finally, (7) hybridization of fluorescently labeled oligo probes to the amplified product allows the interaction to be visualized as distinct fluorescent foci within the cell nucleus or cytoplasm (image from biorender).*

## Generation of CRISPR/Cas9-mediated Indels at the *TWIST1* and *CCNB1* Promoter Regions

CRISPR/Cas9-mediated genome editing was used to generate insertion–deletion (indel) mutations within regulatory regions encompassing the SMAD3 binding site on the *TWIST1* promoter and the TWIST1 binding site on the *CCNB1* promoter in MCF10A cells. Single-guide RNAs (sgRNAs) targeting these transcription factor binding regions were designed using established CRISPR design tools, selecting guides with high predicted on-target efficiency and minimal off-target potential. sgRNA oligonucleotides were cloned into the px458 vector (Addgene #48138), which expresses Streptococcus pyogenes Cas9 and GFP to enable enrichment of transfected cells.

MCF10A cells were cultured under standard conditions and transfected with the sgRNA-containing px458 constructs using Lipofectamine 3000 according to the manufacturer's protocol. Cells were seeded to achieve approximately 70–80% confluency at the time of transfection. Plasmid–lipid complexes were prepared in Opti-MEM, and cells were incubated for 48 hours post-transfection to allow Cas9 expression and genome editing.

Transfected GFP-positive cells were isolated by fluorescence-activated cell sorting (FACS). Single GFP-positive cells were sorted directly into individual wells of 96-well plates (one cell per well) to establish monoclonal populations. Sorted cells were expanded under standard growth conditions until sufficient cell numbers were obtained.

To functionally enrich for clones harboring disruptive indels, expanded clones were subjected to negative selection using transforming growth factor-β (TGF-β). Disruption of the SMAD3 binding site on the *TWIST1* promoter impairs canonical TGF-β/SMAD3 signaling; therefore, clones exhibiting attenuated TGF-β responsiveness were selectively enriched under these conditions.

Genomic DNA from surviving clones was isolated, and the targeted promoter regions were amplified by PCR. CRISPR-induced indels were confirmed by sequencing.

## Cell Cycle Analysis

Cells (~$0.3 \times 10^6$) were harvested by trypsinization, washed with 1X PBS (pH=7.5), and fixed in 70% ice-cold ethanol at 4°C overnight. The fixed cell pellets were resuspended in 1X PBS

(pH=7.5) and treated with RNase A (10 µg; Sigma, R6513-10MG) at 37°C for 45 minutes. Subsequently, propidium iodide (PI; 10 µg; Sigma, P4170-10MG) was added to the samples for DNA staining. The cell suspensions were passed through a 70 µm cell strainer (Corning, CLS431751) and transferred for further analysis. Cell cycle profiling was performed using a fluorescence-activated cell scanner (BD FACSCalibur™, BD Biosciences) with approximately 10,000 events recorded per sample. Data were analyzed using FlowJO (V10.10) software.

### 2.3 Specific to Chapter 5

#### Chromatin Immunoprecipitation

Cells (~$1\times10^7$) were fixed with 1% formaldehyde (v/v) in 1x Phosphate-Buffered Saline (pH=7.5) for 10 min at RT to crosslink protein-DNA interactions. Cross-linking was quenched by adding glycine to a final concentration of 125 mM and incubating for 5 min. Next, the cells were washed twice for 5 minutes each with ice-cold 1X PBS (pH=7.5) and lysed in a lysis buffer (1% SDS (w/v), 10 mM EDTA, 50 mM Tris–HCl, pH 8.1) containing 1x protease inhibitors. The lysates were sonicated using the Covaris S220 series for 30 minutes, at 60% duty cycle, 30 sec on and 30-sec off cycle time, to shear chromatin into fragments of ~200–500 bp, and the efficiency of shearing was confirmed by agarose gel electrophoresis.

Chromatin equivalent to ~25 µg was diluted in ChIP dilution buffer (0.01% SDS (w/v), 1% Triton X-100 (v/v), 1.2 mM EDTA, 16.7 mM Tris–HCl, pH 8.1, 167 mM NaCl) and incubated overnight at 4°C. Primary antibody (4 µg) was used for the pulldown of histone modifications (ChIP: H3K27me3, H3K36me3, and H3) and 8 µg of primary antibody for the pulldown of non-histone antigens (ChIP: Lamin A/C, EZH2, RNA Pol II(Ser2p), and RNA Pol II). The primary antibody (Lamin A/C (ab108595); EZH2 (CST#5246); H3K27me3 (Millipore#07-449); H3K36me3 (#ab9050) and RNA Polymerase II (Ser2p) (Covance (H5) #MMS-129R) or normal IgG (control) (Invitrogen#10500C) was pre-bound to protein A/G agarose beads (~4 hours). The beads were washed sequentially (~500µL) with a low-salt wash buffer (20 mM Tris-HCl (pH 7.5), 150 mM NaCl, 2 mM EDTA, 0.1% SDS, 1% Triton X-100), a high-salt wash buffer (20 mM Tris-HCl (pH 7.5), 500 mM NaCl, 2 mM EDTA, 0.1% SDS, 1% Triton X-100), a LiCl wash buffer (10 mM Tris-HCl (pH 8.0), 250 mM LiCl, 1 mM EDTA, 1% NP-40, 1% sodium deoxycholate), and a TE buffer (10 mM Tris-HCl (pH 8.0), 1 mM EDTA). Chromatin was eluted from the beads using elution buffer (pH=8.5;1% SDS (w/v), 0.1 M $NaHCO_3$) and digested with 2µL of 20 mg/mL proteinase K at 55°C for 30 min. Cross-links

were reversed by incubating the samples at 65°C for ~4–6 hours. The DNA was purified using PCR purification columns (Promega# A9281) and analyzed by RT-qPCR (Figure 2.5). Primer sequences are given in Appendix 6.

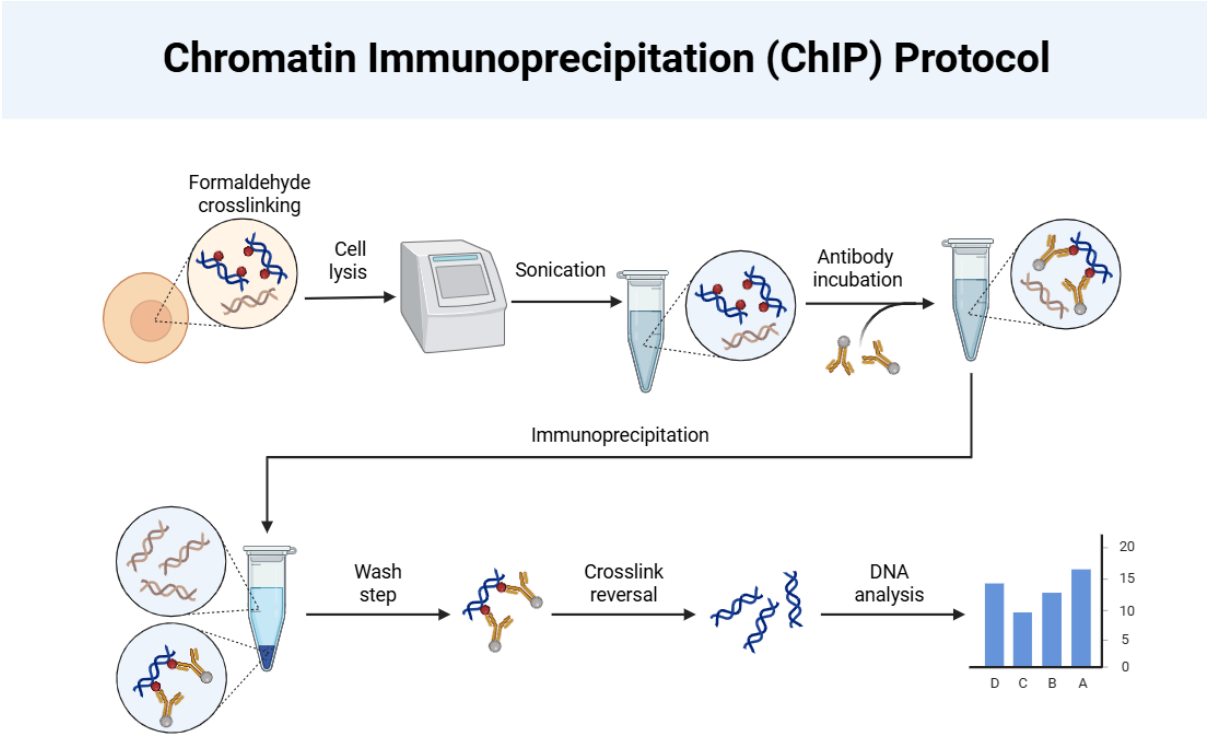


***Figure 2.5: Chromatin Immunoprecipitation (ChIP) Protocol***

*This diagram illustrates the sequential steps of the Chromatin Immunoprecipitation (ChIP) technique, which is used to analyze protein-DNA interactions within the cell. The protocol begins with Formaldehyde crosslinking of the cells to covalently link proteins to the DNA they are bound to. The cells undergo Cell lysis followed by Sonication to shear the DNA into small fragments, leaving the protein-DNA complexes intact. Immunoprecipitation is then performed, which involves Antibody incubation with an antibody specific to the target protein to pull down the desired protein-DNA complex. Following a Wash step, the protein-DNA complex is isolated, and Crosslink reversal is performed to separate the protein from the DNA. Finally, the recovered DNA fragments are subjected to DNA analysis (e.g., qPCR or sequencing) to identify the specific genomic regions where the protein was bound (image from biorender).*

**Flow Cytometry Analysis of CD104 and CD44**

Cells (~1 million) were trypsinized and centrifuged at 10°C for 10 minutes, and the supernatant was aspirated. The cell pellet was resuspended in 0.5–1 mL of 1X PBS (pH=7.5), and formaldehyde was added to a final concentration of 4% for fixation. Cells were incubated for 15 minutes at RT. Following fixation, cells were washed with 1 mL of 1X PBS (pH=7.5) by centrifugation, and the supernatant was discarded. The pellet was resuspended in ~0.5–1 mL of 1X PBS (pH=7.5). The pellet was resuspended in 100 µL of incubation buffer (1% (w/v) BSA in 1X PBS) containing Rabbit anti-CD104 (1:1000; CST#14803T) and Mouse anti-CD44 (1:1000; CST#3570T) primary antibodies. Samples were incubated for 1 hour at RT. After incubation, cells were washed by centrifugation with 1% (w/v) BSA in PBS to remove unbound primary antibodies. Next, the cells were resuspended in 100 µL of diluted secondary antibodies, including anti-Rabbit-Alexa Fluor 564 (Invitrogen#A10042) and anti-Mouse-Alexa Fluor 350 (Invitrogen#A11126) (1:1000, prepared in 1% BSA in PBS). Incubation with a secondary antibody was carried out for 30 minutes at RT. Cells were washed with 1X PBS (pH=7.5), resuspended, and analyzed using a BD FACS Aria (BD Biosciences) flow cytometer. Data analysis was performed using FlowJo (V10.10) software.

**Transwell Migration Assay**

~0.35 million cells per well (MCF7 or MDA-MB-231) were seeded in a 6-well plate and either subjected to stable overexpression of Lamin A or EZH2 or the phosphodeficient (S22A-Lamin A and T345A-EZH2) or phosphomimetic (S22D-Lamin A and T345D-EZH2). The cells were trypsinized, and ~50,000 cells were seeded into the upper chamber of a Transwell insert (8µm pore size, Corning#CLS3422) in serum-free media. Complete media (MCF7-DMEM or MDA-MB-231-RPMI with 10% FBS) (~800 µL) was added to the lower chamber to create a serum gradient for ~36 hours. Non-migrated cells on the upper surface of the membrane were gently removed using a cotton swab. Migrated cells on the lower surface were fixed with 4% paraformaldehyde (pH=7.4) for 10 minutes at RT. The cells are washed twice in 1X PBS (pH=7.5) and stained with DAPI for 2 minutes. The cells were rewashed with 1X PBS (pH=7.5) and visualized under an EVOS microscope at 10X magnification. The threshold was adjusted manually using the Threshold function to isolate the nuclei. To separate closely positioned nuclei, the Watershed function was applied. The total number of nuclei per field was then determined using the "Analyze Particles" function with the following parameters: size = 50–Infinity pixels$^2$, circularity = 0.5–1.0. The average number of nuclei per field was calculated for each condition, and data were analyzed statistically using GraphPad Prism.

**Wound Healing Assay**

MCF10A cells (~0.35 million cells) were either subjected to stable overexpression of Lamin A or EZH2 or the phosphodeficient (S22A-Lamin A and T345A-EZH2) or phosphomimetic (S22D-Lamin A and T345D-EZH2). The cells are treated with 500 ng/mL doxycycline to induce endogenous depletion of Lamin A/C or EZH2 for ~48 hours. EMT was induced by treating the cells with 10 ng/mL of TGF-β. Following ~48 hours of incubation with respective manipulations, cells were trypsinized, and ~50,000 cells were seeded into each well of an ibidi 2-well insert (ibidi #81176) and placed in a 24-well Corning plate overnight. The insert was removed after the cells were attached (~within 12h post-seeding) to create a wound gap, and cell migration into the wound area was monitored for 36 hours using the Operetta High-Content Imaging System. Wound closure was analyzed using the software integrated into the Operetta system.

**Animal Studies**

All animal procedures were conducted following approval from the Institutional Animal Ethics Committee (IISER-P IAEC) at the Indian Institute of Science Education and Research, Pune, in compliance with the Committee for the Purpose of Control and Supervision of Experiments on Animals (CPCSEA), Government of India. Mice were housed in the National Facility for Gene Function in Health and Disease (NFGFHD), IISER Pune, under standard laboratory conditions with unrestricted access to food and water.

**Tumorigenicity Assay in NOD-SCID Mice**

Female NOD-SCID mice (4–6 weeks old, Jackson Laboratory) were used for tumor formation studies. MDA-MB-231 cells expressing either phosphodeficient (S22A-Lamin A and T345A-EZH2) or phosphomimetic (S22D-Lamin A and T345D-EZH2) variants of Lamin A/C or EZH2 were pre-treated with doxycycline (Dox) for 48 hours to induce the knockdown of endogenous Lamin A or EZH2 before injection. Cells (~ $1 \times 10^6$) were resuspended in 100 µL of 1X PBS (pH=7.5) and were injected into the fourth mammary fat pad of each mouse. To sustain knockdown, animals received drinking water supplemented with 1% sucrose and 500 ng/mL doxycycline. Fresh water was replenished every ~72 hours. Tumor growth was monitored, and volume ($mm^3$) was determined using the formula (width × width × length)/2. After five weeks, mice were euthanized, and tumors were harvested for further analysis.

**Tumor Dissociation and Primary Cell Culture**

Excised tumors were finely minced using sterile scalpels in Hank's Balanced Salt Solution (HBSS (pH=7.5)). Tumor digestion was carried out at RT using an enzymatic mixture containing 1 mg/mL collagenase type IV (Sigma, C5138-1G), 0.1 mg/mL hyaluronidase type V (Sigma, H6254-500MG), and 20 mg/mL DNase type IV (Sigma, D5025-15KU) in HBSS (pH=7.5). The digestion was performed in a 50 mL non-vented tissue culture flask on a stir plate. Following enzymatic dissociation, the cell suspension was passed through a 70 μm nylon mesh, centrifuged at 1200 rpm for 5 minutes, and washed twice with HBSS (pH=7.5). The resulting cell pellet was processed either by lysis in Co-IP lysis buffer (pH=7.5) for immunoprecipitation assays or resuspended in a complete RPMI medium for establishing primary cultures. Primary cells were plated onto glass coverslips for immunofluorescence analysis and processed according to standard immunostaining protocols.

**Rescue Experiments**

**Lamin A/C Rescue Experiments**

**MCF7:** MCF7 cells (~1 million cells in a 100mm cell culture dish) were subjected to lentiviral transduction of an inducible shRNA-based Lamin A/C knockdown system and selected using 2 μg/mL of puromycin for 2 days. Subsequently, the puromycin-selected cells were lentivirally transduced with Lamin A-GFP resistant to the shRNA seed sequence of Lamin A. GFP-positive cells were next FACS sorted using BD Aria (BD Biosciences). These cells were transiently transfected with either 2μg of pEGFPN1 (control vector) or TWIST1-GFP for 48 hours. Following transfection, the cells were selected using ~890 μg/mL of G418 for 24 hours. Forty-eight hours post-overexpression, cells were collected for further assays.

**MCF10A:** MCF10A cells (~1 million cells in a 100 mm cell culture dish) were lentivirally transduced with an inducible shRNA-based Lamin A/C knockdown system and selected using 2 μg/mL of puromycin for ~2 days. Subsequently, the puromycin-selected cells were lentivirally transduced with Lamin A-GFP resistant to the shRNA seed sequence of Lamin A. GFP-positive cells were then FACS sorted using BD Aria (BD Biosciences). Cells were treated with 10 ng/mL of TGF-β for 7 days to induce EMT. Cells were collected for further assays.

**MDA-MB-231:** Cells (~1 million cells in a 100mm cell culture dish) were lentivirally transduced with an inducible shRNA-based Lamin A/C knockdown system and selected using

2 μg/mL of puromycin until 100% cell death was observed in non-transduced cells. Subsequently, the puromycin-selected cells were lentivirally transduced with GRHL2-GFP, and positive cells were sorted using FACSAria. Finally, positive cells were lentivirally transduced with Lamin A-GFP and selected by adding 50 μg/mL of hygromycin for 18 hours. Cells were collected for further assays.

**EZH2 Rescue Experiments**

**MCF7:** Cells (~1 million cells in a 100mm cell culture dish) were lentivirally transduced with an inducible shRNA-based EZH2 knockdown system and selected using 2 μg/mL of puromycin for 2 days. Subsequently, the puromycin-selected cells were retrovirally transduced with MSCV-EZH2-FLAG resistant to the shRNA seed sequence of EZH2. Selection was performed by adding 50 μg/mL of hygromycin for 18 hours. These cells were transiently transfected with 2μg either pEGFPN1 (control vector) or TWIST1-GFP for 48 hours. Following transfection, the cells were selected using 890 μg/mL of G418 for 24 hours. Forty-eight hours post-overexpression, cells were collected for further assays.

**MCF10A:** Cells (~1 million cells in a 100mm cell culture dish) were lentivirally transduced with an inducible shRNA-based EZH2 knockdown system and selected using 2 μg/mL of puromycin for ~2 days. Subsequently, the puromycin-selected cells were retrovirally transduced with MSCV-EZH2-FLAG resistant to the shRNA seed sequence of EZH2. Selection was performed by adding 50 μg/mL of hygromycin for 18 hours. EMT was induced by adding 10 ng/mL of TGF-β for 7 days. Additionally, 500 ng/mL of doxycycline was added and replaced every 48 hours.

**MDA-MB-231:** Cells (~1 million cells in a 100mm cell culture dish) were lentivirally transduced with an inducible shRNA-based EZH2 knockdown system and selected using 2 μg/mL of puromycin until 100% cell death was observed in non-transduced cells. Subsequently, the puromycin-selected cells were lentivirally transduced with GRHL2-GFP, and positive cells were sorted using the FACSAria cell sorter. Next, the cells were retrovirally transduced with MSCV-EZH2-FLAG resistant to the shRNA seed sequence of EZH2. Cells were further selected by adding 50 μg/mL of hygromycin for 18 hours.

## 2.5 Cloning of Constructs

**Cloning of shEZH2**

The seed sequence for EZH2 depletion was synthesized as oligos and cloned into a pLKO-Tet-puro vector (Addgene #21915). The pLKO-Tet-puro vector (a gift from Dmitri Wiederschain; Addgene plasmid #21915) was digested with AgeI (R3552S) and EcoRI (R0101S) (20 U) and purified using a gel extraction kit (Qiagen) according to the manufacturer's protocol. Complementary oligonucleotides encoding the shRNA sequence were denatured at 95°C, annealed in a buffer containing 0.1 M NaCl and 10 mM Tris-HCl (pH 7.4), and allowed to cool at RT slowly. The annealed oligonucleotides (4 ng) were ligated into 20 ng of digested and gel-purified pLKO-Tet-puro vector using 350 U of T4 DNA ligase (TAKARA Cat. no. 2011A) at 37°C for 3 h. The ligation reaction was transformed into $CaCl_2$-treated competent Escherichia coli DH5α cells via heat shock at 42°C. Transformed bacteria were plated on LB agar containing ampicillin (100 µg/ml) and incubated overnight at 37°C. Positive clones were screened by restriction enzyme digestion with XhoI to confirm the presence of the insert and further validated by Sanger sequencing. Cloning primer sequences are given in Appendix 7.

**Site-Directed Mutagenesis**

Lamin A S22D and S22A mutants were created by amplifying pLVX-EF1a-GFP-Lamin A-IRES-Hygromycin (Addgene# 134867) using PCR with overlapping mutagenic primers to generate phospho-mimetic and phospho-deficient mutants, as described previously. Similarly, in MSCV-hygro-F-EZH2 (Addgene# 24926), Threonine at the 345$^{th}$ position was mutated to Alanine and Aspartate to generate phospho-deficient and phosphomimetic mutants, respectively, by amplifying the entire plasmid with overlapping mutagenic primers. For generating the shRNA-resistant Lamin A construct (pLVX-EF1a-GFP-LaminA-IRES-Hygromycin), we mutated 3 interspersed bases in the seed sequence by PCR amplifying the pLVX-EF1a-GFP-LaminA-IRES-Hygromycin plasmid with overlapping mutagenic primers. Similarly, we introduced mutations in three bases within the seed sequence to generate the Flag-EZH2 construct (MSCVhygro-F-EZH2) resistant to shRNA. This was achieved through PCR amplification of the MSCV-hygro-F-EZH2 plasmid using mutagenic primers. For all the mutations mentioned above, the PCR reaction consisted of forward primer (0.3 µM), reverse primer (0.3 µM), template DNA (5 ng), and 2X PCR mix (R047A) (5 µL) in a final volume of 10µL. Next, the reactions were incubated with 20 units of DpnI (Cat. no. 1235A) for 3 hours at 37 °C. 2µL of the reaction mixture was transformed into E. coli DH5α cells, and the clones were further validated and confirmed using Sanger sequencing Appendix 7.

**Cloning of Domain Deletion Mutants**

The ΔHead (1-29), ΔRod (31–387), ΔIgG (428-549), and ΔTail (550-664) mutants of Lamin A/C were created by amplifying the parent construct, i.e., pLVX-EF1a-GFP-Lamin A-IRES-Hygromycin, using inverse PCR and back-to-back primers. The amplicons were further gel-purified and subsequently incubated with 10U of DpnI (Cat. no. 1235A). Next, 10U of T4 PNK (Cat. no. 2021A) and 350U of T4 DNA Ligase (Cat. no. 2011A) were added. Post ligation, the reactions were transformed into E. coli DH5α cells and were further screened using colony PCR (95°C for 3 min; 30 cycles of 95°C for 30 sec, 55–60°C for 30 sec, 72°C for 1 min; final extension at 72°C for 5 min; hold at 4°C). Similarly, the Δ1-300, Δ301-500, Δ501-746 deletion mutants in Flag-EZH2 were created using inverse PCR by amplifying MSCV-hygro-F-EZH2. Further, the amplicons were processed for ligation and were later transformed and screened using colony PCR. For all the mutations mentioned above, the PCR reaction volume was set to 10µL. The reactions were incubated with 20 units of DpnI (Cat. no. 1235A) for 3 hours at 37°C. The T4 PNK reactions were incubated at 37°C for 45 mins, utilizing 10 units/10uL reaction volume of T4 PNK enzyme for 100ng of gel-extracted PCR amplified DNA. Subsequently, 5µL of the previous reaction was used for the ligation reaction. The ligation reaction was carried out at 16°C overnight, using 350U of T4 DNA ligase. 5µL of the reaction mixture was transformed into E. coli DH5α cells and was further screened using colony PCR and Sanger sequencing Appendix 7.

**Statistical Analysis**

All statistical analyses were performed using GraphPad Prism version 8.4 (GraphPad Software, San Diego, CA, USA). Data are presented as mean ± standard deviation (SD) unless otherwise specified. Comparisons between the two groups were conducted using an unpaired two-tailed Student's t-test. For multiple-group comparisons, one-way or two-way analysis of variance (ANOVA) followed by Tukey's or Sidak's post hoc test was used, as appropriate (normality and variance were confirmed before applying ANOVA). Statistical significance was defined as $p < 0.05$. Sample sizes and replicates for each experiment are detailed in the figure legends.

# Chapter 3: Decoding the Role of Nuclear Lamins in EMT–MET Dynamics and Chromatin Remodeling

## 3.1 Introduction

Epithelial–mesenchymal plasticity (EMP) encompasses a dynamic and reversible spectrum of phenotypic states that span the continuum between epithelial and mesenchymal identities. At the two extremes lie epithelial–mesenchymal transition (EMT) and mesenchymal–epithelial transition (MET), which enable cells to interconvert in response to developmental cues, environmental stimuli, or pathological conditions (Derynck and Weinberg, 2019). EMT is a fundamental developmental process that is co-opted during wound healing, fibrosis, and tumor progression (Nakaya and Sheng, 2008). It enables epithelial cells to lose apico-basal polarity and intercellular adhesion while gaining migratory and invasive capabilities. MET, conversely, restores epithelial traits and is often crucial for metastatic colonization at secondary sites in cancer (Kim et al., 2019). Together, these transitions bestow cells with phenotypic plasticity, contributing to heterogeneity, drug resistance, and immune evasion in tumors (Dongre and Weinberg, 2019).

While extensive research has elucidated the signaling pathways and transcriptional networks orchestrating EMT and MET (Nieto et al., 2016), the role of nuclear architecture and chromatin organization in modulating EMP is still emerging. In this context, A-type lamins, Lamin A and Lamin C, have gained attention as key players linking nuclear structure to transcriptional regulation (González-Romero et al., 2008). These intermediate filament proteins, encoded by the LMNA gene via alternative splicing, form a meshwork beneath the inner nuclear membrane known as the nuclear lamina. In addition to their architectural role, lamins influence diverse cellular processes including DNA repair, mechanotransduction, senescence, and epigenetic regulation (McLaughlin-Drubin et al., 2013).

Recent findings suggest that lamins are not merely passive scaffolds but active participants in maintaining cell identity and suppressing inappropriate plasticity (Stephens et al., 2018). Perturbations in lamin levels, particularly Lamin A/C, are associated with altered nuclear mechanics, chromatin remodeling, and transcriptional reprogramming—hallmarks of EMT (Fudenberg et al., 2016). Significantly, lamins interface with chromatin-modifying enzymes and contribute to the organization of lamina-associated domains (LADs), thereby modulating large-scale gene expression programs (Kind et al., 2013).

Understanding how lamins influence EMT and MET has profound implications in cancer biology. In epithelial tumors, loss or misregulation of Lamin A/C has been correlated with

enhanced invasiveness, metastatic potential, and therapy resistance (Margueron et al., 2008). Conversely, forced expression or stabilization of Lamin A/C can suppress EMT and impede metastatic dissemination (Ibarra and Hetzer, 2015). These observations suggest that lamins act as key gatekeepers of phenotypic stability, influencing the ability of cells to undergo and reverse EMT.

Moreover, lamins regulate the nuclear availability and activity of transcription factors, and physically interact with epigenetic repressors such as EZH2, the catalytic subunit of the Polycomb Repressive Complex 2 (PRC2) (Deb et al., 2014). Through these interactions, lamins may influence histone modification landscapes during EMT, thereby integrating mechanical, structural, and transcriptional signals that guide cell fate transitions.

In this chapter, we explore the role of lamins in modulating epithelial–mesenchymal plasticity by dissecting four significant aspects:

1. **EMT and MET Induction** – Validation of EMT (TWIST in MCF7 and TGF-β in MCF10A) and MET (GRHL2 in MDA-MB-231).

2. **Effect of EMT on Lamins** – A discussion on how EMT alters the expression, localization, and function of nuclear lamins.

3. **Effect of Lamins on EMT** – Examination of how changes in Lamin A/C levels impact EMT transcriptional programs and phenotypic outcomes.

4. **Chromatin Modifications** – Insight into how lamin-associated changes in chromatin organization and histone modifications contribute to transcriptional reprogramming during EMT/MET.

By integrating structural, transcriptional, and epigenetic dimensions, this chapter aims to highlight the central role of lamins in maintaining cellular identity and regulating the plasticity that underpins cancer progression and metastasis.

## 3.2 Results

### 3.2.1 Induction and Reversal of Epithelial–Mesenchymal Transition (EMT)

The epithelial-to-mesenchymal transition (EMT) and its reverse process, mesenchymal-to-epithelial transition (MET), are fundamental biological programs that play pivotal roles not only in embryonic development but also in cancer progression, particularly in carcinomas (Youle and Strasser, 2008). EMT is a dynamic and reversible process in which epithelial cells lose their cell–cell junctions, apico-basal polarity, and adhesion, and acquire a spindle-shaped, motile mesenchymal phenotype (Wong et al., 2009; Gonzalo, 2014). This transition promotes cellular migration, invasion into surrounding tissues, resistance to apoptosis, and immune evasion (Schuettengruber and Cavalli, 2009; Boumendil et al., 2019). In contrast, MET enables mesenchymal-like cells to reacquire epithelial characteristics, a step that is often essential for colonization and outgrowth at metastatic sites (Towbin et al., 2012; Gdula et al., 2013). These transitions are regulated by complex networks involving transcription factors, signaling pathways, and chromatin-modifying enzymes that together govern epithelial–mesenchymal plasticity (Lin et al., 2013; Briand and Collas, 2018).

To explore the molecular basis of EMT and MET in breast cancer, we utilized three breast cell lines representing a spectrum of epithelial and mesenchymal states: MCF7 (luminal epithelial, tumorigenic), MCF10A (non-tumorigenic epithelial), and MDA-MB-231 (basal-like, highly mesenchymal and invasive). These cell lines provided robust models for inducing EMT and MET under controlled experimental conditions. We authenticated the identity of these cell lines by bright field imaging (Figure 3.1A) and karyotyping (Figure 3.1B).

Morphological characterization using phalloidin staining and confocal microscopy revealed distinct differences across the cell lines. MDA-MB-231 cells displayed an elongated, spindle-like morphology, indicative of mesenchymal characteristics, with a high aspect ratio (AR: 7.19 ± 1.80), reflecting cellular elongation. In contrast, MCF7 and MCF10A cells showed rounded, compact, cobblestone-like epithelial morphology with significantly lower aspect ratios (MCF7: AR: 1.06 ± 0.62; MCF10A: AR: 1.09 ± 0.59) (Figure 3.1D).

At the molecular level, immunoblotting and immunofluorescence confirmed that MDA-MB-231 cells expressed high levels of Vimentin—a mesenchymal cytoskeletal marker—and low levels of E-cadherin, a hallmark of epithelial junctions. On the other hand, MCF7 cells displayed strong E-cadherin expression with low or negligible Vimentin, consistent with their epithelial identity (Figures 3.1C, 3.1E–3.1G).

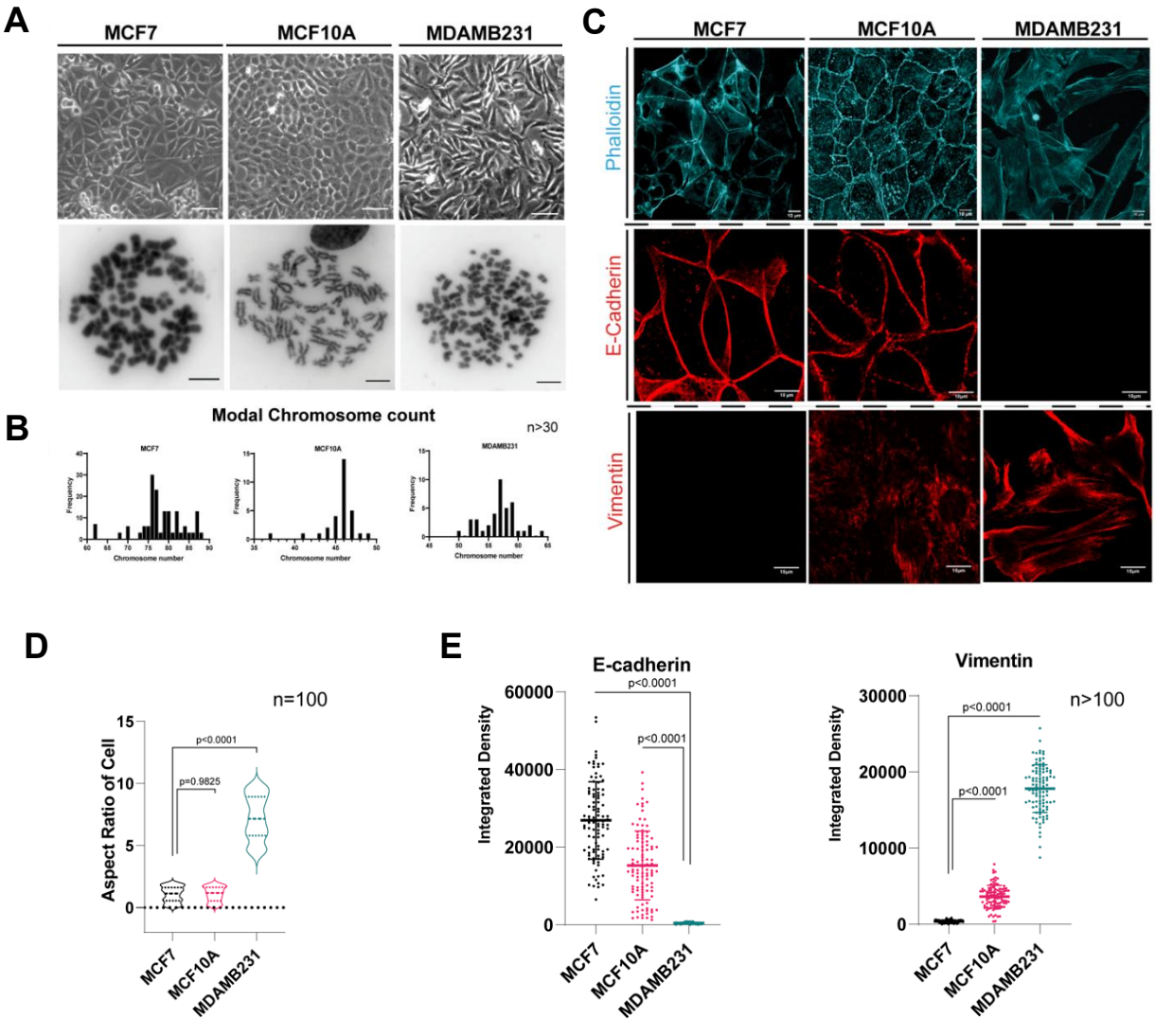

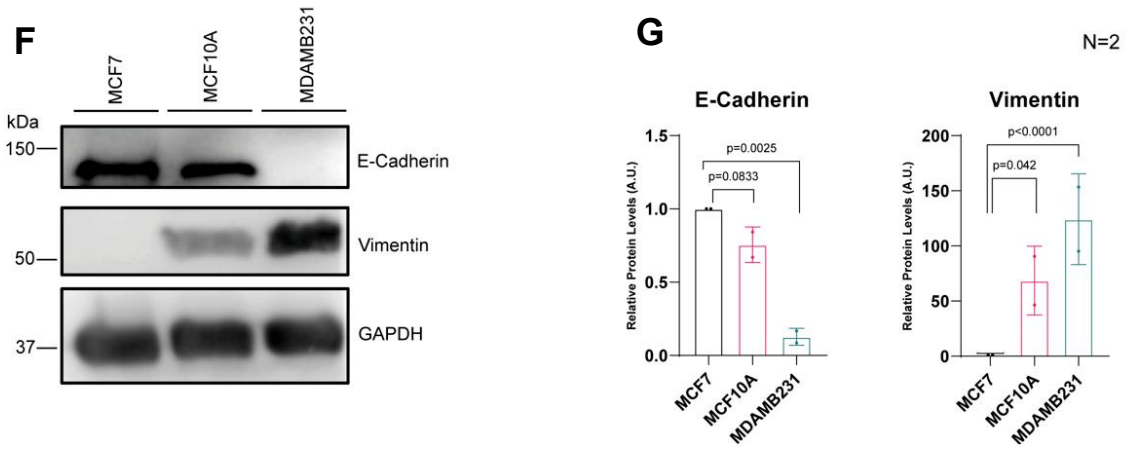


***Figure 3.1 Characterization and authentication of MCF7, MCF10A, and MDA-MB-231 cell systems.***

***(A)*** *Brightfield images (scale bar ~160μm) and metaphase spreads (scale bar, 10 μm) of MCF7, MCF10A, and MDA-MB-231 cells.* ***(B)*** *Quantification of modal chromosome numbers from metaphase spreads, showing modal chromosome numbers of 75, 46, and 58 for MCF7, MCF10A, and MDA-MB-231, respectively.* ***(C)*** *Representative immunofluorescence images of MCF7, MCF10A, and MDA-MB-231 cells stained with Phalloidin (cyan) to visualize F-actin and E-cadherin (red) and Vimentin (red) to assess epithelial and mesenchymal characteristics. Scale bar, ~10 μm.* ***(D)*** *Quantification of cell aspect ratios based on Phalloidin staining in (C).* ***(E)*** *Quantification of the integrated density of E-cadherin and Vimentin in MCF7, MCF10A, and MDA-MB-231 cells (n=200) is shown in (C).* ***(F)*** *Immunoblot analysis of E-cadherin and Vimentin protein levels in MCF7, MCF10A, and MDA-MB-231 cells. GAPDH is used as the loading control.* ***(G)*** *Densitometric quantification of relative E-cadherin and Vimentin protein levels from immunoblots in (F). Data is presented as mean ± SEM from two independent biological replicates. Statistical significance was determined using an unpaired Student's t-test. P values are indicated where significant.*

To experimentally induce EMT in epithelial cells, MCF7 cells were transfected with a GFP-tagged human TWIST1 construct for 48 hours. TWIST1 is a master regulator of EMT that suppresses epithelial genes and activates mesenchymal gene programs. Following TWIST1 expression, immunoblotting revealed a ~75% reduction in E-cadherin and a ~90% increase in Vimentin, alongside upregulation of mesenchymal transcription factors Snail1, Twist1, and Zeb1 (Figure 3.2A). Immunofluorescence imaging supported these findings, demonstrating decreased E-cadherin and increased Vimentin expression (Figures 3.2B, 3.2D).

EMT was induced in MCF10A cells by treatment with TGF-β (10 ng/mL) for seven days (media and 10ng/mL of TGF-β replenished every 48h). TGF-β is a potent EMT inducer that operates through both SMAD-dependent and -independent pathways. Treated cells exhibited marked downregulation of E-cadherin (more than 70%) and increased Vimentin expression (~60%) (Figure 3.2E). Immunofluorescence analysis showed morphological changes consistent with EMT, and expression of transcription factors Snail1, Twist1, and Zeb1 confirmed the mesenchymal reprogramming (Figures 3.2F, 3.2H).

To induce MET, we overexpressed GRHL2 in MDA-MB-231 cells. GRHL2 is an epithelial lineage transcription factor known to oppose EMT and reinforce epithelial characteristics. After ~48 hours of GRHL2 expression, MDA-MB-231 cells expressed E-cadherin at high levels (>95% increase) and exhibited decreased levels of Vimentin (~50%) and mesenchymal transcription factors (Figures 3.2I–3.2L). The phenotypic shift was also evident morphologically, with cells adopting a more epithelial, cobblestone-like architecture. These results establish MCF7, MCF10A, and MDA-MB-231 cells as tractable systems for dissecting EMT/MET dynamics.

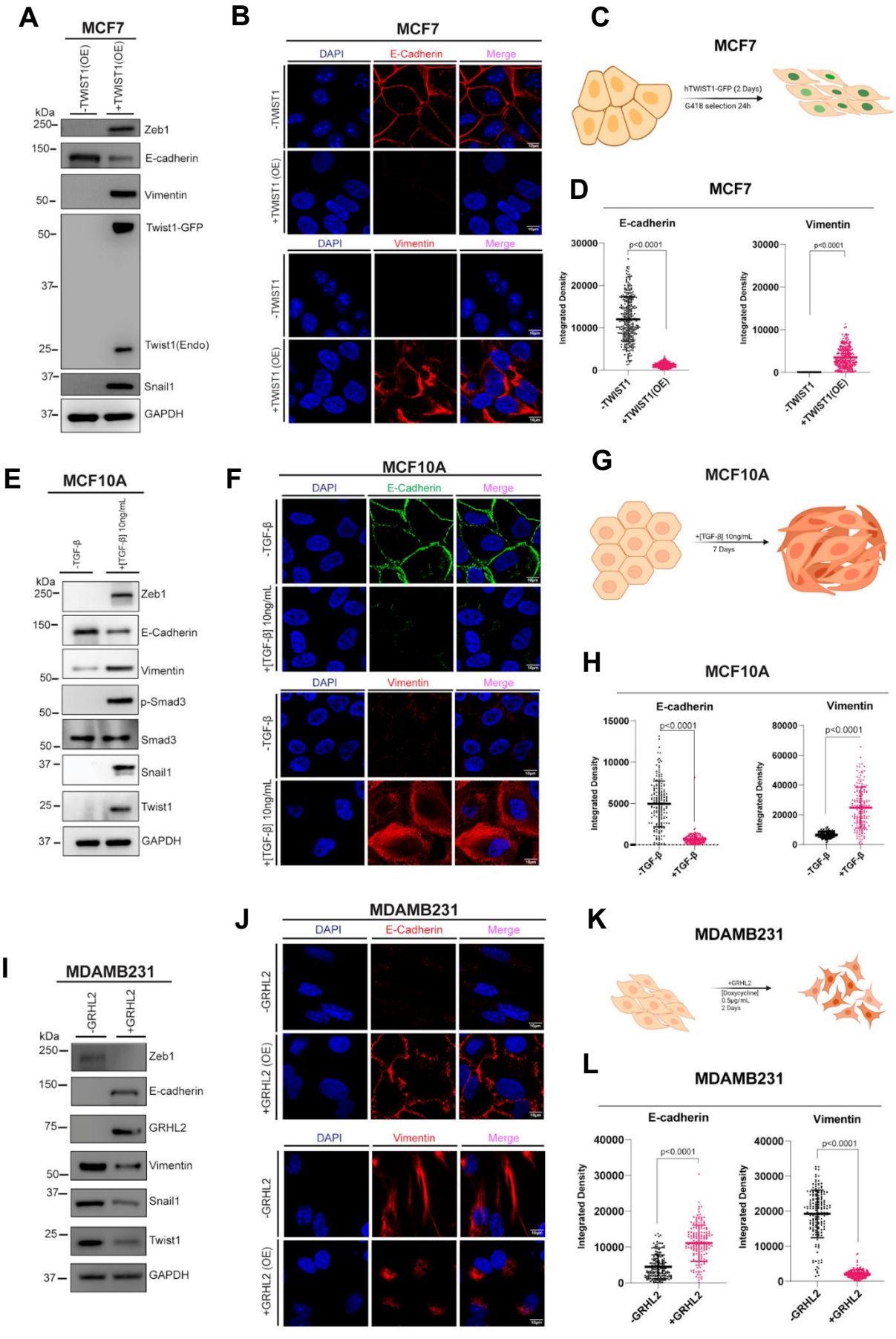
A
MCF7
-TWIST1(OE)
+TWIST1(OE)
kDa
250
150
50
37
25
37
37
Zeb1
E-cadherin
Vimentin
Twist1-GFP
Twist1(Endo)
Snail1
GAPDH
B
MCF7
DAPI
E-Cadherin
Merge
-TWIST1
+TWIST1 (OE)
DAPI
Vimentin
Merge
-TWIST1
+TWIST1 (OE)
C
MCF7
hTWIST1-GFP (2 Days)
G418 selection 24h
D
MCF7
E-cadherin
Vimentin
p<0.0001
p<0.0001
Integrated Density
30000
20000
10000
0
-TWIST1
+TWIST1(OE)
E
MCF10A
-TGF-β
+[TGF-β] 10ng/mL
kDa
250
150
50
50
50
37
25
37
Zeb1
E-Cadherin
Vimentin
p-Smad3
Smad3
Snail1
Twist1
GAPDH
F
MCF10A
DAPI
E-Cadherin
Merge
-TGF-β
+[TGF-β] 10ng/mL
DAPI
Vimentin
Merge
-TGF-β
+[TGF-β] 10ng/mL
G
MCF10A
+[TGF-β] 10ng/mL
7 Days
H
MCF10A
E-cadherin
Vimentin
p<0.0001
p<0.0001
Integrated Density
15000
10000
5000
0
80000
60000
40000
20000
0
-TGF-β
+TGF-β
I
MDAMB231
-GRHL2
+GRHL2
kDa
250
150
75
50
37
25
37
Zeb1
E-cadherin
GRHL2
Vimentin
Snail1
Twist1
GAPDH
J
MDAMB231
DAPI
E-Cadherin
Merge
-GRHL2
+GRHL2 (OE)
DAPI
Vimentin
Merge
-GRHL2
+GRHL2 (OE)
K
MDAMB231
+GRHL2
[Doxycycline]
0.5μg/mL
2 Days
L
MDAMB231
E-cadherin
Vimentin
p<0.0001
p<0.0001
Integrated Density
40000
30000
20000
10000
0
-GRHL2
+GRHL2

***Figure 3.2: Induction and characterization of EMT and MET in breast cancer cell lines***

*(A) Immunoblot analysis of EMT induction in MCF7 cells transiently overexpressing TWIST1-GFP for 48 hours. Control cells were transfected with pEGFPN1. (B) Immunofluorescence analysis of EMT in MCF7 cells overexpressing TWIST1-GFP or control pEGFPN1. E-cadherin and Vimentin are stained in red. Scale bar, 10 μm. (C) Schematic representation of the methodology of EMT induction in MCF7 cells. (D) Scatter plot showing relative changes in the integrated density of E-cadherin and Vimentin in MCF7 cells. Quantification for the data in (B). (n = 242). Data represent mean ± SD from three independent biological replicates. Unpaired Student's t-test was used to calculate p-values. (E) Immunoblot analysis of EMT induction in MCF10A cells treated with 10ng/mL TGF-β for 7 days. (F) Immunofluorescence analysis of EMT in MCF10A cells treated with TGF-β. E-cadherin is stained in green, and Vimentin is stained in red. Scale bar, 10 μm. (G) Schematic representation of the methodology of EMT induction in MCF10A cells. (H) Scatter plot of the integrated density of E-cadherin and Vimentin in MCF10A cells (data shown in (F)) following EMT induction (n > 200). Data represent mean ± SD from three independent biological replicates. Unpaired Student's t-test was used to calculate p-values. (I) Immunoblot analysis of MET induction in MDA-MB-231 cells following doxycycline-induced GRHL2 overexpression for 48 hours. (J) Immunofluorescence analysis of MET in MDA-MB-231 cells overexpressing GRHL2. E-cadherin and Vimentin are stained in red. Scale bar, 10 μm. (K) Schematic representation of the methodology of MET induction in MDA-MB-231 cells. (L) Scatter plot of the integrated density of E-cadherin and Vimentin in MDA-MB-231 cells following MET induction (data shown in (J)) (n = 215). Data represent mean ± SD from three independent biological replicates. Unpaired Student's t-test was used to calculate p-values.*

We also validated by immunoblotting the EM profile of 11 breast cancer cell lines (lysates only) spanning the EM spectra (Le et al., 2018). This revealed the reported EM marker profile. (Figure 3.3A and B).

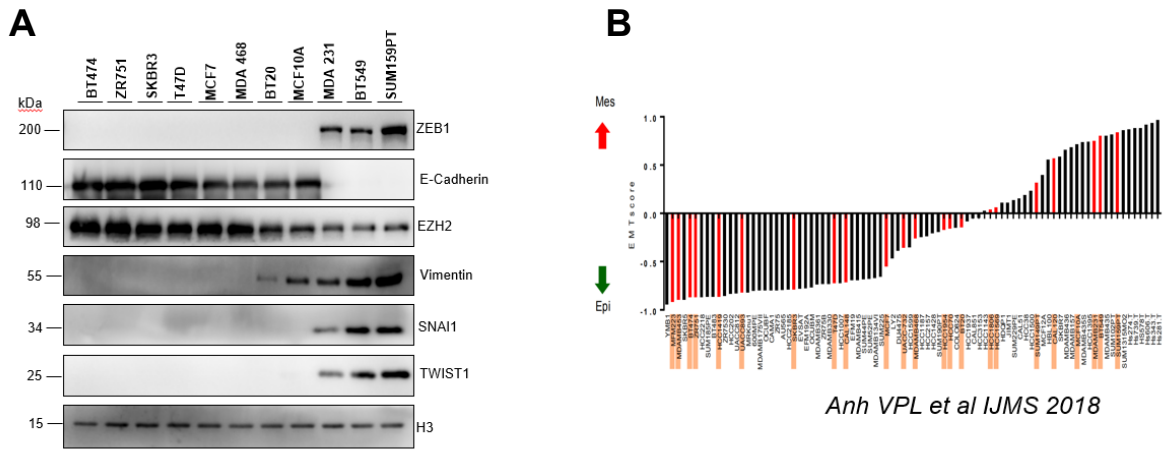


***Figure 3.3: EM profile of breast cancer cells****: (A) 11 cells of breast origin were arranged based on reported EM characteristics with increasing mesenchymal nature (loading control same as figure 3.5J). (MDA 468: MDA-MB-468 and MDA 231: MDA-MB-231) (B) Report showing breast cancer cell lines with epithelial and mesenchymal characteristics*

### 3.2.2 Impact of EMT Induction on Lamin A/C Expression

As cells undergo epithelial-to-mesenchymal transition (EMT), they experience not only a dramatic reshaping of their external morphology and cytoskeletal framework but also profound intracellular and nuclear alterations (Kim et al., 2019). While much attention has been directed toward the reprogramming of transcriptional networks and cytoplasmic structures during EMT, changes in nuclear architecture—particularly involving structural proteins such as lamins—are increasingly recognized as integral to cellular plasticity (Liu et al., 2013; Ha et al., 2014). Nuclear lamins, specifically Lamin A/C (encoded by the *LMNA* gene) and B-type lamins, assemble into a dense fibrous meshwork known as the nuclear lamina, located just beneath the inner nuclear membrane (Laberge et al., 2015; Ebrahimi et al., 2018). This lamina not only provides mechanical support and maintains nuclear shape but also interfaces with chromatin to regulate genome organization and gene expression programs (Eldholm et al., 2014; Laberge et al., 2015).

Among the nuclear lamins, Lamin A/C is particularly sensitive to changes in cellular state and identity. Its expression and post-translational modifications are dynamically regulated during differentiation (Holwerda and de Laat, 2013), in response to mechanical cues (Puisieux et al., 2014), and under pathological conditions such as cancer, where altered Lamin A/C levels have been associated with tumor progression and metastasis (Watanabe et al., 2001; Shimi et al., 2008; Dongre and Weinberg, 2019). Given this context, and considering the extensive cellular and cytoskeletal remodeling intrinsic to EMT, we hypothesized that nuclear architecture—particularly Lamin A/C abundance and organization—might be similarly altered during this transition. Thus, to explore whether EMT induction has consequences for the nuclear lamina, we specifically examined the expression levels and distribution of Lamin A/C during epithelial-mesenchymal transitions.

First, we assessed nuclear morphology following EMT induction in MCF7 cells. Although total nuclear area and volume remained relatively constant, significant reductions in nuclear sphericity and circularity were observed in TWIST1-overexpressing cells (Sphericity: MCF7 = 0.94 ± 0.03; MCF7-TWIST1 = 0.50 ± 0.09, $p < 0.0001$) (Figures 3.4A and 3.4D). These changes reflect a transition to an irregular, elongated nuclear shape typical of mesenchymal cells. By contrast, MET induction via GRHL2 in MDA-MB-231 cells restored nuclear circularity (Sphericity: control = 0.45 ± 0.08; GRHL2 = 0.94 ± 0.03) (Figures 3.4C, 3.4F), indicating reversibility of nuclear architecture alongside phenotypic state.

To explore Lamin expression patterns across breast cancer subtypes, we profiled Lamin A/C, Lamin B1, and B2 levels in 11 breast cancer cell lines with known EMT statuses. We observed a clear trend with Lamin A/C expression progressively lowered in mesenchymal-like lines, while Lamin B1 and B2 levels did not show any trend with increasing mesenchymal cell states (Figure 3.5J). This differential expression points to a potential role of Lamin A/C in maintaining epithelial nuclear architecture.

Subsequently, we analyzed Lamin A/C expression following EMT induction in MCF7 and MCF10A cells. In both systems, EMT was associated with a significant reduction in Lamin A/C protein levels (Figures 3.5A–F). Conversely, GRHL2-induced MET in MDA-MB-231 cells resulted in a robust increase in Lamin A/C (Figures 3.5G–I). Notably, B-type lamin levels remained largely unaffected (Figures 3.4G–3.4J). Quantitative PCR showed that LMNA transcript levels remained constant across EMT/MET conditions (Figure 3.5K), indicating that Lamin A/C regulation is likely post-transcriptional.

These results highlight Lamin A/C as a dynamically regulated nuclear component that responds to epithelial-mesenchymal transitions, reinforcing the notion that nuclear structure is intimately tied to cell identity.

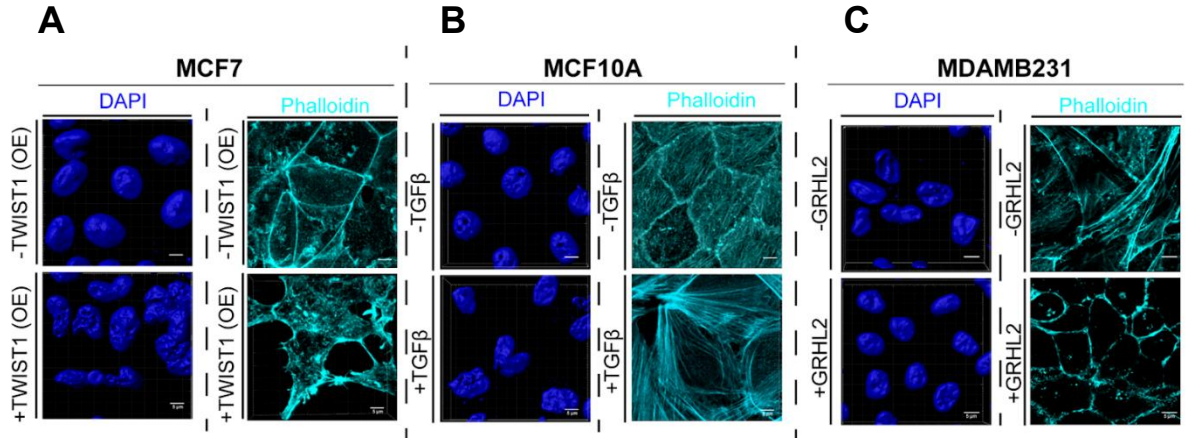

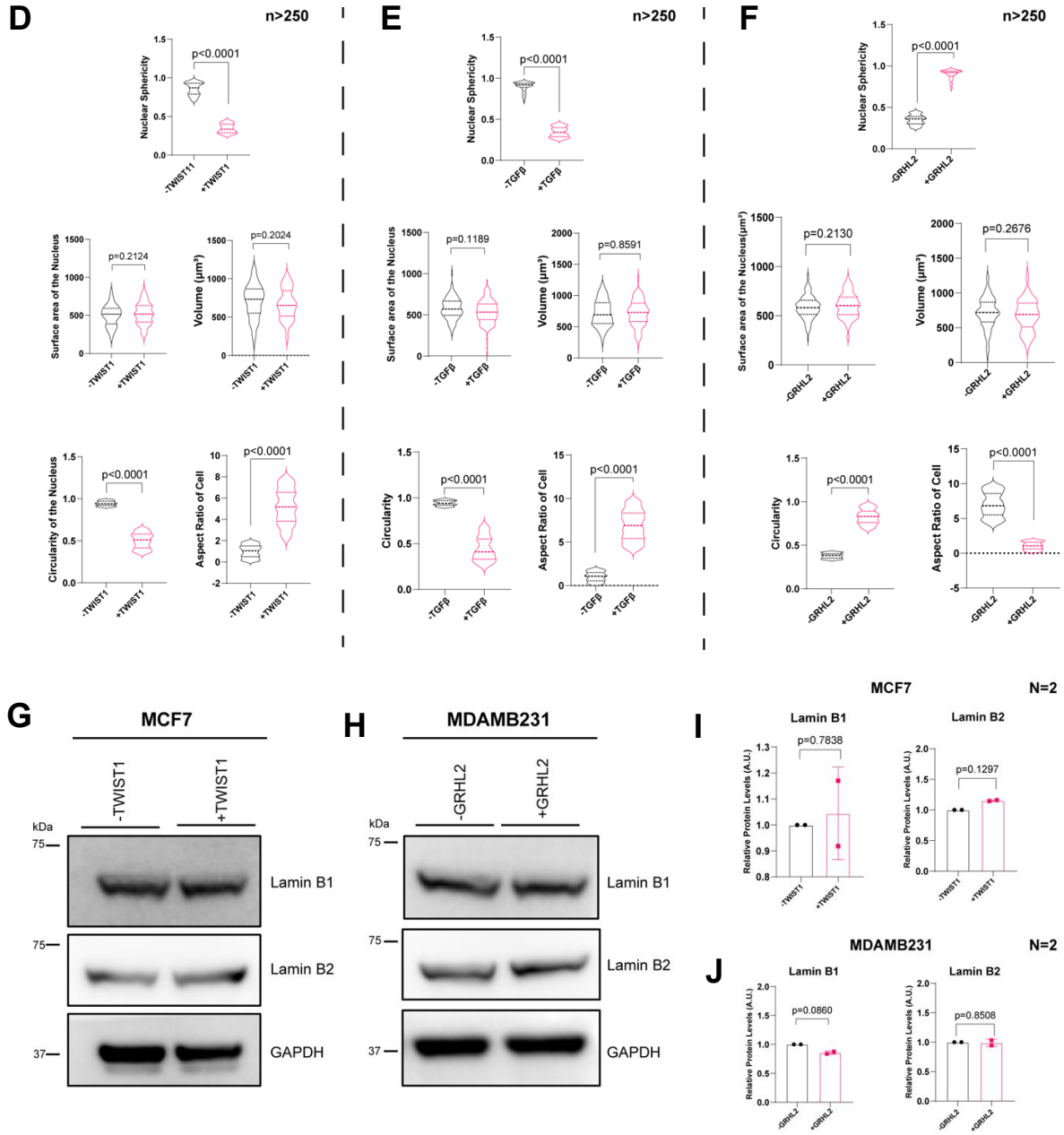


***Figure 3.4. Nuclear Architecture Remodeling and Lamin B Dynamics During EMT and MET.***

***(A–C)*** *3D reconstruction of nuclei (DAPI) and mid-optic section of the cytoskeleton (Phalloidin, cyan) in MCF7 cells overexpressing pEGFP-N1 or TWIST1-GFP (A), MCF10A cells induced with 10 ng/mL TGF-β (B), and MDA-MB-231 cells overexpressing GRHL2 (C) (Scale bar ~5µm).* ***(D–F)*** *Quantification of nuclear sphericity, surface area, volume, circularity, and cell aspect ratio in MCF7 (D), MCF10A (E), and MDA-MB-231 (F) cells. Data represent n>250 cells. An unpaired Student's t-test was used for statistical analysis.* ***(G, H)***

*Immunoblot analysis of Lamin B1 and Lamin B2 levels following EMT induction by TWIST1 in MCF7 cells (G) and MET induction by GRHL2 in MDA-MB-231 cells (H). (I, J) Quantification of relative Lamin B1 and Lamin B2 protein levels from (G, H). Data represent mean ± SEM from two independent biological replicates. An unpaired Student's t-test was used for statistical analysis.*

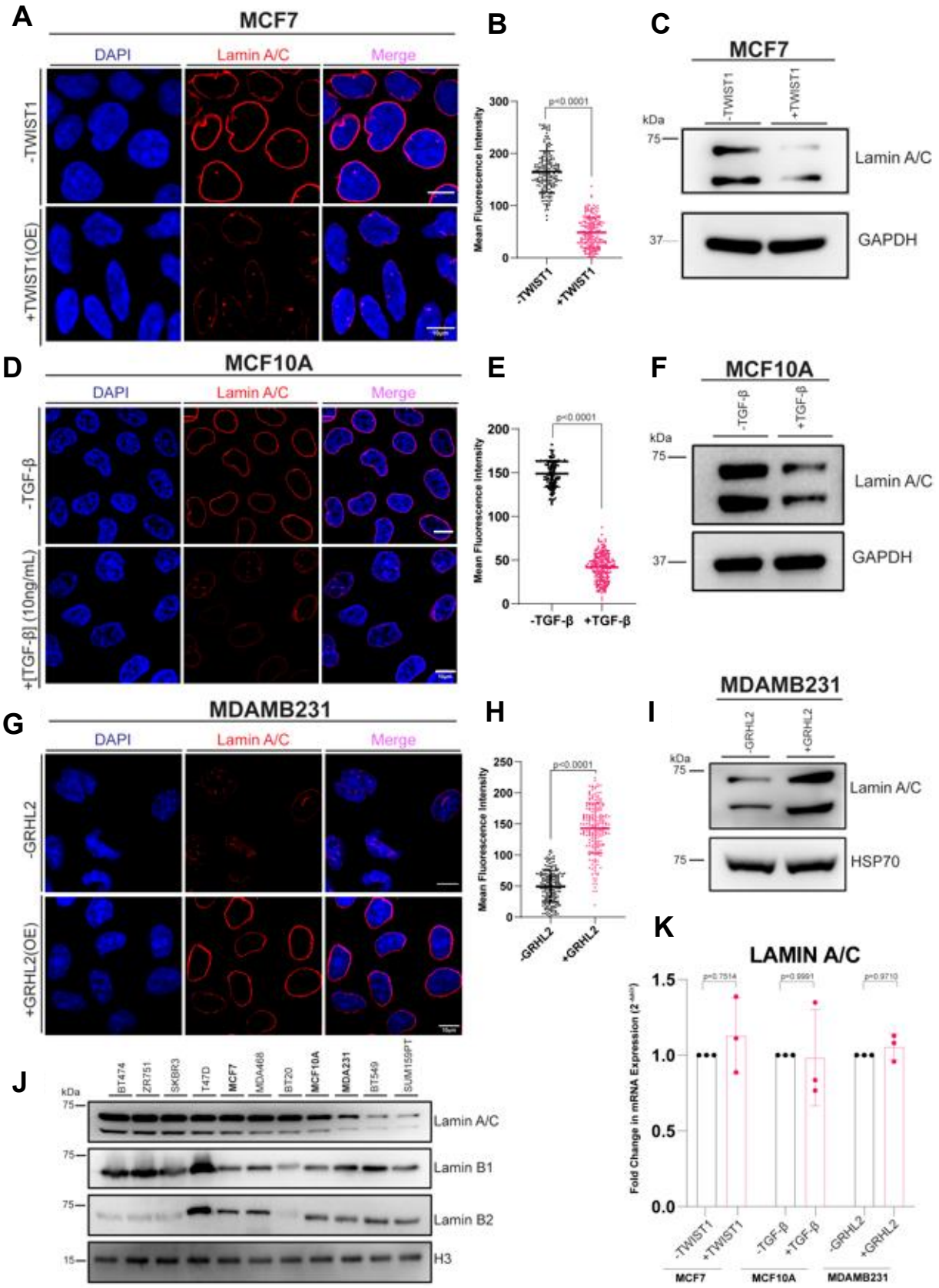


***Figure 3.5: Impact of EMT induction on Lamin A/C expression***

*(A, D, G) Immunofluorescence analysis of Lamin A/C (red) in MCF7 (A), MCF10A (D), and*

*MDA-MB-231 (G) cells undergoing EMT or MET. (B, E, H) Mean fluorescence intensity of Lamin A/C quantified by line scan analysis across the nucleus in MCF7 (B), MCF10A (E), and MDA-MB-231 (H) cells. Data represent mean ± SD from three independent biological replicates (n > 250). Unpaired Student's t-test was used to calculate p-values. (C, F, I) Immunoblot analysis of total Lamin A/C protein levels in MCF7 (C), MCF10A (F), and MDA-MB-231 (I) cells upon EMT (C, F) or MET (I) induction. GAPDH (C, F) and HSP70 (I) serve as loading controls. (J) Immunoblot analysis of Lamin A/C, Lamin B1, and Lamin B2 levels across 11 breast cancer cell lines with increasing mesenchymal characteristics. Histone H3 serves as the loading control. (K) RT-qPCR analysis of LMNA transcript levels in MCF7 and MCF10A cells undergoing EMT and in MDA-MB-231 cells undergoing MET. Data represent mean ± SD from three independent biological replicates (N = 3, n = 9). Unpaired Student's t-test was used to calculate p-values.*

### 3.2.3 Stability of Lamin A/C upon EMT

During epithelial–mesenchymal transition (EMT), we observed a pronounced reduction in the overall protein levels of Lamin A/C, while the corresponding LMNA transcript levels remained essentially unchanged. This lack of concordance between mRNA and protein expression strongly suggests that Lamin A/C downregulation occurs through post-transcriptional mechanisms rather than through transcriptional repression. Given the central role of Lamin A/C in maintaining nuclear architecture and chromatin organization, we next sought to determine whether EMT influences the protein stability of Lamin A/C.

To investigate this, we performed a cycloheximide (CHX) chase assay to monitor Lamin A/C degradation dynamics under epithelial and mesenchymal conditions. MCF7 cells stably expressing TWIST1, a well-established EMT transcription factor, were used to induce a mesenchymal phenotype, while cells transfected with the empty vector served as epithelial controls. Both cell populations were treated with CHX (10 μg/mL) to inhibit de novo protein synthesis, thereby allowing the assessment of Lamin A/C turnover solely as a function of degradation. Whole-cell lysates were harvested with Urea buffer (8 M urea, 1% SDS, 50 mM Tris-HCl pH 7.5, 150 mM NaCl, 1 mM EDTA, 1 mM DTT, and freshly added 1x protease and phosphatase inhibitor cocktails) at 0, 2, 4, 8, 12, and 24 hours after CHX treatment, and Lamin A/C levels were analyzed by immunoblotting and normalized to β-actin.

In epithelial control cells, Lamin A/C levels remained relatively stable throughout the 24-hour time course, consistent with the long half-life and low basal turnover rate typically associated with nuclear lamins under homeostatic conditions. In contrast, TWIST1-expressing cells displayed a progressive and time-dependent reduction in Lamin A/C protein abundance, with a marked decrease evident after 8 hours and a near-complete loss by 24 hours. This accelerated decline in Lamin A/C levels under mesenchymal conditions indicates a substantial reduction in protein stability, suggesting that EMT triggers mechanisms that actively promote Lamin A/C degradation (Figure 3.6A and B).

To determine the pathway responsible for this enhanced turnover, we examined the effect of proteasome inhibition on Lamin A/C stability. TWIST1-expressing MCF7 cells were co-treated with MG132 (1 μM), a potent proteasome inhibitor, along with CHX. Remarkably, the co-treatment prevented Lamin A/C degradation, with protein levels remaining comparable to those observed in untreated controls even after 8 hours of CHX exposure. This rescue effect

upon MG132 treatment clearly implicates the ubiquitin–proteasome system as the primary route mediating Lamin A/C degradation during EMT (Figure 3.6C and D).

Together, these findings demonstrate that EMT induction by TWIST1 leads to a significant destabilization of Lamin A/C through a proteasome-dependent degradation mechanism. The selective targeting of Lamin A/C for proteasomal turnover during EMT likely represents an adaptive process to remodel the nuclear lamina and alter chromatin organization, thereby facilitating the transcriptional and structural reprogramming necessary for mesenchymal transition. This post-translational regulation of Lamin A/C underscores the dynamic interplay between nuclear architecture and cellular plasticity, providing mechanistic insight into how the nuclear envelope contributes to the epigenetic and phenotypic remodeling associated with EMT.

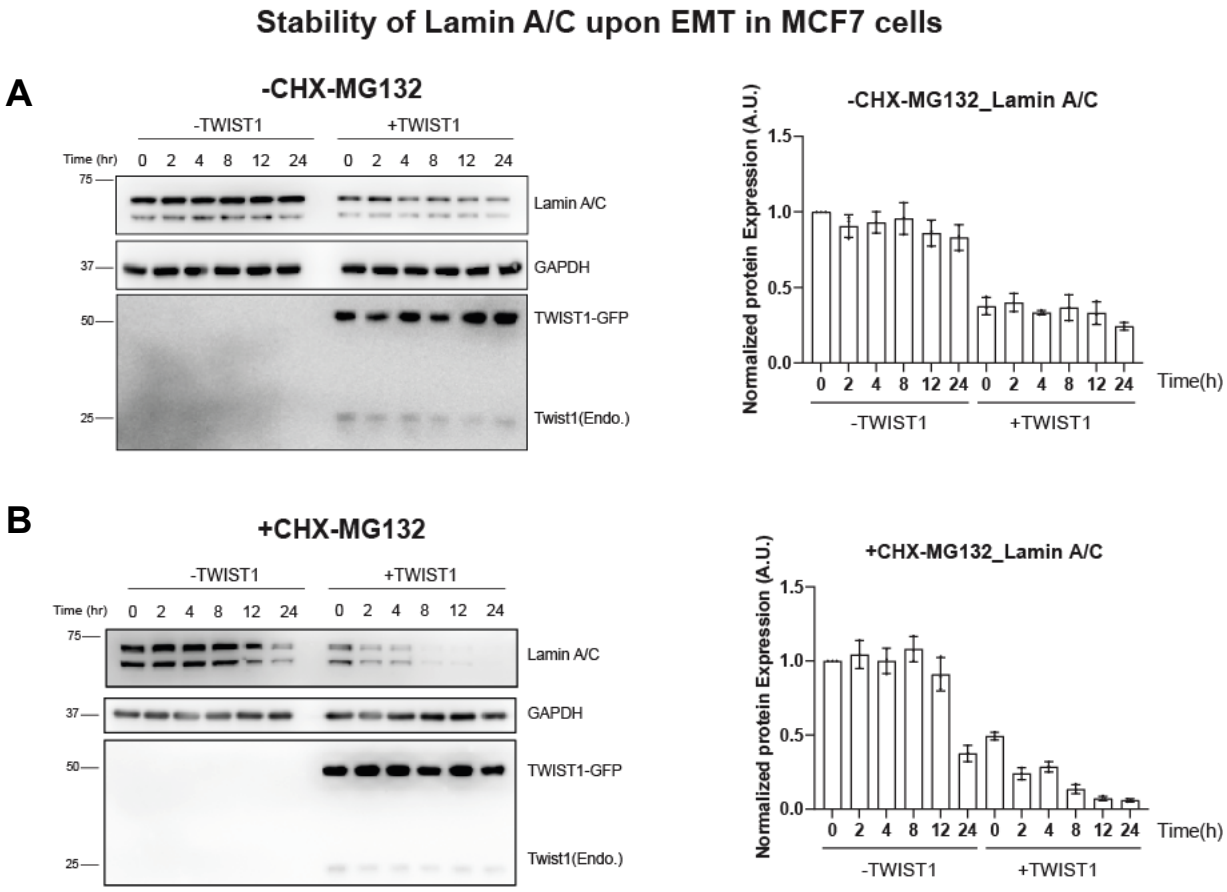

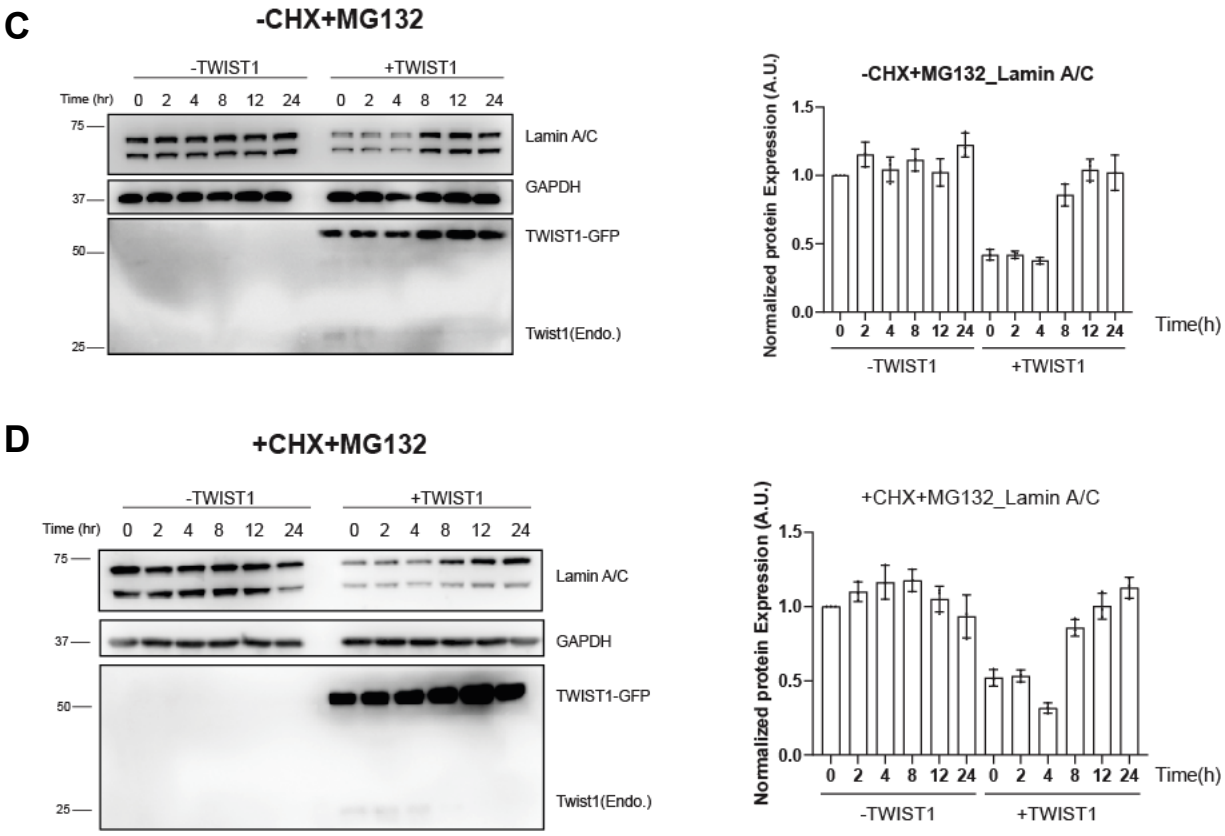


***Figure 3.6 Cycloheximide (CHX) chase assay to evaluate Lamin A/C stability in MCF7 cells.***

***(A)*** *Untreated control (–CHX/–MG132).* ***(B)*** *CHX treatment alone (+CHX/–MG132).* ***(C)*** *MG132 treatment alone (–CHX/+MG132).* ***(D)*** *Combined CHX and MG132 treatment (+CHX/+MG132). MCF7 cells with or without TWIST1 expression were treated with cycloheximide (10 µg/mL) in the presence or absence of MG132 (1 µM) and harvested at the indicated time points. Protein lysates were subjected to immunoblotting for Lamin A/C, GAPDH (loading control), and TWIST1. Representative immunoblots are shown along with quantification of Lamin A/C levels normalized to GAPDH. Bar graphs represent the mean ± SD of three independent experiments.*

### 3.2.4 Effect of Lamin A/C Perturbation on EMT and MET

To dissect the functional role of Lamin A/C in regulating EMT and MET, we conducted RNA-sequencing in MCF10A cells following siRNA-mediated depletion of Lamin A/C. Differential gene expression analysis identified strong upregulation of genes associated with EMT, cell migration, adhesion dynamics, and tumor progression. Gene Ontology (GO) analysis revealed enrichment in biological processes related to cell-cell adhesion disassembly, cytoskeletal reorganization, and secondary tumor formation (Figure 3.8C). GSEA showed enrichment of hallmark gene sets, including epithelial-mesenchymal transition, wound healing, and focal adhesion (Figures 3.8D).

Consistent with these analyses, Lamin A/C depletion led to increased expression of mesenchymal markers such as VIM, SNAI1, TWIST1, and ZEB1. Simultaneously, epithelial markers including CDH1 (E-cadherin), OCLN, and CLDN1 were significantly downregulated, indicative of a complete EMT program (Figures 3.8A, 3.8B). These effects were recapitulated in MCF7 cells, where Lamin A/C depletion also promoted mesenchymal gene expression and suppressed epithelial gene expression (Figure 3.8E and 3.8H).

Protein-level validations confirmed the transcriptomic findings. Immunoblotting and immunofluorescence demonstrated ~70% reduction in E-cadherin and ~65% increase in Vimentin upon Lamin A/C knockdown in both MCF7 and MCF10A cells (Figures 3.8E,3.8F, 3.8H and 3.8I).

To evaluate whether restoring Lamin A expression could reverse mesenchymal traits, we overexpressed Lamin A in MDA-MB-231 cells after knocking down endogenous Lamin A/C. This intervention led to a dramatic re-expression of E-cadherin (>95%) and downregulation of Vimentin and mesenchymal transcription factors (Figures 3.7K, 3.8G and 3.8J). The cells also reverted to a more epithelial morphology, as reflected by reduced elongation and increased nuclear circularity.

We further examined whether B-type lamins play a similar role. However, depletion of Lamin B1 or B2 in MCF7 and MDA-MB-231 cells did not significantly alter EMT markers (Figures 3.7M, 3.7N), suggesting that A-type lamins have a unique role in regulating EMT/MET dynamics.

Collectively, these data underscore the pivotal function of Lamin A/C as a modulator of epithelial-mesenchymal plasticity. Its expression is dynamically regulated during EMT and MET, and its manipulation directly impacts cellular identity, morphology, and transcriptional programs. These findings provide critical insights into how alterations in nuclear architecture contribute to cancer cell plasticity and metastatic competence.

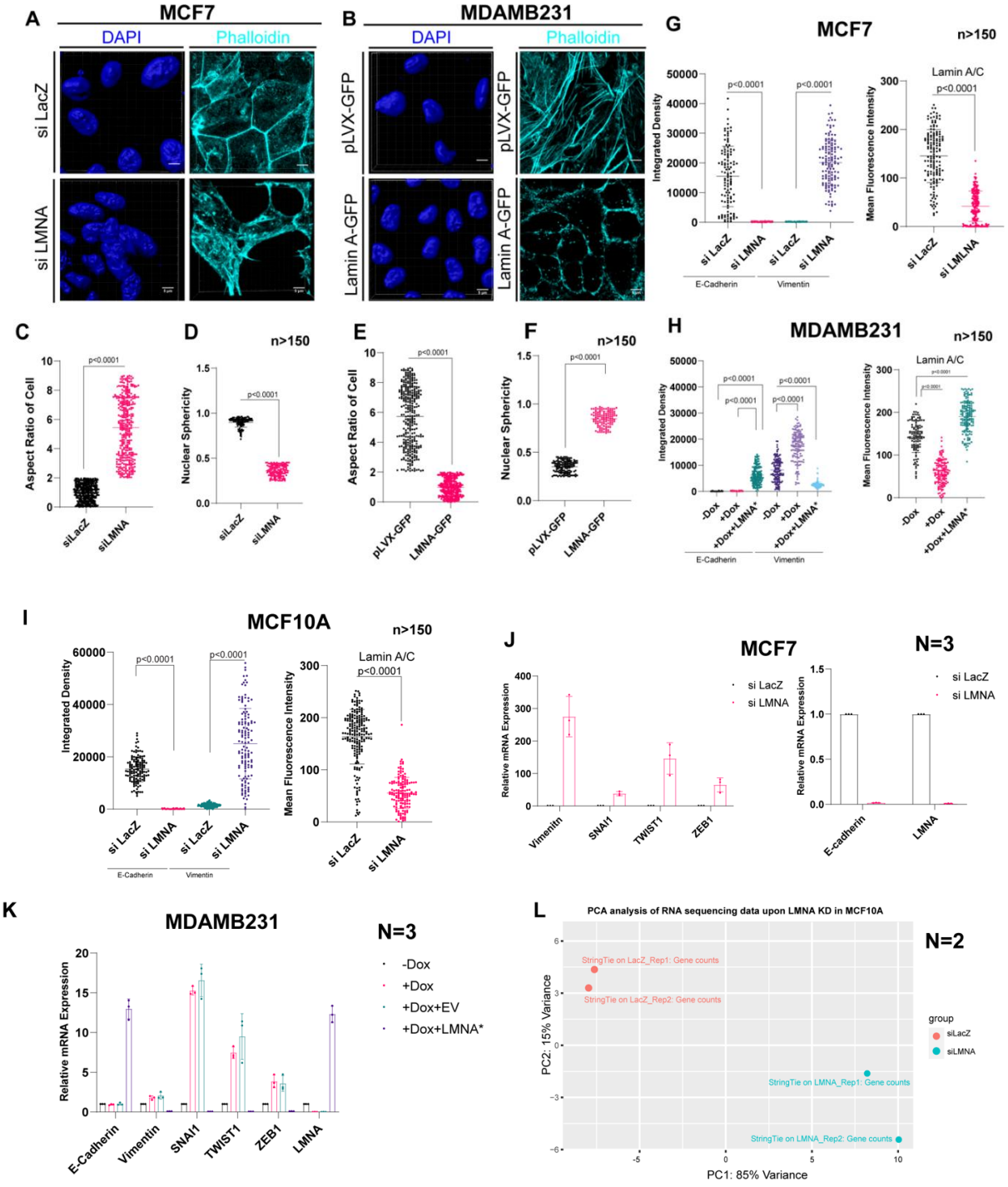

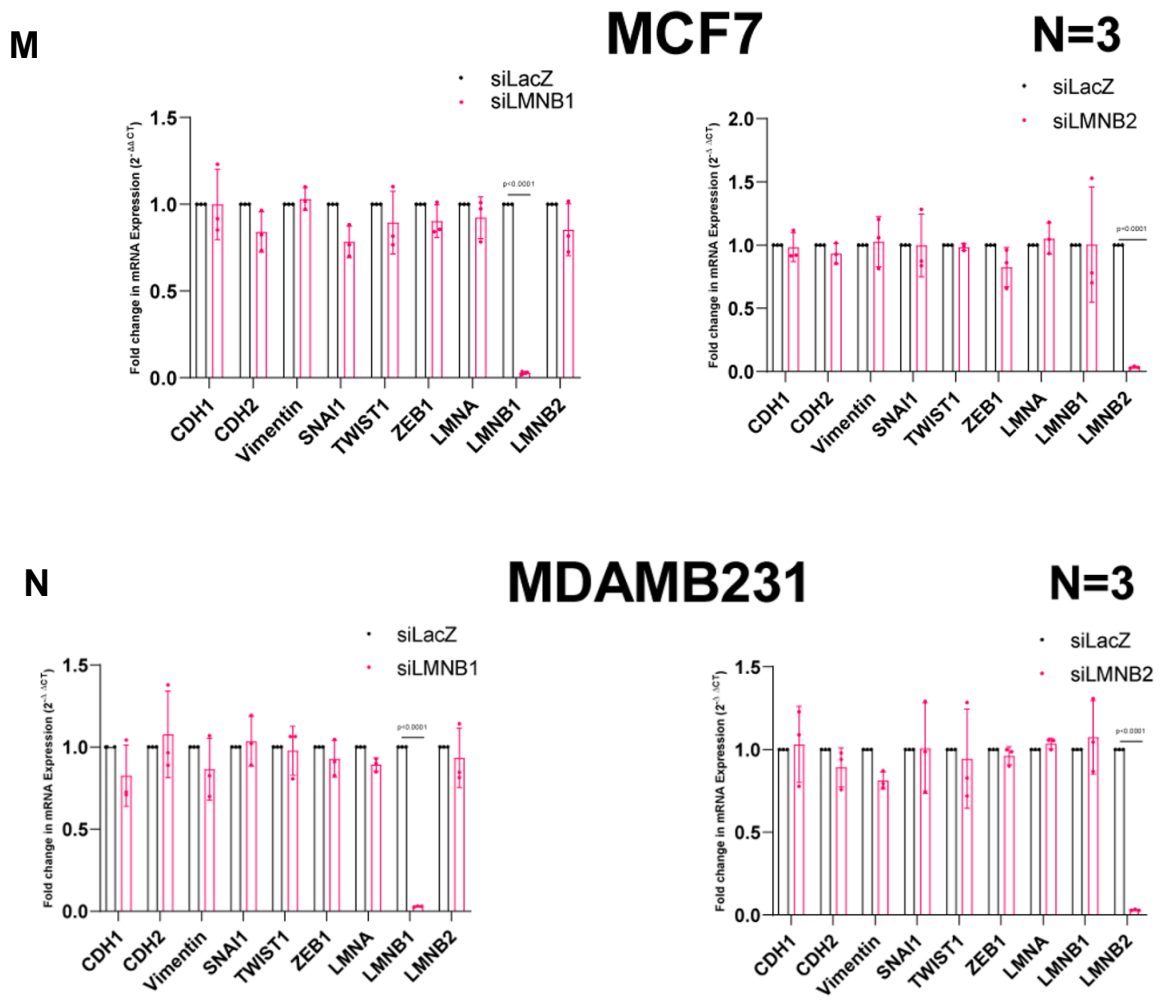


***Figure 3.7: Effects of A and B-type Lamin perturbation on nuclear morphology and EMT marker expression.***

***(A, B)*** *Representative 3D nuclear reconstructions and mid-optical sections of MCF7 cells upon Lamin A/C knockdown (A) and MDA-MB-231 cells upon Lamin A overexpression (B).* ***(C, D)*** *Scatter plots quantifying the aspect ratio (C) and nuclear sphericity (D) in MCF7 cells upon Lamin A/C knockdown (n = 164).* ***(E, F)*** *Scatter plots quantifying the aspect ratio (E) and nuclear sphericity (F) in MDA-MB-231 cells upon Lamin A overexpression (n > 150). Statistical significance was determined using an unpaired Student's t-test.* ***(G, H)*** *Scatter plots showing the integrated density of E-cadherin and Vimentin in MCF7 upon Lamin A/C knockdown (G) and MDA-MB-231 cells following Lamin A overexpression (H). Mean fluorescence intensity of Lamin A/C is shown to indicate knockdown (G) or overexpression (H) efficiency (n >150). Statistical significance was determined using an unpaired Student's t-test (G) or one-way ANOVA (H).* ***(I)*** *Scatter plot quantifying the integrated density of E-cadherin*

*and Vimentin in MCF10A cells upon Lamin A/C knockdown. Mean fluorescence intensity of Lamin A/C is shown to confirm knockdown efficiency. Statistical significance was determined using an unpaired Student's t-test.* ***(J, K)*** *RT-qPCR analysis of EMT marker transcript levels in MCF7 upon Lamin A/C depletion (J) and MDA-MB-231 upon Lamin A overexpression (K).* ***(L)*** *Principal component analysis (PCA) illustrates the reproducibility of RNA sequencing datasets between control and Lamin A/C knockdown MCF10A samples from two independent biological replicates.* ***(M, N)*** *RT-qPCR analysis of EMT marker transcript levels following Lamin B1 and Lamin B2 knockdown in MCF7 (M) and MDA-MB-231 (N) cells.*

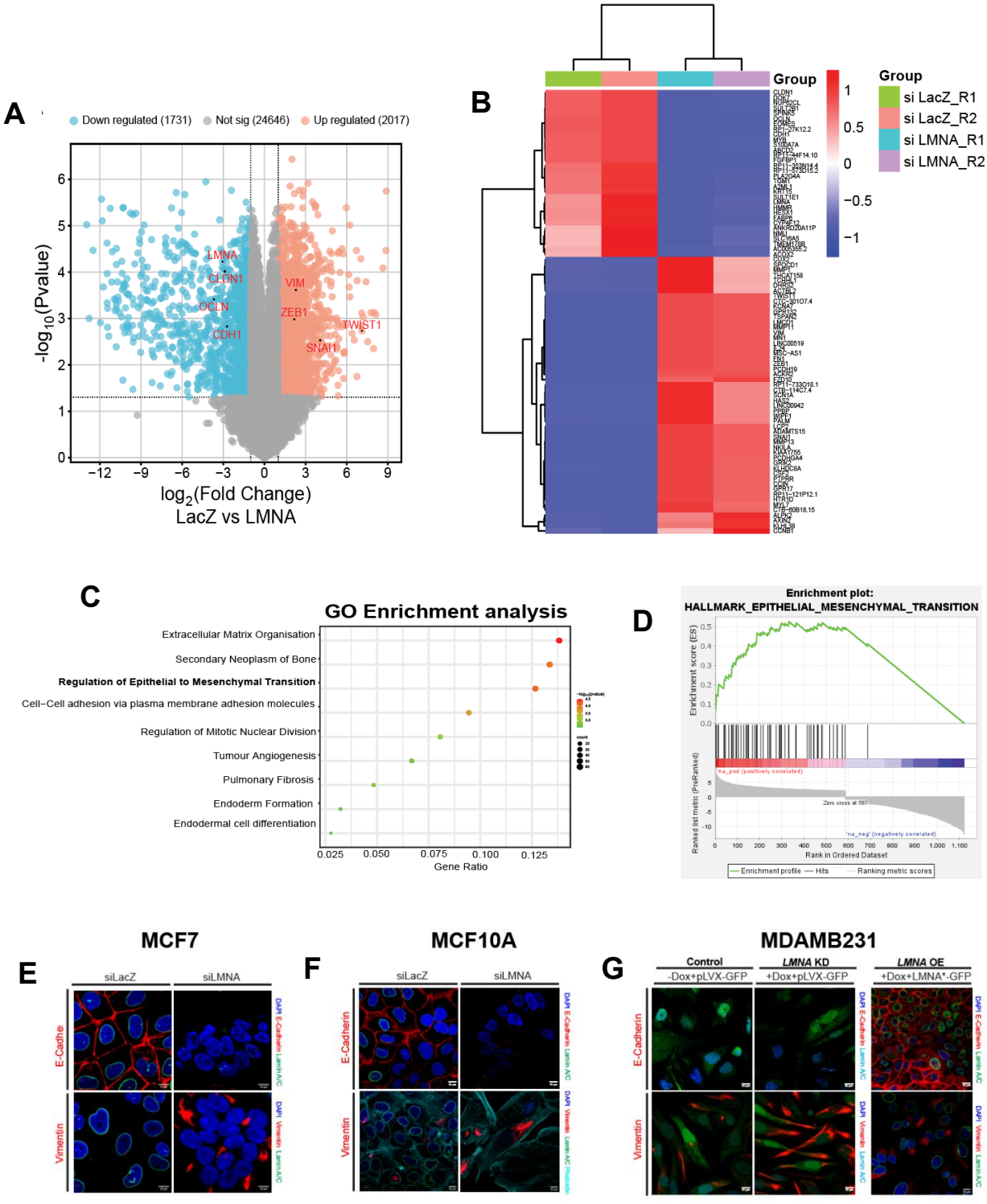
A
Down regulated (1731)
Not sig (24646)
Up regulated (2017)
-log10(Pvalue)
log2(Fold Change)
LacZ vs LMNA
LMNA
CLDN1
OCLN
CDH1
VIM
ZEB1
SNAI1
TWIST1
B
Group
si LacZ_R1
si LacZ_R2
si LMNA_R1
si LMNA_R2
C
GO Enrichment analysis
Extracellular Matrix Organisation
Secondary Neoplasm of Bone
Regulation of Epithelial to Mesenchymal Transition
Cell–Cell adhesion via plasma membrane adhesion molecules
Regulation of Mitotic Nuclear Division
Tumour Angiogenesis
Pulmonary Fibrosis
Endoderm Formation
Endodermal cell differentiation
Gene Ratio
D
Enrichment plot:
HALLMARK_EPITHELIAL_MESENCHYMAL_TRANSITION
Enrichment score (ES)
Ranked list metric (PreRanked)
Rank in Ordered Dataset
Enrichment profile
Hits
Ranking metric scores
E
MCF7
siLacZ
siLMNA
E-Cadherin
Vimentin
F
MCF10A
siLacZ
siLMNA
E-Cadherin
Vimentin
G
MDAMB231
Control
-Dox+pLVX-GFP
LMNA KD
+Dox+pLVX-GFP
LMNA OE
+Dox+LMNA*-GFP
E-Cadherin
Vimentin

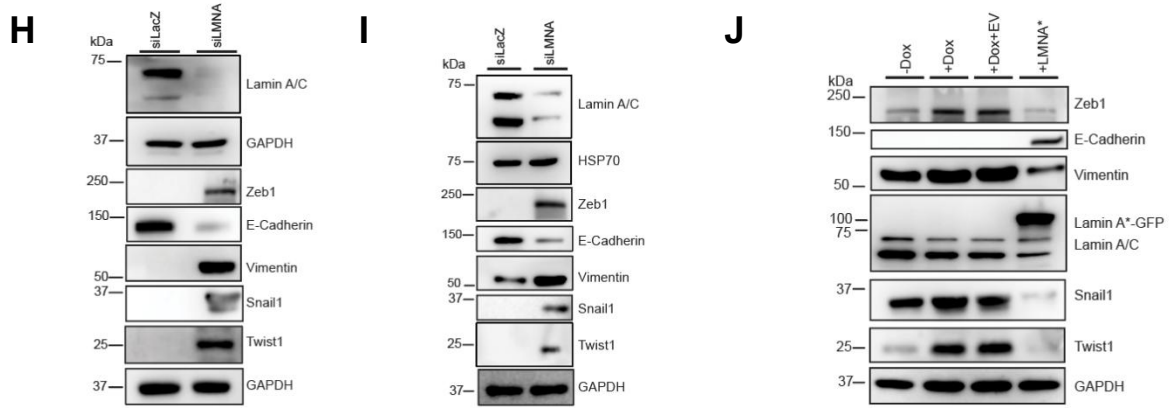


***Figure 3.8: Effect of Lamin A/C perturbation on EMT and MET*** *(A) Volcano plot of differentially expressed genes in MCF10A cells upon Lamin A/C knockdown. Blue, red, and grey indicate downregulated, upregulated, and non-significant genes, respectively. (B) Heatmap of the top differentially expressed genes in MCF10A cells upon Lamin A/C knockdown. Blue and red indicate downregulated and upregulated genes, respectively (n = 2 biological replicates). (C) GO enrichment analysis of differentially expressed genes ($p \leq 0.05$), showing the most enriched biological processes. (D) GSEA plot showing EMT pathway enrichment upon Lamin A/C knockdown (NES = 3.337). (E, F) Immunofluorescence analysis of MCF7 (E) and MCF10A (F) cells upon Lamin A/C knockdown. Lamin A/C (green), E-cadherin or Vimentin (red), and Phalloidin (Cyan). Scale bars, 10 µm. (G) Immunofluorescence analysis of MDA-MB-231 cells overexpressing Lamin A*-GFP upon endogenous Lamin A/C depletion. E-cadherin (top panel) or Vimentin (bottom panel) (red), and Lamin A/C (-Dox and +Dox panels only) (cyan). Scale bar, 10 µm. (H–J) Immunoblot analysis of EMT markers in MCF7 (H), MCF10A cells upon Lamin A/C knockdown (I), and MDA-MB-231 (J) cells upon Lamin A overexpression. RNA sequencing was performed in two independent biological replicates. All other experiments were performed in three biological replicates. Lamin A* denotes a wild-type Lamin A construct engineered to be resistant to doxycycline-induced depletion of endogenous Lamin A/C.*

### 3.2.5 Lamin A/C Regulates Heterochromatin Organization During EMT and MET

Given our findings that Lamin A/C expression dynamically responds to epithelial–mesenchymal transitions and that its depletion promotes mesenchymal gene expression programs, we next examined whether these changes extend to chromatin-level regulation. Nuclear lamins, particularly Lamin A/C, are not only architectural components of the nuclear envelope but also key regulators of genome organization and gene expression. A growing body of evidence suggests that Lamin A/C physically associates with specific regions of the genome known as LADs. These LADs are typically enriched for transcriptionally repressive, heterochromatic histone modifications such as H3K9me3 (trimethylation of histone H3 at lysine 9) and H3K27me3 (trimethylation of histone H3 at lysine 27). These histone marks are well-established indicators of compacted chromatin states and are crucial for maintaining epigenetic silencing in differentiated epithelial cells.

To investigate whether EMT and MET modulate global heterochromatin levels, we first assessed the abundance of H3K9me3 and H3K27me3 in epithelial cells undergoing mesenchymal reprogramming. Immunoblotting of whole-cell lysates revealed that upon EMT induction—either through TWIST1 overexpression in MCF7 cells or prolonged TGF-β treatment in MCF10A cells—there was a significant reduction in global heterochromatic content. Specifically, the total levels of both H3K9me3 and H3K27me3 were reduced by approximately 50%, suggesting a genome-wide relaxation of chromatin (Figures 3.9A(i) and 3.9B(i)). This decrease in repressive chromatin marks aligns with the observed transcriptional activation of mesenchymal genes, which are typically silenced in epithelial cells through heterochromatic repression.

In contrast, the process of MET led to an opposite trend. When GRHL2 was overexpressed in MDA-MB-231 cells—driving a shift from a mesenchymal to an epithelial phenotype—we observed a ~60% increase in H3K9me3 and H3K27me3 levels (Figure 3.9C(i)). This increase in heterochromatic marks coincided with repression of mesenchymal transcription factors and restoration of epithelial gene expression, suggesting that the re-establishment of epithelial identity involves chromatin compaction and epigenetic silencing of mesenchymal programs.

To directly test whether Lamin A/C contributes to the observed changes in chromatin state, we next examined the effect of Lamin A/C perturbation on heterochromatin levels in both epithelial and mesenchymal contexts. Knockdown of Lamin A/C in epithelial MCF7 and

MCF10A cells led to a substantial reduction in H3K27me3 and H3K9me3 levels, each by approximately 50% (Figures 3.9A(ii) and 3.9B(ii)). This loss of heterochromatin mirrored the changes observed during EMT induction, further supporting the notion that Lamin A/C is essential for maintaining a compact chromatin landscape in epithelial cells. Given that LADs are frequently enriched with these heterochromatic marks, it is plausible that Lamin A/C depletion leads to detachment of LADs from the nuclear periphery and subsequent chromatin decompaction.

To determine whether Lamin A/C is sufficient to restore heterochromatin in a mesenchymal context, we overexpressed Lamin A in MDA-MB-231 cells, which generally exhibit low endogenous Lamin A/C levels and reduced heterochromatic content. Remarkably, Lamin A overexpression led to a significant increase in both H3K9me3 and H3K27me3 levels (Figure 3.9C(ii)), consistent with a more repressive chromatin environment. This suggests that Lamin A/C does not merely correlate with heterochromatin levels but actively contributes to their maintenance. B-Type Lamins do not show interaction with EZH2 while retaining their interaction with other heterochromatin markers like G9a (Figure 3.9F and 3.9G)

Taken together, these results provide strong evidence that Lamin A/C plays a central role in orchestrating chromatin organization during phenotypic transitions. By stabilizing heterochromatin and preserving repressive histone modifications, Lamin A/C acts as a gatekeeper of epithelial identity and epigenetic integrity. The loss of Lamin A/C during EMT facilitates chromatin relaxation and activation of mesenchymal programs, while its re-expression during MET re-establishes a silenced chromatin state conducive to epithelial differentiation. These findings underscore the integral connection between nuclear lamina composition, epigenetic architecture, and transcriptional plasticity in breast cancer progression.

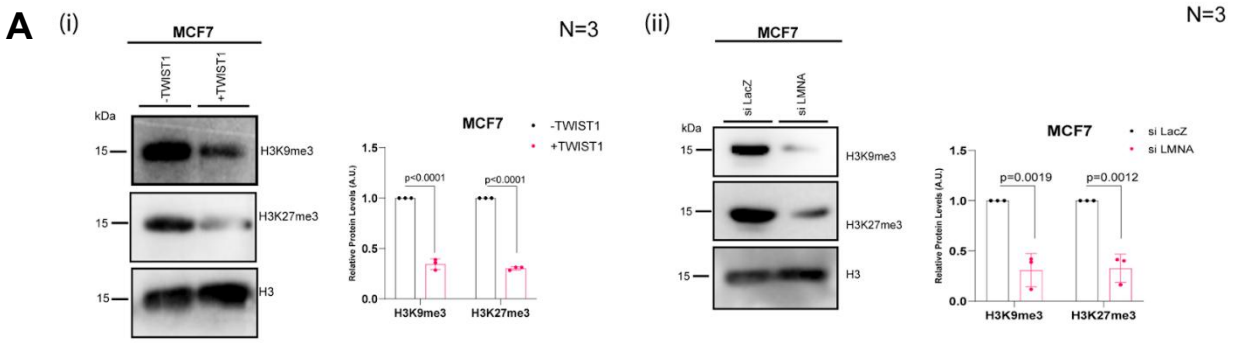

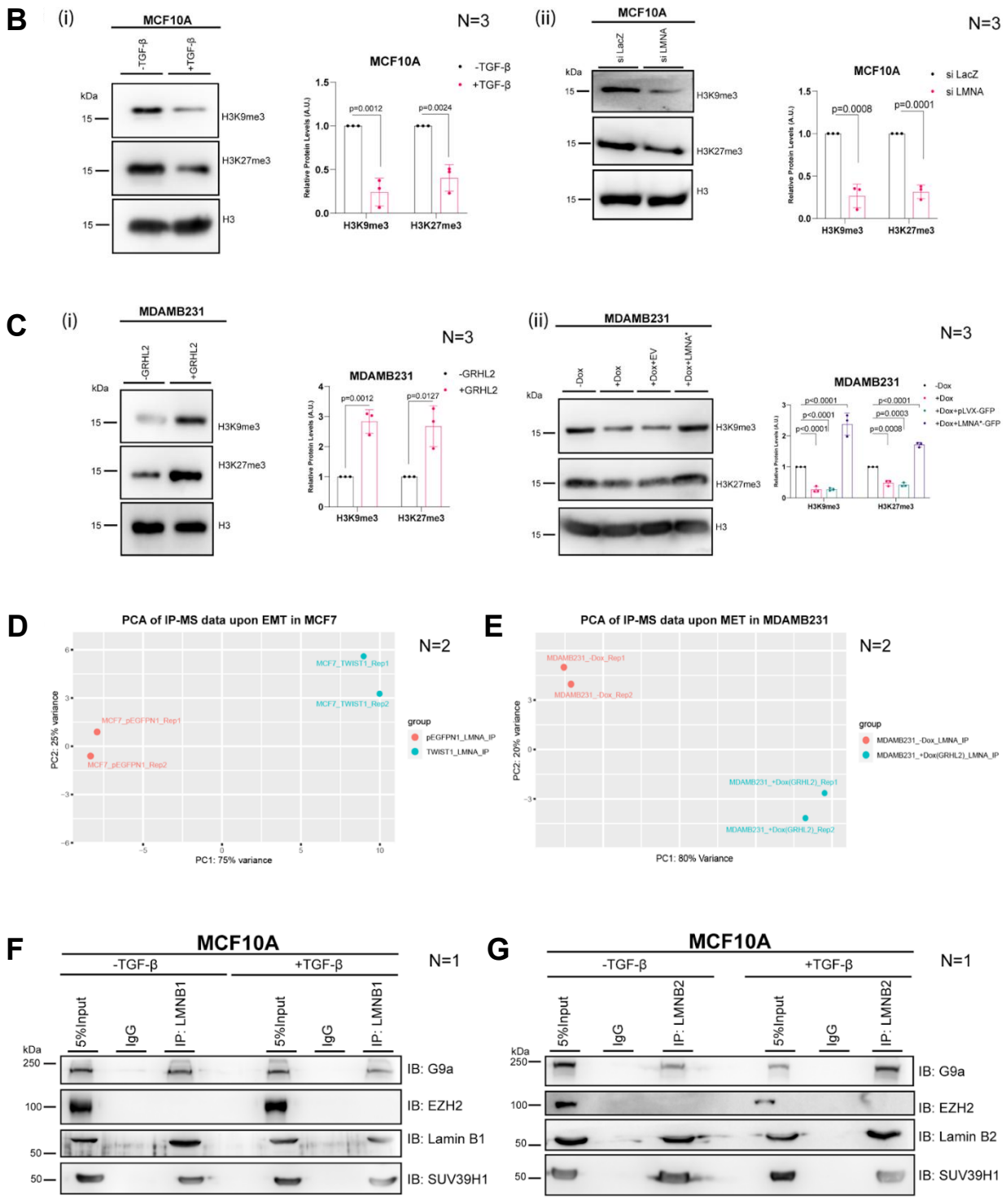


***Figure 3.9 Regulation of repressive histone modifications during EMT and MET.***

***(A)*** *Immunoblot analysis of H3K9me3 and H3K27me3 upon (i) TWIST1-induced EMT, (ii) Lamin A/C knockdown in MCF7* ***(B)*** *Immunoblot analysis of H3K9me3 and H3K27me3 upon (i) TGF-β-induced EMT, (ii) Lamin A/C knockdown in MCF10A Cells* ***(C)*** *Immunoblot analysis of H3K9me3 and H3K27me3 upon (i) GRHL2-induced MET (ii) Lamin A overexpression in*

*MDA-MB-231 cells. Densitometric quantification of H3K9me3 and H3K27me3 relative to total H3 in EMT (MCF7, MCF10A) and MET (MDA-MB-231) is given alongside the immunoblot. Data represent mean ± S.D. from three independent biological replicates; P-values were determined by unpaired Student's t-test.* ***(D, E)*** *PCA plots of mass spectrometry datasets showing replicate reproducibility upon EMT (MCF7) and MET (MDA-MB-231).* ***(F, G)*** *Co-immunoprecipitation of Lamin B1 (F) and Lamin B2 (G) in MCF10A upon TGF-β-induced EMT, followed by immunoblotting for EZH2, Suv39H1, and G9a.*

### 3.3 Discussion and Conclusion

The results presented in this chapter shed new light on the multifaceted role of Lamin A/C in regulating epithelial–mesenchymal plasticity in breast cancer. Through an integrative approach combining molecular, cellular, and genomic analyses, we establish Lamin A/C as a determinant of cellular identity, chromatin architecture, and transcriptional state during EMT and MET. The dynamic remodeling of the nuclear lamina and its profound influence on gene regulation point to a deeper and more nuanced understanding of how intracellular structural components govern cancer cell plasticity (Scheller et al., 2020; Wilson et al., 2020).

A cascade of morphological and molecular changes marks the induction of EMT. Our experimental systems—employing TWIST1 overexpression and TGF-β treatment in epithelial cells—consistently drove mesenchymal reprogramming, as evidenced by increased Vimentin, decreased E-cadherin, and upregulation of EMT transcription factors. These results reinforce the view that EMT is a transcriptionally regulated program, facilitated by external cues and internal regulators that collectively dismantle epithelial architecture while constructing a mesenchymal identity (Flavahan et al., 2016; Karoutas et al., 2019). Inversely, GRHL2-induced MET demonstrated the reversibility of this transition, suggesting that epithelial identity can be reinstated under suitable transcriptional influence (Cho et al., 2019).

Within this framework, the dynamic regulation of Lamin A/C emerged as a key feature of EMT and MET. Lamin A/C levels decreased consistently with EMT induction and increased with MET, highlighting their strong correlation with cellular phenotype (Lim and Thiery, 2012; Jolly et al., 2019). Notably, changes in Lamin A/C were not accompanied by alterations in LMNA transcript levels, suggesting post-transcriptional regulatory mechanisms, such as altered protein stability or degradation, are at play (Nava et al., 2020). Nuclear morphology analyses further revealed that Lamin A/C depletion contributes to nuclear deformation and loss of circularity—hallmarks of mesenchymal cells—which are reversed upon MET (Kimura, 2013).

Importantly, functional perturbation of Lamin A/C had profound consequences on cell identity. Depleting Lamin A/C in epithelial cells activated EMT-associated genes and suppressed epithelial markers, as confirmed through transcriptomic profiling and protein validation (Shimi et al., 2008). Conversely, reintroducing Lamin A in mesenchymal MDA-MB-231 cells restored epithelial markers and reversed mesenchymal traits (Gil et al., 2020). These manipulations

directly implicate Lamin A/C as not merely a marker of cellular state but a regulator of the transcriptional programs that define it (Wong and Stewart, 2020).

At the chromatin level, our data elucidate a mechanistic link between Lamin A/C and epigenetic regulation. Lamin A/C depletion led to a marked loss of heterochromatin-associated histone modifications (H3K9me3 and H3K27me3), both of which are essential for transcriptional silencing and maintenance of epithelial identity (Tzur et al., 2006). The reconstitution of Lamin A restored these marks, indicating its functional role in preserving epigenetic repression (Kadota et al., 2020). This underscores the idea that Lamin A/C not only provides nuclear stability but also anchors chromatin domains and maintains the epigenetic landscape required for proper gene regulation (Towbin et al., 2012; Kim et al., 2013).

The findings presented here align with and extend emerging literature on the role of the nuclear lamina in cancer. Previous studies have shown that loss of Lamin A/C correlates with poor differentiation and increased invasiveness in various cancers (Kim et al., 2012; Lu and Kang, 2019). Our work adds mechanistic depth to this observation by showing that Lamin A/C is an active suppressor of EMT and a guardian of epithelial state via transcriptional and chromatin-level mechanisms (Wilson et al., 2020).

Furthermore, these insights may have therapeutic implications. Given the reversibility of EMT and the role of Lamin A/C in this plasticity, modulating Lamin A/C expression or function could represent a strategy to curb metastatic progression or promote differentiation in aggressive tumors (H. Kang et al., 2019). Future studies might explore how Lamin A/C interacts with other chromatin modifiers or whether Lamin A/C levels could serve as a biomarker for therapeutic response in epithelial cancers (Johnstone et al., 2020; Nacev et al., 2020).

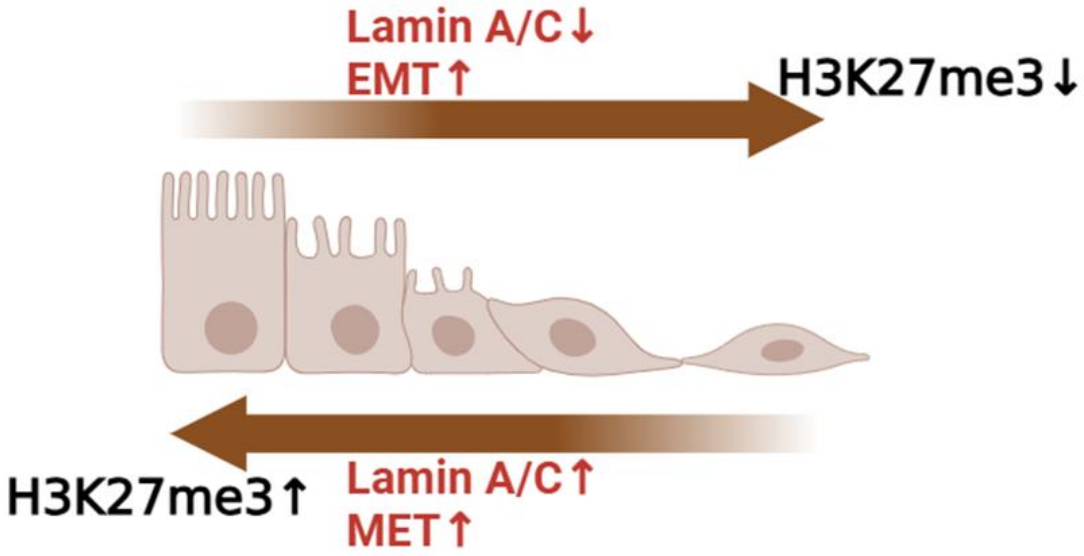


In conclusion, this chapter delineates a comprehensive model wherein Lamin A/C acts as both a sensor and effector of phenotypic plasticity in breast cancer. It integrates structural, transcriptional, and epigenetic layers of regulation to maintain epithelial identity and repress mesenchymal transformation. These findings provide a valuable foundation for understanding how alterations in nuclear architecture contribute to tumor progression and open new avenues for targeting cellular plasticity in cancer therapeutics.

# Chapter 4: Identification of the Unique interaction of Lamin A/C in Epithelial vs Mesenchymal cell States

## 4.1 Introduction

The architecture of the nucleus plays a central role in regulating various cellular functions, including gene expression, chromatin organization, and mechanical stability. Among the structural components of the nucleus, the nuclear lamina, composed predominantly of A-type and B-type lamins, serves as a critical scaffold for maintaining nuclear integrity and organizing the genome (Mitra et al., 2005; Nakaya and Sheng, 2008). Lamin A/C, encoded by the LMNA gene, has been increasingly recognized not only for its structural roles but also for its involvement in signal transduction, chromatin anchoring, and transcriptional regulation (Taddei et al., 2006; Friedl and Gilmour, 2009). Dysregulation of Lamin A/C has been implicated in a variety of human diseases, including muscular dystrophies, lipodystrophies, and cancers (Rossi et al., 2007). In the context of cancer, particularly those of epithelial origin such as breast cancer, alterations in Lamin A/C expression have emerged as pivotal modulators of phenotypic plasticity, including the transitions between epithelial and mesenchymal states (Jolly et al., 2019; Minchell et al., 2020).

Epithelial-to-mesenchymal transition (EMT) and its reverse, mesenchymal-to-epithelial transition (MET), represent dynamic and reversible processes during which cells undergo profound changes in morphology, adhesion, and gene expression. EMT endows epithelial cells with migratory and invasive capabilities and contributes to metastasis, stemness, and resistance to therapy (Flavahan et al., 2016; Cho et al., 2019). Conversely, MET is essential for metastatic colonization and the re-establishment of epithelial traits at distant sites (Cho et al., 2019). This bidirectional plasticity is orchestrated by a network of transcriptional regulators, signaling pathways, and epigenetic modifications. Despite extensive characterization of EMT/MET transcription factors such as SNAI1, TWIST1, ZEB1, and GRHL2, relatively little is known about how nuclear structural components, such as Lamin A/C, integrate with these pathways to influence cell fate decisions (Ikegami et al., 2020).

Emerging evidence points to a close association between the nuclear lamina and the transcriptional machinery that governs EMT and MET. Lamin A/C has been shown to modulate nuclear stiffness and chromatin compartmentalization, two properties that undergo substantial remodeling during EMT (Holwerda and de Laat, 2013; Kadota et al., 2020). Given the differences in nuclear morphology between epithelial and mesenchymal cells—where epithelial nuclei are generally more spherical and compact, while mesenchymal nuclei tend to be elongated and deformed—it is plausible that changes in Lamin A/C expression and

localization contribute to or are affected by the EMT process (Lim and Thiery, 2012). In addition, LADs, which are enriched in repressive histone marks such as H3K27me3 and H3K9me3 (Margueron et al., 2008; de Magalhães, 2013). These heterochromatic regions contribute to transcriptional silencing of lineage-inappropriate genes and are reorganized during EMT and MET (Taddei et al., 2006; Kim et al., 2012). Thus, Lamin A/C may influence gene expression patterns not only through physical nuclear structure but also by modulating the epigenetic landscape (Earle et al., 2020).

In light of these observations, the central objective of this chapter is to characterize the unique interaction of Lamin A/C in epithelial versus mesenchymal cell states. By integrating morphological analysis, molecular assays, and transcriptomic profiling, we examine how Lamin A/C expression and function are modulated during EMT and MET, and conversely, how Lamin A/C depletion or overexpression influences cellular phenotype. We also investigate the relationship between Lamin A/C and chromatin organization, particularly the regulation of heterochromatic histone marks, to determine whether Lamin A/C contributes to the maintenance of transcriptionally repressive environments characteristic of the epithelial state (Nakaya and Sheng, 2008; Kong et al., 2012).

To this end, we utilize well-characterized breast cancer cell lines representing epithelial (MCF7, MCF10A) and mesenchymal (MDA-MB-231) states. EMT is induced through TWIST1 overexpression or TGF-β treatment, while MET is driven via GRHL2 expression. These models provide a robust framework to dissect the role of Lamin A/C in controlling cell identity and plasticity (Andronov et al., 2019). Our findings highlight that Lamin A/C levels inversely correlate with mesenchymal traits and directly influence the transcriptional and epigenetic states associated with EMT/MET (Khot et al., 2020; Scheller et al., 2020). Notably, while Lamin A/C depletion promotes mesenchymal reprogramming, its reintroduction reinstates epithelial characteristics, reinforcing its role as a master regulator of phenotypic stability.

Furthermore, we address the specificity of Lamin A/C function by contrasting its role with that of B-type lamins. Despite structural similarities and shared localization at the nuclear periphery, B-type lamins do not exhibit the same regulatory effects on EMT markers or heterochromatin status (Wong and Stewart, 2020), underscoring a distinct and non-redundant role for Lamin A/C. This distinction reinforces the hypothesis that A-type lamins possess

unique molecular interactions in epithelial versus mesenchymal contexts, which are essential for maintaining cell state fidelity.

Collectively, this chapter aims to provide a comprehensive view of how Lamin A/C contributes to epithelial–mesenchymal plasticity through structural, transcriptional, and epigenetic mechanisms. By elucidating the unique interactions of Lamin A/C in different cellular states, we uncover novel insights into the regulation of EMT/MET, with potential implications for understanding metastatic progression and therapeutic resistance in breast cancer.

## 4.2 Results

### Comprehensive Functional Analysis of Lamin A (LMNA) Interactors: Integration of GO and KEGG Pathway Enrichment Studies

Lamin A (LMNA) serves as both a structural scaffold and a regulatory hub in nuclear organization. While its role in maintaining nuclear integrity was first characterized in the 1980s (Aebi et al., 1986), contemporary studies reveal its participation in diverse cellular processes, including RNA metabolism (Brabletz et al., 2018) and mechanotransduction (Jiang et al., 2015). This integrated analysis combines multiple omics approaches to elucidate multifaceted roles of Lamin A functions.

**Nuclear Architecture and Organization**

The cellular component analysis revealed the critical role of Lamin A in nuclear architecture organization. The enrichment of nuclear pore complex components (20-fold, $p<10^{-35}$) (Figure 4.1) aligns with super-resolution microscopy studies demonstrating direct LMNA-NUP153 interactions essential for nuclear transport competency (Boumendil et al., 2019). The spliceosomal complex associations correlate with the ability of Lamin A to organize nuclear speckles containing SRSF1 and other splicing factors (Flavahan et al., 2016).

The nuclear-ER membrane network enrichment supports biochemical evidence of LMNA-mediated tethering between these organelles, facilitating calcium signaling (De Cecco et al., 2019). Chromatin anchoring functions are evidenced by the direct binding of Lamin A/C to LADs (lamina-associated domains), which maintains heterochromatin positioning (Youle and Strasser, 2008).

**Molecular Functions**

Beyond structural roles, LMNA exhibits diverse biochemical activities. The nucleic acid binding capacities (snRNA binding $p<10^{-40}$) correlate with CLIP-seq data showing LMNA-

RNA interactions (Lu and Kang, 2019). The unexpected SNARE binding activity (Fold Enrichment=12.3) matches recent BioID studies identifying VAMP3 as a novel LMNA partner (Figure 4.1) (Andronov et al., 2019).

Transcription factor binding enrichment supports ChIP-seq data demonstrating LMNA's occupancy at regulatory regions of mechanosensitive genes (Bian et al., 2013). The DNA repair functions align with the role of Lamin A/C in recruiting 53BP1 to double-strand breaks (Redwood et al., 2011).

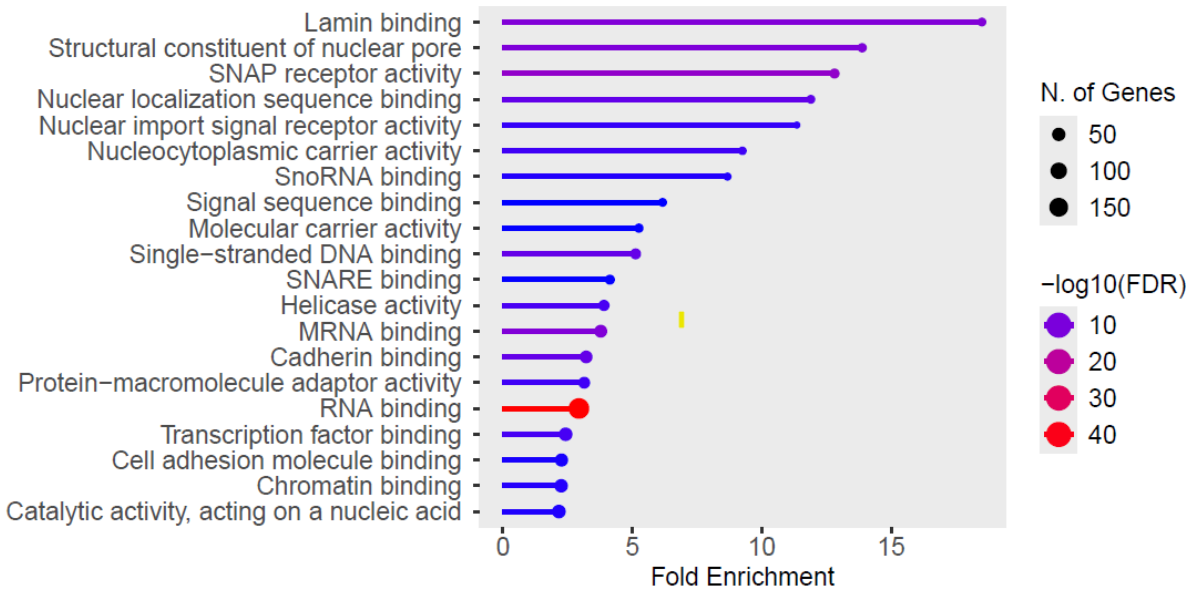


***Figure 4.1.*** *Bubble plot summarizing the molecular function enrichment derived from Lamin A/C proteomics data. Each bubble represents a significantly enriched molecular function category identified among Lamin A/C–A/C-associated proteins. Bubble size corresponds to the number of proteins associated with each molecular function, while bubble color indicates the level of statistical significance (adjusted* p-*value). This analysis highlights the functional distribution of Lamin A/C–interacting proteins, with prominent enrichment in pathways related to chromatin organization, transcriptional regulation, and structural molecular activity.*

**Biological Processes**

RNA processing enrichment (FDR<$10^{-50}$) corresponds with transcriptomic studies showing widespread splicing defects in LMNA mutants (Lund et al., 2015). The viral process association matches proteomic evidence of interaction of Lamin A with viral capsid proteins (Figure 4.2) (Bian et al., 2013).

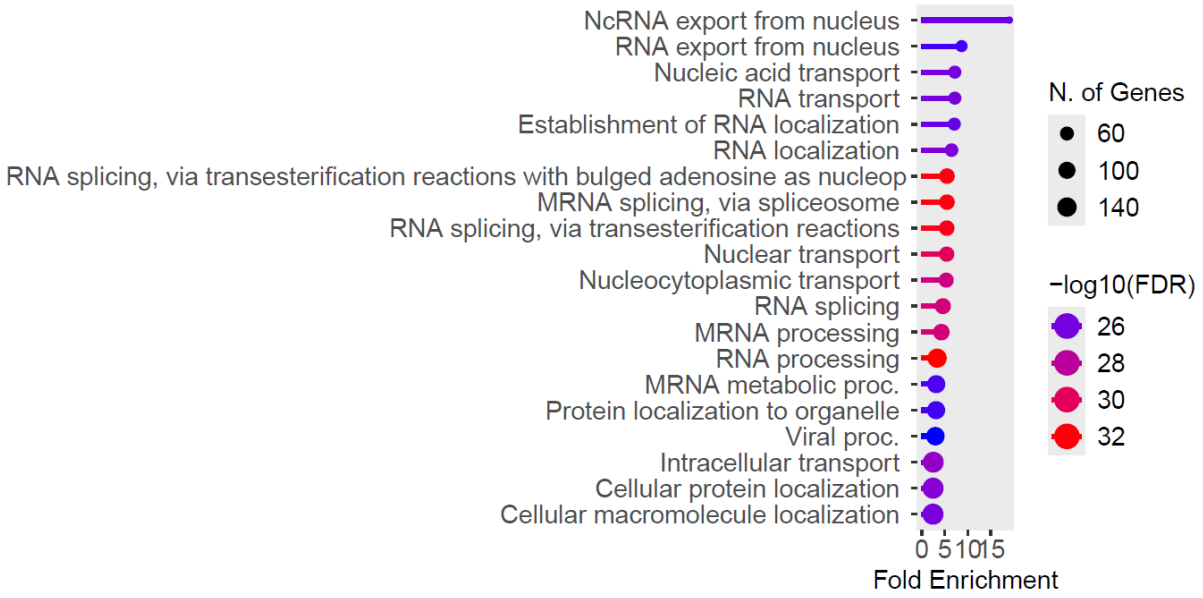


***Figure 4.2:*** *Bubble plot depicting enriched biological process categories derived from Lamin A/C proteomics data. Each bubble represents a significantly enriched biological process associated with Lamin A/C–interacting proteins. Bubble size reflects the number of proteins contributing to each process, while bubble color indicates statistical significance (false discovery rate, FDR). Prominent enrichment of RNA processing–related processes (FDR <* $10^{-50}$*) is consistent with reported splicing defects in* LMNA *mutant cells, and enrichment of viral process–related terms aligns with known interactions between Lamin A and viral capsid proteins.*

**KEGG Pathway Analysis**

The SNARE pathway enrichment (Fold=13.2) is supported by live-cell imaging showing the requirement of Lamin A for nuclear envelope vesicle fusion (Olmos et al., 2022). DNA repair pathway associations correlate with increased γH2AX foci in LMNA-deficient cells (Figure 4.3) (Jolly et al., 2015).

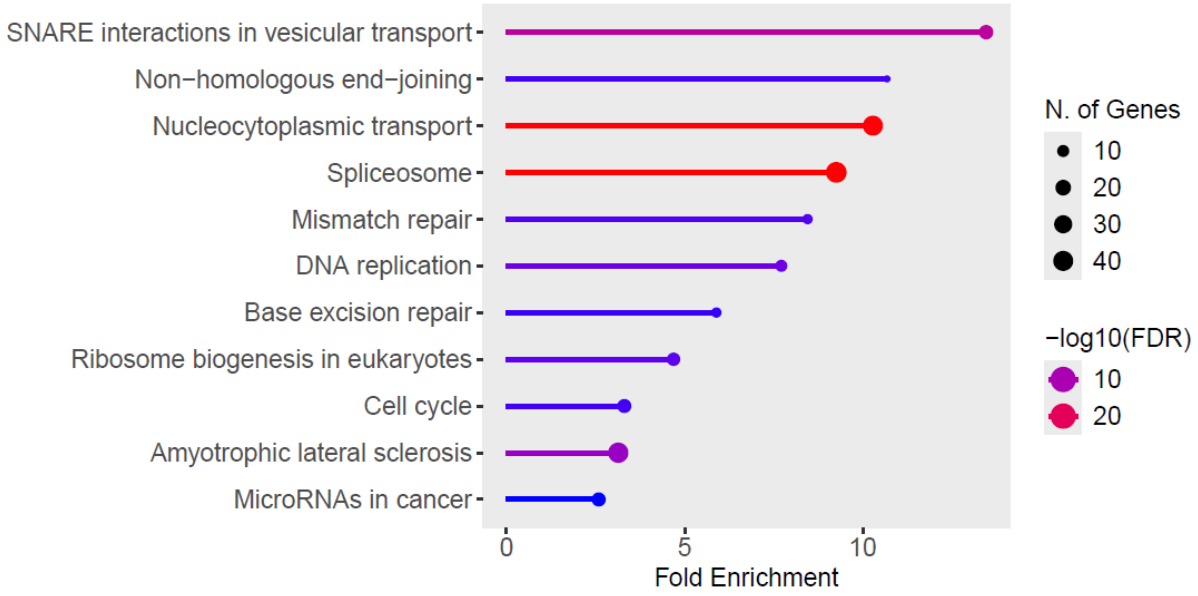


***Figure 4.3:*** *Bubble plot illustrating significantly enriched KEGG pathways identified from Lamin A/C proteomics data. Each bubble represents an enriched KEGG pathway associated with Lamin A/C–A/C-interacting proteins. Bubble size corresponds to the number of proteins mapped to each pathway, while bubble color denotes the level of statistical significance (false discovery rate, FDR). The analysis highlights key cellular pathways linked to Lamin A/C function, providing pathway-level insight into its roles in nuclear organization and regulatory processes.*

Integrated Model

This explains how LMNA mutations cause diverse pathologies: transport defects (HGPS, p.R527C), splicing errors (DCM, p.R190W), and genome instability (progeria, p.G608G) (Johnstone et al., 2020).

Synthesizing these multi-omics analyses reveals LMNA as a central node in a complex cellular network that integrates nuclear structure with diverse functional outputs. The protein serves as: (1) a structural scaffold maintaining nuclear integrity; (2) an organizer of nuclear subcompartments; (3) a regulator of gene expression through chromatin interactions and RNA processing; and (4) a participant in novel processes such as membrane trafficking and host defense. (Figure 4.4)

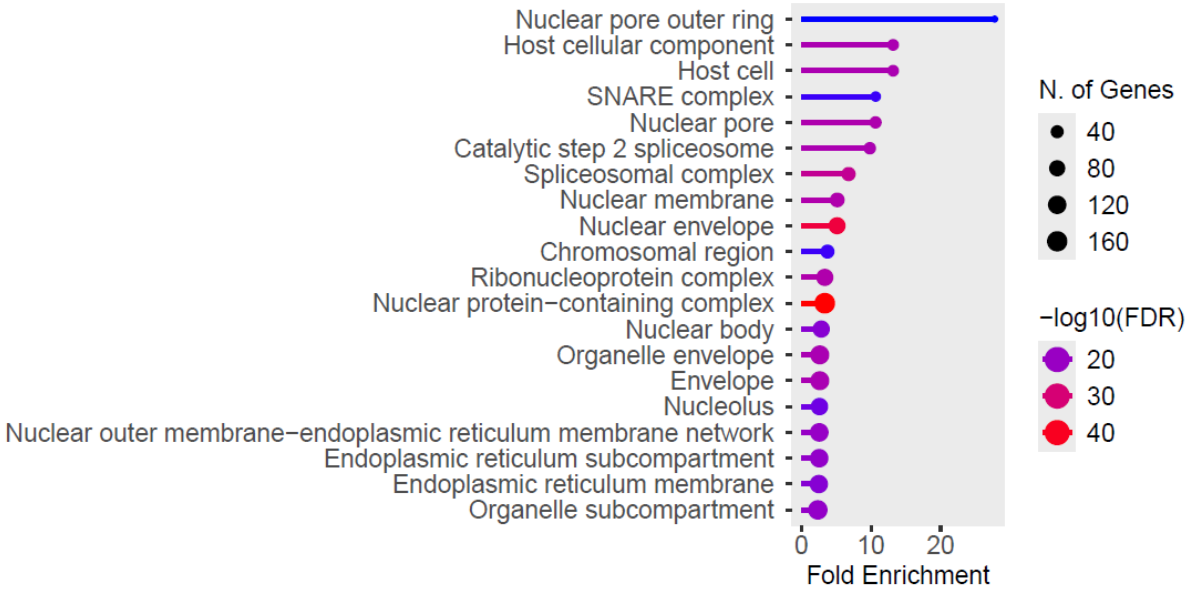


***Figure 4.4*** *This integrated model explains how LMNA mutations can lead to such diverse clinical manifestations, as perturbations at any level of this network can have cascading effects on cellular homeostasis. The tissue-specificity of laminopathy phenotypes likely reflects differential dependence on these various LMNA functions across cell types.*

**Therapeutic Implications and Future Directions**

The comprehensive functional mapping of LMNA interactions suggests several promising therapeutic strategies. Targeting nuclear transport defects, correcting aberrant splicing patterns, or enhancing DNA repair efficiency could potentially ameliorate disease phenotypes. The

novel associations with membrane trafficking pathways identified in this analysis may inspire innovative treatment approaches focused on maintaining nuclear envelope dynamics.
Future research should focus on elucidating the mechanistic basis of the newly identified roles, particularly in vesicular transport and viral defense. Additionally, tissue-specific analyses of LMNA interaction networks (Figure 4.5) may help explain the selective vulnerability of specific cell types in different laminopathies.

This integrated multi-omics analysis significantly expands our understanding of LMNA biology, moving beyond its classical structural role to reveal participation in diverse cellular processes. The findings provide a framework for understanding laminopathy pathogenesis and identify novel targets for therapeutic intervention. By connecting nuclear architecture to functional outputs across multiple biological scales, this work establishes LMNA as a central integrator of cellular homeostasis with far-reaching implications for human health and disease.

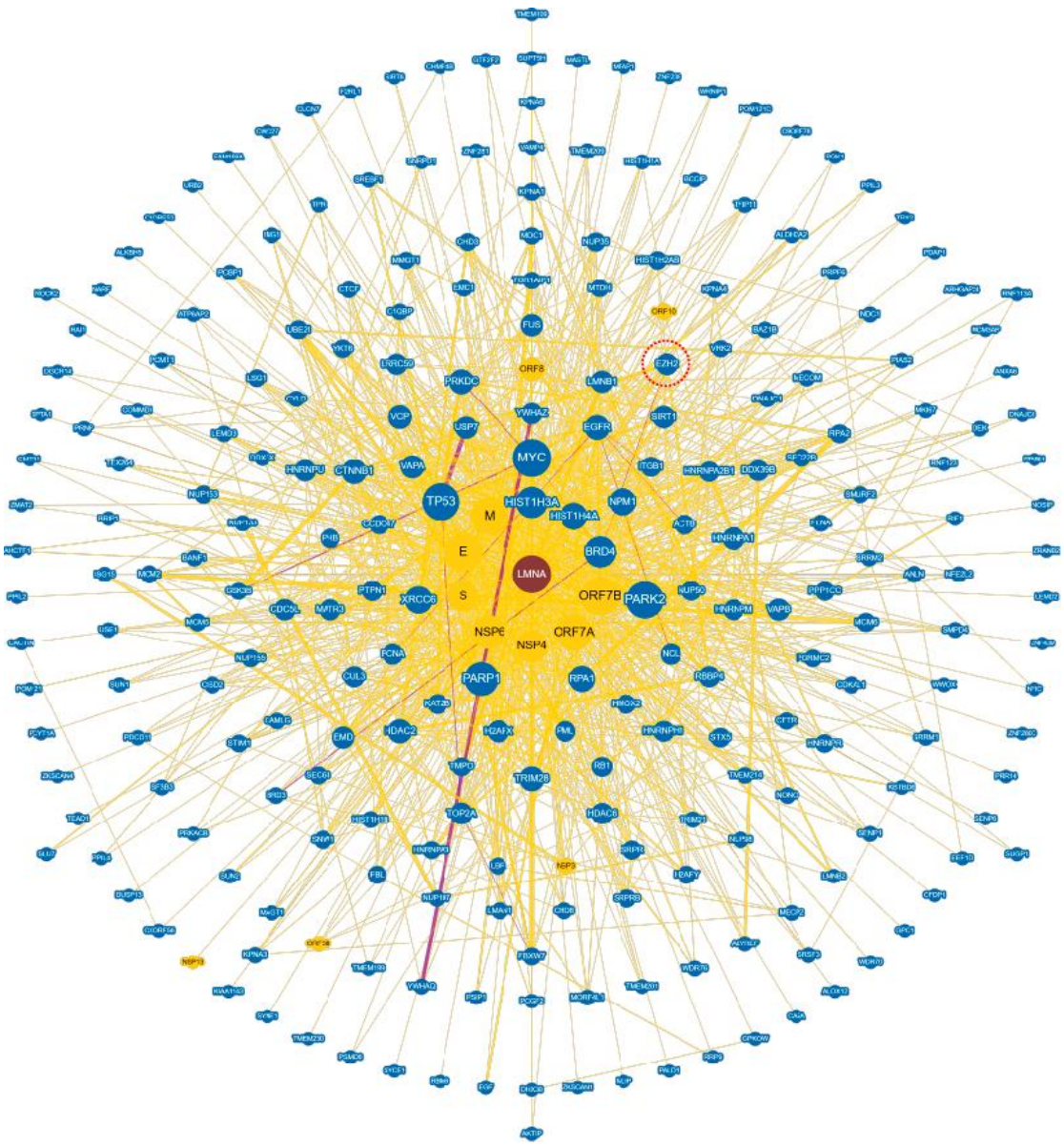


**Figure 4.5: Protein interaction network centered on Lamin A/C (LMNA).**

*This network visualizes the interaction landscape of Lamin A/C (LMNA) and its associated host proteins. LMNA is shown as the central red node, with node size proportional to its interaction degree. Direct LMNA interactors are displayed as larger yellow/orange nodes, while secondary and tertiary interacting host proteins are represented as blue nodes arranged toward the periphery. EZH2 is highlighted in a dotted red circle. The radial layout highlights LMNA as a significant structural and regulatory hub linked to multiple signaling, chromatin, and cytoskeletal proteins, including TP53, MYC, BRD4, PARP1, and others. This visualization underscores the extensive molecular network connected to Lamin A/C and its potential influence on diverse cellular pathways relevant to nuclear architecture, gene regulation, and disease-associated mechanisms.*

### 4.2.1 Lamin A/C Interactome Dynamics During EMT and MET Transitions

In light of established associations between nuclear lamins and chromatin-remodeling complexes, we sought to investigate whether the interactome of Lamin A/C is differentially regulated during epithelial–mesenchymal transition (EMT) and mesenchymal–epithelial transition (MET). To this end, we performed co-immunoprecipitation (Co-IP) of Lamin A/C followed by mass spectrometry (MS) analysis to profile its protein–protein interactors across different cellular states.

In MCF7 epithelial control cells, MS identified 44 unique Lamin A/C interactors, including EZH2, NUDT21, LIMA1, EEF1G, CPSF6, and H2AFX. Upon EMT induction via TWIST1 overexpression (MCF7-TWIST1), the Lamin A/C interactome expanded to include 90 unique interactors, such as CCNB1, phosphorylated CDK1 (pCDK1), PGK2, AMOT, EFHD1, and LDHB. A subset of 49 proteins, including LMNB1, LMNB2, EHMT2, SUV39H1, and PRRX1, were common across both epithelial and mesenchymal MCF7 states (Figure 4.6A).

Similarly, in the basal-like mesenchymal MDA-MB-231 cell line, 103 unique Lamin A/C interactors were detected in control conditions, including CCNB1, pCDK1, DDX17, LDHA, and GOT2. Upon GRHL2-mediated MET induction, the interactome shifted to include 71 distinct proteins such as EZH2, H4C1, NONO, ILF2, and UBC. Notably, 72 proteins, including LMNB1, LMNB2, CBX5, EHMT2, and SUV39H1, were shared between the mesenchymal and MET-induced states (Figure 4.6B) (consistence between the replicates were assessed by PCA plot mentioned in Figure3.9D and 3.9E).

Gene Ontology (GO) enrichment analysis revealed functional differences in the Lamin A/C interactome across cellular states. In epithelial MCF7 cells, Lamin A/C interactors were predominantly involved in gene expression regulation, mRNA metabolism, ribonucleoprotein complex assembly, and mRNA stability. By contrast, EMT induction led to enrichment in pathways related to cell cycle regulation, mitotic nuclear envelope disassembly, and DNA damage repair (Figure 4.6C). Interestingly, GRHL2-induced MET in MDA-MB-231 cells reinstated Lamin A/C interactions with gene regulatory proteins such as EZH2, consistent with a reversion to epithelial-like functions (Figure 4.6D). These results collectively suggest that the Lamin A/C interactome is subject to dynamic remodeling during EMT and MET, reflective of the distinct transcriptional and functional landscapes characteristic of each cell state.

A prominent observation emerging from our interactome analysis was the reversible interaction between Lamin A/C and the histone methyltransferase EZH2. This interaction was detected in epithelial MCF7 cells and re-established during GRHL2-driven MET in MDA-MB-231 cells, but was absent in mesenchymal contexts—namely, TWIST1-induced EMT in MCF7 and basal-like MDA-MB-231 cells. Conversely, interaction between Lamin A/C and pCDK1 was prominent in mesenchymal cells but lost upon MET induction (Figures 4.6E and 4.6F). These findings point to a reciprocal switch in Lamin A/C's binding partners, wherein it associates with chromatin regulators such as EZH2 in epithelial states, and cell cycle regulators like pCDK1 in mesenchymal states, highlighting a cell state–dependent reprogramming of the Lamin A/C interactome linked to epithelial–mesenchymal plasticity (EMP).

To validate these interactions, we performed Lamin A/C Co-IP followed by immunoblotting for EZH2 across EMT and MET transitions. Consistent with MS data, Co-IP confirmed a loss of Lamin A/C–EZH2 interaction upon EMT induction, and its restoration during MET (Figures 4.6G–I). Notably, neither Lamin B1 nor Lamin B2 interacted with EZH2, underscoring the specificity of the Lamin A/C–EZH2 association. However, consistent with prior reports (49, 50), both B-type lamins retained interactions with methyltransferases G9a and SUV39H1, which remained unchanged upon EMT in MCF10A cells (Figures 3.9F and 3.9G).

To further substantiate the Lamin A/C–EZH2 interaction, we employed a proximity ligation assay (PLA) under EMT and MET conditions. A significant (~10-fold) reduction in PLA foci was observed upon EMT, indicating a disruption of the Lamin A/C–EZH2 complex (Figures 4.6J and 4.6L). In contrast, GRHL2-induced MET led to a marked increase in PLA signals (~10-fold) relative to control MDA-MB-231 cells, confirming the re-establishment of this interaction (Figures 4.6K and 4.6M).

To understand the temporal dynamics of this interaction, we conducted a time-course experiment using TGF-β to induce EMT, followed by TGF-β withdrawal to promote MET. Immunoprecipitation of Lamin A/C at defined intervals (12 to 168 hours for EMT; 12 to 120 hours for MET) revealed a progressive loss of EZH2 interaction, culminating in complete dissociation by ~72 hours post-EMT induction. Upon TGF-β withdrawal, the Lamin A/C–EZH2 interaction was progressively restored, with re-association evident after ~72 hours of MET (Figure 4.6N). These results support the notion that the Lamin A/C–EZH2 interaction is both dynamic and reversible in response to cellular plasticity cues.

Collectively, our findings demonstrate that EMT disrupts, while MET restores, the interaction between Lamin A/C and EZH2, correlating with alterations in heterochromatin-associated features. Moreover, the mutually exclusive interactions of Lamin A/C with EZH2 and pCDK1 underscore its dual role in epigenetic regulation and cell cycle control, depending on the cell's phenotypic state. This context-specific modulation of Lamin A/C interactions provides critical mechanistic insight into how nuclear architecture contributes to the regulation of epithelial–mesenchymal plasticity and highlights Lamin A/C as a central integrator of nuclear structure and function during cancer progression.

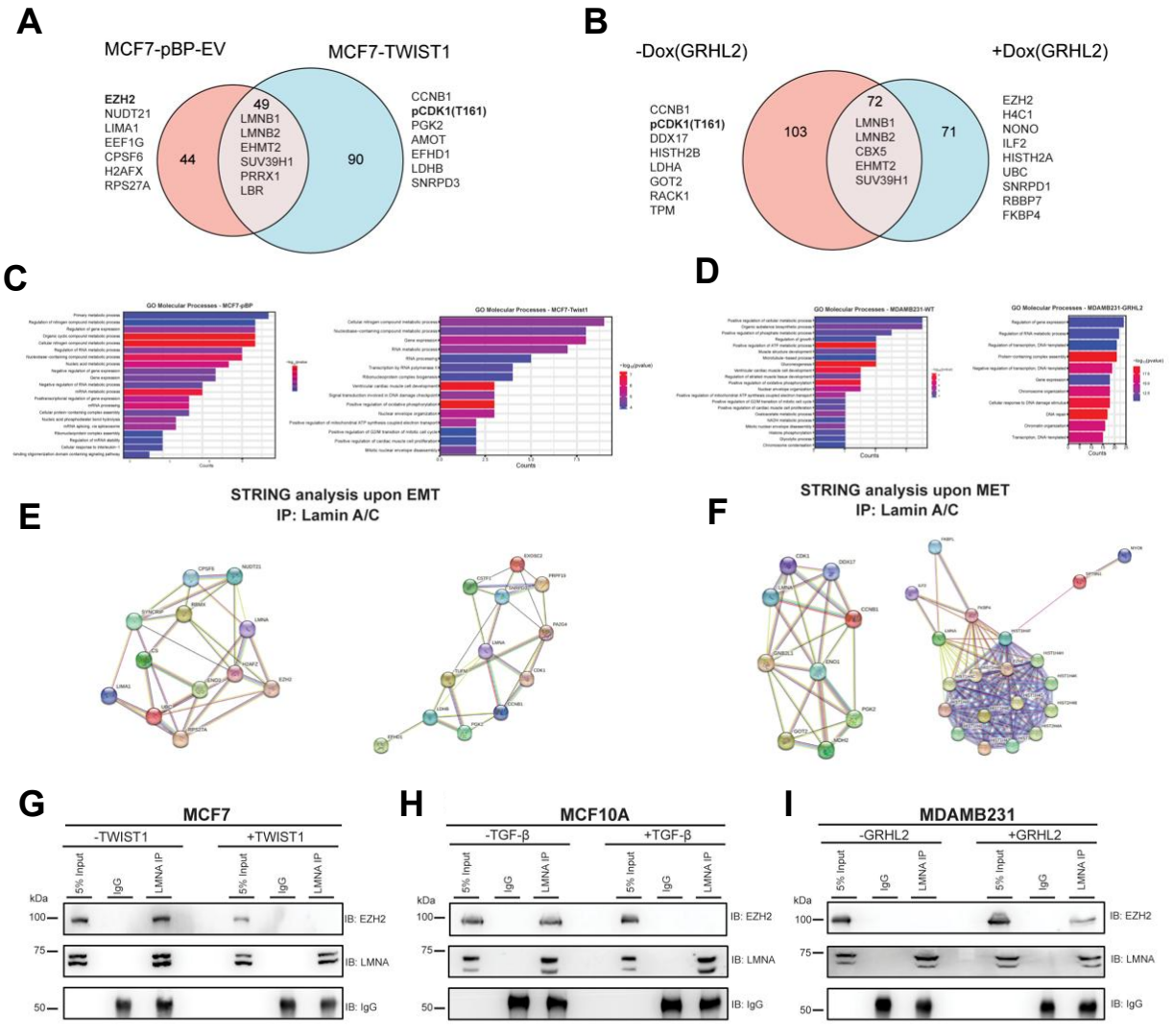

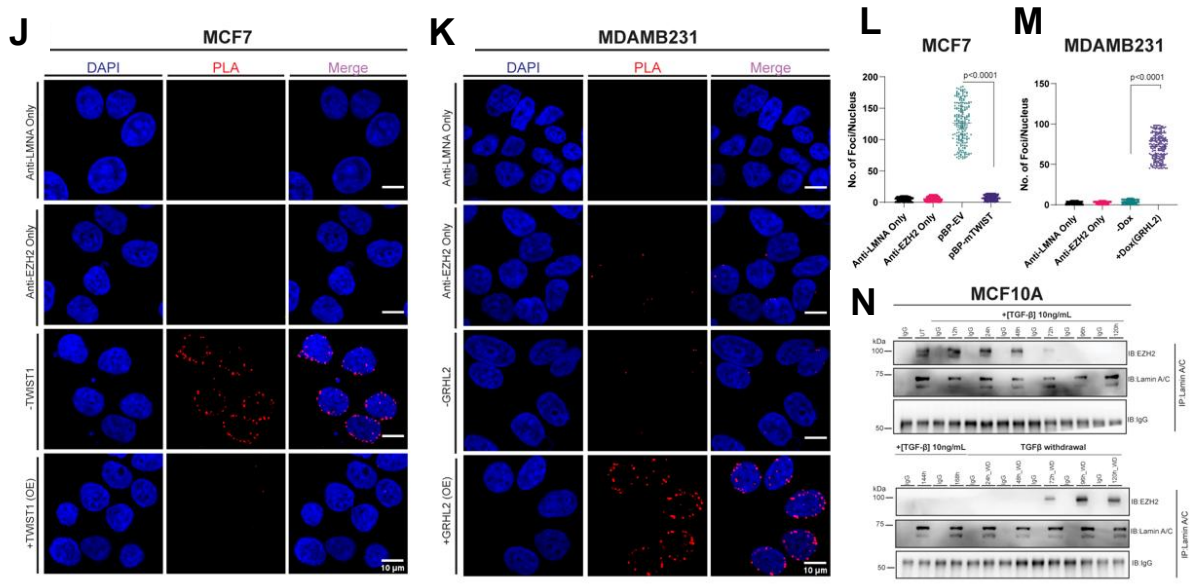


***Figure 4.6: Dynamic Remodeling of the Lamin A/C Interactome During EMT and MET***

*(A, B) Venn diagrams showing unique and shared Lamin A/C interactors identified by IP-MS in MCF7 vs. MCF7-TWIST1 (A) and MDA-MB-231 vs. MDA-MB-231-GRHL2 (B) cells. (C, D) Gene Ontology (GO) pathway enrichment analysis of Lamin A/C interactors in MCF7 vs. MCF7-TWIST1 (C) and MDA-MB-231 vs. MDA-MB-231-GRHL2 (D) cells, categorized by molecular function and cellular process. (E, F) Representative STRING network analysis of Lamin A/C interactors in MCF7 vs. MCF7-TWIST1 (E) and MDA-MB-231 vs. MDA-MB-231-GRHL2 (F) cells. (G–I) Co-immunoprecipitation of Lamin A/C in MCF7 (G), MCF10A (H), and MDA-MB-231 (I) cells upon EMT or MET induction, followed by immunoblotting for EZH2 and Lamin A/C. IgG serves as the isotype control and shows an approximately equal amount of antibody is used for immunoprecipitation. (J, K) Proximity ligation assay (PLA) detecting Lamin A/C–EZH2 interaction in MCF7 (J) and MDA-MB-231 (K) cells upon EMT or MET induction. PLA signal in red. Scale bar: 10 µm. (L, M) Quantification of PLA signal in MCF7 (L) and MDA-MB-231 (M) cells. Data represent mean ± S.D. from three independent biological replicates. p-values calculated by one-way ANOVA. (N) Time-course analysis of Lamin A/C–EZH2 interaction, by immunoprecipitation of Lamin A/C in MCF10A cells during EMT progression (12 h to 168h (7 days) post-TGF-β) and MET recovery (5 days post-TGF-β withdrawal (WD)), assessed by co-immunoprecipitation and immunoblotting. IgG serves as the isotype control.*

### 4.2.2 Structural Basis of Lamin A/C–EZH2 Interaction

To delineate the molecular interface mediating the Lamin A/C–EZH2 interaction, we adopted a combined computational and experimental approach designed to identify and validate specific residues involved in this protein–protein interaction. Recognizing the potential complexity and specificity of nuclear interactions, we first employed the High Ambiguity Driven protein–protein DOCKing (HADDOCK) platform—an advanced, information-driven molecular docking tool that integrates experimental data, biochemical constraints, and structural information into the docking process. HADDOCK is particularly well-suited for analyzing transient and partially flexible interactions like those expected between nuclear proteins involved in chromatin organization and transcriptional repression. By incorporating our knowledge of conserved domain architecture and charge complementarity, our in-silico modeling predicted a specific interaction interface between the N-terminal head domain of Lamin A/C and the 130-150 aa of EZH2.

More specifically, the simulations identified residues Arg25 and Arg28 in Lamin A/C's N-terminal head as forming a potential electrostatic interface with acidic residues Asp136 and Asp140 on EZH2. These residues lie within functionally conserved domains—the coil 1A region of Lamin A and the non-catalytic domain of EZH2—suggesting not only structural compatibility but also potential functional relevance. These computational predictions were visualized using molecular modeling software and ranked based on binding energy scores and interface residue contacts (Figure 4.7A). The predicted residues are situated in regions known to remain solvent-accessible and structurally flexible, supporting their capacity to mediate specific interactions under physiological conditions.

To experimentally validate these predictions, we designed a panel of deletion constructs for both Lamin A/C and EZH2, carefully preserving their nuclear localization signals (NLS) to ensure faithful subnuclear targeting. These constructs were expressed in HEK293T cells, a system chosen for its high transfection efficiency and suitability for biochemical co-immunoprecipitation (Co-IP) assays. Lamin A was tagged with GFP to allow fluorescence-based tracking and immunoprecipitation, while EZH2 constructs were FLAG-tagged for reciprocal pull-downs.

Initial Co-IP experiments using full-length GFP-Lamin A and a series of FLAG-tagged EZH2 deletion mutants revealed that the central domain of EZH2, specifically the region spanning

Ala301–Ala500, was necessary and sufficient for interaction with Lamin A (Figure 4.7C). This region encompasses part of the pre-SET and SET domains of EZH2, which are known to mediate interactions with nucleosomal substrates and regulatory partners. To confirm the reciprocal nature of this binding, we performed reverse Co-IP using FLAG-EZH2 and a panel of Lamin A truncation mutants. These experiments pinpointed the N-terminal head domain of Lamin A (amino acids 1–70) as the critical region mediating interaction with EZH2 (Figure 4.7B).

Together, these results confirm a stable and specific interaction between Lamin A/C and EZH2, mediated through structurally defined and conserved domains. This interaction provides a mechanistic basis for the previously observed colocalization of Lamin A/C and EZH2 at the nuclear periphery and supports the notion that Lamin A/C may serve as a structural scaffold for epigenetic regulators. Given EZH2's role as the catalytic subunit of the Polycomb Repressive Complex 2 (PRC2), which deposits the transcriptionally repressive H3K27me3 mark, our findings raise the possibility that Lamin A/C facilitates the spatial sequestration or targeting of PRC2 to specific heterochromatic regions. This interface thus represents a convergence point between nuclear architecture and epigenetic silencing, with potential implications for regulating gene expression during EMT/MET and in cancer-associated phenotypic plasticity.

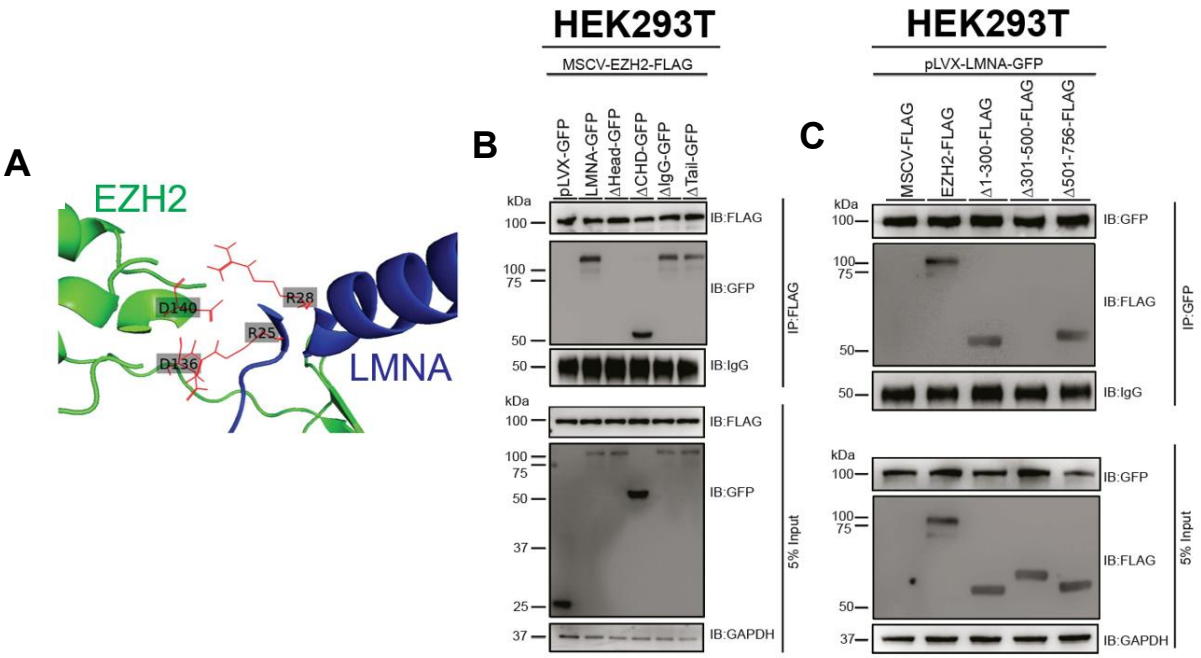

***Figure 4.7: (A)*** *HADDOCK docking model of the Lamin A–EZH2 complex, highlighting interactions between aspartate residues in EZH2 (D136, D140) and arginine residues in Lamin A (R25, R28)* ***(B)*** *Co-immunoprecipitation of FLAG in HEK293T cells co-transfected with full-length EZH2-FLAG and Lamin A-GFP deletion mutants (ΔHead 1-29, ΔRod 31-387, ΔIgG 428-549, ΔTail 550-664 of Lamin A). (C) Co-immunoprecipitation of GFP in HEK293T cells co-transfected with full-length Lamin A-GFP and EZH2-FLAG deletion mutants (Δ1-300, Δ301-500, Δ501-746 of EZH2).*

**Interaction with other PRC2 components**

Among key regulators of transcriptional repression, the Polycomb Repressive Complex 2 (PRC2) plays a central role by catalyzing trimethylation of histone H3 at lysine 27 (H3K27me3) through its catalytic subunit EZH2, in conjunction with the structural components SUZ12 and EED (Heaphy et al., 2011; Coschi et al., 2014). Given the emerging evidence that Lamin A/C and PRC2 components may converge at repressive chromatin domains (Celeste et al., 2002; Chin et al., 2006), we sought to determine whether Lamin A/C interacts with PRC2 components beyond EZH2, which we had previously shown to associate with Lamin A/C (Figure 4.6G-I).

To address this, co-immunoprecipitation assays were performed using nuclear extracts from MCF10A cells under basal epithelial conditions. Lamin A/C was immunoprecipitated, and the presence of core PRC2 components EZH2, SUZ12, and EED in the immunoprecipitates was assessed by immunoblotting. The results revealed a specific and robust interaction between Lamin A/C and EZH2, while no detectable association was observed with SUZ12 or EED. These findings indicate that Lamin A/C selectively interacts with the catalytic subunit of PRC2, rather than forming a complex with the complete PRC2 machinery. This selective interaction suggests that Lamin A/C may influence EZH2 function independently of its canonical PRC2 activity, potentially modulating EZH2 localization or stability at the nuclear periphery (Margueron et al., 2008; H. Kang et al., 2019) (Figure 4.8A).

To further probe whether the integrity of the PRC2 complex is maintained during epithelial–mesenchymal transition (EMT), we performed reciprocal co-immunoprecipitation experiments in MCF10A cells treated with TGF-β to induce EMT. EZH2 was immunoprecipitated, and the association with SUZ12 and EED was examined. Despite EMT induction, EZH2 remained tightly associated with SUZ12 and EED, confirming that the PRC2 complex remains intact under these conditions. This observation indicates that the Lamin A/C–EZH2 interaction is independent of the canonical PRC2 assembly, further supporting the notion of a distinct Lamin A/C–EZH2 module that may function separately from the established PRC2 complex (Figure 4.8B).

Taken together, these results suggest that Lamin A/C forms a specific, independent association with EZH2, without engaging other core PRC2 components. This interaction likely represents a mechanism through which Lamin A/C contributes to the establishment of repressive

chromatin domains at the nuclear periphery, potentially modulating gene expression programs associated with epithelial–mesenchymal plasticity. By selectively engaging EZH2, Lamin A/C may act as a spatial organizer of repressive chromatin, coordinating nuclear architecture with epigenetic regulation during cellular transitions.

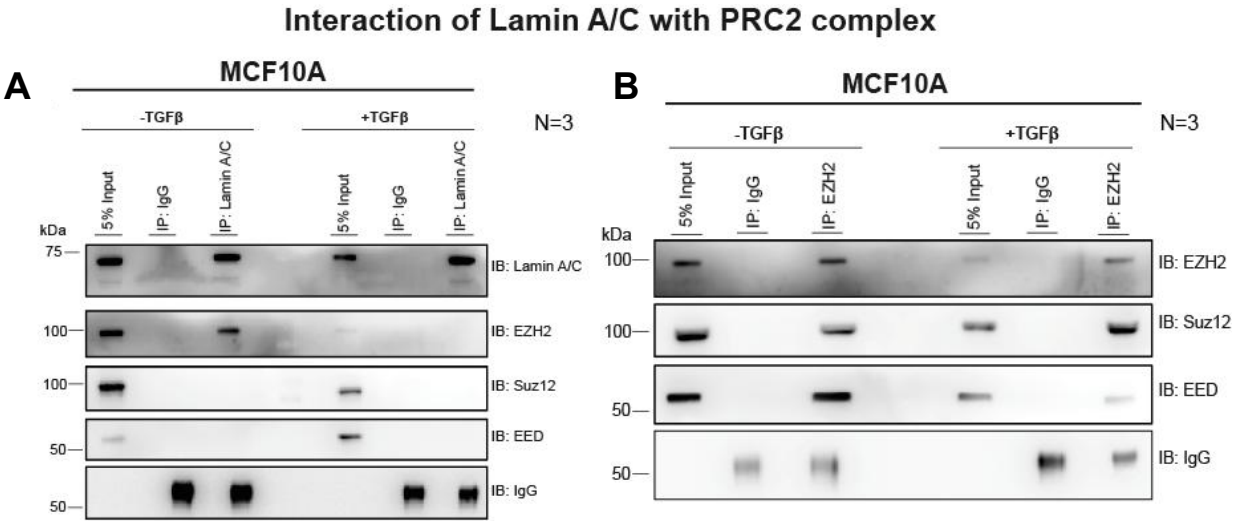


***Figure 4.8: Lamin–chromatin regulator interactions***

***(A)*** *CoIP of Lamin A/C in MCF10A cells induced to undergo EMT by TGF-β treatment, followed by IB for PRC2 subunits EED and SUZ12.* ***(B)*** *CoIP of EZH2 in MCF10A cells induced to undergo EMT by TGF-β treatment, followed by IB for PRC2 subunits EED and SUZ12.*

### 4.2.3 Phosphorylation-Dependent Modulation by CDK1

Having identified the structural interface mediating the Lamin A/C–EZH2 interaction, we next sought to elucidate the regulatory mechanisms governing the stability and dynamics of this complex. Protein–protein interactions within the nucleus are often modulated by post-translational modifications, which can influence binding affinity, complex formation, subcellular localization, and protein turnover. Among these, phosphorylation stands out as a highly versatile regulatory mechanism that responds rapidly to cellular cues and controls numerous processes, including cell cycle progression, transcription, and chromatin remodeling.

Sequence analysis of both Lamin A/C and EZH2 revealed multiple conserved consensus motifs for Cyclin-Dependent Kinase 1 (CDK1), a serine/threonine kinase that plays a central role in cell cycle regulation and mitotic entry. Specifically, Ser22 on Lamin A/C and Thr345 on EZH2 were found within high-confidence CDK1 consensus sequences (Figure 4.9A), prompting the hypothesis that CDK1-mediated phosphorylation might modulate the Lamin A/C–EZH2 complex.

To explore this hypothesis, we performed immunoprecipitation followed by mass spectrometry (IP-MS) to identify kinases co-precipitating with Lamin A/C in mesenchymal-like cellular models. Using Twist1-overexpressing MCF7 cells and untreated MDA-MB-231 cells—both of which exhibit strong mesenchymal characteristics—we consistently detected strong enrichment of CDK1 within Lamin A/C-associated protein complexes. This finding suggested a functional interaction between CDK1 and Lamin A/C during EMT, possibly influencing its interaction with EZH2 (Figures 4.9B–D).

To validate and spatially resolve this interaction in situ, we employed Proximity Ligation Assay (PLA) in MCF10A cells undergoing TGF-β-induced EMT. This highly sensitive technique confirmed a significant increase in the Lamin A/C-phospho-CDK1 (T161) interaction following EMT induction (Figures 4.9E), indicating that CDK1 activity is spatially coupled with Lamin A/C in cells undergoing phenotypic plasticity.

Further support for this model came from Co-IP experiments performed across a panel of breast cancer cell lines (MCF7, MCF10A, and MDA-MB-231) with varying degrees of epithelial or mesenchymal traits. These assays showed that CDK1 physically associates with Lamin A/C predominantly in mesenchymal-like cells, while this interaction is significantly diminished in epithelial cells or in those undergoing MET (Figures 4.9B–D).

To assess the phosphorylation status of relevant residues, we performed western blot analysis using phospho-specific antibodies. EMT induction consistently led to elevated levels of phospho-CDK1 (T161), phospho-Lamin A/C (S22), and phospho-EZH2 (T345), indicating enhanced CDK1 kinase activity during the transition to a mesenchymal state. Quantitative densitometric analysis revealed significantly increased ratios of pLMNA(S22)/LMNA and pEZH2(T345)/EZH2 during EMT compared to control or MET conditions (Figures 4.9I-4.9L). This coordinated phosphorylation pattern correlated negatively with Lamin A/C–EZH2 complex formation, suggesting a mechanistic model wherein CDK1-dependent phosphorylation at these key regulatory residues disrupts their interaction.

Taken together, these results provide compelling evidence that CDK1 acts as a post-translational regulator of the Lamin A/C–EZH2 complex. The phosphorylation of Lamin A/C at Ser22 and EZH2 at Thr345 likely introduces structural or electrostatic changes that reduce their binding affinity, thereby disassembling the nuclear complex. This mechanism may serve as a molecular switch to modulate chromatin-associated repression complexes during EMT, promoting transcriptional reprogramming and phenotypic plasticity. These findings add a crucial layer of regulatory insight into the nuclear architecture–epigenetic interface and underscore the importance of kinase signaling in modulating epithelial–mesenchymal dynamics.

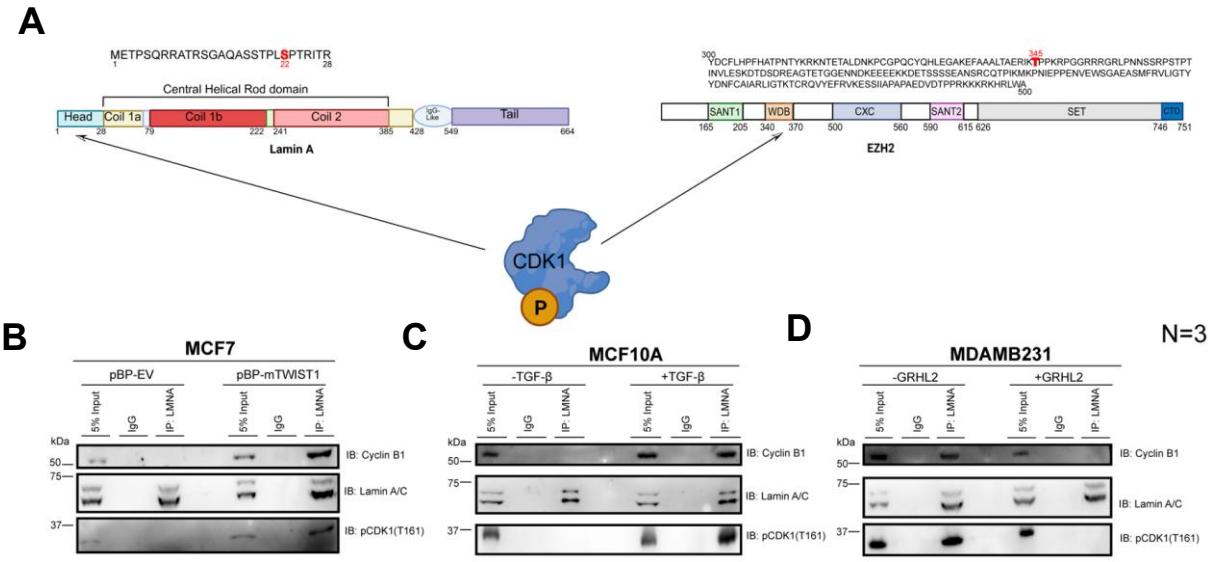

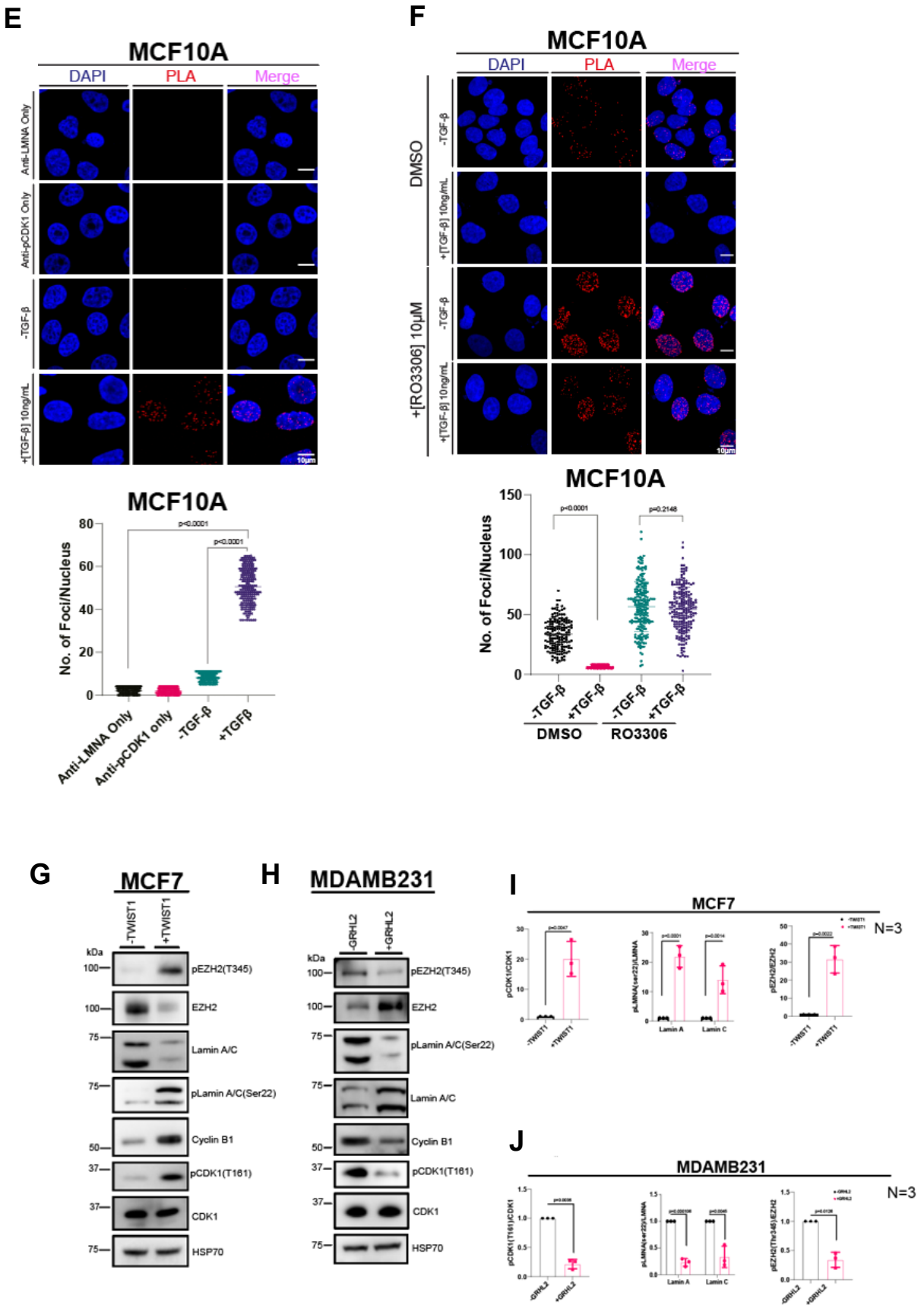


*Figure 4.9: Phosphorylation of Lamin A/C-EZH2 by pCDK1*

***(A)*** *Schematic representation of pCDK1 (T161)-mediated phosphorylation sites (amino acids in the interacting domain, with phosphorylation-sensitive residues marked in red) on Lamin A/C and EZH2.* ***(B–D)*** *Co-immunoprecipitation of Lamin A/C following (B) Twist1-mediated EMT induction in MCF7, (C) TGF-β-mediated EMT induction in MCF10A, and (D) GRHL2-mediated MET induction in MDA-MB-231. Immunoprecipitates were analysed for Cyclin B1 and pCDK1 (T161). Experiments were performed in three independent biological replicates. (E) Proximity ligation assay (PLA) detecting Lamin A/C–pCDK1(T161) interaction in MCF10A cells treated with 10 ng/mL TGF-β for 7 days. Scale bar, ~10 μm. (F) PLA detecting Lamin A/C–EZH2 interaction in MCF10A cells treated with DMSO or 10 μM RO3306 for 18 h in the presence or absence of TGF-β for 7 days. Scale bar, ~10 μm.* ***(G, H)*** *Immunoblot analysis of phosphorylated EZH2 (T345), Lamin A/C (S22), and CDK1 (T161) following (G) EMT in MCF7 and (H) MET in MDA-MB-231.* ***(I, J)*** *Quantification of pEZH2:EZH2, pLMNA: LMNA, and pCDK1:CDK1 ratios in (I) MCF7 following EMT and (J) MDA-MB-231 following MET. Data are from three independent biological replicates.*

### 4.2.4 Functional Rescue of Lamin A/C–EZH2 Interaction by CDK1 Inhibition

To evaluate the functional consequences of CDK1-mediated phosphorylation on the interaction between Lamin A/C and EZH2, we pharmacologically inhibited CDK1 activity in the context of epithelial–mesenchymal transition (EMT). Given our earlier findings that phosphorylation at specific residues (Lamin A/C Ser22 and EZH2 Thr345) disrupts their interaction and that these modifications are upregulated during EMT, we hypothesized that inhibiting CDK1 would stabilize the Lamin A/C–EZH2 complex and potentially restrain EMT progression.

We employed RO-3306, a selective small-molecule inhibitor of CDK1, to test this hypothesis in a controlled EMT model. MCF10A cells were first treated with TGF-β for 150 hours to induce EMT, a condition that results in robust mesenchymal reprogramming characterized by loss of epithelial traits and upregulation of EMT-associated transcription factors. After EMT induction, the cells were treated with RO-3306 (10 μM) for 18 hours to inhibit CDK1 activity. Proximity Ligation Assay (PLA) was then performed to assess the in situ proximity between Lamin A/C and EZH2, which serves as a readout for complex formation.

Strikingly, CDK1 inhibition led to a dramatic restoration of the Lamin A/C–EZH2 interaction. Quantitative analysis of PLA signal intensity revealed nearly a 10-fold increase in the number of PLA puncta in RO-3306–treated cells compared to TGF-β-only controls (Figure 4.9E and F). This result strongly supports the conclusion that CDK1 activity is a negative regulator of the Lamin A/C–EZH2 complex. The rapid and robust recovery of the PLA signal following CDK1 inhibition also implies that this regulatory mechanism is reversible and dynamic, allowing cells to modulate chromatin-associated interactions in response to kinase signaling.

We next sought to determine whether disruption of CDK1 activity would also affect the progression of EMT at the molecular level (Schematic representation in Figure 4.10A). To this end, we analyzed the expression of canonical EMT markers by immunoblotting and immunofluorescence. As expected, TGF-β–treated MCF10A cells showed strong induction of mesenchymal transcription factors ZEB1, SNAI1, and TWIST1, along with a pronounced increase in Vimentin protein levels. Concomitantly, E-cadherin, a hallmark epithelial marker, was markedly downregulated, consistent with EMT induction. However, upon treatment with RO-3306, there was a substantial reversal of these changes: the expression levels of ZEB1, SNAI1, and TWIST1 were significantly reduced, and Vimentin protein levels declined.

Notably, E-cadherin expression was either maintained at basal levels or modestly upregulated, suggesting a partial reversal of EMT (Figures: 4.10C, 4.10E and 4.10K).

To assess the generalizability of this effect, we extended the analysis to a second EMT model using Twist1-overexpressing MCF7 cells. Similar to the results observed in MCF10A cells, inhibition of CDK1 in this model resulted in a suppression of mesenchymal phenotypes. Cells exhibited decreased expression of mesenchymal markers and showed partial reversion to epithelial-like morphology (4Figures: 4.10B, 4.10D, and 4.10F). These findings confirm that the effects of CDK1 inhibition are not restricted to a single model system but rather reflect a broader regulatory role for CDK1 in maintaining EMT-associated transcriptional programs.

Taken together, these results establish a direct functional link between CDK1 activity and the stability of the Lamin A/C–EZH2 complex. By phosphorylating key residues on both interaction partners, CDK1 disrupts the complex, thereby allowing chromatin reorganization and transcriptional reprogramming required for EMT. Inhibiting CDK1 restores the Lamin A/C–EZH2 interaction and attenuates mesenchymal gene expression, effectively countering EMT progression. These findings point to CDK1 not only as a cell cycle regulator but also as a critical modulator of nuclear structure–epigenetic interactions and epithelial–mesenchymal plasticity. This insight could have significant implications for therapeutic strategies aimed at halting metastasis by targeting EMT at the level of nuclear architecture.

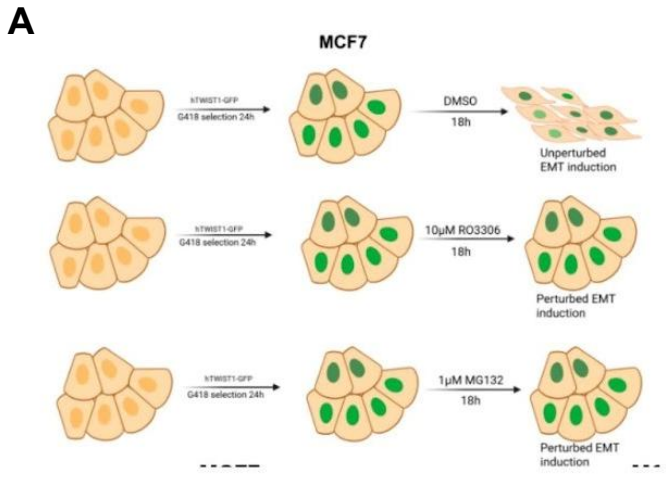

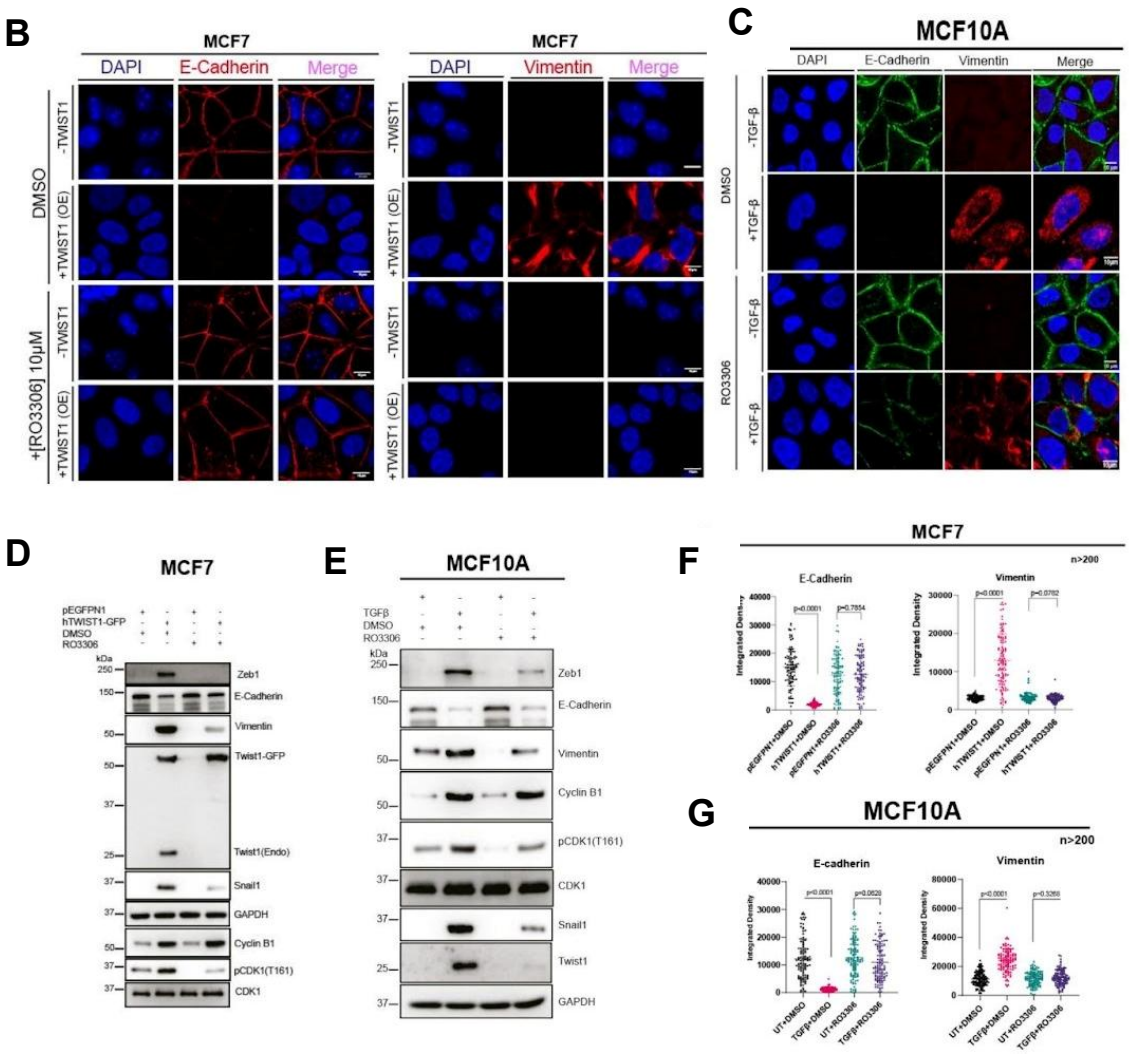


***Figure 4.10:*** *(A) Schematic representation of the methodology of RO3306 and MG132 experiment in MCF7 cells. (B) Immunofluorescence of MCF7 cells transiently transfected with pEGFP-N1 or Twist1-GFP and treated with 10μM RO3306 for 18 hours. E-cadherin or Vimentin stained in red. Scale bar, ~10 μm. (C) Immunofluorescence assay of MCF10A cells to check the effect of RO3306 on EMT. E-Cadherin is stained in green and Vimentin in red. Nucleus is visualized by DAPI (blue). Scale bar ~ 10μm. (D) Immunoblotting for EMT markers in MCF7 treated with RO3306 and Twist1-GFP in MCF7. (E) Immunoblotting to check the effect of RO3306 on EMT markers in the presence and absence of 10ng/mL TGF-β. (F) Quantification for the data in (B). (G) Quantification for the data in (C).*

### 4.2.5 Role of EZH2 Degradation in Disrupting the Interaction

CDK1 has previously been reported to phosphorylate EZH2 at Thr345, a post-translational modification that serves as a recognition cue for ubiquitin ligases, thereby targeting EZH2 for proteasomal degradation. This regulatory axis is particularly relevant in proliferative and

differentiation contexts where precise control of epigenetic silencing is required. In the context of epithelial–mesenchymal transition (EMT), where EZH2 plays a key role in reinforcing transcriptional repression of mesenchymal genes via H3K27 trimethylation, the phosphorylation-dependent degradation of EZH2 may serve to loosen repressive chromatin constraints and promote mesenchymal reprogramming.

To investigate whether CDK1-mediated degradation of EZH2 contributes to the disruption of the Lamin A/C–EZH2 interaction during EMT, we pharmacologically inhibited proteasomal activity using MG132, a potent and reversible proteasome inhibitor. TGF-β-treated MCF10A cells—undergoing robust EMT—were exposed to MG132 at a concentration of 1 μM for 18 hours. Following treatment, immunofluorescence staining was performed to assess the subnuclear distribution and colocalization of Lamin A/C and EZH2.

Remarkably, MG132 treatment restored the proximity of Lamin A/C and EZH2 in TGF-β-treated cells, as evidenced by enhanced nuclear colocalization (Figure 4.11A). In untreated EMT conditions, EZH2 staining appeared more diffuse, consistent with degradation, whereas MG132-exposed cells exhibited distinct perinuclear colocalization with Lamin A/C, similar to patterns observed in epithelial states. This observation strongly supports the model wherein proteasomal degradation of EZH2—triggered by CDK1-mediated phosphorylation—is a key event that destabilizes the Lamin A/C–EZH2 complex during EMT.

To further probe the functional impact of EZH2 stabilization on EMT phenotypes, we evaluated the expression of key epithelial and mesenchymal markers following MG132 treatment. TGF-β-treated MCF10A cells (and TWIST1 mediated EMT induction in MCF7) demonstrated elevated expression of canonical mesenchymal markers such as Vimentin, ZEB1, and TWIST1, alongside downregulation of epithelial marker E-cadherin. However, upon MG132 treatment, this gene expression profile was partially reversed: mesenchymal markers declined, and epithelial features, including E-cadherin localization at cell–cell junctions, were restored (Figure 4.11B-4.11F). These findings were corroborated by morphological changes, wherein MG132-treated cells displayed more epithelial-like, cobblestone morphology compared to the elongated and spindle-shaped appearance typical of EMT-induced cells.

The partial reversal of EMT upon EZH2 stabilization suggests that the degradation of EZH2 is not merely a downstream consequence of EMT but may actively drive the transition by dismantling chromatin-based repression mechanisms that maintain epithelial identity. Since

EZH2 is the catalytic subunit of the Polycomb Repressive Complex 2 (PRC2), its degradation would impair global H3K27me3 deposition, leading to transcriptional derepression of genes promoting mesenchymal states or inhibiting epithelial programs.

Collectively, these results reveal a multi-tiered regulatory mechanism wherein CDK1 not only phosphorylates Lamin A/C and EZH2 to disrupt their interaction directly but also induces proteasomal degradation of EZH2 to reinforce this dissociation. By destabilizing the Lamin A/C–EZH2 complex, CDK1 facilitates chromatin remodeling and transcriptional reprogramming necessary for EMT progression. Importantly, inhibition of the proteasome is sufficient to restore this interaction and partially revert EMT, highlighting a novel axis of epigenetic regulation that couples nuclear architecture with proteostasis and kinase signaling.

These findings further position the Lamin A/C–EZH2 interaction as a critical node in controlling cellular plasticity and underscore the potential of targeting the CDK1–EZH2–proteasome axis for modulating EMT in cancer therapy.

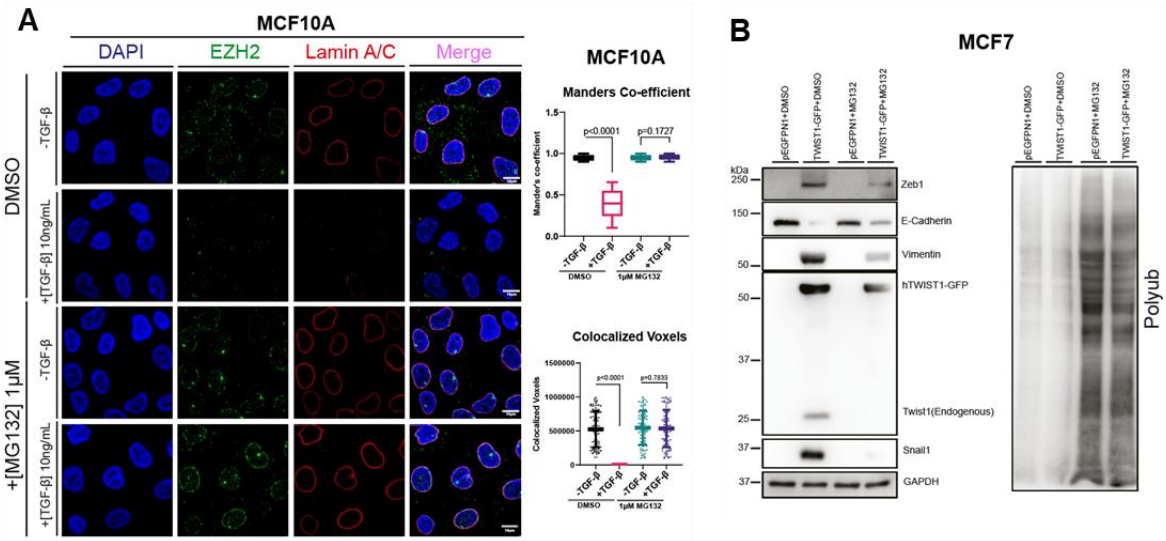

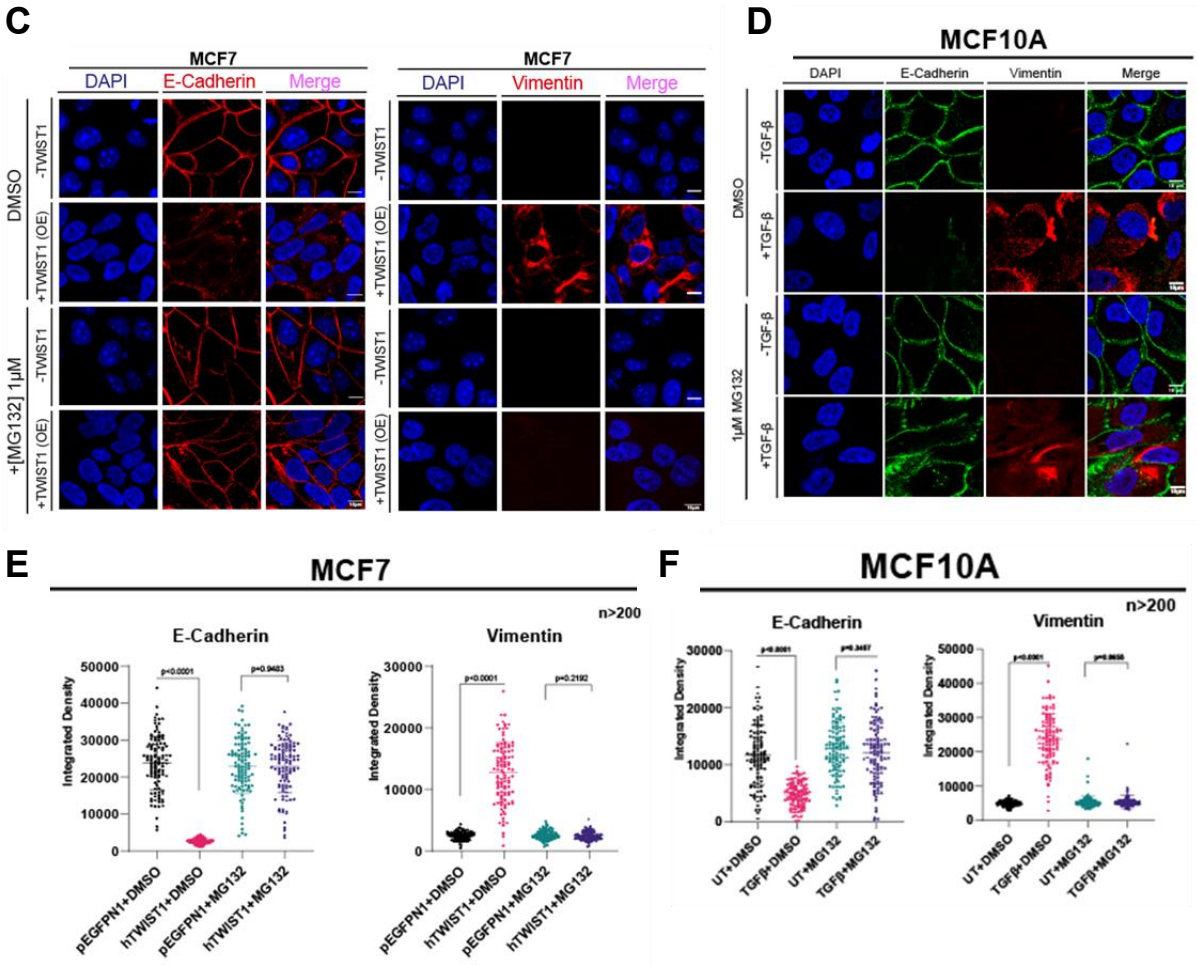


***Figure 4.11:*** *(A) Immunofluorescence and quantification of colocalized voxels and Mander's coefficient for Lamin A/C (Red) and EZH2(Green) in MCF10A cells ± TGF-β and 1 μM MG132. (B) Immunoblotting for EMT markers in MCF7 cells treated with MG132 and Twist1-GFP in MCF7. (C) Immunofluorescence of MCF7 cells treated with MG132 and transiently overexpressing hTWIST1-GFP and stained for E-cadherin and Vimentin (red). Scale bar, ~10 μm. (D) Immunofluorescence assay of MCF10A cells to check the effect of MG132 on EMT. E-Cadherin is stained in green and Vimentin in red. Nucleus is visualized by DAPI (blue). Scale bar ~ 10μm. (E) Quantification of the data in (C). (F) Quantification of the data in (D).*

### 4.2.6 Dissecting the Role of CDK1 Activity Versus Cell Cycle Phase

Given that CDK1 is a mitotic kinase activated during G2/M transition, we questioned whether EMT-associated CDK1 functions are due to its enzymatic activity or merely reflect G2/M cell cycle accumulation. FACS analysis demonstrated that EMT induction increased the G2/M population by ~30%, whereas MET induction via GRHL2 overexpression decreased G2/M occupancy (Figure 4.12A).

To decouple CDK1 activity from G2/M accumulation, we used nocodazole (10 μM, 18 h) to arrest Twist1-overexpressing MCF7 cells in G2/M without inhibiting CDK1 activity. Nocodazole treatment failed to alter EMT markers, suggesting that G2/M accumulation alone is insufficient to impact EMT progression (Figures 4.12B and 4.12C). Thus, CDK1 kinase activity, not cell cycle phase, is necessary for EMT.

In summary, our study uncovers a critical regulatory axis involving Lamin A/C, EZH2, and CDK1 that governs EMT progression in breast epithelial cells. The key insights are:

1. Lamin A/C and EZH2 form a direct complex via their conserved structural domains.
2. CDK1 phosphorylates Lamin A/C and EZH2 at specific sites, weakening their interaction.
3. Phosphorylation of EZH2 by CDK1 targets it for proteasomal degradation.
4. Dissociation of Lamin A/C–EZH2 complex alters chromatin structure and gene expression patterns to favor EMT.
5. CDK1 inhibition restores Lamin A/C–EZH2 interaction and suppresses EMT, offering potential therapeutic avenues.
6. CDK1 enzymatic activity, rather than cell cycle phase alone, is essential for these processes.

These findings highlight the convergence of nuclear structural components and epigenetic regulators under the control of cell cycle kinases in modulating dynamic cell state transitions. Targeting this axis may serve as a novel strategy to counteract EMT-driven metastasis in breast cancer and other malignancies.

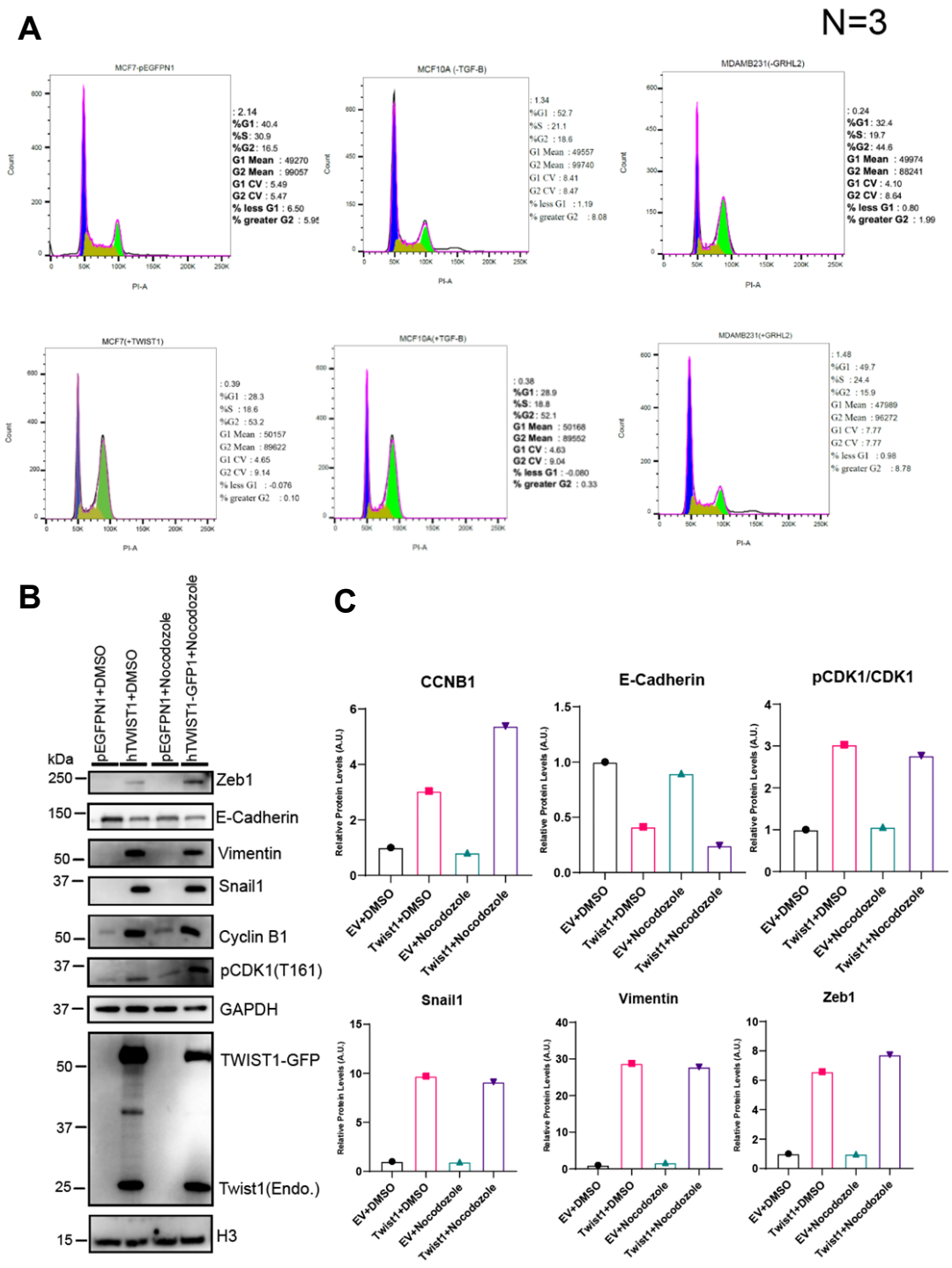


***Figure 4.12:*** *(A) FACS histogram showing cell cycle distribution following EMT (MCF7, MCF10A) and MET (MDA-MB-231). (B) Immunoblot analysis of EMT markers in MCF7 cells overexpressing TWIST1 with G2/M arrest induced by 10 µM nocodazole for 18 h (N=1).* ***(C)*** *Quantification for the data in (B).*

Epithelial–mesenchymal transition (EMT) is closely intertwined with cell cycle dynamics, as progression through specific cell cycle phases may be required to coordinate chromatin remodeling, transcriptional reprogramming, and cytoskeletal reorganization. Previous studies have reported varying effects of EMT on cell cycle distribution. For instance, Vega et al., 2004 observed that EMT in MDCK cells was accompanied by a reduction in Cyclin D1 levels and accumulation of cells in G1 phase, but they did not detect an enrichment in G2/M. This finding highlights the potential context dependence of cell cycle regulation during EMT, which may vary according to cell type and EMT subtype.

To systematically investigate the impact of EMT on the cell cycle in breast epithelial cells, we performed a double-thymidine block and release experiment in MCF10A cells, followed by EMT induction using TGF-β. In contrast to the observations reported by Vega et al., we found that Cyclin D1 levels remained largely unaltered following EMT induction, indicating that G1/S progression was not impaired. Notably, Cyclin B1 expression was substantially upregulated, with approximately a 25-fold increase at the mRNA level and ~15-fold increase at the protein level in mesenchymal cells. These results suggest an accumulation of cells in G2/M rather than G1 (Figure 4.13A and B).

To complement these molecular analyses, we performed flow cytometry, which revealed a ~3-fold increase in the G2/M fraction in TGF-β–treated MCF10A cells compared to controls. BrdU incorporation assays demonstrated comparable DNA synthesis between untreated and treated cells, further ruling out a G1/S block. Together, these data indicate that EMT induction is not associated with G1/S arrest but instead promotes accumulation of cells in the G2 phase of the cell cycle (Figure 4.13C and D).

To more precisely define the stage of accumulation within G2/M, we assessed phosphorylation of histone H3 at serine 10 (H3S10p), a marker of late mitosis. Two complementary approaches were used: (i) immunofluorescence in unsynchronized populations revealed that the fraction of H3S10p-positive cells dropped dramatically from ~19% in untreated cells to ~0.67% in TGF-β–treated cells; (ii) western blotting of synchronized, FACS-sorted G2/M populations confirmed a marked reduction in total H3S10p signal in mesenchymal cells. This pattern, when considered alongside elevated Cyclin B1 and pCDK1(T161) levels, unchanged Cyclin D1 after release from thymidine block, and unchanged BrdU incorporation, strongly indicates that EMT induces accumulation in either late S or early G2, rather than G1/S or late mitosis (Figure 4.13E-G).

These findings are consistent with previous reports suggesting that EMT-inducing transcription factors, including TWIST1 and SNAI1, can promote a G2/M delay to facilitate cellular reprogramming (Lee et al., 2010; Laberge et al., 2015). We propose that the apparent discrepancy with Vega et al. likely reflects differences in cellular context and EMT subtype: Vega et al. studied Type 1 EMT in MDCK cells and neural plate development in mouse embryos, whereas our study examines Type 3 EMT in human breast epithelial cells (Kalluri and Weinberg, 2009).

In summary, EMT induction in MCF10A cells is characterized by an enrichment in early G2, associated with active CDK1 signaling. This cell cycle context may provide a permissive environment for Lamin A/C–EZH2 dissociation, nuclear envelope remodeling, and chromatin reorganization, thereby facilitating the transcriptional and structural changes required for the mesenchymal phenotype. These observations underscore the close interdependence of cell cycle dynamics and EMT-associated nuclear reprogramming.

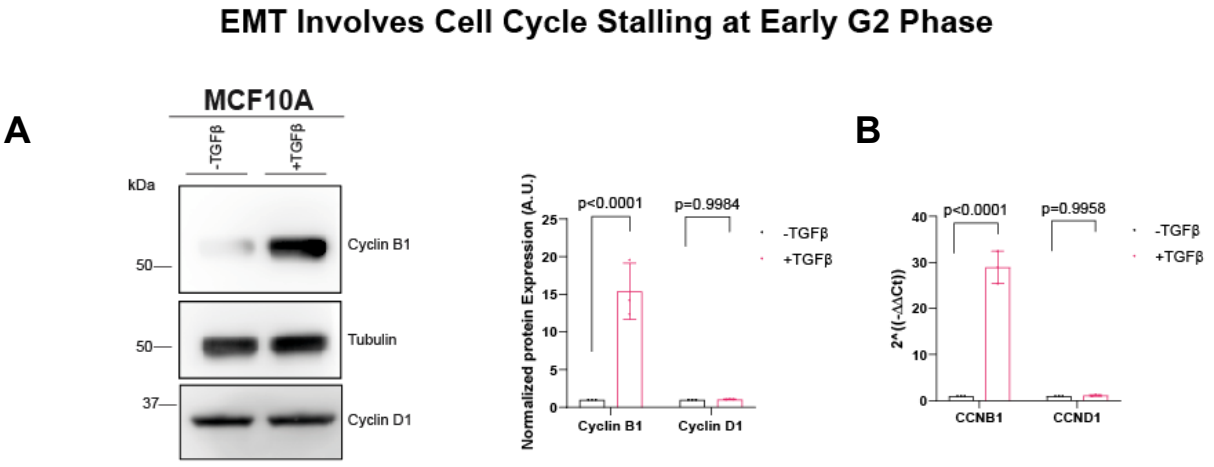

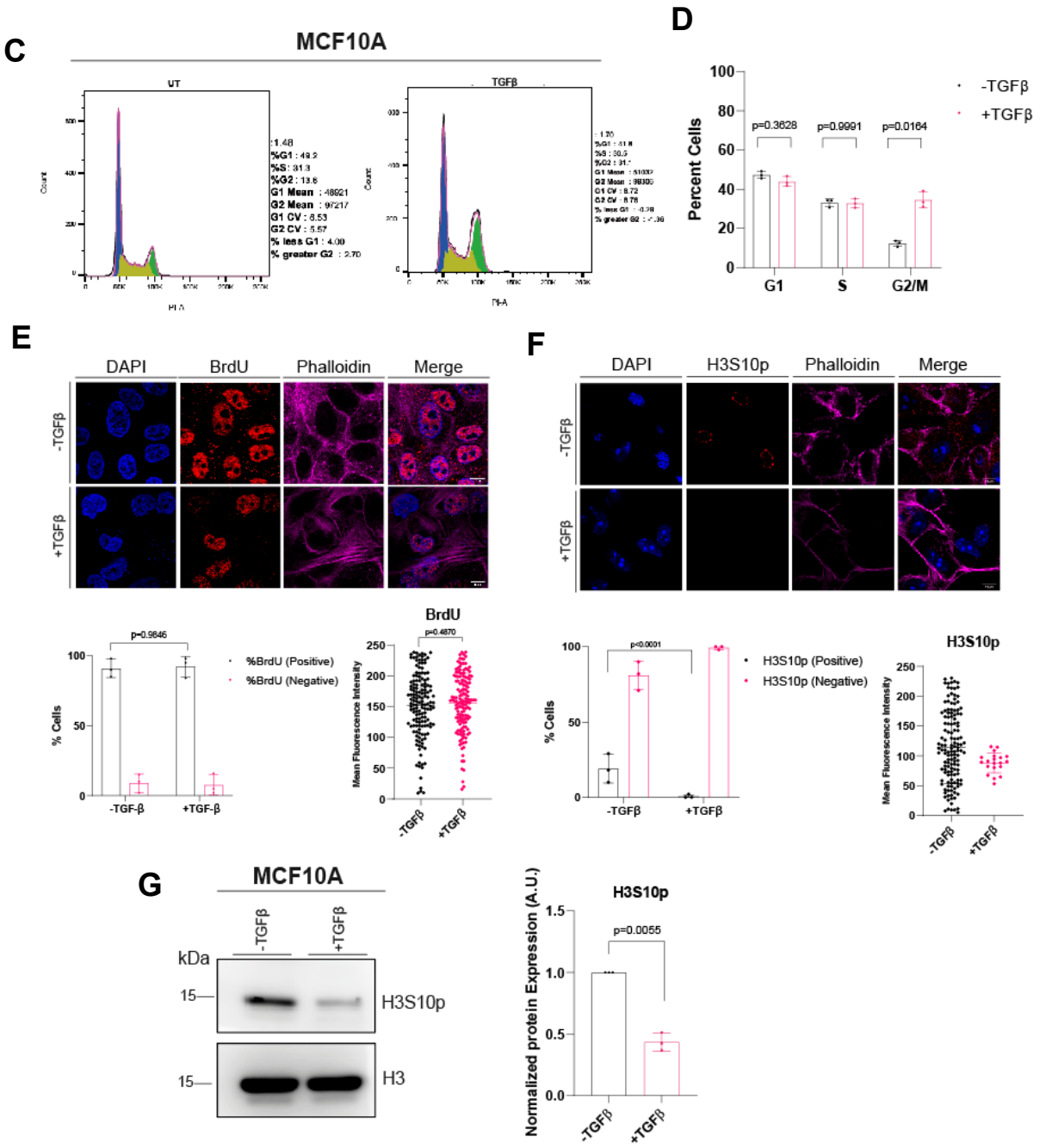


***Figure 4.13: TGFβ treatment induces cell cycle arrest and inhibits cell proliferation in MCF10A cells.*** *(A) Western blot analysis and quantification of Cyclin B1 and Cyclin D1 expression in MCF10A cells in the presence and absence of TGFβ. Tubulin serves as a loading control; bar graphs represent normalized protein levels (mean ± SD, n=3). (B) RT-PCR showing normalized mRNA levels of CCNB1 and CCND1 in the presence and absence of TGFβ (mean ± SD, n=3). (C) Flow cytometry analysis of DNA content to assess cell cycle phases, comparing untreated (UT) and TGFβ-treated cells. (D) Quantification of cell population distribution in G1, S, and G2/M phases following TGFβ treatment (mean ± SD, n=3). (E) Representative immunofluorescence images and quantification of %cells that are BrdU-*

*positive and BrdU-negative upon EMT induction by TGFβ. Phalloidin stains the actin cytoskeleton, and DAPI stains nuclei. Scale bar ~10μm (F) Immunofluorescence and quantification of %cells that are positive for H3S10 phosphorylation upon TGFβ treatment. (G) Western blot analysis and quantification of H3S10p levels from FACS-sorted G2 cells in MCF10A cells treated with TGFβ (mean ± SD, n=3). (H) Western blot for pCDK1 (T161) and total CDK1 with quantification upon EMT in MCF10A cells. Data are expressed as mean ± SD from triplicate experiments; statistical significance was determined using Student's t-test.*

### 4.2.7 pCDK1(T161): An Intermediate Player in EMT Progression in Breast Cancer Cells

We observed a notable increase in phosphorylated CDK1 at threonine 161 [pCDK1(T161)] levels during epithelial–mesenchymal transition (EMT), which was reversed upon mesenchymal–epithelial transition (MET). This observation prompted us to investigate the significance of elevated pCDK1 levels during EMT. Given that CDK1 activity is tightly regulated by Cyclin B1 (CCNB1), we assessed CCNB1 transcript and protein levels during EMT and MET. Both mRNA and protein levels of CCNB1 were upregulated during EMT and decreased upon MET, mirroring the pattern observed for pCDK1 (Figure 4.9G-I).

To explore the mechanism underlying transcriptional upregulation of CCNB1 during EMT, we used ChIP-Atlas to identify potential transcription factors that may bind to the CCNB1 promoter within the -1 kb region. This analysis revealed a putative TWIST1 binding site at the -108 position of the CCNB1 promoter, consistent with prior studies implicating TWIST1 in CCNB1 regulation (Kwok et al., 2007).

To test whether TWIST1 directly regulates CCNB1 transcription and thereby influences CDK1 activation, we overexpressed TWIST1 in the presence of SIS3, an inhibitor of Smad3 phosphorylation and TGFβ signaling. TWIST1 overexpression was able to rescue the inhibition of TGFβ signaling by SIS3, confirming that TWIST1 can bypass the requirement for Smad3 phosphorylation in promoting EMT. This result suggests that TWIST1 exerts its effects by directly binding DNA and regulating the transcription of downstream genes (Figure 4.14A-C).

We then validated TWIST1 binding to the CCNB1 promoter using ChIP-PCR. Further, ChIP assays revealed increased occupancy of transcriptional elongation marks H3K36me3 and RNA Polymerase II (Ser2p) at the +1 kb transcription start site of CCNB1 upon TWIST1 overexpression, confirming transcriptional activation.

To directly test the functional relevance of TWIST1 binding to the CCNB1 promoter, we generated CRISPR-based indels specifically at the TWIST1 binding site (-108) on the CCNB1 promoter, while leaving TWIST1 binding at other genomic sites intact. ChIP-PCR confirmed loss of TWIST1 binding at this specific site. When these CRISPR-edited MCF10A cells were treated with TGFβ, they failed to undergo EMT — mesenchymal markers were not upregulated, and epithelial markers remained unchanged — unlike wild-type MCF10A cells, which responded with canonical EMT marker shifts. These results underscore the critical role of TWIST1-mediated CCNB1 transcription in EMT induction (Figure 4.14D).

Curious about the upstream regulation of TWIST1, particularly its early activation during EMT, we performed promoter motif analysis and identified a Smad Binding Element (SBE) within the TWIST1 promoter, suggesting regulation by phosphorylated Smad3. Using CRISPR, we introduced indels at the Smad3 binding site of the TWIST1 promoter. These cells failed to upregulate TWIST1, CCNB1, or pCDK1 in response to TGFβ, indicating that Smad3 directly activates TWIST1 transcription, which in turn governs downstream CCNB1 and CDK1 activity (Figure 4.14E).

To delineate the signaling cascade, we treated MCF10A cells with either SIS3 (Smad3 inhibitor) or RO3306 (CDK1 inhibitor), followed by TGFβ stimulation. Both inhibitors abrogated EMT induction. Interestingly, Twist1 levels remained elevated upon TGFβ treatment in RO3306-treated cells, whereas SIS3-treated cells did not upregulate Twist1. This confirms that TWIST1 activation occurs upstream of CCNB1 transcription and CDK1 activation, and that Smad3 phosphorylation is essential for Twist1 induction (Figure 4.14A).

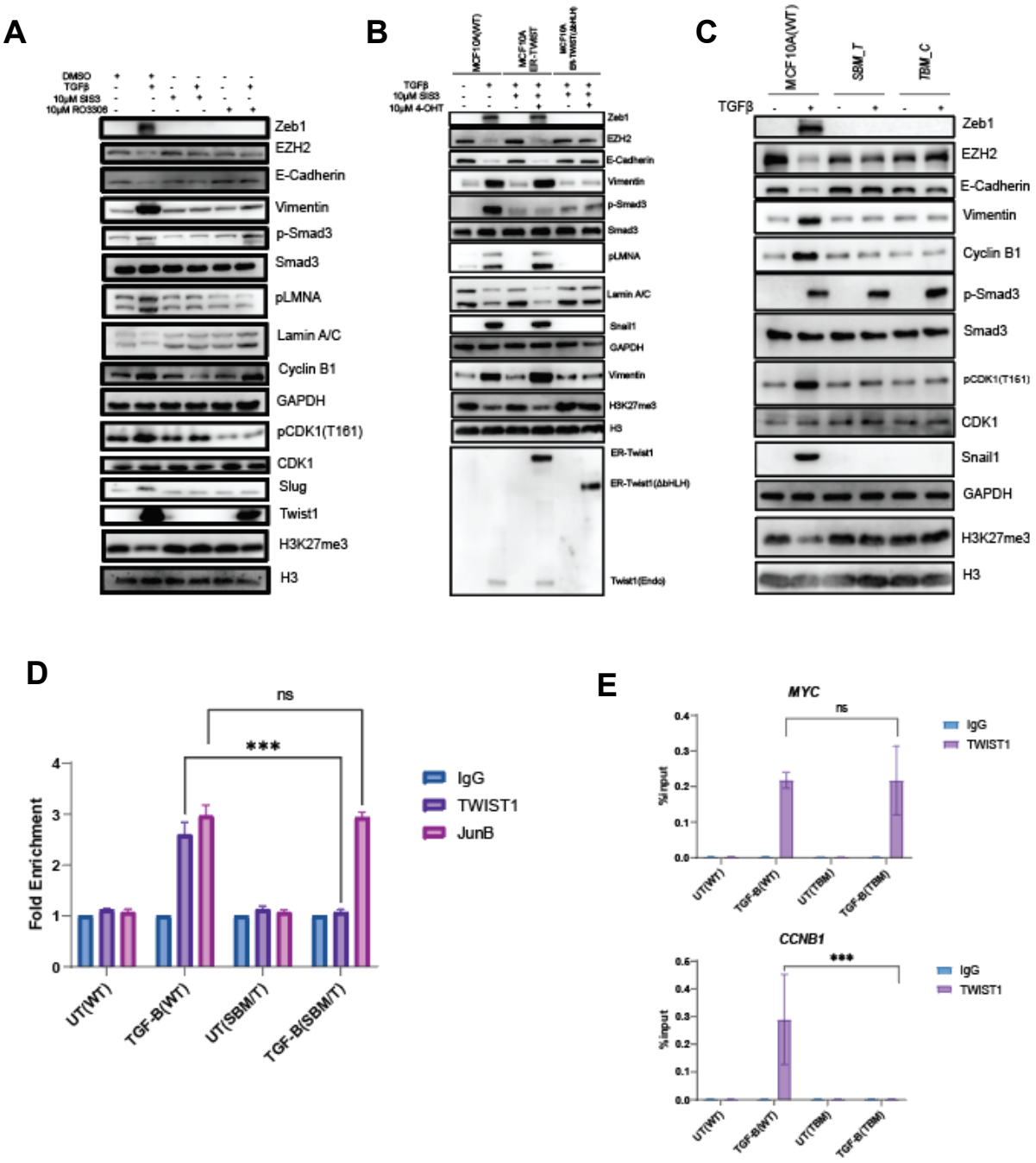


***Figure 4.14: Mechanistic Insights into Chromatin-Mediated Regulation of EMT via Lamin A–EZH2 Interaction***

*(A) Immunoblotting analysis of epithelial–mesenchymal (EM) markers in MCF10A cells to dissect upstream and downstream events leading to the disruption of the Lamin A–EZH2 interaction during EMT. Cells were treated with CDK1 inhibitor RO-3306 and Smad3 phosphorylation inhibitor SIS3 to assess their respective roles. (B) Functional assessment of Twist1 and a DNA-binding deficient mutant, Twist1(ΔbHLH), in rescuing EMT progression*

*under TGF-β signaling. The assay demonstrates that chromatin binding of Twist1 is essential for EMT advancement. (C) CRISPR-based mutants targeting Smad3 binding sites on the Twist1 promoter and Twist1 binding sites on the CCNB1 promoter were generated to delineate transcriptional regulatory dependencies in EMT progression. (D, E) ChIP-qPCR validating the genomic promoter mutation in (D) Smad3 binding site in Twist1 promoter (SBM/T) (E) Twist1 binding site in CCNB1 promoter (TBM)*

### 4.2.8 Preservation of Lamin A/C–EZH2 Interaction Following Disruption of Twist1–CCNB1 and Smad3–Twist1 Promoter Binding

In the preceding section, we demonstrated that targeted CRISPR–Cas9–mediated indels disrupting Twist1 binding at the CCNB1 promoter and Smad3 binding at the TWIST1 promoter markedly attenuated EMT-associated phenotypes in MCF10A cells, despite sustained exposure to TGF-β. These results indicate that canonical TGF-β signaling alone is insufficient to drive a complete EMT program in the absence of intact transcription factor–promoter interactions within the Smad3–Twist1–cell cycle regulatory axis. Thus, perturbation of these key transcriptional nodes functionally uncouples upstream TGF-β signaling from its downstream transcriptional and phenotypic outputs. Given our earlier observations that TGF-β–induced EMT is accompanied by disruption of the Lamin A/C–EZH2 complex, we next investigated whether such promoter-specific disruptions also influence the status of the Lamin A/C–EZH2 interaction.

To directly address this question, we assessed Lamin A/C–EZH2 proximity using proximity ligation assay (PLA) in MCF10A cells harboring CRISPR-induced indels at either (i) the Twist1 binding site within the CCNB1 promoter or (ii) the Smad3 binding site within the TWIST1 promoter. In control cells, TGF-β treatment led to a pronounced reduction in Lamin A/C–EZH2 PLA signal, consistent with dissociation of this complex during EMT progression. In striking contrast, cells bearing indels at either regulatory locus retained robust Lamin A/C–EZH2 proximity following TGF-β exposure. This preservation of interaction was reproducible and comparable across both genetic perturbations, indicating that disruption of Twist1–CCNB1 or Smad3–Twist1 promoter engagement is sufficient to block the TGF-β–dependent disassembly of the Lamin A/C–EZH2 complex (Figure 4.15).

These findings suggest that loss of Lamin A/C–EZH2 interaction is not a direct or inevitable consequence of TGF-β receptor activation, but rather depends on the successful execution of specific transcriptional programs downstream of Smad3 and Twist1. Intact Smad3 occupancy at the TWIST1 promoter and Twist1 binding at the CCNB1 promoter appear to act as critical molecular checkpoints that link extracellular TGF-β signaling to nuclear architectural remodeling. When these promoter-level interactions are disrupted, Lamin A/C remains stably associated with EZH2, implying that the Lamin–PRC2 regulatory module becomes refractory to upstream EMT-inducing signals.

Importantly, the maintenance of Lamin A/C–EZH2 proximity in these CRISPR-edited cells occurs in a context where EMT progression is attenuated, underscoring a close relationship between transcriptional state and epigenetic organization. This observation supports a model in which Lamin A/C–EZH2 dissociation is contingent upon productive transcriptional reprogramming rather than serving as a purely upstream driver of EMT. At the same time, it highlights a mechanistic separation between partial EMT-related responses and the broader chromatin reconfiguration typically associated with a complete EMT.

Collectively, these data position the Lamin A/C–EZH2 interaction as a sensitive integrator of transcriptional competence within the TGF-β–Twist1 signaling network. Rather than acting as a passive responder to extracellular cues, the Lamin A/C–dependent chromatin scaffold appears to sense and respond to the integrity of specific transcription factor–promoter interactions. Disruption of these interactions effectively insulates nuclear architecture from TGF-β–driven remodeling, reinforcing the concept that Lamin A/C–mediated chromatin organization functions as a regulatory checkpoint that coordinates transcriptional control with epigenetic state during EMT.

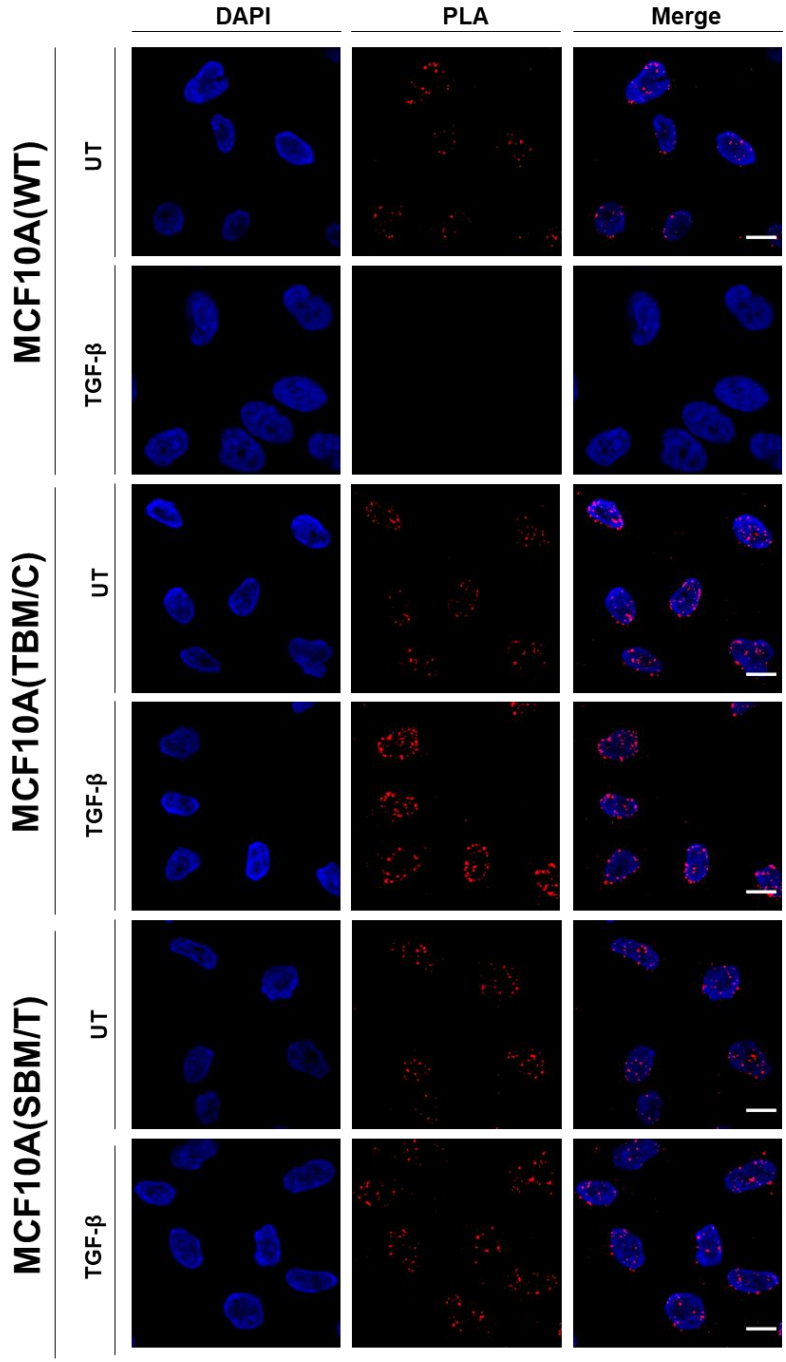


***Figure 4.15: Lamin A–EZH2 Interaction in CRISPR Mutants Targeting Smad3 and Twist1 Regulatory Sites***

*Proximity ligation assay (PLA) illustrating Lamin A–EZH2 interactions in MCF10A wild-type cells, Smad3 binding site mutants on the Twist1 promoter, and Twist1 binding site mutants on the CCNB1 promoter, under control conditions and upon TGF-β treatment. The assay reveals the requirement of intact Smad3–Twist1 and Twist1–CCNB1 transcriptional axes for preserving the Lamin A–EZH2 interaction*

### 4.2.9 Role of CDK1 phosphorylation in Lamin A and EZH2 phosphorylation and EMT progression

Cellular plasticity during epithelial–mesenchymal transition (EMT) is orchestrated by a complex interplay between transcriptional regulators, chromatin modifiers, and structural components of the nucleus. Lamin A/C, a key component of the nuclear lamina, has emerged as a critical regulator of chromatin organization and gene expression through its interactions with epigenetic modulators such as EZH2, the catalytic subunit of the Polycomb Repressive Complex 2 (PRC2). While Lamin A/C–EZH2 interactions contribute to the maintenance of repressive chromatin domains, the mechanisms regulating the stability of this complex during EMT remain unclear. Given that EMT is tightly linked to cell cycle progression and that CDK1 is a central mitotic kinase known to phosphorylate nuclear and chromatin-associated proteins, we hypothesized that CDK1-mediated phosphorylation could influence Lamin A/C–EZH2 association and thereby modulate EMT progression.

To test this hypothesis, we first investigated whether CDK1 activity directly affects the Lamin A/C–EZH2 interaction. Co-immunoprecipitation assays were performed in MCF10A cells arrested at the G1/S boundary using thymidine. Lamin A/C was immunoprecipitated from cells expressing either wild-type CDK1, a phosphomimetic mutant (T161D), or non-phosphorylatable mutants. In thymidine-arrested cells expressing wild-type or non-phosphorylatable CDK1, the Lamin A/C–EZH2 interaction remained intact, indicating that basal Lamin A/C–EZH2 binding is stable in the absence of mitotic phosphorylation events. In contrast, expression of the phosphomimetic CDK1 (T161D) mutant led to a clear disruption of the Lamin A/C–EZH2 interaction (Figure 4.16B). These results demonstrate that CDK1-mediated phosphorylation is sufficient to weaken or destabilize the Lamin A/C–EZH2 complex, likely by inducing conformational or post-translational changes in one or both proteins that reduce their binding affinity.

Having established that CDK1 activity can modulate Lamin A/C–EZH2 stability, we next assessed the functional consequences of this regulation on EMT progression. Thymidine-arrested MCF10A cells failed to undergo EMT upon TGF-β treatment, as evidenced by the retention of epithelial morphology and persistent expression of epithelial markers. This observation underscores the requirement of cell cycle progression for effective EMT induction. Remarkably, ectopic expression of the phosphomimetic CDK1 (T161D) mutant in thymidine-arrested cells restored EMT progression, resulting in characteristic mesenchymal

morphological changes, including spindle-like cell shape, loss of cell–cell adhesion, and upregulation of mesenchymal markers. These findings indicate that CDK1 activity is not only sufficient to disrupt the Lamin A/C–EZH2 complex but also capable of driving EMT even in the context of cell cycle arrest (Figure 4.16A).

Taken together, these results provide compelling evidence that CDK1 serves as a key regulator linking cell cycle progression, Lamin A/C–EZH2 dynamics, and EMT. The disruption of the Lamin A/C–EZH2 interaction by CDK1-mediated phosphorylation likely facilitates chromatin reorganization required for the transcriptional programs underlying EMT. This mechanistic connection highlights how post-translational modifications by cell cycle kinases can integrate nuclear architecture, epigenetic regulation, and phenotypic plasticity in epithelial cells undergoing mesenchymal transition.

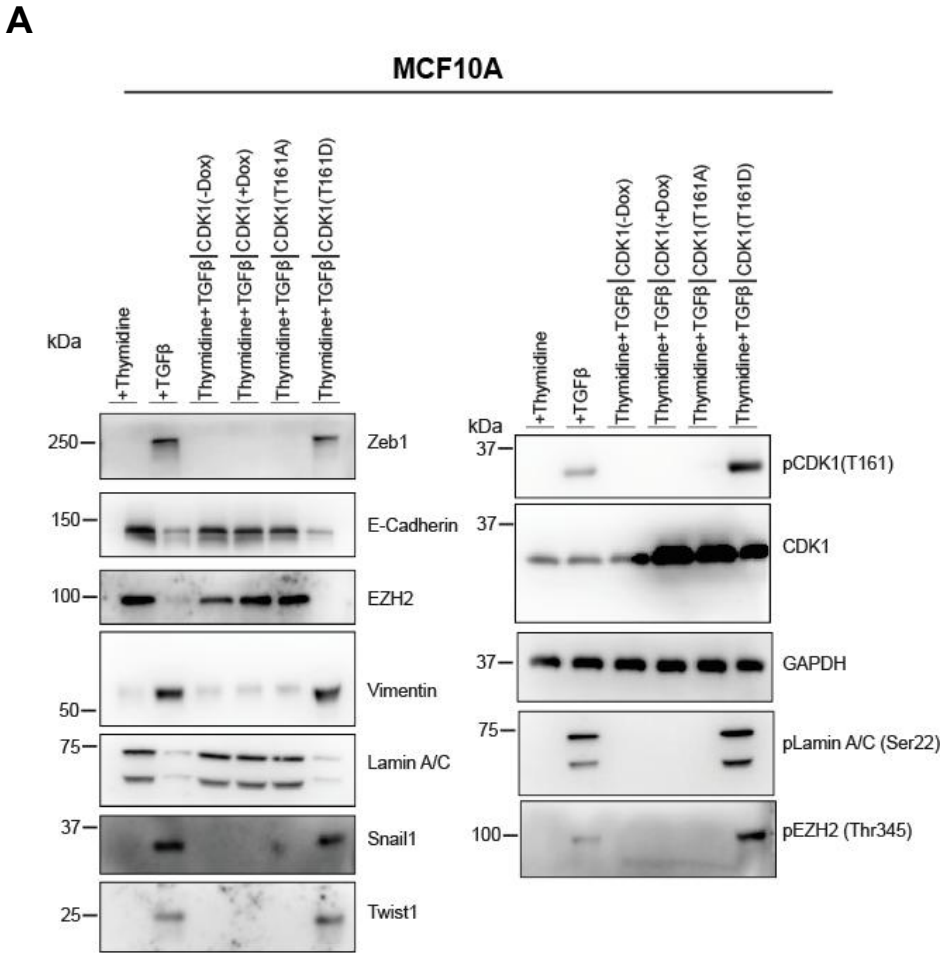

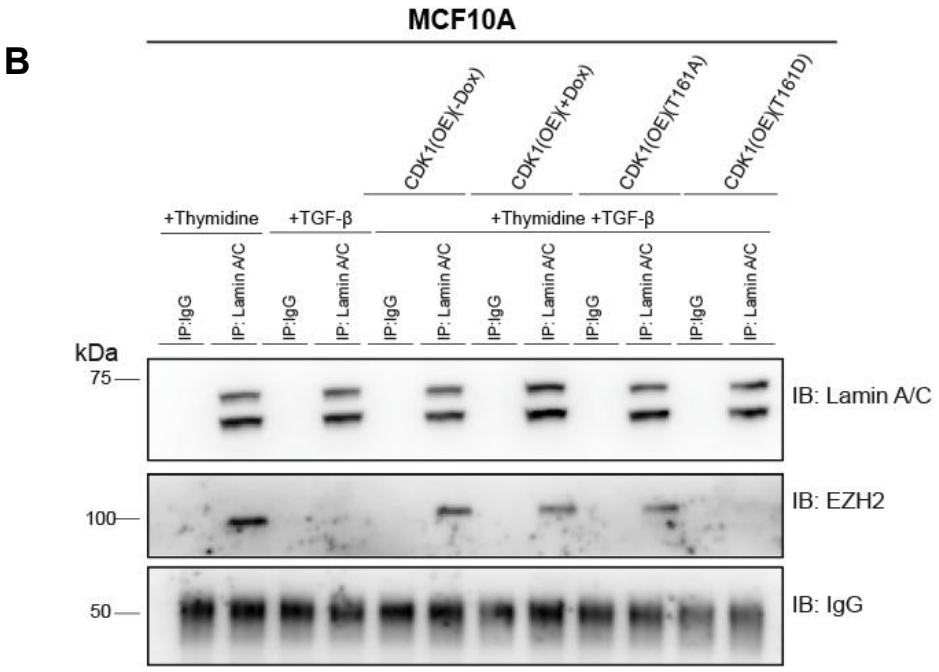


***Figure 4.16. Effect of CDK1 phosphomutants on EMT and Lamin A/C- EZH2 complex.***

***(A)*** *MCF10A cells synchronized at the G1 phase by double thymidine block were treated with 10 ng/mL TGFβ to induce EMT. The role of CDK1 phosphorylation site mutants (T161A, T161D) was assessed by doxycycline-inducible overexpression in thymidine-arrested cells.* ***(B)*** *Co-immunoprecipitation in G1-synchronized MCF10A cells treated with TGFβ and overexpressing CDK1 phosphomutants to validate the interaction of Lamin A/C with EZH2.*

### 4.2.10 Regulatory Role of Phosphorylation in Lamin A/C–EZH2 Interaction

Post-translational modifications, particularly phosphorylation, are crucial modulators of protein–protein interactions, often influencing structural conformation, subcellular localization, and complex formation. Phosphorylation of nuclear lamins is known to regulate nuclear architecture and chromatin organization, both of which are fundamental processes in EMT and MET. Given the central roles of Lamin A/C and EZH2 in chromatin dynamics and transcriptional regulation, we hypothesized that phosphorylation at specific residues might influence their mutual interaction and, consequently, impact cell state transitions during EMT/MET.

Cyclin-Dependent Kinase 1 (CDK1) has been previously implicated in phosphorylating nuclear lamins, thereby disrupting the nuclear lamina during mitosis and remodeling chromatin structure. To explore whether CDK1-mediated phosphorylation modulates the Lamin A/C–EZH2 interaction, we focused on two well-characterized phosphorylation sites: Serine 22 (S22) on Lamin A/C and Threonine 345 (T345) on EZH2—both of which fall within CDK1 consensus motifs and are reported to regulate protein–protein interactions.

Since deletion experiments had revealed that the N-terminal head domain of Lamin A interacts with amino acids 301–500 of EZH2, we systematically examined known CDK1 target sites within these regions. Site-directed mutagenesis (SDM) was performed for T19 and S22 in Lamin A, and for T345, T350, and T487 in EZH2. Among these, only Lamin A (S22) showed interaction with EZH2 (T345), while no detectable binding was observed for any of the other phospho-site combinations. This selective interaction further justified focusing on the S22 and T345 sites for downstream mechanistic studies.

To functionally dissect the roles of these residues, we generated phospho-deficient (S22A and T345A) and phosphomimetic (S22D and T345D) mutants of Lamin A and EZH2, respectively. To assess the influence of Lamin A/C phosphorylation, we engineered stable, doxycycline-inducible Lamin A/C knockdown MCF7 cell lines, subsequently rescued with shRNA-resistant constructs expressing either wild-type Lamin A, the phospho-deficient S22A variant, or the phosphomimetic S22D variant, all tagged with GFP for selection and visualization. To ensure uniform expression, GFP-positive cells were isolated via FACS. EMT was induced by transient overexpression of TWIST1-GFP for ~48 hours, followed by G418 selection to enrich TWIST1-expressing populations (Figure 4.17A). Co-immunoprecipitation (Co-IP) of Lamin A/C

followed by immunoblotting for EZH2 revealed that both wild-type Lamin A and the S22A mutant retained their ability to interact with EZH2, regardless of EMT induction. Conversely, the S22D variant failed to interact with EZH2 under any condition. These results suggest that phosphorylation at S22 of Lamin A/C disrupts its binding to EZH2, highlighting the requirement for an unphosphorylated state to maintain this interaction (Figure 4.17C).

We next tested the generalizability of this finding in a MET context using MDA-MB-231 cells overexpressing GRHL2. Stable cell lines expressing shRNA-resistant versions of full-length Lamin A, S22A, or S22D were generated. Consistent with our observations in MCF7 cells, the wild-type and S22A Lamin A variants displayed robust interaction with EZH2, whereas the S22D phosphomimetic did not. This reinforces the notion that S22 phosphorylation consistently inhibits Lamin A/C–EZH2 complex formation during both EMT and MET transitions (Figure 4.17D).

To assess whether EZH2 phosphorylation independently regulates this interaction, we generated phospho-deficient (T345A) and phosphomimetic (T345D) EZH2 mutants. Co-IP experiments were conducted in both MCF7 (± TWIST1) and MDA-MB-231 (± GRHL2) backgrounds. In both cell types, full-length EZH2 and the T345A variant retained strong interactions with Lamin A/C, irrespective of cell state. However, the T345D phosphomimetic mutant failed to interact with Lamin A/C, indicating that phosphorylation at T345 impairs complex formation (Figures 4.17E, 4.17F).

To evaluate the combinatorial impact of phosphorylation on both Lamin A/C and EZH2 simultaneously, we performed co-transfection experiments using combinations of wild-type, phospho-deficient, and phosphomimetic forms of Lamin A and EZH2, followed by co-immunoprecipitation of FLAG-tagged EZH2 to assess binding efficiency. These experiments revealed that the interaction between Lamin A and EZH2 was abolished if either protein was expressed in its phosphomimetic form, regardless of the phosphorylation status of the other. In other words, a single phosphorylation-mimicking mutation—either Lamin A(S22D) or EZH2(T345D)—was sufficient to disrupt the interaction, underscoring the sensitivity of the complex to phosphorylation at either site as seen by immunofluorescence assay (Figure 4.17G-J).

Together, these findings demonstrate that phosphorylation at either Lamin A/C S22 or EZH2 T345 is sufficient to abrogate the Lamin A/C–EZH2 interaction. This highlights the

phosphorylation status of both proteins as a pivotal determinant in regulating the formation of this nuclear complex. These results support a model in which CDK1-mediated phosphorylation of either component leads to disassembly of the Lamin A/C–EZH2 complex, facilitating chromatin reorganization and gene expression changes that drive EMT.

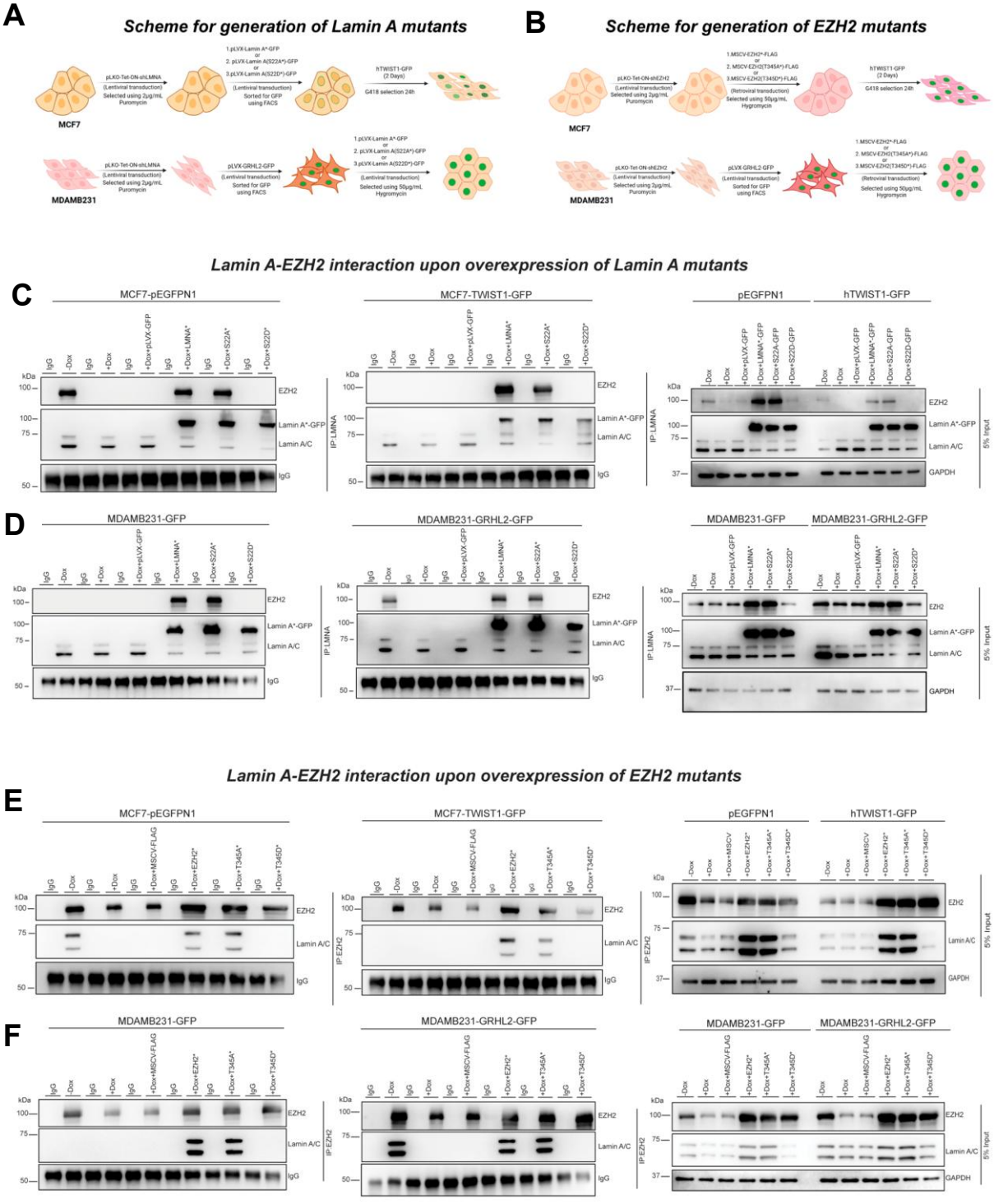

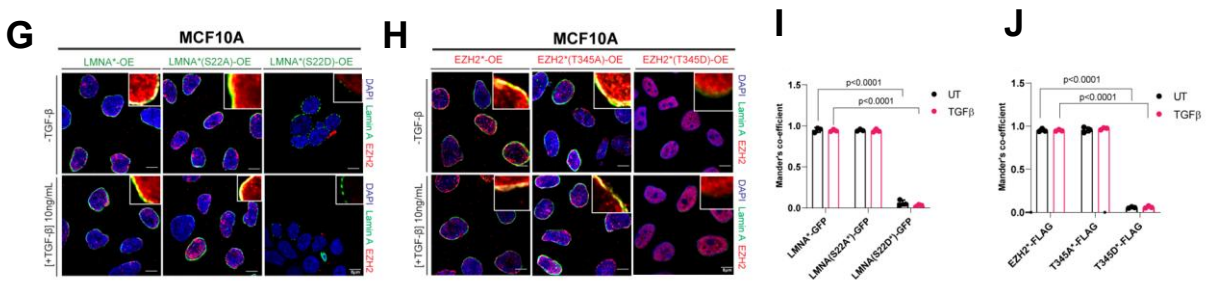


***Figure 4.17 Phosphorylation-dependent regulation of Lamin A/C–EZH2 binding in epithelial-mesenchymal and mesenchymal-epithelial transitions***

*(A, B) Schematic representation of the workflow for generating stable cell lines with inducible knockdown of Lamin A (A) or EZH2 (B), followed by rescue with wild-type (WT), phosphodeficient, or phosphomimetic mutants. (C, D) Co-immunoprecipitation of Lamin A in MCF7 and MDA-MB-231 cells after doxycycline-induced Lamin A/C depletion and rescue with WT, phosphodeficient (S22A), or phosphomimetic (S22D) Lamin A. TWIST1-GFP was transiently overexpressed in MCF7 cells, and GRHL2-GFP was stably overexpressed in MDA-MB-231 cells. (E, F) Co-immunoprecipitation of EZH2 in MCF7 and MDA-MB-231 cells after doxycycline-induced EZH2 depletion and rescue with WT, phosphodeficient (T345A), or phosphomimetic (T345D) EZH2. TWIST1-GFP was transiently overexpressed in MCF7 cells, and GRHL2-GFP was stably overexpressed in MDA-MB-231 cells. (G) Immunofluorescence images of MCF10A cells showing the extent of colocalization between Lamin A (WT, phosphodeficient (S22A), or phosphomimetic (S22D)) and EZH2 in the presence or absence of TGF-β. Lamin A-GFP is shown in green, and EZH2 is stained in red. Scale bar, ~10 µm. (H) Immunofluorescence images of MCF10A cells showing the extent of colocalization between EZH2 (WT, phosphodeficient (S22A), or phosphomimetic (S22D)) and Lamin A in the presence or absence of TGF-β. EZH2 is stained in red, and Lamin A is shown in green. Scale bar, ~10 µm. (I, J) Quantification of Lamin A and EZH2 colocalization in MCF10A cells using Mander's coefficient.*

### 4.2.11 CDK1-Mediated Phosphorylation Reveals S22 of Lamin A and T345 of EZH2 as the Dominant Determinants of Their Interaction

The nuclear lamina protein Lamin A/C plays a central role in chromatin organization and transcriptional regulation through its interactions with multiple epigenetic regulators, including Polycomb group proteins. Enhancer of zeste homolog 2 (EZH2), the catalytic subunit of the Polycomb repressive complex 2 (PRC2), mediates transcriptional repression via trimethylation of histone H3 at lysine 27 (H3K27me3) and has been widely implicated in epithelial–mesenchymal transition (EMT), cellular plasticity, and cancer progression (Margueron and Reinberg, 2011; Kim and Roberts, 2016). Our earlier findings established a phosphorylation-dependent interaction between Lamin A/C and EZH2, centred on Lamin A serine 22 (S22) and EZH2 threonine 345 (T345), and demonstrated that disruption of this interaction promotes epithelial–mesenchymal plasticity.

Cyclin-dependent kinase 1 (CDK1) is a well-characterized mitotic kinase known to phosphorylate both Lamin A/C and EZH2 at multiple residues, thereby regulating nuclear envelope dynamics, chromatin association, and protein–protein interactions (Peter et al., 1990; Wei et al., 2011). In addition to Lamin A S22 and EZH2 T345, several other CDK1 phosphorylation sites have been reported, including Lamin A S19 and EZH2 T350 and T487 (Heald and McKeon, 1990; Kaneko et al., 2010). Given the clustering of these residues within or proximal to the Lamin A–EZH2 interaction interface, it remained unclear whether multiple CDK1-dependent phosphorylation events collectively regulate this interaction or whether a single dominant site governs complex stability and downstream epithelial–mesenchymal (EM) phenotypes.

To address this, we systematically interrogated the contribution of additional CDK1 phosphorylation sites on Lamin A and EZH2 using phosphodeficient and phosphomimetic mutants, and assessed their impact on Lamin A–EZH2 interaction and epithelial–mesenchymal status in non-transformed mammary epithelial cells.

Deletion mapping experiments revealed that Lamin A interacts with EZH2 within the 301–500 amino acid region, while EZH2 preferentially associates with the N-terminal head domain of Lamin A. Sequence analysis of these interacting regions highlighted multiple consensus CDK1 phosphorylation motifs on both proteins, suggesting potential multilayered phosphoregulation of the Lamin A–EZH2 complex.

In addition to the previously characterized Lamin A S22 and EZH2 T345 sites, we focused on Lamin A S19 and EZH2 T350 and T487, all of which have been reported as bona fide CDK1 targets in existing literature. To examine their functional relevance, phosphodeficient (alanine substitution) and phosphomimetic (aspartate substitution) mutants were generated for Lamin A (S19A and S19D) and EZH2 (T350A/D and T487A/D). These constructs were individually expressed in MCF10A cells, followed by co-immunoprecipitation assays to assess their ability to interact with the endogenous binding partner.

Co-immunoprecipitation experiments using Lamin A as the bait demonstrated that the phosphomimetic Lamin A S19D mutant retained robust interaction with EZH2, comparable to Lamin A wild-type. In contrast, the phosphodeficient Lamin A S19A mutant failed to interact with EZH2, even upon TGF-β stimulation. Notably, Lamin A wild-type maintained interaction under basal conditions, consistent with previous observations. These results indicate that phosphorylation status at S19 does not function as a regulatory switch for Lamin A–EZH2 interaction, and that loss of interaction observed under EMT-inducing conditions is not phenocopied by S19 phosphomutation alone (Figure 4.18A).

Parallel analyses with EZH2 mutants yielded similar conclusions. Neither phosphodeficient nor phosphomimetic mutations at EZH2 T350 altered its interaction with Lamin A under basal conditions. However, TGF-β treatment resulted in a marked loss of interaction for both T350A and T350D mutants, whereas EZH2 wild-type retained its association with Lamin A under identical conditions. An analogous pattern was observed for EZH2 T487A and T487D mutants, which displayed no intrinsic defects in Lamin A binding but exhibited interaction loss specifically upon TGF-β stimulation, in contrast to EZH2 wild-type (Figures 4.18B and C).

To determine whether these phosphorylation events influence epithelial–mesenchymal plasticity, we assessed the EM profiles of all mutant-expressing MCF10A cells. Across all Lamin A S19 and EZH2 T350/T487 phosphomutants, no significant alterations in epithelial or mesenchymal marker expression were observed relative to wild-type controls. Changes in EM status were detected exclusively upon TGF-β treatment, indicating that these additional phosphorylation sites do not independently modulate epithelial–mesenchymal identity (Figures 4.18D – F).

Collectively, these data demonstrate that, despite the presence of multiple CDK1 phosphorylation sites within the Lamin A–EZH2 interaction interface, only Lamin A S22 and

EZH2 T345 act as functionally dominant residues governing complex stability and epithelial–mesenchymal regulation.

This systematic phosphomutational analysis establishes that CDK1-mediated phosphorylation of Lamin A and EZH2 is not globally permissive or redundant with respect to their interaction. Instead, the Lamin A S22 and EZH2 T345 residues constitute a single, predominant phosphoregulatory axis that dictates Lamin A–EZH2 complex integrity and epithelial–mesenchymal plasticity. Additional CDK1 phosphorylation sites on Lamin A (S19) and EZH2 (T350 and T487), although biochemically validated, do not contribute to interaction dynamics or EM phenotypic outcomes in MCF10A cells. These findings underscore a high degree of site specificity in phosphorylation-dependent regulation of nuclear lamina–chromatin crosstalk and reinforce the central role of the Lamin A(S22)–EZH2(T345) module in controlling EMT-associated epigenetic remodeling.

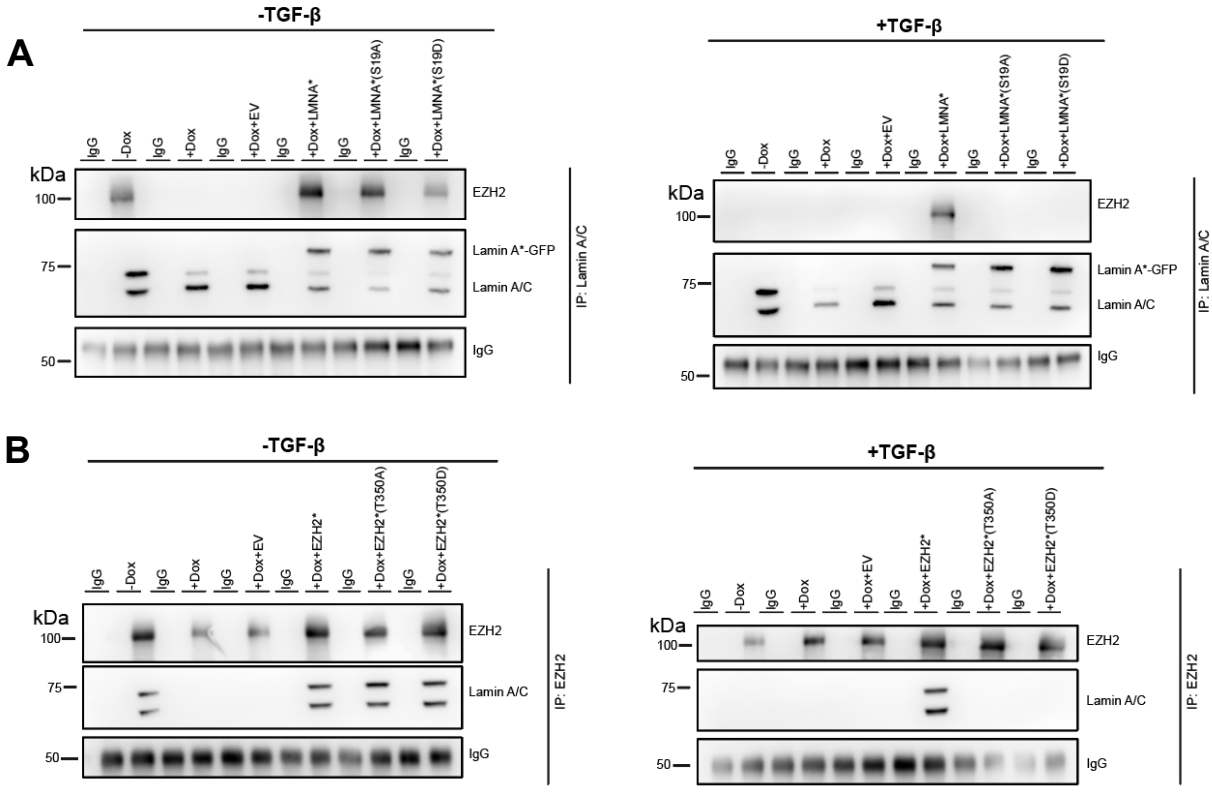

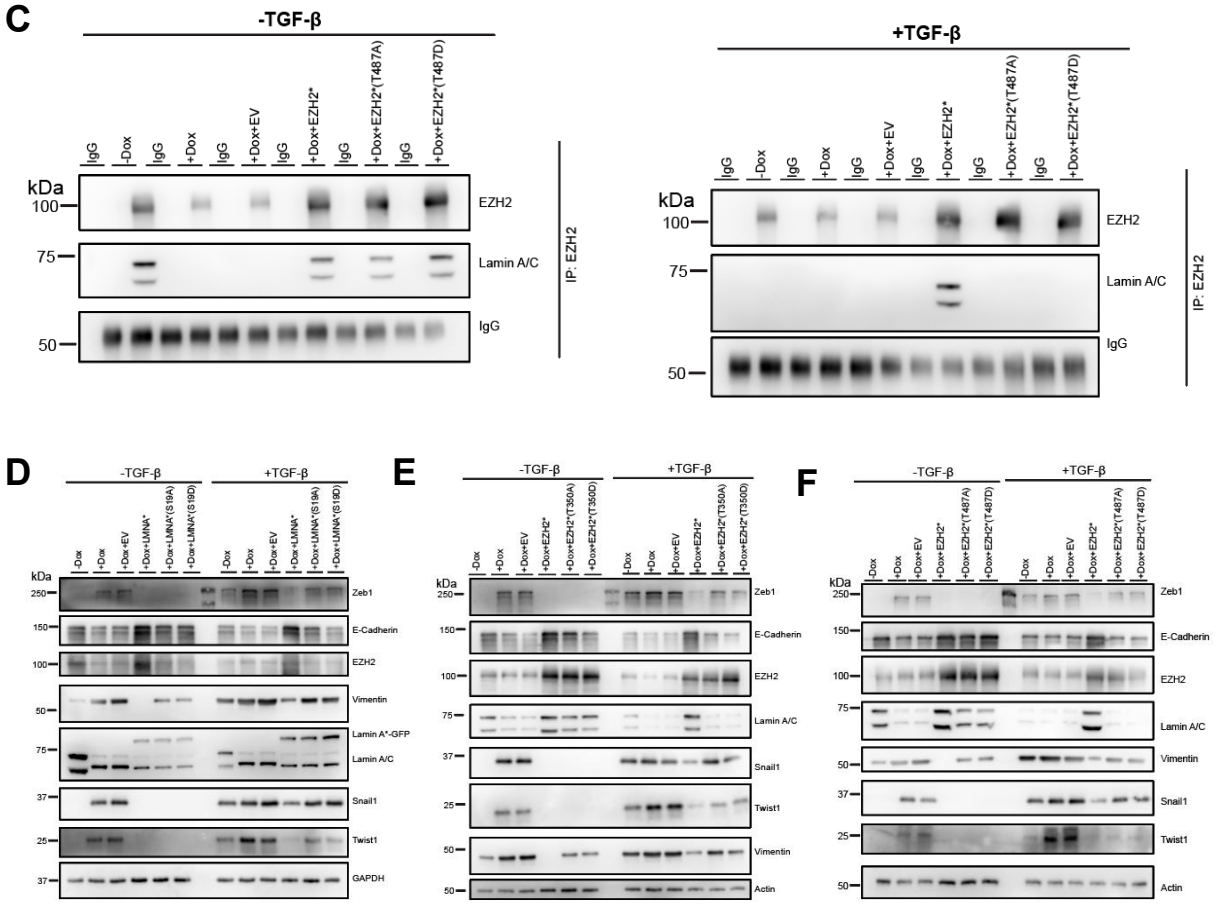


***Figure 4.18: Relavance of other Lamin A and EZH2 phosphomutants on Lamin A and EZH2 interaction and EM status in MCF10A cells****: (A) CoIP of Lamin A/C and immunoblot of EZH2 in MCF10A cells overexpressing Lamin A (S19) phosphomutants (B) CoIP of EZH2 and immunoblot of Lamin A/C in MCF10A cells overexpressing EZH2 (T350) phosphomutants (C) CoIP of EZH2 and immunoblot of Lamin A/C in MCF10A cells overexpressing Lamin A (T487) phosphomutants (D) EM status profiling of MCF10A cells overexpressing Lamin A(S19) phosphomutants (E) EM status profiling of MCF10A cells overexpressing EZH2(T350) phosphomutants (F) EM status profiling of MCF10A cells overexpressing EZH2(T487) phosphomutants.*

### 4.2.12 Phosphorylation-Dependent Modulation of Lamin A/C and EZH2 Influences CDK1 Activation and Cell Cycle Progression

To further investigate the functional impact of Lamin A/C and EZH2 phosphorylation on cell cycle dynamics, we performed fluorescence-activated cell sorting (FACS)-based cell cycle profiling in MCF10A cells expressing different phospho-mutants of these proteins. Both Lamin A/C and EZH2 are known to participate in diverse cellular processes, including nuclear architecture, chromatin organization, and transcriptional regulation. However, their role in modulating cell cycle progression during epithelial–mesenchymal transition (EMT) remains largely unexplored. Our earlier observations indicated that the phosphorylation status of Lamin A at Ser22 and EZH2 at Thr345 correlates with changes in the levels of phosphorylated CDK1 at threonine 161 [pCDK1(T161)], a key marker of CDK1 activation that is required for G2/M phase transition. To understand the mechanistic link between these post-translational modifications and cell cycle progression, we systematically evaluated how various phospho-deficient and phospho-mimetic mutants of Lamin A and EZH2 influence the distribution of cells across different phases of the cell cycle.

We first validated the expression of the mutant constructs through immunoblotting and confirmed that the wild-type, phospho-deficient (Lamin A S22A and EZH2 T345A), and phospho-mimetic (Lamin A S22D and EZH2 T345D) forms were robustly expressed in MCF10A cells. Immunoblot analysis revealed that cells expressing either wild-type or phospho-deficient forms exhibited notably reduced levels of pCDK1(T161) compared to uninduced MCF10A controls. In contrast, overexpression of the phospho-mimetic Lamin A(S22D) and EZH2(T345D) led to a significant increase in pCDK1(T161) levels, suggesting that phosphorylation at these specific residues may play a role in enhancing CDK1 activation.

We next performed FACS-based cell cycle profiling to assess how these phosphorylation-dependent changes in pCDK1 levels influenced the progression through the cell cycle. Cells were fixed, stained with propidium iodide, and analyzed for DNA content to determine their distribution across G1, S, and G2/M phases. Strikingly, MCF10A cells treated with TGF-β, or cells in which Lamin A/C and EZH2 were depleted using siRNA-mediated knockdown, showed a pronounced accumulation in the G2/M phase, with approximately 30% of the population residing in this compartment. Similarly, overexpression of the phospho-mimetic Lamin A(S22D) and EZH2(T345D) mutants also resulted in a comparable enrichment of cells in the G2/M phase. These data collectively point towards a role for phosphorylated Lamin A

and EZH2 in promoting progression toward mitosis, likely through the activation of the CDK1–Cyclin B1 complex (Figures 4.13 and 4.14).

In contrast, cells overexpressing full-length Lamin A or EZH2, as well as their respective phospho-deficient variants (S22A and T345A), showed a clear accumulation in the G1 phase, with a lower proportion of cells transitioning into G2/M. These results indicate that the non-phosphorylatable forms of Lamin A and EZH2 may inhibit CDK1 activation and act as suppressors of G2/M progression. Interestingly, the cell cycle profiles of these cells closely resembled those of the uninduced MCF10A control population, suggesting that phosphorylation at these specific residues acts as a molecular switch regulating CDK1 activity and cell cycle transition (Figures 4.19 and 4.20).

Collectively, these findings underscore the importance of Lamin A/C and EZH2 phosphorylation in modulating CDK1 activation and cell cycle dynamics during EMT. Phosphorylation of Lamin A at Ser22 and EZH2 at Thr345 appears to facilitate the accumulation of cells in G2/M, potentially preparing the cells for division and epigenetic reprogramming associated with EMT. This cell cycle shift could also serve as a permissive state for transcriptional and chromatin alterations that drive mesenchymal features, thereby linking cell cycle regulation with cell fate transitions. Moreover, these results provide a mechanistic basis for how post-translational modifications of nuclear and epigenetic regulators converge on CDK1 activity to influence the EMT process in breast epithelial cells.

Future studies could explore how these phosphorylation events are temporally regulated during EMT and whether CDK1 directly phosphorylates Lamin A/C or EZH2 in a feedback loop to sustain the mesenchymal state. Additionally, pharmacological modulation of these pathways may open new avenues for interfering with EMT-associated cancer progression and metastasis.

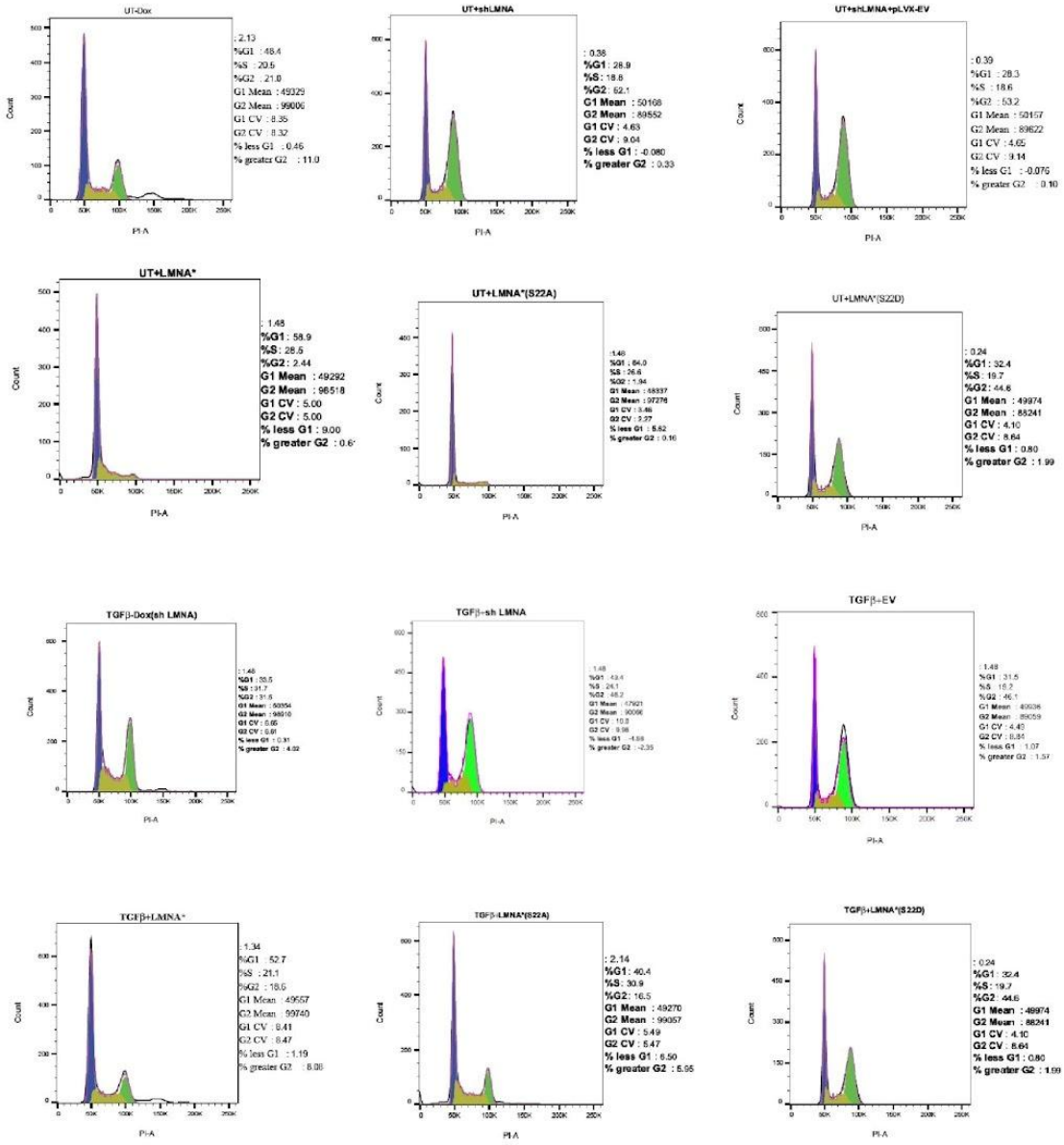


***Figure 4.19: FACS-based cell cycle profiling of Lamin A mutants:*** *MCF10A cells - Wild-type, phosphodeficient (S22A), and phosphomimetic (S22D) were analyzed for any possible changes in the cell cycle profile.*

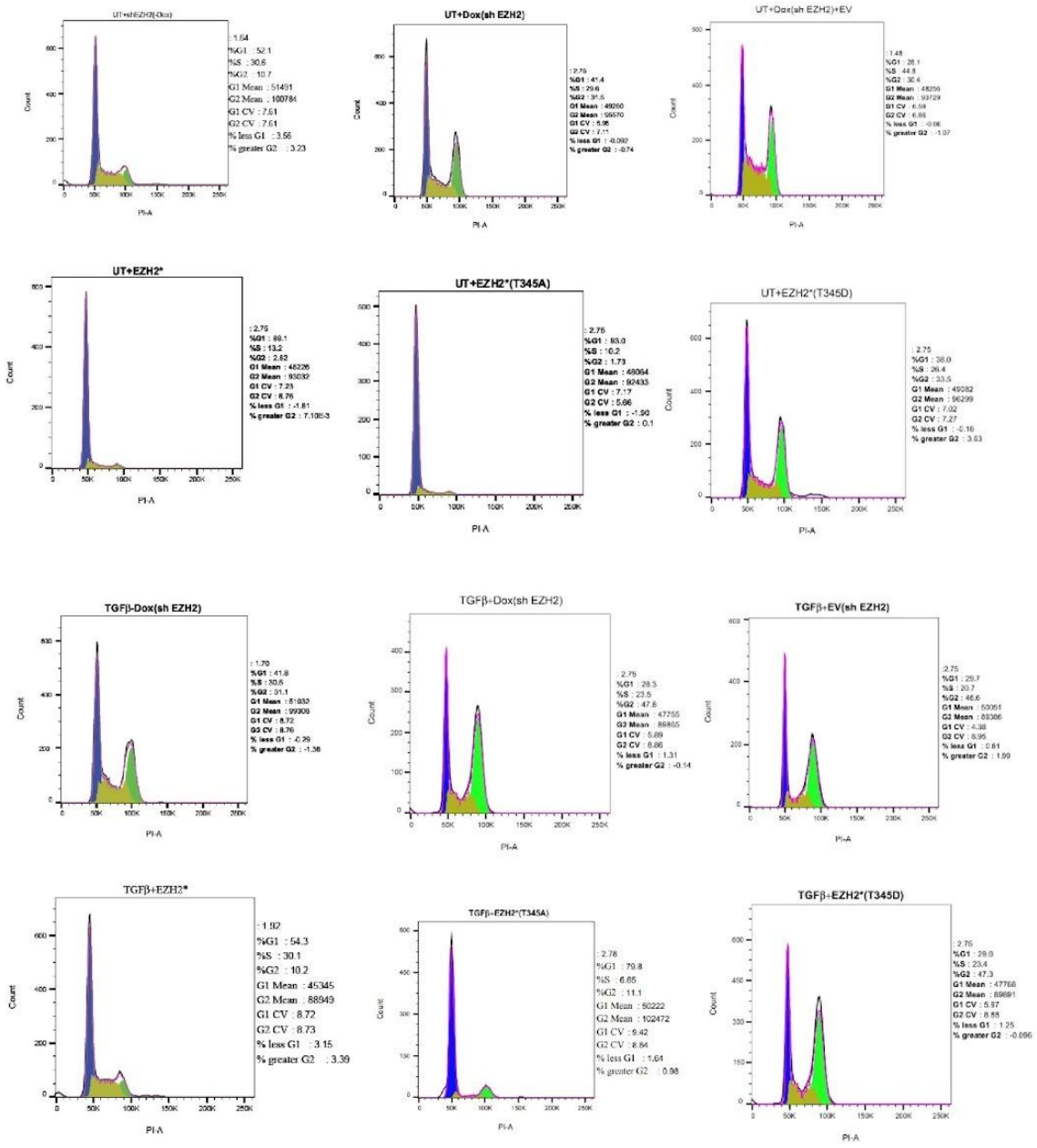


***Figure 4.20: FACS-based cell cycle profiling of EZH2 mutants:*** *MCF10A cells - Wild-type, phosphodeficient (T345A), and phosphomimetic (T345D) were analyzed for any possible changes in the cell cycle profile.*

### 4.2.13 Delineation of Cell Cycle Status by BrdU and H3S10p Staining in Lamin A/C and EZH2 Phosphomutants

To complement the flow cytometry–based cell cycle analysis and to obtain finer resolution of the specific cell cycle phases affected by phosphorylation status, we employed 5-bromo-2'-deoxyuridine (BrdU) incorporation and phospho-histone H3 (Ser10) (H3S10p) staining assays in MCF10A cells expressing phospho-deficient (S22A, T345A) and phospho-mimetic (S22D, T345D) mutants of Lamin A/C and EZH2, respectively.

BrdU incorporation provides a sensitive and quantitative measure of DNA synthesis during the S-phase of the cell cycle, allowing discrimination of cells actively engaged in replication from those arrested in G1 or G2. Across all phospho-mutant and full-length constructs, we observed comparable BrdU staining intensities, with no significant difference in the fraction of BrdU-positive nuclei. This observation indicates that neither the phospho-deficient nor the phospho-mimetic forms of Lamin A/C and EZH2 impede DNA synthesis or cause an arrest at the G1/S transition. Thus, phosphorylation at these residues does not appear to interfere with S-phase entry or completion (Figure 4.21A and B).

In contrast, H3S10p staining, which marks chromatin condensation during late G2 and mitosis, revealed striking differences between mutant forms. Cells expressing full-length or phospho-deficient (S22A/T345A) variants of Lamin A/C and EZH2 showed a robust population of H3S10p-positive nuclei, consistent with active progression through mitosis. The presence of distinct mitotic figures and condensed chromatin further confirmed regular cell cycle transit into and through M phase.

However, cells expressing phospho-mimetic (S22D/T345D) mutants exhibited a pronounced reduction in H3S10p-positive nuclei. Despite maintaining regular BrdU incorporation, these cells displayed markedly fewer mitotic cells by immunofluorescence and reduced overall H3S10p intensity by western blotting. This pattern suggests that although these cells complete DNA synthesis, they fail to transition into mitosis, consistent with an accumulation in early G2 as identified by PI-FACS analysis (Figure 4.21C and D).

Collectively, these results provide a refined understanding of how phosphorylation status at key regulatory residues on Lamin A/C and EZH2 impacts cell cycle progression. The combination of BrdU incorporation and H3S10p staining offers complementary and precise delineation of the cell cycle state, enabling us to distinguish between defects in S-phase entry

and G2/M transition. Importantly, these findings demonstrate that phospho-mimetic activation of Lamin A/C (S22D) or EZH2 (T345D) selectively impairs the G2-to-M transition, resulting in early G2 accumulation without affecting DNA replication.

Mechanistically, this supports the hypothesis that CDK1-mediated phosphorylation of Lamin A/C and EZH2 plays a functional role in coupling chromatin remodeling with cell cycle progression. The inability of phospho-mimetic mutants to proceed into mitosis may reflect premature or constitutive activation of phosphorylation-dependent dissociation events (such as Lamin A/C–EZH2 complex disruption), leading to altered nuclear architecture or defective checkpoint regulation. Together, these data establish that phosphorylation at Lamin A/C-S22 and EZH2-T345 is a critical determinant of cell cycle timing and nuclear reorganization during EMT.

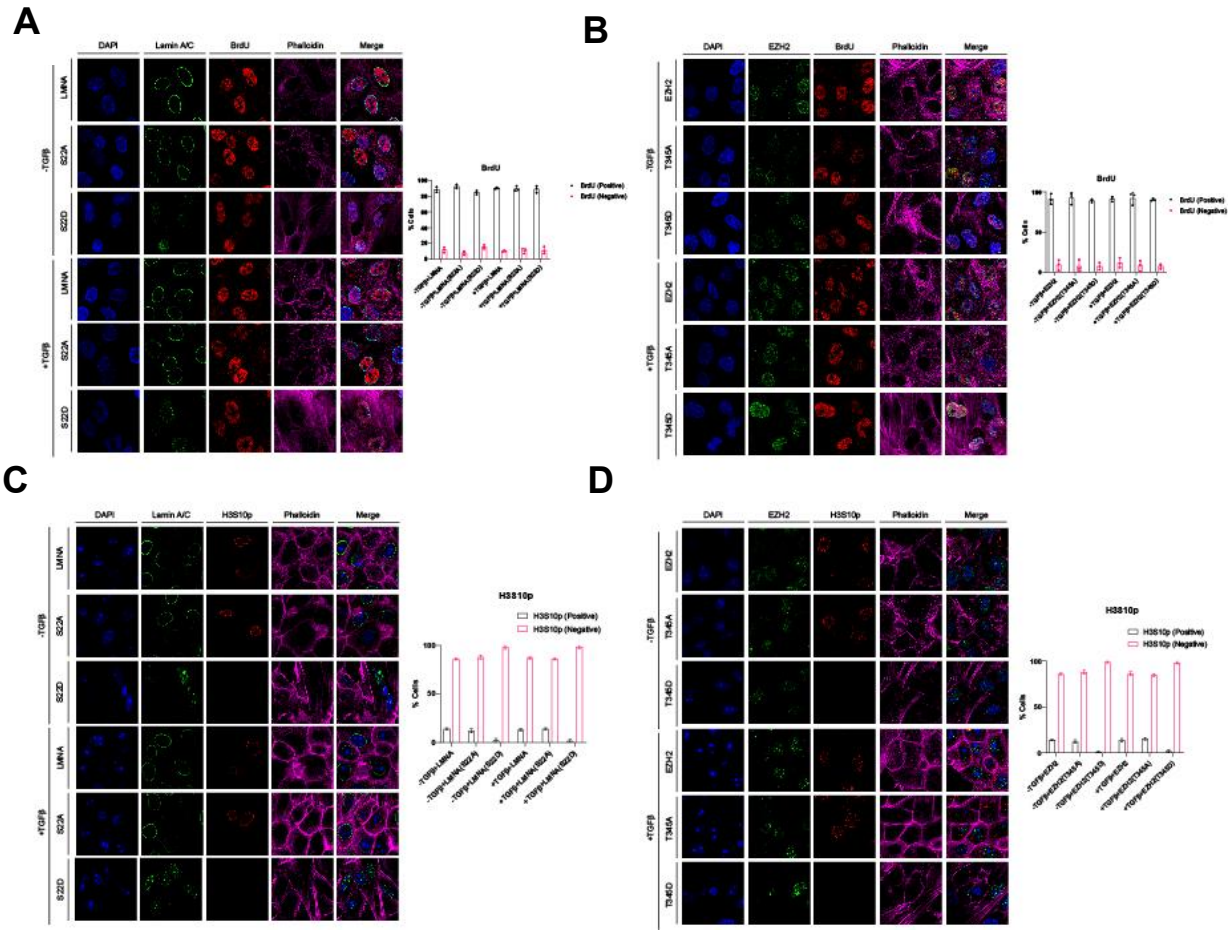


***Figure 4.21. Cell cycle analysis of MCF10A cells overexpressing Lamin A/C and EZH2 phospho-mutants.***

***(A)*** *BrdU incorporation assay in MCF10A cells expressing Lamin A variants.* ***(B)*** *BrdU incorporation assay in MCF10A cells expressing EZH2 variants.* ***(C)*** *H3S10 phosphorylation (H3S10p) staining to quantify the percentage of cells in G2/M phase for Lamin A variants.* ***(D)*** *H3S10p staining to quantify the percentage of cells in G2/M phase for EZH2 variants. All experiments were performed in at least three independent biological replicates.*

## 4.14 PRMT1-Dependent Arginine Methylation of EZH2 and Its Context-Specific Role in Epithelial–Mesenchymal Plasticity

Post-translational modifications (PTMs) of EZH2 play a critical role in fine-tuning its non-canonical functions beyond Polycomb Repressive Complex 2 (PRC2)-mediated histone methylation. In addition to phosphorylation, EZH2 is subject to arginine methylation, a modification catalyzed predominantly by protein arginine methyltransferase 1 (PRMT1), the primary type I PRMT responsible for the majority of asymmetric dimethylarginine marks in mammalian cells. PRMT1-mediated methylation has been implicated in the regulation of transcriptional control, RNA metabolism, DNA damage responses, and signal transduction through modification of both histone and non-histone substrates (Blanc and Richard, 2017).

Li et al. (2020) reported that arginine methylation of EZH2 is required for mesenchymal cell migration, suggesting that this modification may contribute to EMT-associated phenotypes. However, whether EZH2 arginine methylation universally regulates epithelial–mesenchymal plasticity across different cellular contexts, and how it integrates with other PTMs such as phosphorylation, remains unclear. Given our findings that CDK1-dependent phosphorylation of EZH2 at T345 disrupts its interaction with Lamin A/C and promotes EMT, we sought to examine the contribution of PRMT1-mediated arginine methylation of EZH2 in our epithelial and mesenchymal breast cancer model systems.

To assess the involvement of PRMT1 in regulating EZH2 function during epithelial–mesenchymal transitions, we first examined the interaction between EZH2 and PRMT1 by co-immunoprecipitation assays in MCF7 cells undergoing EMT and in MDA-MB-231 cells undergoing MET. In epithelial MCF7 control cells, EZH2 exhibited a detectable interaction with PRMT1. Notably, this association was markedly reduced upon EMT induction by TWIST1 overexpression, indicating that the EZH2–PRMT1 interaction is dynamically regulated during epithelial-to-mesenchymal conversion. These observations suggest that PRMT1-mediated methylation of EZH2 may be preferentially associated with an epithelial cellular state (Figure 4.22A).

In contrast, in the mesenchymal MDA-MB-231 cell line, EZH2–PRMT1 interaction was undetectable irrespective of the epithelial reprogramming status induced by GRHL2 expression. This finding indicates a strong cell-type dependency in EZH2–PRMT1 association

and suggests that PRMT1-mediated regulation of EZH2 may be dispensable in inherently mesenchymal breast cancer cells (Figure 4.22B).

To directly interrogate the functional relevance of EZH2 arginine methylation, we analyzed the effects of targeted EZH2 mutations in MCF7 cells. The arginine-to-lysine substitution at residue R342 (R342K), designed to abrogate arginine methylation, did not alter the interaction of EZH2 with Lamin A/C and did not promote EMT-associated phenotypic changes. Importantly, cells expressing the R342K mutant retained epithelial characteristics comparable to wild-type EZH2-expressing cells (Figure 4.22C).

In contrast, phosphomimetic EZH2 T345D variants, either alone or in combination with the R342K substitution, failed to bind Lamin A/C and robustly promoted mesenchymal features. These results demonstrate that phosphorylation at T345 is the dominant regulatory modification controlling EZH2–Lamin A/C interaction and EMT progression in MCF7 cells. The lack of phenotypic impact of the methylation-deficient R342K mutant further indicates that EZH2 arginine methylation is not required for EMT induction in this epithelial breast cancer context (Figure 4.22D).

Collectively, these findings suggest that while EZH2 can interact with PRMT1 in epithelial cells, loss of this interaction during EMT does not appear to be a primary driver of epithelial–mesenchymal plasticity. Instead, CDK1-mediated phosphorylation of EZH2 emerges as the critical regulatory switch governing its dissociation from Lamin A/C and subsequent EMT progression.

In summary, our data reveal that the interaction between EZH2 and PRMT1 is highly cell-type and context dependent, being detectable in epithelial MCF7 cells but absent in mesenchymal MDA-MB-231 cells. Functional disruption of EZH2 arginine methylation through the R342K mutation does not impact Lamin A/C binding or EMT status in MCF7 cells, indicating that PRMT1-mediated methylation of EZH2 is not essential for epithelial–mesenchymal plasticity in this system. These findings contrast with earlier reports implicating EZH2 arginine methylation in mesenchymal migration, underscoring the context-specific nature of EZH2 regulation.

Importantly, our results position phosphorylation of EZH2 at T345 as the dominant post-translational modification governing its functional disengagement from Lamin A/C and its pro-

EMT activity. This highlights a hierarchical regulation of EZH2 by distinct PTMs and emphasizes that phosphorylation-dependent mechanisms, rather than arginine methylation, drive EMT in epithelial breast cancer cells. These insights are integrated into the Discussion section to reconcile differences with prior studies and to underscore the multifaceted, context-dependent regulation of EZH2 during cancer cell plasticity.

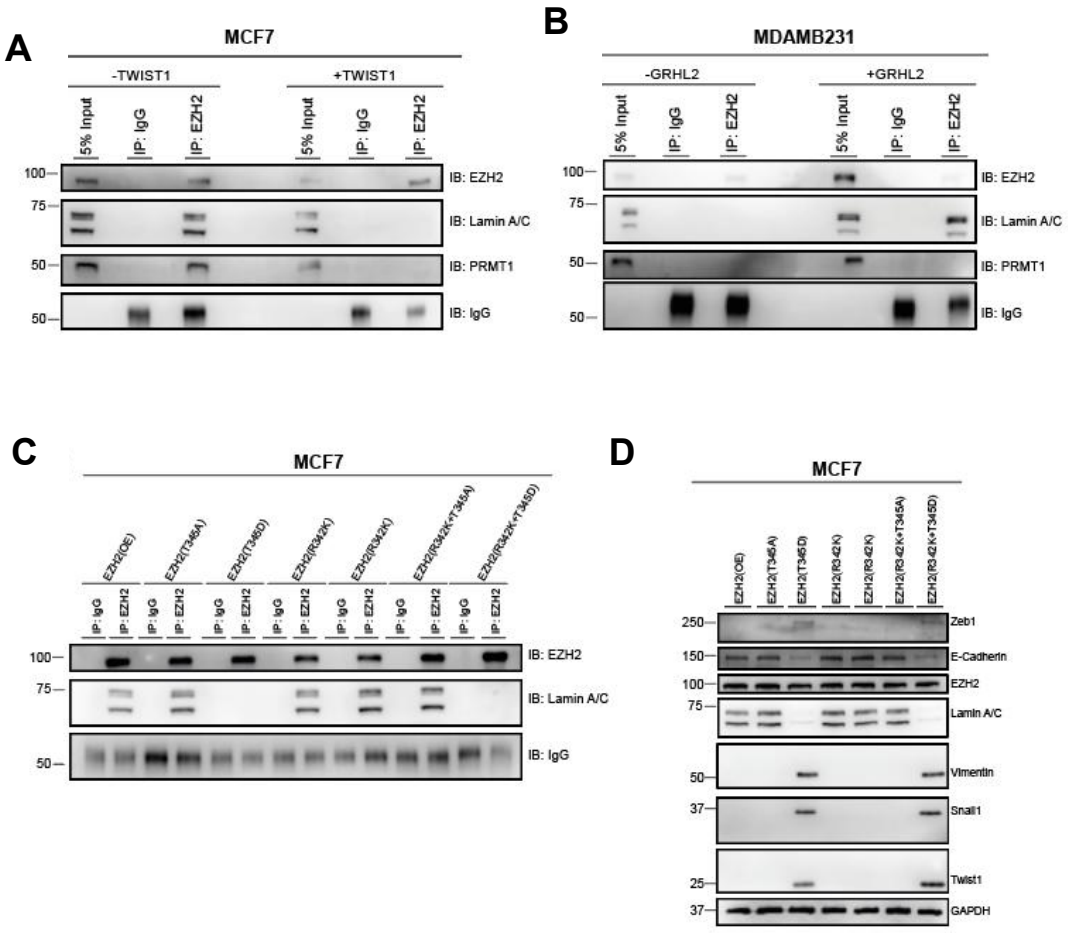


***Figure 4.22***: ***Co-immunoprecipitation and functional analysis of wild-type and EZH2 mutants in breast cancer cells.*** *(A) MCF7 cells in the presence and absence of TWIST1 were subjected to immunoprecipitation with EZH2 and immunoblotted for EZH2, Lamin A/C, and PRMT1. (B) CoIP analyses performed in MDA-MB-231 cells with or without GRHL2 overexpression. (C) CoIP analysis of wild-type EZH2 and EZH2 mutants (T345A, T345D, R342K, R342K+T345A, R342K+T345D) in MCF7 cells, examining interactions with Lamin A/C. (D) Western blot analysis of EMT markers (Zeb1, E-cadherin, Vimentin, Snail, Twist1) in MCF7 cells expressing wild-type or EZH2 mutants (T345A, T345D, R342K, R342K+T345A, R342K+T345D) to assess their effects on EMT regulation. GAPDH serves as a loading control. (N=1)*

## 4.3 Discussion and Conclusion

Epithelial–mesenchymal transition (EMT) and its reversal, mesenchymal–epithelial transition (MET), are highly dynamic processes central to developmental plasticity and metastatic progression in carcinomas. While the roles of transcription factors, chromatin remodelers, and signaling pathways in EMT/MET have been widely studied, how nuclear architectural components, such as the nuclear lamina, integrate with epigenetic regulators to mediate this plasticity remains poorly understood. In this chapter, we have explored a novel mechanistic axis involving Lamin A/C and EZH2, unveiling how their interaction is modulated through post-translational phosphorylation, ultimately impacting epithelial–mesenchymal plasticity (EMP).

### 4.3.1 A Novel Regulatory Nexus: Lamin A/C–EZH2 Complex

One of the most significant findings from this work is the identification of a previously underappreciated complex between Lamin A/C and EZH2, a catalytic subunit of the Polycomb Repressive Complex 2 (PRC2). The nuclear lamina has conventionally been associated with structural support and genome organization, whereas EZH2's role has been primarily confined to transcriptional repression through H3K27me3 deposition. Our results provide compelling evidence that Lamin A/C and EZH2 physically interact in both epithelial (MCF7) and mesenchymal (MDA-MB-231) contexts, linking structural and epigenetic regulators into a functional complex.

Importantly, we show that this interaction is dynamically modulated during EMT and MET. The disruption of the Lamin A/C–EZH2 interaction upon EMT induction (via TWIST1) and restoration upon MET (via GRHL2) highlights its potential role as a structural epigenetic switch that fine-tunes the epithelial or mesenchymal identity of a cell. This adds a new layer of complexity to EMP regulation, extending beyond transcriptional circuits and chromatin remodeling to include the nuclear architectural landscape.

### 4.3.2 Phosphorylation as a Molecular Toggle

A significant novel insight of this chapter lies in delineating the role of CDK1-mediated phosphorylation in regulating the Lamin A/C–EZH2 interaction. Using site-directed mutagenesis, we uncovered that specific phosphorylation at Serine 22 (S22) on Lamin A and Threonine 345 (T345) on EZH2—both canonical CDK1 sites—abrogates their binding. These

modifications were not arbitrary: deletion mapping and focused mutagenesis showed that only S22 (among T19/S22) and T345 (among T345, T350, T487) were functionally relevant for the interaction.

Our co-transfection and co-immunoprecipitation experiment further revealed that even phosphorylation at a single site on either Lamin A/C or EZH2 is sufficient to prevent complex formation, underscoring a finely tuned regulation mechanism. These findings establish phosphorylation as a critical molecular toggle that switches the interaction on or off in response to cellular signals, such as mitotic progression or EMT induction.

This has important implications: while CDK1 activity peaks during mitosis, its transient activation during EMT has been reported in cancer cells. We propose that phosphorylation-induced dissociation of the Lamin A/C–EZH2 complex may facilitate chromatin decompaction and transcriptional reprogramming, creating a permissive state for mesenchymal gene expression.

To further probe the functional consequences of CDK1 activity during EMT, we performed FACS-based cell cycle profiling in MCF10A cells expressing wild-type, phosphodeficient, and phosphomimetic mutants of Lamin A and EZH2. Interestingly, cells expressing phosphomimetic Lamin A (S22D) or EZH2 (T345D) showed elevated pCDK1(T161) levels and accumulated in the G2/M phase (~30%), comparable to cells treated with TGF-β or depleted for Lamin A/C and EZH2. In contrast, cells expressing wild-type or phosphodeficient mutants (S22A or T345A) predominantly resided in the G1 phase, indicating low CDK1 activity. These results suggest that phosphorylation of Lamin A/C and EZH2 not only disrupts their interaction but also actively promotes CDK1-mediated cell cycle progression—an event that may be critical for EMT-linked transcriptional reprogramming and chromatin remodeling.

### 4.3.3 Functional Relevance and Broader Implications

From a functional standpoint, the disruption of Lamin A/C–EZH2 interaction during EMT likely contributes to global chromatin remodeling. Lamin A/C is known to tether lamina-associated domains (LADs), many of which correspond to repressed heterochromatin. EZH2, on the other hand, reinforces repressive states through H3K27 trimethylation. Their interaction could thus serve to stabilize repressed genomic regions in epithelial states. Disassembly of this complex during EMT might lead to the release of genomic loci from the nuclear periphery, enabling the activation of mesenchymal genes.

Additionally, we uncovered a novel regulatory cascade linking TGF-β signaling to CCNB1 transcription via TWIST1, which directly impacts CDK1 activation and EMT progression. Through ChIP-Atlas analysis and validation using ChIP-PCR and transcriptional occupancy assays, we demonstrated that TWIST1 binds the -108 region of the CCNB1 promoter, enhancing its transcription. The upregulation of CCNB1 subsequently increases pCDK1(T161), linking transcriptional and cell cycle machinery in a unified EMT program.

CRISPR-mediated disruption of the TWIST1 binding site at the CCNB1 promoter abrogated TGF-β-induced EMT in MCF10A cells, despite intact global TWIST1 expression and binding at other loci. Cells harboring this mutation failed to upregulate mesenchymal markers or repress epithelial genes and maintained their epithelial identity upon TGF-β treatment. Moreover, we identified a Smad3 binding site upstream of the TWIST1 promoter, and CRISPR-based deletion of this region abolished TWIST1 induction and downstream CCNB1-CDK1 axis activation. These findings delineate a Smad3–TWIST1–CCNB1–CDK1 regulatory axis that integrates transcriptional and post-translational control to enforce EMT commitment.

### 4.3.4 Novel Perspectives and Future Directions

#### Nuclear Structural–Epigenetic Integration

The Lamin A/C–EZH2 interaction represents an important integration point between nuclear mechanics and chromatin regulation. Future studies may uncover how changes in nuclear stiffness, deformability, or mechanical stress affect this interaction and EMT progression.

#### Temporal Regulation During Cell Cycle and EMT

Our findings suggest a temporal axis of regulation in which CDK1 activity and Lamin A/C–EZH2 complex formation are dynamically modulated in response to EMT signaling. The discovery that phosphorylated Lamin A/C and EZH2 drive G2/M accumulation and CDK1 activation supports the existence of a cyclical regulatory loop involving mitotic kinases and EMT-associated transcriptional programs.

#### Implications for Cancer Therapy

EZH2 inhibitors are currently in clinical trials for various cancers. Our findings suggest that the efficacy of these inhibitors might be modulated by Lamin A/C expression or phosphorylation status. Conversely, targeting upstream kinases (e.g., CDK1 or Smad3) that regulate this interaction could offer a new angle to suppress EMT and metastasis, especially in tumors showing aberrant EMT plasticity or resistance to therapy.

**Role in Aging and Laminopathies**

Given that Lamin A mutations are central to progeroid syndromes and certain cancers, it would be of interest to determine whether phosphorylation-mediated uncoupling from EZH2 contributes to ageing-related chromatin dysfunction or to tumor progression in laminopathies.

**Conclusion**

In conclusion, our study identifies and characterizes a dynamic and phosphorylation-sensitive interaction between Lamin A/C and EZH2, with direct implications for epithelial–mesenchymal plasticity. By elucidating how phosphorylation at CDK1-specific sites on either protein disrupts their complex formation, we uncover a novel regulatory mechanism that links nuclear architecture, epigenetic repression, and phenotypic state transitions. Furthermore, we define a transcriptionally coupled pathway—Smad3–TWIST1–CCNB1–CDK1—that coordinates with Lamin A/C–EZH2 dynamics to control cell cycle status and EMT progression. This work provides a conceptual framework for further dissecting the interplay between structural and regulatory proteins in cancer progression and cell fate plasticity.

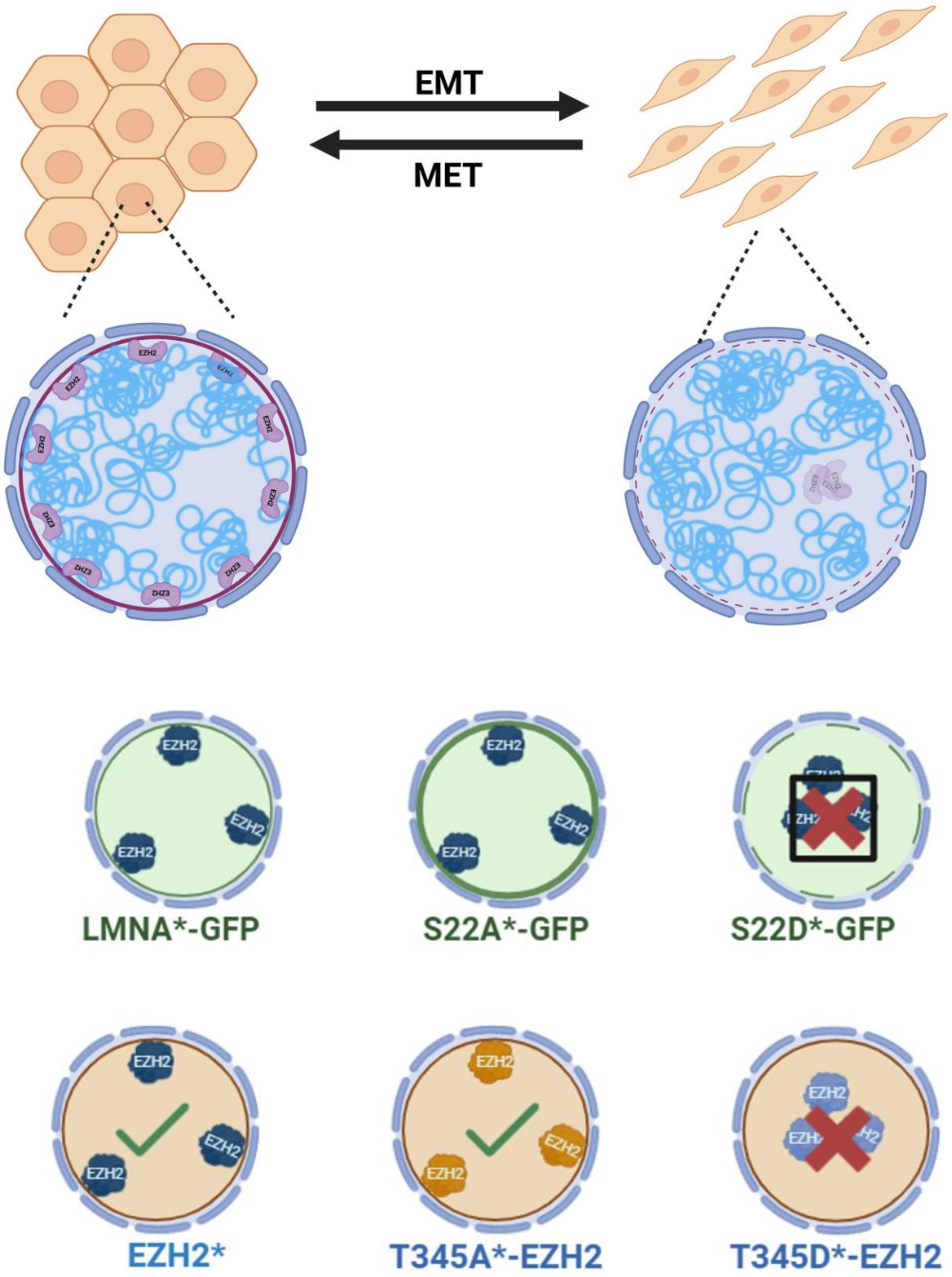
EMT
MET
EZH2
LMNA*-GFP
S22A*-GFP
S22D*-GFP
EZH2*
T345A*-EZH2
T345D*-EZH2

# Chapter 5: Functional Consequences of Lamin A-EZH2 Interaction

## 5.1 Introduction

Epithelial–mesenchymal transition (EMT) and its reversal, mesenchymal–epithelial transition (MET), represent fundamental biological processes that underlie diverse developmental and pathological contexts, including embryogenesis, wound healing, fibrosis, and cancer metastasis. In carcinomas, EMT facilitates the dissociation of epithelial tumor cells from the primary tumor mass, endowing them with migratory and invasive capabilities essential for the dissemination and colonization of distant organs. MET, on the other hand, enables re-epithelialization at secondary sites, facilitating metastatic outgrowth. Importantly, these transitions do not occur in a binary fashion but are instead regulated through a dynamic continuum of intermediate or "hybrid" epithelial/mesenchymal (E/M) states. The molecular underpinnings of this epithelial–mesenchymal plasticity (EMP) remain incompletely understood, but accumulating evidence points to a coordinated interplay of transcriptional, epigenetic, and post-translational mechanisms.

Among the emerging regulators of EMP are nuclear lamins and chromatin modifiers that together orchestrate nuclear organization, epigenetic landscape, and transcriptional identity. Lamin A/C, encoded by the LMNA gene, forms a key structural component of the nuclear lamina and contributes to genome organization through chromatin tethering and nuclear stiffness. Beyond its mechanical role, Lamin A/C interacts with epigenetic enzymes to influence gene silencing and maintain cell identity. A particularly intriguing interaction is that between Lamin A/C and Enhancer of Zeste Homolog 2 (EZH2), the catalytic component of the Polycomb Repressive Complex 2 (PRC2), which mediates histone H3 lysine 27 trimethylation (H3K27me3) to repress transcription of developmental and differentiation-associated genes.

Recent studies, including our own, have revealed that Lamin A/C and EZH2 form a functional complex that suppresses EMT and supports epithelial differentiation. However, this complex is dynamically regulated by post-translational modifications, especially phosphorylation. CDK1 phosphorylates both Lamin A/C and EZH2 at specific residues (S22 in Lamin A/C and T345 in EZH2), which modulates their interaction and subcellular localization. Phosphorylation at these sites disrupts their complex formation, resulting in derepression of EMT transcription factors such as SNAI1, ZEB1, and TWIST1. This phosphorylation-dependent switch may represent a key regulatory node in EMT plasticity and tumor progression.

This chapter seeks to unravel the functional consequences of Lamin A/C–EZH2 interaction and its disruption by phosphorylation in regulating EMP in breast cancer models. Through a combination of molecular, cellular, and in vivo approaches, we dissect how alterations in the phosphorylation state of Lamin A/C and EZH2 affect chromatin organization, gene expression, cell morphology, migration, invasion, and metastatic potential. Specifically, we explore:

- **Lamin A/C Promotes a Repressed Chromatin Microenvironment Suppressing EMT:** Here, we show that Lamin A/C supports a repressive chromatin environment enriched for H3K27me3 and other heterochromatic markers. Loss of Lamin A/C or disruption of its complex with EZH2 alters the nuclear epigenetic landscape and upregulates mesenchymal transcriptional programs.
- **Phosphorylation-Dependent Modulation of the Lamin A/C–EZH2 Axis Regulates Epithelial–Mesenchymal Plasticity:** Through site-directed mutagenesis, we demonstrate that CDK1-mediated phosphorylation at S22 of Lamin A and T345 of EZH2 abolishes their interaction, enabling mesenchymal transdifferentiation. Phosphomimetic mutants drive EMT even in the absence of canonical inducers like TGF-β, while phosphodeficient variants sustain epithelial identity.
- **Functional Impact of Lamin A/C–EZH2 Disruption on Cell Invasion and Migration:** In vitro transwell assays reveal that disruption of the Lamin A/C–EZH2 axis enhances cellular invasion and migration. This functional transition mirrors the phenotypic and molecular hallmarks of EMT and suggests that loss of the Lamin A/C–EZH2 complex potentiates pro-metastatic behavior.
- **Lamin A/C–EZH2 Axis Modulates TGF-β–Induced Migration in MCF10A Cells:** TGF-β is a well-characterized EMT inducer. In this section, we show that the Lamin A/C–EZH2 complex attenuates TGF-β-induced cell migration. Cells expressing phosphomimetic Lamin A or EZH2 mutants exhibit an exaggerated migratory response, underscoring the sensitizing effect of phosphorylation on EMT signaling.
- **Phosphorylation-Dependent Modulation of Hybrid Epithelial/Mesenchymal States by Lamin A/C and EZH2:** Using CD104/CD44-based flow cytometry, we delineate the hybrid E/M population and demonstrate that phosphorylation of Lamin A and EZH2 stabilizes this hybrid state. In contrast, phosphodeficient forms promote complete MET, effectively bypassing the hybrid phenotype. This finding positions the Lamin A/C–EZH2 interaction as a critical determinant of EMP state transitions.

- **Phosphorylation-Dependent Regulation of Tumorigenic Potential in Breast Cancer Models:** Orthotopic xenograft experiments show that phosphomimetic Lamin A and EZH2 mutants significantly increase tumor growth and volume. Tumors derived from phosphodeficient mutants grow slowly and display more epithelial histology, supporting the suppressive role of the Lamin A/C–EZH2 complex in tumorigenesis.
- **Phosphorylation-Dependent Regulation of Metastatic Spread in Breast Cancer Models:** Histopathological examination of lung tissues from tumor-bearing mice reveals that phosphorylation of Lamin A and EZH2 enhances metastatic dissemination. The presence of densely stained, pleomorphic nuclei in lung lesions correlates with phosphomimetic status, further affirming the functional link between phosphorylation, EMT plasticity, and metastasis.

Collectively, the findings presented in this chapter illuminate a novel and critical regulatory circuit wherein the phosphorylation state of Lamin A/C and EZH2 governs the epigenetic suppression or activation of EMT programs. The phosphorylation-sensitive Lamin A/C–EZH2 axis emerges as a master regulator of epithelial–mesenchymal fate decisions and metastatic potential in breast cancer. Understanding this axis offers new insights into the chromatin-level control of cellular plasticity and suggests potential therapeutic targets for modulating EMP and limiting metastatic progression.

## 5.2 Results

### 5.2.1 Lamin A/C Promotes a Repressed Chromatin Microenvironment Suppressing EMT

Epithelial–mesenchymal transition (EMT) is a reversible and dynamic cellular program that enables epithelial cells to acquire mesenchymal features, including enhanced motility, invasiveness, and resistance to apoptosis. This process plays a central role in embryonic development, tissue repair, fibrosis, and cancer metastasis. The transition from an epithelial to a mesenchymal state involves widespread transcriptional reprogramming, changes in cell morphology, and remodeling of the cytoskeleton. Central to this process is the activation of a set of transcription factors known as EMT inducers—such as SNAI1, TWIST1, and ZEB1—which orchestrate the repression of epithelial markers (e.g., E-cadherin) and activation of mesenchymal genes.

While extensive research has delineated the roles of EMT-inducing transcription factors, signaling cascades (e.g., TGF-β, WNT, Notch), and chromatin regulators in promoting EMT, the role of nuclear architecture and structural nuclear proteins in restraining EMT remains

underexplored. The nuclear lamina, a filamentous meshwork underlying the inner nuclear membrane, is composed primarily of A-type and B-type lamins. Lamin A/C, encoded by the LMNA gene, has been traditionally viewed as a key structural protein maintaining nuclear shape and mechanical stability. However, emerging evidence suggests that Lamin A/C also plays an active role in chromatin organization and transcriptional repression by anchoring heterochromatin domains at the nuclear periphery.

In this chapter, we investigate the role of Lamin A/C in maintaining a repressive chromatin environment that suppresses the activation of EMT transcription factors and thereby preserves epithelial identity. Building on our earlier observations that Lamin A/C interacts with EZH2—the catalytic component of Polycomb Repressive Complex 2 (PRC2)—we sought to dissect how this interaction functions in regulating the transcriptional silencing of EMT-associated genes. EZH2 mediates transcriptional repression by catalyzing the trimethylation of histone H3 at lysine 27 (H3K27me3), a hallmark of facultative heterochromatin. We hypothesized that Lamin A/C anchors EZH2-enriched repressive chromatin at the promoters of mesenchymal transcription factors and that this repression is dynamically regulated via CDK1-mediated phosphorylation.

To explore this hypothesis, we first depleted Lamin A/C in MCF7 epithelial breast cancer cells and performed transcriptome-wide RNA sequencing. This analysis revealed a significant upregulation of mesenchymal transcription factors, including SNAI1, TWIST1, and ZEB1, upon Lamin A/C depletion. These findings suggest that Lamin A/C is critical for maintaining the transcriptional repression of key EMT inducers. Given the known role of EZH2 in mediating H3K27me3-dependent repression, we proposed a cooperative model in which Lamin A/C, EZH2, and H3K27me3 converge at the promoters of mesenchymal genes to enforce transcriptional silencing.

To validate this model, we utilized ChIP-Atlas, a publicly available chromatin immunoprecipitation (ChIP)-sequencing resource, and identified strong enrichment of Lamin A and EZH2 binding at the -1 kb promoter regions of SNAI1, TWIST1, and ZEB1 in epithelial cell lines such as HepG2 and MCF7. We then established MCF7 cell lines stably expressing phosphodeficient or phosphomimetic mutants of Lamin A (S22A and S22D, respectively) and EZH2 (T345A and T345D, respectively). ChIP-PCR assays were performed on these cells to quantify the enrichment of Lamin A/C, EZH2, and H3K27me3 at the -1 kb regions of the EMT-TF promoters (Figure 5.1A).

In wild-type MCF7 cells, we observed robust enrichment of Lamin A/C, EZH2, and H3K27me3 at the promoters of SNAI1, TWIST1, and ZEB1, suggesting that these loci are transcriptionally repressed. EMT induction via TWIST1 overexpression led to a marked decrease in the binding of Lamin A/C and EZH2, as well as reduced H3K27me3 enrichment. Notably, Lamin A/C knockdown alone was sufficient to reduce EZH2 and H3K27me3 occupancy at these loci, supporting the idea that Lamin A/C serves as a stabilizing scaffold for PRC2 at specific gene promoters.

To evaluate transcriptional activity, we performed ChIP-PCR for transcription elongation-associated markers, including H3K36me3 and RNA Polymerase II phosphorylated at serine 2 (RNA Pol II Ser2P), at the +1 kb regions of SNAI1, TWIST1, and ZEB1. In control cells, these markers showed low enrichment, indicating a repressed transcriptional state. However, both Lamin A/C depletion and TWIST1 overexpression significantly increased the occupancy of H3K36me3 and RNA Pol II Ser2P, consistent with enhanced transcriptional elongation of EMT-TFs.

We next investigated the role of CDK1-mediated phosphorylation in modulating Lamin A/C–EZH2–chromatin interactions. Overexpression of full-length Lamin A or its phosphodeficient mutant (S22A) preserved the repressive chromatin environment, as evidenced by sustained binding of Lamin A/C, EZH2, and H3K27me3 at EMT-TF promoters, even in the presence of EMT stimuli. In contrast, expression of the phosphomimetic Lamin A mutant (S22D) resulted in a dramatic loss of these repressive marks, accompanied by increased H3K36me3 and RNA Pol II Ser2P, indicating transcriptional activation (Figure 5.1B and D).

A similar regulatory pattern was observed for EZH2 phosphorylation. Overexpression of wild-type or phosphodeficient EZH2 (T345A) retained Lamin A/C and H3K27me3 enrichment at mesenchymal promoters. Conversely, expression of the phosphomimetic EZH2 mutant (T345D) disrupted this occupancy, leading to elevated levels of transcription elongation markers. These results demonstrate that phosphorylation at CDK1 sites on either Lamin A/C or EZH2 can disrupt their interaction and chromatin binding, resulting in the derepression of mesenchymal gene expression (Figure 5.2A -B).

Together, these findings reveal a phosphorylation-sensitive regulatory axis in which Lamin A/C and EZH2 collaboratively maintain a repressive chromatin landscape that silences mesenchymal transcription factors in epithelial cells. The loss or post-translational

modification of Lamin A/C or EZH2 compromises this repression, tipping the balance toward EMT induction. This chapter thus uncovers a critical mechanistic link between nuclear architecture, chromatin regulation, and epithelial–mesenchymal plasticity, offering new insights into how cellular identity is epigenetically safeguarded against phenotypic reprogramming.

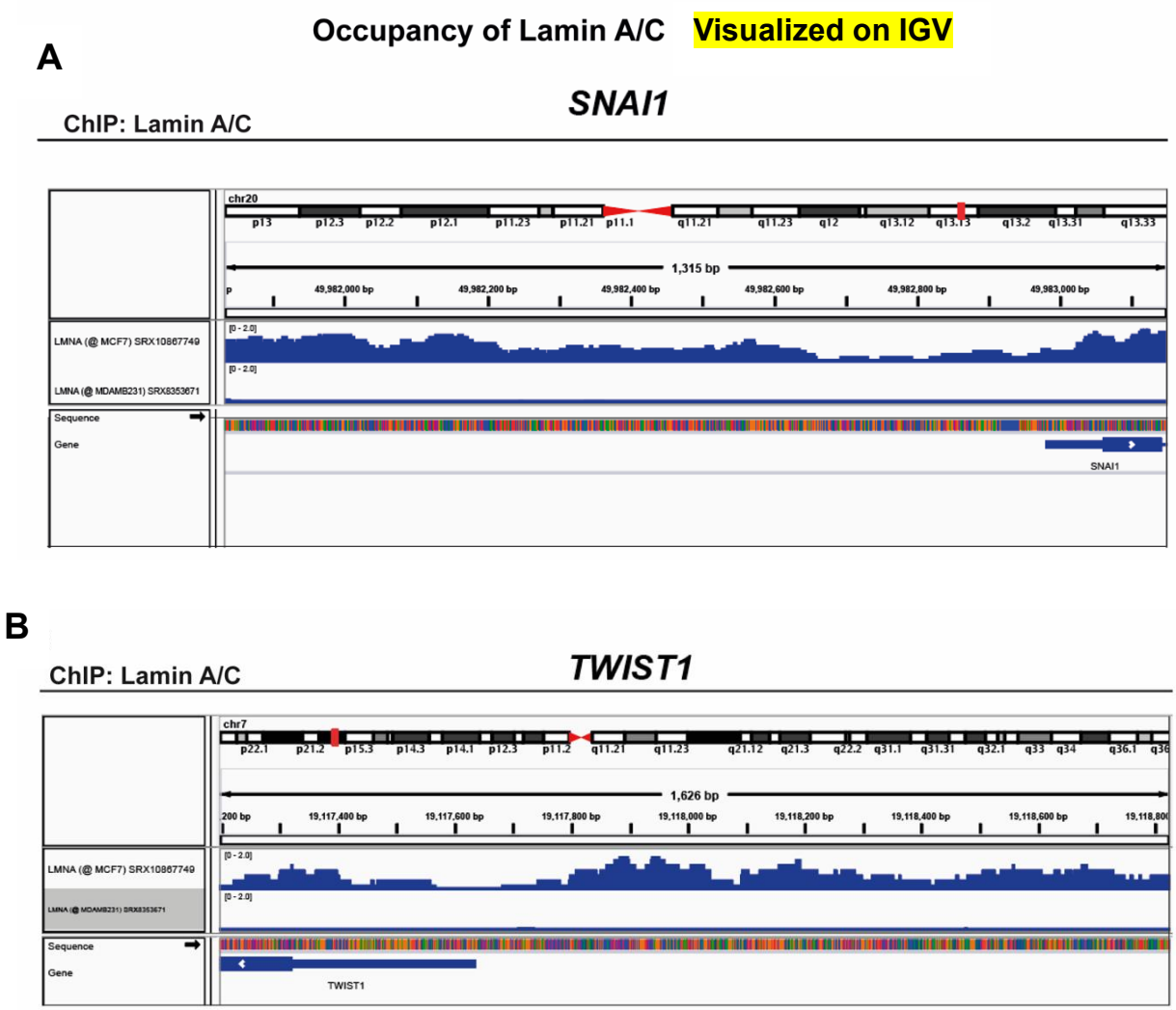

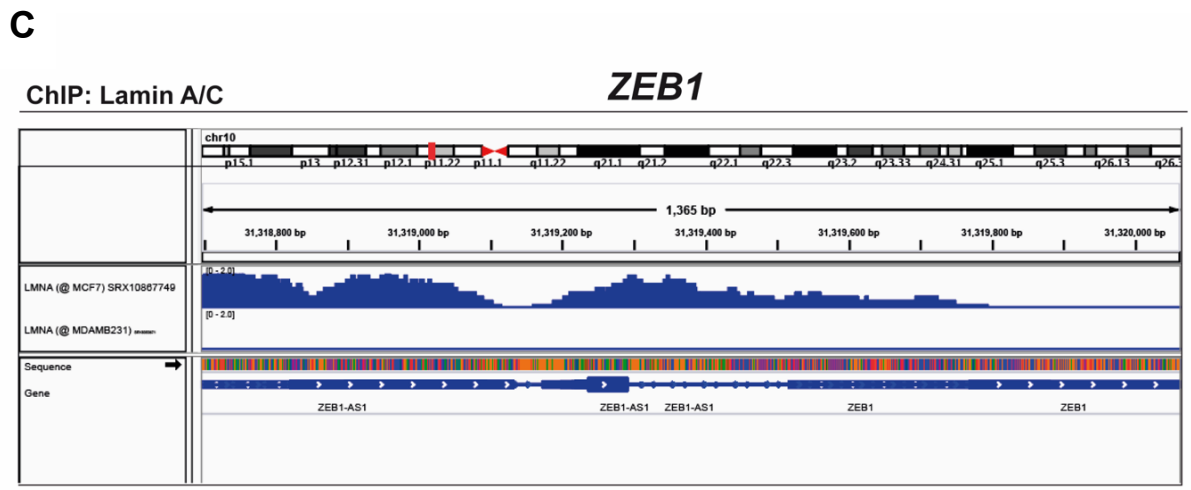


***Figure 5.1**: ChIPAtlas data of MCF7 and MDA-MB-231 cells showing occupancy of Lamin A/C in the -1kb region of (A) SNAI1, (B) TWIST1 and (C) ZEB1*

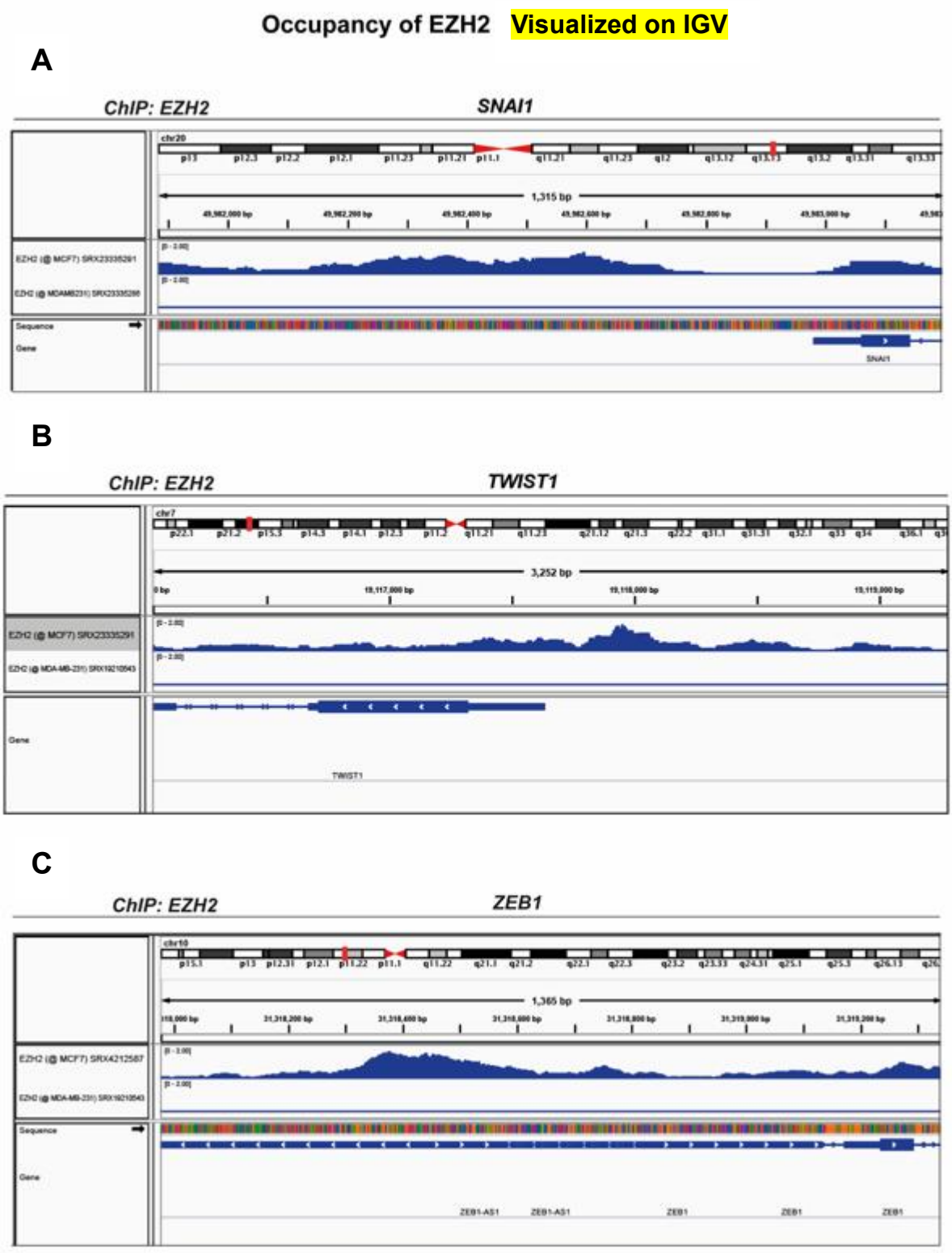


***Figure 5.2:*** *ChIPAtlas data of MCF7 and MDA-MB-231 cells showing occupancy of EZH2 in the -1kb region of (A) SNAI1, (B) TWIST1 and (C) ZEB1*

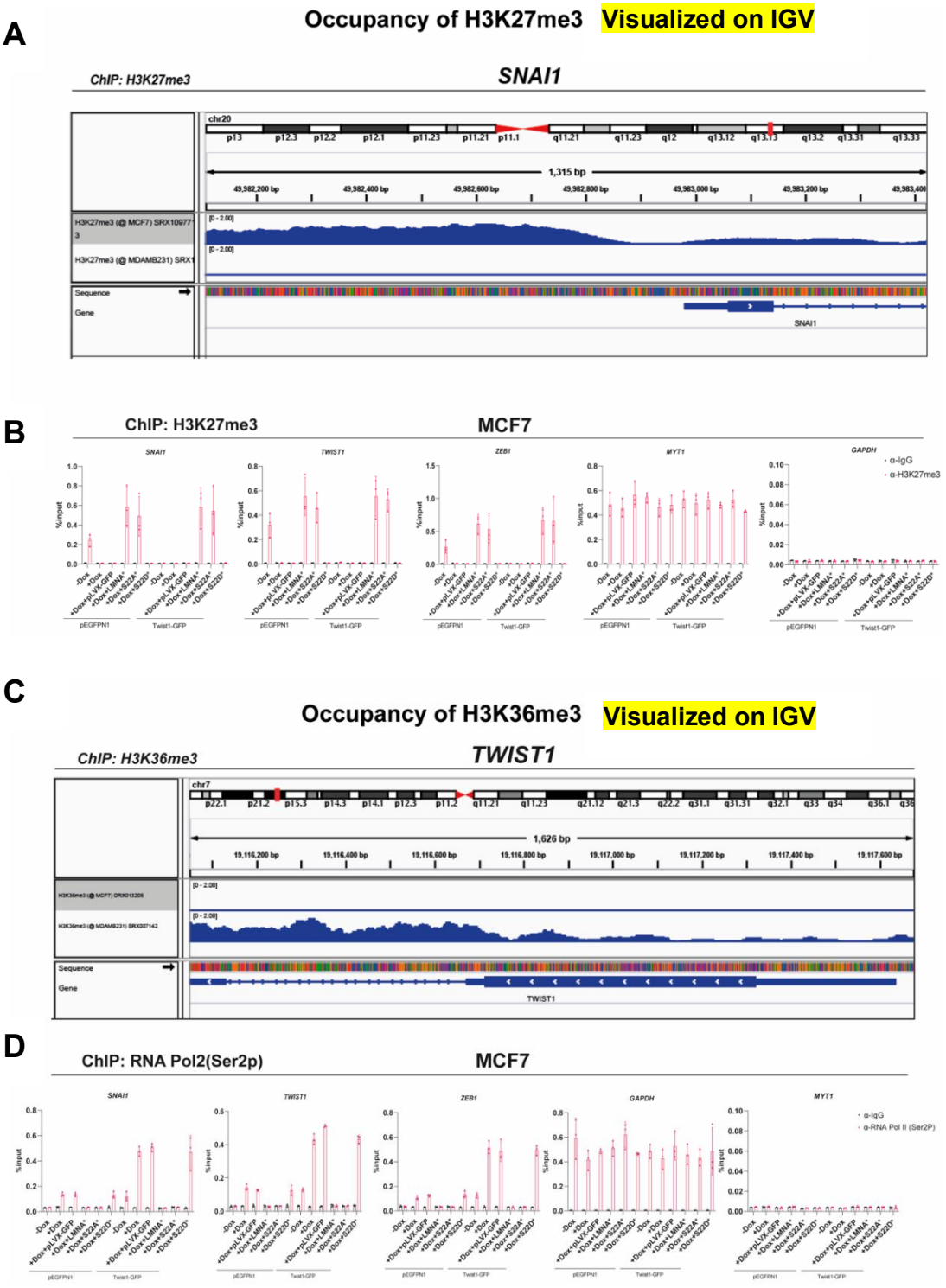


***Figure 5.3***: *(A) ChIPAtlas data showing the occupancy of H3K27me3 on the -1kb region of SNAI1 in MCF7 and MDA-MB-231 cells (B) ChIP-qPCR showing the occupancy of H3K27me3 in phosphomutants of Lamin A/C in MCF7 (C) ChIPAtlas data showing the occupancy of H3K36me3 on the +1kb region of SNAI1 in MCF7 and MDA-MB-231 cells (D) ChIP-qPCR showing the occupancy of RNA polymerase (Ser2p) in phosphomutants of Lamin A/C in MCF7.*

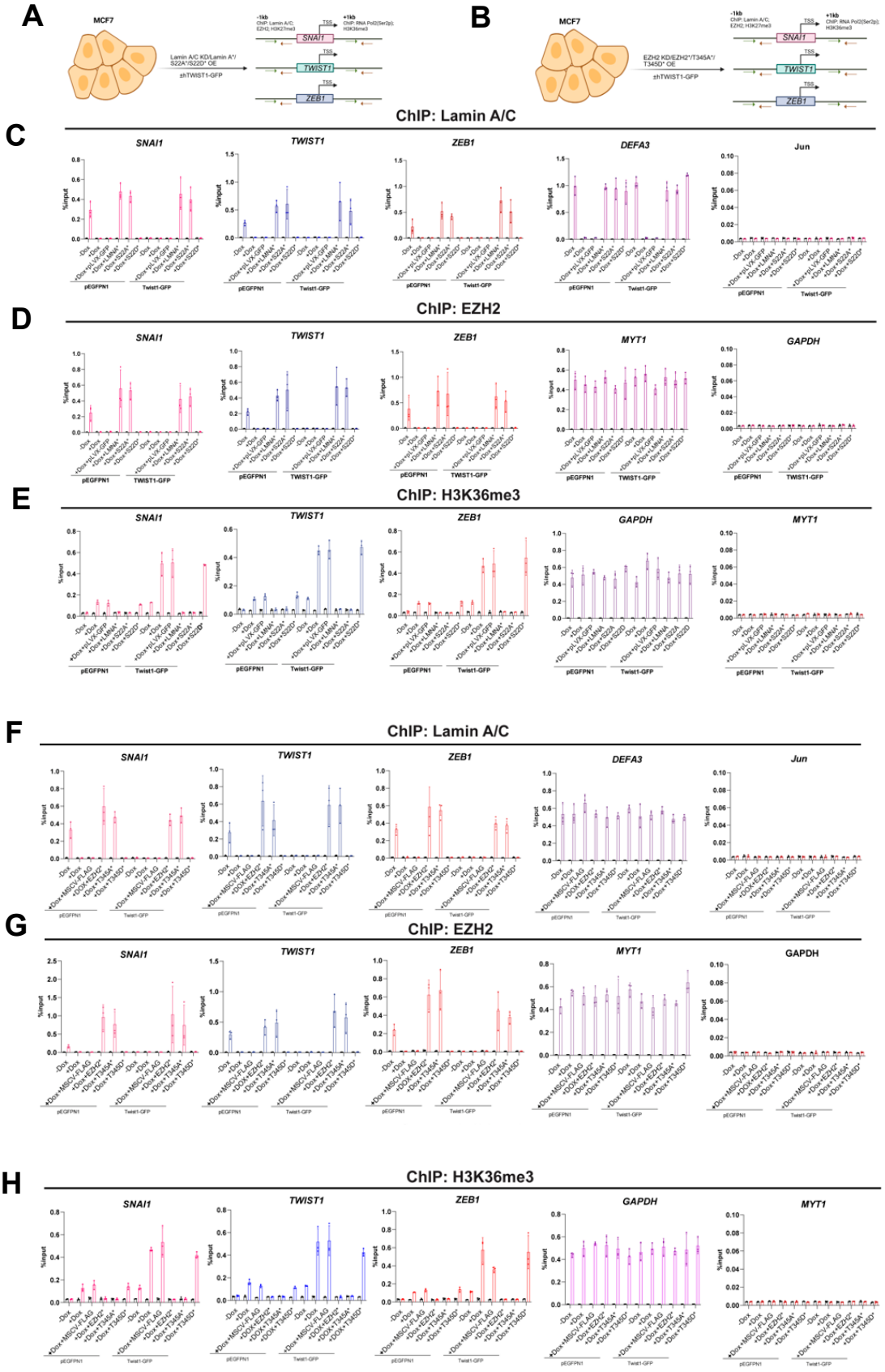
A
MCF7
Lamin A/C KD/Lamin A*/S22A*/S22D* OE
±hTWIST1-GFP
SNAI1
TWIST1
ZEB1
B
MCF7
EZH2 KD/EZH2*/T345A*/T345D* OE
±hTWIST1-GFP
C
ChIP: Lamin A/C
SNAI1
TWIST1
ZEB1
DEFA3
Jun
D
ChIP: EZH2
SNAI1
TWIST1
ZEB1
MYT1
GAPDH
E
ChIP: H3K36me3
SNAI1
TWIST1
ZEB1
GAPDH
MYT1
F
ChIP: Lamin A/C
SNAI1
TWIST1
ZEB1
DEFA3
Jun
G
ChIP: EZH2
SNAI1
TWIST1
ZEB1
MYT1
GAPDH
H
ChIP: H3K36me3
SNAI1
TWIST1
ZEB1
GAPDH
MYT1

***Figure 5.4: Lamin A/C and EZH2 Cooperatively Regulate Chromatin to Suppress Mesenchymal Transcription Factors and Maintain Epithelial Identity.*** *(A) Schematic representation of chromatin immunoprecipitation (ChIP) experiments performed in MCF7 cells overexpressing TWIST1-GFP, following knockdown (KD) of Lamin A/C or overexpression (OE) of full-length Lamin A or phospho-mutant Lamin A (S22A: phospho-deficient; S22D: phospho-mimetic). ChIP was performed using antibodies against Lamin A/C, EZH2, H3K27me3 (-1kb of TSS), and RNA Polymerase II (Ser2P) and H3K36me3 (+1kb of TSS) at the promoters of key mesenchymal transcription factors SNAI1, TWIST1, and ZEB1. (B) Schematic representation of ChIP analysis in MCF7 cells with EZH2 knockdown or overexpression of full-length or phospho-mutant EZH2 (T345A: phospho-deficient; T345D: phospho-mimetic) in the context of TWIST1-GFP induction. Promoter occupancy of Lamin A/C, EZH2, and associated histone modifications (H3K27me3 and H3K36me3), as well as RNA Pol II (Ser2P), was examined at the transcription start sites (TSS) of SNAI1, TWIST1, and ZEB1. Green and red arrows indicate primers for the qPCR experiment. (C–E) Chromatin immunoprecipitation (ChIP) PCR analysis in MCF7 cells stably transduced with full-length Lamin A, phosphodeficient (S22A), or phosphomimetic (S22D) variants, followed by transient transfection with pEGFP-N1 (control) or TWIST1-GFP for 48 h. ChIP occupancy of (A) Lamin A, (B) EZH2 at the -1 kb regions, and (C) H3K36me3 at the +1 kb regions of SNAI1, TWIST1, and ZEB1 was assessed. DEFA3 (C), MYT1 (D), and GAPDH(E) served as positive controls, while Jun (A), GAPDH +1 kb (B), and MYT1(C) were negative controls for Lamin A/C, EZH2, and H3K36me3, respectively. (F–H) ChIP PCR analysis in MCF7 cells stably transduced with full-length EZH2, phosphodeficient (T345A), or phosphomimetic (T345D) variants, followed by transient transfection with pEGFP-N1 or TWIST1-GFP for 48 h. ChIP occupancy of (F) Lamin A, (G) EZH2 at the -1 kb regions, and (H) H3K36me3 at the +1 kb regions of SNAI1, TWIST1, and ZEB1 was assessed. DEFA3 (F) and MYT1 (G) and GAPDH(H) served as positive controls, while Jun (F), GAPDH +1 kb (G), and MYT1(H) were negative controls for Lamin A/C, EZH2, and H3K36me3, respectively. Data represent mean ± SD from three independent experiments.*

### 5.2.2 Phosphorylation-Dependent Modulation of the Lamin A/C–EZH2 Axis Regulates Epithelial–Mesenchymal Plasticity

We next sought to determine how phosphorylation of Lamin A/C and EZH2 impacts their interaction and its broader consequences on epithelial–mesenchymal (EM) plasticity. Given that the Lamin A/C–EZH2 complex plays a critical role in chromatin organization and transcriptional regulation, we hypothesized that phosphorylation at specific residues could act as a molecular switch to disrupt this interaction, thereby facilitating EM transitions. To test this hypothesis, we engineered stable cell lines with inducible knockdown of endogenous Lamin A/C and EZH2, followed by overexpression of either full-length, phosphodeficient, or phosphomimetic mutants of these proteins. Specifically, for Lamin A, the serine 22 residue (S22) was mutated to alanine (S22A) to mimic a dephosphorylated state and to aspartate (S22D) to mimic phosphorylation. Similarly, for EZH2, we used threonine 345 (T345) to generate the phosphodeficient (T345A) and phosphomimetic (T345D) mutants.

To dissect the functional impact of these mutations, we established a model system wherein Lamin A/C and EZH2 could be depleted and selectively reconstituted with these engineered variants. Overexpression of the phosphomimetic Lamin A mutant (S22D) disrupted the interaction with EZH2 and led to a robust mesenchymal phenotype. This was characterized by significant upregulation of mesenchymal markers such as Vimentin, TWIST1, SNAI1, and ZEB1, along with a marked reduction in the epithelial marker E-cadherin. These changes occurred in the absence of external EMT inducers, underscoring the sufficiency of Lamin A phosphorylation at S22 in initiating EMT-like transitions. In contrast, cells expressing either wild-type Lamin A or the phosphodeficient mutant (S22A), both of which retained the ability to bind EZH2, maintained epithelial morphology and marker expression, even under conditions that typically induce EMT, such as TGF-β treatment or TWIST1 overexpression. Immunofluorescence analyses (Figure 5.5A-E) and immunoblotting data (Figures 5.6A-B) consistently demonstrated that the Lamin A–EZH2 complex acts as a repressor of mesenchymal gene expression. Phosphorylation at S22 effectively dismantles this complex, allowing EMT-promoting transcription factors to be expressed.

Supporting this model, we observed that overexpression of either full-length Lamin A or the S22A mutant was sufficient to enforce a robust epithelial state in MDA-MB-231 cells, which are otherwise mesenchymal by default. These cells exhibited high E-cadherin levels and repressed mesenchymal markers, even in the absence of GRHL2-mediated MET induction.

Conversely, cells with Lamin A/C knockdown or overexpressing the S22D phosphomimetic variant failed to undergo MET, maintaining high expression of mesenchymal factors. Notably, even co-overexpression of GRHL2 and the Lamin A (S22D) mutant, or GRHL2 overexpression in Lamin A/C knockdown backgrounds, only partially restored epithelial features. This was evidenced by immunofluorescence, quantitative image analyses (Figure 5.5F-J), and immunoblotting. These observations highlight the indispensable role of the Lamin A–EZH2 complex in facilitating MET and repressing mesenchymal transcriptional programs.

To further explore the phosphorylation-dependent regulation of this complex, we introduced phosphodeficient (T345A) and phosphomimetic (T345D) EZH2 mutants into cells with EZH2 depletion. In epithelial cell lines such as MCF7 and MCF10A, overexpression of the T345D mutant, which is unable to interact with Lamin A/C, resulted in EMT-like phenotypes. These cells displayed decreased E-cadherin expression and elevated levels of mesenchymal markers, even without EMT-inducing stimuli. On the other hand, cells overexpressing wild-type EZH2 or the phosphodeficient T345A variant retained epithelial characteristics and resisted EMT induction by TGF-β or TWIST1. This underscores the necessity of the Lamin A/C–EZH2 interaction in safeguarding epithelial identity and resisting mesenchymal transition.

In mesenchymal MDA-MB-231 cells, overexpression of wild-type or T345A EZH2 mutants led to MET, marked by increased E-cadherin levels and decreased mesenchymal markers. Remarkably, this MET occurred independent of GRHL2 overexpression, suggesting that the reconstitution of Lamin A/C–EZH2 interaction is itself sufficient to trigger epithelial gene programs. In contrast, overexpression of T345D EZH2 or depletion of EZH2 resulted in the persistence of mesenchymal features. Even when combined with GRHL2 overexpression, these cells displayed only partial MET, maintaining a hybrid phenotype with co-expression of epithelial and mesenchymal markers. These findings were validated through immunofluorescence (Figure 5.5O-R) and immunoblotting (Figure 5.6C and F).

In summary, these data provide compelling evidence that the Lamin A/C–EZH2 complex operates as a phosphorylation-sensitive regulatory module that suppresses mesenchymal gene expression and facilitates epithelial identity. Disruption of this complex through CDK1-mediated phosphorylation represents a key mechanistic event that enables cells to undergo EMT. Conversely, inhibition or prevention of phosphorylation preserves this interaction and supports MET, even in otherwise mesenchymal cell types. The precise nature of the S22–T345 interaction axis, as demonstrated through mutational, co-transfection, and co-

immunoprecipitation experiments, offers novel insights into how reversible post-translational modifications fine-tune nuclear architecture and chromatin-based gene regulation. These findings position the Lamin A/C–EZH2 complex as a critical molecular switch that governs EM plasticity, with significant implications in understanding the mechanisms driving metastatic progression and identifying potential therapeutic targets in cancer treatment.

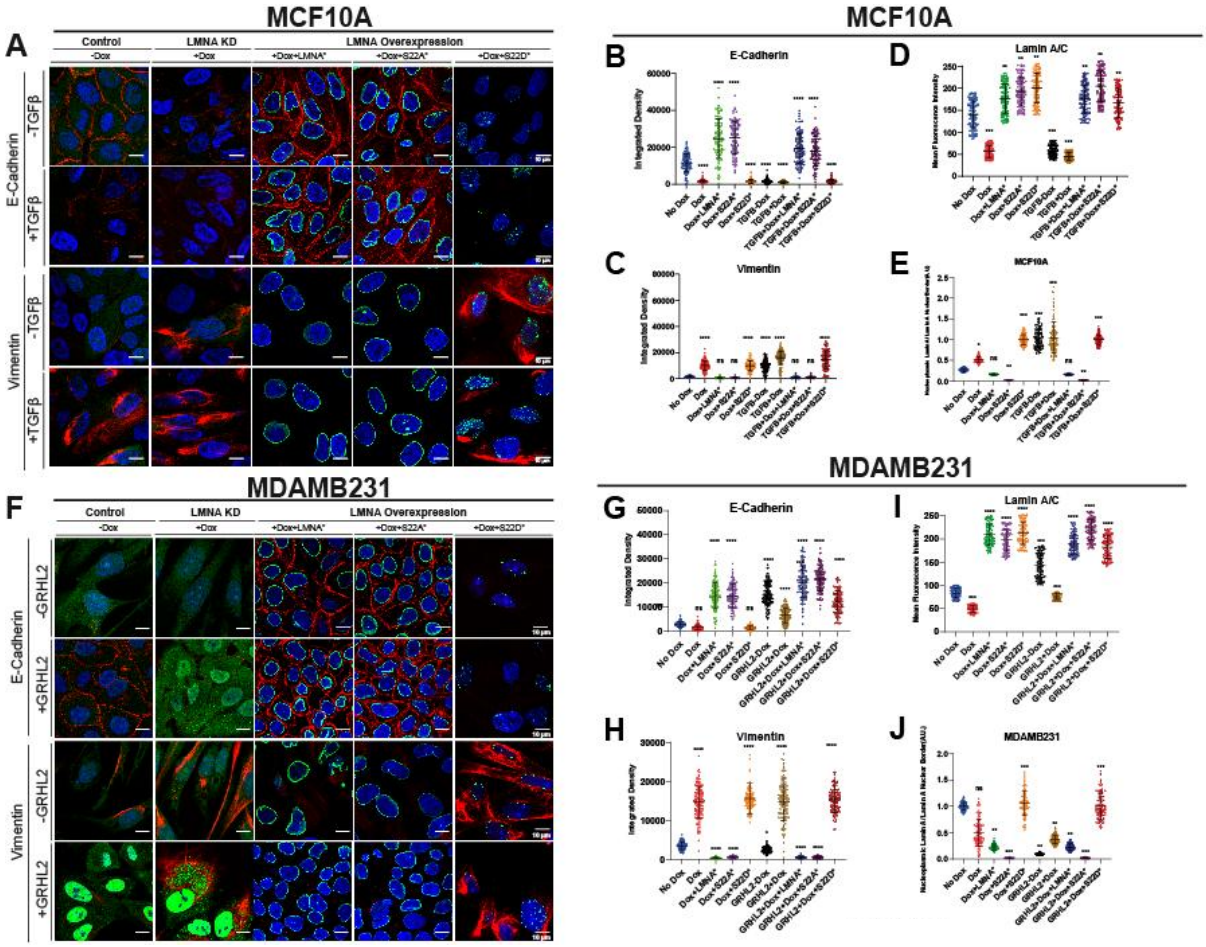

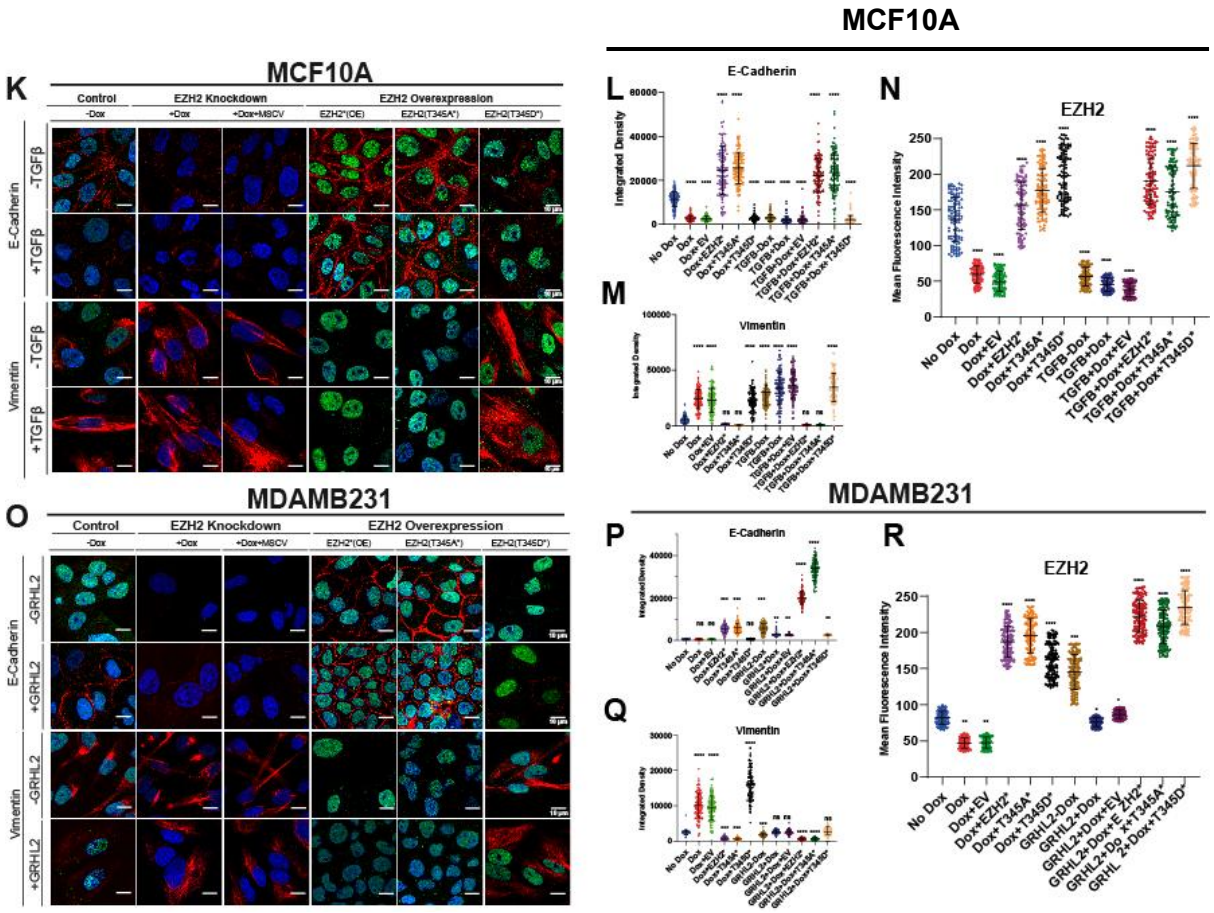


***Figure 5.5: Phosphorylation state of EZH2 and Lamin A modulates epithelial and mesenchymal marker expression.***

***(A)*** *Representative mid-optical sections of MCF10A cells overexpressing phosphodeficient or phosphomimetic forms of Lamin A (green), immunostained for E-cadherin and Vimentin (red) in MCF10A cells in the presence or absence of TGF-β induction. The nucleus is visualized by DAPI (blue). Scale bar ~10μm. Scatter plots depict the integrated density of (B) E-cadherin and (C) Vimentin signals in (A). (D) Mean fluorescence intensity of Lamin A validating knockdown or overexpression. (E) Scatter plot representing the ratio of nucleoplasmic Lamin A to nuclear peripheral Lamin A.*

***(F)*** *Representative mid-optical sections of MDA-MB-231 cells overexpressing phosphodeficient or phosphomimetic forms of Lamin A (green), immunostained for E-cadherin and Vimentin (red). Nucleus is visualized by DAPI (blue). Scale bar ~10μm. Scatter plots depict the integrated density of (G) E-cadherin and (H) Vimentin signals in (F). (I) Mean fluorescence intensity of Lamin A validating knockdown or overexpression. (J) Scatter plot representing the ratio of nucleoplasmic Lamin A to nuclear peripheral Lamin A.*

***(K)*** *Representative mid-optical sections of MCF10A cells overexpressing phosphodeficient or phosphomimetic forms of EZH2 (green), immunostained for E-cadherin and Vimentin (red). Nucleus is visualized by DAPI (blue). Scale bar ~10µm. Scatter plots depict the integrated density of (L) E-cadherin and (M) Vimentin signals in (K). (N) Mean fluorescence intensity of EZH2 validating knockdown or overexpression*

***(O)*** *Representative mid-optical sections of MDA-MB-231 cells overexpressing phosphodeficient or phosphomimetic forms of EZH2 (green), immunostained for E-cadherin and Vimentin (red). Nucleus is visualized by DAPI (blue). Scale bar ~10µm. Scatter plots depict the integrated density of (P) E-cadherin and (Q) Vimentin signals in (O). (R) Mean fluorescence intensity of EZH2 validating knockdown or overexpression*

*Data represent mean ± S.D. (n = 110 cells, N = 3). Two-way ANOVA was used for statistical analysis.*

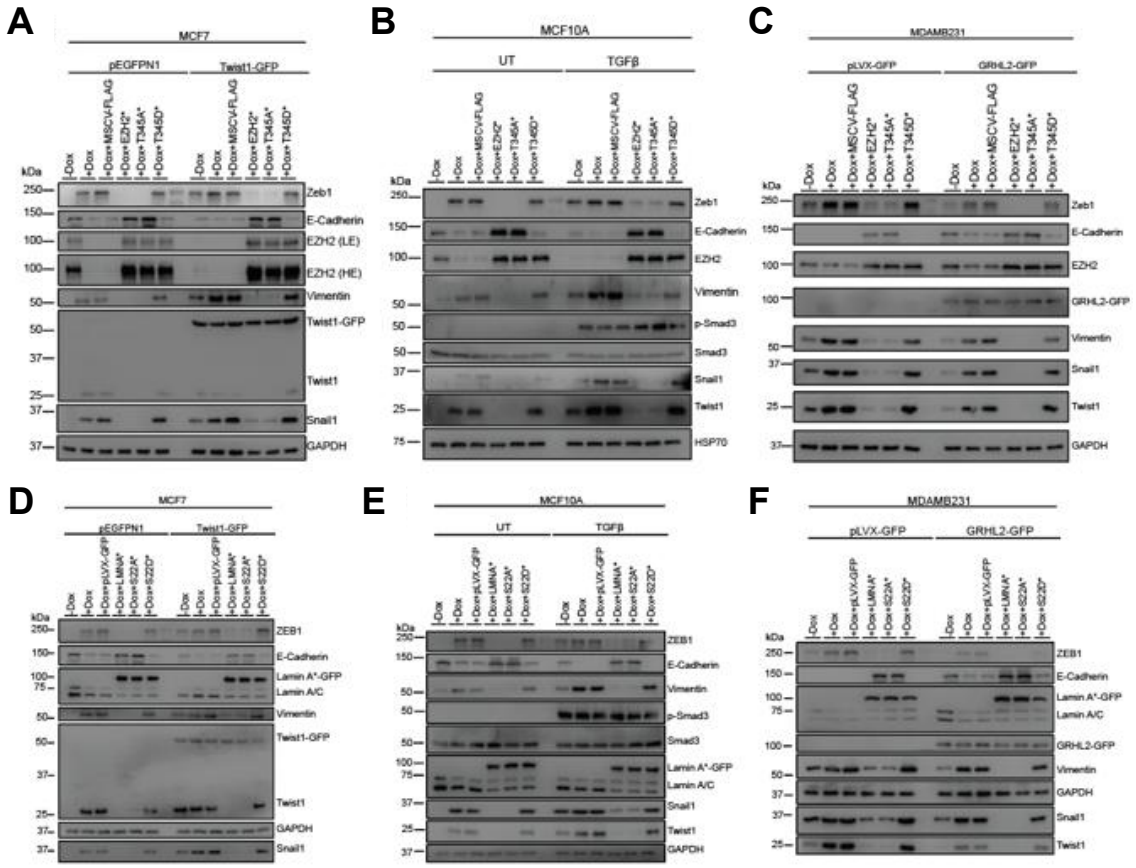


***Figure 5.6: Phosphorylation-dependent regulation of EZH2 and Lamin A/C during EMT and MET.***

***(A, B)*** *Western blot analysis of EMT marker expression in MCF7 and MCF10A cells upon Lamin A/C knockdown and rescue with WT, phospho-deficient (S22A), or phospho-mimetic (S22D) Lamin A-GFP. EMT was induced by TWIST1 overexpression (~48 h) in MCF7 cells or by 10ng/mL TGF-β (~7 days) in MCF10A cells* ***(D, E).*** *Western blot analysis of EMT marker expression in MCF7 and MCF10A cells upon EZH2 knockdown and rescue with WT, phospho-deficient (T345A), or phospho-mimetic (T345D) EZH2-FLAG. EMT was induced by TGF-β (~7 days) in MCF10A cells or by TWIST1 overexpression (~48 h) in MCF7 cells* ***(C, F).*** *Western blot analysis of epithelial-mesenchymal (EM) marker expression in MDA-MB-231 cells following knockdown and rescue experiments. (C) EM marker expression in cells with Lamin A/C knockdown was rescued with WT, phospho-deficient (S22A), or phospho-mimetic (S22D) Lamin A/C. MET was induced by GRHL2 overexpression. (F) EM marker expression in cells with EZH2 knockdown was rescued with WT, phospho-deficient (T345A), or phospho-mimetic (T345D) EZH2. (G) Schematic representation of the effect of mutants on Lamin A-EZH2 association and the EM status of cells.*

### 5.2.3 Functional Impact of Lamin A/C–EZH2 Disruption on Cell Invasion

To elucidate the functional consequences of Lamin A/C–EZH2 interaction in modulating epithelial–mesenchymal plasticity, we systematically evaluated the invasive potential of cells under conditions that disrupt or stabilize this interaction. Given the established role of epithelial–mesenchymal transition (EMT) in enhancing the invasive capacity of tumor cells, we hypothesized that disruption of the Lamin A/C–EZH2 complex via phosphorylation may serve as a molecular mechanism enabling enhanced cellular invasiveness. To test this, we employed a series of invasion and migration assays in both epithelial-like MCF7 and mesenchymal-like MDA-MB-231 cell lines under various genetic perturbation models designed to modulate the phosphorylation state of these key regulatory proteins.

In MCF7 cells, which are typically non-invasive and exhibit strong epithelial characteristics, we transiently overexpressed human TWIST1 (hTWIST1), a canonical EMT-inducing transcription factor. This allowed us to induce EMT and assess how different phosphorylation states of Lamin A and EZH2 influence the resulting phenotype. We generated multiple isogenic MCF7 cell lines with stable knockdown of endogenous Lamin A/C or EZH2 and subsequently reconstituted them with either full-length, phosphodeficient, or phosphomimetic versions of the proteins. Invasion assays using Matrigel-coated transwell inserts revealed that TWIST1 overexpression alone increased invasion potential, as expected. Notably, when Lamin A/C or EZH2 were depleted, a further ~30% increase in cell invasion was observed, indicating that these proteins usually act to suppress invasive behavior. This effect was phenocopied by the overexpression of the phosphomimetic Lamin A (S22D) or EZH2 (T345D) mutants, both of which disrupt the Lamin A/C–EZH2 interaction. In contrast, cells expressing the phosphodeficient mutants (Lamin A: S22A and EZH2: T345A), which retain the interaction, exhibited reduced invasion and migration compared to control cells, even under EMT-inducing conditions. Quantitative analysis of the migration assays further supported these findings, with phosphodeficient constructs reducing cell migration by approximately 20% relative to the parental or TWIST1-transfected cells (Figure 5.8A and B).

These results underscore the inhibitory role of the Lamin A/C–EZH2 complex in governing invasive potential in epithelial cancer cells. The phosphomimetic mutants, by disrupting this interaction, likely derepress mesenchymal transcription programs and extracellular matrix degradation, hallmark features of an invasive phenotype. These data highlight phosphorylation-dependent destabilization of the Lamin A/C–EZH2 complex as a key event promoting EMT-

associated cell invasion. In a broader context, the modulation of cell behavior through specific post-translational modifications of nuclear envelope components points to an intricate link between nuclear architecture and dynamic cellular responses during cancer progression (Figure 5.7A and B).

To examine whether these findings were retained in a more mesenchymal background, we next turned to MDA-MB-231 cells, which are intrinsically highly motile and invasive because of their basal-like, mesenchymal phenotype. In this context, GRHL2 overexpression led to a pronounced reduction in both cell migration and invasion, consistent with its established role as a transcription factor that promotes MET and suppresses invasive behavior (Figure 5.7C). These results confirmed that GRHL2 is capable of driving a more epithelial-like state even in a highly aggressive breast cancer cell line. However, this anti-invasive effect was significantly attenuated when either Lamin A or EZH2 was depleted in GRHL2-overexpressing cells. Despite the continued presence of GRHL2, cells with reduced Lamin A or EZH2 expression regained migratory and invasive capacity, indicating that GRHL2 alone is not sufficient to fully enforce the epithelial program. Rather, the Lamin A/C–EZH2 axis appears to be required for the complete execution of GRHL2-mediated suppression of invasion (Figure 5.7D).

These findings suggest that GRHL2 does not function in isolation, but instead cooperates with a downstream chromatin regulatory module involving Lamin A/C and EZH2. In this model, GRHL2 likely initiates epithelial reprogramming, while the Lamin A/C–EZH2 complex contributes to the stabilization and maintenance of that state through nuclear and chromatin-associated mechanisms. The partial reversal of the GRHL2 phenotype upon Lamin A or EZH2 depletion implies that this axis acts as a necessary effector arm for GRHL2-driven MET. In other words, GRHL2 may set the transcriptional direction toward epithelial identity, but the Lamin A/C–EZH2 complex is needed to consolidate that shift and suppress the invasive mesenchymal phenotype.

This interpretation is further supported by the fact that disruption of the Lamin A/C–EZH2 interaction enhances invasion even in the presence of GRHL2, underscoring a functional interdependence between these factors. Thus, the data point to a model in which GRHL2 and the Lamin A/C–EZH2 module operate in a coordinated manner to regulate epithelial plasticity. GRHL2 serves as an upstream MET-promoting factor, whereas Lamin A/C–EZH2 functions as a critical downstream or cooperative component that translates this transcriptional program into a stable anti-invasive phenotype (Figure 5.7D). The inability of GRHL2 to fully suppress

invasion in the absence of Lamin A or EZH2 highlights the importance of this regulatory axis in maintaining epithelial integrity. Collectively, these observations support the idea that the Lamin A/C–EZH2 complex is an essential participant in the GRHL2-mediated control of cell invasiveness and that phosphorylation-sensitive regulation of this complex may represent a key switch governing epithelial–mesenchymal plasticity.

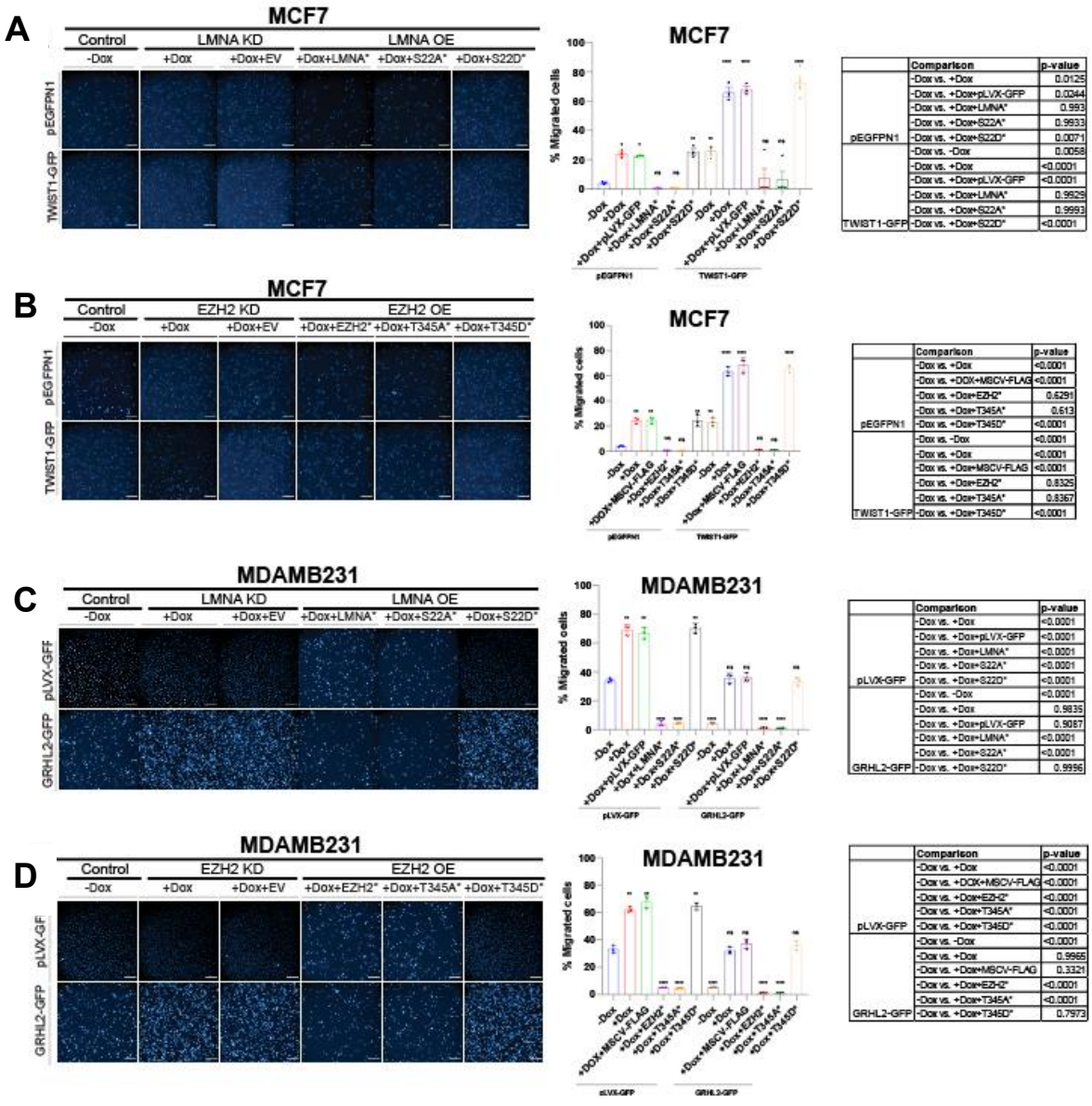


| | Comparison | p-value |
|---|---|---|
| pEGFPN1 | -Dox vs. +Dox | 0.0125 |
| | -Dox vs. +Dox+pLVX-GFP | 0.0244 |
| | -Dox vs. +Dox+LMNA* | 0.993 |
| | -Dox vs. +Dox+S22A* | 0.9933 |
| | -Dox vs. +Dox+S22D* | 0.0071 |
| TWIST1-GFP | -Dox vs. -Dox | 0.0058 |
| | -Dox vs. +Dox | <0.0001 |
| | -Dox vs. +Dox+pLVX-GFP | <0.0001 |
| | -Dox vs. +Dox+LMNA* | 0.9929 |
| | -Dox vs. +Dox+S22A* | 0.9993 |
| | -Dox vs. +Dox+S22D* | <0.0001 |

| | Comparison | p-value |
|---|---|---|
| pEGFPN1 | -Dox vs. +Dox | <0.0001 |
| | -Dox vs. +DOX+MSCV-FLAG | <0.0001 |
| | -Dox vs. +Dox+EZH2* | 0.6291 |
| | -Dox vs. +Dox+T345A* | 0.613 |
| | -Dox vs. +Dox+T345D* | <0.0001 |
| TWIST1-GFP | -Dox vs. -Dox | <0.0001 |
| | -Dox vs. +Dox | <0.0001 |
| | -Dox vs. +Dox+MSCV-FLAG | <0.0001 |
| | -Dox vs. +Dox+EZH2* | 0.8325 |
| | -Dox vs. +Dox+T345A* | 0.8367 |
| | -Dox vs. +Dox+T345D* | <0.0001 |

| | Comparison | p-value |
|---|---|---|
| pLVX-GFP | -Dox vs. +Dox | <0.0001 |
| | -Dox vs. +Dox+pLVX-GFP | <0.0001 |
| | -Dox vs. +Dox+LMNA* | <0.0001 |
| | -Dox vs. +Dox+S22A* | <0.0001 |
| | -Dox vs. +Dox+S22D* | <0.0001 |
| GRHL2-GFP | -Dox vs. -Dox | <0.0001 |
| | -Dox vs. +Dox | 0.9835 |
| | -Dox vs. +Dox+pLVX-GFP | 0.9087 |
| | -Dox vs. +Dox+LMNA* | <0.0001 |
| | -Dox vs. +Dox+S22A* | <0.0001 |
| | -Dox vs. +Dox+S22D* | 0.9996 |

| | Comparison | p-value |
|---|---|---|
| pLVX-GFP | -Dox vs. +Dox | <0.0001 |
| | -Dox vs. +DOX+MSCV-FLAG | <0.0001 |
| | -Dox vs. +Dox+EZH2* | <0.0001 |
| | -Dox vs. +Dox+T345A* | <0.0001 |
| | -Dox vs. +Dox+T345D* | <0.0001 |
| GRHL2-GFP | -Dox vs. -Dox | <0.0001 |
| | -Dox vs. +Dox | 0.9965 |
| | -Dox vs. +Dox+MSCV-FLAG | 0.3321 |
| | -Dox vs. +Dox+EZH2* | <0.0001 |
| | -Dox vs. +Dox+T345A* | <0.0001 |
| | -Dox vs. +Dox+T345D* | 0.7973 |

***Figure 5.7: Lamin A and EZH2 phosphorylation regulate migration. (A, B)*** *Representative DAPI images and quantification of MCF7 cell migration in a serum gradient upon overexpression of Lamin A (A) or EZH2 (B) mutants, with or without TWIST1 overexpression.* ***(C, D)*** *Representative DAPI images and quantification of MDA-MB-231 cell migration in a serum gradient upon overexpression of Lamin A (C) or EZH2 (D) mutants, with or without GRHL2 overexpression.*

### 5.2.4 Lamin A/C–EZH2 Axis Modulates TGF-β–Induced Migration in MCF10A Cells

To further dissect the mechanistic role of the Lamin A/C–EZH2 interaction in epithelial–mesenchymal plasticity, we performed migration assays using the non-tumorigenic human mammary epithelial cell line MCF10A. These cells represent a valuable model for studying early EMT events, as they respond robustly to TGF-β—a well-characterized inducer of EMT and cellular motility. The objective was to investigate whether the phosphorylation-dependent disruption of the Lamin A/C–EZH2 complex contributes to the migratory phenotype observed during TGF-β signaling.

In control conditions, MCF10A cells exhibited relatively low basal migration, consistent with their epithelial character. Upon stimulation with TGF-β, however, there was a marked increase in cell migration, reflecting EMT induction. To explore the contribution of Lamin A/C and EZH2 to this migratory shift, we employed siRNA-mediated depletion strategies and generated overexpression constructs of both wild-type and phosphorylation mutants of Lamin A and EZH2. Specifically, we used phosphodeficient (S22A for Lamin A and T345A for EZH2) and phosphomimetic (S22D and T345D) variants to assess the functional relevance of CDK1-mediated phosphorylation on this axis.

Depletion of Lamin A/C or EZH2 alone was sufficient to enhance cell migration, phenocopying the effect of TGF-β treatment. Importantly, this increase in migration was not merely additive when combined with TGF-β stimulation, suggesting that Lamin A/C and EZH2 function downstream of or in convergence with the TGF-β signaling pathway to repress migratory potential. These results underscore the repressive role of the Lamin A/C–EZH2 complex in maintaining epithelial cell behavior and suggest that its disruption is a necessary event in the acquisition of migratory capacity during EMT.

When full-length Lamin A or EZH2 was overexpressed in MCF10A cells, we observed a significant reduction in basal cell migration, reinforcing their role as suppressors of motility. Intriguingly, the phosphodeficient variants S22A and T345A exhibited an even more substantial inhibitory effect on migration, indicating that the unphosphorylated forms of these proteins are functionally competent in repressing motility and likely form a more stable repressive complex. These effects were particularly notable in the presence of TGF-β, where full-length and phosphodeficient Lamin A or EZH2 significantly blunted TGF-β-induced migration. This suggests that these unmodified forms actively counteract EMT signaling

cascades, maintaining the epithelial phenotype and restraining cellular motility even in the presence of a potent EMT inducer.

Conversely, overexpression of phosphomimetic mutants Lamin A S22D or EZH2 T345D, which are designed to mimic constitutive phosphorylation and disrupt interaction with one another, exacerbated the migratory response. In the absence of TGF-β, these phosphomimetic variants alone were sufficient to increase cell migration, indicating that phosphorylation-dependent dissociation of the Lamin A/C–EZH2 complex removes an intrinsic barrier to motility. When combined with TGF-β treatment, the effect was even more pronounced, suggesting a synergistic interaction between external EMT signals and internal post-translational modifications of nuclear lamins and chromatin modifiers.

These findings with quantitative data show statistically significant differences in migration between control, knockdown, and overexpression conditions under both basal and TGF-β-stimulated states. These data clearly establish that the phosphorylation status of Lamin A/C and EZH2 is a critical determinant of epithelial cell migration, influencing the cell's ability to respond to external pro-migratory cues such as TGF-β (Figure 5.8A and B).

Collectively, these results support a model in which the Lamin A/C–EZH2 complex acts as a gatekeeper of epithelial identity, repressing migration through its influence on chromatin state and transcriptional programming. Phosphorylation by CDK1 or other mitotic kinases likely serves as a switch to disengage this complex, thereby sensitizing cells to EMT-inducing signals and promoting motility. This mechanism links nuclear envelope dynamics and epigenetic regulation to broader aspects of cellular behavior and may represent a targetable vulnerability in epithelial-derived cancers with high migratory and metastatic potential.

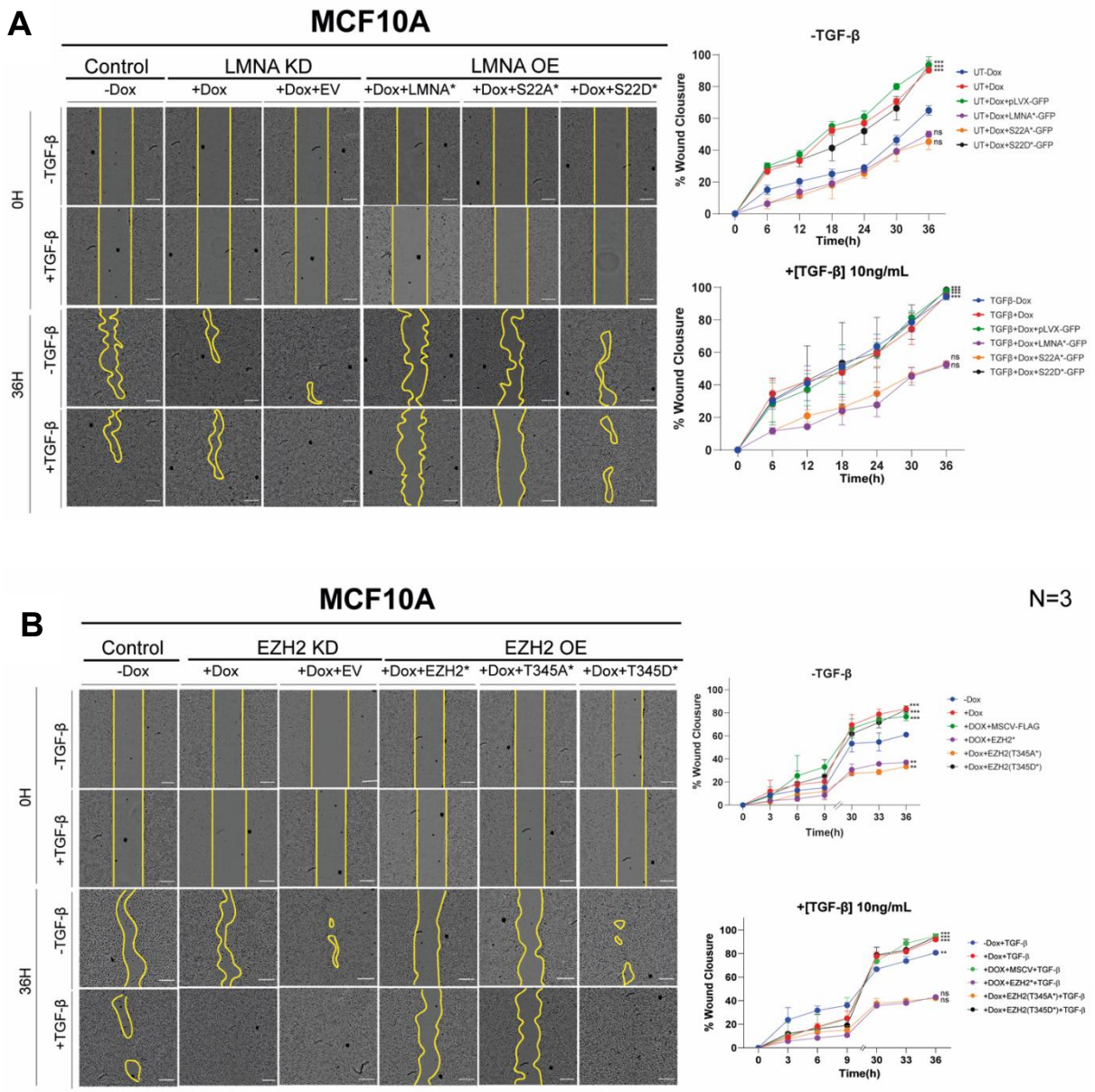


***Figure 5.8: Lamin A and EZH2 phosphorylation regulate migration.***

***(A)*** *Bright-field images showing the migration of untreated or TGF-β-treated MCF10A cells undergoing wound-healing assay following Lamin A/C depletion or overexpression of Lamin A, Lamin A (S22A), or Lamin A (S22D).* ***(B)*** *Bright-field images showing the migration of untreated or TGF-β-treated MCF10A cells undergoing wound-healing assay following EZH2 depletion or overexpression of EZH2, EZH2 (T345A), or EZH2 (T345D).*

### 5.2.5 Phosphorylation-Dependent Modulation of Hybrid Epithelial/Mesenchymal States by Lamin A/C and EZH2

To uncover the role of Lamin A/C and EZH2 phosphorylation in modulating epithelial-mesenchymal plasticity, we investigated the dynamics of hybrid epithelial/mesenchymal (E/M) phenotypes using surface marker-based flow cytometry. Hybrid states, typified by co-expression of CD104 and CD44, represent transitional cell identities with high metastatic and stem-like potential. We aimed to determine whether the phosphorylation state of Lamin A/C and EZH2 influences the stabilization or bypassing of this hybrid population under EMT and MET conditions.

Upon TWIST1-induced EMT in MCF7 cells, we observed a marked phenotypic transition from epithelial (CD104+CD44−) to mesenchymal (CD104−CD44+) states via a hybrid intermediate (CD104+CD44+). Flow cytometric analysis revealed a progressive accumulation of CD104+CD44+ cells during EMT induction, confirming the intermediate nature of this population during transition. However, overexpression of either full-length Lamin A or EZH2 in these TWIST1-overexpressing cells abrogated the formation of hybrid cells and directly promoted a reversion to an epithelial phenotype (CD104+CD44−). These observations suggest that Lamin A and EZH2, in their unmodified states, are potent repressors of mesenchymal gene expression and can effectively override intermediate hybrid programs even under strong EMT-inducing conditions.

In stark contrast, the phosphomimetic mutants Lamin A S22D and EZH2 T345D yielded an accumulation of hybrid CD104+CD44+ cells even in the absence of exogenous EMT stimuli. This accumulation suggests that phosphorylation at these specific sites impairs the ability of Lamin A/C and EZH2 to enforce a complete epithelial or mesenchymal identity, thereby stabilizing the cells in a hybrid state. These findings indicate that phosphorylation of Lamin A at serine 22 and EZH2 at threonine 345 disrupts their chromatin binding or repressor activity, thereby partially de-repressing EMT transcription factors such as SNAI1, TWIST1, and ZEB1. The inability of cells to fully commit to either epithelial or mesenchymal identities results in their entrapment in a metastable hybrid state—a condition associated with heightened plasticity and tumor aggressiveness.

We extended this investigation into the context of GRHL2-mediated MET in mesenchymal MDA-MB-231 cells. GRHL2 overexpression led to a phenotypic shift toward CD104+CD44−

epithelial cells, consistent with successful MET induction. Notably, co-expression of full-length or phosphodeficient Lamin A (S22A) and EZH2 (T345A) synergized with GRHL2 to entirely suppress the hybrid population and restore a robust epithelial identity. In contrast, the presence of phosphomimetic Lamin A or EZH2 mutants in the GRHL2 background failed to promote complete MET, resulting in persistent CD104+CD44+ hybrid cells (Figures 5.9C and D). These data support a model in which the phosphorylation-sensitive repression activity of Lamin A and EZH2 is necessary for the complete execution of MET.

Collectively, our results show that while GRHL2 acts as a transcriptional inducer of epithelial fate, Lamin A and EZH2 are required at the chromatin level to lock in this fate by repressing mesenchymal gene programs. Importantly, the phosphorylation state of these proteins serves as a molecular switch: the phosphodeficient mutants enforce epithelial commitment and suppress hybrid states, while the phosphomimetic forms allow EMT-TFs to remain active, thereby facilitating the persistence of plastic hybrid phenotypes.

Flow cytometric analysis performed under these various conditions further reinforced these findings (Figures 5.9A and B). In conditions promoting hybrid phenotypes—either through the presence of phosphomimetic Lamin A/EZH2 or partial depletion of these proteins—there was a consistent increase in CD104+CD44+ cells. This trend was observed regardless of the presence of strong EMT or MET drivers, indicating that phosphorylation of Lamin A/C and EZH2 is sufficient to modulate the balance between plasticity and lineage commitment.

These findings offer a mechanistic understanding of how Lamin A/C and EZH2 post-translational modifications regulate epithelial-mesenchymal plasticity. The inability of phosphorylated forms to enforce chromatin compaction and repression of EMT-TFs allows for the stabilization of hybrid states, which are now understood to be more than just transient intermediates. Instead, they represent a stable, selectable, and biologically significant phenotype that supports tumor dissemination and therapeutic resistance.

In summary, this set of results highlights that the hybrid E/M state is not merely a passage through EMT/MET but a regulated node within the plasticity network. The Lamin A/C–EZH2 complex emerges as a phosphorylation-sensitive epigenetic gatekeeper that governs the entry into or exit from this hybrid state. Interventions that prevent the phosphorylation of these proteins—or pharmacologically stabilize their chromatin-associated states—may provide a powerful therapeutic strategy to curtail cancer plasticity and progression.

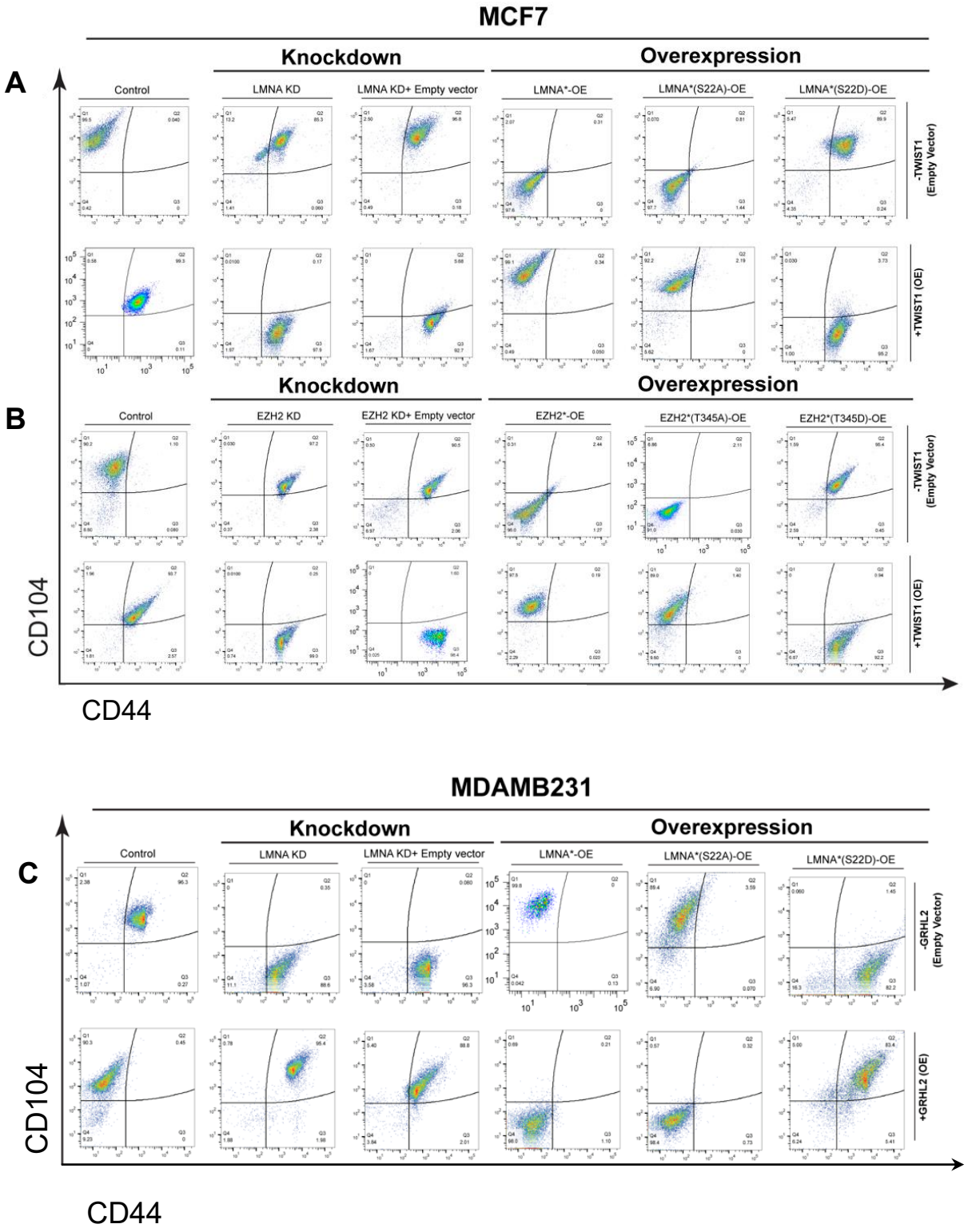
MCF7
Knockdown
Overexpression
A
Control
LMNA KD
LMNA KD+ Empty vector
LMNA*-OE
LMNA*(S22A)-OE
LMNA*(S22D)-OE
-TWIST1 (Empty Vector)
+TWIST1 (OE)
Knockdown
Overexpression
B
Control
EZH2 KD
EZH2 KD+ Empty vector
EZH2*-OE
EZH2*(T345A)-OE
EZH2*(T345D)-OE
-TWIST1 (Empty Vector)
+TWIST1 (OE)
CD104
CD44
MDAMB231
Knockdown
Overexpression
C
Control
LMNA KD
LMNA KD+ Empty vector
LMNA*-OE
LMNA*(S22A)-OE
LMNA*(S22D)-OE
-GRHL2 (Empty Vector)
+GRHL2 (OE)
CD104
CD44

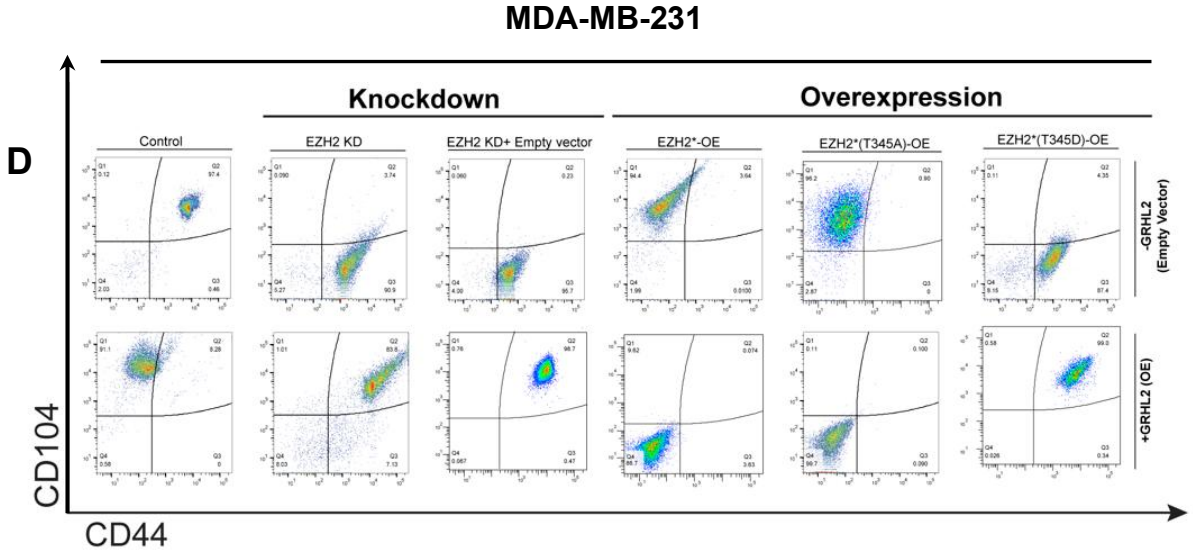


***Figure 5.9: Lamin A/C and EZH2 perturbation alter CD104 and CD44 FACS distribution profile in response to EMT and MET induction.***

***(A)*** *FACS scatter representing the percentage of MCF7 cells in each quadrant upon Lamin A/C depletion or overexpression of mutants of Lamin A (S22A or S22D) in the presence and absence of TWIST1-mediated EMT.*

***(B)*** *FACS scatter representing the percentage of MCF7 cells in each quadrant upon EZH2 depletion or overexpression of mutants of EZH2 (T345A or T345D) in the presence and absence of TWIST1-mediated EMT.*

***(C)*** *FACS scatter representing the percentage of MDA-MB-231 cells in each quadrant upon Lamin A/C depletion or overexpression of mutants of Lamin A (S22A or S22D) in the presence and absence of GRHL2-mediated MET.*

***(D)*** *FACS scatter representing the percentage of MDA-MB-231 cells in each quadrant upon Lamin A/C depletion or overexpression of mutants of EZH2 (T345A or T345D) in the presence and absence of GRHL2-mediated MET.*

### 5.2.6 Phosphorylation-Dependent Regulation of Tumorigenic Potential in Breast Cancer Models

To explore the functional implications of phosphorylation on Lamin A/C and EZH2 in the context of breast cancer progression, we investigated the tumorigenic potential of their phosphodeficient and phosphomimetic variants using an orthotopic xenograft model. Given our previous findings that phosphorylation of Lamin A at serine 22 (S22) and EZH2 at threonine 345 (T345) disrupts their interaction and promotes mesenchymal traits, we hypothesized that these post-translational modifications would enhance tumor formation in vivo. To test this, we utilized the highly aggressive triple-negative breast cancer cell line MDA-MB-231, which exhibits an intrinsic mesenchymal phenotype and high metastatic potential.

We generated stable MDA-MB-231 cell lines overexpressing either phosphodeficient (Lamin A: S22A and EZH2: T345A) or phosphomimetic (Lamin A: S22D and EZH2: T345D) forms of Lamin A and EZH2. Approximately one million cells from each engineered line were orthotopically injected into the mammary fat pad of immunodeficient female NOD-SCID mice, aged six weeks. Tumor volume was measured every 3 days using calipers, and final tumor burden was recorded at the termination of the study after five weeks.

Strikingly, mice injected with cells expressing phosphomimetic Lamin A (S22D) or EZH2 (T345D) developed significantly larger tumors compared to their phosphodeficient counterparts. Quantitative analysis revealed an increase in both tumor volume and final tumor weight in the phosphomimetic groups, suggesting enhanced tumorigenic capacity. In contrast, mice bearing tumors derived from cells expressing phosphodeficient Lamin A (S22A) or EZH2 (T345A) showed significantly restrained tumor growth, reinforcing the suppressive role of the Lamin A/C–EZH2 complex in vivo. These findings are consistent with in vitro assays showing that phosphorylation of these proteins enhances mesenchymal traits, which are often associated with increased invasiveness, metastatic potential, and poor prognosis in breast cancer (Figure 5.10A-F).

To further validate the molecular mechanisms underlying these phenotypic differences, we isolated tumor-derived cells from each group and performed co-immunoprecipitation assays following triple enzyme digestion to preserve chromatin–protein interactions. In tumors derived from the S22A group, Lamin A/C maintained its interaction with EZH2, consistent with its phosphodeficient state and ability to sustain chromatin repression at mesenchymal loci.

In contrast, in tumors expressing Lamin A (S22D), this interaction was abrogated. Instead, Lamin A was found to preferentially associate with phosphorylated CDK1 (pCDK1-T161), suggesting that phosphorylation at S22 not only disrupts Lamin A/C–EZH2 binding but also redirects Lamin A to engage in CDK1-mediated regulatory pathways (Figure 5.10A, C, and E).

A similar pattern was observed in immunoprecipitation assays for EZH2. The phosphodeficient EZH2 (T345A) retained its interaction with Lamin A/C, whereas the phosphomimetic variant (T345D) lost this binding and instead displayed enhanced interaction with pCDK1. These reciprocal interaction profiles underscore a switch-like mechanism whereby phosphorylation at specific residues redirects the molecular associations of Lamin A/C and EZH2, resulting in divergent transcriptional programs and cellular behaviors. Such reprogramming may contribute to increased plasticity, loss of epithelial integrity, and acquisition of stem-like and tumorigenic properties (Figure 5.10B, D, and F).

To complement these biochemical findings, we performed immunofluorescence assays on MDA-MB-231 cells expressing each variant. Cells overexpressing the phosphodeficient variants (S22A and T345A) exhibited classical epithelial morphology characterized by cobblestone appearance, increased cell–cell adhesion, and cortical localization of E-cadherin. In contrast, cells expressing the phosphomimetic variants (S22D and T345D) retained elongated, spindle-shaped morphology with reduced cell–cell contact and increased Vimentin expression, consistent with mesenchymal features. These results directly link the phosphorylation status of Lamin A and EZH2 to structural and molecular hallmarks of EMT (Figure 5.11C and D).

Taken together, these data provide compelling in vivo and in vitro evidence that phosphorylation at S22 of Lamin A and T345 of EZH2 enhances the tumorigenic potential of breast cancer cells by disrupting their chromatin-associated repressive functions and promoting mesenchymal properties. Notably, these findings extend the functional consequences of Lamin A/C–EZH2 interactions beyond transcriptional regulation and chromatin remodeling to include critical roles in tumor initiation and progression.

Importantly, these results offer a mechanistic basis for understanding how EM plasticity is modulated in vivo and underscore the therapeutic potential of targeting the phosphorylation machinery or stabilizing the Lamin A/C–EZH2 complex. Intervening at the level of post-

translational modifications may prove to be a promising strategy to restore epithelial characteristics, restrict EMT, and ultimately suppress tumor progression in aggressive breast cancer subtypes. These insights not only reinforce the central role of nuclear architecture in tumor biology but also open new avenues for translational applications in oncology.

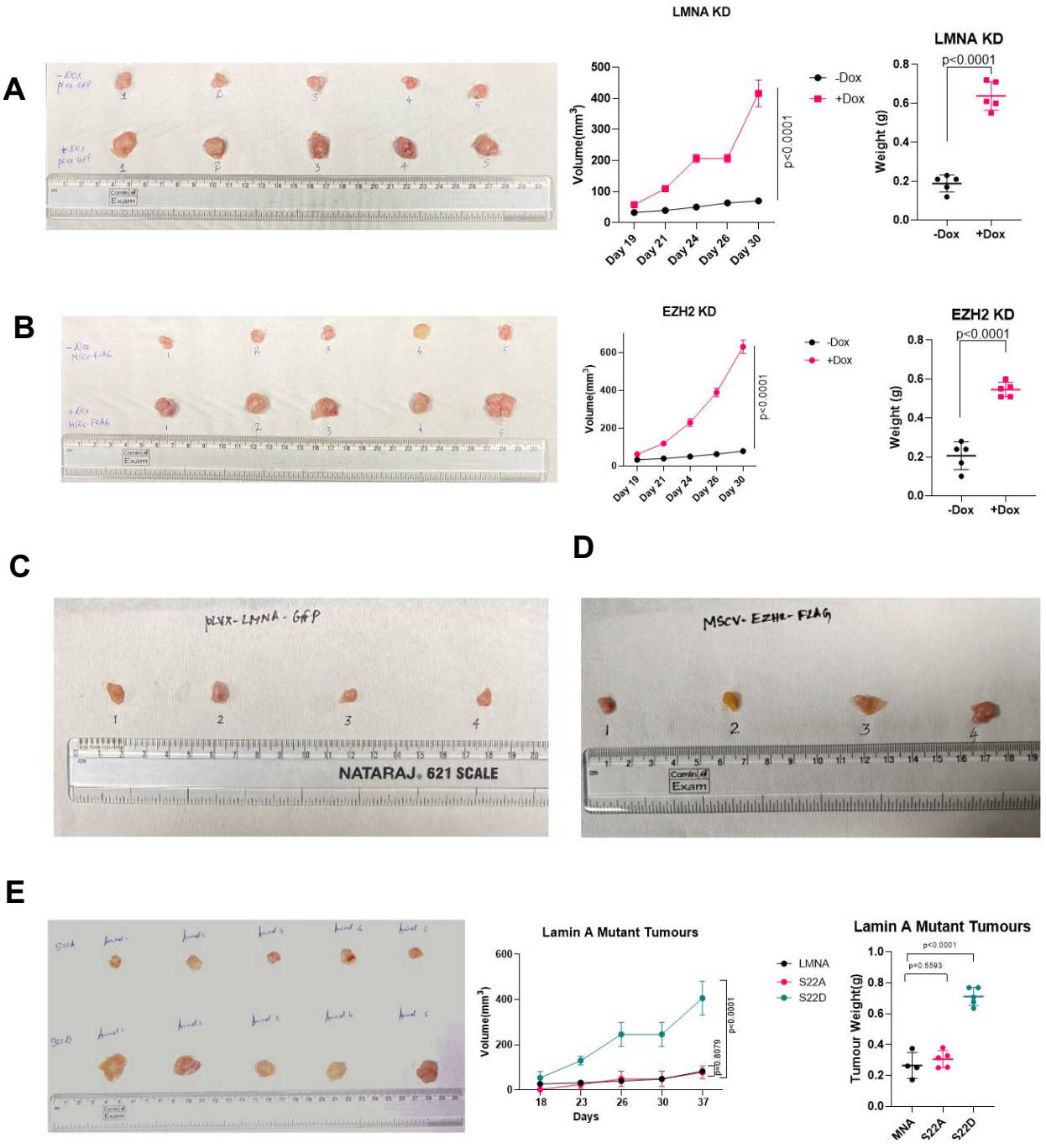

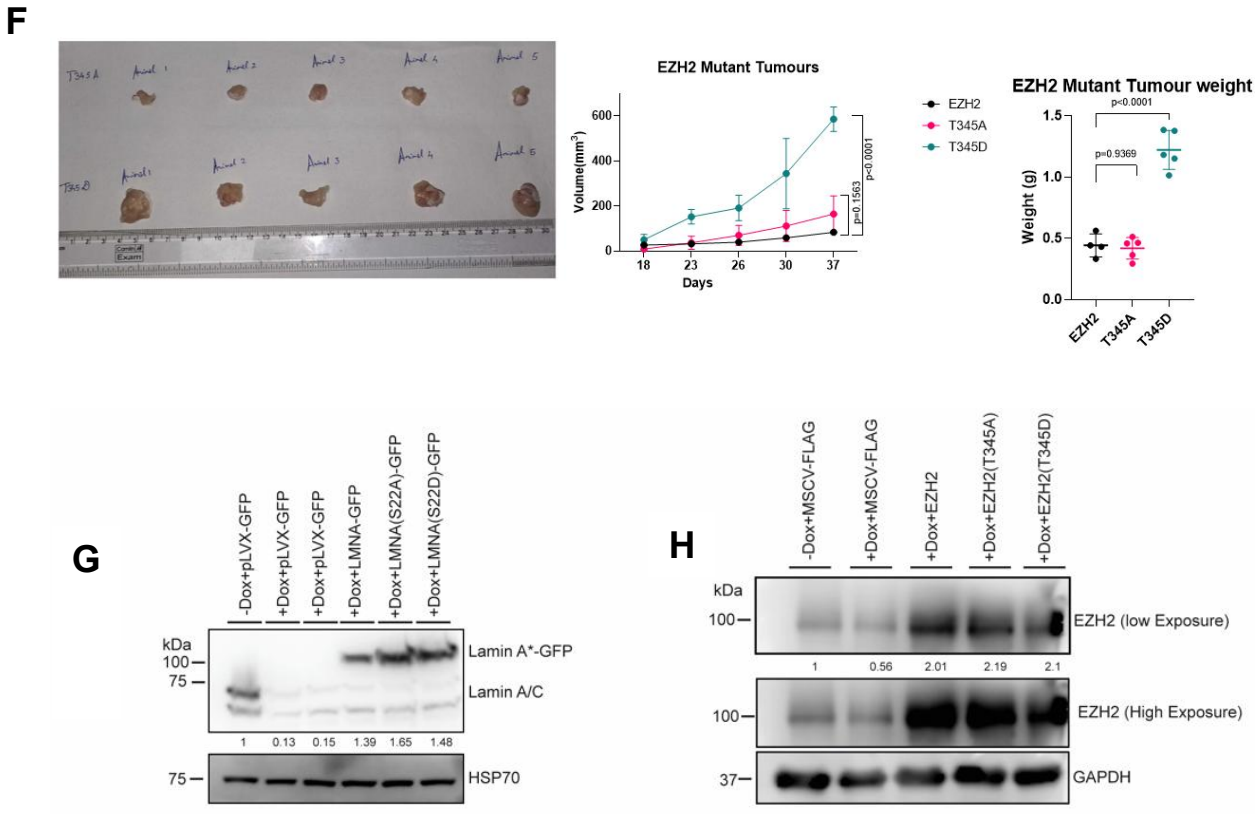


***Figure 5.10: Tumour formation in NOD-SCID mice***

*(A) Comparison of tumour formation capabilities in MDA-MB-231 cells, in Lamin A/C knockdown. Knockdown was induced by the addition of 500 ng/mL of doxycycline in drinking water. (B) Comparison of tumour formation capabilities in MDA-MB-231 cells, in EZH2 knockdown. Knockdown was induced by the addition of 500 ng/mL of doxycycline in drinking water. (C) Overexpression of full-length Lamin A in the presence of endogenous Lamin A/C depletion. Graphs compare the volume ($mm^3$) of tumours and the weight of tumours in (g). (D) Overexpression of full-length EZH2 in the presence of endogenous EZH2 depletion. Graphs compare the volume ($mm^3$) of tumours and the weight of tumours in (g). (E) Overexpression of phosphodeficient (S22A) and phosphomimetic (S22D) in the presence of endogenous Lamin A/C depletion. Graphs compare the volume ($mm^3$) of tumours and the weight of tumours in (g). (F) Overexpression of phosphodeficient (T345A) and phosphomimetic (T345D) in the presence of endogenous EZH2 depletion. Graphs compare the volume ($mm^3$) of tumours and the weight of tumours in (g). Immunoblot validating the extent of knockdown and overexpression from tumours(G) Lamin A (H) EZH2.*

### 5.2.7 Post-Translational Control of Lamin A/C–EZH2 Binding Modulates Epithelial–Mesenchymal Plasticity

To gain deeper insight into the regulatory significance of the Lamin A/C–EZH2 interaction in the context of epithelial–mesenchymal plasticity, we examined the impact of phosphorylation at key regulatory residues through a combination of co-immunoprecipitation and phenotypic assays. While our earlier findings established a dynamic interaction between Lamin A/C and EZH2 in vitro, we next sought to validate whether this interaction was preserved in primary tumor-derived cells and whether post-translational modifications modulate their association and downstream functional consequences.

We performed immunoprecipitation assays using lysates from primary tumor-derived cells transfected with wild-type or phospho-mutant forms of Lamin A and EZH2. Lamin A harboring a serine-to-alanine mutation at residue 22 (S22A), which renders it phosphodeficient and mimics the dephosphorylated state, robustly co-precipitated with EZH2, suggesting that phosphorylation at S22 negatively regulates Lamin A/C–EZH2 complex formation. Conversely, the phosphomimetic Lamin A mutant (S22D), designed to mimic constitutive phosphorylation, failed to associate with EZH2 and instead exhibited enhanced binding to phosphorylated CDK1 (pCDK1-T161), indicating a competitive shift in interaction partners (Figure 5.11A and B). This supports the hypothesis that phosphorylation of Lamin A at S22 by CDK1 disrupts its interaction with chromatin regulators such as EZH2 and facilitates association with cell cycle kinases, potentially promoting mitotic chromatin reorganization and loss of repressive chromatin marks.

A complementary pattern was observed when we immunoprecipitated EZH2. The phosphodeficient EZH2 mutant (T345A), which cannot be phosphorylated at threonine 345, retained its association with Lamin A/C. In contrast, the phosphomimetic mutant (T345D), simulating a constitutively phosphorylated state, preferentially interacted with pCDK1 rather than Lamin A/C. These results suggest a bidirectional phosphorylation-dependent mechanism in which both Lamin A/C and EZH2 are modulated by CDK1-mediated phosphorylation to dynamically regulate their interaction during the epithelial–mesenchymal transition (EMT).

To examine the phenotypic consequences of these molecular interactions, we assessed cellular morphology by immunofluorescence in MDA-MB-231 cells expressing either wild-type or mutant forms of Lamin A and EZH2. Cells expressing phosphodeficient Lamin A (S22A) or

EZH2 (T345A) displayed an epithelial-like morphology, characterized by a cobblestone appearance, increased cell–cell junctions (Figure 5.11C and D). In contrast, cells expressing the phosphomimetic forms (S22D or T345D) retained a mesenchymal phenotype, marked by elongated spindle-shaped morphology, disrupted cell–cell contacts, and prominent actin-rich protrusions. These observations further support a model in which phosphorylation at specific residues on Lamin A and EZH2 disrupts their interaction, favoring a chromatin state permissive to mesenchymal gene expression and metastatic traits.

Taken together, our findings highlight a phosphorylation-dependent regulatory axis involving Lamin A/C, EZH2, and CDK1. Phosphorylation acts as a molecular switch that controls the stability of the Lamin A/C–EZH2 complex, influencing nuclear architecture and epigenetic repression during EMT. The preferential interaction of phosphomimetic mutants with pCDK1 suggests a role for mitotic signaling in reprogramming the nuclear lamina–chromatin interface, thereby facilitating epigenetic plasticity essential for cancer progression. These insights reveal a potential vulnerability that could be exploited to therapeutically stabilize the Lamin A/C–EZH2 complex and inhibit mesenchymal transition in aggressive breast cancers.

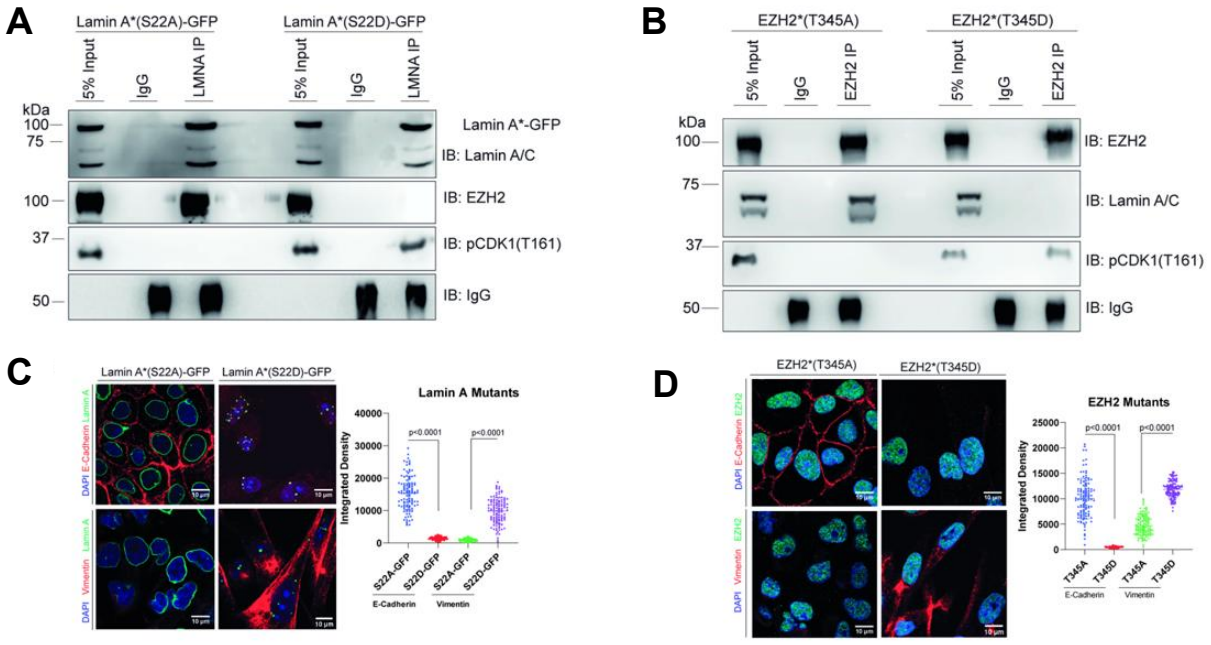


***Figure 5.11: Post-Translational Control of Lamin A/C–EZH2 Binding Modulates Epithelial–Mesenchymal Plasticity***

*(A) Immunoprecipitation of Lamin A/C from tumor lysates followed by immunoblotting for EZH2 and phospho-CDK1.*

*(B) Immunoprecipitation of EZH2 from tumor lysates followed by immunoblotting for Lamin A/C and phospho-CDK1.*

*(C) Immunofluorescence of tumor-derived MDA-MB-231 cells stained for E-cadherin, Vimentin (red), and Lamin A (GFP). Scale bar: 10 μm. Quantification of integrated density of E-Cadherin and Vimentin upon overexpression of phosphomutants of Lamin A. Data represent mean ± SD. Statistical significance was determined using an unpaired two-tailed Student's t-test.*

*(D) Immunofluorescence of tumor-derived MDA-MB-231 cells stained for E-cadherin, Vimentin (red), and EZH2 (green). Scale bar: 10 μm. Quantification of integrated density of E-Cadherin and Vimentin upon overexpression of phosphomutants of EZH2. Data represent mean ± SD. Statistical significance was determined using an unpaired two-tailed Student's t-test.*

### 5.2.8 Phosphorylation-Dependent Regulation of Metastatic Spread in Breast Cancer Models

To assess whether these post-translational modifications influence not only primary tumor growth but also the metastatic propensity of tumor cells, we conducted a comprehensive histopathological evaluation of the lungs from xenografted mice approximately six weeks post-fat pad inoculation of MDA-MB-231 cells. These cells were engineered to stably overexpress either phosphodeficient (S22A and T345A) or phosphomimetic (S22D and T345D) forms of Lamin A and EZH2, respectively. At the endpoint, lung tissues were harvested, formalin-fixed, and paraffin-embedded for sectioning and hematoxylin and eosin (H&E) staining. The stained tissue sections were systematically examined under a microscope to assess the presence, distribution, and morphology of metastatic lesions.

Microscopic analysis revealed striking differences between the groups. In animals injected with cells expressing phosphomimetic Lamin A (S22D) or EZH2 (T345D), the lungs showed widespread metastatic involvement, with numerous tumor foci distributed throughout the lung parenchyma. These metastatic foci were characterized by dense hematoxylin staining, indicating high nuclear content, and featured abnormally shaped, pleomorphic nuclei—hallmarks of malignant transformation and aggressive cellular proliferation. The tumor cells infiltrated alveolar spaces extensively, forming irregular, poorly demarcated clusters that disrupted the standard lung architecture. These histological features are indicative of high metastatic efficiency and support a functional role for the phosphomimetic forms in promoting systemic dissemination (Figure 5.12).

In stark contrast, lung tissues obtained from mice harboring tumors derived from cells overexpressing phosphodeficient Lamin A (S22A) or EZH2 (T345A) exhibited either no detectable metastases or sparse, well-contained foci. When present, these lesions were significantly smaller in size, well circumscribed, and localized to limited regions of the lung parenchyma. The nuclear morphology within these foci was comparatively more regular, and the staining intensity was markedly reduced, reflecting a less aggressive histological phenotype. These observations strongly support a model wherein the dephosphorylated states of Lamin A and EZH2 act as metastasis-suppressive factors, likely through the maintenance of epithelial features and repression of EMT-associated gene expression.

Quantitative analysis of metastatic scores—derived from the number and size of metastatic foci per lung section—further substantiated these findings. Mice in the phosphomimetic groups consistently exhibited higher metastatic scores compared to their phosphodeficient counterparts. This quantification aligns with the qualitative histological observations and provides a robust statistical basis for concluding that phosphorylation of Lamin A and EZH2 facilitates the metastatic cascade.

Collectively, these data provide compelling in vivo evidence that phosphorylation at S22 of Lamin A and T345 of EZH2 significantly enhances the tumorigenic and metastatic potential of breast cancer cells by disrupting chromatin-associated repressive functions and promoting a mesenchymal cellular phenotype. The phosphorylation events appear to functionally inactivate the Lamin A–EZH2 complex, facilitating transcriptional de-repression of EMT drivers such as TWIST1, ZEB1, and SNAI1. This, in turn, primes the cells for increased invasion, migration, and metastatic colonization.

Importantly, these findings underscore a mechanistic framework for understanding how epithelial–mesenchymal plasticity is regulated in vivo and highlight the translational potential of therapeutically targeting the phosphorylation machinery. Inhibiting kinases like CDK1 or enhancing phosphatase activity to maintain Lamin A and EZH2 in their unphosphorylated, interaction-competent states may represent novel strategies to suppress EMT, maintain epithelial integrity, and restrict metastatic progression in aggressive breast cancer subtypes. These insights extend the role of nuclear architecture proteins from structural regulators to dynamic modulators of cell fate and malignant behavior, offering new avenues for clinical intervention.

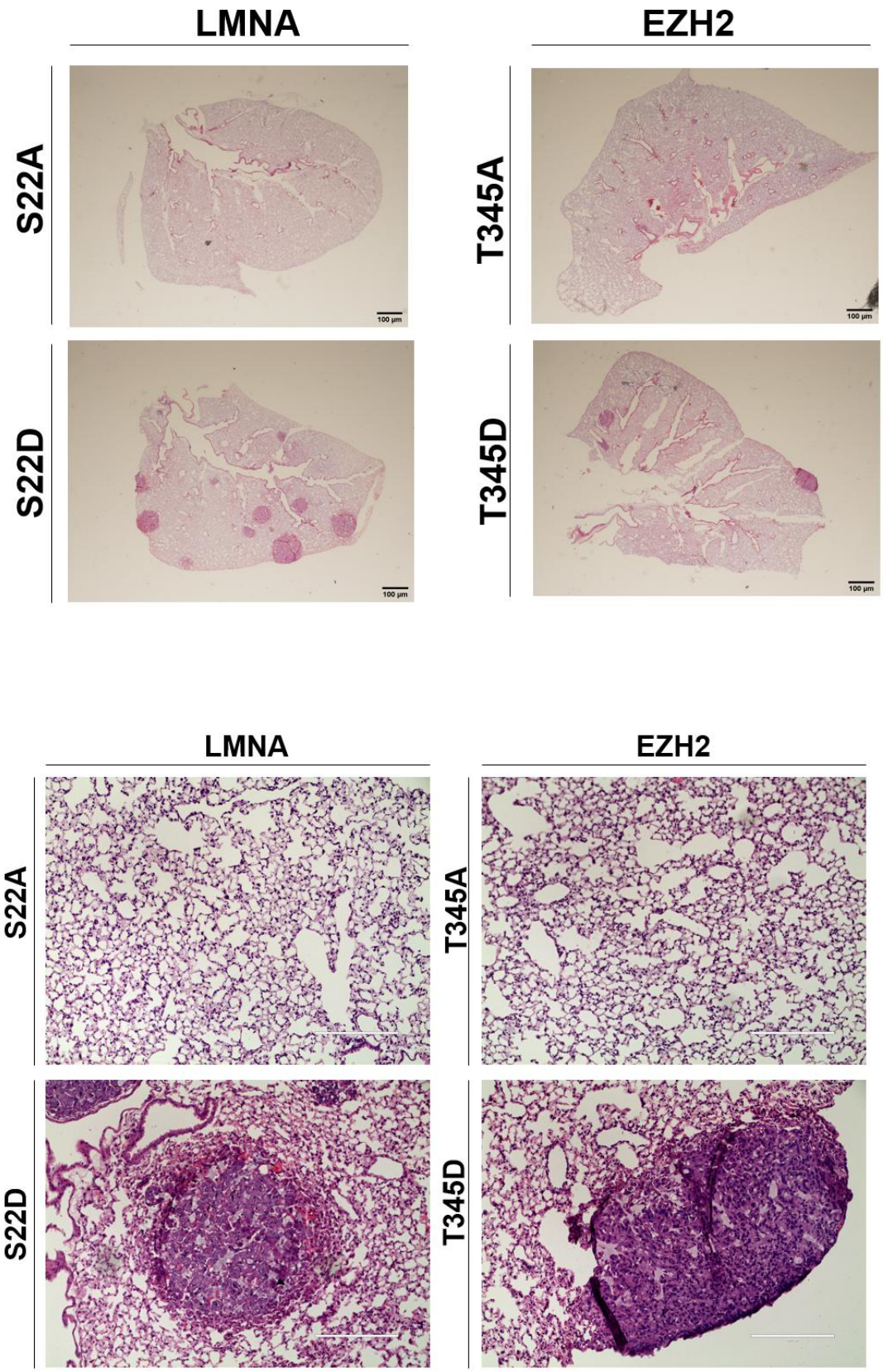


*Figure 5.12: Dependence on Lamin and EZH2 phosphorylation for breast to lung metastasis*

*(A) H&E staining of female NOD-SCID mice with MDA-MB-231 cells (Lamin A phospho-mutants) injected in the mammary fat pad and scored for metastatic nodules in the entire lung section ~6 weeks post injection (taken under 1x).*

*(B) H&E staining of female NOD-SCID mice with MDA-MB-231 cells (EZH2 phospho-mutants) injected in the mammary fat pad and scored for metastatic nodules in the entire lung section ~6 weeks post-injection (taken under 1x).*

*(C) H&E staining of female NOD-SCID mice with MDA-MB-231 cells (Lamin A phospho-mutants) injected in the mammary fat pad and the extent of tumour infiltration in the lung parenchyma (taken under 20x).*

*(D) H&E staining of female NOD-SCID mice with MDA-MB-231 cells (EZH2 phospho-mutants) injected in the mammary fat pad and the extent of tumour infiltration in the lung parenchyma (taken under 20x).*

### 5.2.9 Resistance to Cisplatin

Resistance to platinum-based chemotherapy remains a major clinical challenge in breast cancer, particularly in tumors exhibiting epithelial–mesenchymal plasticity and heightened epigenetic adaptability. Cisplatin exerts its cytotoxic effects primarily through the formation of DNA intra- and interstrand crosslinks, leading to replication stress, DNA damage response activation, and ultimately apoptosis. However, cancer cells frequently evade cisplatin-induced cell death through alterations in chromatin organization, DNA repair capacity, and transcriptional reprogramming (Galluzzi et al., 2012; Kelland, 2007).

Nuclear architecture proteins and epigenetic regulators have emerged as key modulators of therapy response. Lamin A/C, a core component of the nuclear lamina, plays a critical role in maintaining nuclear integrity, chromatin tethering, and genome stability. Alterations in Lamin A/C expression or post-translational modifications have been linked to cancer progression, altered mechanotransduction, and resistance to genotoxic stress (Swift et al., 2013; Bell and Lammerding, 2016). Similarly, EZH2, the catalytic subunit of the Polycomb Repressive Complex 2 (PRC2), mediates trimethylation of histone H3 at lysine 27 (H3K27me3) and is frequently overexpressed or hyperactivated in aggressive cancers, where it promotes transcriptional repression programs associated with stemness, EMT, and drug resistance (Kim and Roberts, 2016; McCabe et al., 2012).

Recent studies, including our own, indicate that phosphorylation of Lamin A/C at serine 22 and EZH2 at threonine 345—both CDK1-targeted residues—functionally alters their chromatin association and protein–protein interactions. Given the established link between epigenetic plasticity and chemoresistance, we investigated whether phosphorylation-mimicking versus phosphorylation-deficient forms of Lamin A/C and EZH2 differentially regulate cellular sensitivity to cisplatin.

To assess the impact of Lamin A/C and EZH2 phosphorylation on chemotherapeutic response, cells expressing phosphomimetic mutants Lamin A(S22D) or EZH2(T345D) were compared with cells expressing their corresponding phosphodeficient counterparts Lamin A(S22A) and EZH2(T345A). Cell viability following cisplatin treatment was quantified using standard metabolic viability assays across a range of drug concentrations.

Cells expressing the phosphomimetic Lamin A(S22D) mutant exhibited significantly higher viability upon cisplatin exposure compared with Lamin A(S22A)-expressing cells. This enhanced survival was evident across multiple cisplatin doses, indicating a robust shift in drug sensitivity rather than a dose-specific effect. Similarly, expression of EZH2(T345D) conferred a pronounced resistance to cisplatin-induced cytotoxicity relative to the EZH2(T345A) mutant, which showed markedly reduced viability under identical treatment conditions. Notably, cells harboring the phosphodeficient mutants displayed increased susceptibility to cisplatin, consistent with impaired adaptive stress responses (Figure 5.13A and B).

These findings suggest that phosphorylation at Lamin A serine 22 and EZH2 threonine 345 promotes a cellular state permissive to chemoresistance. Mechanistically, the phosphomimetic forms are associated with reduced Lamin A/C–EZH2 interaction, as shown earlier in this study, potentially facilitating redistribution of EZH2 away from lamina-associated heterochromatin toward more dynamic chromatin regions. Such redistribution may enable rapid transcriptional reprogramming and enhanced DNA damage tolerance. In line with this, EZH2 phosphorylation has been previously implicated in non-canonical, PRC2-independent functions, including regulation of DNA damage response genes and cell cycle progression (Cha et al., 2017).

Moreover, phosphorylation-dependent weakening of Lamin A/C–chromatin interactions may increase nuclear deformability and alter chromatin compaction, features that have been linked to resistance against DNA-damaging agents (Gonzalez-Sandoval et al., 2015). Together, these effects likely converge to enhance cellular survival following cisplatin treatment by modulating both epigenetic repression programs and nuclear structural constraints.

In summary, our data demonstrate that phosphomimetic forms of Lamin A(S22D) and EZH2(T345D) confer a clear survival advantage under cisplatin treatment compared with their phosphodeficient counterparts. These results identify phosphorylation of Lamin A/C and EZH2 as a critical regulatory node linking nuclear architecture, epigenetic plasticity, and chemotherapeutic response. Notably, the heightened cisplatin resistance observed in the phosphomimetic context supports a model in which CDK1-driven phosphorylation disrupts the Lamin A/C–EZH2 axis, enabling adaptive chromatin reorganization and transcriptional flexibility. This phosphorylation-dependent mechanism may contribute to therapy resistance in aggressive breast cancers and highlights potential opportunities for targeting cell cycle–epigenetic crosstalk to overcome chemoresistance.

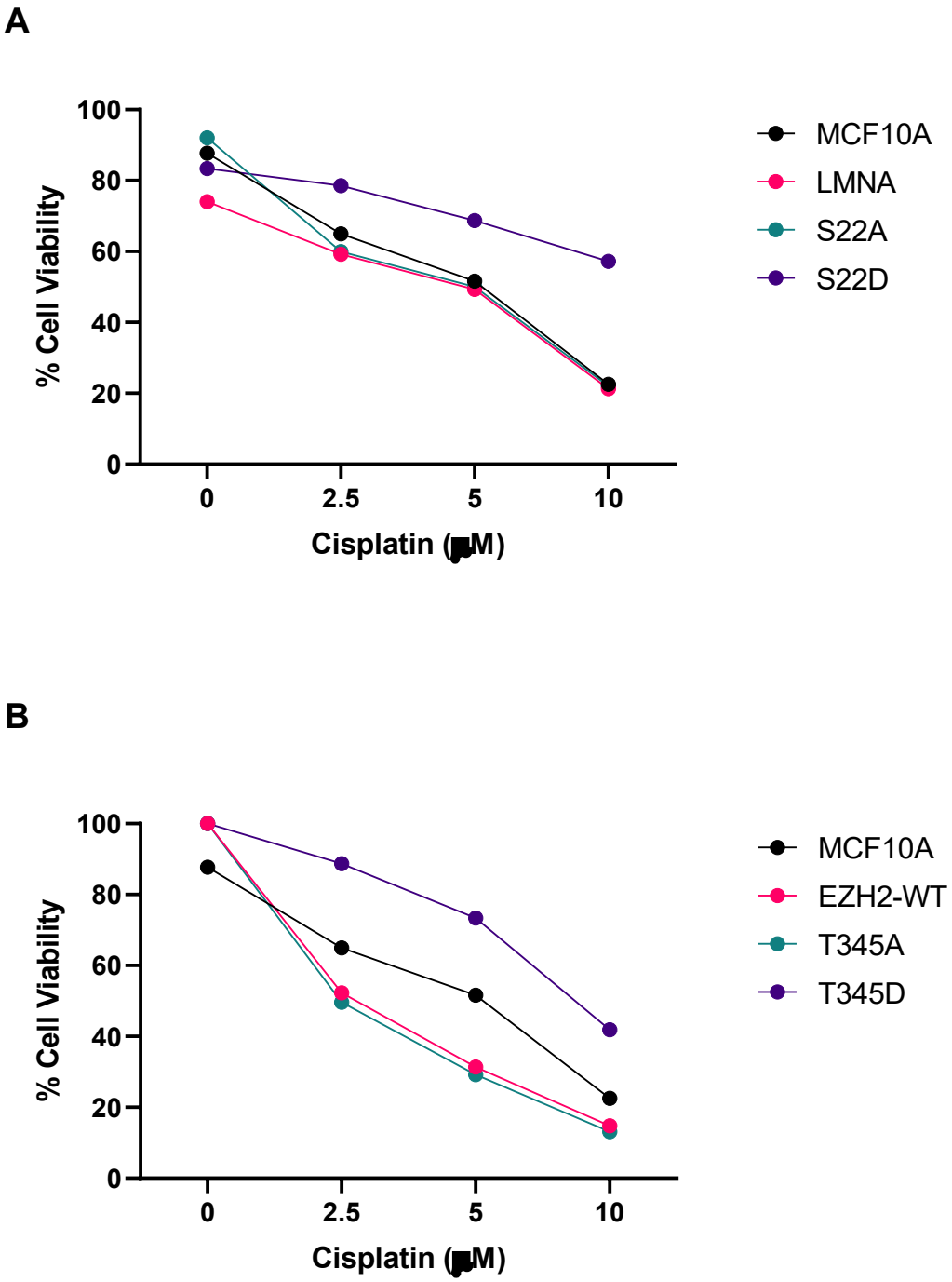


***Figure 5.13: Drug sensitivity assay for cisplatin in phosphomutants of MCF10A cells:*** *(A) %cell viability in MCF10A cells treated with various concentrations of cisplatin expressing phosphomutants of Lamin A (N=1); (B) %cell viability in MCF10A cells treated with various concentrations of cisplatin expressing phosphomutants of EZH2 (N=1)*

## 5.3 Discussion and Conclusion

The intricate balance between epithelial and mesenchymal states—commonly referred to as epithelial–mesenchymal plasticity (EMP)—is increasingly recognized as a central feature of cancer progression, particularly in aggressive and therapy-resistant breast cancer subtypes. This study identifies a pivotal, phosphorylation-sensitive regulatory module involving Lamin A/C and EZH2, which orchestrates chromatin remodeling, gene repression, and phenotypic transitions during EMT and MET. Through a combination of biochemical, cellular, and in vivo approaches, this work uncovers novel mechanistic insights into how Lamin A/C and EZH2 jointly suppress mesenchymal programs, and how their phosphorylation-dependent disruption contributes to tumor invasiveness and metastatic competence.

### 5.3.1 Lamin A/C–EZH2 Interaction as a Chromatin-Associated Repressor Module

One of the fundamental discoveries of this study is the identification of a direct and dynamic interaction between Lamin A/C and the histone methyltransferase EZH2, mediated through the head domain of Lamin A and the 301–500 amino acid region of EZH2. This interaction is tightly regulated by phosphorylation, particularly at S22 in Lamin A and T345 in EZH2—sites targeted by CDK1. The Lamin A/C–EZH2 complex associates with heterochromatic regions and appears to function as an epigenetic repressor of EMT-promoting transcription factors such as TWIST1, ZEB1, and SNAI1. This complex is preferentially stabilized in epithelial cells and reestablished during MET, suggesting that it plays a functional role in maintaining epithelial integrity.

### 5.3.2 Phosphorylation as a Molecular Switch Driving EMP

Phosphorylation at specific residues—S22 in Lamin A and T345 in EZH2—emerges as a critical regulatory mechanism that controls the assembly and disassembly of the Lamin A/C–EZH2 complex. Our data show that the phosphomimetic mutants (S22D and T345D), which mimic constitutive phosphorylation, abolish Lamin A/C–EZH2 interaction and promote mesenchymal characteristics in multiple in vitro and in vivo systems. Conversely, phosphodeficient mutants (S22A and T345A) maintain this interaction, repress mesenchymal markers, and stabilize epithelial identity even in the presence of strong EMT inducers such as TGF-β or TWIST1. These findings provide a compelling model in which phosphorylation acts as a reversible switch toggling chromatin accessibility and EMT/MET transitions.

### 5.3.3 Implications for Cell Migration, Invasion, and Hybrid E/M States

Functionally, disruption of the Lamin A/C–EZH2 axis through phosphorylation enhances cell migration and invasion. This is not only evident in traditional EMT contexts but also extends to TGF-β–driven migration in non-transformed epithelial cells such as MCF10A. Furthermore, our data reveal that phosphorylation-sensitive disruption of the Lamin A/C–EZH2 complex promotes the stabilization of hybrid epithelial/mesenchymal (E/M) states—transcriptionally and functionally distinct subpopulations that are now known to contribute to metastasis, tumor heterogeneity, and drug resistance.

Interestingly, while canonical EMT inducers promote a continuum of E/M states, the expression of phosphomimetic Lamin A or EZH2 traps cells in these intermediate states, preventing complete reversion to epithelial identity even under MET-inducing conditions. This suggests that phosphorylation of Lamin A/C and EZH2 not only activates mesenchymal gene expression but also blocks epigenetic remodeling needed for MET, thereby reinforcing a metastable, plastic phenotype.

### 5.3.4 In Vivo Relevance: Tumorigenicity and Metastatic Potential

In orthotopic xenograft models, phosphomimetic Lamin A and EZH2 variants resulted in significantly higher tumor volumes and more aggressive histopathological features compared to their phosphodeficient counterparts. Lung metastasis studies further confirmed that phosphorylation promotes systemic dissemination, with dense, pleomorphic metastatic lesions observed in animals injected with cells expressing the phosphomimetic forms. These in vivo findings strongly validate the concept that post-translational modifications of nuclear structural and chromatin-regulatory proteins serve as master regulators of cancer aggressiveness.

### 5.3.5 Translational Outlook

This study has uncovered a potential vulnerability in breast cancer progression—namely, the phosphorylation-sensitive disassembly of a chromatin-bound, tumor-suppressive complex. Inhibiting kinases such as CDK1 or boosting the activity of specific phosphatases to maintain Lamin A and EZH2 in their dephosphorylated, interaction-competent states may offer therapeutic benefit. Such strategies could stabilize epithelial phenotypes, prevent metastasis, and reduce intratumoral heterogeneity by eliminating hybrid E/M populations.

Furthermore, Lamin A and EZH2 phosphorylation status could serve as predictive biomarkers for EMT status and metastatic risk, providing clinical tools for disease stratification and therapy customization. Future research should explore the regulatory networks upstream of CDK1 in various breast cancer subtypes and identify pharmacological agents that can modulate this axis with specificity.

### 5.3.6 Conclusion

In summary, this chapter delineates a novel, phosphorylation-sensitive regulatory axis that governs epithelial–mesenchymal plasticity in breast cancer. The Lamin A/C–EZH2 complex acts as a repressor of mesenchymal gene expression, and its disruption through CDK1-mediated phosphorylation promotes EMT, invasion, hybrid E/M states, tumor growth, and metastasis. These findings extend the functional landscape of nuclear lamins and polycomb group proteins from structural and epigenetic regulators to central modulators of cancer plasticity and malignancy. Targeting the phosphorylation machinery associated with this axis opens up new avenues for anti-metastatic therapies and underscores the importance of nuclear architecture in cancer progression.

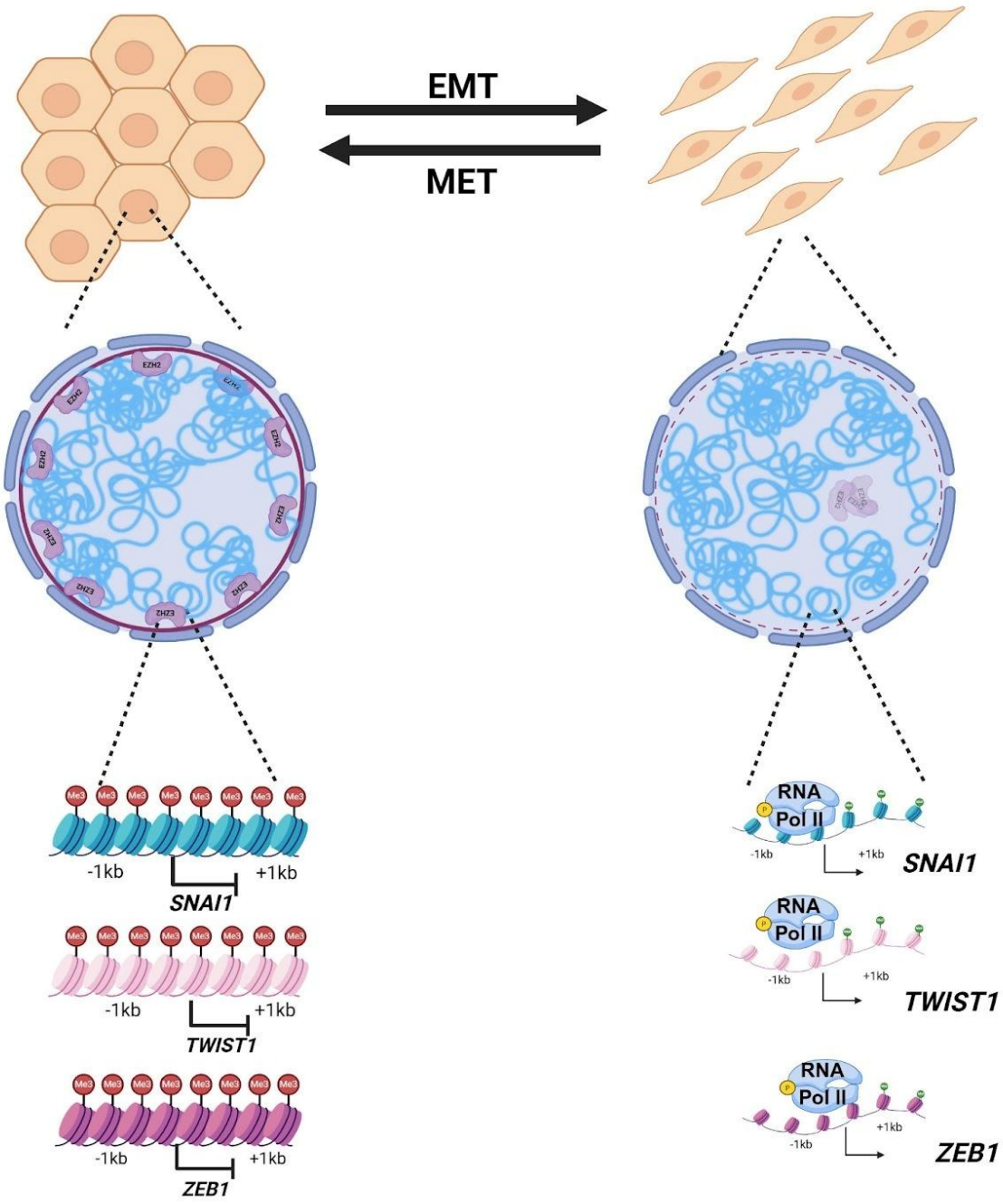
EMT
MET
EZH2
Me3
-1kb
+1kb
SNAI1
TWIST1
ZEB1
RNA
Pol II
P

# Chapter 6: Discussion and Future Outlook

## 6.1 Summary of Key Results

Cancer progression is not merely a function of uncontrolled proliferation, but a complex interplay of genetic, epigenetic, and post-translational modifications that dynamically regulate cellular states. In the context of breast cancer, epithelial-to-mesenchymal transition (EMT) and its reverse, mesenchymal-to-epithelial transition (MET), have emerged as central processes underpinning metastasis, therapy resistance, and cellular plasticity. This thesis delves into the molecular mechanisms regulating epithelial-mesenchymal plasticity (EMP) in breast cancer, with a focus on the nuclear lamina protein Lamin A/C and the Polycomb group protein EZH2, elucidating a novel phosphorylation-dependent axis that governs the transition between epithelial, mesenchymal, and hybrid cellular states.

In this study, we uncover a novel, phosphorylation-sensitive interaction between the inner nuclear envelope protein Lamin A/C and the histone methyltransferase EZH2, revealing its pivotal role in regulating epithelial–mesenchymal (EM) plasticity. Using a combination of models of epithelial-to-mesenchymal transition (EMT) and its reversal (MET), we show that Lamin A/C interacts with EZH2 in epithelial cells, establishing a repressive chromatin environment over the SNAI1, TWIST1, and ZEB1 loci, which encode key mesenchymal transcription factors (EMT-TFs). This interaction is disrupted upon EMT induction via CDK1-mediated phosphorylation of both Lamin A/C and EZH2, thereby facilitating the activation of EMT-TFs. Through gain- and loss-of-function studies using phosphomimetic and phosphodeficient variants of Lamin A (S22D/S22A) and EZH2 (T345D/T345A), we define the critical regulatory role of phosphorylation in modulating EMT. In vivo, phosphomimetic forms of these proteins significantly promote tumor growth and mesenchymal traits, while phosphodeficient forms maintain epithelial characteristics, resulting in an approximately five-fold reduction in tumor volume. These findings position the Lamin A–EZH2 complex as a crucial epigenetic checkpoint regulated by phosphorylation during cancer progression.

## 6.2 Rewiring the Lamin A Interactome During EMT and MET

Proteomic analyses further demonstrate a remodeling of the Lamin A interactome in response to EMT and MET. In epithelial states, Lamin A/C preferentially binds chromatin repressors (EZH2, EHMT2), RNA splicing regulators (NUDT21, CPSF6), and chromatin compaction proteins (LIMA1). During EMT, these associations shift toward cell cycle regulators (pCDK1,

CCNB1), implying a switch from transcriptional repression to proliferative signaling. These dynamic interaction profiles position Lamin A as a sensor that toggles between genome stability and proliferation in a phosphorylation-dependent manner (Celeste et al., 2002).

Importantly, these interactions are specific to Lamin A/C and not recapitulated by B-type lamins, which instead interact with alternate methyltransferases (e.g., G9a, SUV39H1) in a phosphorylation-independent fashion. This underscores the unique regulatory capacity of Lamin A/C in modulating EMP (Sciacovelli and Frezza, 2017).

### 6.3 Rewiring Chromatin Repression through the Lamin A/C–EZH2 Complex

Historically regarded as a static structural component of the nucleus, Lamin A/C has gained attention as a dynamic modulator of gene expression, nuclear mechanics, and lineage commitment. This thesis provides compelling evidence that Lamin A/C functions beyond its architectural role, anchoring epigenetic regulators at the nuclear periphery to repress lineage-inappropriate transcriptional programs (Goldman et al., 2002). The direct interaction between Lamin A/C and EZH2 enables the spatial sequestration and recruitment of PRC2 to repressive domains, promoting chromatin compaction and epithelial stability.

A central finding of this work is the identification of a previously uncharacterized interaction between Lamin A/C and EZH2 that functions as a chromatin-associated repressive complex. This interaction is anchored by specific residues within the head domain of Lamin A (Arg25, Arg28) and the central domain of EZH2 (amino acids 301–500), validated by both in silico docking and co-immunoprecipitation experiments. Functionally, this interaction is essential for repressing mesenchymal genes, preserving epithelial identity, and facilitating MET (Lukášová et al., 2017).

Importantly, this complex is sensitive to CDK1-mediated phosphorylation at conserved sites—S22 in Lamin A and T345 in EZH2. Phosphorylation at these sites disrupts their interaction and triggers a cascade of transcriptional and phenotypic changes that favor EMT. This post-translational modification represents a key molecular switch, integrating cell cycle progression and chromatin state to coordinate cellular plasticity (Mitra et al., 2005).

During EMT, phosphorylation of Lamin A/C and EZH2 disrupts this repressive complex. Phosphomimetic variants of Lamin A (S22D) and EZH2 (T345D) not only impair Lamin A/C–EZH2 binding but also trigger chromatin relaxation, enhanced EMT-TF expression, and

mesenchymal phenotypes. Conversely, phosphodeficient forms preserve repressive chromatin landscapes and suppress mesenchymal transition even under pro-EMT stimuli such as TGF-β and TWIST1. This demonstrates that phosphorylation operates as a molecular gatekeeper for epigenetic plasticity and state transitions.


**Figure 6.1:** *Heatmap illustrating co-relation of extent of Lamin A/C expression with CDH1 (E-cadherin), TWIST1, SNAI1 and ZEB1 expression across various cancers*

### 6.4 Phosphorylation-Dependent Modulation of EMP

One of the most significant contributions of this study lies in demonstrating how phosphorylation regulates EMP in a context-dependent manner. Using phosphomimetic and phosphodeficient mutants of Lamin A and EZH2, it was shown that phosphorylation abrogates their interaction, promoting mesenchymal traits, while dephosphorylated forms restore epithelial features and suppress EMT. These findings were consistent across multiple models, including MCF7, MCF10A, and MDA-MB-231 cell lines, and corroborated by in vivo tumor xenograft studies.

This work also provides mechanistic insight into how EMT is modulated not just by transcription factors but also by nuclear structure and chromatin dynamics. It shifts the focus from classical signaling pathways to epigenetic and nuclear architectural regulators, offering a new lens through which to understand tumor plasticity.

Epithelial-to-mesenchymal transition (EMT) and its reverse, mesenchymal-to-epithelial transition (MET), are tightly regulated, reversible processes that orchestrate cellular transitions

during development, wound healing, and disease. In cancer, the plasticity of EMT/MET enables tumor cells to dynamically acquire phenotypic features that facilitate invasion, survival, and metastatic colonization. This thesis identifies and characterizes a novel epigenetic regulatory axis governed by the inner nuclear envelope protein Lamin A/C and the chromatin modifier EZH2, which acts as a phosphorylation-sensitive molecular switch for epithelial–mesenchymal plasticity (EMP) in breast cancer.

Through an integrated set of biochemical, transcriptomic, epigenomic, and in vivo approaches, this work reveals that Lamin A/C physically interacts with EZH2 in epithelial cells, forming a nuclear lamina-associated repressive complex that silences EMT transcription factors (SNAI1, TWIST1, ZEB1) via deposition of the heterochromatic mark H3K27me3. This interaction is shown to be phosphorylation-sensitive—specifically modulated by CDK1-mediated phosphorylation at S22 of Lamin A and T345 of EZH2. Loss of interaction via phosphorylation destabilizes the chromatin-bound EZH2 complex, leading to transcriptional de-repression of mesenchymal programs. This post-translational regulation creates a mechanistically compelling model that links cell cycle progression with nuclear structure, chromatin state, and transcriptional plasticity.

### 6.5 Functional Consequences on Migration, Invasion, and Tumorigenicity

Beyond the molecular interactions, the Lamin A/C–EZH2 axis was shown to have profound functional consequences on cell behavior. Disruption of this complex through phosphorylation enhanced cell invasion, migration, and anchorage-independent growth. These phenotypes were not merely in vitro artifacts but translated into significant increases in tumor size and metastatic burden in orthotopic mouse models.

Furthermore, CDK1 activity and its effect on Lamin A and EZH2 were found to promote the accumulation of hybrid epithelial/mesenchymal (E/M) states—transcriptionally distinct subpopulations with high metastatic and stem-like potential. These findings support a model wherein phosphorylation acts not only as a molecular off-switch for chromatin repression but also as a selector of intermediate phenotypic states that are functionally poised for metastasis.

### 6.6 Tumor Growth and Metastasis: Phosphorylation Drives Malignancy

In vivo xenograft experiments validate the role of Lamin A/C–EZH2 phosphorylation in tumor progression. Phosphomimetic mutants exhibit larger tumor volumes, increased invasiveness,

and elevated metastatic burden, while phosphodeficient forms suppress tumorigenicity and restore epithelial features. Histopathological analysis of lung metastases reveals extensive dissemination, nuclear pleomorphism, and hyperchromasia in phosphomimetic groups—hallmarks of high-grade malignancy.

This confirms that post-translational disruption of Lamin A–EZH2 interaction is not merely a cellular phenotype but a driver of systemic cancer progression. The phosphorylation-dependent axis thus serves as a critical regulatory node linking nuclear architecture, chromatin remodeling, and metastatic competence.

### 6.7 EMP and the Hybrid State: A Selectable Metastatic Intermediate

Another novel insight provided by this work is the identification of the hybrid E/M state as a selectable and regulated phenotype, rather than a passive transition. Overexpression of phosphomimetic Lamin A or EZH2 stabilized the CD104+CD44+ population—a hallmark of hybrid identity. Even under pro-MET conditions induced by GRHL2, these phosphomimetic variants resisted reversion to a fully epithelial phenotype, highlighting the dominant influence of Lamin A/C–EZH2 phosphorylation status in maintaining plasticity (Kröger et al., 2019).

This has substantial implications for metastasis and therapy resistance. Hybrid states have been linked to enhanced survival under stress, immune evasion, and chemoresistance. By revealing a regulatory mechanism that maintains or resolves hybrid identity, this thesis provides a potential therapeutic target for intercepting plasticity-driven tumor evolution (Johnstone et al., 2020).

### 6.8 Hybrid E/M States: Lamin A/C–EZH2 Axis as a Regulator of Phenotypic Stability

The hybrid epithelial/mesenchymal (E/M) state has emerged as a functionally distinct, metastable phenotype that confers adaptive advantages such as collective migration, stemness, and drug tolerance. This work uncovers that the Lamin A/C–EZH2 complex regulates not only the binary EMT/MET switch but also the maintenance or resolution of hybrid states. In the absence of Lamin A–EZH2 interaction (via phosphorylation or knockdown), cells accumulate in a CD104+CD44+ hybrid state, which is poorly responsive to MET-inducing signals. This is particularly evident in GRHL2-mediated MET, where phosphomimetic mutants fail to drive complete epithelial transition (Heaphy et al., 2011).

This finding challenges the notion of hybrid states as passive intermediates and positions them as actively regulated, selectable configurations governed by chromatin modifiers and nuclear lamina dynamics. The interplay between CDK1 activity, Lamin A/C–EZH2 interaction, and EMT-TF expression thus defines an axis that balances cellular plasticity and commitment.

### 6.9 Intrinsic Heterogeneity in EMT and MET Model Systems

Epithelial–mesenchymal plasticity (EMP) encompasses a spectrum of phenotypic states between the epithelial and mesenchymal poles, often giving rise to heterogeneous cell populations with varying degrees of marker expression and functional attributes. To investigate this phenomenon, we employed three widely used human breast cell models representing distinct positions along the epithelial–mesenchymal spectrum: MCF7, MCF10A, and MDA-MB-231, and induced EMT or MET through different stimuli—TWIST1 overexpression in MCF7, TGF-β treatment in MCF10A, and restoration of MET in mesenchymal MDA-MB-231 cells. Across these systems, we observed substantial intra-population heterogeneity in the expression of canonical epithelial (E-Cadherin) and mesenchymal (Vimentin) markers, as well as in surface marker profiles based on CD104 (β4-integrin) and CD44.

### 6.10 Baseline Heterogeneity in Untreated States

At baseline, MCF7 cells exhibited a predominantly epithelial phenotype, with uniform E-Cadherin membrane localization and negligible Vimentin expression, consistent with their luminal epithelial origin. However, immunofluorescence and immunoblotting revealed a small subset of cells with reduced E-Cadherin and faint cytoplasmic Vimentin, suggestive of a pre-existing hybrid or primed state. This subtle heterogeneity was further reflected in flow cytometry, where **CD104** expression showed a unimodal but broad distribution, and **CD44** expression, while generally low, showed a tail of intermediate-expressing cells (Lu and Kang, 2019). Hybrid E/M cells exhibit intermediate activation of Snai1/Zeb1/Twist1 (2-5x E baseline, 30-70% M levels), enabling coexistence of epithelial/mesenchymal markers through partial Lamin A/C–EZH2 disruption and miR-200/Zeb1 oscillation.

In contrast, MCF10A cells—although non-tumorigenic and often classified as epithelial—demonstrated more evident heterogeneity in both marker expression and surface phenotype. Immunostaining revealed a mosaic pattern of E-Cadherin, with some cells showing strong junctional localization and others displaying cytoplasmic or patchy membrane staining. Vimentin was detectable at low levels in a significant fraction of cells even under basal

conditions, indicative of their basal-like plasticity. FACS analysis confirmed a bimodal distribution of CD104, and a continuum of CD44 expression, supporting their intermediate or poised EMP status.

MDA-MB-231 cells, by contrast, displayed hallmarks of a fully mesenchymal phenotype with high, uniform expression of Vimentin and loss of E-Cadherin. However, both protein and transcript analysis identified rare cell subsets expressing low but detectable levels of E-Cadherin, suggesting potential for MET under appropriate cues. CD104 was nearly absent across the population, whereas CD44 levels were uniformly high, consistent with a mesenchymal and stem-like phenotype. Nonetheless, a minor fraction of CD44^low cells was consistently observed, indicating residual phenotypic variability.

### 6.11 Induced Heterogeneity Upon EMT and MET

Upon TWIST1-induced EMT in MCF7 cells, we observed a graded loss of E-Cadherin and concomitant induction of Vimentin. Notably, this transition was not binary; instead, the population split into multiple intermediate states. Immunofluorescence revealed the coexistence of cells with retained E-Cadherin but cytoplasmic Vimentin, alongside cells with complete E-Cadherin loss and high Vimentin expression. FACS analysis mirrored this with a substantial increase in CD44^high/CD104^low cells, but also revealed CD44^int/CD104^int populations that may represent partial or hybrid EMT states. These observations emphasize that TWIST1 does not enforce a uniform EMT program but instead promotes a spectrum of epithelial-to-mesenchymal transition states.

Similarly, TGF-β–induced EMT in MCF10A cells amplified pre-existing heterogeneity. While a significant fraction of cells lost E-Cadherin and gained Vimentin, a substantial subpopulation retained partial epithelial characteristics, showing E-Cadherin-Vimentin co-expression. This was paralleled by the emergence of a CD44^high/CD104^low population, though a CD44 /CD104 subset persisted, further supporting a continuum of EMT states rather than a terminal mesenchymal conversion. These results align with recent studies demonstrating that TGF-β signaling can promote stable intermediate EMT phenotypes rather than a complete transition.

In MDA-MB-231 cells subjected to MET-inducing conditions, a gradual gain of epithelial features was observed in a subset of cells. Specifically, re-expression of E-Cadherin was evident in small clusters, accompanied by a moderate reduction in Vimentin expression. These cells frequently re-expressed CD104 and exhibited reduced CD44 levels, giving rise to a

$CD104^{+}/CD44^{low}$ population that had been virtually absent at baseline. Importantly, this population remained minor, underscoring the inefficiency and heterogeneity of MET induction in this aggressive mesenchymal background.

### 6.12 Implications of Heterogeneity in EMP Models

These findings collectively reveal that EMP, whether spontaneous or induced, is rarely uniform across a cell population. Instead, EMT and MET transitions are marked by intrinsic cellular heterogeneity, reflected both in classical epithelial/mesenchymal markers and in cell surface marker expression. The presence of hybrid E/M states—cells that co-express E-Cadherin and Vimentin, or cells with intermediate CD44 and CD104 levels—suggests plasticity and the ability to transition between phenotypes reversibly. This has profound implications for interpreting functional assays, drug response, and in vivo behavior, as subpopulations may differentially contribute to invasion, stemness, and metastasis.

The observed FACS profiles support a continuum model of EMP, rather than discrete states. Importantly, CD104 and CD44 serve as effective surrogate markers for tracking these transitions, and their co-expression patterns can help resolve mixed populations where canonical markers like E-Cadherin and Vimentin alone are insufficient. In particular, CD44^int/CD104^int populations may represent metastable or plastic states, highly relevant for studying epigenetic and transcriptional regulation of EMT/MET.

In summary, our model systems capture diverse trajectories and outcomes of EMT/MET, and the cellular heterogeneity uncovered here underlines the need for high-resolution analysis in EMP research. Understanding and harnessing this heterogeneity may be key to targeting phenotypically plastic cancer cell subsets that escape conventional therapies.

### 6.13 Lamin A/C and EZH2 as Integrators of Nuclear Structure and Transcriptional Repression

This work extends the role of Lamin A/C from a structural scaffold to a dynamic regulator of transcription and chromatin state. Similarly, EZH2 is redefined here not just as a histone methyltransferase but as a phosphorylation-sensitive component of a nuclear repressor complex that interacts with nuclear lamina architecture. Together, these findings expand the functional repertoire of nuclear envelope proteins and Polycomb group proteins in cancer biology.

Moreover, the study emphasizes the dual regulation of Lamin A/C and EZH2 through cell cycle machinery—particularly CDK1—highlighting the intersection of mitotic signaling and long-term transcriptional reprogramming. This positions Lamin A/C and EZH2 as nodes in a regulatory network that senses proliferative signals and modulates chromatin architecture accordingly, influencing cell fate decisions in both development and disease.

### 6.14 Translational Implications: Targeting the Lamin A–EZH2–CDK1 Axis

The findings presented here offer new avenues for diagnostic and therapeutic interventions. Phosphorylated forms of Lamin A (S22) and EZH2 (T345) emerge as potential biomarkers of EMT status and metastatic capacity. Analysis of clinical proteomic datasets (e.g., CPTAC) supports these findings, revealing increased pLMNA(S22) and pEZH2(T345) levels in tumor tissues across breast cancer stages.

Functionally, restoring Lamin A–EZH2 interaction—either through CDK1 inhibition, proteasomal stabilization, or phosphatase modulation—may reinforce epithelial identity and suppress metastasis. However, therapeutic strategies involving global EZH2 inhibition must be approached cautiously, as disrupting Lamin A–EZH2-mediated repression may inadvertently promote EMP in some contexts. Stratified approaches targeting upstream kinase activity or selectively stabilizing Lamin A/C–EZH2 complexes may offer a more precise means of reprogramming tumor cell identity.

**A**

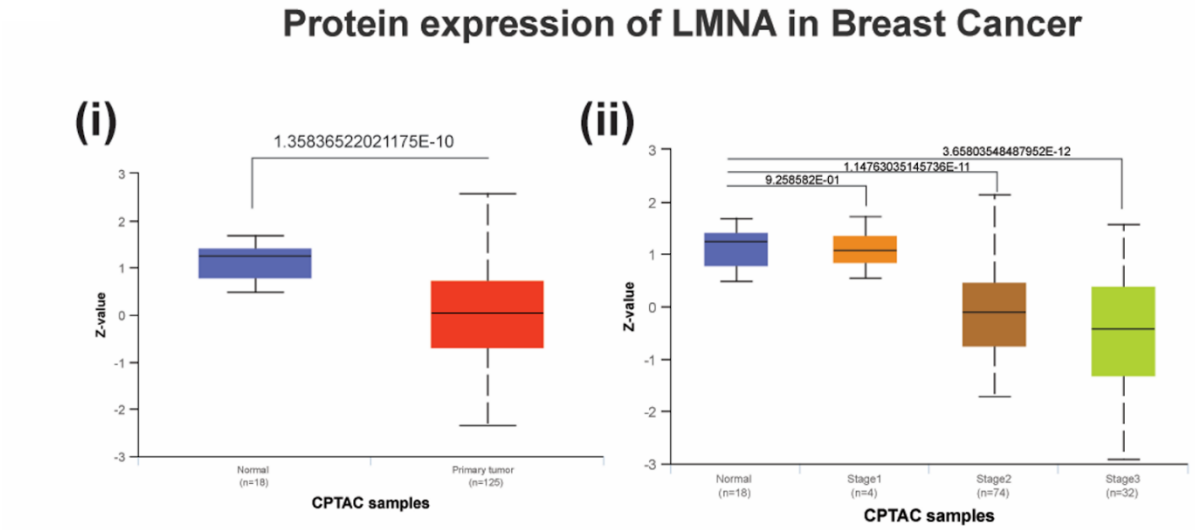

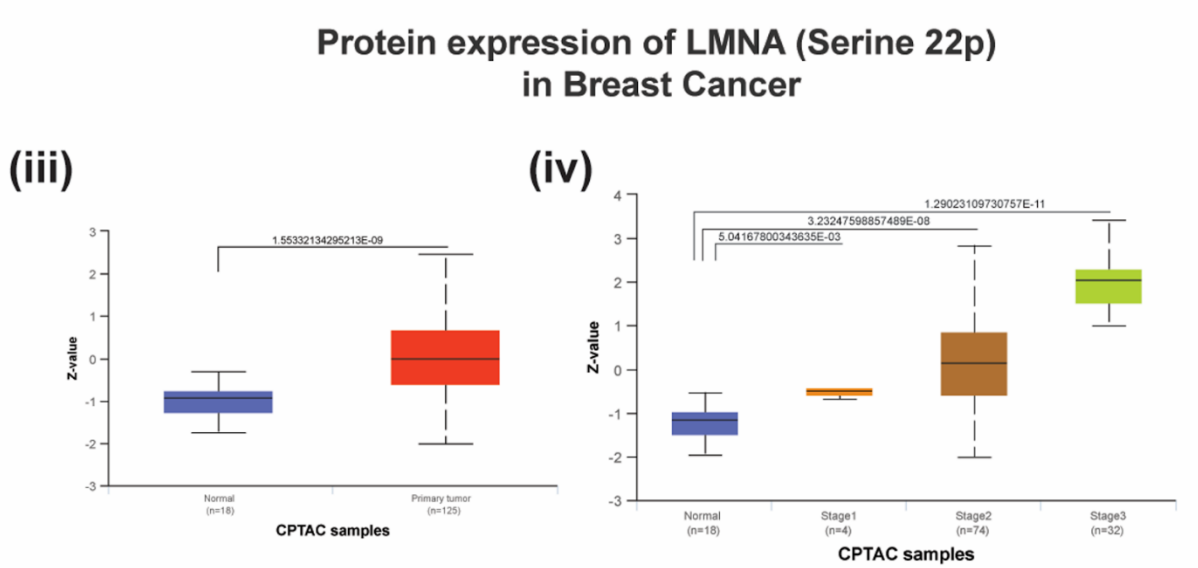
Protein expression of LMNA (Serine 22p)
in Breast Cancer
(iii)
1.55332134295213E-09
Z-value
Normal (n=18)
Primary tumor (n=125)
CPTAC samples
(iv)
1.29023109730757E-11
3.23247598857489E-08
5.04167800343635E-03
Z-value
Normal (n=18)
Stage1 (n=4)
Stage2 (n=74)
Stage3 (n=32)
CPTAC samples

B

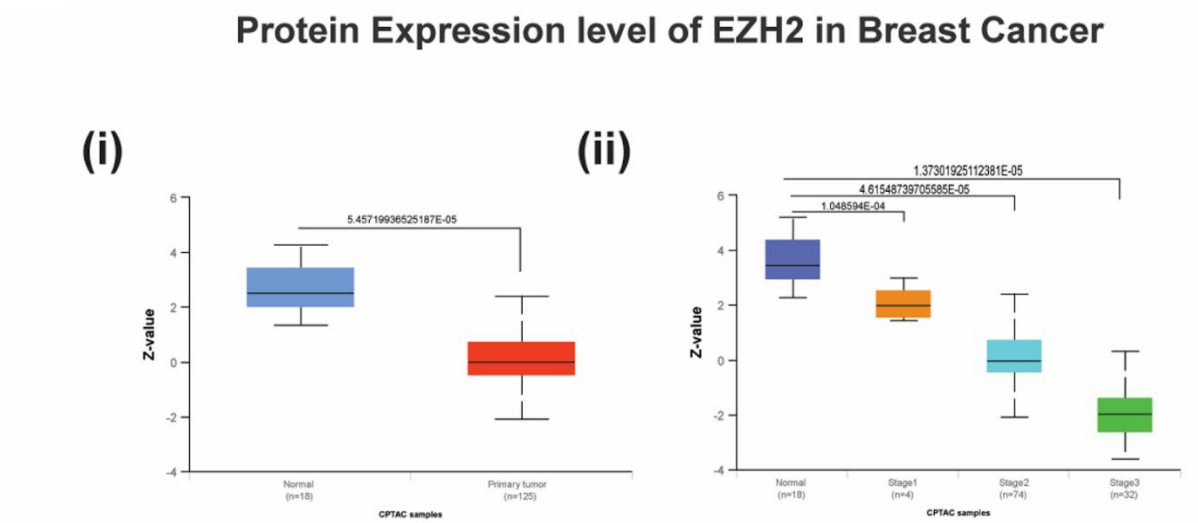
Protein Expression level of EZH2 in Breast Cancer
(i)
5.45719936525187E-05
Z-value
Normal (n=18)
Primary tumor (n=125)
CPTAC samples
(ii)
1.37301925112381E-05
4.61548739705585E-05
1.048594E-04
Z-value
Normal (n=18)
Stage1 (n=4)
Stage2 (n=74)
Stage3 (n=32)
CPTAC samples

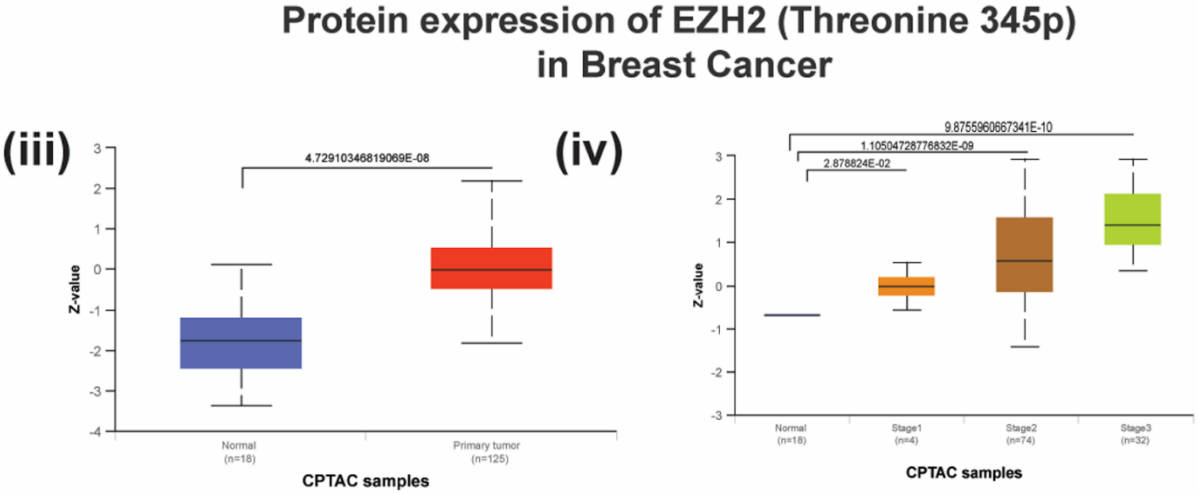
Protein expression of EZH2 (Threonine 345p)
in Breast Cancer
(iii)
4.72910346819069E-08
Z-value
Normal (n=18)
Primary tumor (n=125)
CPTAC samples
(iv)
9.87559606673412E-10
1.10504728776832E-09
2.878824E-02
Z-value
Normal (n=18)
Stage1 (n=4)
Stage2 (n=74)
Stage3 (n=32)
CPTAC samples

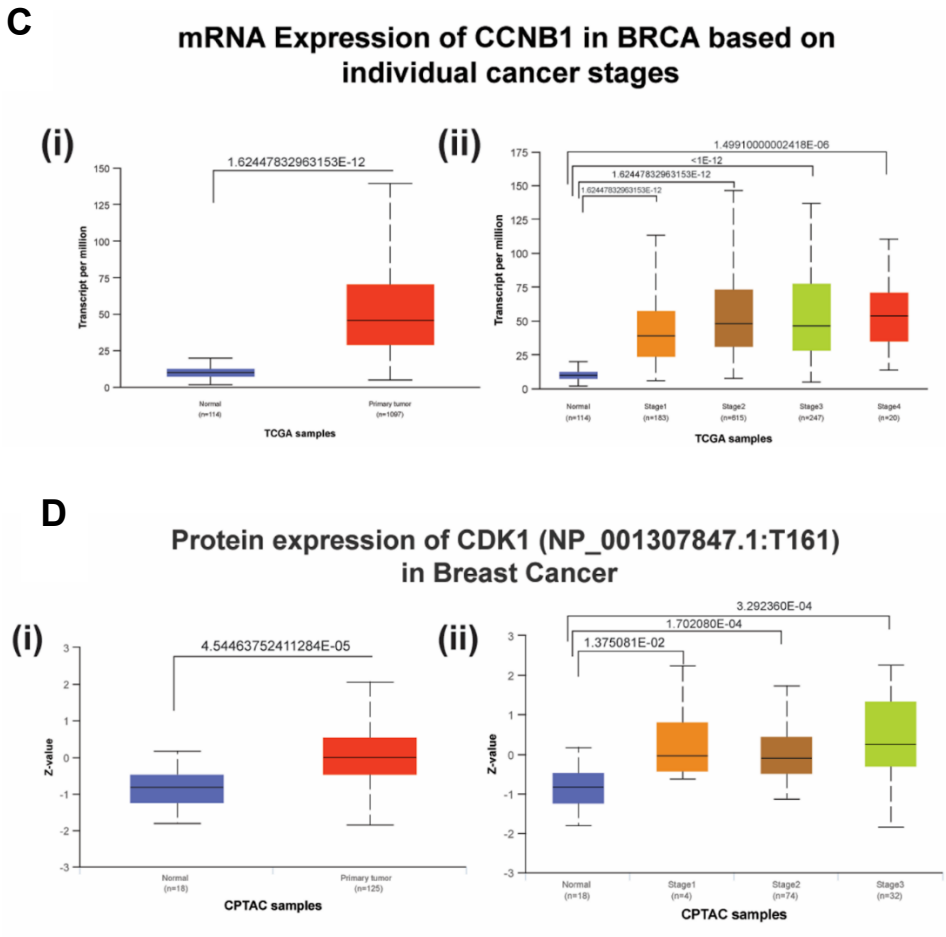


***Figure 6.2: Proteomic, transcriptomic, and co-immunoprecipitation analysis of Lamin A/C, EZH2, CCNB1, and CDK1 in normal and tumor conditions.***

***(A)*** *Clinical Proteomic Tumor Analysis Consortium (CPTAC)-based proteomic analysis of total Lamin A/C expression in normal and tumor tissues* ***(i)*** *and its stratification across tumor stages (Stage I–III)* ***(ii)****. Analysis of phosphorylated Lamin A/C (Ser22) levels in normal versus tumor tissues* ***(iii)*** *and across tumor stages* ***(iv)****.* ***(B)*** *Comparative analysis of total EZH2 protein expression in normal versus tumor tissues* ***(i)*** *and its stage-specific distribution (Stage I–III)* ***(ii)****. Quantification of phosphorylated EZH2 (Thr345) in normal and tumor tissues* ***(iii)*** *and across tumor stages* ***(iv)****.* ***(C)*** *TCGA-based differential expression analysis of CCNB1 mRNA in normal versus tumor tissues* ***(i)*** *and across tumor stages (Stage I-IV)* ***(ii)****.* ***(D)*** *CPTAC-based proteomic analysis of phosphorylated CDK1 (Thr161) in normal versus tumor tissues* ***(i)*** *and across tumor stages (Stage I–III)* ***(ii)****.*

## 6.15 Conclusion and Future Perspectives

This thesis establishes a phosphorylation-sensitive Lamin A/C–EZH2 complex as a novel epigenetic module that governs epithelial–mesenchymal plasticity in breast cancer. By modulating chromatin accessibility at EMT-TF loci, this complex orchestrates phenotypic transitions, cellular invasiveness, and metastatic spread. Phosphorylation by CDK1 disrupts this complex, promoting mesenchymal traits, hybrid states, and tumor progression.

The body of work presented in this thesis uncovers a critical phosphorylation-sensitive axis involving Lamin A/C and EZH2 that governs epithelial-mesenchymal plasticity in breast cancer. This axis acts as a repressive checkpoint that must be overcome for EMT to proceed. Its disruption via phosphorylation facilitates mesenchymal gene expression, hybrid state stabilization, and ultimately promotes tumor progression and metastasis.

These findings lay the groundwork for several promising research directions:

1. **Therapeutic Targeting of the Phosphorylation Machinery**: CDK1 emerges as a candidate kinase whose activity modulates EMP via Lamin A and EZH2 phosphorylation. Inhibitors targeting CDK1 or strategies that enhance phosphatase activity may help stabilize the epithelial state and curb metastasis.
2. **Biomarker Development**: Phosphorylation status of Lamin A and EZH2 could serve as a prognostic marker for EMP, tumor aggressiveness, or response to therapy. Future work should validate these markers in clinical breast cancer samples.
3. **Hybrid E/M State as a Therapeutic Vulnerability**: Given its role in metastasis and resistance, targeting the hybrid state directly—by enforcing Lamin A/C–EZH2 interaction or repressing mesenchymal genes—may be a viable strategy to limit tumor plasticity.
4. **Role in Other Cancers and Systems**: While this thesis focuses on breast cancer, the Lamin A/C–EZH2 axis may function similarly in other epithelial cancers. Comparative studies in additional models could broaden the applicability of these findings.
5. **Nuclear Mechanics and Chromatin Architecture**: Given Lamin A's role in nuclear stiffness and chromatin organization, further studies could integrate mechanical and epigenetic perspectives to understand better how cellular microenvironments influence EMP.

6. **Phosphatase Identification:** Identifying phosphatases that reverse Lamin A and EZH2 phosphorylation could reveal novel drug targets and regulators of EMP reversibility.
7. **Temporal Dynamics and Therapy Resistance:** Longitudinal tracking of Lamin A–EZH2 phosphorylation status during chemotherapy could clarify its role in therapy-induced plasticity and resistance.
8. **Organoid and Patient-Derived Models:** Incorporating 3D organoid systems and patient-derived xenografts will enhance translational relevance and validate therapeutic strategies targeting this axis.

In summary, this work highlights a previously unrecognized axis of nuclear epigenetic control in breast cancer plasticity and metastasis. Targeting the phosphorylation status of Lamin A and EZH2 or their regulatory kinases may offer a potent strategy to constrain tumor heterogeneity, suppress metastatic dissemination, and enhance therapeutic response in aggressive breast cancers.

## References


Aebi, U., Cohn, J., Buhle, L., Gerace, L., 1986. The nuclear lamina is a meshwork of intermediate-type filaments. Nature 323, 560–564. https://doi.org/10.1038/323560a0

Aiello, N.M., Kang, Y., 2019. Context-dependent EMT programs in cancer metastasis. J. Exp. Med. 216, 1016–1026. https://doi.org/10.1084/jem.20181827

Aird, K.M., Zhang, R., 2013. Detection of senescence-associated heterochromatin foci (SAHF). Methods Mol. Biol. 965, 185–196. https://doi.org/10.1007/978-1-62703-239-1_12

Almeida, M., Pintacuda, G., Masui, O., Koseki, Y., Gdula, M., Cerase, A., Brown, D., Mould, A., Innocent, C., Nakayama, M., Schermelleh, L., Nesterova, T.B., Koseki, H., Brockdorff, N., 2017. PCGF3/5-PRC1 initiates Polycomb recruitment in X chromosome inactivation. Science 356, 1081–1084. https://doi.org/10.1126/science.aal2512

Andronov, L., Ouararhni, K., Stoll, I., Klaholz, B.P., Hamiche, A., 2019. CENP-A nucleosome clusters form rosette-like structures around HJURP during G1. Nat. Commun. 10, 4436. https://doi.org/10.1038/s41467-019-12383-3

Ano Bom, A.P.D., Rangel, L.P., Costa, D.C.F., de Oliveira, G.A.P., Sanches, D., Braga, C.A., Gava, L.M., Ramos, C.H.I., Cepeda, A.O.T., Stumbo, A.C., De Moura Gallo, C.V., Cordeiro, Y., Silva, J.L., 2012. Mutant p53 aggregates into prion-like amyloid oligomers and fibrils: implications for cancer. J. Biol. Chem. 287, 28152–28162. https://doi.org/10.1074/jbc.M112.340638

Antony, J., Gimenez, G., Taylor, T., Khatoon, U., Day, R., Morison, I.M., Horsfield, J.A., 2020. BET inhibition prevents aberrant RUNX1 and ERG transcription in STAG2 mutant leukaemia cells. J. Mol. Cell Biol. 12, 397–399. https://doi.org/10.1093/jmcb/mjz114

Barnhart, M.C., Kuich, P.H.J.L., Stellfox, M.E., Ward, J.A., Bassett, E.A., Black, B.E., Foltz, D.R., 2011. HJURP is a CENP-A chromatin assembly factor sufficient to form a functional de novo kinetochore. J. Cell Biol. 194, 229–243. https://doi.org/10.1083/jcb.201012017

Baugh, E.H., Ke, H., Levine, A.J., Bonneau, R.A., Chan, C.S., 2018. Why are there hotspot mutations in the TP53 gene in human cancers? Cell Death Differ. 25, 154–160. https://doi.org/10.1038/cdd.2017.180

Bian, Q., Khanna, N., Alvikas, J., Belmont, A.S., 2013. \beta-Globin cis-elements determine differential nuclear targeting through epigenetic modifications. J. Cell Biol. 203, 767–783. https://doi.org/10.1083/jcb.201305027

Bjerke, L., Mackay, A., Nandhabalan, M., Burford, A., Jury, A., Popov, S., Bax, D.A., Carvalho, D., Taylor, K.R., Vinci, M., Bajrami, I., McGonnell, I.M., Lord, C.J., Reis, R.M., Hargrave, D., Ashworth, A., Workman, P., Jones, C., 2013. Histone H3.3. mutations drive pediatric glioblastoma through upregulation of MYCN. Cancer Discov. 3, 512–519. https://doi.org/10.1158/2159-8290.CD-12-0426

Bohl, C.R., Harihar, S., Denning, W.L., Sharma, R., Welch, D.R., 2014. Metastasis suppressors in breast cancers: mechanistic insights and clinical potential. J. Mol. Med. 92, 13–30. https://doi.org/10.1007/s00109-013-1109-y

Boija, A., Klein, I.A., Sabari, B.R., Dall'Agnese, A., Coffey, E.L., Zamudio, A.V., Li, C.H., Shrinivas, K., Manteiga, J.C., Hannett, N.M., Abraham, B.J., Afeyan, L.K., Guo, Y.E., Rimel, J.K., Fant, C.B., Schuijers, J., Lee, T.I., Taatjes, D.J., Young, R.A., 2018. Transcription Factors Activate Genes through the Phase-Separation Capacity of Their Activation Domains. Cell 175, 1842-1855.e16. https://doi.org/10.1016/j.cell.2018.10.042

Boumendil, C., Hari, P., Olsen, K.C.F., Acosta, J.C., Bickmore, W.A., 2019. Nuclear pore density controls heterochromatin reorganization during senescence. Genes Dev. 33, 144–149. https://doi.org/10.1101/gad.321117.118

Bouwman, P., Aly, A., Escandell, J.M., Pieterse, M., Bartkova, J., van der Gulden, H., Hiddingh, S., Thanasoula, M., Kulkarni, A., Yang, Q., Haffty, B.G., Tommiska, J., Blomqvist, C., Drapkin, R., Adams, D.J., Nevanlinna, H., Bartek, J., Tarsounas, M., Ganesan, S., Jonkers, J., 2010. 53BP1 loss rescues BRCA1 deficiency and is associated with triple-negative and BRCA-mutated breast cancers. Nat. Struct. Mol. Biol. 17, 688–695. https://doi.org/10.1038/nsmb.1831

Brabletz, T., Kalluri, R., Nieto, M.A., Weinberg, R.A., 2018. EMT in cancer. Nat. Rev. Cancer 18, 128–134. https://doi.org/10.1038/nrc.2017.118

Briand, N., Collas, P., 2018. Laminopathy-causing lamin A mutations reconfigure lamina-associated domains and local spatial chromatin conformation. Nucl. Austin Tex 9, 216–226. https://doi.org/10.1080/19491034.2018.1449498

Bustin, S.A., Benes, V., Garson, J.A., Hellemans, J., Huggett, J., Kubista, M., Mueller, R., Nolan, T., Pfaffl, M.W., Shipley, G.L., Vandesompele, J., Wittwer, C.T., 2009. The MIQE guidelines: minimum information for publication of quantitative real-time PCR experiments. Clin. Chem. 55, 611–622. https://doi.org/10.1373/clinchem.2008.112797

Celeste, A., Petersen, S., Romanienko, P.J., Fernandez-Capetillo, O., Chen, H.T., Sedelnikova, O.A., Reina-San-Martin, B., Coppola, V., Meffre, E., Difilippantonio, M.J., Redon, C., Pilch, D.R., Olaru, A., Eckhaus, M., Camerini-Otero, R.D., Tessarollo, L., Livak, F., Manova, K., Bonner, W.M., Nussenzweig, M.C., Nussenzweig, A., 2002. Genomic instability in mice lacking histone H2AX. Science 296, 922–927. https://doi.org/10.1126/science.1069398

Chan, K.-M., Fang, D., Gan, H., Hashizume, R., Yu, C., Schroeder, M., Gupta, N., Mueller, S., James, C.D., Jenkins, R., Sarkaria, J., Zhang, Z., 2013. The histone H3.3K27M mutation in pediatric glioma reprograms H3K27 methylation and gene expression. Genes Dev. 27, 985–990. https://doi.org/10.1101/gad.217778.113

Chang, A.T., Liu, Y., Ayyanathan, K., Benner, C., Jiang, Y., Prokop, J.W., Paz, H., Wang, D., Li, H.-R., Fu, X.-D., Rauscher, F.J., Yang, J., 2015. An evolutionarily conserved DNA architecture determines target specificity of the TWIST family bHLH transcription factors. Genes Dev. 29, 603–616. https://doi.org/10.1101/gad.242842.114

Chen, H., Tian, Y., Shu, W., Bo, X., Wang, S., 2012. Comprehensive identification and annotation of cell type-specific and ubiquitous CTCF-binding sites in the human genome. Plos One 7, e41374. https://doi.org/10.1371/journal.pone.0041374

Chin, K., DeVries, S., Fridlyand, J., Spellman, P.T., Roydasgupta, R., Kuo, W.-L., Lapuk, A., Neve, R.M., Qian, Z., Ryder, T., Chen, F., Feiler, H., Tokuyasu, T., Kingsley, C., Dairkee, S., Meng, Z., Chew, K., Pinkel, D., Jain, A., Ljung, B.M., Esserman, L., Albertson, D.G., Waldman, F.M., Gray, J.W., 2006. Genomic and transcriptional aberrations linked to breast cancer pathophysiologies. Cancer Cell 10, 529–541. https://doi.org/10.1016/j.ccr.2006.10.009

Cho, S., Vashisth, M., Abbas, A., Majkut, S., Vogel, K., Xia, Y., Ivanovska, I.L., Irianto, J., Tewari, M., Zhu, K., Tichy, E.D., Mourkioti, F., Tang, H.-Y., Greenberg, R.A., Prosser, B.L., Discher, D.E., 2019. Mechanosensing by the Lamina Protects against Nuclear Rupture, DNA Damage, and Cell-Cycle Arrest. Dev. Cell 49, 920-935.e5. https://doi.org/10.1016/j.devcel.2019.04.020

Coschi, C.H., Ishak, C.A., Gallo, D., Marshall, A., Talluri, S., Wang, J., Cecchini, M.J., Martens, A.L., Percy, V., Welch, I., Boutros, P.C., Brown, G.W., Dick, F.A., 2014. Haploinsufficiency of an RB-E2F1-Condensin II complex leads to aberrant replication and aneuploidy. Cancer Discov. 4, 840–853. https://doi.org/10.1158/2159-8290.CD-14-0215

Crompton, B.D., Stewart, C., Taylor-Weiner, A., Alexe, G., Kurek, K.C., Calicchio, M.L., Kiezun, A., Carter, S.L., Shukla, S.A., Mehta, S.S., Thorner, A.R., de Torres, C., Lavarino, C., Suñol, M., McKenna, A., Sivachenko, A., Cibulskis, K., Lawrence, M.S., Stojanov, P., Rosenberg, M., Ambrogio, L., Auclair, D., Seepo, S., Blumenstiel, B., DeFelice, M., Imaz-Rosshandler, I., Schwarz-Cruz Y Celis, A., Rivera, M.N., Rodriguez-Galindo, C., Fleming, M.D., Golub, T.R., Getz, G., Mora, J., Stegmaier, K., 2014. The genomic landscape of pediatric Ewing sarcoma. Cancer Discov. 4, 1326–1341. https://doi.org/10.1158/2159-8290.CD-13-1037

Cronshaw, J.M., Krutchinsky, A.N., Zhang, W., Chait, B.T., Matunis, M.J., 2002. Proteomic analysis of the mammalian nuclear pore complex. J. Cell Biol. 158, 915–927. https://doi.org/10.1083/jcb.200206106

Cucco, F., Palumbo, E., Camerini, S., D'Alessio, B., Quarantotti, V., Casella, M.L., Rizzo, I.M., Cukrov, D., Delia, D., Russo, A., Crescenzi, M., Musio, A., 2018. Separase prevents genomic instability by controlling replication fork speed. Nucleic Acids Res. 46, 267–278. https://doi.org/10.1093/nar/gkx1172

Datta, S.R., Brunet, A., Greenberg, M.E., 1999. Cellular survival: a play in three Akts. Genes Dev. 13, 2905–2927. https://doi.org/10.1101/gad.13.22.2905

De Cecco, M., Ito, T., Petrashen, A.P., Elias, A.E., Skvir, N.J., Criscione, S.W., Caligiana, A., Brocculi, G., Adney, E.M., Boeke, J.D., Le, O., Beauséjour, C., Ambati, J., Ambati, K., Simon, M., Seluanov, A., Gorbunova, V., Slagboom, P.E., Helfand, S.L., Neretti, N., Sedivy, J.M., 2019. L1 drives IFN in senescent cells and promotes age-associated inflammation. Nature 566, 73–78. https://doi.org/10.1038/s41586-018-0784-9

de Magalhães, J.P., 2013. How ageing processes influence cancer. Nat. Rev. Cancer 13, 357–365. https://doi.org/10.1038/nrc3497

Deb, S., Xu, H., Tuynman, J., George, J., Yan, Y., Li, J., Ward, R.L., Mortensen, N., Hawkins, N.J., McKay, M.J., Ramsay, R.G., Fox, S.B., 2014. RAD21 cohesin overexpression is a prognostic and predictive marker exacerbating poor prognosis in KRAS mutant colorectal carcinomas. Br. J. Cancer 110, 1606–1613. https://doi.org/10.1038/bjc.2014.31

Dechat, T., Adam, S.A., Taimen, P., Shimi, T., Goldman, R.D., 2010. Nuclear lamins. Cold Spring Harb. Perspect. Biol. 2, a000547. https://doi.org/10.1101/cshperspect.a000547

Dechat, T., Pfleghaar, K., Sengupta, K., Shimi, T., Shumaker, D.K., Solimando, L., Goldman, R.D., 2008. Nuclear lamins: major factors in the structural organization and function of the nucleus and chromatin. Genes Dev. 22, 832–853. https://doi.org/10.1101/gad.1652708

Dechat, T., Shimi, T., Adam, S.A., Rusinol, A.E., Andres, D.A., Spielmann, H.P., Sinensky, M.S., Goldman, R.D., 2007. Alterations in mitosis and cell cycle progression caused by a mutant lamin A known to accelerate human aging. Proc. Natl. Acad. Sci. U. S. A. 104, 4955–4960. https://doi.org/10.1073/pnas.0700854104

Demmerle, J., Koch, A.J., Holaska, J.M., 2012. The nuclear envelope protein emerin binds directly to histone deacetylase 3 (HDAC3) and activates HDAC3 activity. J. Biol. Chem. 287, 22080–22088. https://doi.org/10.1074/jbc.M111.325308

Derynck, R., Weinberg, R.A., 2019. EMT and cancer: more than meets the eye. Dev. Cell 49, 313–316. https://doi.org/10.1016/j.devcel.2019.04.026

Diepenbruck, M., Christofori, G., 2016. Epithelial-mesenchymal transition (EMT) and metastasis: yes, no, maybe? Curr. Opin. Cell Biol. 43, 7–13. https://doi.org/10.1016/j.ceb.2016.06.002

Dittmer, T.A., Sahni, N., Kubben, N., Hill, D.E., Vidal, M., Burgess, R.C., Roukos, V., Misteli, T., 2014. Systematic identification of pathological lamin A interactors. Mol. Biol. Cell 25, 1493–1510. https://doi.org/10.1091/mbc.E14-02-0733

Dongre, A., Weinberg, R.A., 2019. New insights into the mechanisms of epithelial-mesenchymal transition and implications for cancer. Nat. Rev. Mol. Cell Biol. 20, 69–84. https://doi.org/10.1038/s41580-018-0080-4

Earle, A.J., Kirby, T.J., Fedorchak, G.R., Isermann, P., Patel, J., Iruvanti, S., Moore, S.A., Bonne, G., Wallrath, L.L., Lammerding, J., 2020. Mutant lamins cause nuclear envelope rupture and DNA damage in skeletal muscle cells. Nat. Mater. 19, 464–473. https://doi.org/10.1038/s41563-019-0563-5

Ebrahimi, H., Masuda, H., Jain, D., Cooper, J.P., 2018. Distinct “safe zones” at the nuclear envelope ensure robust replication of heterochromatic chromosome regions. eLife 7. https://doi.org/10.7554/eLife.32911

Eldholm, V., Haugen, A., Zienolddiny, S., 2014. CTCF mediates the TERT enhancer-promoter interactions in lung cancer cells: identification of a novel enhancer region involved in the regulation of TERT gene. Int. J. Cancer 134, 2305–2313. https://doi.org/10.1002/ijc.28570

Favreau, C., Dubosclard, E., Ostlund, C., Vigouroux, C., Capeau, J., Wehnert, M., Higuet, D., Worman, H.J., Courvalin, J.-C., Buendia, B., 2003. Expression of lamin A mutated in the carboxyl-terminal tail generates an aberrant nuclear phenotype similar to that observed in cells from patients with Dunnigan-type partial lipodystrophy and Emery-Dreifuss muscular dystrophy. Exp. Cell Res. 282, 14–23. https://doi.org/10.1006/excr.2002.5669

Fischer, K.R., Durrans, A., Lee, S., Sheng, J., Li, F., Wong, S.T.C., Choi, H., El Rayes, T., Ryu, S., Troeger, J., Schwabe, R.F., Vahdat, L.T., Altorki, N.K., Mittal, V., Gao, D., 2015. Epithelial-to-mesenchymal transition is not required for lung metastasis but contributes to chemoresistance. Nature 527, 472–476. https://doi.org/10.1038/nature15748

Flavahan, W.A., Drier, Y., Liau, B.B., Gillespie, S.M., Venteicher, A.S., Stemmer-Rachamimov, A.O., Suvà, M.L., Bernstein, B.E., 2016. Insulator dysfunction and oncogene activation in IDH mutant gliomas. Nature 529, 110–114. https://doi.org/10.1038/nature16490

Friedl, P., Gilmour, D., 2009. Collective cell migration in morphogenesis, regeneration and cancer. Nat. Rev. Mol. Cell Biol. 10, 445–457. https://doi.org/10.1038/nrm2720

Fudenberg, G., Imakaev, M., Lu, C., Goloborodko, A., Abdennur, N., Mirny, L.A., 2016. Formation of chromosomal domains by loop extrusion. Cell Rep. 15, 2038–2049. https://doi.org/10.1016/j.celrep.2016.04.085

Fukagawa, T., Nogami, M., Yoshikawa, M., Ikeno, M., Okazaki, T., Takami, Y., Nakayama, T., Oshimura, M., 2004. Dicer is essential for formation of the heterochromatin structure in vertebrate cells. Nat. Cell Biol. 6, 784–791. https://doi.org/10.1038/ncb1155

Gdula, M.R., Poterlowicz, K., Mardaryev, A.N., Sharov, A.A., Peng, Y., Fessing, M.Y., Botchkarev, V.A., 2013. Remodeling of three-dimensional organization of the nucleus during terminal keratinocyte differentiation in the epidermis. J. Invest. Dermatol. 133, 2191–2201. https://doi.org/10.1038/jid.2013.66

Geigl, J.B., Obenauf, A.C., Schwarzbraun, T., Speicher, M.R., 2008. Defining “chromosomal instability”. Trends Genet. 24, 64–69. https://doi.org/10.1016/j.tig.2007.11.006

Gesson, K., Rescheneder, P., Skoruppa, M.P., von Haeseler, A., Dechat, T., Foisner, R., 2016. A-type lamins bind both hetero- and euchromatin, the latter being regulated by lamina-associated polypeptide 2 alpha. Genome Res. 26, 462–473. https://doi.org/10.1101/gr.196220.115

Gil, L., Niño, S.A., Chi-Ahumada, E., Rodríguez-Leyva, I., Guerrero, C., Rebolledo, A.B., Arias, J.A., Jiménez-Capdeville, M.E., 2020. Perinuclear Lamin A and Nucleoplasmic Lamin B2 Characterize Two Types of Hippocampal Neurons through Alzheimer’s Disease Progression. Int. J. Mol. Sci. 21. https://doi.org/10.3390/ijms21051841

Goldberg, A.D., Banaszynski, L.A., Noh, K.-M., Lewis, P.W., Elsaesser, S.J., Stadler, S., Dewell, S., Law, M., Guo, X., Li, X., Wen, D., Chapgier, A., DeKelver, R.C., Miller, J.C., Lee, Y.-L., Boydston, E.A., Holmes, M.C., Gregory, P.D., Greally, J.M., Rafii, S., Yang, C., Scambler, P.J., Garrick, D., Gibbons, R.J., Higgs, D.R., Cristea, I.M., Urnov, F.D., Zheng, D., Allis, C.D., 2010. Distinct factors control histone variant H3.3 localization at specific genomic regions. Cell 140, 678–691. https://doi.org/10.1016/j.cell.2010.01.003

Goldman, R.D., Gruenbaum, Y., Moir, R.D., Shumaker, D.K., Spann, T.P., 2002. Nuclear lamins: building blocks of nuclear architecture. Genes Dev. 16, 533–547. https://doi.org/10.1101/gad.960502

González-Romero, R., Méndez, J., Ausió, J., Eirín-López, J.M., 2008. Quickly evolving histones, nucleosome stability and chromatin folding: all about histone H2A.Bbd. Gene 413, 1–7. https://doi.org/10.1016/j.gene.2008.02.003

Gonzalo, S., 2014. DNA damage and lamins. Adv. Exp. Med. Biol. 773, 377–399. https://doi.org/10.1007/978-1-4899-8032-8_17

Guo, G., Sun, X., Chen, C., Wu, S., Huang, P., Li, Z., Dean, M., Huang, Y., Jia, W., Zhou, Q., Tang, A., Yang, Z., Li, X., Song, P., Zhao, Xiaokun, Ye, R., Zhang, S., Lin, Zhao, Qi, M., Wan, S., Xie, L., Fan, F., Nickerson, M.L., Zou, X., Hu, X., Xing, L., Lv, Z., Mei, H., Gao, S., Liang, C., Gao, Z., Lu, J., Yu, Y., Liu, C., Li, L., Fang, X., Jiang, Z., Yang, J., Li, C., Zhao, Xin, Chen, J., Zhang, F., Lai, Y., Lin, Zheguang, Zhou, F., Chen, H., Chan, H.C., Tsang, S., Theodorescu, D., Li, Y., Zhang, X., Wang, Jian, Yang, H., Gui, Y., Wang, Jun, Cai, Z., 2013. Whole-genome and whole-exome sequencing of bladder cancer identifies frequent alterations in genes involved in sister chromatid cohesion and segregation. Nat. Genet. 45, 1459–1463. https://doi.org/10.1038/ng.2798

Ha, M., Kraushaar, D.C., Zhao, K., 2014. Genome-wide analysis of H3.3 dissociation reveals high nucleosome turnover at distal regulatory regions of embryonic stem cells. Epigenetics Chromatin 7, 38. https://doi.org/10.1186/1756-8935-7-38

Hanahan, D., Weinberg, R.A., 2011. Hallmarks of cancer: the next generation. Cell 144, 646–674. https://doi.org/10.1016/j.cell.2011.02.013

Hanssen, L.L.P., Kassouf, M.T., Oudelaar, A.M., Biggs, D., Preece, C., Downes, D.J., Gosden, M., Sharpe, J.A., Sloane-Stanley, J.A., Hughes, J.R., Davies, B., Higgs, D.R., 2017. Tissue-specific CTCF-cohesin-mediated chromatin architecture delimits enhancer interactions and function in vivo. Nat. Cell Biol. 19, 952–961. https://doi.org/10.1038/ncb3573

Harada, T., Swift, J., Irianto, J., Shin, J.-W., Spinler, K.R., Athirasala, A., Diegmiller, R., Dingal, P.C.D.P., Ivanovska, I.L., Discher, D.E., 2014. Nuclear lamin stiffness is a barrier to 3D migration, but softness can limit survival. J. Cell Biol. 204, 669–682. https://doi.org/10.1083/jcb.201308029

Hartman, H.B., Yu, J., Alenghat, T., Ishizuka, T., Lazar, M.A., 2005. The histone-binding code of nuclear receptor co-repressors matches the substrate specificity of histone deacetylase 3. EMBO Rep. 6, 445–451. https://doi.org/10.1038/sj.embor.7400391

Heaphy, C.M., de Wilde, R.F., Jiao, Y., Klein, A.P., Edil, B.H., Shi, C., Bettegowda, C., Rodriguez, F.J., Eberhart, C.G., Hebbar, S., Offerhaus, G.J., McLendon, R., Rasheed, B.A., He, Y., Yan, H., Bigner, D.D., Oba-Shinjo, S.M., Marie, S.K.N., Riggins, G.J., Kinzler, K.W., Vogelstein, B., Hruban, R.H., Maitra, A., Papadopoulos, N., Meeker, A.K., 2011. Altered telomeres in tumors with ATRX and DAXX mutations. Science 333, 425. https://doi.org/10.1126/science.1207313

Holaska, J.M., Wilson, K.L., 2007. An emerin “proteome”: purification of distinct emerin-containing complexes from HeLa cells suggests molecular basis for diverse roles including gene regulation, mRNA splicing, signaling, mechanosensing, and nuclear architecture. Biochemistry 46, 8897–8908. https://doi.org/10.1021/bi602636m

Holwerda, S.J.B., de Laat, W., 2013. CTCF: the protein, the binding partners, the binding sites and their chromatin loops. Philos. Trans. R. Soc. Lond. B. Biol. Sci. 368, 20120369. https://doi.org/10.1098/rstb.2012.0369

Ibarra, A., Benner, C., Tyagi, S., Cool, J., Hetzer, M.W., 2016. Nucleoporin-mediated regulation of cell identity genes. Genes Dev. 30, 2253–2258. https://doi.org/10.1101/gad.287417.116

Ibarra, A., Hetzer, M.W., 2015. Nuclear pore proteins and the control of genome functions. Genes Dev. 29, 337–349. https://doi.org/10.1101/gad.256495.114

Ikegami, K., Secchia, S., Almakki, O., Lieb, J.D., Moskowitz, I.P., 2020. Phosphorylated Lamin A/C in the Nuclear Interior Binds Active Enhancers Associated with Abnormal Transcription in Progeria. Dev. Cell 52, 699-713.e11. https://doi.org/10.1016/j.devcel.2020.02.011

Iwabuchi, K., Hashimoto, M., Matsui, T., Kurihara, T., Shimizu, H., Adachi, N., Ishiai, M., Yamamoto, K., Tauchi, H., Takata, M., Koyama, H., Date, T., 2006. 53BP1 contributes to survival of cells irradiated with X-ray during G1 without Ku70 or Artemis. Genes Cells 11, 935–948. https://doi.org/10.1111/j.1365-2443.2006.00989.x

Jha, D.K., Strahl, B.D., 2014. An RNA polymerase II-coupled function for histone H3K36 methylation in checkpoint activation and DSB repair. Nat. Commun. 5, 3965. https://doi.org/10.1038/ncomms4965

Jiang, L., Xiao, L., Sugiura, H., Huang, X., Ali, A., Kuro-o, M., Deberardinis, R.J., Boothman, D.A., 2015. Metabolic reprogramming during TGF\beta1-induced epithelial-to-mesenchymal transition. Oncogene 34, 3908–3916. https://doi.org/10.1038/onc.2014.321

Johnstone, S.E., Reyes, A., Qi, Y., Adriaens, C., Hegazi, E., Pelka, K., Chen, J.H., Zou, L.S., Drier, Y., Hecht, V., Shoresh, N., Selig, M.K., Lareau, C.A., Iyer, S., Nguyen, S.C., Joyce, E.F., Hacohen, N., Irizarry, R.A., Zhang, B., Aryee, M.J., Bernstein, B.E., 2020. Large-Scale Topological Changes Restrain Malignant Progression in Colorectal Cancer. Cell 182, 1474-1489.e23. https://doi.org/10.1016/j.cell.2020.07.030

Jolly, M.K., Boareto, M., Huang, B., Jia, D., Lu, M., Ben-Jacob, E., Onuchic, J.N., Levine, H., 2015. Implications of the hybrid epithelial/mesenchymal phenotype in metastasis. Front. Oncol. 5, 155. https://doi.org/10.3389/fonc.2015.00155

Jolly, M.K., Somarelli, J.A., Sheth, M., Biddle, A., Tripathi, S.C., Armstrong, A.J., Hanash, S.M., Bapat, S.A., Rangarajan, A., Levine, H., 2019. Hybrid epithelial/mesenchymal phenotypes promote metastasis and therapy resistance across carcinomas. Pharmacol. Ther. 194, 161–184. https://doi.org/10.1016/j.pharmthera.2018.09.007

Kadota, S., Ou, J., Shi, Y., Lee, J.T., Sun, J., Yildirim, E., 2020. Nucleoporin 153 links nuclear pore complex to chromatin architecture by mediating CTCF and cohesin binding. Nat. Commun. 11, 2606. https://doi.org/10.1038/s41467-020-16394-3

Kalluri, R., Weinberg, R.A., 2009. The basics of epithelial-mesenchymal transition. J. Clin. Invest. 119, 1420–1428. https://doi.org/10.1172/JCI39104

Kang, H., Kim, H., Lee, S., Youn, H., Youn, B., 2019. Role of metabolic reprogramming in epithelial¯mesenchymal transition (EMT). Int. J. Mol. Sci. 20. https://doi.org/10.3390/ijms20082042

Kang, X., Wang, J., Li, C., 2019. Exposing the Underlying Relationship of Cancer Metastasis to Metabolism and Epithelial-Mesenchymal Transitions. iScience 21, 754–772. https://doi.org/10.1016/j.isci.2019.10.060

Karoutas, A., Szymanski, W., Rausch, T., Guhathakurta, S., Rog-Zielinska, E.A., Peyronnet, R., Seyfferth, J., Chen, H.-R., de Leeuw, R., Herquel, B., Kimura, H., Mittler, G., Kohl, P., Medalia, O., Korbel, J.O., Akhtar, A., 2019. The NSL complex maintains nuclear architecture stability via lamin A/C acetylation. Nat. Cell Biol. 21, 1248–1260. https://doi.org/10.1038/s41556-019-0397-z

Kasper, L.H., Brindle, P.K., Schnabel, C.A., Pritchard, C.E., Cleary, M.L., van Deursen, J.M., 1999. CREB binding protein interacts with nucleoporin-specific FG repeats that activate transcription and mediate NUP98-HOXA9 oncogenicity. Mol. Cell. Biol. 19, 764–776. https://doi.org/10.1128/MCB.19.1.764

Khot, M., Sreekumar, D., Jahagirdar, S., Kulkarni, A., Hari, K., Faseela, E.E., Sabarinathan, R., Jolly, M.K., Sengupta, K., 2020. Twist1 induces chromosomal instability (CIN) in colorectal cancer cells. Hum. Mol. Genet. 29, 1673–1688. https://doi.org/10.1093/hmg/ddaa076

Kim, E., Kim, M., Woo, D.-H., Shin, Y., Shin, J., Chang, N., Oh, Y.T., Kim, H., Rheey, J., Nakano, I., Lee, C., Joo, K.M., Rich, J.N., Nam, D.-H., Lee, J., 2013. Phosphorylation of EZH2 activates STAT3 signaling via STAT3 methylation and promotes tumorigenicity of glioblastoma stem-like cells. Cancer Cell 23, 839–852. https://doi.org/10.1016/j.ccr.2013.04.008

Kim, J.H., Youn, Y., Kim, K.-T., Jang, G., Hwang, J.-H., 2019. Non-SMC condensin I complex subunit H mediates mature chromosome condensation and DNA damage in pancreatic cancer cells. Sci. Rep. 9, 17889. https://doi.org/10.1038/s41598-019-54478-3

Kim, J.-K., Louhghalam, A., Lee, G., Schafer, B.W., Wirtz, D., Kim, D.-H., 2017. Nuclear lamin A/C harnesses the perinuclear apical actin cables to protect nuclear morphology. Nat. Commun. 8, 2123. https://doi.org/10.1038/s41467-017-02217-5

Kim, S.-Y., Rhee, J.G., Song, X., Prochownik, E.V., Spitz, D.R., Lee, Y.J., 2012. Breast cancer stem cell-like cells are more sensitive to ionizing radiation than non-stem cells: role of ATM. Plos One 7, e50423. https://doi.org/10.1371/journal.pone.0050423

Kimura, H., 2013. Histone modifications for human epigenome analysis. J. Hum. Genet. 58, 439–445. https://doi.org/10.1038/jhg.2013.66

Kind, J., Pagie, L., Ortabozkoyun, H., Boyle, S., de Vries, S.S., Janssen, H., Amendola, M., Nolen, L.D., Bickmore, W.A., van Steensel, B., 2013. Single-cell dynamics of genome-nuclear lamina interactions. Cell 153, 178–192. https://doi.org/10.1016/j.cell.2013.02.028

Kojic, A., Cuadrado, A., De Koninck, M., Giménez-Llorente, D., Rodríguez-Corsino, M., Gómez-López, G., Le Dily, F., Marti-Renom, M.A., Losada, A., 2018. Distinct roles of cohesin-SA1 and cohesin-SA2 in 3D chromosome organization. Nat. Struct. Mol. Biol. 25, 496–504. https://doi.org/10.1038/s41594-018-0070-4

Kong, L., Schäfer, G., Bu, H., Zhang, Yong, Zhang, Yuxiang, Klocker, H., 2012. Lamin A/C protein is overexpressed in tissue-invading prostate cancer and promotes prostate cancer cell

growth, migration and invasion through the PI3K/AKT/PTEN pathway. Carcinogenesis 33, 751–759. https://doi.org/10.1093/carcin/bgs022

Kröger, C., Afeyan, A., Mraz, J., Eaton, E.N., Reinhardt, F., Khodor, Y.L., Thiru, P., Bierie, B., Ye, X., Burge, C.B., Weinberg, R.A., 2019. Acquisition of a hybrid E/M state is essential for tumorigenicity of basal breast cancer cells. Proc. Natl. Acad. Sci. U. S. A. 116, 7353–7362. https://doi.org/10.1073/pnas.1812876116

Kuga, T., Nie, H., Kazami, T., Satoh, M., Matsushita, K., Nomura, F., Maeshima, K., Nakayama, Y., Tomonaga, T., 2014. Lamin B2 prevents chromosome instability by ensuring proper mitotic chromosome segregation. Oncogenesis 3, e94. https://doi.org/10.1038/oncsis.2014.6

Kwok, W.K., Ling, M.-T., Yuen, H.F., Wong, Y.-C., Wang, X., 2007. Role of p14ARF in TWIST-mediated senescence in prostate epithelial cells. Carcinogenesis 28, 2467–2475. https://doi.org/10.1093/carcin/bgm185

Labade, A.S., Karmodiya, K., Sengupta, K., 2016. HOXA repression is mediated by nucleoporin Nup93 assisted by its interactors Nup188 and Nup205. Epigenetics Chromatin 9, 54. https://doi.org/10.1186/s13072-016-0106-0

Laberge, R.-M., Sun, Y., Orjalo, A.V., Patil, C.K., Freund, A., Zhou, L., Curran, S.C., Davalos, A.R., Wilson-Edell, K.A., Liu, S., Limbad, C., Demaria, M., Li, P., Hubbard, G.B., Ikeno, Y., Javors, M., Desprez, P.-Y., Benz, C.C., Kapahi, P., Nelson, P.S., Campisi, J., 2015. MTOR regulates the pro-tumorigenic senescence-associated secretory phenotype by promoting IL1A translation. Nat. Cell Biol. 17, 1049–1061. https://doi.org/10.1038/ncb3195

Lambert, A.W., Pattabiraman, D.R., Weinberg, R.A., 2017. Emerging biological principles of metastasis. Cell 168, 670–691. https://doi.org/10.1016/j.cell.2016.11.037

Lamouille, S., Xu, J., Derynck, R., 2014. Molecular mechanisms of epithelial-mesenchymal transition. Nat. Rev. Mol. Cell Biol. 15, 178–196. https://doi.org/10.1038/nrm3758

Landt, S.G., Marinov, G.K., Kundaje, A., Kheradpour, P., Pauli, F., Batzoglou, S., Bernstein, B.E., Bickel, P., Brown, J.B., Cayting, P., Chen, Y., DeSalvo, G., Epstein, C., Fisher-Aylor, K.I., Euskirchen, G., Gerstein, M., Gertz, J., Hartemink, A.J., Hoffman, M.M., Iyer, V.R., Jung, Y.L., Karmakar, S., Kellis, M., Kharchenko, P.V., Li, Q., Liu, T., Liu, X.S., Ma, L., Milosavljevic, A., Myers, R.M., Park, P.J., Pazin, M.J., Perry, M.D., Raha, D., Reddy, T.E., Rozowsky, J., Shoresh, N., Sidow, A., Slattery, M., Stamatoyannopoulos, J.A., Tolstorukov, M.Y., White, K.P., Xi, S., Farnham, P.J., Lieb, J.D., Wold, B.J., Snyder, M., 2012. ChIP-seq guidelines and practices of the ENCODE and modENCODE consortia. Genome Res. 22, 1813–1831. https://doi.org/10.1101/gr.136184.111

Larson, J.D., Kasper, L.H., Paugh, B.S., Jin, H., Wu, G., Kwon, C.-H., Fan, Y., Shaw, T.I., Silveira, A.B., Qu, C., Xu, R., Zhu, X., Zhang, Junyuan, Russell, H.R., Peters, J.L., Finkelstein, D., Xu, B., Lin, T., Tinkle, C.L., Patay, Z., Onar-Thomas, A., Pounds, S.B., McKinnon, P.J., Ellison, D.W., Zhang, Jinghui, Baker, S.J., 2019. Histone H3.3 K27M accelerates spontaneous brainstem glioma and drives restricted changes in bivalent gene expression. Cancer Cell 35, 140-155.e7. https://doi.org/10.1016/j.ccell.2018.11.015

Le, A., Szaumkessel, M., Tan, T., Thiery, J.-P., Thompson, E., Dobrovic, A., 2018. DNA Methylation Profiling of Breast Cancer Cell Lines along the Epithelial Mesenchymal Spectrum—Implications for the Choice of Circulating Tumour DNA Methylation Markers. Int. J. Mol. Sci. 19, 2553. https://doi.org/10.3390/ijms19092553

Lee, J.-J., Lee, J.-H., Ko, Y.-G., Hong, S.I., Lee, J.-S., 2010. Prevention of premature senescence requires JNK regulation of Bcl-2 and reactive oxygen species. Oncogene 29, 561–575. https://doi.org/10.1038/onc.2009.355

Leiserson, M.D.M., Vandin, F., Wu, H.-T., Dobson, J.R., Eldridge, J.V., Thomas, J.L., Papoutsaki, A., Kim, Y., Niu, B., McLellan, M., Lawrence, M.S., Gonzalez-Perez, A., Tamborero, D., Cheng, Y., Ryslik, G.A., Lopez-Bigas, N., Getz, G., Ding, L., Raphael, B.J., 2015. Pan-cancer network analysis identifies combinations of rare somatic mutations across pathways and protein complexes. Nat. Genet. 47, 106–114. https://doi.org/10.1038/ng.3168

Leong, H.S., Robertson, A.E., Stoletov, K., Leith, S.J., Chin, C.A., Chien, A.E., Hague, M.N., Ablack, A., Carmine-Simmen, K., McPherson, V.A., Postenka, C.O., Turley, E.A., Courtneidge, S.A., Chambers, A.F., Lewis, J.D., 2014. Invadopodia are required for cancer cell extravasation and are a therapeutic target for metastasis. Cell Rep. 8, 1558–1570. https://doi.org/10.1016/j.celrep.2014.07.050

Lim, J., Thiery, J.P., 2012. Epithelial-mesenchymal transitions: insights from development. Development 139, 3471–3486. https://doi.org/10.1242/dev.071209

Lin, C.-J., Conti, M., Ramalho-Santos, M., 2013. Histone variant H3.3 maintains a decondensed chromatin state essential for mouse preimplantation development. Development 140, 3624–3634. https://doi.org/10.1242/dev.095513

Little, M.H., McMahon, A.P., 2012. Mammalian kidney development: principles, progress, and projections. Cold Spring Harb. Perspect. Biol. 4. https://doi.org/10.1101/cshperspect.a008300

Liu, B., Wang, Z., Zhang, L., Ghosh, S., Zheng, H., Zhou, Z., 2013. Depleting the methyltransferase Suv39h1 improves DNA repair and extends lifespan in a progeria mouse model. Nat. Commun. 4, 1868. https://doi.org/10.1038/ncomms2885

Lopez, J., Tait, S.W.G., 2015. Mitochondrial apoptosis: killing cancer using the enemy within. Br. J. Cancer 112, 957–962. https://doi.org/10.1038/bjc.2015.85

Lovisa, S., LeBleu, V.S., Tampe, B., Sugimoto, H., Vadnagara, K., Carstens, J.L., Wu, C.-C., Hagos, Y., Burckhardt, B.C., Pentcheva-Hoang, T., Nischal, H., Allison, J.P., Zeisberg, M., Kalluri, R., 2015. Epithelial-to-mesenchymal transition induces cell cycle arrest and parenchymal damage in renal fibrosis. Nat. Med. 21, 998–1009. https://doi.org/10.1038/nm.3902

Lu, W., Kang, Y., 2019. Epithelial-Mesenchymal Plasticity in Cancer Progression and Metastasis. Dev. Cell 49, 361–374. https://doi.org/10.1016/j.devcel.2019.04.010

Lukášová, E., Kovarˇík, A., Bacˇíková, A., Falk, M., Kozubek, S., 2017. Loss of lamin B receptor is necessary to induce cellular senescence. Biochem. J. 474, 281–300. https://doi.org/10.1042/BCJ20160459

Lupiáñez, D.G., Kraft, K., Heinrich, V., Krawitz, P., Brancati, F., Klopocki, E., Horn, D., Kayserili, H., Opitz, J.M., Laxova, R., Santos-Simarro, F., Gilbert-Dussardier, B., Wittler, L., Borschiwer, M., Haas, S.A., Osterwalder, M., Franke, M., Timmermann, B., Hecht, J., Spielmann, M., Visel, A., Mundlos, S., 2015. Disruptions of topological chromatin domains cause pathogenic rewiring of gene-enhancer interactions. Cell 161, 1012–1025. https://doi.org/10.1016/j.cell.2015.04.004

Mahen, R., Hattori, H., Lee, M., Sharma, P., Jeyasekharan, A.D., Venkitaraman, A.R., 2013. A-type lamins maintain the positional stability of DNA damage repair foci in mammalian nuclei. Plos One 8, e61893. https://doi.org/10.1371/journal.pone.0061893

Maishman, L., Obado, S.O., Alsford, S., Bart, J.-M., Chen, W.-M., Ratushny, A.V., Navarro, M., Horn, D., Aitchison, J.D., Chait, B.T., Rout, M.P., Field, M.C., 2016. Co-dependence between trypanosome nuclear lamina components in nuclear stability and control of gene expression. Nucleic Acids Res. 44, 10554–10570. https://doi.org/10.1093/nar/gkw751

Malashicheva, A., Bogdanova, M., Zabirnyk, A., Smolina, N., Ignatieva, E., Freilikhman, O., Fedorov, A., Dmitrieva, R., Sjöberg, G., Sejersen, T., Kostareva, A., 2015. Various lamin A/C mutations alter expression profile of mesenchymal stem cells in mutation specific manner. Mol. Genet. Metab. 115, 118–127. https://doi.org/10.1016/j.ymgme.2015.04.006

Margueron, R., Li, G., Sarma, K., Blais, A., Zavadil, J., Woodcock, C.L., Dynlacht, B.D., Reinberg, D., 2008. Ezh1 and Ezh2 maintain repressive chromatin through different mechanisms. Mol. Cell 32, 503–518. https://doi.org/10.1016/j.molcel.2008.11.004

Marullo, F., Cesarini, E., Antonelli, L., Gregoretti, F., Oliva, G., Lanzuolo, C., 2016. Nucleoplasmic Lamin A/C and Polycomb group of proteins: An evolutionarily conserved interplay. Nucl. Austin Tex 7, 103–111. https://doi.org/10.1080/19491034.2016.1157675

Mattioli, E., Andrenacci, D., Garofalo, C., Prencipe, S., Scotlandi, K., Remondini, D., Gentilini, D., Di Blasio, A.M., Valente, S., Scarano, E., Cicchilitti, L., Piaggio, G., Mai, A., Lattanzi, G., 2018. Altered modulation of lamin A/C-HDAC2 interaction and p21 expression during oxidative stress response in HGPS. Aging Cell 17, e12824. https://doi.org/10.1111/acel.12824

McCord, R.P., Nazario-Toole, A., Zhang, H., Chines, P.S., Zhan, Y., Erdos, M.R., Collins, F.S., Dekker, J., Cao, K., 2013. Correlated alterations in genome organization, histone methylation, and DNA-lamin A/C interactions in Hutchinson-Gilford progeria syndrome. Genome Res. 23, 260–269. https://doi.org/10.1101/gr.138032.112

McLaughlin-Drubin, M.E., Park, D., Munger, K., 2013. Tumor suppressor p16INK4A is necessary for survival of cervical carcinoma cell lines. Proc. Natl. Acad. Sci. U. S. A. 110, 16175–16180. https://doi.org/10.1073/pnas.1310432110

Meyer-Schaller, N., Cardner, M., Diepenbruck, M., Saxena, M., Tiede, S., Lüönd, F., Ivanek, R., Beerenwinkel, N., Christofori, G., 2019. A Hierarchical Regulatory Landscape during the Multiple Stages of EMT. Dev. Cell 48, 539-553.e6. https://doi.org/10.1016/j.devcel.2018.12.023

Minchell, N.E., Keszthelyi, A., Baxter, J., 2020. Cohesin causes replicative DNA damage by trapping DNA topological stress. Mol. Cell 78, 739-751.e8. https://doi.org/10.1016/j.molcel.2020.03.013

Mitra, S.K., Hanson, D.A., Schlaepfer, D.D., 2005. Focal adhesion kinase: in command and control of cell motility. Nat. Rev. Mol. Cell Biol. 6, 56–68. https://doi.org/10.1038/nrm1549

Mohammad, F., Helin, K., 2017. Oncohistones: drivers of pediatric cancers. Genes Dev. 31, 2313–2324. https://doi.org/10.1101/gad.309013.117

Moir, R.D., Spann, T.P., Herrmann, H., Goldman, R.D., 2000. Disruption of nuclear lamin organization blocks the elongation phase of DNA replication. J. Cell Biol. 149, 1179–1192. https://doi.org/10.1083/jcb.149.6.1179

Moly, P.K., Cooley, J.R., Zeltzer, S.L., Yatskievych, T.A., Antin, P.B., 2016. Gastrulation EMT Is Independent of P-Cadherin Downregulation. PLOS ONE 11, e0153591. https://doi.org/10.1371/journal.pone.0153591

Nacev, B.A., Jones, K.B., Intlekofer, A.M., Yu, J.S.E., Allis, C.D., Tap, W.D., Ladanyi, M., Nielsen, T.O., 2020. The epigenomics of sarcoma. Nat. Rev. Cancer 20, 608–623. https://doi.org/10.1038/s41568-020-0288-4

Nakaya, Y., Sheng, G., 2008. Epithelial to mesenchymal transition during gastrulation: an embryological view. Dev. Growth Differ. 50, 755–766. https://doi.org/10.1111/j.1440-169X.2008.01070.x

Narita, Masashi, Nũnez, S., Heard, E., Narita, Masako, Lin, A.W., Hearn, S.A., Spector, D.L., Hannon, G.J., Lowe, S.W., 2003. Rb-mediated heterochromatin formation and silencing of E2F target genes during cellular senescence. Cell 113, 703–716. https://doi.org/10.1016/s0092-8674(03)00401-x

Nava, M.M., Miroshnikova, Y.A., Biggs, L.C., Whitefield, D.B., Metge, F., Boucas, J., Vihinen, H., Jokitalo, E., Li, X., García Arcos, J.M., Hoffmann, B., Merkel, R., Niessen, C.M., Dahl, K.N., Wickström, S.A., 2020. Heterochromatin-Driven Nuclear Softening Protects the Genome against Mechanical Stress-Induced Damage. Cell 181, 800-817.e22. https://doi.org/10.1016/j.cell.2020.03.052

Nelson, D.M., Jaber-Hijazi, F., Cole, J.J., Robertson, N.A., Pawlikowski, J.S., Norris, K.T., Criscione, S.W., Pchelintsev, N.A., Piscitello, D., Stong, N., Rai, T.S., McBryan, T., Otte, G.L., Nixon, C., Clark, W., Riethman, H., Wu, H., Schotta, G., Garcia, B.A., Neretti, N., Baird, D.M., Berger, S.L., Adams, P.D., 2016. Mapping H4K20me3 onto the chromatin landscape of senescent cells indicates a function in control of cell senescence and tumor suppression through preservation of genetic and epigenetic stability. Genome Biol. 17, 158. https://doi.org/10.1186/s13059-016-1017-x

Nieto, M.A., Huang, R.Y.-J., Jackson, R.A., Thiery, J.P., 2016. EMT: 2016. Cell 166, 21–45. https://doi.org/10.1016/j.cell.2016.06.028

Ogiyama, Y., Schuettengruber, B., Papadopoulos, G.L., Chang, J.-M., Cavalli, G., 2018. Polycomb-Dependent Chromatin Looping Contributes to Gene Silencing during Drosophila Development. Mol. Cell 71, 73-88.e5. https://doi.org/10.1016/j.molcel.2018.05.032

Panier, S., Boulton, S.J., 2014. Double-strand break repair: 53BP1 comes into focus. Nat. Rev. Mol. Cell Biol. 15, 7–18. https://doi.org/10.1038/nrm3719

Pastushenko, I., Brisebarre, A., Sifrim, A., Fioramonti, M., Revenco, T., Boumahdi, S., Van Keymeulen, A., Brown, D., Moers, V., Lemaire, S., De Clercq, S., Minguijón, E., Balsat, C., Sokolow, Y., Dubois, C., De Cock, F., Scozzaro, S., Sopena, F., Lanas, A., D'Haene, N., Salmon, I., Marine, J.-C., Voet, T., Sotiropoulou, P.A., Blanpain, C., 2018. Identification of the tumour transition states occurring during EMT. Nature 556, 463–468. https://doi.org/10.1038/s41586-018-0040-3

Peric-Hupkes, D., Meuleman, W., Pagie, L., Bruggeman, S.W.M., Solovei, I., Brugman, W., Gräf, S., Flicek, P., Kerkhoven, R.M., van Lohuizen, M., Reinders, M., Wessels, L., van Steensel, B., 2010. Molecular maps of the reorganization of genome-nuclear lamina interactions during differentiation. Mol. Cell 38, 603–613. https://doi.org/10.1016/j.molcel.2010.03.016

Puisieux, A., Brabletz, T., Caramel, J., 2014. Oncogenic roles of EMT-inducing transcription factors. Nat. Cell Biol. 16, 488–494. https://doi.org/10.1038/ncb2976

Rajagopalan, H., Lengauer, C., 2004. Aneuploidy and cancer. Nature 432, 338–341. https://doi.org/10.1038/nature03099

Ray-Gallet, D., Woolfe, A., Vassias, I., Pellentz, C., Lacoste, N., Puri, A., Schultz, D.C., Pchelintsev, N.A., Adams, P.D., Jansen, L.E.T., Almouzni, G., 2011. Dynamics of histone H3 deposition in vivo reveal a nucleosome gap-filling mechanism for H3.3 to maintain chromatin integrity. Mol. Cell 44, 928–941. https://doi.org/10.1016/j.molcel.2011.12.006

Redwood, A.B., Perkins, S.M., Vanderwaal, R.P., Feng, Z., Biehl, K.J., Gonzalez-Suarez, I., Morgado-Palacin, L., Shi, W., Sage, J., Roti-Roti, J.L., Stewart, C.L., Zhang, J., Gonzalo, S., 2011. A dual role for A-type lamins in DNA double-strand break repair. Cell Cycle 10, 2549–2560. https://doi.org/10.4161/cc.10.15.16531

Reis-Sobreiro, M., Chen, J.-F., Novitskaya, T., You, S., Morley, S., Steadman, K., Gill, N.K., Eskaros, A., Rotinen, M., Chu, C.-Y., Chung, L.W.K., Tanaka, H., Yang, W., Knudsen, B.S., Tseng, H.-R., Rowat, A.C., Posadas, E.M., Zijlstra, A., Di Vizio, D., Freeman, M.R., 2018. Emerin deregulation links nuclear shape instability to metastatic potential. Cancer Res. 78, 6086–6097. https://doi.org/10.1158/0008-5472.CAN-18-0608

Rossi, D.J., Bryder, D., Seita, J., Nussenzweig, A., Hoeijmakers, J., Weissman, I.L., 2007. Deficiencies in DNA damage repair limit the function of haematopoietic stem cells with age. Nature 447, 725–729. https://doi.org/10.1038/nature05862

Santi, S., Cenni, V., Capanni, C., Lattanzi, G., Mattioli, E., 2020. PCAF Involvement in Lamin A/C-HDAC2 Interplay during the Early Phase of Muscle Differentiation. Cells 9. https://doi.org/10.3390/cells9071735

Sati, S., Bonev, B., Szabo, Q., Jost, D., Bensadoun, P., Serra, F., Loubiere, V., Papadopoulos, G.L., Rivera-Mulia, J.-C., Fritsch, L., Bouret, P., Castillo, D., Gelpi, J.L., Orozco, M., Vaillant, C., Pellestor, F., Bantignies, F., Marti-Renom, M.A., Gilbert, D.M., Lemaitre, J.-M., Cavalli, G., 2020. 4D Genome Rewiring during Oncogene-Induced and Replicative Senescence. Mol. Cell 78, 522-538.e9. https://doi.org/10.1016/j.molcel.2020.03.007

Scheller, L., Schmollack, M., Bertschi, A., Mansouri, M., Saxena, P., Fussenegger, M., 2020. Phosphoregulated orthogonal signal transduction in mammalian cells. Nat. Commun. 11, 3085. https://doi.org/10.1038/s41467-020-16895-1

Schuettengruber, B., Cavalli, G., 2009. Recruitment of polycomb group complexes and their role in the dynamic regulation of cell fate choice. Development 136, 3531–3542. https://doi.org/10.1242/dev.033902

Sciacovelli, M., Frezza, C., 2017. Metabolic reprogramming and epithelial-to-mesenchymal transition in cancer. FEBS J. 284, 3132–3144. https://doi.org/10.1111/febs.14090

Shi, L., Wen, H., Shi, X., 2017. The histone variant H3.3 in transcriptional regulation and human disease. J. Mol. Biol. 429, 1934–1945. https://doi.org/10.1016/j.jmb.2016.11.019

Shimi, T., Pfleghaar, K., Kojima, S., Pack, C.-G., Solovei, I., Goldman, A.E., Adam, S.A., Shumaker, D.K., Kinjo, M., Cremer, T., Goldman, R.D., 2008. The A- and B-type nuclear lamin networks: microdomains involved in chromatin organization and transcription. Genes Dev. 22, 3409–3421. https://doi.org/10.1101/gad.1735208

Solomon, D.A., Kim, T., Diaz-Martinez, L.A., Fair, J., Elkahloun, A.G., Harris, B.T., Toretsky, J.A., Rosenberg, S.A., Shukla, N., Ladanyi, M., Samuels, Y., James, C.D., Yu, H., Kim, J.-S., Waldman, T., 2011. Mutational inactivation of STAG2 causes aneuploidy in human cancer. Science 333, 1039–1043. https://doi.org/10.1126/science.1203619

Strohecker, A.M., White, E., 2014. Targeting mitochondrial metabolism by inhibiting autophagy in BRAF-driven cancers. Cancer Discov. 4, 766–772. https://doi.org/10.1158/2159-8290.CD-14-0196

Taddei, A., Van Houwe, G., Hediger, F., Kalck, V., Cubizolles, F., Schober, H., Gasser, S.M., 2006. Nuclear pore association confers optimal expression levels for an inducible yeast gene. Nature 441, 774–778. https://doi.org/10.1038/nature04845

Tait, S.W.G., Green, D.R., 2010. Mitochondria and cell death: outer membrane permeabilization and beyond. Nat. Rev. Mol. Cell Biol. 11, 621–632. https://doi.org/10.1038/nrm2952

Taylor, A.M., Shih, J., Ha, G., Gao, G.F., Zhang, X., Berger, A.C., Schumacher, S.E., Wang, C., Hu, H., Liu, J., Lazar, A.J., Network, C.G.A.R., Cherniack, A.D., Beroukhim, R., Meyerson, M., 2018. Genomic and functional approaches to understanding cancer aneuploidy. Cancer Cell 33, 676-689.e3. https://doi.org/10.1016/j.ccell.2018.03.007

Towbin, B.D., González-Aguilera, C., Sack, R., Gaidatzis, D., Kalck, V., Meister, P., Askjaer, P., Gasser, S.M., 2012. Step-wise methylation of histone H3K9 positions heterochromatin at the nuclear periphery. Cell 150, 934–947. https://doi.org/10.1016/j.cell.2012.06.051

Turinetto, V., Orlando, L., Sanchez-Ripoll, Y., Kumpfmueller, B., Storm, M.P., Porcedda, P., Minieri, V., Saviozzi, S., Accomasso, L., Cibrario Rocchietti, E., Moorwood, K., Circosta, P., Cignetti, A., Welham, M.J., Giachino, C., 2012. High basal \gammaH2AX levels sustain self-renewal of mouse embryonic and induced pluripotent stem cells. Stem Cells 30, 1414–1423. https://doi.org/10.1002/stem.1133

Tzur, Y.B., Wilson, K.L., Gruenbaum, Y., 2006. SUN-domain proteins: “Velcro” that links the nucleoskeleton to the cytoskeleton. Nat. Rev. Mol. Cell Biol. 7, 782–788. https://doi.org/10.1038/nrm2003

Vassilev, L.T., Tovar, C., Chen, S., Knezevic, D., Zhao, X., Sun, H., Heimbrook, D.C., Chen, L., 2006. Selective small-molecule inhibitor reveals critical mitotic functions of human CDK1. Proc. Natl. Acad. Sci. U. S. A. 103, 10660–10665. https://doi.org/10.1073/pnas.0600447103

Vega, S., Morales, A.V., Ocaña, O.H., Valdés, F., Fabregat, I., Nieto, M.A., 2004. Snail blocks the cell cycle and confers resistance to cell death. Genes Dev. 18, 1131–1143. https://doi.org/10.1101/gad.294104

Wandke, C., Kutay, U., 2013. Enclosing chromatin: reassembly of the nucleus after open mitosis. Cell 152, 1222–1225. https://doi.org/10.1016/j.cell.2013.02.046

Wang, G.G., Cai, L., Pasillas, M.P., Kamps, M.P., 2007. NUP98-NSD1 links H3K36 methylation to Hox-A gene activation and leukaemogenesis. Nat. Cell Biol. 9, 804–812. https://doi.org/10.1038/ncb1608

Wang, G.G., Song, J., Wang, Z., Dormann, H.L., Casadio, F., Li, H., Luo, J.-L., Patel, D.J., Allis, C.D., 2009. Haematopoietic malignancies caused by dysregulation of a chromatin-binding PHD finger. Nature 459, 847–851. https://doi.org/10.1038/nature08036

Wang, J., Nikhil, K., Viccaro, K., Chang, L., Jacobsen, M., Sandusky, G., Shah, K., 2017. The Aurora-A-Twist1 axis promotes highly aggressive phenotypes in pancreatic carcinoma. J. Cell Sci. 130, 1078–1093. https://doi.org/10.1242/jcs.196790

Watanabe, T., Wu, T.T., Catalano, P.J., Ueki, T., Satriano, R., Haller, D.G., Benson, A.B., Hamilton, S.R., 2001. Molecular predictors of survival after adjuvant chemotherapy for colon cancer. N. Engl. J. Med. 344, 1196–1206. https://doi.org/10.1056/NEJM200104193441603

Wei, Y., Chen, Y.-H., Li, L.-Y., Lang, J., Yeh, S.-P., Shi, B., Yang, C.-C., Yang, J.-Y., Lin, C.-Y., Lai, C.-C., Hung, M.-C., 2011. CDK1-dependent phosphorylation of EZH2 suppresses methylation of H3K27 and promotes osteogenic differentiation of human mesenchymal stem cells. Nat. Cell Biol. 13, 87–94. https://doi.org/10.1038/ncb2139

White, E., 2012. Deconvoluting the context-dependent role for autophagy in cancer. Nat. Rev. Cancer 12, 401–410. https://doi.org/10.1038/nrc3262

Wilson, K.L., Foisner, R., 2010. Lamin-binding Proteins. Cold Spring Harb. Perspect. Biol. 2, a000554. https://doi.org/10.1101/cshperspect.a000554

Wilson, M.M., Weinberg, R.A., Lees, J.A., Guen, V.J., 2020. Emerging Mechanisms by which EMT Programs Control Stemness. Trends Cancer 6, 775–780. https://doi.org/10.1016/j.trecan.2020.03.011

Wong, L.H., Ren, H., Williams, E., McGhie, J., Ahn, S., Sim, M., Tam, A., Earle, E., Anderson, M.A., Mann, J., Choo, K.H.A., 2009. Histone H3.3 incorporation provides a unique and functionally essential telomeric chromatin in embryonic stem cells. Genome Res. 19, 404–414. https://doi.org/10.1101/gr.084947.108

Wong, X., Stewart, C.L., 2020. The Laminopathies and the Insights They Provide into the Structural and Functional Organization of the Nucleus. Annu. Rev. Genomics Hum. Genet. 21, 263–288. https://doi.org/10.1146/annurev-genom-121219-083616

Wood, A.M., Rendtlew Danielsen, J.M., Lucas, C.A., Rice, E.L., Scalzo, D., Shimi, T., Goldman, R.D., Smith, E.D., Le Beau, M.M., Kosak, S.T., 2014. TRF2 and lamin A/C interact to facilitate the functional organization of chromosome ends. Nat. Commun. 5, 5467. https://doi.org/10.1038/ncomms6467

Xu, H., Yan, M., Patra, J., Natrajan, R., Yan, Y., Swagemakers, S., Tomaszewski, J.M., Verschoor, S., Millar, E.K., van der Spek, P., Reis-Filho, J.S., Ramsay, R.G., O'Toole, S.A., McNeil, C.M., Sutherland, R.L., McKay, M.J., Fox, S.B., 2011. Enhanced RAD21 cohesin expression confers poor prognosis and resistance to chemotherapy in high grade luminal, basal and HER2 breast cancers. Breast Cancer Res. 13, R9. https://doi.org/10.1186/bcr2814

Xu, Y., Qin, L., Sun, T., Wu, H., He, T., Yang, Z., Mo, Q., Liao, L., Xu, J., 2017. Twist1 promotes breast cancer invasion and metastasis by silencing Foxa1 expression. Oncogene 36, 1157–1166. https://doi.org/10.1038/onc.2016.286

Yamazaki, T., Souquere, S., Chujo, T., Kobelke, S., Chong, Y.S., Fox, A.H., Bond, C.S., Nakagawa, S., Pierron, G., Hirose, T., 2018. Functional Domains of NEAT1 Architectural lncRNA Induce Paraspeckle Assembly through Phase Separation. Mol. Cell 70, 1038-1053.e7. https://doi.org/10.1016/j.molcel.2018.05.019

Yang, J.-M., Bhattacharya, S., West-Foyle, H., Hung, C.-F., Wu, T.-C., Iglesias, P.A., Huang, C.-H., 2018. Integrating chemical and mechanical signals through dynamic coupling between cellular protrusions and pulsed ERK activation. Nat. Commun. 9, 4673. https://doi.org/10.1038/s41467-018-07150-9

Yang, L., Besschetnova, T.Y., Brooks, C.R., Shah, J.V., Bonventre, J.V., 2010. Epithelial cell cycle arrest in G2/M mediates kidney fibrosis after injury. Nat. Med. 16, 535–43, 1p following 143. https://doi.org/10.1038/nm.2144

Ye, J., Zhang, Y., Cui, H., Liu, J., Wu, Y., Cheng, Y., Xu, H., Huang, X., Li, S., Zhou, A., Zhang, X., Bolund, L., Chen, Q., Wang, J., Yang, H., Fang, L., Shi, C., 2018. WEGO 2.0: a web tool for analyzing and plotting GO annotations, 2018 update. Nucleic Acids Res. 46, W71–W75. https://doi.org/10.1093/nar/gky400

Yin, L., Jiang, L.-P., Shen, Q.-S., Xiong, Q.-X., Zhuo, X., Zhang, L.-L., Yu, H.-J., Guo, X., Luo, Y., Dong, J., Kong, Q.-P., Yang, C.-P., Chen, Y.-B., 2017. NCAPH plays important roles in human colon cancer. Cell Death Dis. 8, e2680. https://doi.org/10.1038/cddis.2017.88

Youle, R.J., Strasser, A., 2008. The BCL-2 protein family: opposing activities that mediate cell death. Nat. Rev. Mol. Cell Biol. 9, 47–59. https://doi.org/10.1038/nrm2308

Yusufzai, T.M., Tagami, H., Nakatani, Y., Felsenfeld, G., 2004. CTCF tethers an insulator to subnuclear sites, suggesting shared insulator mechanisms across species. Mol. Cell 13, 291–298. https://doi.org/10.1016/s1097-2765(04)00029-2

Zeitlin, S.G., Baker, N.M., Chapados, B.R., Soutoglou, E., Wang, J.Y.J., Berns, M.W., Cleveland, D.W., 2009. Double-strand DNA breaks recruit the centromeric histone CENP-A. Proc. Natl. Acad. Sci. U. S. A. 106, 15762–15767. https://doi.org/10.1073/pnas.0908233106

Zhang, X., Cook, P.C., Zindy, E., Williams, C.J., Jowitt, T.A., Streuli, C.H., MacDonald, A.S., Redondo-Muñoz, J., 2016. Integrin \alpha4\beta1 controls G9a activity that regulates epigenetic changes and nuclear properties required for lymphocyte migration. Nucleic Acids Res. 44, 3031–3044. https://doi.org/10.1093/nar/gkv1348

Zhao, L., Yang, Y., Yin, S., Yang, T., Luo, J., Xie, R., Long, H., Jiang, L., Zhu, B., 2017. CTCF promotes epithelial ovarian cancer metastasis by broadly controlling the expression of metastasis-associated genes. Oncotarget 8, 62217–62230. https://doi.org/10.18632/oncotarget.19216

Zheng, L., Baumann, U., Reymond, J.-L., 2004. An efficient one-step site-directed and site-saturation mutagenesis protocol. Nucleic Acids Res. 32, e115. https://doi.org/10.1093/nar/gnh110

Zhou, L., Panté, N., 2010. The nucleoporin Nup153 maintains nuclear envelope architecture and is required for cell migration in tumor cells. FEBS Lett. 584, 3013–3020. https://doi.org/10.1016/j.febslet.2010.05.038

# Appendix 1

## Sequences of siRNA

| Gene | Sequence |
|---|---|
| si LMNA | 5’ CAGUCUGCUGAGAGGAACA 3’ |
| si LacZ | 5’ CGUACGCGGAAUACUUCGA 3’ |
| siLMNB1 | 5’ AGACAAAGAGAGAGAGAUG 3’ |
| siLMNB2 | 5’ GAGCAGGAGAUGACGGAGA 3’ |

# Appendix 2

## List of plasmids

| Plasmid | Addgene Number | Vector |
|---|---|---|
| pEGFPN1-hTwist1-GFP | This thesis | Transient transfection |
| pBP-mTWIST1 | 1783 | Retroviral vector |
| pLVX-GRHL2-GFP | Ruby Yun-Ju Huang | Lentiviral vector |
| pLKO-Tet-on-GRHL2 | Ruby Yun-Ju Huang | Lentiviral vector |
| pLKO-Tet-on-shLMNA | This thesis | Lentiviral vector |
| pLKO-Tet-on-shEZH2 | This thesis | Lentiviral vector |
| pLVX-LMNA-GFP(shResistant) | This thesis | Lentiviral vector |
| pLVX-LMNA(S22A)-GFP(shResistant) | This thesis | Lentiviral vector |
| pLVX-LMNA(S22D)-GFP(shResistant) | This thesis | Lentiviral vector |
| MSCV-EZH2-FLAG(shResistant) | This thesis | Retroviral vector |
| MSCV-EZH2(T345A)-FLAG(shResistant) | This thesis | Retroviral vector |
| MSCV-EZH2(T345D)-FLAG(shResistant) | This thesis | Retroviral vector |
| psPAX2 | 12260 | Lentiviral vector |
| pMD2G | 12259 | Lentiviral vector |
| Gag.Pol | 14887 | Retroviral vector |
| VSV-G | 8454 | Retroviral vector |
| ΔHead-LMNA-GFP | This thesis | Lentiviral vector |
| Δcentral helical rod-LMNA-GFP | This thesis | Lentiviral vector |
| ΔIgG-LMNA-GFP | This thesis | Lentiviral vector |
| Δtail-LMNA-GFP | This thesis | Lentiviral vector |
| Δ1-300-EZH2-FLAG | This thesis | Retroviral vector |
| Δ301-500-EZH2-FLAG | This thesis | Retroviral vector |
| Δ501-756-EZH2-FLAG | This thesis | Retroviral vector |

# Appendix 3

## List of antibodies used

| IMMUNOFLOURSCENCE ASSAY | | | | |
|---|---|---|---|---|
| **Host** | **Antibody** | **Vendor** | **Cat No** | **Dilution** |
| Mouse | E-Cadherin | Abcam | ab1416 | 1:1000 |
| Rabbit | Vimentin | Abcam | ab92547 | 1:1000 |
| Rabbit | Lamin A/C | Abcam | ab108595 | 1:1000 |
| Mouse | Lamin A/C | Abcam | ab40567 | 1:50 |
| Rabbit | EZH2 | Cell Signaling Technology | 5246S | 1:1000 |
| Rabbit | pCDK1 | Cell Signaling Technology | 9114S | 1:1000 |
| Mouse | BrdU | Abcam | ab8955 | 1:1000 |
| Rabbit | H3S10p | Cell Signaling Technology | 3377S | 1:1000 |

# Appendix 4

## List of antibodies

| IMMUNOBLOTTING | | | | |
|---|---|---|---|---|
| **Host** | **Antibody** | **Vendor** | **Cat No** | **Dilution** |
| Rabbit | Zeb1 | Cell Signaling Technology | 3396T | 1:1000 |
| Rabbit | EZH2(Thr345p) | Cell Signaling Technology | 45153S | 1:1000 |
| Rabbit | EZH2 | Cell Signaling Technology | 5246S | 1:1000 |
| Mouse | E-Cadherin | Abcam | ab1416 | 1:1000 |
| Rabbit | Vimentin | Abcam | ab92547 | 1:1000 |
| Rabbit | pSmad3 | Abcam | ab52903 | 1:1000 |
| Rabbit | Smad3 | Abcam | ab28379 | 1:1000 |
| Rabbit | Lamin A/C(Ser22p) | Cell Signaling Technology | 13448T | 1:1000 |
| Rabbit | Lamin A/C | Abcam | ab108595 | 1:1000 |
| Rabbit | Cyclin B1 | Cell Signaling Technology | 12231S | 1:1000 |
| Rabbit | CDK1(Thr161p) | Cell Signaling Technology | 9114S | 1:1000 |
| Mouse | CDK1 | Cell Signaling Technology | 9116S | 1:1000 |
| Rabbit | Lamin B1 | Abcam | ab20396 | 1:1000 |
| Mouse | Lamin B2 | Abcam | ab8983 | 1:1000 |
| Rabbit | Suv39H1 | Cell Signaling Technology | 8729T | 1:1000 |
| Rabbit | G9a | Cell Signaling Technology | 68851T | 1:1000 |
| Rabbit | HSP70 | Abcam | ab181606 | 1:1000 |
| Rabbit | GAPDH | Sigma-Aldrich | G9545 | 1:7000 |
| Rabbit | Snail1 | Cell Signaling Technology | 3879S | 1:1000 |
| Mouse | Twist1 | Abcam | ab50887 | 1:1000 |
| Rabbit | H3K27me3 | Millipore | 07-449 | 1:1000 |
| Rabbit | H3K9me3 | Abcam | ab176916 | 1:1000 |
| Rabbit | H3 | Abcam | ab1791 | 1:3000 |
| Rabbit | N-terminal GFP | Sigma-Aldrich | G1544 | 1:1000 |
| Rabbit | Anti-FLAG | Cell Signaling Technology | 14793T | 1:1000 |
| Rabbit | GRHL2 | Sigma-Aldrich | HPA004820 | 1:1000 |

# Appendix 5

## List of primers used for RT-qPCR

| Gene | Forward Primer | Reverse Primer |
|---|---|---|
| E-Cadherin | TGGTACCTGGCAAGATGCAG | GGGGGCTTCATTCACATCCA |
| Vimentin | CTCTGGCACGTCTTGACCTT | TTGCGCTCCTGAAAAACTGC |
| Zeb1 | GAGAGGATCATGGCGGATGG | TTACACCCAGACTGCGTCAC |
| Snail1 | CTCGGACCTTCTCCCGAATG | AAAGTCCTGTGGGGCTGATG |
| Twist1 | GCGCTGGGGAAGATCATC | GGTCTGAATCTTGCTCAGCTT |
| Lamin A/C | CTCCACTGGGGAAGAAGTGG | CCCATCTCTTGTATGATGCTGC |
| Lamin B1 | AGCTAAGTGCAGGGAGCTATG | TCATGCGGCTTTCCATCAGT |
| Lamin B2 | TTTTCCACCAACAGGGGGAC | ACGTTCTGGCAGTTCGCTTA |
| GAPDH | CGAGATCCCTCCAAAATCAAG | GCAGAGATGATGACCCTTTTG |

# Appendix 6

## List of primers used for ChIP-qPCR

| Gene | Forward Primer | Reverse Primer |
|---|---|---|
| SNAI1_-1kb | AAAGGCCGTGGCATTTCAAG | CATTGACGAGGGAAACGCAC |
| TWIST1_-1kb | TGGGTCGTTGTAGAGGGGAA | CCTTGGAGTTCCAAAGGCCA |
| ZEB1_-1kb | TTGCTGGCTTGTGGACATGA | GTGACAGGGGAAATCAGGCA |
| DEFA3_-1kb | TCTCACATTGGCACGTCCTC | TAACACAAGAGAGTGCGCGT |
| GAPDH_+1kb | GGGCTTGTGTCAAGGTGAGA | CGAAGCAAGCAAGGCTGTTT |
| MYT1_+1kb | AGCCATGTCTGAAGGCACTC | TGCATTGGCTTTTTGGCCTT |

# Appendix 7

## List of primers used in cloning

| Plasmid | | Cloning Primer sequence |
|---|---|---|
| Lamin A _shRNA resistant_F | | AAAGAATTCatggagaccccgtcccag |
| Lamin A _shRNA resistant_R | | aaaggatccttacatgatgctgcagt |
| EZH2_shRNA resistant_1F | | gacagctcaaacggttcagaag |
| EZH2_shRNA resistant_1R | | cttctgaaccgtttgagctgtc |
| EZH2T345A_F | | CTGAGCGGATAAAGGCACCACCTAAACGC |
| EZH2T345A_R | | GCGTTTAGGTGGTGCCTTTATCCGCTCAG |
| EZH2T345D_F | | TGCTGAGCGGATAAAGGACCCACCTAAACGCCCAG |
| EZH2T345D_R | | CTGGGCGTTTAGGTGGGTCCTTTATCCGCTCAGCA |
| Lamin A S22A_F | | CACTCCGCTGGCGCCCACCC |
| Lamin A S22A_R | | CGGGTGGGCGCCAGCGGAGTG |
| Lamin A S22D_F | | CTCCACTCCGCTGGATCCCACCCGCAT |
| Lamin A S22D_R | | ATGCGGGTGGGATCCAGCGGAGTGGAG |
| ΔHead (1-29)_R | | ctgcagccgggtgatgcg |
| ΔHead (1-29)_F | | caggagaaggaggacctgcaggagctc |
| ΔRod (31–387)_R | | ctgcagccgggtgatgcg |
| ΔRod (31–387)_F | | cgcctgtcccccagccct |
| ΔIgG (428-549)_R | | tgcgtgctgtgagaagct |
| ΔIgG (428-549)_F | | gttgaggacgacgaggatgag |
| ΔTail (550-664)_R | | ctcatcctcgtcgtcctcaaccacagt |
| ΔTail (550-664)_F | | ggatcccgcccctctccct |
| EZH2 del(1-300)_R | | ggtggccaggatctaattc |
| EZH2 del(1-300)_F | | tatgactgcttcctacatccc |
| EZH2 del(301-500)_R | | atacttaaaacatcgtcgacagaagag |
| EZH2 del(301-500)_F | | aaaaggaaacatcggttgtgg |
| EZH2 del(501-746)_R | | tttcttctttcttggaggagtgtc |
| EZH2 del(501-746)_F | | ggcatcgaacgagaaatggaa |

## List of publications

1. **Balaji AK**, Santam Saha, Kundan Sengupta; Phosphorylation-dependent modulation of the Lamin A/C–EZH2 complex regulates epithelial–mesenchymal plasticity; Nucleic acids research – 2026 Nucleic Acids Research, 2026, gkaf1464 https://doi.org/10.1093/nar/gkaf1464

2. Saha, S., **Balaji AK**, Meel, S., Notani, D., & Sengupta, K. (2025). Fibrillarin regulates epithelial integrity via EZH2-mediated modulation of scribble expression. Cell Reports, 44(12), 116608. https://doi.org/10.1016/j.celrep.2025.116608

3. **Balaji AK**, Saha S, Deshpande S, Poola D and Sengupta K (2022), Nuclear envelope, chromatin organizers, histones, and DNA: The many achilles heels exploited across cancers. Front. Cell Dev. Biol. 10:1068347. doi: 10.3389/fcell.2022.1068347

*Nucleic Acids Research*, 2026, **54**, gkaf1464
https://doi.org/10.1093/nar/gkaf1464
**Gene regulation, Chromatin and Epigenetics**

# Phosphorylation-dependent modulation of the Lamin A/C–EZH2 complex regulates epithelial–mesenchymal plasticity

**Balaji AK, Santam Saha, Kundan Sengupta** *

B-216, Chromosome Biology Lab, Biology, Indian Institute of Science Education and Research (IISER), Pune, Dr Homi Bhabha Road, Pashan, Pune 411008, Maharashtra, India

*To whom correspondence should be addressed. Email: kunsen@iiserpune.ac.in

## Abstract

Epithelial-to-mesenchymal transition (EMT) is essential for normal development and cancer progression. However, how nuclear Lamins regulate EMT is unclear. Here, we show that Lamin A/C modulates the epithelial–mesenchymal (E-M) plasticity of cells through its interaction with the chromatin organizer, EZH2. The overexpression of Lamin A reinforces an epithelial identity, while its depletion promotes a mesenchymal phenotype. This positions Lamin A/C as a crucial modulator of Epithelial-Mesenchymal plasticity. Furthermore, CDK1-mediated phosphorylation of Lamin A/C (Ser22) and EZH2 (Thr345) disrupts Lamin A/C–EZH2 interaction, destabilizing EZH2, with a concomitant decrease in the occupancy of the heterochromatin mark (H3K27me3) on the *SNAI1*, *TWIST1*, and *ZEB1* promoters, thereby facilitating a transition towards mesenchymal transcriptional programs. Conversely, phosphodeficient Lamin A/C (S22A) and EZH2 (T345A) mutants restore epithelial identity, highlighting a regulatory role of the Lamin A/C–EZH2 axis in maintaining epithelial homeostasis. *In vivo*, xenograft assays in NOD-SCID mice reveal that while phosphorylated Lamin A/C or EZH2 promote tumor growth and metastasis, phospho-deficient mutants markedly suppress it. Lamin A/C–EZH2 interaction regulates the expression of E–M-associated transcription factors, highlighting the role of this interaction in modulating transcriptional plasticity, thereby serving as a potential therapeutic target for regulating metastasis in breast cancers.

## Graphical abstract

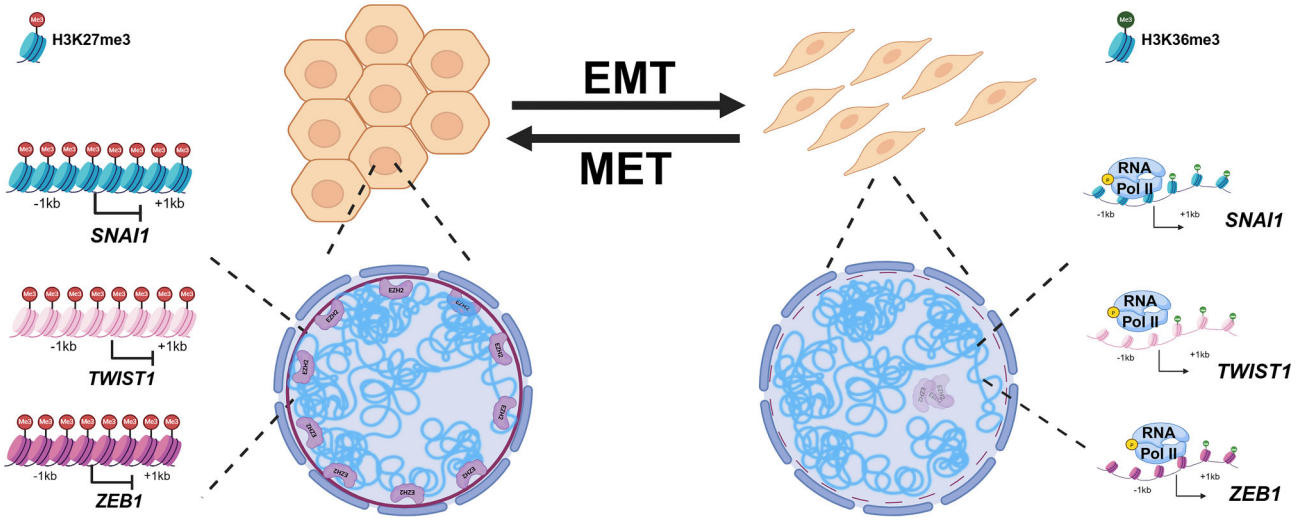


## Introduction

Epithelial-to-Mesenchymal Transition (EMT) and Mesenchymal-to-Epithelial Transition (MET) are fundamental biological processes that play critical roles in embryonic development, wound healing, and tissue homeostasis [1]. EMT is essential for gastrulation, somite formation and neural crest cell migration, while the converse of EMT i.e. MET is essential for organogenesis, such as kidney development and the formation of epithelial somites surrounding the core of mesenchymal cells [2, 3]. During EMT, epithelial cells show

**Received:** June 3, 2025. **Revised:** November 26, 2025. **Accepted:** November 30, 2025

loss of polarity and cell–cell adhesion, which confer migratory and invasive characteristics that are typical of mesenchymal cells [4]. Conversely, MET induces enhanced cell–cell adhesion, decreases motility, restoring epithelial characteristics, enabling tissue differentiation and organogenesis [5]. While these processes are essential for normal physiology, they are subverted during cancer progression, fibrosis, and organ dysfunction [6]. EMT facilitates cells to invade the surrounding tissues and MET is crucial for the colonization of metastatic cells and integration into the secondary tissue. Rather than representing a binary switch, epithelial-to-mesenchymal plasticity (EMP) encompasses hybrid epithelial–mesenchymal (E-M) states that confer metastatic competence and survival advantages. Lineage-tracing and single-cell studies reveal that these hybrid states often underlie tumor dissemination, metastatic colonization, resistance to chemotherapy and recurrence, making it imperative to understand how tumor cells dynamically modulate EMP during cancer progression [7–10]. The transition between these phenotypic states (E and M) involves an intricate coordination among transcription factors, signalling pathways, and epigenetic mechanisms. However, the underlying mechanisms on how each of these processes crosstalk with one another are not fully understood [11].

During EMT, epithelial factors such as E-cadherin are downregulated, while mesenchymal markers—Vimentin, N-cadherin, and fibronectin—are upregulated, driven by transcription factors TWIST1, SNAI1, and ZEB1 [12]. Conversely, during MET, the activity of these transcription factors is attenuated, re-expressing epithelial factors, and suppressing mesenchymal properties [13]. However, the crosstalk between nuclear architecture and chromatin organization in regulating EM plasticity is unclear.

Lamin A/C, a core component of the nuclear lamina, provides structural support to the nucleus and maintains genome organization. It regulates chromatin architecture and gene expression, and its depletion increases nuclear deformability, alters chromatin accessibility, and enhances cellular plasticity [14–18]. Despite these broad nuclear functions, its direct role in EMT or MET remains unclear.

Lamin A/C regulates transcriptional programs through interactions with chromatin modifiers and transcriptional repressors. Notably, the Polycomb Repressive Complex 2 (PRC2), a histone methyltransferase, silences target genes via deposition of the repressive mark H3K27me3 [19, 20]. This connection suggests that Lamin A/C could modulate EM plasticity by coordinating with PRC2 components, such as EZH2 (the catalytic subunit of PRC2), thereby linking integrity of nuclear lamina to epigenetic regulation and transcriptional control. EZH2 is a well-established epigenetic regulator implicated in EMT [21]. However, the mechanisms by which Lamin A/C modulates EZH2 activity and if this interaction impacts E–M plasticity are largely unknown. Considering the central importance of epigenetic regulation in cancer initiation and progression, understanding the interplay between nuclear and chromatin organizers, namely Lamin A/C and EZH2 respectively, will uncover novel therapeutic targets to modulate EMT and MET dynamics in aggressive malignancies.

Here, we systematically investigate the role of Lamin A/C and EZH2 in EMT and MET using well-characterized paradigms of mammary breast epithelial cells and breast cancers. We demonstrate that depletion of Lamin A/C or EZH2 facilitates EMT, whereas its overexpression promotes MET, underscoring its role in maintaining epithelial identity. Furthermore, we identify that CDK1-mediated phosphorylation regulates the interaction between Lamin A/C-EZH2 altering their chromatin occupancy during EMT and MET. Integrative analyses involving transcriptomic, proteomic, and functional data, collectively provide crucial mechanistic insights into how nuclear Lamins contribute to EM plasticity. By elucidating the interplay between Lamin A/C and EZH2, this study elucidates the functional relevance of the interactome of nuclear Lamins in cancer progression. Our findings highlight the regulatory role of the phosphorylation of Lamin A/C in modulating EMT and implicate the Lamin A/C-EZH2 axis as a key target for novel therapeutic interventions in metastatic breast cancers.

## Materials and methods

### Cell culture

Immortalized human breast epithelial cell line MCF10A (CRL-10317) and cancer cell lines MCF7 (HTB-22), and MDAMB231 (HTB-26) were obtained from ATCC. MCF10A cells were maintained in Dulbecco's modified Eagle's medium (DMEM)/F12 (1:1) supplemented with 5% horse serum, EGF (20 ng/ml), hydrocortisone (0.5 mg/ml), cholera toxin (0.1 mg/ml), insulin (10 mg/ml), and 1% penicillin–streptomycin. MCF7 and MDAMB231 cells were cultured in DMEM and Roswell Park Memorial Institute (RPMI), respectively, supplemented with 10% fetal bovine serum (FBS), 1% L-glutamine, and 1% penicillin–streptomycin. All cells were grown at 37°C with 5% $CO_2$. The cell types were validated based on morphology (Supplementary Fig. S1A), chromosome numbers (Supplementary Fig. S1B), and profile of key E and M markers (Supplementary Fig. S1C–G). Furthermore, 4′,6-diamidino-2-phenylindole (DAPI) staining did not show any visible extranuclear staining, negating mycoplasma contamination.

### EMT induction in MCF7 upon TWIST1 overexpression

MCF7 cells (∼0.35 million) were seeded in six-well plates and allowed to adhere for ∼10–12 h, to attain a confluency of ∼50%. Cells were independently transfected with 2 μg of pEGFPN1 (Empty vector) or TWIST1 in Opti-MEM using polyethyleneimine (PEI; Sigma #408727-100ML) at a ratio of 1:3 plasmid: branched PEI. After ∼6 h post-transfection, Opti-MEM was replaced with DMEM containing 10% FBS. Transfected cells were selected with G418 (890 μg/ml, Roche #4727878001) for 24 h. Cells were harvested for reverse transcriptase-polymerase chain reaction (RT-PCR), immunofluorescence assay, or immunoblotting at ∼48 h post-transfection to assess for expression of E and M marks, respectively [22, 23].

### TGF-β mediated EMT induction

MCF10A cells (∼0.15 million) were seeded at a confluency of (∼30%–40%) in each well of a six-well plate and allowed to adhere overnight (∼16 h). MCF10A cells were treated with recombinant human TGF-β1 (10 ng/ml, PeproTech, #100-21) to induce EMT in complete growth medium. Media containing fresh TGF-β1 was replenished every ∼48 h for a total duration of 7 days. Control cells were maintained in complete media without TGF-β [24, 25].

### GRHL2 mediated MET induction

MET was induced by overexpression of GRHL2 using the lentiviral vector pLVX-TetOn-Puro-GRHL2 (gift from Dr Ruby Yun-Ju Huang, National Taiwan University). Lentiviral particles were generated by transfecting HEK293T cells ($\sim 1 \times 10^6$) with 8 μg plasmid DNA using branched PEI (1:3 DNA:PEI ratio). Viral supernatants collected at 48 and 72 h, were filtered using a 0.45 μm filter and used to transduce MDAMB231 cells ($\sim 1 \times 10^6$) in the presence of 8 μg/ml polybrene (Sigma #H9268). Cells were selected with puromycin (2 μg/ml, 2 days) and GRHL2 overexpression was validated by immunoblotting (Fig. 1I) [26, 27].

### small interfering RNA (siRNA) transfection

MCF7, MCF10A, and MDA-MB-231 cells (~0.35 million) were seeded in six-well plates or 35 mm dishes ~24 h prior to transfection. Cells were cultured in Opti-MEM and transfected with 50 nM siRNA using 4 μl of RNAiMAX (Invitrogen #13778150). After ~6 h, Opti-MEM was replaced with DMEM with 10% FBS for a total duration of ~48 h. Cells were harvested for immunofluorescence assay, RT-PCR, or immunoblotting post-transfection.

### Retroviral transduction

HEK293T cells (~1 million) were transfected with ~8 μg of the retroviral plasmid of interest (Supplementary Table 4), 4 μg of packaging plasmid Gag-Pol (Plasmid #14887), and VSV-G (2 μg, Plasmid #14888) using PEI (~42 μl), in the ratio of DNA:PEI = 1:3 (w/v). Viral supernatant (~8 ml) was collected ~48 h post-transfection from HEK293T cells and added to ~0.35 million cells (~1.5 ml; seeded at ~0.35 million cells per well in a six-well plate). Polybrene (10 μg/ml ~10 μl Sigma #H9268) was added to facilitate viral attachment and entry. This procedure was repeated at ~72 h post-transfection. Cells were selected using puromycin (2 μg/ml, Gibco #A1113802; for pBabe-Puro constructs) for ~48 h or hygromycin (50 μg/ml, Gibco #10687010; for MSCV-F-Hygro constructs) for ~24 h [28].

### Lentiviral transduction

HEK293T cells were co-transfected with the transfer vector (8 μg), packaging plasmid psPAX2 (4 μg; Addgene #12260), and envelope plasmid pMD2.G (2 μg; Addgene #12259) using PEI (DNA:PEI = 1:3, w/v). Viral supernatants were collected at 48 and 72 h post-transfection and used to transduce target cells ($\sim 3.5 \times 10^5$ cells/well in a six-well plate) in the presence of 10 μg/ml polybrene. Transduced cells were selected with 2 μg/ml puromycin for 2 days [29].

### Immunofluorescence

Cells ($\sim 3.5 \times 10^5$) were seeded on 22 × 22 mm coverslips and fixed with 4% paraformaldehyde in 1× phosphate buffered saline (PBS; pH 7.4) for 15 min at room temperature (RT), followed by permeabilization with 0.5% Triton X-100 for 10 min. After blocking with 1% bovine serum albumin (BSA) in 1× PBS for 30 min, cells were incubated with primary antibodies for 90 min at RT. Cells were incubated with Alexa Fluor-conjugated secondary antibodies (488 or 568; Invitrogen, 1:1000) for 1 h, followed by DAPI counterstaining (0.05 μg/ml, 2 min). Coverslips were mounted in SlowFade Gold Antifade Reagent (Invitrogen, S36937) and stored at 4°C until imaging. Dilutions and Catalogue numbers of antibodies used are listed in Supplementary Table 4.

### Imaging and acquisition parameters

Confocal microscopy was performed using a Zeiss LSM 710 microscope (Carl Zeiss, Thornwood, NJ, USA) equipped with a 63 × Plan-Apochromat 1.4 NA oil immersion objective and an AxioCam MRm Rev.3 charge-coupled device camera (Zeiss). Images were acquired at a zoom of 1.0 as Z-stacks at a resolution of 512 × 512 pixels per frame with an 8-bit pixel depth per channel. Voxel size was set to 0.105 μm × 0.105 μm × 0.34 μm, with line averaging of 4.0 in sequential three-channel mode. Fluorescence signals were detected appropriately with filters for DAPI, Alexa Fluor-488, and Alexa Fluor-568. Image processing and analysis were performed using ImageJ software.

### Immunoblotting

Cells were lysed in Radioimmunoprecipitation Assay (RIPA) buffer [50 mM Tris–HCl, pH 7.4–8.0, 150 mM NaCl, 1% NP-40, 0.1% sodium dodecyl sulphate (SDS), 0.5% sodium deoxycholate, 1 mM ethylenediaminetetraacetic acid (EDTA)] supplemented with protease and phosphatase inhibitors (Roche) for 10 min at 4°C. Protein concentration was determined using the Bicinchoninic Acid (BCA) assay. Equal amounts of protein were resolved on 12.5% sodium dodecyl sulphate–polyacrylamide gel electrophoresis (SDS–PAGE) and transferred to Polyvinylidene Fluoride (PVDF) membranes (0.45 μm; Millipore #IPVH00010) at 100 V for 2 h at 4°C. Membranes were blocked in 5% milk or 5% BSA in TBST (20 mM Tris–HCl, pH 7.5, 150 mM NaCl, 0.1% Tween-20) for 1 h and incubated overnight at 4°C with primary antibodies (1:1000 unless stated otherwise) against E-Cadherin, Vimentin, ZEB1, EZH2, pEZH2(T345), Lamin A/C, pLamin A/C(S22), pSmad3, Smad3, SUV39H1, Lamin B1, Lamin B2, Cyclin B1, Snail1, GRHL2, pCDK1, Twist1, GAPDH (1:7000) H3K27me3, H3K9me3, and H3 (1:3000). After washing, membranes were incubated with horseradish peroxidase-conjugated secondary antibodies (anti-rabbit #111-035-003; anti-mouse #515-035-003; Jackson Labs; 1:10 000) for 1 h at RT. Bands were visualized using ECL substrate (Bio-Rad #1705061) and imaged on LAS4000 (GE). Densitometric quantification was performed using ImageJ. Dilutions and Catalogue numbers of primary antibodies used are listed in Supplementary Table 4.

## RT-PCR

### RNA isolation

Cells ($\sim 3 \times 10^5$) were seeded in six-well plates and lysed in 1 ml TRIzol reagent (Invitrogen #15596018). Chloroform (100 μl per 500 μl TRIzol) was added, and samples were vortexed, incubated for 10 min at RT, and centrifuged at 12 000 × *g* for 15 min at 4°C. The aqueous phase was mixed with an equal volume of isopropanol, incubated for 15 min, and centrifuged at 12 000 × *g* for 15 min at 4°C. RNA pellets were washed with 70% ethanol, air-dried, and resuspended in nuclease-free water. RNA concentration and purity were measured using a NanoDrop spectrophotometer.

### Complementary DNA synthesis and quantitative real-time PCR

Complementary DNA was synthesized from 1 μg total RNA using the PrimeScript RT Reagent Kit (Takara #6110B) with oligo(dT) and random hexamer primers. Quantitative PCR was performed using TB Green Premix Ex Taq II (Takara #RR820W) on a Bio-Rad CFX96 system under the following conditions: 95°C for 30 s, followed by 40 cycles of 95°C for 5 s and 60°C for 30 s. Melt-curve analysis (60–95°C, 0.3°C/s) confirmed amplicon specificity. Relative gene expression was calculated using the $2^{-\Delta\Delta Ct}$ method with GAPDH as the internal control and untreated samples as the reference.

### Co-immunoprecipitation

Cells (~1 × $10^7$) were lysed in co-immunoprecipitation (Co-IP) buffer (50 mM Tris–HCl, pH 8.0, 300 mM NaCl, 0.5% NP-40) supplemented with protease inhibitors (Roche #5892970001) and incubated on ice for 15 min. Lysates were cleared by centrifugation at 14 000 rpm for 15 min at 4°C, and protein concentration was determined by BCA assay. For each reaction, 2 μg of antibody or normal rabbit IgG (control) was pre-bound to Protein A–Sepharose beads (Roche #P3391) for 4 h at 4°C. Equal amounts of lysate (~500 μg total protein) were added and incubated overnight at 4°C with rotation. Beads were washed 5–6 times with a cold Co-IP buffer and eluted in 2 × Laemmli buffer at 95°C for 10 min. Eluates were resolved by SDS–PAGE and analyzed by immunoblotting. Antibodies used: anti-Lamin A/C (Abcam #ab108595), anti-EZH2 (CST #5246), and normal rabbit IgG (Invitrogen #10500C).

### Chromatin immunoprecipitation

Cells (~1 × $10^7$) were crosslinked with 1% formaldehyde in 1× PBS (pH 7.5) for 10 min at RT, and the reaction was quenched with 125 mM glycine for 5 min. Cells were washed twice with cold PBS and lysed in a buffer containing 1% SDS, 10 mM EDTA, and 50 mM Tris–HCl (pH 8.1) supplemented with protease inhibitors. Chromatin was sonicated (Covaris S220; 60% duty cycle, 30 s on/off for 30 min) to ~200–500 bp fragments, verified by agarose gel electrophoresis.

For each IP, 25 μg of chromatin was diluted in ChIP dilution buffer (0.01% SDS, 1% Triton X-100, 1.2 mM EDTA, 16.7 mM Tris–HCl, pH 8.1, 167 mM NaCl) and incubated overnight at 4°C with antibody-bound Protein A/G agarose beads. The following antibodies were used: Lamin A/C (Abcam #ab108595), EZH2 (CST #5246), H3K27me3 (Millipore #07-449), H3K36me3 (Abcam #ab9050), RNA Pol II (Ser2p; Covance #MMS-129R), and control IgG (Invitrogen #10500C). Beads were sequentially washed with low-salt, high-salt, LiCl, and TE buffers and eluted in 1% SDS, 0.1 M $NaHCO_3$. Eluates were treated with proteinase K (2 μl, 20 mg/ml, 55°C, 30 min), and crosslinks were reversed at 65°C for 4–6 h. DNA was purified using PCR purification columns (Promega #A9281) and analyzed by qPCR [30, 31].

### Co-IP and mass spectrometry analysis

Endogenous Lamin A/C–interacting proteins were identified by Co-IP followed by Liquid Chromatography-Tandem Mass Spectrometry (LC–MS/MS) analysis [32, 33]. Briefly, MCF7−TWIST1(EV), MCF7+TWIST1, MDAMB231−Dox (−GRHL2), and MDAMB231+Dox (+GRHL2) cells (~1 × $10^7$) were lysed in Co-IP buffer (50 mM Tris–HCl, pH 7.5; 150 mM NaCl; 1% NP-40) containing protease inhibitors. Clarified lysates (1 mg) were incubated overnight at 4°C with Protein A magnetic beads (SureBeads, Bio-Rad #161-4013) pre-bound to anti-Lamin A/C antibody (2 μg, Abcam #ab108595) or control IgG (Invitrogen #10500C). Immunocomplexes were washed, eluted in 2 × Laemmli buffer at 95°C, and resolved by SDS–PAGE.

Coomassie-stained gel bands (~2 cm) were excised, reduced (10 mM Dithiothreitol (DTT)), alkylated (55 mM iodoacetamide), and digested with sequencing-grade trypsin (Promega #V5111). Peptides were extracted, desalted on C18 columns, and analyzed on a Sciex TripleTOF 6600 mass spectrometer coupled to an Eksigent nano-LC 425 system. Data were processed using ProteinPilot (v2.0.1, Sciex) and searched against the human UniProt database.

The Lamin A/C interactome under EMT and MET conditions is provided in Supplementary Tables 2 and 3, respectively. The mass spectrometry (MS) data are available in the PRIDE repository (Dataset ID: PXD060831).

### RNA sequencing

MCF10A cells (~0.35 million) were plated in six-well plates or 35 mm dishes around 24 h before transfection. The cells were maintained in Opti-MEM and transfected with 50 nM siRNA using 4 μl of RNAiMAX (Invitrogen #13778150). Transfection (was for ~6 h), after which the Opti-MEM medium was replaced with complete media, and the cells were incubated for ~48 h. Following transfection, MCF10A cells were collected in 1 ml TRIzol, and RNA sequencing (RNA-Seq) was outsourced to Medgenome, Bangalore. Quality control checks for the two independent biological replicates were confirmed through RNA Integrity Number (RIN) number analysis (RIN = 10, for all samples). RNA-Seq data are provided in Supplementary Table 1. The datasets have been deposited in Gene Expression Omnibus under accession number GSE289750.

### Cell cycle analysis

Cells (~0.3 million) were harvested by trypsinization, washed with 1× PBS (pH = 7.5), and fixed in 70% ice-cold ethanol at 4°C, overnight. The fixed cell pellets were resuspended in 1× PBS and treated with RNase A (10 μg; Sigma, R6513-10MG) at 37°C for 45 min. Subsequently, propidium iodide (PI; 10 μg; Sigma, P4170-10MG) was added to the samples for DNA staining. The cell suspensions were passed through a 70 μm cell strainer (Corning, CLS431751) and processed for further analysis. Cell cycle profiling was performed using a fluorescence-activated cell scanner (BD FACSCalibur™, BD Biosciences) with approximately 10,000 events recorded per sample. Data were analyzed using FlowJO (V10.10) software.

### Transwell migration (Boyden-chamber assay)

Cells (~3.5 × $10^5$) were seeded in six-well plates and subjected to overexpression of Lamin A or EZH2, or their phosphodeficient (S22A-Lamin A, T345A-EZH2) or phosphomimetic (S22D-Lamin A, T345D-EZH2) variants. Approximately 5 × $10^4$ cells were seeded in the upper chamber of 8 μm pore Transwell inserts (Corning #CLS3422) in serum-free media. Complete media (DMEM for MCF7 or RPMI for MDAMB231, 10% FBS) was added to the lower chamber and cells were allowed to migrate for ~36 h. Nonmigrated

cells were removed, and migrated cells were fixed with 4% paraformaldehyde for 10 min, washed, and stained with DAPI for 2 min. Nuclei were imaged at 10× on an EVOS microscope. Images were processed using the Threshold and Watershed functions, and nuclei were quantified with the "Analyze Particles" function (size 50 – ∞ pixels$^2$, circularity 0.5–1.0). Average nuclei per field were calculated and analyzed using imageJ.

### Wound healing (scratch wound assay)

MCF10A cells (~3.5 × $10^5$) were subjected to overexpression of Lamin A or EZH2, or their phosphodeficient (S22A-Lamin A, T345A-EZH2) or phosphomimetic (S22D-Lamin A, T345D-EZH2) variants. Cells were treated with 500 ng/ml doxycycline for ~48 h to induce endogenous Lamin A/C or EZH2 depletion, and EMT was induced with 10 ng/ml TGF-β. After ~48 h, ~5 × $10^4$ cells were seeded per well in ibidi two-well inserts (ibidi #81176) in a 24-well plate overnight. Inserts were removed to create a wound gap, and migration into the wound area was monitored for 36 h (in assay media) using the Operetta High-Content Imaging System. Snapshots of wound closure was quantified with the integrated software in the Operetta Imaging System.

### Animal studies

All animal procedures were conducted following approval from the Institutional Animal Ethics Committee (IISER-Pune/IAEC/2024–01/08) at the Indian Institute of Science Education and Research, Pune, in compliance with the Committee for the Purpose of Control and Supervision of Experiments on Animals (CPCSEA), Government of India. Mice were housed in the National Facility for Gene Function in Health and Disease (NFGFHD), IISER Pune, under standard laboratory conditions with unrestricted access to food and water.

### *In vivo* tumor formation assay in NOD-SCID Mice

Female NOD-SCID mice (4–6 weeks old; Jackson Laboratory) were used for *in vivo* tumor formation studies. MDAMB231 cells expressing full-length (Lamin A or EZH2) or phosphodeficient (S22A-Lamin A, T345A-EZH2) or phosphomimetic (S22D-Lamin A, T345D-EZH2) variants were pre-treated with doxycycline for 48 h to deplete endogenous Lamin A/C or EZH2. Approximately 1 × $10^6$ cells in 100 µl PBS were injected into the fourth mammary fat pad of each mouse. Knockdown was maintained via drinking water containing 1% sucrose and 500 ng/ml doxycycline, replenished every 72 h. Tumor growth was monitored, and volumes were calculated as (width$^2$ × length)/2. Mice were euthanized after 5 weeks, and tumors were harvested for analysis.

### Tumor dissociation and primary cell culture

Excised tumors were minced using a scalpel and enzymatically digested in Hank's Balanced Salt Solution (HBSS) (Gibco, #14025050) containing collagenase IV (1 mg/ml, Sigma #C5138-1G), hyaluronidase V (0.1 mg/ml, Sigma #H6254-500MG), and DNase IV (20 mg/ml, Sigma #D5025-15KU) at RT. The suspension was filtered through a 70 µm mesh, centrifuged (1200 rpm, 5 min), and washed twice with HBSS. Cells were either lysed for Co-IP or plated in RPMI (Gibco, #11875093) for primary culture.

### Proximity ligation assay

PLA was performed using the Duolink in Situ Detection Kit (Sigma #DUO92008) following the manufacturer's protocol. Cells were treated with cytoskeletal (CSK) buffer (10 mM PIPES, pH 6.8, 100 mM NaCl, 300 mM sucrose, 3 mM $MgCl_2$, 1 mM Ethylene Glycol Tetraacetic Acid (EGTA)), fixed in 4% Paraformaldehyde (PFA) (pH 7.4, 12 min), permeabilized with 0.5% Triton X-100 (10 min), and blocked with Duolink Blocking Solution (30 min, RT). Primary antibodies—Mouse anti-Lamin A/C (Jol2, Abcam #ab40567, 1:50), Rabbit anti-EZH2 (D2C9, CST #5246, 1:1000), and Rabbit anti-Phospho-cdc2 (Thr161, CST #9114, 1:500)—were applied overnight at 4°C.

PLA probes (anti-Mouse PLUS and anti-Rabbit MINUS, 1:5) were added and incubated at 37°C for 1 h, followed by ligation (Duolink ligase, 1 U/µl, 1:40) and amplification (Duolink polymerase, 10 U/µl, 1:80). Nuclei were counterstained with DAPI using Duolink Mounting Medium (#DUO82040).

### Imaging and acquisition parameters

PLA images were acquired on a Zeiss anisotropy microscope (Carl Zeiss, Thornwood, NJ, USA) with a 63×/1.4 NA oil objective and AxioCam MRm Rev.3 camera using ZEN software. Z-stacks (512 × 512 pixels, 8-bit) were captured with a voxel size of 0.105 × 0.105 × 0.34 µm and line averaging of 4 in sequential two-channel mode. Fluorescence was detected for DAPI and Alexa Fluor-568. Images were processed and analyzed using ImageJ.

### Statistical analysis

All statistical analyses were performed using GraphPad Prism version 8.4 (GraphPad Software, San Diego, CA, USA). Data are presented as mean ± standard deviation (SD) unless otherwise specified. Comparisons between the two groups were conducted using an unpaired two-tailed Student's *t*-test. For multiple-group comparisons, one-way or two-way analysis of variance (ANOVA) followed by Tukey's or Sidak's *post hoc* test was used, as appropriate. Statistical significance was defined as $P < 0.05$. Sample sizes and replicates for each experiment are detailed in the figure legends.

## Results

### Induction and reversal of EMT

EMT is a dynamic and reversible cellular process that plays a pivotal role in cancer progression [34]. EMT is involved in ~90% of cancers of epithelial origin, which increases cell migration while MET facilitates colonization and metastasis [35].

To elucidate the mechanisms that regulate EMT and MET, we selected three well-established cell types derived from the human breast, namely MCF7, MCF10A, and MDAMB231 [36]. The authenticity of these cell lines was validated by evaluating modal chromosome numbers (Supplementary Fig. S1A and B). We also performed phalloidin staining, followed by confocal imaging (Supplementary Fig. S1C), which showed an increased aspect ratio (AR) of mesenchymal [MDAMB231 cells (AR: 7.19±1.80)], as compared to epithelial cells [MCF7 (AR: 1.06±0.62) and MCF10A (AR: 1.09±0.59); Supplementary Fig. S1D]. Furthermore, immunoblotting and immunofluorescence assays at the single-cell level underscore

the epithelial nature of MCF7 cells, characterized by high E-cadherin expression and low Vimentin levels. In sharp contrast, MDA-MB-231 cells are mesenchymal, with relatively higher Vimentin and lower E-cadherin levels (Supplementary Fig. S1C and E–G).

We induced EMT in MCF7 cells by overexpressing hTWIST1-GFP for ∼48 h. Immunoblotting analysis revealed a ∼75% reduction in E-cadherin and a ∼90% increase in Vimentin levels. Additionally, key mesenchymal transcription factors—Snail1, Twist1, and Zeb1—were significantly upregulated at the protein level (Fig. 1A). We corroborated these findings with immunofluorescence staining, which showed a decrease in E-cadherin and an increase in Vimentin expression in MCF7 cells overexpressing hTWIST1-GFP (Fig. 1B and D, methodological illustration in Fig. 1C), consistent with the immunoblot data. We treated MCF10A cells with TGF-β (10 ng/ml) for 7 days, which resulted in a striking reduction in E-cadherin expression (>70%) and a concomitant increase in Vimentin (∼60%; Fig. 1E), consistent with EMT induction [24]. Immunofluorescence staining of these cells also showed a significant upregulation of Vimentin and downregulation of E-cadherin (Fig. 1F and H, methodological illustration in Fig. 1G). Furthermore, transcription factors that mark mesenchymal cells (Snail1, Twist1, and Zeb1) were significantly upregulated at the protein level (Fig. 1E).

We next overexpressed the transcription factor GRHL2 in the mesenchymal MDAMB231 cells for ∼48 h [26, 27]. GRHL2 is a transcription factor that suppresses EMT by directly activating E-cadherin and repressing mesenchymal programs, thereby promoting MET, which makes it a useful model to study the reversibility of EMT [37, 38]. Overexpression of GRHL2 showed a striking increase in E-cadherin (>95%), decrease in Vimentin and mesenchymal transcription factors levels, leading to a transition in epithelial phenotype (Fig. 1I–L). Taken together, these representative cell lines derived from the E–M spectrum, serve as suitable models for studying EMT and its reversibility MET, offering a framework to investigate their regulatory mechanisms in the context of mammary epithelial and breast cancer respectively.

## Impact of EMT induction on nuclear topology and Lamin A/C expression

EMT is accompanied by significant changes in cellular morphology and cytoskeletal organization. Altered cytoskeletal organization directly impacts nuclear morphology [39]. We examined the extent of changes in nuclear morphology upon EMT by overexpressing TWIST1 in MCF7 cells. This showed a significant decrease in the circularity and sphericity [from 0.94 ± 0.03 to 0.50 ± 0.09 in MCF7-TWIST1 cells ($P < 0.0001$)] of the nucleus, with no significant changes in either surface area or volume (Supplementary Fig. S2A–D). In contrast, GRHL2-mediated MET induction, restored nuclear shapes consistent with epithelial-like cells, with increased sphericity (from 0.45 ± 0.08 to 0.94 ± 0.03 in MDAMB231 +GRHL2 cells; Supplementary Fig. S2E and F). Taken together, these data reveal significant changes in nuclear morphology upon EMT or MET induction.

We next assessed the protein levels of Lamin A/C and B-type lamins, as lamins define nuclear structure and function [39, 40]. While EMT induction in the epithelial cells (MCF7 and MCF10A) showed a marked reduction in Lamin A/C levels (Fig. 2A–F), the levels of B-type Lamins were relatively unaltered (Supplementary Fig. S2G, H). Conversely, Lamin A/C levels were upregulated upon GRHL2-driven MET in MDAMB231 cells (Fig. 2G–I), without any significant changes in the expression levels of B-type lamins (Supplementary Fig. S2I and J).

We quantified the levels of A- and B-type lamins across a panel of 11 breast cancer cell lines spanning the EM spectrum [36]. Interestingly, Lamin A/C showed a progressive decline with increasing mesenchymal characteristics, whereas B-type lamin levels did not display such a trend (Fig. 2J), suggesting a selective downregulation of Lamin A/C during EMT.

Importantly, transcript levels of *LMNA* remained unchanged upon both EMT and MET (Fig. 2K), indicating that Lamin A/C is post-transcriptionally regulated [41]. To further determine if EMT impacts the stability of Lamin A/C, we performed a time-course cycloheximide (CHX) chase assay in MCF7 cells. TWIST1 overexpression, followed by CHX treatment (10 μg/ml) showed a temporal reduction in Lamin A/C protein levels, whereas Lamin A/C remained unaltered in control cells (Empty vector) over the same duration (Supplementary Fig. S3A and B). Furthermore, co-treatment with 1 μM MG132 and CHX restored the stability of Lamin A/C protein after ∼8 h upon TWIST1 overexpression (Supplementary Fig. S3C and D), suggesting that EMT induces Lamin A/C degradation via a proteasome-dependent pathway.

Collectively, these results demonstrate that EM plasticity is associated with changes in Lamin A/C expression and nuclear morphology, with Lamin A/C being regulated by post-translational degradation during EMT.

## Lamin A/C determines EM identity

To investigate the role of Lamin A/C in EM plasticity, we performed RNA-Seq analysis upon Lamin A/C depletion in MCF10A cells. Differential gene expression analysis (DESeq2) revealed a robust upregulation of mesenchymal-associated genes including *VIM, SNAI1, TWIST1,* and *ZEB1,* which were among the top 50 upregulated genes, accompanied by downregulation of epithelial markers such as *CLDN1, OCLN,* and *CDH1* (Fig. 3A and B) [42]. Consistent with these observations, Gene Ontology (GO) analysis showed a significant enrichment ($P < .05$) of genes associated with EMT regulation, cell migration, secondary neoplasms, cell–cell adhesion, and regulation of mitotic nuclear division (Fig. 3C) [43]. Kyoto Encyclopedia of Genes and Genomes (KEGG) pathway analysis revealed modulation of signalling pathways implicated in ECM–receptor interaction, TGF-β signalling pathway and regulation of actin cytoskeleton, while GO Cellular Component analysis highlighted ECM organization and cell migration (Supplementary Fig. S4A and B) [44]. Furthermore, Gene Set Enrichment Analysis (GSEA) enriched for cell adhesion and migration-related gene sets, both hallmarks of EMT (Fig. 3D; Principal Component Analysis (PCA) analyses of RNA seq data between independent replicates Supplementary Fig. S4C).

To validate these results in an independent epithelial context, Lamin A/C was depleted in MCF7 cells. Lamin A/C depletion showed an increase in the AR of MCF7 cells [si Lamin A/C: mean ± SD = 5.49 ± 2.09, si LacZ (control) mean ± SD = 1.02 ± 0.58] [Supplementary Fig. S5A, A(i), and A(ii)]. In contrast, overexpression of Lamin A in MDAMB231 cells, revealed the acquisition of cobblestone-like epithelial morphol-

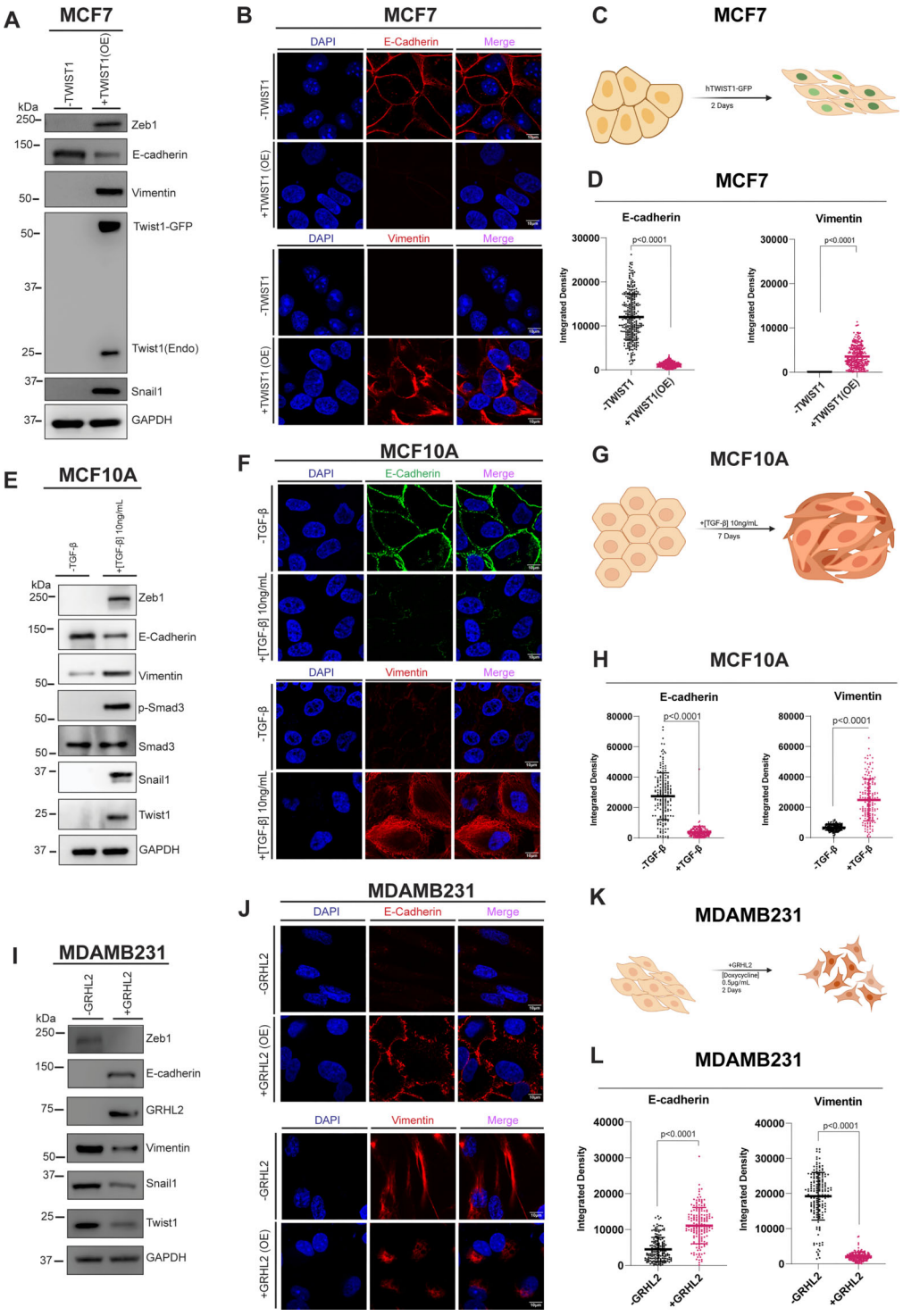


**Figure 1.** Induction and characterization of EMT and MET in breast cancer cell lines. **(A)** Immunoblot analysis of EMT induction in MCF7 cells transiently overexpressing TWIST1-GFP for 48 h. Cells were transfected with 2 μg of pEGFPN1 or hTWIST1-GFP **(B)** Immunofluorescence analysis of EMT in MCF7 cells overexpressing TWIST1-GFP or control pEGFPN1. E-cadherin and Vimentin (red), nucleus (DAPI, blue). Scale bar ∼10 μm **(C)** Schematic representation of EMT induction in MCF7 cells **(D)** Scatter plot of immunofluorescence assay, showing relative changes in the integrated density of E-cadherin and Vimentin in MCF7 cells. Quantification for panel (B) ($n = 200$). Data represent mean ± standard deviation (SD) from $N = 3$ independent biological replicates. **(E)** Immunoblot analysis of EMT induction in MCF10A cells treated with 10 ng/ml TGF-β for 7 days **(F)** Immunofluorescence analysis of EMT in MCF10A cells treated with TGF-β. E-cadherin (green); Vimentin (red); nucleus (blue, DAPI). Scale bar ∼10 μm **(G)** Schematic representation of EMT induction in MCF10A cells **(H)** Scatter plot of immunofluorescence assay, showing relative changes in the integrated density of E-cadherin and Vimentin in MCF10A cells [data shown in panel (F)] following EMT induction ($n = 200$). Data represent mean ± SD from $N = 3$ independent biological replicates **(I)** Immunoblot analysis of MET induction in MDAMB231 cells following doxycycline-induced GRHL2 overexpression for 48 h **(J)** Immunofluorescence analysis of MET in MDAMB231 cells overexpressing GRHL2. E-cadherin and Vimentin (red), nucleus (blue, DAPI). Scale bar ∼10 μm **(K)** Schematic representation of MET induction in MDAMB231 cells **(L)** Scatter plot of immunofluorescence assay, showing relative changes in the integrated density of E-cadherin and Vimentin in MDAMB231 cells following MET induction [data shown in panel (J)] ($n = 200$). Data represent mean ± SD from three independent biological replicates. Unpaired Student's *t*-test was used to compute the *P*-value.

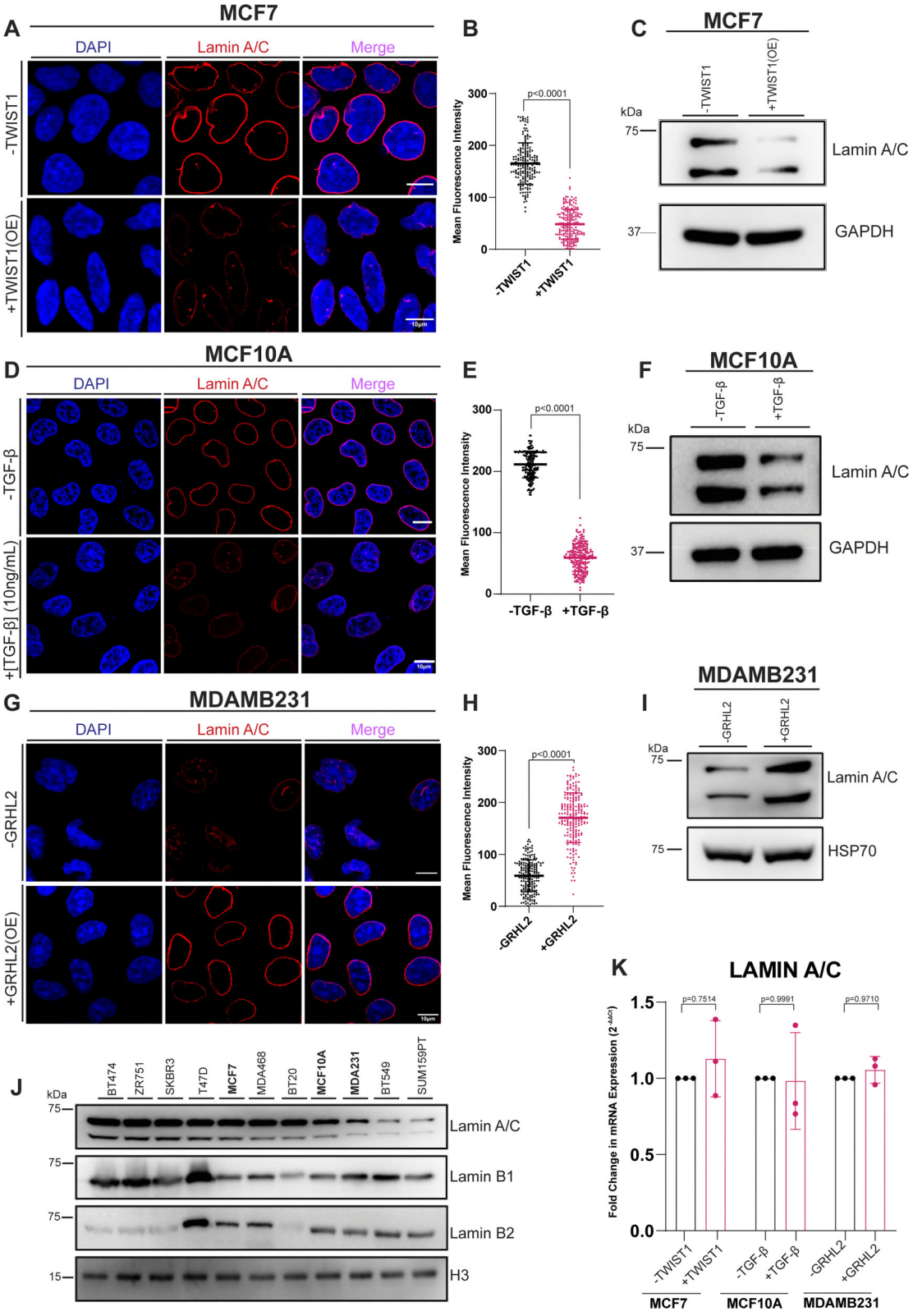


**Figure 2.** Impact of EMT induction on Lamin A/C expression. **(A, D, G)** Immunofluorescence analysis of Lamin A/C (red) in MCF7 **(A)**, MCF10A **(D)**, and MDAMB231 **(G)** cells upon EMT **(A, D)** or MET **(G)** nucleus (DAPI, blue). Scale bar ∼10 μm. **(B, E, H)** Mean fluorescence intensity of Lamin A/C quantified by line scan analysis across the nucleus in MCF7 **(B)**, MCF10A **(E)**, and MDAMB231 **(H)** cells. Data represent mean ± SD from $N = 3$ independent biological replicates ($n = 250$). Unpaired Student's *t*-test was used to calculate *P*-values. **(C, F, I)** Immunoblot analysis of total Lamin A/C protein levels in MCF7 **(C)**, MCF10A **(F)**, and MDAMB231 **(I)** cells upon EMT **(C, F)** or MET **(I)** induction. GAPDH **(C, F)** and HSP70 **(I)** are loading controls. **(J)** Immunoblot analysis of Lamin A/C, Lamin B1, and Lamin B2 levels across 11 cell lines of breast origin with increasing mesenchymal characteristics. Loading control: Histone H3 **(K)** RT-qPCR analysis of LMNA transcript levels in MCF7 and MCF10A upon EMT and MET in MDAMB231 cells. Data represent mean ± SD ($N = 3$, $n = 9$). Unpaired Student's *t*-test was used to compute the *P*-values. Means are compared between **(B)** −Twist1 (control) and +Twist1; **(E)** −TGFβ (control) and **(H)** +TGFβ; −GRHL2 (control) and +GRHL2, statistical significance, *P*-value <0.05.

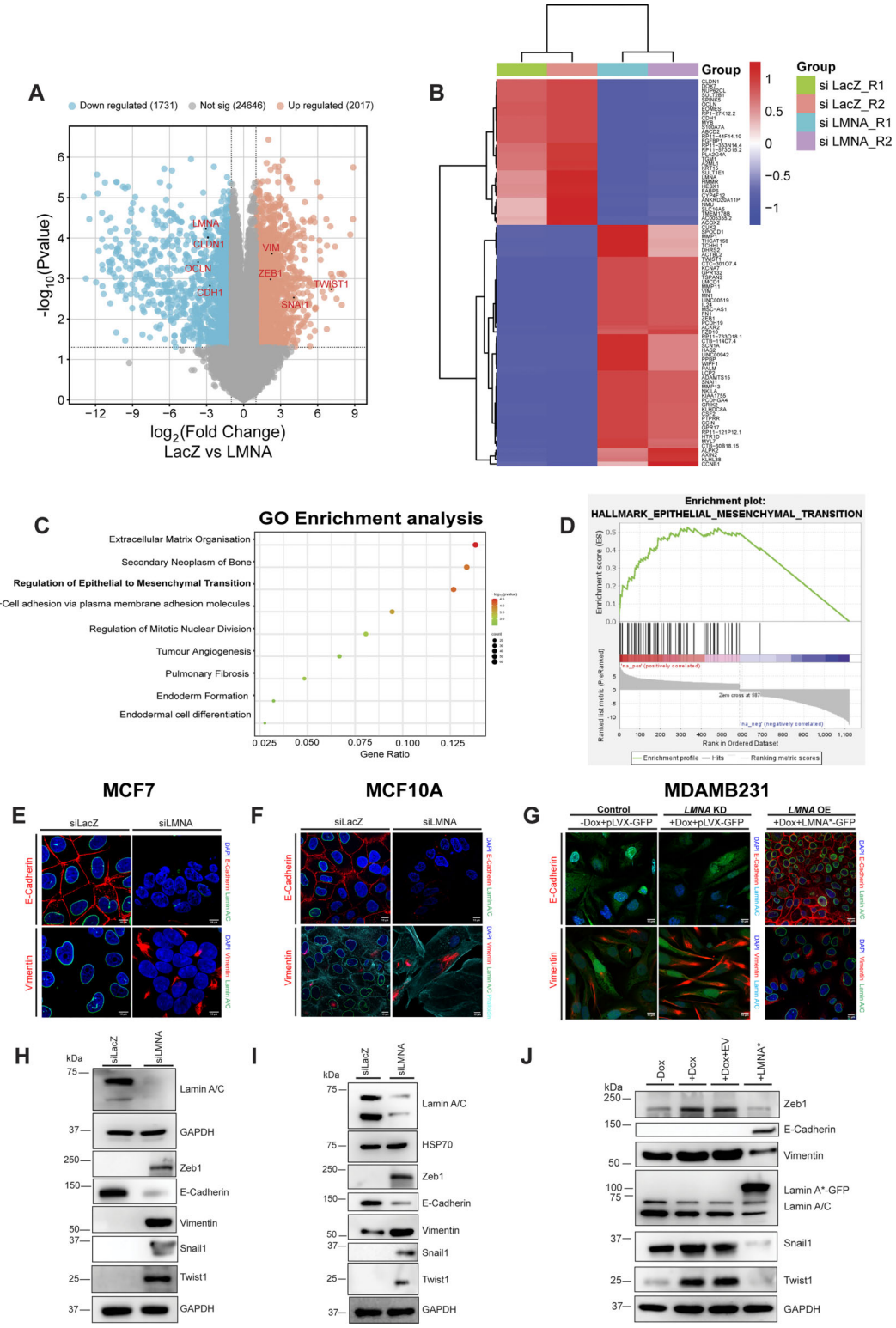


**Figure 3.** Effect of Lamin A/C perturbation on EMT and MET. **(A)** Volcano plot showing differentially expressed genes in MCF10A cells upon Lamin A/C knockdown. Downregulated, upregulated, and nonsignificant genes. **(B)** Heatmap of the top 50 [$P$ <0.05; $\log_2$ Fold Change (FC) > 2] differentially expressed genes in MCF10A cells upon Lamin A/C knockdown. Downregulated and upregulated genes, respectively ($N = 2$ biological replicates). **(C)** GO enrichment analysis of differentially expressed genes ($P \leq 0.05$), showing the most enriched biological processes. **(D)** GSEA plot showing enrichment for EMT upon Lamin A/C knockdown (normalized enrichment score = 3.337). **(E, F)** Immunofluorescence analysis of MCF7 **(E)** and MCF10A **(F)** cells upon Lamin A/C knockdown. Lamin A/C, E-cadherin or Vimentin, and phalloidin. Nucleus (DAPI). Scale bars, ~10 μm **(G)** Immunofluorescence analysis of MDAMB231 cells overexpressing Lamin A*-GFP upon endogenous Lamin A/C depletion. E-cadherin (top panel) or Vimentin (bottom panel), and Lamin A/C (−Dox and +Dox panels only). Nucleus (DAPI). Scale bar ~10 μm. (**H–J**) Immunoblot analysis of EMT markers in MCF7 **(H)**, MCF10A **(I)** cells upon Lamin A/C knockdown, and MDAMB231 **(J)** cells upon Lamin A overexpression. RNA-Seq was performed in $N = 2$ independent biological replicates. Lamin A* denotes a full-length Lamin A construct resistant to doxycycline-induced depletion of endogenous Lamin A/C. Statistical significance, $P$-value <0.05.

ogy. This was corroborated by quantifications of AR, which showed a shift towards an epithelial-like architecture of cells [Supplementary Fig. S5B, B(i), and B(ii)].

Immunofluorescence analyses in both MCF10A and MCF7 cells showed a ∼70% reduction in E-cadherin and a ∼65% increase in Vimentin upon Lamin A/C loss (Fig. 3E and F; quantification: Supplementary Fig. S5C and D). Transcriptional upregulation of mesenchymal factors (*VIM, SNAI1, TWIST1*, and *ZEB1*) and decreased *CDH1*, was consistent with the mesenchymal morphology in MCF7 cells upon Lamin A/C depletion (Supplementary Fig. S5F). Immunoblotting showed a decrease in E-cadherin and increase in the levels of Vimentin, Snail1, Twist1, and Zeb1 in Lamin A/C–depleted cells (Fig. 3H and I).

In contrast, Lamin A overexpression in MDAMB231 cells (upon endogenous Lamin A/C depletion) showed a significant upregulation in the transcript levels of E-cadherin (∼95% increase), and downregulation of mesenchymal regulators (*VIM, SNAI1, TWIST1*, and *ZEB1*; Supplementary Fig. S5G). Immunoblotting and immunofluorescence analyses reiterate these effects, showing enhanced E-cadherin expression and suppression of mesenchymal markers (Fig. 3G and J; quantification: Supplementary Fig. S5E).

We also determined the EM status in MCF7 and MDAMB231 cells upon depleting B-type Lamins (Lamin B1 and Lamin B2). Depletion of B-type Lamins did not significantly alter the expression of EM markers underscoring a specific role of Lamin A/C in regulating EM plasticity (Supplementary Fig. S5H and I).

## Impact of EMT or MET induction on the lamin interactome

Nuclear Lamins play a critical role in the maintenance of nuclear integrity, chromatin organization and gene regulation [45]. Lamina-associated domains (LADs) are genomic regions enriched for nuclear Lamins and are marked by histone marks H3K9me3 and H3K27me3 associated predominantly with heterochromatin [46, 47]. We next performed immunoblotting upon EMT induction, which showed a decrease (∼50%) in the total levels of H3K9me3 and H3K27me3, suggesting a marked decrease in inactive histone marks [Supplementary Fig. S6A(i) and B(i)]. In contrast, MET induction increased levels of these heterochromatic marks by ∼60% [Supplementary Fig. S6C(i)]. Notably, Lamin A/C knockdown in the epithelial cells (MCF7 and MCF10A) also showed a significant reduction (∼50%) in H3K27me3 and H3K9me3, reinforcing the functional association between Lamin A/C and chromatin compaction [Supplementary Fig. S6A(ii) and B(ii)]. Furthermore, Lamin A overexpression, showed an increase in H3K27me3 and H3K9me3 in MDAMB231 cells [Supplementary Figure S6C(ii)], consistent with the role of Lamin A/C in the maintenance of heterochromatin [48].

Given the dynamic changes in heterochromatin markers during EMT and MET, we next examined whether the interactors of Lamin A/C are differentially enriched across E and M states [19, 49, 50]. We performed Co-IP followed by MS to identify the sub-interactome of Lamin A/C in the epithelial and mesenchymal states. While, MS analyses identified 44 unique protein-protein interactors, including EZH2, in Lamin A/C pull-downs from epithelial MCF7 cells, 90 unique interactors including CCNB1 and pCDK1, among others were detected upon EMT induction in MCF7-TWIST1 cells. A total of 49 interactions (LMNB1, LMNB2, EHMT2, SUV39H1, PRRX1) were common to both the control and Twist1 overexpressing MCF7 cells (Fig. 4A; PCA analysis Supplementary Fig. S6D). In contrast, MET induction in MDA-MB-231 cells markedly reconfigures the Lamin A/C interactome. In control cells, 103 unique interactors were identified involving (CCNB1 and pCDK1). In contrast, GRHL2 mediated MET-induction revealed 71 distinct interactors, including (EZH2). Notably, 72 proteins, including (LMNB1, LMNB2, CBX5, EHMT2, SUV39H1) were consistently associated with Lamin A/C in both control and GRHL2-overexpressing MDAMB231 cells (Fig. 4B; PCA analysis Supplementary Fig. S6E).

GO pathway enrichment analysis of the Lamin A/C interactome in epithelial MCF7 cells revealed that its interacting partners are primarily involved in the regulation of gene expression, messenger RNA (mRNA) metabolic processes, ribonucleoprotein complex assembly, and regulation of mRNA stability. In contrast, Twist1-mediated EMT shows a shift in the Lamin A/C interactome, enriching for pathways related to cell cycle regulation, nuclear envelope disassembly and DNA damage repair (Supplementary Fig. S7A and B). Remarkably, GRHL2-mediated MET re-established interactions between Lamin A/C and proteins involved in gene expression regulation, such as EZH2 (Supplementary Fig. S7C and D). These findings suggest that the Lamin A/C interactome is dynamically reprogrammed during EMT and MET, reflecting the functional requirements of epithelial versus mesenchymal cell states [51].

A key finding from the mass spectroscopy studies unravelled dynamic Lamin A/C interactome as it showed a reversible association with histone methyltransferase EZH2, which was enriched in MCF7 and upon MET induction in MDAMB231 cells. Interestingly, Lamin A/C-EZH2 interaction was undetectable in (i) MDAMB231 cells (ii) upon Twist1 induction in MCF7 cells. In contrast, Lamin A/C interacts with phosphorylated CDK1 (pCDK1) predominantly in the mesenchymal cells (MCF7-TWIST1 and control: MDAMB231). However, this interaction was undetectable upon MET induction (Fig. 4C and D). Taken together, these findings suggest a switch in the interactions of Lamin A/C, consistent with the cellular state, with Lamin A/C involved in chromatin-modifying functions via EZH2 in epithelial cells, while in mesenchymal states, Lamin A/C facilitates cell cycle regulation through its interaction with pCDK1.

To validate these findings, we performed Co-IP of Lamin A/C followed by immunoblotting for EZH2 upon EMT and MET induction. Co-IP results showed a loss of the Lamin A/C–EZH2 interaction upon EMT induction and its restoration during MET (Fig. 4E–G). Furthermore, immunoprecipitation with either of the B-type Lamins (Lamin B1 or B2), did not show an interaction with EZH2, indicating that this association with EZH2 is specific to Lamin A/C. However, both the B-type Lamins interact with the methyltransferases G9a and SUV39H1, consistent with previous studies [52]. Of note, these interactions with the B-type Lamins were unaltered upon EMT induction in MCF10A cells (Supplementary Fig. S7E and F).

To further determine if Lamin A/C interacts with PRC2 components other than EZH2, we performed Co-IP of Lamin A/C, followed by immunoblotting for PRC2 components—EED and Suz12—in MCF10A cells. This showed a specific association with EZH2, but not with other PRC2 components

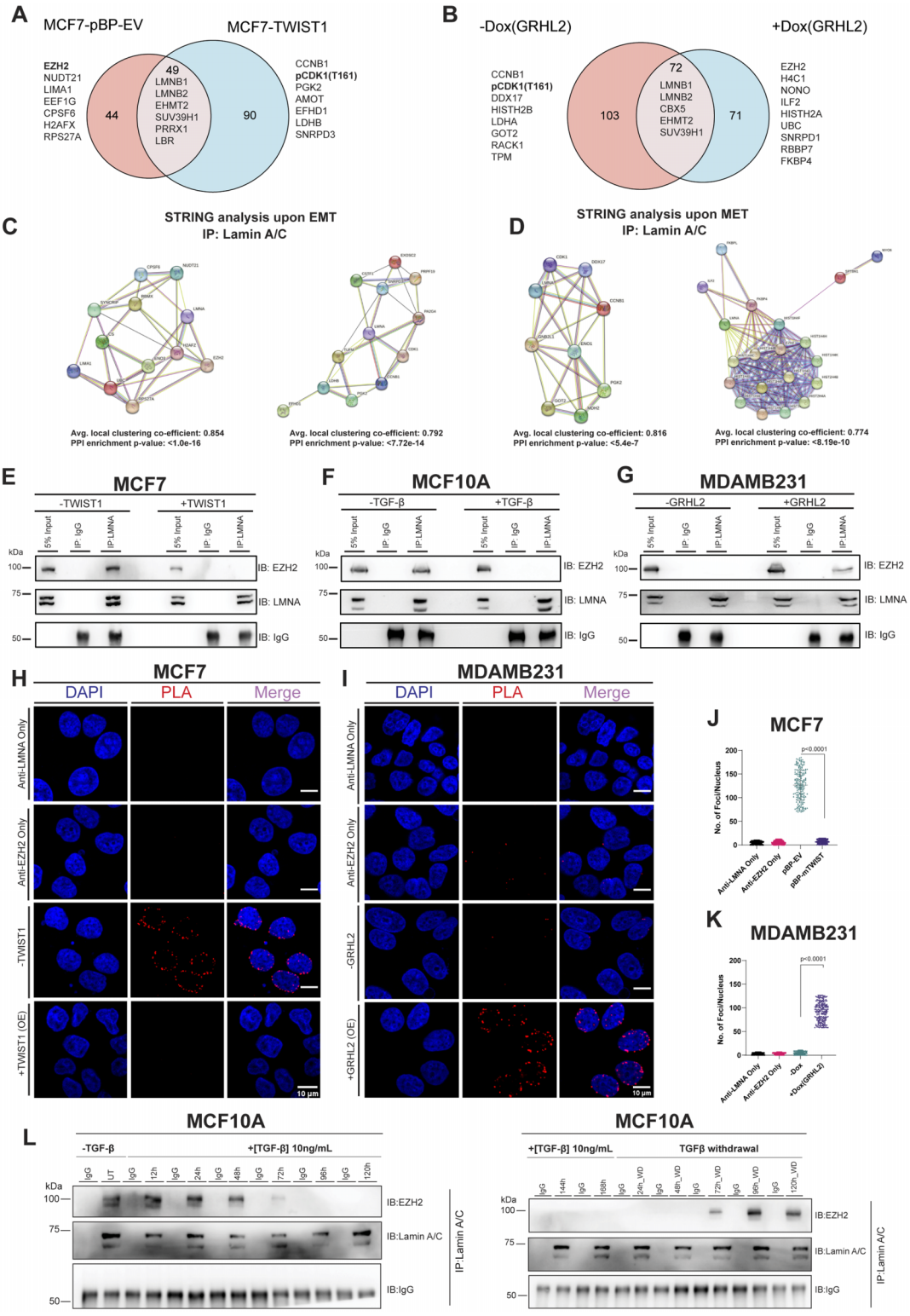


**Figure 4.** Dynamic Remodeling of the Lamin A/C Interactome During EMT and MET. **(A, B)** Venn diagrams showing unique and common interactors of Lamin A/C identified by (Immunoprecipitation - Mass Spectroscopy) IP-MS in MCF7 versus MCF7-TWIST1 **(A)** and MDAMB231 versus MDAMB231-GRHL2 **(B)**. **(C, D)** Representative STRING network analysis of Lamin A/C interactors in MCF7 versus MCF7-TWIST1 **(C)** and MDAMB231 versus MDAMB231-GRHL2 **(D)**. **(E–G)** Co-IP of Lamin A/C in MCF7 **(E)**, MCF10A **(F)**, and MDAMB231 **(G)** cells upon EMT **(E, F)** or MET **(G)** induction, followed by immunoblotting for EZH2 and Lamin A/C. IgG: isotype control, an approximately equal amount of antibody is used for immunoprecipitation. **(H, I)** Proximity ligation assay (PLA) detects Lamin A/C–EZH2 interaction in MCF7 **(H)** and MDAMB231 **(I)** cells upon EMT **(H)** or MET **(I)** induction. PLA signal (red), nucleus (blue, DAPI). Scale bar: ∼10 µm. **(J, K)** Quantification of PLA signal in MCF7 **(J)** and MDAMB231 **(K)** cells. Data represent mean ± SD from $N = 3$, independent biological replicates, and $P$-values calculated by one-way ANOVA and means are compared between pBp-EV and pBP-Twist **(J)** and −Dox (GRHL2) and +Dox (GRHL2) **(K)**. **(L)** Time-course analysis of Lamin A/C–EZH2 interaction by immunoprecipitation of Lamin A/C in MCF10A cells during EMT progression [∼12 to ∼168 h (∼7 days) post-TGF-β treatment] and MET recovery [5 days post-TGF-β withdrawal (WD)], assessed by Co-IP and immunoblotting. IgG: isotype control, statistical significance, $P$-value <0.05.

such as SUZ12 or EED (Supplementary Fig. S7G). To assess the integrity of the PRC2 complex upon EMT, EZH2 was immunoprecipitated from TGF-β-treated MCF10A cells, where it retained its association with SUZ12 and EED, indicating that the Lamin A/C–EZH2 interaction is independent of the PRC2 complex (Supplementary Fig. S7H).

To further substantiate the interaction between Lamin A/C and EZH2, we performed PLA upon EMT and MET induction. We detected a striking decrease (∼10-fold) in the number of PLA foci upon EMT induction, suggesting a loss of Lamin A/C–EZH2 interaction (Fig. 4H and J). In contrast, GRHL2-mediated MET induction re-established the interaction between Lamin A/C and EZH2, as demonstrated by a significantly higher number (∼10-fold) of PLA foci (Fig. 4I and K).

To investigate the temporal dynamics of the Lamin A/C–EZH2 interaction, we performed a time-course assay following EMT induction via TGF-β treatment and subsequent MET induction by withdrawal of TGF-β. Immunoprecipitation of Lamin A/C at different time points [∼12–168 h (∼7 days)] revealed a progressive loss of interaction with EZH2, with complete dissociation at ∼72 h post-EMT induction. Conversely, withdrawal of TGF-β [∼12–120 h (∼5 days)] restored Lamin A/C–EZH2 interaction after ∼72 h (Fig. 4L). These findings further corroborate a dynamic and reversible association between Lamin A/C and EZH2. In summary, these studies reveal that EMT induction disrupts the Lamin A/C–EZH2 interaction, with a concomitant decrease in heterochromatin marks, while MET promotes this interaction and re-establishes heterochromatin marks.

## CDK1-mediated phosphorylation regulates Lamin A/C–EZH2 interaction and EMT progression

To address the molecular basis of Lamin A/C–EZH2 interaction, we performed HADDOCK, which predicted an interface between the head domain of Lamin A/C (Arg25, Arg28) and EZH2 (Asp136, Asp140; Supplementary Fig. S8A) [53]. We co-overexpressed GFP-tagged Lamin A and FLAG-tagged EZH2 deletion constructs into HEK293T cells. Co-IP revealed that Lamin A binds to EZH2 at the Ala301–Ala500 region, whereas reverse Co-IP (using Lamin A deletion constructs) shows that EZH2 interacts with the head domain of Lamin A (Fig. 5A and B).

Putative CDK1 phosphorylation sites were identified to be the region of interaction (through deletion experiments) between Lamin A/C and EZH2 (Supplementary Fig. S8B), suggesting CDK1 regulation. IP-MS also showed CDK1 enrichment with Lamin A/C in Twist1-overexpressing MCF7 and untreated MDAMB231 cells. PLA demonstrated that EMT induction in MCF10A cells enhanced the interaction of Lamin A/C with phosphorylated CDK1 (pCDK1-T161; Fig. 5C and F), which was further corroborated by Co-IP. In contrast, induction of MET in MDAMB231 cells abolished this interaction (Supplementary Fig. S8C–E).

Since CDK1 phosphorylates Lamin A/C and EZH2 independently, immunoblotting revealed increased ratios of pLMNA(S22)/LMNA and pEZH2(T345)/EZH2 along with elevated pCDK1-T161 levels during EMT, whereas MET induction markedly decreased these phosphorylation events (Supplementary Fig. S8F–I) [54, 55]. To address the effect of altered CDK1 activity during EMT/MET on cell cycle, we performed FACS profiling, which showed an increase in cell numbers in G2/M upon EMT (in MCF7 and MCF10A) and decreased cell numbers in G2/M upon MET (in MDAMB231; Supplementary Fig. S8J and K). We surmised that increased CDK1 activity could destabilize Lamin A/C–EZH2 binding during EMT. To validate this finding, we performed PLA, which showed a loss of Lamin A/C–EZH2 interaction upon EMT induction, which was restored upon CDK1 inhibition with RO-3306 (∼10-fold increase in PLA signal; Fig. 5D and G).

MCF10A cells treated with TGF-β showed an increase in mesenchymal markers (ZEB1, SNAI1, TWIST1, Vimentin) and reduction in E-cadherin. To determine if CDK1 inhibition alters the dynamics of EMT markers, EMT-induced cells were treated with the CDK1 inhibitor (RO-3306). This showed the attenuation of mesenchymal markers, while E-cadherin expression was sustained (Supplementary Fig. S9A and C–E). A similar effect was observed in Twist1-overexpressing MCF7 cells, where CDK1 inhibition suppressed EMT induction (Fig. 5H and K, and Supplementary Fig. S9I).

Since CDK1 phosphorylates EZH2 at Thr345, leading to its proteasomal degradation, we asked if phosphorylation contributes to the dissociation of EZH2 from Lamin A/C. Upon EMT induction, Lamin A/C levels were markedly reduced, resulting in the loss of colocalization with EZH2. However, this interaction was restored when cells were treated with the proteasomal inhibitor MG132 (Fig. 5I). Interestingly, MG132 treatment also attenuated EMT-associated phenotypic changes (Fig. 5J and L, and Supplementary Fig. S9B, F–H, and J).

To further assess the consequence of increased CDK1 activity in regulating cell cycle and EM status of cells, we synchronized MCF10A cells by double-thymidine block followed by release and treated cells with TGF-β. While Cyclin D1 levels remained unaltered, Cyclin B1 was upregulated at both mRNA (∼25-fold) and protein (∼15-fold) levels in mesenchymal cells (Supplementary Fig. S10A and B). Flow cytometry showed a ∼3-fold increase in the G2/M sub-population (Supplementary Fig. S10C and D). BrdU incorporation assays showed no changes in the intensity of BrdU, negating a G1 arrest (Supplementary Fig. S10E).

To determine the state of cells at G2/M, we examined the levels of H3S10p - a marker of late mitosis [56]. Immunofluorescence showed a marked reduction of H3S10p-positive cells in TGF-β-treated cells (∼0.67 ± 0.08%; control: ∼19 ± 7.8%; Supplementary Fig. S10F). Consistently, immunoblotting of synchronized, and FACS-sorted G2/M cells revealed reduced H3S10p in EMT-induced cells (Supplementary Fig. S10G). These results collectively indicate that the cells undergoing EMT are arrested at the late S-to-early G2 transition.

We next asked whether CDK1 activity per se, rather than cell cycle arrest, is essential for EMT. In Twist1-overexpressing MCF7 cells, nocodazole-induced prometaphase arrest did not impair EMT, whereas CDK1 inhibition with RO-3306 markedly suppressed EMT (Supplementary Fig. S11A). Similarly, TGF-β did not induce EMT in thymidine-arrested MCF10A cells, but ectopic overexpression of a phosphomimetic CDK1 mutant (T161D) restored EMT progression (Supplementary Fig. S11B).

To directly test whether CDK1 activity regulates Lamin A/C–EZH2 stability, we performed Co-IP assays in thymidine-arrested MCF10A cells expressing CDK1 phosphomutants. The Lamin A/C–EZH2 interaction was disrupted

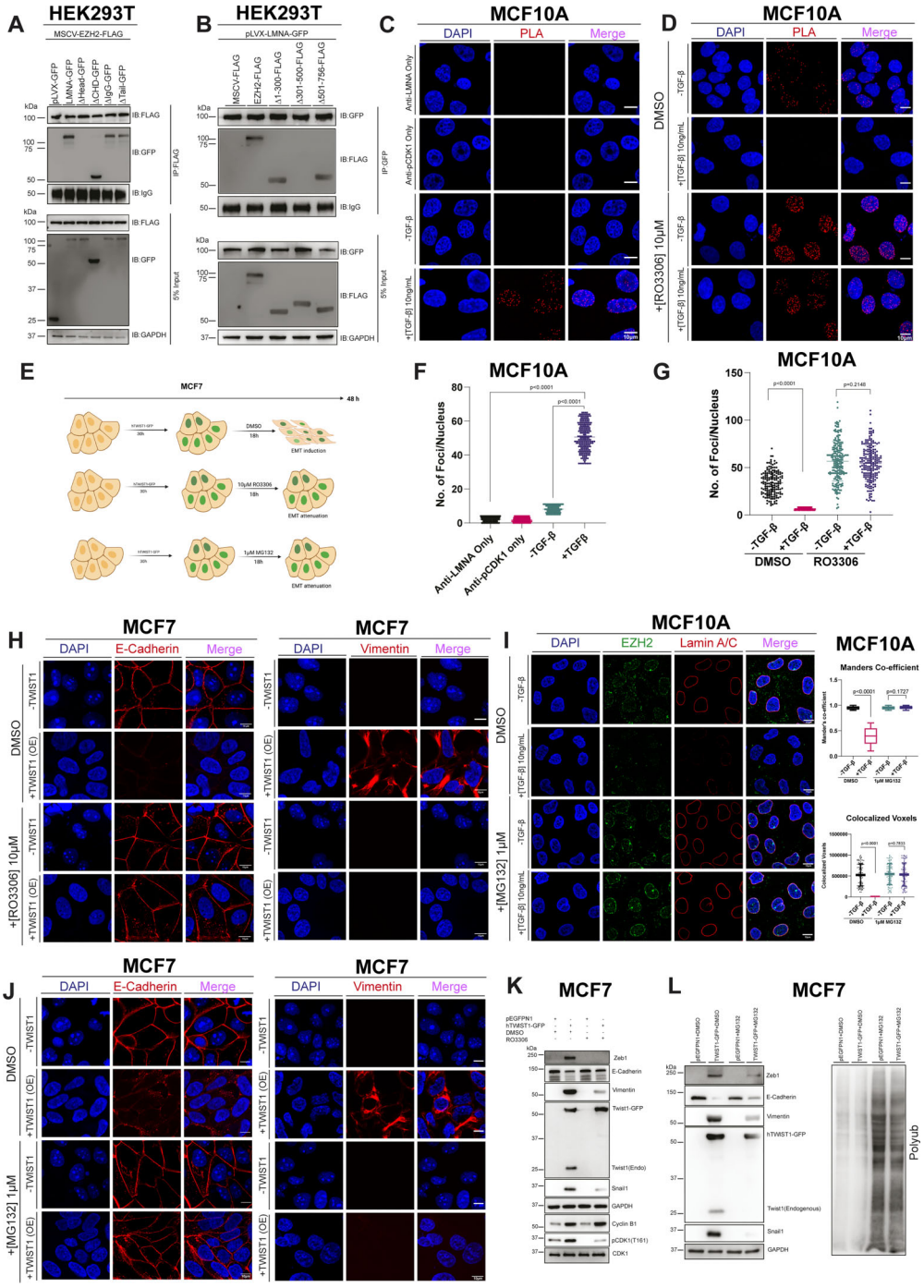


**Figure 5.** CDK1-mediated phosphorylation regulates Lamin A/C–EZH2 interaction and EMT progression. **(A)** Co-IP of FLAG in HEK293T cells co-transfected with full-length EZH2-FLAG and Lamin A-GFP deletion mutants (ΔHead 1–29, ΔRod 31–387, ΔIgG 428–549, ΔTail 550–664 of Lamin A). **(B)** Co-IP of GFP in HEK293T cells co-transfected with full-length Lamin A-GFP and EZH2-FLAG deletion mutants (Δ1–300, Δ301–500, Δ501–746 of EZH2). **(C)** PLA detects Lamin A/C–pCDK1(T161) interaction in MCF10A cells treated with 10 ng/ml TGF-β for ∼7 days. Nucleus (DAPI), PLA signal in red. Scale bar ∼10 μm **(D)** PLA detects Lamin A/C– EZH2 interaction in MCF10A cells treated with DMSO or 10 μM RO3306 for ∼18 h in the ± TGF-β for ∼7 days, nucleus (DAPI). PLA signal in red. Scale bar ∼10 μm. **(E)** Schematic representation of RO3306 and MG132 treatment in MCF7 cells **(F)** Quantification of PLA foci/nucleus of the data in **(C)**. *P*-values were calculated using ANOVA. Means are compared between +TGFβ and –TGFβ (control) conditions with the single antibody control. **(G)** Quantification of PLA foci/nucleus of the data in **(D)**. Statistical significance was determined using unpaired Student's *t*-tests. Means are compared between +TGFβ and –TGFβ (control) conditions within each group (DMSO and RO-3306). **(H)** Immunofluorescence of MCF7 cells transiently transfected with pEGFP-N1 or Twist1-GFP and treated with 10 μM RO3306 for 18 h. nucleus (DAPI). Scale bar ∼10 μm **(I)** Immunofluorescence and quantification of colocalized voxels and Mander's coefficient for Lamin A/C and EZH2 in MCF10A cells ± TGF-β and 1 μM MG132. Nucleus (DAPI). Scale bar ∼10 μm. Statistical significance was determined using unpaired Student's *t*-tests. Means are compared between +TGFβ and –TGFβ (control) conditions within each treatment group (DMSO and RO-3306). **(J)** Immunofluorescence of MCF7 cells treated with MG132 and transient overexpression of hTWIST1-GFP and stained for E-cadherin and Vimentin ; nucleus (DAPI). Scale bar ∼10 μm. **(K)** Immunoblotting for EMT markers in MCF7 treated with RO3306 and Twist1-GFP in MCF7 **(L)** Immunoblotting for EMT markers in MCF7 cells treated with MG132 and Twist1-GFP in MCF7. For all experiments, data are represented as mean ± SD from $N = 3$ three independent biological replicates, statistical significance, *P*-value <0.05.

upon expression of the phosphomimetic mutant (T161D; Supplementary Fig. S11C).

In summary, these findings suggest that EMT progression is driven by elevated CDK1 activity leading to late S-to-early G2 arrest. CDK1 phosphorylates Lamin A/C and EZH2, disrupts the Lamin A/C–EZH2 complex and promotes EZH2 degradation, thereby facilitating EMT [57–59].

## Regulatory role of phosphorylation in the interaction of Lamin A/C–EZH2

Phosphorylation of nuclear lamins regulate nuclear organization and chromatin dynamics [60, 61]. Since Lamin A/C and EZH2 are involved in chromatin organization and transcriptional regulation, we surmised that perturbing their phosphorylation sites could modulate EMT/MET. Furthermore, CDK1-mediated phosphorylation impacts lamin organization, prompting an in-depth analysis of how CDK1 phosphorylation affects Lamin A/C–EZH2 binding. Specifically, Serine 22 (S22) in Lamin A/C and Threonine 345 (T345) in EZH2—both established CDK1 phosphorylation sites with roles in protein–protein interactions and nuclear dynamics—were selected for site-directed mutagenesis to mimic either a phosphorylated (phosphomimetic: Lamin A–S22D, EZH2–T345D) or nonphosphorylated (phospho-deficient: Lamin A–S22A, EZH2–T345A) state [62].

Lamin A/C knockdown lines (doxycycline-inducible) of MCF7 cells were generated, followed by ectopic overexpression of (i) GFP–Lamin A (shRNA resistant), (ii) S22A, and (iii) S22D constructs. To ensure homogeneity, GFP-positive cells were FACS-sorted. Additionally, TWIST1-GFP was transiently overexpressed (∼48 h) and selected with G418 to enrich TWIST1-expressing cells [(Fig. 6A), schematic for generation of EZH2 mutants (Fig. 6B)]. Immunoprecipitation of Lamin A/C followed by immunoblotting for EZH2 showed that full-length Lamin A and S22A retained their interaction with EZH2, independent of TWIST1-induced EMT, whereas the S22D variant did not bind to EZH2, irrespective of EMT status. These results indicate that phosphorylation at S22 disrupts Lamin A/C–EZH2 interaction (Fig. 6C).

We adopted a similar strategy in MDAMB231 cells stably expressing GRHL2 to induce MET. Consistent with findings in MCF7, full-length Lamin A and S22A interacted with EZH2, while the S22D variant did not (Fig. 6D). Thus, phosphorylation at Ser22 consistently inhibits Lamin A/C–EZH2 interaction during both EMT and MET.

To further delineate the role of EZH2 phosphorylation, T345A and T345D mutants were tested in MCF7 (±TWIST1) and MDAMB231 (±GRHL2) cells. In both contexts, full-length EZH2 and T345A retained their interaction with Lamin A/C, whereas the T345D variant failed to bind Lamin A/C (Fig. 6E and F).

Taken together, these data demonstrate that phosphorylation at either S22 in Lamin A/C or T345 in EZH2 prevents complex formation. We further validated the interaction between the mutants of Lamin A/C and EZH2 through immunofluorescence studies and found that the full length (control) and phosphodeficient mutants interact with each other (Lamin A/C and EZH2), while phosphomimetic mutants lost the interaction irrespective of the presence of TGF-β (Fig. 6G–J).

To determine if there is a requirement for dual phosphorylation of Lamin A and EZH2, we co-transfected HEK293T cells with combinations of Lamin A–GFP and EZH2–FLAG (wild-type, phospho-deficient, or phospho-mimetic). Co-IP revealed robust binding only when both proteins are in their unphosphorylated or phospho-deficient forms. Notably, phosphorylation of either Lamin A or EZH2 alone was sufficient to weaken or abolish this interaction. Lamin A/C–EZH2 complex is sensitive to phosphorylation of either partner. Therefore, the disruption of this interaction does not require both interacting partners to be phosphorylated (Supplementary Fig. S12A). Importantly, the localization of the Lamin A and EZH2 mutants was validated by immunofluorescence assays, which predominantly showed a nuclear localization (Supplementary Fig. S12B and C).

Since phosphorylation impacts cell cycle dynamics, we next examined how phosphomutants of Lamin A/C and EZH2 affect cell cycle progression. MCF10A cells expressing Lamin A or EZH2 mutants were synchronized by double-thymidine block and released (for ∼18 h), followed by FACS profiling. Notably, phosphomimetic mutants (∼25%–30%) showed an increased number of cells in G2/M compared with full-length and phospho-deficient forms (∼6%–9%; Supplementary Fig. S13A and B). To further examine the effect of phosphomutants of Lamin A and EZH2 on cell cycle, we performed PI-FACS, BrdU incorporation, and H3S10p staining. BrdU incorporation was comparable across full-length, phospho-deficient, and phospho-mimetic constructs (∼85% BrdU positive cells), which excluded G1 arrest (Supplementary Fig. S13C and D). However, H3S10p staining revealed that full-length and phospho-deficient mutants progressed normally through mitosis (∼10% H3S10p-positive cells), whereas phospho-mimetic mutants (S22D, T345D) stalled at G2/M as indicated by PI-FACS, but displayed markedly reduced H3S10p positivity (<2%), suggesting an arrest in late S-to early G2 phase of the cell cycle (Supplementary Fig. S13E and F).

## Lamin A and EZH2 phosphorylation determines the dynamics of EMT

We next sought to determine the effect of Lamin A-EZH2 phosphorylation on EM plasticity. To address this question, we generated cell lines expressing either phosphodeficient or phosphomimetic mutants of Lamin A (S22A or S22D) and EZH2 (T345A or T345D) in the background of endogenous protein depletion.

Remarkably, the overexpression of the phosphomimetic Lamin A mutant (S22D) disrupts the Lamin A–EZH2 interaction, showing a pronounced mesenchymal phenotype, characterized by the upregulation of Vimentin, TWIST1, SNAI1, and ZEB1, and downregulation of E-cadherin, notwithstanding the absence of EMT inducers. In contrast, cells expressing either full-length Lamin A or the phosphodeficient mutant (S22A) retain their interaction with EZH2 and their epithelial features, even under EMT-inducing conditions such as TGF-β or TWIST1 overexpression (Fig. 7A, E, and F; quantification in Supplementary Fig. S14A–E).

Similarly, overexpression of full length or the phosphodeficient Lamin A (S22A) mutant (both capable of binding EZH2), was sufficient to induce a robust epithelial state, marked by high E-cadherin levels and reduced mesenchymal markers, even without GRHL2-mediated MET induction. In contrast, knockdown of Lamin A/C or overexpression of Lamin A (S22D)—which does not interact with EZH2—

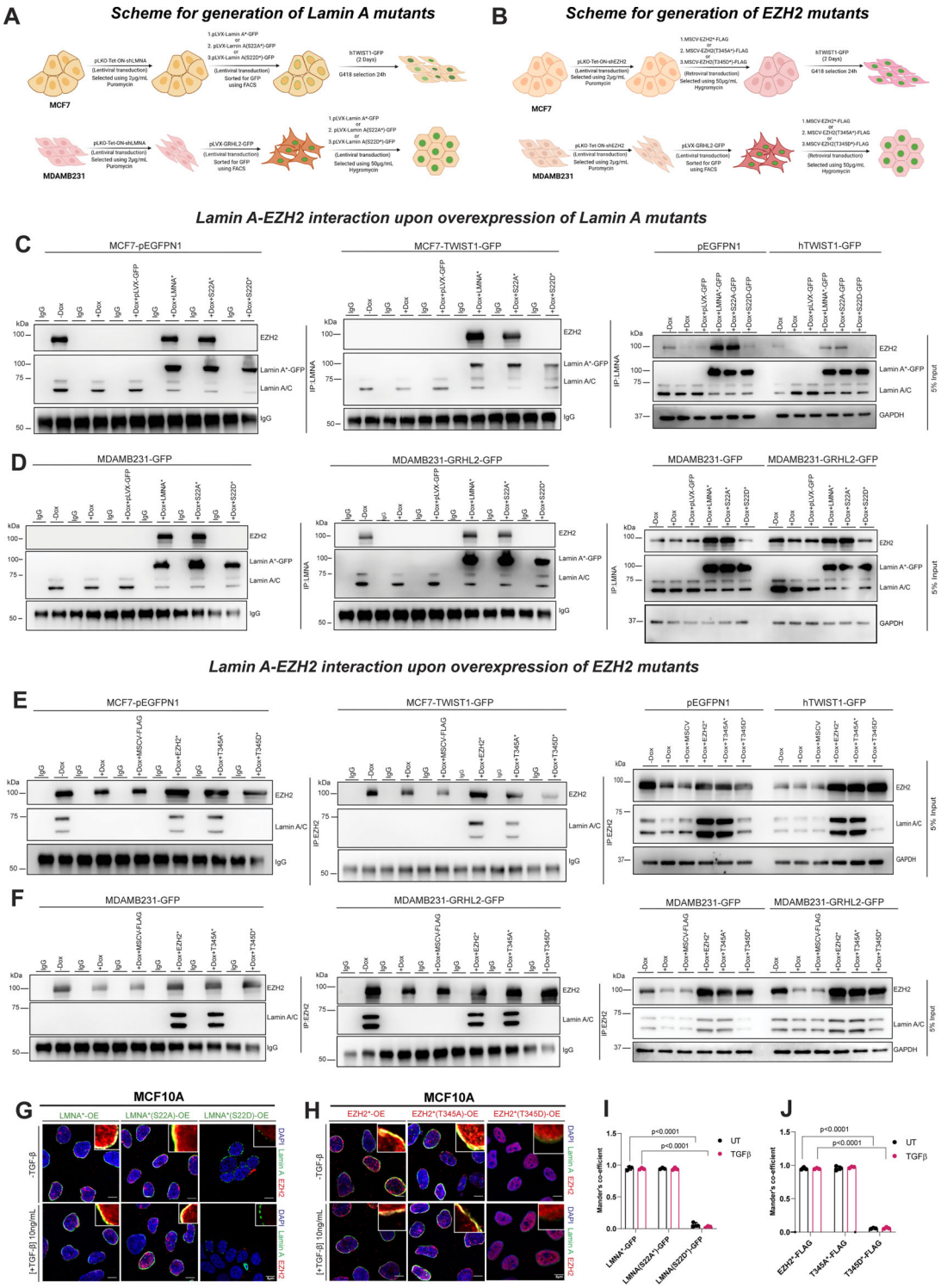


**Figure 6.** Phosphorylation-dependent regulation of Lamin A/C–EZH2 binding in EMT and MET. **(A, B)** Schematic representation of the workflow for generating stable cell lines with inducible knockdown of Lamin A **(A)** or EZH2 **(B)**, followed by rescue with full-length, phosphodeficient, or phosphomimetic mutants. **(C, D)** Co-IP of Lamin A in MCF7 and MDAMB231 cells after doxycycline-induced Lamin A/C depletion and rescue with full-length, phosphodeficient (S22A), or phosphomimetic (S22D) Lamin A. TWIST1-GFP was transiently overexpressed in MCF7 cells, and GRHL2-GFP was stably overexpressed in MDAMB231 cells. **(E, F)** Coimmunoprecipitation of EZH2 in MCF7 and MDAMB231 cells after doxycycline-induced EZH2 depletion and rescue with full-length, phosphodeficient (T345A), or phosphomimetic (T345D) EZH2. TWIST1-GFP was transiently overexpressed in MCF7 cells, and GRHL2-GFP was stably overexpressed in MDAMB231 cells. **(G)** Immunofluorescence images of MCF10A cells showing the extent of colocalization between Lamin A [full-length, phosphodeficient (S22A), or phosphomimetic (S22D)] and EZH2 ± TGF-β. Nucleus (DAPI). Scale bar ∼10 μm. **(H)** Immunofluorescence images of MCF10A cells showing the extent of colocalization between EZH2 [full-length, phosphodeficient (T345A), or phosphomimetic (T345D)] nucleus (DAPI). Scale bar ∼10 μm. **(I, J)** Quantification of Lamin A and EZH2 colocalization in MCF10A cells using Mander's coefficient. Unpaired Student's *t*-test was used to compute the *P*-value. Means are compared between **(I)** LMNA-GFP (UT; control) versus LMNA-S22D (UT) and LMNA-GFP (TGFβ; control) versus LMNA-S22D (TGFβ). **(J)** EZH2-FLAG (UT; control) versus EZH2-T345D (UT) and EZH2-FLAG (TGFβ; control) versus EZH2-T345D (TGFβ). Statistical significance, *P*-value <0.05.

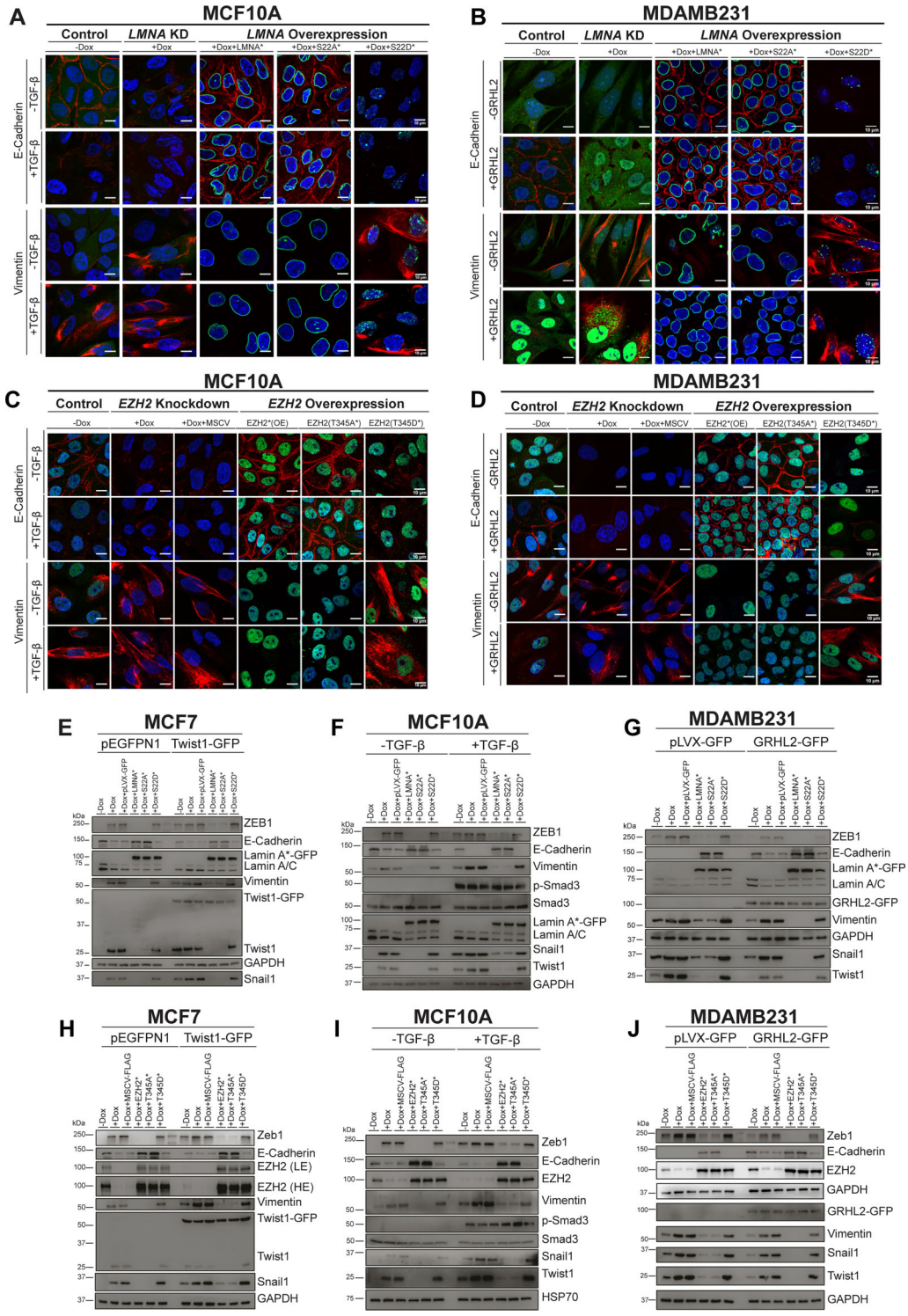


**Figure 7.** Phosphorylation-dependent regulation of EZH2 and Lamin A/C during EMT and MET. Representative mid-optical sections of immunofluorescence images showing the effect of Lamin A and EZH2 mutants on EMT (in MCF10A) and MET (in MDAMB231). MCF10A **(A, C)** and MDAMB231 **(B, D)**. Cells were transduced with full-length, phospho-deficient, or phospho-mimetic constructs of Lamin A **(A, B)** or EZH2 **(C, D)** following doxycycline-induced knockdown (0.5 μg/ml, 48 h) of endogenous Lamin A/C or EZH2. EMT was induced in MCF10A cells by TGF-β treatment (10 ng/ml, ∼7 days), while MET was induced in MDAMB231 cells by stable, constitutive overexpression of GRHL2. EZH2 was immunostained in green; E-cadherin and Vimentin were immunostained in red. Lamin A constructs were GFP-tagged. Nucleus (blue, DAPI). Scale bar ∼10 μm. **(E, F)** Immunoblot analysis of EMT marker expression in MCF7 and MCF10A cells upon Lamin A/C knockdown and rescue with full-length, phospho-deficient (S22A), or phospho-mimetic (S22D) Lamin A-GFP. EMT was induced by TWIST1 overexpression (∼48 h) in MCF7 cells or by 10ng/ml TGF-β (∼7 days) in MCF10A cells. **(G)** EM marker expression in cells with Lamin A/C knockdown was rescued with full-length, phospho-deficient (S22A) or phospho-mimetic (S22D) Lamin A/C. MET was induced by GRHL2 overexpression. **(H, I)** Immunoblot analysis of EMT marker expression in MCF7 and MCF10A cells upon EZH2 knockdown and rescue with full-length, phospho-deficient (T345A), or phospho-mimetic (T345D) EZH2-FLAG. EMT was induced by TGF-β (∼7 days) in MCF10A cells or by TWIST1 overexpression (∼48 h) in MCF7 cells. **(J)** EM marker expression in cells with EZH2 knockdown rescued with full-length, phospho-deficient (T345A), or phospho-mimetic (T345D) EZH2. MET was induced by GRHL2 overexpression.

resulted in the persistence of mesenchymal characteristics (Fig. 7B and G). Notably, MDAMB231 cells exhibited partial MET upon co-overexpression of GRHL2 and Lamin A (S22D), or GRHL2 overexpression combined with Lamin A/C depletion (Supplementary Fig. S14F–J). This reinforces the significance of the Lamin A–EZH2 interaction in facilitating MET and repressing mesenchymal genes.

To delineate the role of EZH2 phosphorylation in this regulatory axis, we introduced phosphodeficient (T345A) and phosphomimetic (T345D) EZH2 mutants in the background of EZH2 depletion in epithelial (MCF7, MCF10A) and mesenchymal (MDAMB231) cells. In MCF7 and MCF10A cells, overexpression of the phosphomimetic EZH2 mutant (T345D)—deficient in Lamin A/C binding—shows an EMT-like phenotype, including loss of E-cadherin and induction of mesenchymal markers, independent of external EMT induction. Conversely, overexpression of full length EZH2 or the phosphodeficient EZH2 mutant (T345A), which retains its interaction with Lamin A/C, maintained epithelial properties and resists EMT induction, even in the presence of TWIST1 or TGF-β (Fig. 7C, H, and I; quantification: Supplementary Fig. S14K–N).

Overexpression of full length or phosphodeficient EZH2 (T345A) promoted MET in MDAMB231 cells, consistent with elevated E-cadherin and suppression of mesenchymal markers, independent of GRHL2 overexpression. However, overexpression of the phosphomimetic EZH2 (T345D) or EZH2 knockdown (both of which abrogate Lamin A/C interaction), exacerbated mesenchymal properties. Overexpression of EZH2 (full length) or EZH2 (T345A) in the background of GRHL2 overexpression, facilitates transition of MDAMB231 cells to an epithelial-like phenotype [EZH2(OE) and EZH2(T345A)—E-cadherin (integrated density): 2108 ± 516 and 3560 ± 532, respectively], whereas EZH2 (T345D) or EZH2 depletion only partially reversed cells to an epithelial phenotype [EZH2(T345D)—E-cadherin (integrated density): 320 ± 58] as it maintains mesenchymal marker expression and a hybrid phenotype [Fig. 7D and J; quantification: Supplementary Fig. S14O–R).

Collectively, these data demonstrate that phosphorylation at Lamin A (S22) or EZH2 (T345) disrupts Lamin A/C–EZH2 interaction, activating mesenchymal transcription factors, thereby promoting EMT. In contrast, phosphodeficient mutants that preserve this interaction sustain epithelial identity and enable MET.

## Lamin A/C promotes chromatin compaction suppressing EMT

To investigate the functional consequences of Lamin A/C–EZH2 interaction, we examined the effects of CDK1-mediated phosphorylation of Lamin A/C or EZH2 on the expression of mesenchymal transcription factors *SNAI1*, *TWIST1*, and *ZEB1*. RNA-Seq following Lamin A/C depletion in MCF10A cells showed a significant upregulation of these transcription factors, indicating a role of Lamin A/C in their transcriptional repression. This indicates that Lamin A/C and repressive chromatin factors work in coordination, which may arise from spatial–epigenetic coupling, whereby Lamin A/C anchors PRC2-enriched chromatin at the nuclear periphery, promoting robust H3K27me3 deposition and enforcing transcriptional repression at key EMT-regulatory loci.

Analysis of publicly available ChIP-seq data sets from ChIP-Atlas revealed an enrichment of Lamin A, EZH2, and H3K27me3 at the −1 kb regions of the SNAI1, TWIST1, and ZEB1 promoters in epithelial MCF7 cells, and a loss of this occupancy in mesenchymal MDAMB231 cells (Lamin A/C: Supplementary Fig. S15A–C; EZH2: Supplementary Fig. S16A–C, H3K27me3: Supplementary Fig. S17A) [63]. We overexpressed phosphodeficient or phosphomimetic mutants of Lamin A or EZH2 in MCF7 cells and performed ChIP-qPCR at the −1 kb regions of SNAI1, TWIST1, and ZEB1 (Fig. 8A and B). Twist mediated EMT induction showed a marked reduction of Lamin A/C, EZH2, and H3K27me3 occupancy on SNAI1, TWIST1, and ZEB1 promoters, but were otherwise enriched on these promoters in untreated MCF7 cells (control). Lamin A/C depletion markedly reduced EZH2 and H3K27me3 occupancy, while control regions (MYT1, positive control; *GAPDH*, negative control) showed no differences in their occupancy (Fig. 8C and D, and Supplementary Fig. S17B).

ChIP-qPCR for transcriptional elongation markers revealed reduced occupancy of H3K36me3 and RNA polymerase II Ser2P at the +1 kb regions of *SNAI1*, *TWIST1*, and *ZEB1* in control MCF7 cells, consistent with a reduced expression of mesenchymal genes in epithelial cells. However, Lamin A/C depletion and TWIST1 overexpression significantly increased the enrichment of H3K36me3 and RNA Pol II Ser2P on the promoters of mesenchymal transcription factors (Fig. 8E and Supplementary Fig. S17C and D).

We next analyzed the effect of Lamin A phosphorylation. Overexpression of full-length Lamin A or the phosphodeficient mutant S22A preserved Lamin A/C, EZH2, and H3K27me3 occupancy at the −1 kb regions of SNAI1, TWIST1, and ZEB1, even under EMT-inducing conditions. In contrast, the phosphomimetic mutant S22D showed reduced enrichment of Lamin A (Fig. 8C), EZH2 (Fig. 8D), and H3K27me3 (Supplementary Fig. S17B) at these loci, accompanied by increased H3K36me3 (Fig. 8E) and RNA Pol II Ser2P (Supplementary Fig. S17D) at the +1 kb regions of SNAI1, TWIST1, and ZEB1. A similar regulatory mechanism was observed for EZH2 phosphorylation. Overexpression of full-length EZH2 or the phosphodeficient mutant T345A enhanced Lamin A/C, EZH2, and H3K27me3 occupancy at the −1 kb regions of SNAI1, TWIST1, and ZEB1. Conversely, the phosphomimetic mutant T345D reduced this enrichment, with a corresponding increase in H3K36me3 and RNA Pol II Ser2P occupancy at the +1 kb regions (Fig. 8F–H, and Supplementary Fig. S18A and B). This was corroborated by analysis of primer efficiency profiles (Supplementary Fig. S18C–F).

Taken together, these findings demonstrate that Lamin A/C facilitates EZH2 mediated deposition of H3K27me3 on mesenchymal gene promoters. Furthermore, CDK1-mediated phosphorylation of either protein disrupts this repression, thereby facilitating EMT.

## Impact of Lamin A/C–EZH2 phosphorylation on cancer progression

To investigate the functional role of Lamin A/C–EZH2 interaction in EM plasticity, we performed cell migration, and tumor induction assays. We performed Boyden-chamber assay (transwell to quantify migration) for MCF7 and MDAMB231 cells. In MCF7 cells, transient overexpression of hTwist1 followed by depletion of Lamin A/C or EZH2 increased migration by ∼30%. Similarly, overexpression of the phosphomimetic mutants Lamin A (S22D) or EZH2 (T345D) en-

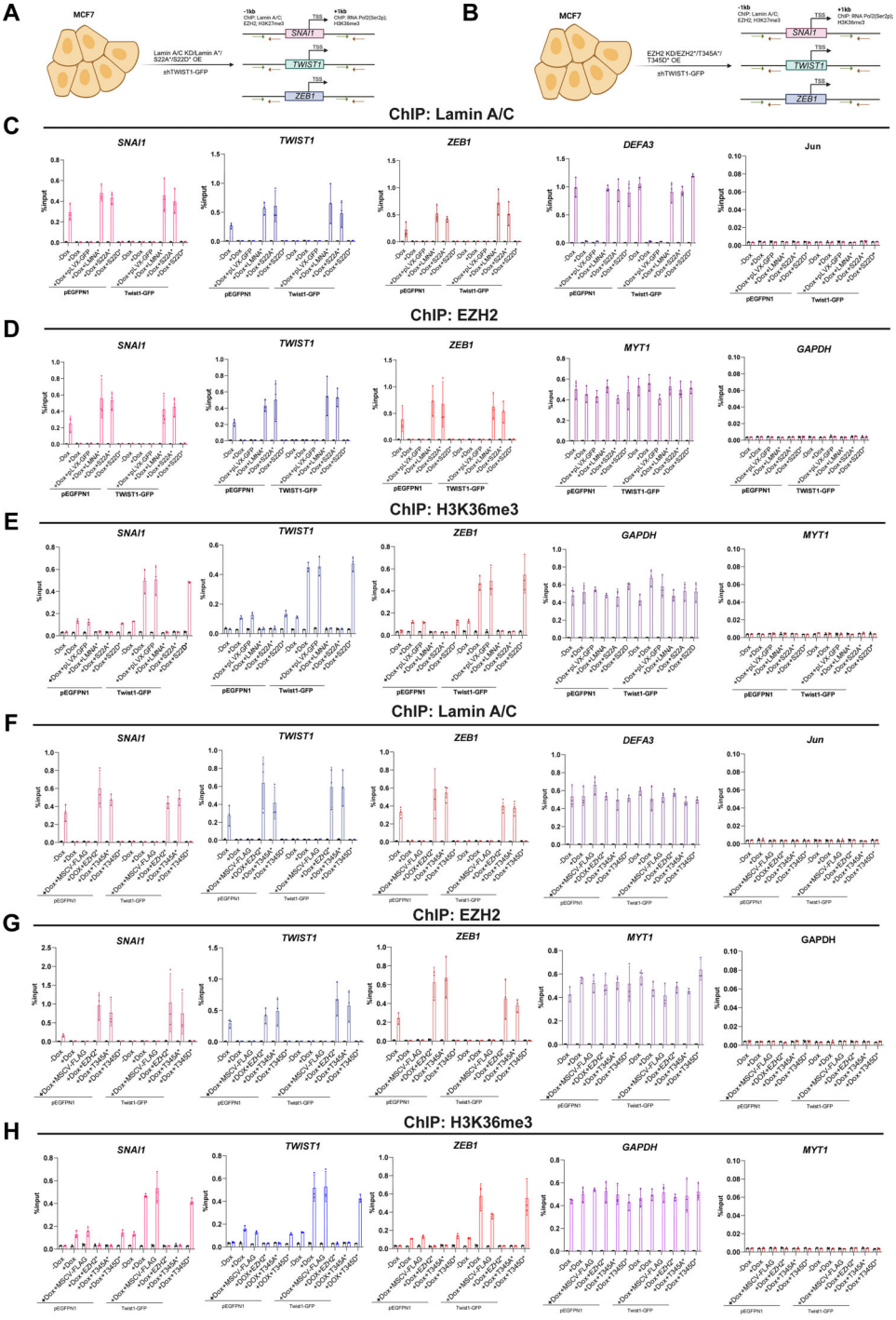


**Figure 8.** Lamin A/C promotes chromatin compaction suppressing EMT. **(A)** Schematic representation of chromatin immunoprecipitation (ChIP) experiments performed in MCF7 cells overexpressing TWIST1-GFP, following knockdown (KD) of Lamin A/C or overexpression (OE) of full-length Lamin A or phospho-mutant Lamin A (S22A: phospho-deficient; S22D: phospho-mimetic). ChIP was performed using antibodies against Lamin A/C, EZH2, H3K27me3 [−1 kb of transcription start sites (TSS)], and RNA Polymerase II (Ser2P) and H3K36me3 (+1 kb of TSS) at the promoters of key mesenchymal transcription factors SNAI1, TWIST1, and ZEB1. **(B)** Schematic representation of ChIP analysis in MCF7 cells with EZH2 knockdown or overexpression of full-length or phospho-mutant EZH2 (T345A: phospho-deficient; T345D: phospho-mimetic) in the context of TWIST1-GFP induction. Promoter occupancy of Lamin A/C, EZH2, and associated histone modifications (H3K27me3 and H3K36me3), as well as RNA Pol II (Ser2P), was examined at the TSS of SNAI1, TWIST1, and ZEB1. Green and red arrows indicate primers for the qPCR experiment. (**C–E**) ChIP PCR analysis in MCF7 cells stably transduced with full-length Lamin A, phosphodeficient (S22A), or phosphomimetic (S22D) variants, followed by transient transfection with pEGFP-N1 (control) or TWIST1-GFP for 48 h. ChIP occupancy of **(C)** Lamin A, **(D)** EZH2 at the −1 kb regions, and **(E)** H3K36me3 at the +1 kb regions of SNAI1, TWIST1, and ZEB1 were assessed. DEFA3 **(C)**, MYT1 **(D)**, and GAPDH **(E)** served as positive controls, while Jun **(C)**, GAPDH +1 kb **(D)**, and MYT1 **(E)** were negative controls for Lamin A/C, EZH2, and H3K36me3 respectively. (**F–H**) ChIP PCR analysis in MCF7 cells stably transduced with full-length EZH2, phosphodeficient (T345A), or phosphomimetic (T345D) variants, followed by transient transfection with pEGFP-N1 or TWIST1-GFP for 48 h. ChIP occupancy of **(F)** Lamin A, **(G)** EZH2 at the −1 kb regions, and **(H)** H3K36me3 at the +1 kb regions of SNAI1, TWIST1, and ZEB1 was assessed. DEFA3 **(F)**, MYT1 **(G)**, and GAPDH **(H)** served as positive controls, while Jun **(F)**, GAPDH +1 kb **(G)**, and MYT1 **(H)** were negative controls for Lamin A/C, EZH2, and H3K36me3 respectively. Data represent mean ± SD from three independent experiments.

hanced migration, whereas overexpression of the full-length proteins or their phosphodeficient mutants (Lamin A S22A, EZH2 T345A) reduced migration by ∼20% (Supplementary Fig. S19A and B). In MDAMB231 cells, GRHL2 overexpression reduced migration, while depletion of Lamin A or EZH2 increased migration. When GRHL2 was overexpressed in cells lacking Lamin A or EZH2, migration was further elevated compared to GRHL2 overexpression alone. Consistently, the phosphomimetic Lamin A (S22D) and EZH2 (T345D) variants enhanced migration than their full-length or phosphodeficient counterparts (Supplementary Fig. S19C and D). We performed wound healing assays to determine the migratory ability of MCF10A cells. Depletion of Lamin A/C or EZH2 increased cell migration, comparable to that induced by TGF-β. While, overexpression of full-length Lamin A or EZH2, as well as their phosphodeficient mutants (S22A, T345A), suppressed migration in both untreated and TGF-β-treated cells. In contrast, the phosphomimetic mutants (S22D, T345D) enhanced migration, even in the absence of TGF-β (Supplementary Fig. S20A and B).

To investigate the *in vivo* implications of Lamin A (S22A and S22D) and EZH2 (T345A and T345D) mutants to form tumors, we orthotopically injected MDA-MB-231 cells ($\sim 1 \times 10^6$), overexpressing (i) full length (Lamin A or EZH2 – control), (ii) phospho-deficient (Lamin A S22A; EZH2 T345A) (iii) phospho-mimetic (Lamin A S22D; EZH2 T345D) forms into the mammary fat pad of female NOD-SCID mice (∼6 weeks old). Tumour volume was monitored, and the experiment was terminated after ∼5 weeks (Validation of Lamin A and EZH2 knockdown and overexpression are shown in Supplementary Fig. S21A and B). Both phosphomimetic Lamin A (S22D) and EZH2 (T345D) exhibited a marked increase in tumor growth, as reflected by both tumor volume and final tumor weight (Fig. 9A–F), as compared to their full-length and phospho-deficient counterparts (full length control in Supplementary Fig. S21C–H).

Previous studies have consistently shown that the lungs are a frequent site of metastasis in breast cancers. We therefore performed H&E staining of lung sections and quantified metastatic nodules to determine whether Lamin A and EZH2 phosphomutants (with respect to the full-length control) affect metastatic dissemination [64, 65]. Mice injected with phospho-mimetic mutants (S22D-Lamin A and T345D-EZH2) showed a significantly higher metastatic burden, whereas full length (LMNA-WT and EZH2-WT) and phospho-deficient mutants (S22A-Lamin A and T345A-EZH2) did not form detectable lung metastases. These findings demonstrate that CDK1-dependent phosphorylation of Lamin A/C and EZH2 promotes both primary tumor growth and *in vivo* metastatic dissemination of breast cancer cells (Fig. 9G and H; full length control in Supplementary Fig. S21I–L).

To further address the significance of the Lamin A/C-EZH2 interaction, we performed triple enzyme digestion followed by immunoprecipitation on primary tumor-derived cells. Phosphodeficient Lamin A (S22A) maintained its interaction with EZH2, whereas the phosphomimetic Lamin A (S22D) preferentially interacted with phosphorylated CDK1 (pCDK1-T161; Fig. 9I). Similarly, immunoprecipitation of EZH2 revealed that the phosphodeficient EZH2 (T345A) interacted with Lamin A/C, while phosphomimetic EZH2 (T345D) interacted with pCDK1 (Fig. 9J).

We performed immunofluorescence assays in cells (cultured for ∼72 h) derived from the tumors (the EM state could not be examined *in situ*, as the subsequent assays necessitated culturing and expansion of cells). These assays also reveal morphological characteristics since the cells expressing phosphodeficient Lamin A or EZH2 mutants showed an epithelial-like morphology, whereas those expressing phosphomimetic mutants retained a mesenchymal phenotype (Fig. 9K–N).

In summary, these findings underscore a crucial role for Lamin A and EZH2 phosphorylation in modulating EM plasticity. Phosphomimetic modifications favour mesenchymal properties, whereas phosphodeficient or full-length variants reinforce epithelial characteristics.

## Discussion

### Summary of key results

In this study, we uncover a phosphorylation-sensitive interaction between the inner nuclear envelope protein Lamin A/C and the histone methyltransferase EZH2, revealing its pivotal role in regulating EM plasticity. Using a combination of models of EMT and its reversal (MET), we show that Lamin A/C interacts with EZH2 in epithelial cells, which renders a repressive chromatin environment on *SNAI1, TWIST1*, and *ZEB1* loci that encode for mesenchymal transcription factors (EMT-TF). To ensure comparable expression of empty vector and TWIST1 (in MCF7) or GRHL2 overexpression (in MDAMB231 cells; EGFP panel is included in Supplementary Fig. S25A–D). This interaction is disrupted upon EMT induction through CDK1-mediated phosphorylation of both Lamin A/C and EZH2, facilitating EMT-TF activation (Fig. 10). Phosphomimetic and phosphodeficient variants of Lamin A (S22D/S22A) and EZH2 (T345D/T345A) reveal their regulatory role of phosphorylation in controlling EMT. *In vivo*, phosphomimetic forms promote tumor growth and metastasis, whereas phosphodeficient forms maintain epithelial characteristics, decreasing tumor growth potential. These findings implicate Lamin A–EZH2 interaction as a critical epigenetic checkpoint modulated by phosphorylation in cancer progression.

### Lamins and EMT: contributions of A- and B-type lamins

Nuclear lamins regulate nuclear architecture with genome organization and transcriptional control, and their altered expression or modification profoundly impacts cancer cell behavior by modulating nuclear mechanics and chromatin accessibility [66].

Lamin A/C restricts EMT by reinforcing nuclear stiffness and limiting chromatin openness. Its reduction decreases nuclear rigidity, increases chromatin accessibility, and promotes invasion by enhancing mesenchymal gene expression [67, 68].

Lamin B1, in contrast, acts as a context-dependent EMT regulator. Its loss in lung cancer cells suppresses E-cadherin, elevates fibronectin and N-cadherin, and activates rearranged during transfection proto-oncogene and MAPK/PI3K–AKT signaling, suggesting an EMT-restraining role [69]. Lamin B1 enrichment at TAD boundaries supports EMT programs, and its depletion disrupts them in NMuMG cells [70]. However, in our study, Lamin B1 levels remained stable, and depletion of Lamin B1 or B2 had no effect on EMT, indicating cell-type-specific variability. While Lamin B2 contributes to nuclear in-

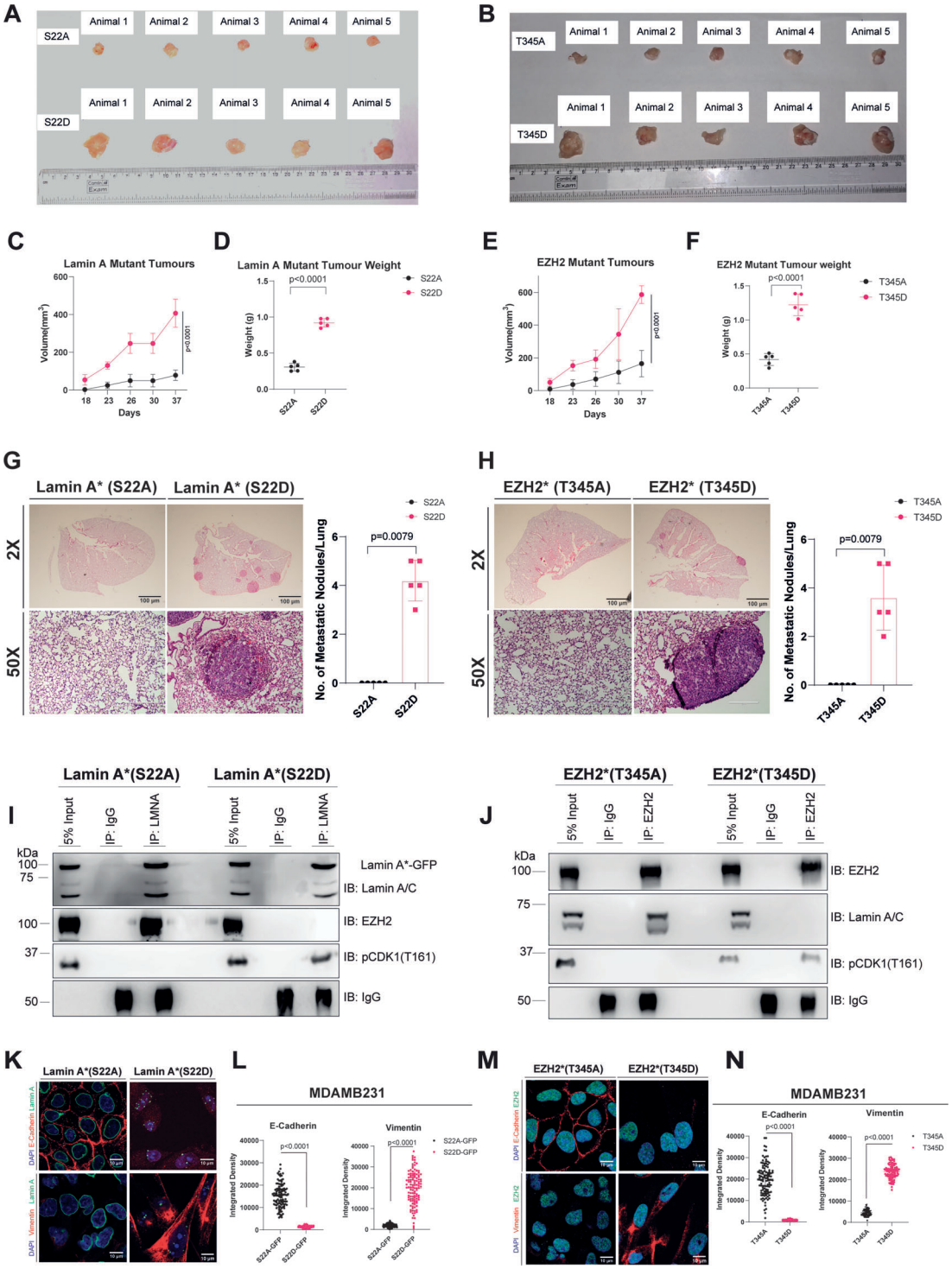


**Figure 9.** Impact of Lamin A/C–EZH2 phosphorylation on tumor progression. **(A, B)** Representative images of excised tumors from NOD-SCID female mice injected with MDAMB231 cells expressing either phospho-mutant Lamin A **(A)** or EZH2 **(B)**. $N = 5$ mice per group. **(C, D)** Quantification of tumor volume **(C)** and tumor weight **(D)** from Lamin A phospho-mutant xenografts. **(E, F)** Quantification of tumor volume **(E)** and tumor weight **(F)** from EZH2 phosphomutant xenografts. **(G)** Representative Hematoxylin and Eosin (H&E) images (2×, 50×) of lung metastases from MDA-MB-231 cells expressing phosphodeficient (S22A) or phosphomimetic (S22D) Lamin A. **(H)** Representative H&E images (2×, 50×) of lung metastases from MDA-MB-231 cells expressing phosphodeficient (T345A) or phosphomimetic (T345D) EZH2. Quantification of the number of nodules per lung is given alongside the H&E images. **(I)** Immunoprecipitation of Lamin A/C from tumor lysates followed by immunoblotting for EZH2 and phospho-CDK1 **(J)** Immunoprecipitation of EZH2 from tumor lysates followed by immunoblotting for Lamin A/C and phospho-CDK1 **(K)** Immunofluorescence of tumor-derived MDAMB231 cells stained for E-cadherin, Vimentin (red), and Lamin A (GFP). Nucleus (blue, DAPI). Scale bar ∼10 μm. **(L)** Quantification of the integrated density of E-Cadherin and Vimentin upon overexpression of phosphomutants of Lamin A. Data represent mean ± SD. Statistical significance was determined using an unpaired two-tailed Student's *t*-test, *P*-value <0.05 **(M)** Immunofluorescence of tumor-derived MDAMB231 cells stained for E-cadherin, Vimentin and EZH2. Nucleus (DAPI). Scale bar ∼10 μm. **(N)** Quantification of the integrated density of E-Cadherin and Vimentin upon overexpression of phosphomutants of EZH2. Data represent mean ± SD. Statistical significance was determined using an unpaired two-tailed Student's *t*-test. Means are compared between phosphodeficient (control) and phosphomimetic mutants.

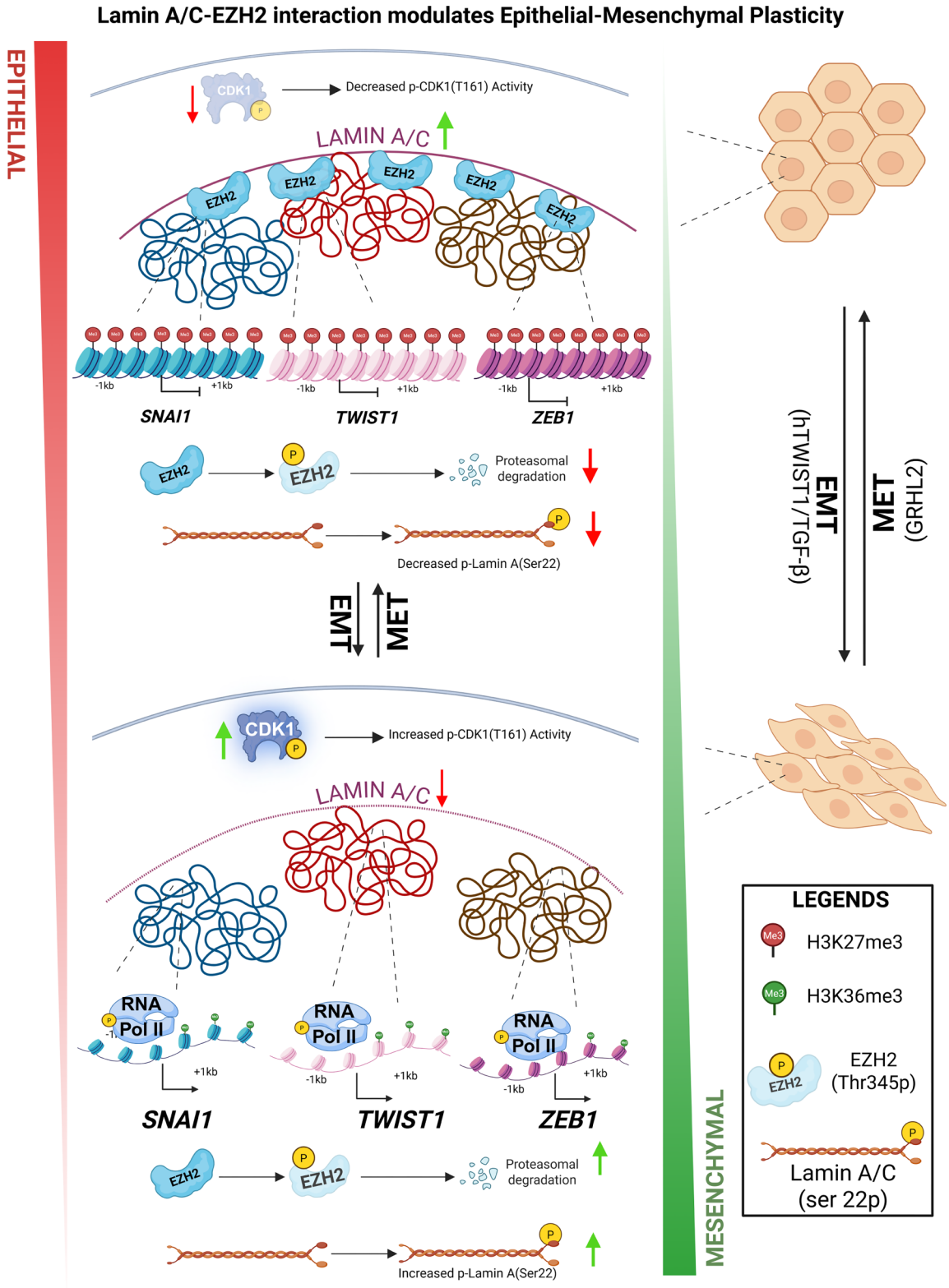


**Figure 10.** Lamin A/C-EZH2 interaction modulates EM plasticity. This schematic illustrates the dynamic regulation of EMT and MET by Lamin A/C–EZH2 signaling. In epithelial cells (top), high Lamin A/C levels promote the sequestration of EZH2 at the nuclear lamina, diminishing the transcriptional activation and expression of key EMT transcription factors (SNAI1, TWIST1, ZEB1) by enforcing H3K27me3-mediated repression at their promoters. Reduced CDK1 activity leads to reduced phosphorylation on both Lamin A/C (Ser22) and EZH2 (Thr345), limiting EZH2 degradation and further stabilizing chromatin repression. During EMT, increased CDK1 activity and phosphorylation of Lamin A/C (Ser22) and EZH2 (Thr345), results in proteasomal degradation of EZH2 which releases the repressive chromatin state, recruits active RNA polymerase II to EMT gene promoters, and upregulates EMT transcription factors, promoting mesenchymal properties. Created in BioRender. Sengupta, K.
(Schematic illustration of EMT and MET regulation by Lamin A/C-EZH2).

tegrity and metastasis in other cancers, it did not impact EMT in breast cancer [45, 71].

Overall, Lamin A/C consistently functions as a repressive scaffold maintaining epithelial identity, whereas B-type lamins show context-dependent roles. Loss or modification of Lamin A/C represents a critical step enabling EMT and invasiveness of cancer cells.

## Coordination of Lamin A/C–PRC2 Interactions regulate EM Plasticity

Previous studies have reported divergent patterns of EZH2 expression during EMT, suggesting that its regulation may be context dependent [72]. While some reports did not observe a reduction of EZH2 in mesenchymal-like cells, our data reveal a modest but consistent decrease in EZH2 upon EMT induction and restoration during MET. This aligns with recent studies indicating that attenuation of PRC2/EZH2 function accompanies mesenchymal transition. Specifically, loss or dysfunction of PRC2 promotes a quasi-mesenchymal trajectory and enhance metastatic traits, implicating PRC2 as an organizer of the epithelial state [73]. In lung carcinoma cells, inhibition or knockout of EZH2 induces mesenchymal gene expression and a shift toward the mesenchymal phenotype [74], while in breast cancer models, EZH2 sustains epithelial identity by repressing mesenchymal programs [75]. Reduction in EZH2 levels, was undetected in other studies [76], underscoring that the relationship between EZH2 expression and EMT may vary across cellular contexts and experimental systems.

Since EZH2 levels are modulated during EMT, we next explored whether changes in the sub-interactome of Lamin A/C could explain these dynamics, focusing on Lamin A/C as a potential scaffold coordinating PRC2 activity and chromatin organization.

## Lamin A/C–mediated chromatin reorganization during EMT and MET

Beyond its structural role, Lamin A/C serves as a dynamic scaffold that coordinates chromatin modifiers and transcriptional regulators to control EM plasticity. In epithelial MCF7 cells, Lamin A/C interacts with EZH2—the catalytic subunit of PRC2 responsible for H3K27 trimethylation—as well as other chromatin organizers such as NUDT21, LIMA1, and EHMT2 [67, 68]. During EMT, this interaction is lost, coinciding with Lamin A/C association with phosphorylated CDK1 and CCNB1, indicating a potential shift in the functional role of Lamin from chromatin organization to proliferative signaling [67].

A-type lamins associate with both euchromatin and heterochromatin, and loss of LAP2$\alpha$ redistributes Lamin A/C toward heterochromatin with altered histone modifications [77]. Similarly, reduced Lamin A/C decreases H3K27me3 levels and reorganizes, activating mesenchymal genes. Thus, Lamin A/C preserves a repressive chromatin environment, and its loss promotes chromatin relaxation and mesenchymal gene activation.

The Lamin A/C–EZH2 interaction is re-established upon MET, restoring PRC2 scaffolding and epithelial identity. [78]. Unlike A-type lamins, B-type lamins interact with G9a and SUV39H1, unaffected during EMT, emphasizing their distinct functional roles [45, 71].

Overall, Lamin A/C functions as a phosphorylation-dependent hub linking chromatin organization and cell cycle signaling. Its dynamic interaction with PRC2 and post-translationally modified EZH2 integrates nuclear architecture and epigenetic regulation to control EM plasticity, with MET-driven restoration of the Lamin A/C–EZH2 complex reinstating epithelial chromatin states.

## pCDK1, Lamin A/C, and EMT–MET dynamics

During EMT, Lamin A/C associates with pCDK1 (T161), coinciding with loss of Lamin A/C–EZH2 interaction. BrdU incorporation in MCF10A cells undergoing EMT did not show G1 arrest, while decreased H3S10 phosphorylation indicated EMT-associated cell cycle arrest occurs between late S and early G2 phase.

Mechanistically, pCDK1 phosphorylates Lamin A/C and EZH2, disrupting their interaction, relieving PRC2-mediated H3K27me3 repression at mesenchymal loci, and activating EMT transcriptional programs. Upon MET, Lamin A/C–EZH2 interactions are restored, reinstating epithelial chromatin and transcriptional repression [67, 76].

These results are consistent with the finding that CDK1 phosphorylation modulates EMT, and frequently correlates with cell cycle stalling at late S/early G2 transition, coupling proliferative signalling with transcriptional reprogramming [57–59]. In line with recent studies highlighting the role of EMT-inducing transcription factors in late S/early G2-phase regulation, replication stress, and DNA damage responses [79–83], certain partial or metastatic EMT states are associated with transient G1 arrest or reduced proliferation, underscoring the temporal and contextual plasticity of EMT–cell cycle coupling [84, 85].

Collectively, our data suggest that cells undergoing EMT show cell cycle arrest at late S or early G2 phase, enabling pCDK1-dependent remodeling of Lamin A/C scaffolds, dissociation and degradation of EZH2, leading to activation of mesenchymal programs. Restoration of the Lamin A/C–EZH2 complex during MET underscores the reversible coupling between cell-cycle state, nuclear organization, and EM plasticity.

## Decoding EMT plasticity through Lamin A and EZH2 phosphorylation

EMT and MET occur along a continuum, with hybrid epithelial/mesenchymal (E/M) states serving as key intermediates in tumor progression and metastasis. This hybrid population, marked by CD104 and CD44 co-expression [86].

During TWIST1-induced EMT, cells acquire a mesenchymal-like ($CD104^{+}CD44^{+}$) phenotype (Supplementary Fig. S22A and B), whereas overexpression of Lamin A or EZH2, with or without TWIST1, restores epithelial identity ($CD104^{+}CD44^{-}$), bypassing the hybrid state. In contrast, phospho-mimetic mutants (Lamin A S22D, EZH2 T345D) enrich hybrid populations in MCF7 cells, indicating that phosphorylation disrupts chromatin binding and repression of EMT-TFs such as SNAI1, TWIST1, and ZEB1. Under GRHL2-driven MET in MDA-MB-231 cells, these mutants maintain hybrid populations despite epithelial cues (GRHL2 overexpression).

Rescue experiments reveal that a complete commitment to an epithelial state requires unphosphorylated Lamin A and EZH2. Phospho-deficient mutants (S22A, T345A) restore epithelial identity ($CD104^{+}CD44^{-}$), while phospho-mimetic forms sustain hybrid states (Supplementary Figs S22C and D,

and S23A–D), consistent with Lamin A phosphorylation promoting nuclear softening and chromatin decondensation [87].

Overall, the hybrid E/M state is a regulated phenotype governed by post-translational modifications of Lamin A and EZH2. Phosphorylation-dependent disruption of their interaction enhances EM plasticity and sustains hybrid populations linked to metastasis.

### Implications for diagnosis and treatment

The Lamin A–EZH2 interaction and their phosphorylation states offer potential diagnostic and therapeutic avenues. Phosphorylated Lamin A (S22) and EZH2 (T345) may serve as markers of mesenchymal transition and metastatic potential, detectable by mass spectrometry or immunohistochemistry to refine EMT-based prognosis.

CPTAC proteomics showed increased pLMNA(Ser22) and decreased total LMNA with tumor progression (Supplementary Fig. S24A), paralleled by elevated pEZH2(T345) and reduced total EZH2 (Supplementary Fig. S24B). TCGA data further revealed progressive CCNB1 upregulation and increased pCDK1(T161) across tumor stages, linking CDK1–CCNB1 activity to malignancy (Supplementary Fig. S24C and D) [88, 89].

Therapeutically, inhibiting CDK1 or stabilizing the Lamin A–EZH2 complex could restore heterochromatin and suppress EMT-TFs, promoting a less aggressive phenotype. However, broad PRC2 inhibition may disrupt Lamin A–EZH2 tumor-suppressive functions, emphasizing patient-tailored approaches. The reversibility of this interaction highlights tumor plasticity and its potential as a target to drive cells toward a more differentiated, less malignant state.

### Limitations and future perspectives

This study identifies a phosphorylation-dependent Lamin A–EZH2 mechanism regulating EMT, but several aspects remain unresolved. The universality of this pathway beyond breast and liver carcinoma (HepG2; Supplementary Fig. S24E) needs validation, as tissue-specific factors may influence its function.

Although *in vivo* data support a phosphorylation-dependent Lamin A–EZH2 interaction in primary tumors, its role during metastasis and under therapeutic stress remains unclear. Determining whether EMT involves cell-cycle arrest specifically in late S or early G2 phases will further refine our understanding of this mechanism. Future studies employing high-resolution cell-cycle mapping approaches, such as short BrdU/EdU pulse labeling, combined DNA-content analysis with replication and mitotic markers, or single-cell cell-cycle indexing will be essential to definitively distinguish late S from early G2 states and clarify their contribution to EMT regulation.

Additionally, the phosphatases responsible for Lamin A and EZH2 dephosphorylation are yet to be identified. These enzymes are likely to mediate complex disassembly and chromatin reorganization, influencing EMT reversibility. Elucidating these regulatory layers will be key to fully defining the Lamin A–EZH2–CDK1 axis and its therapeutic relevance in tumor progression and chemoresistance.

## Acknowledgements

We thank Ruby Yun-Ju Huang (National Taiwan University, Taiwan) for generously providing the GRHL2 constructs that were critical to this study. RNA sequencing was carried out by MedGenome (Bengaluru), and we acknowledge their contribution. We are grateful to the core facilities at IISER Pune, including the Mass Spectrometry Facility, Microscopy Facility, NFGFHD, and the FACS Facility, for their technical assistance. We also acknowledge the Revvity–IISER Pune Center of Excellence for providing access to the Operetta system. We thank Khushi Salvi and Madhura Kulkarni for providing protein lysates from breast cancer cell lines. We sincerely thank Richa Rikhy (IISER-Pune) for kindly providing PLA kits and reagents, as well as for valuable discussions throughout the course of this work. We are thankful to Anish Pandey for his help with HADDOCK simulations. Illustrations were created using BioRender, and we acknowledge their contribution to the visual presentation of our work. We thank Sanjeev Galande for providing access to the Covaris S220 for chromatin shearing. We thank Ellora Sen, NBRC, New Delhi, for her generous support with antibodies. We thank Sorab Dalal, ACTREC, Mumbai, for generously providing CDK1 construct. We thank Ajay S. Labade and CBL, IISER-Pune for insightful discussions during the preparation of this manuscript.

*Author contributions*: Balaji AK (Conceptualization [lead], Data curation [lead], Formal analysis [lead], Investigation [lead], Methodology [lead], Visualization [lead], Writing – original draft [equal], Writing – review & editing [equal], Santam Saha (Conceptualization [supporting], Data curation [supporting], Formal analysis [supporting], Methodology [supporting], Resources [supporting], Writing – original draft [supporting], Writing – review & editing [supporting], Kundan Sengupta (Conceptualization [lead], Formal analysis [supporting], Funding acquisition [lead], Investigation [lead], Methodology [supporting], Project administration [lead], Resources [supporting], Supervision [lead], Validation [supporting], Writing – original draft [supporting], Writing – review & editing [equal])

## Supplementary data

Supplementary data is available at NAR online.

## Conflict of interest

None declared.

## Funding

We gratefully acknowledge funding support from ANRF, Department of Science and Technology, Science and Engineering Research Board (grant #CRG/2020/002563), Ministry of Education-STARS (grant #MoE-STARS/STARS-2/2023-0603), Department of Biotechnology (DBT) MedDevice (grant #BT/PR49745/MED/32/925/2023), Department of Biotechnology (BT/PR52973/MED/30/2535/2024), Intermediate Fellowship of the Wellcome Trust–DBT India Alliance (grant #500164/Z/09/Z) and Intramural funding from IISER-Pune.

## Data availability

The RNA sequencing data generated in this study have been deposited in the Gene Expression Omnibus under accession number GSE289750.

The mass spectrometry proteomics data are available via the PRIDE repository with the dataset identifier PXD060831.

## References


1. Thiery JP, Acloque H, Huang RYJ *et al.* Epithelial–mesenchymal transitions in development and disease. *Cell* 2009;139:871–90. https://doi.org/10.1016/j.cell.2009.11.007
2. Acloque H, Adams MS, Fishwick K *et al.* Epithelial–mesenchymal transitions: the importance of changing cell state in development and disease. *J Clin Invest* 2009;119:1438–49. https://doi.org/10.1172/JCI38019
3. Little MH, McMahon AP. Mammalian kidney development: principles, progress, and projections. *Cold Spring Harb Perspect Biol* 2012;4:a008300.
4. Kalluri R, Weinberg RA. The basics of epithelial–mesenchymal transition. *J Clin Invest* 2009;119:1420–8. https://doi.org/10.1172/JCI39104
5. Pitsidianaki I, Morgan J, Adams J *et al.* Mesenchymal-to-epithelial transitions require tissue-specific interactions with distinct laminins. *J Cell Biol* 2021;220:e202010154.
6. Brabletz T, Kalluri R, Nieto MA *et al.* EMT in cancer. *Nat Rev Cancer* 2018;18:128–34. https://doi.org/10.1038/nrc.2017.118
7. Jolly MK, Boareto M, Huang B *et al.* Implications of the hybrid epithelial/mesenchymal phenotype in metastasis. *Front Oncol* 2015;5:155. https://doi.org/10.3389/fonc.2015.00155
8. Jolly MK, Somarelli JA, Sheth M *et al.* Hybrid epithelial/mesenchymal phenotypes promote metastasis and therapy resistance across carcinomas. *Pharmacol Ther* 2019;194:161–84. https://doi.org/10.1016/j.pharmthera.2018.09.007
9. Pastushenko I, Mauri F, Song Y *et al.* Fat1 deletion promotes hybrid EMT state, tumour stemness and metastasis. *Nature* 2021;589:448–55. https://doi.org/10.1038/s41586-020-03046-1
10. Pastushenko I, Brisebarre A, Sifrim A *et al.* Identification of the tumour transition states occurring during EMT. *Nature* 2018;556:463–8. https://doi.org/10.1038/s41586-018-0040-3
11. Liu Q-L, Luo M, Huang C *et al.* Epigenetic regulation of epithelial to mesenchymal transition in the cancer metastatic cascade: implications for cancer therapy. *Front Oncol* 2021;11:657546. https://doi.org/10.3389/fonc.2021.657546
12. Lamouille S, Xu J, Derynck R. Molecular mechanisms of epithelial–mesenchymal transition. *Nat Rev Mol Cell Biol* 2014;15:178–96. https://doi.org/10.1038/nrm3758
13. Nieto MA, Huang RYJ, Jackson RA *et al.* EMT: 2016. *Cell* 2016;166:21–45. https://doi.org/10.1016/j.cell.2016.06.028
14. Solovei I, Wang AS, Thanisch K *et al.* LBR and lamin A/C sequentially tether peripheral heterochromatin and inversely regulate differentiation. *Cell* 2013;152:584–98. https://doi.org/10.1016/j.cell.2013.01.009
15. Kim J-K, Louhghalam A, Lee G *et al.* Nuclear lamin A/C harnesses the perinuclear apical actin cables to protect nuclear morphology. *Nat Commun* 2017;8:2123. https://doi.org/10.1038/s41467-017-02217-5
16. Capo-Chichi CD, Yeasky TM, Smith ER *et al.* Nuclear envelope structural defect underlies the main cause of aneuploidy in ovarian carcinogenesis. *BMC Cell Biol* 2016;17:37. https://doi.org/10.1186/s12860-016-0114-8
17. Wong KM, Song J, Wong YH. CTCF and EGR1 suppress breast cancer cell migration through transcriptional control of Nm23-H1. *Sci Rep* 2021;11:491. https://doi.org/10.1038/s41598-020-79869-9
18. Wang R-R, Qiu X, Pan R *et al.* Dietary intervention preserves β cell function in mice through CTCF-mediated transcriptional reprogramming. *J Exp Med* 2022;219:e20211779.
19. Cesarini E, Mozzetta C, Marullo F *et al.* Lamin A/C sustains PcG protein architecture, maintaining transcriptional repression at target genes. *J Cell Biol* 2015;211:533–51. https://doi.org/10.1083/jcb.201504035
20. Siegenfeld AP, Roseman SA, Roh H *et al.* Polycomb-lamina antagonism partitions heterochromatin at the nuclear periphery. *Nat Commun* 2022;13:4199. https://doi.org/10.1038/s41467-022-31857-5
21. Cardenas H, Zhao J, Vieth E *et al.* EZH2 inhibition promotes epithelial-to-mesenchymal transition in ovarian cancer cells. *Oncotarget* 2016;7:84453–67. https://doi.org/10.18632/oncotarget.11497
22. Xu Y, Qin L, Sun T *et al.* Twist1 promotes breast cancer invasion and metastasis by silencing Foxa1 expression. *Oncogene* 2017;36:1157–66. https://doi.org/10.1038/onc.2016.286
23. Zhang Y-Q, Wei X-L, Liang Y-K *et al.* Over-expressed twist associates with markers of epithelial mesenchymal transition and predicts poor prognosis in breast cancers via ERK and Akt activation. *PLoS One* 2015;10:e0135851. https://doi.org/10.1371/journal.pone.0135851
24. Paul I, Bolzan D, Youssef A *et al.* Parallelized multidimensional analytic framework applied to mammary epithelial cells uncovers regulatory principles in EMT. *Nat Commun* 2023;14:688. https://doi.org/10.1038/s41467-023-36122-x
25. Zhang J, Tian X-J, Zhang H *et al.* TGF-β-induced epithelial-to-mesenchymal transition proceeds through stepwise activation of multiple feedback loops. *Sci Signal* 2014;7:ra91. https://doi.org/10.1126/scisignal.2005304
26. Werner S, Frey S, Riethdorf S *et al.* Dual roles of the transcription factor grainyhead-like 2 (GRHL2) in breast cancer. *J Biol Chem* 2013;288:22993–3008. https://doi.org/10.1074/jbc.M113.456293
27. Chung VY, Tan TZ, Ye J *et al.* The role of GRHL2 and epigenetic remodeling in epithelial–mesenchymal plasticity in ovarian cancer cells. *Commun Biol* 2019;2:272. https://doi.org/10.1038/s42003-019-0506-3
28. Eremenko E, Taylor ZV, Khand B *et al.* An optimized protocol for the retroviral transduction of mouse CD4 T cells. *STAR Protocols* 2021;2:100719. https://doi.org/10.1016/j.xpro.2021.100719
29. Tan JYM, Tan JC, Wang C *et al.* Protocol for the simultaneous activation and lentiviral transduction of primary human T cells with artificial T cell receptors. *STAR Protocols* 2025;6:103685. https://doi.org/10.1016/j.xpro.2025.103685
30. Landt SG, Marinov GK, Kundaje A *et al.* ChIP-seq guidelines and practices of the ENCODE and modENCODE consortia. *Genome Res* 2012;22:1813–31. https://doi.org/10.1101/gr.136184.111
31. Bustin SA, Benes V, Garson JA *et al.* The MIQE guidelines: minimum information for publication of quantitative real-time PCR experiments. *Clin Chem* 2009;55:611–22. https://doi.org/10.1373/clinchem.2008.112797
32. Kumar K, Mhetre A, Ratnaparkhi GS *et al.* A Superfamily-wide activity atlas of serine hydrolases in *Drosophila melanogaster*. *Biochemistry* 2021;60:1312–24. https://doi.org/10.1021/acs.biochem.1c00171
33. Lagundžin D, Krieger KL, Law HCH *et al.* An optimized co-immunoprecipitation protocol for the analysis of endogenous protein-protein interactions in cell lines using mass spectrometry. *STAR Protocols* 2022;3:101234. https://doi.org/10.1016/j.xpro.2022.101234
34. Gaponova AV, Rodin S, Mazina AA *et al.* Epithelial-mesenchymal transition: role in cancer progression and the perspectives of antitumor treatment. *Acta Naturae* 2020;12:4–23. https://doi.org/10.32607/actanaturae.11010
35. Dongre A, Weinberg RA. New insights into the mechanisms of epithelial–mesenchymal transition and implications for cancer. *Nat Rev Mol Cell Biol* 2019;20:69–84. https://doi.org/10.1038/s41580-018-0080-4
36. Le AVP, Szaumkessel M, Tan TZ *et al.* DNA methylation profiling of breast cancer cell lines along the epithelial mesenchymal spectrum-implications for the choice of circulating tumour DNA methylation markers. *Int J Mol Sci* 2018;19:2553.
37. Cieply B, Riley P, Pifer PM *et al.* Suppression of the epithelial–mesenchymal transition by Grainyhead-like-2. *Cancer*

*Res* 2012;72:2440–53. https://doi.org/10.1158/0008-5472.CAN-11-4038
38. Wang Z, Coban B, Wu H *et al.* GRHL2-controlled gene expression networks in luminal breast cancer. *Cell Commun Signal* 2023;21:15. https://doi.org/10.1186/s12964-022-01029-5
39. Alisafaei F, Jokhun DS, Shivashankar GV *et al.* Regulation of nuclear architecture, mechanics, and nucleocytoplasmic shuttling of epigenetic factors by cell geometric constraints. *Proc Natl Acad Sci USA* 2019;116:13200–9. https://doi.org/10.1073/pnas.1902035116
40. de Leeuw R, Gruenbaum Y, Medalia O. Nuclear Lamins: thin filaments with major functions. *Trends Cell Biol* 2018;28:34–45. https://doi.org/10.1016/j.tcb.2017.08.004
41. Comaills V, Kabeche L, Morris R *et al.* Genomic instability is induced by persistent proliferation of cells undergoing epithelial-to-mesenchymal transition. *Cell Rep* 2016;17:2632–47. https://doi.org/10.1016/j.celrep.2016.11.022
42. Love MI, Huber W, Anders S. Moderated estimation of fold change and dispersion for RNA-seq data with DESeq2. *Genome Biol* 2014;15:550. https://doi.org/10.1186/s13059-014-0550-8
43. Ye J, Zhang Y, Cui H *et al.* WEGO 2.0: a web tool for analyzing and plotting GO annotations, 2018 update. *Nucleic Acids Res* 2018;46:W71–5. https://doi.org/10.1093/nar/gky400
44. Baldarelli RM, Smith CM, Finger JH *et al.* The mouse Gene Expression Database (GXD): 2021 update. *Nucleic Acids Res* 2021;49:D924–31. https://doi.org/10.1093/nar/gkaa914
45. Zheng X, Hu J, Yue S *et al.* Lamins organize the global three-dimensional genome from the nuclear periphery. *Mol Cell* 2018;71:802–15. https://doi.org/10.1016/j.molcel.2018.05.017e7.
46. Guelen L, Pagie L, Brasset E *et al.* Domain organization of human chromosomes revealed by mapping of nuclear lamina interactions. *Nature* 2008;453:948–51. https://doi.org/10.1038/nature06947
47. van Steensel B, Belmont AS. Lamina-associated domains: links with chromosome architecture, heterochromatin, and gene repression. *Cell* 2017;169:780–91. https://doi.org/10.1016/j.cell.2017.04.022
48. Wang Y, Elsherbiny A, Kessler L *et al.* Lamin A/C-dependent chromatin architecture safeguards naïve pluripotency to prevent aberrant cardiovascular cell fate and function. *Nat Commun* 2022;13:6663. https://doi.org/10.1038/s41467-022-34366-7
49. Liu B, Wang Z, Zhang L *et al.* Depleting the methyltransferase Suv39h1 improves DNA repair and extends lifespan in a progeria mouse model. *Nat Commun* 2013;4:1868. https://doi.org/10.1038/ncomms2885
50. Karoutas A, Szymanski W, Rausch T *et al.* The NSL complex maintains nuclear architecture stability via lamin A/C acetylation. *Nat Cell Biol* 2019;21:1248–60. https://doi.org/10.1038/s41556-019-0397-z
51. Ontology Consortium G, Aleksander SA, Balhoff J *et al.* The Gene Ontology knowledgebase in 2023. *Genetics* 2023;224:iyad031. https://doi.org/10.1093/genetics/iyad031
52. Kaneshiro JM, Capitanio JS, Hetzer MW. Lamin B1 overexpression alters chromatin organization and gene expression. *Nucleus* 2023;14:2202548. https://doi.org/10.1080/19491034.2023.2202548
53. de Vries SJ, van Dijk M, Bonvin AMJJ. The HADDOCK web server for data-driven biomolecular docking. *Nat Protoc* 2010;5:883–97. https://doi.org/10.1038/nprot.2010.32
54. Wu SC, Zhang Y. Cyclin-dependent kinase 1 (CDK1)-mediated phosphorylation of enhancer of zeste 2 (Ezh2) regulates its stability. *J Biol Chem* 2011;286:28511–9. https://doi.org/10.1074/jbc.M111.240515
55. Jeong S, Ahn J, Jo I *et al.* Cyclin-dependent kinase 1 depolymerizes nuclear lamin filaments by disrupting the head-to-tail interaction of the lamin central rod domain. *J Biol Chem* 2022;298:102256. https://doi.org/10.1016/j.jbc.2022.102256
56. Hendzel MJ, Wei Y, Mancini MA *et al.* Mitosis-specific phosphorylation of histone H3 initiates primarily within pericentromeric heterochromatin during G2 and spreads in an ordered fashion coincident with mitotic chromosome condensation. *Chromosoma* 1997;106:348–60. https://doi.org/10.1007/s004120050256
57. Yang L, Besschetnova TY, Brooks CR *et al.* Epithelial cell cycle arrest in G2/M mediates kidney fibrosis after injury. *Nat Med* 2010;16:535–43. https://doi.org/10.1038/nm.2144
58. Lovisa S, LeBleu VS, Tampe B *et al.* Epithelial-to-mesenchymal transition induces cell cycle arrest and parenchymal damage in renal fibrosis. *Nat Med* 2015;21:998–1009. https://doi.org/10.1038/nm.3902
59. Hu S, Lu Y, Yu G *et al.* Epithelial–mesenchymal transition couples with cell cycle arrest at various stages. bioRxiv, https://doi.org/10.1101/2025.02.24.639880, 28 February 2025, preprint: not peer reviewed.
60. Kochin V, Shimi T, Torvaldson E *et al.* Interphase phosphorylation of lamin A. *J Cell Sci* 2014;127:2683–96.
61. Ikegami K, Secchia S, Almakki O *et al.* Phosphorylated Lamin A/C in the nuclear interior binds active enhancers associated with abnormal transcription in progeria. *Dev Cell* 2020;52:699–713. https://doi.org/10.1016/j.devcel.2020.02.011
62. Liu S, Xiong F, Dou Z *et al.* Phosphorylation of Lamin A/C regulates the structural integrity of the nuclear envelope. *J Biol Chem* 2025;301:108033. https://doi.org/10.1016/j.jbc.2024.108033
63. Zou Z, Ohta T, Miura F *et al.* ChIP-Atlas 2021 update: a data-mining suite for exploring epigenomic landscapes by fully integrating ChIP-seq, ATAC-seq and Bisulfite-seq data. *Nucleic Acids Res* 2022;50:W175–82. https://doi.org/10.1093/nar/gkac199
64. Medeiros B, Allan AL. Molecular mechanisms of breast cancer metastasis to the lung: clinical and experimental perspectives. *Int J Mol Sci* 2019;20:2272.
65. Zhang J, Xie Q, Huo X *et al.* Impact of intestinal dysbiosis on breast cancer metastasis and progression. *Front Oncol* 2022;12:1037831. https://doi.org/10.3389/fonc.2022.1037831
66. Capo-chichi CD, Cai KQ, Simpkins F *et al.* Nuclear envelope structural defects cause chromosomal numerical instability and aneuploidy in ovarian cancer. *BMC Med* 2011;9:28. https://doi.org/10.1186/1741-7015-9-28
67. Danielsson BE, George Abraham B, Mäntylä E *et al.* Nuclear lamina strain states revealed by intermolecular force biosensor. *Nat Commun* 2023;14:3867. https://doi.org/10.1038/s41467-023-39563-6
68. Fan J-R, Chang S-N, Chu C-T *et al.* AKT2-mediated nuclear deformation leads to genome instability during epithelial–mesenchymal transition. *iScience* 2023;26:106992. https://doi.org/10.1016/j.isci.2023.106992
69. Jia Y, Vong JSL, Asafova A *et al.* Lamin B1 loss promotes lung cancer development and metastasis by epigenetic derepression of RET. *J Exp Med* 2019;216:1377–95. https://doi.org/10.1084/jem.20181394
70. Pascual-Reguant L, Blanco E, Galan S *et al.* Lamin B1 mapping reveals the existence of dynamic and functional euchromatin lamin B1 domains. *Nat Commun* 2018;9:3420. https://doi.org/10.1038/s41467-018-05912-z
71. Wazir U, Ahmed MH, Bridger JM *et al.* The clinicopathological significance of lamin A/C, lamin B1 and lamin B receptor mRNA expression in human breast cancer. *Cell Mol Biol Lett* 2013;18:595–611. https://doi.org/10.2478/s11658-013-0109-9
72. Tiwari N, Tiwari VK, Waldmeier L *et al.* Sox4 is a master regulator of epithelial–mesenchymal transition by controlling Ezh2 expression and epigenetic reprogramming. *Cancer Cell* 2013;23:768–83. https://doi.org/10.1016/j.ccr.2013.04.020
73. Zhang Y, Donaher JL, Das S *et al.* Genome-wide CRISPR screen identifies PRC2 and KMT2D-COMPASS as regulators of distinct EMT trajectories that contribute differentially to metastasis. *Nat Cell Biol* 2022;24:554–64. https://doi.org/10.1038/s41556-022-00877-0

74. Gallardo A, Molina A, Asenjo HG *et al.* EZH2 endorses cell plasticity to non-small cell lung cancer cells facilitating mesenchymal to epithelial transition and tumour colonization. *Oncogene* 2022;41:3611–24. https://doi.org/10.1038/s41388-022-02375-x
75. Gallardo A, López-Onieva L, Belmonte-Reche E *et al.* EZH2 represses mesenchymal genes and upholds the epithelial state of breast carcinoma cells. *Cell Death Dis* 2024;15:609. https://doi.org/10.1038/s41419-024-07011-y
76. Li Z, Wang D, Lu J *et al.* Methylation of EZH2 by PRMT1 regulates its stability and promotes breast cancer metastasis. *Cell Death Differ* 2020;27:3226–42. https://doi.org/10.1038/s41418-020-00615-9
77. Gesson K, Rescheneder P, Skoruppa MP *et al.* A-type lamins bind both hetero- and euchromatin, the latter being regulated by lamina-associated polypeptide 2 alpha. *Genome Res* 2016;26:462–73. https://doi.org/10.1101/gr.196220.115
78. Blanc RS, Richard S. Arginine methylation: the coming of age. *Mol Cell* 2017;65:8–24. https://doi.org/10.1016/j.molcel.2016.11.003
79. Johnson N, Cai D, Kennedy RD *et al.* Cdk1 participates in BRCA1-dependent S phase checkpoint control in response to DNA damage. *Mol Cell* 2009;35:327–39. https://doi.org/10.1016/j.molcel.2009.06.036
80. Schuhwerk H, Kleemann J, Gupta P *et al.* The EMT transcription factor ZEB1 governs a fitness-promoting but vulnerable DNA replication stress response. *Cell Rep* 2022;41:111819. https://doi.org/10.1016/j.celrep.2022.111819
81. Akhmetkaliyev A, Alibrahim N, Shafiee D *et al.* EMT/MET plasticity in cancer and Go-or-Grow decisions in quiescence: the two sides of the same coin? *Mol Cancer* 2023;22:90. https://doi.org/10.1186/s12943-023-01793-z
82. Schuhwerk H, Brabletz T. Mutual regulation of TGFβ-induced oncogenic EMT, cell cycle progression and the DDR. *Semin Cancer Biol* 2023;97:86–103. https://doi.org/10.1016/j.semcancer.2023.11.009
83. Perelli L, Zhang L, Mangiameli S *et al.* Evolutionary fingerprints of epithelial-to-mesenchymal transition. *Nature* 2025;640:1083–92. https://doi.org/10.1038/s41586-025-08671-2
84. Vega S, Morales AV, Ocaña OH *et al.* Snail blocks the cell cycle and confers resistance to cell death. *Genes Dev* 2004;18:1131–43. https://doi.org/10.1101/gad.294104
85. Pastushenko I, Blanpain C. EMT transition states during tumor progression and metastasis. *Trends Cell Biol* 2019;29:212–26. https://doi.org/10.1016/j.tcb.2018.12.001
86. Kröger C, Afeyan A, Mraz J *et al.* Acquisition of a hybrid E/M state is essential for tumorigenicity of basal breast cancer cells. *Proc Natl Acad Sci USA* 2019;116:7353–62.
87. Buxboim A, Swift J, Irianto J *et al.* Matrix elasticity regulates lamin-A,C phosphorylation and turnover with feedback to actomyosin. *Curr Biol* 2014;24:1909–17. https://doi.org/10.1016/j.cub.2014.07.001
88. Chandrashekar DS, Bashel B, Balasubramanya SAH *et al.* UALCAN: a portal for facilitating tumor subgroup gene expression and survival analyses. *Neoplasia* 2017;19:649–58. https://doi.org/10.1016/j.neo.2017.05.002
89. Chandrashekar DS, Karthikeyan SK, Korla PK *et al.* UALCAN: an update to the integrated cancer data analysis platform. *Neoplasia* 2022;25:18–27. https://doi.org/10.1016/j.neo.2022.01.001



**Received:** June 3, 2025. **Revised:** November 26, 2025. **Accepted:** November 30, 2025

Cell Reports

Article

# Fibrillarin regulates epithelial integrity via EZH2-mediated modulation of scribble expression

## Graphical abstract

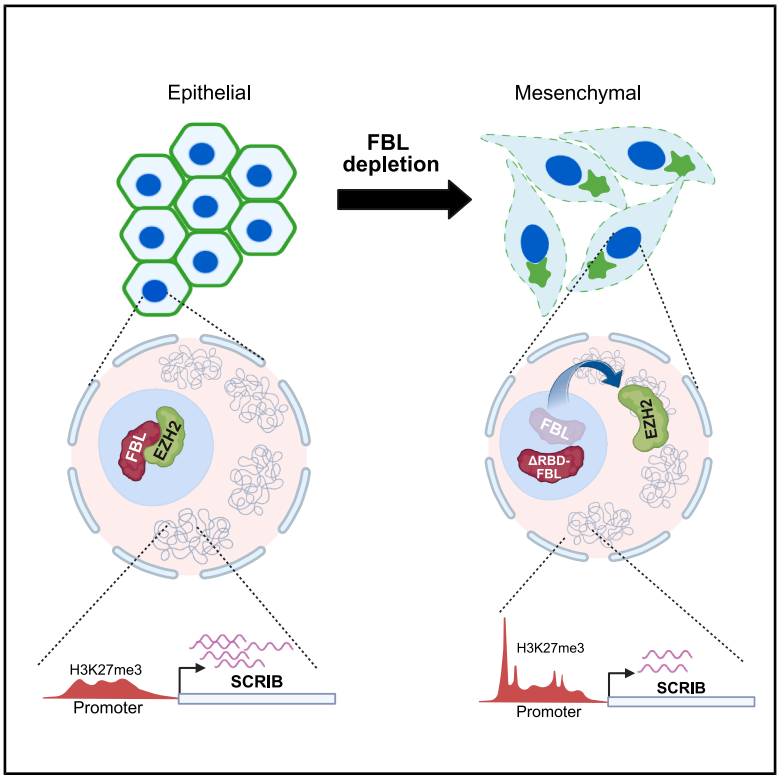


## Authors

Santam Saha, Balaji A.K., Sweety Meel, Dimple Notani, Kundan Sengupta

## Correspondence

kunsen@iiserpune.ac.in

## In brief

Saha et al. reveal that fibrillarin, a nucleolar protein, safeguards epithelial integrity by preventing EZH2-driven repression of Scribble. Fibrillarin loss disrupts cell-cell junctions, induces epithelial-to-mesenchymal transition (EMT), and enhances cell migration, uncovering a crucial link between nucleolar function and cancer progression.

## Highlights

- Fibrillarin maintains epithelial stability by regulating cell-cell adhesion
- FBL depletion shuttles EZH2 out of the nucleoli
- FBL loss drives EZH2 relocalization and repression of Scribble
- Prolonged FBL depletion promotes epithelial-to-mesenchymal transition (EMT) and metastasis

Saha et al., 2025, Cell Reports *44*, 116608
December 23, 2025 
https://doi.org/10.1016/j.celrep.2025.116608

CellPress

Cell Reports

CellPress
OPEN ACCESS

Article

# Fibrillarin regulates epithelial integrity via EZH2-mediated modulation of scribble expression

Santam Saha,[1] Balaji A.K.,[1] Sweety Meel,[2] Dimple Notani,[2] and Kundan Sengupta[1,3,*]
[1]B-216, Chromosome Biology Lab (CBL), Biology, Indian Institute of Science Education and Research (IISER), Dr. Homi Bhabha Road, Pashan, 411008 Pune, Maharashtra, India
[2]National Center for Biological Sciences (NCBS), Tata Institute of Fundamental Research (TIFR), 560065 Bangalore, Karnataka, India
[3]Lead contact
*Correspondence: kunsen@iiserpune.ac.in
https://doi.org/10.1016/j.celrep.2025.116608

## SUMMARY

Fibrillarin (FBL) is a nucleolar protein critical for rRNA biogenesis. We show that FBL is essential for the maintenance of epithelial integrity through its regulation of cell-cell adhesion proteins. RNA-seq analyses upon FBL depletion revealed deregulation of adhesion- and apical membrane organization-associated pathways. FBL loss deregulates cell polarity via increased deposition of H3K27me3 on the SCRIB promoter, driven by the localization of a subpopulation of EZH2 from the nucleolus to the nucleoplasm. Disrupting the FBL-EZH2 interaction increases cell migration, underscoring a requirement for retaining EZH2 also in the nucleolus. Furthermore, FBL depletion induces EMT in breast epithelial cells, owing to increased levels of mesenchymal factors (Snail1, Twist1, and Zeb1) and activation of Akt. Since Scribble tethers PHLPP1 and PTEN to antagonize Akt, repression of Scribble induces EMT. In summary, FBL safeguards epithelial integrity, by regulating the expression of Scribble, uncovering an FBL-EZH2 axis in EMT and metastasis.

## INTRODUCTION

The nucleolar protein fibrillarin (FBL) is a highly conserved 2′-*O*-methyltransferase involved in ribosomal RNA (rRNA) biogenesis.[1] As a core component of the C/D box small nucleolar ribonucleoprotein (snoRNP) complex, FBL catalyzes 2′-*O*-methylation of ribose in rRNA, which enhances ribosomal stability and function.[2,3] This modification occurs through the base pairing of C/D box snoRNAs with rRNA, positioning FBL at target sites, to transfer a methyl (-$CH_3$) group from S-adenosyl methionine (SAM) to the 2′-hydroxyl (-OH) of ribose.[4] Methylation imparts stability to rRNA, facilitating ribosome assembly while ensuring translational fidelity and adaptation to cellular stress.[5] FBL also methylates histone H2A (H2AQ104me) at glutamine residues. This H2AQme modification plays a role in epigenetic regulation, impacting the transcription of ribosomal DNA (rDNA) by altering its interaction with the FACT complex, which facilitates nucleosome reorganization at the rDNA promoter.[6] FBL also mediates 2′-*O*-methylation of peroxidasin (Pxdn) mRNAs, especially at the 5′ cap (Cap 0 to Cap 1/Cap 2), enhancing their stability.[7] Elevated FBL expression is implicated in aggressive cancers such as breast cancer, hepatocellular carcinoma, and colorectal cancer[8–10] where it drives aberrant ribosome biogenesis, correlating with enhanced cell proliferation and poor prognosis.[8] Mechanistically, elevated FBL levels enhance 2′-*O*-methylation of rRNA, which increases the efficiency of internal ribosome entry site (IRES)-mediated translation of oncogenic mRNAs FGF1, FGF2, MYC, and VEGFA.[8] In contrast, reduced levels of FBL are associated with poor prognosis of patients with early-stage breast cancer.[11]

Emerging evidence suggests that the oncogenic functions of FBL extend beyond ribosome biogenesis to influence gene expression programs that govern cell identity and behavior. One such critical process is the epithelial-to-mesenchymal transition (EMT), a cell state transition that reshapes epithelial identity and function, closely associated with cancer progression and metastasis. EMT is characterized by a gradual loss of epithelial morphology and the acquisition of mesenchymal properties, facilitating increased motility and invasiveness. The epithelial morphology is characterized by prominent cell-cell adhesion, apico-basal polarity, and the organization of cells into structured, functional sheets. Central to these functions are cell adhesion molecules and junctional complexes, particularly E-cadherin (epithelial cadherin, CDH1), tight junction complexes, and crucial polarity regulators such as Scribble, which function synergistically to maintain epithelial integrity. E-cadherin, a calcium-dependent transmembrane glycoprotein, mediates homophilic interactions between adjacent cells and forms a key component of adherens junctions. Its cytoplasmic domain binds to β-catenin and p120-catenin, anchoring the complex to F-actin (filamentous actin).[12,13] E-cadherin functions as a key determinant of epithelial organization, and its decrease or altered localization facilitates EMT. While type 1 EMT is associated with normal development, type 3 EMT is associated with cancer progression.[14,15] Complementing adherens junctions, tight junctions occupy the most apical position in the junctional complex. They are composed of transmembrane proteins such as claudins, occludin, and junctional adhesion molecules (JAMs). These proteins interact with scaffold proteins, including ZO-1, ZO-2, and ZO-3, which in turn connect the

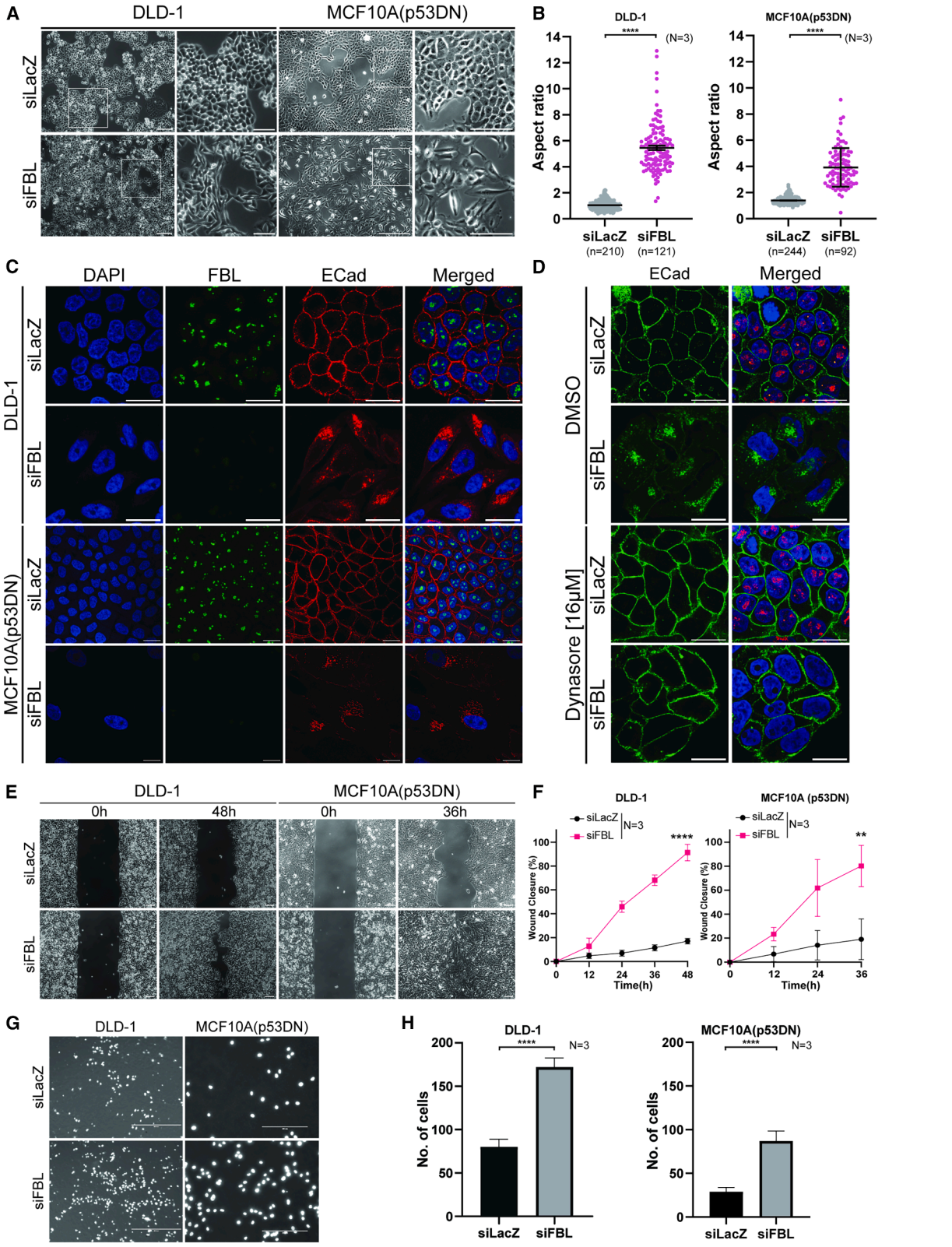


*(legend on next page)*

junctions to the actin cytoskeleton. These structures are crucial in establishing epithelial polarity and paracellular permeability. The key polarity protein Scribble, a keystone component of the Scribble-Lgl-Dlg complex, localizes to the basolateral membrane and is critical for maintaining epithelial architecture by suppressing apical polarity signals and promoting the formation of adherens and tight junctions.[16,17] Disruption of Scribble function results in the loss of polarity and induction of EMT. The physical and functional interplay between E-cadherin-mediated adherens junctions, tight junctions, and Scribble is critical for epithelial homeostasis, and their dysregulation is a common feature of tissue remodeling, inflammation, and tumorigenesis.[18,19]

Here, we have unraveled a novel role of FBL in the maintenance of epithelial integrity, thereby preventing cell migration and EMT. Our study uncovers a previously unrecognized role of FBL in the maintenance of epithelial homeostasis beyond its canonical function in ribosome biogenesis. We demonstrate that FBL depletion induces a striking loss of the classical cobblestone morphology of epithelial cells, characterized by the destabilization of adherens and tight junctions in two independent epithelial cell lines, namely, DLD-1 (colorectal cancer) and MCF10A (breast epithelial). This is driven by the mislocalization of E-cadherin via endocytosis, which disrupts cell-cell adhesion. Mechanistically, we uncover a direct link between FBL and the epigenetic regulation of cell adhesion genes. Loss of FBL transcriptionally represses Scribble expression (a key polarity protein) via enhanced deposition of the inactive histone mark (H3K27me3) on the SCRIB promoter. This is mediated by the translocation of a subpopulation of EZH2 from the nucleolus to the nucleoplasm. Notably, pharmacological inhibition of EZH2 rescues Scribble expression, restoring epithelial integrity and establishing FBL as a key regulator of epithelial stability. Concomitant with the loss of cell-cell adhesion, FBL depletion induces EMT, with the upregulation of Snail, Twist1, Zeb1, and pAkt. Strikingly, disruption of the FBL-EZH2 interaction for prolonged duration induces EMT in MCF10A(p53DN) breast cells, underscoring the functional significance of this interaction in retaining a nucleolar pool of EZH2 that safeguards epithelial integrity.

Taken together, these findings uncover a novel role of FBL in restraining EMT, preserving epithelial identity by maintaining cell-cell junction proteins. Our study, for the first time, highlights a novel function of FBL as a therapeutic target in cancers of epithelial origin, crucial for maintaining the integrity of epithelial cells and preventing metastasis.

## RESULTS

### FBL depletion disrupts cell-cell adhesion and alters cell morphology

FBL is a highly conserved nucleolar protein localized within the dense fibrillar compartment (DFC) of the nucleolus.[20] Increased levels of FBL enhance cell proliferation and chemoresistance in breast and colorectal cancer cells.[8,9] In contrast, reduced levels of FBL correlate with poor prognosis in breast cancers.[11]

We depleted FBL in two independent epithelial cell lines: colorectal cancer DLD-1 ($TP53^{WT/S241F}$) and breast epithelial MCF10A ($TP53^{WT/WT}$) cells. Since FBL is involved in rRNA biogenesis and maturation,[3,4] disrupting rRNA biogenesis stabilizes p53, enhancing cell death.[21–24] FBL depletion in MCF10A cells showed a significant increase in cell death (~60%), owing to the wild-type status of TP53 in MCF10A cells ($TP53^{WT/WT}$). We therefore created MCF10A cells stably expressing dominant-negative p53 (hereafter MCF10A(p53DN)) by transducing cells with a pBabe-Hygro-p53DD construct, which maintained cell viability of ~95%, upon FBL depletion (Figure S3B).[25–27]

Remarkably, FBL depletion caused a loss of the classical cobblestone morphology of epithelial cells (Figure 1A). Independent depletion of FBL showed a ~70%–80% knockdown in both epithelial cell types (Figure S1C(i–iii)), along with a significant increase in cell elongation, with an increased aspect ratio in both cell lines (DLD-1 [~5.8-fold ± 1.0] and MCF10A(p53DN) [~2.35-fold ± 0.5]; Figure 1B). Furthermore, FBL knockdown significantly altered the subcellular localization of the cell adhesion protein E-cadherin. Specifically, E-cadherin was internalized into the cytoplasm of cells (~72.5% ± 12.5%), resulting in loss of cell-cell adhesion (Figures 1C and S1A(i–ii); Videos S1

**Figure 1. FBL depletion leads to loss of cell-cell junctions and enhanced cell migration**

(A) Phase-contrast images of siLacZ (control) and siFBL-transfected DLD-1 and MCF10A(p53DN) cells for ~48 and ~36 h, respectively, showing elongated, spindle-shaped cells and loss of cobblestone morphology. Scale bar, ~150 μm. Scale bar for insets, 150 μm ($N = 3$).

(B) Quantification of the aspect ratio of cells upon FBL depletion in (1) DLD-1 (knockdown for ~48 h) and (2) MCF10A(p53DN) (knockdown for ~48 h) cells ($N = 3$). Unpaired $t$ test was performed to calculate the $p$ values. The data were pooled from $n = 331$ (DLD-1) and $n = 336$ (MCF10A(p53DN)) cells from $N = 3$ independent biological replicates.

(C) Representative images of immunofluorescence showing FBL (green), E-cadherin (red), and nucleus (DAPI; blue) in DLD-1 and MCF10A(p53DN) cells, respectively, upon FBL depletion ($n \geq 90$), for ~48 and 36 h, respectively. FBL depletion shows distinct relocalization of E-cadherin. The data were pooled from DLD-1 ($n = 180$) and MCF10A ($n = 181$) cells from $N = 3$ independent biological replicates. Scale bar, ~20 μm. Quantification in Figure S1A(i–ii).

(D) Representative immunofluorescence staining of E-cadherin (Ecad; green), FBL (red), and nucleus (DAPI; blue) in control and FBL-depleted cells (FBL depletion for ~48 h; $n \geq 339$), pooled from $N = 3$ independent biological replicates, with DMSO control and 16 μm Dynasore. Scale bar, ~20 μm. Quantification in Figure S1D(ii).

(E) Representative phase-contrast images showing scratch wound assays performed on DLD-1 and MCF10A(p53DN) cells in control (siLacZ) and FBL-depleted ($N = 3$) cells. Scale bar, ~100 μm.

(F) Quantification of Figure 1E showing a significant increase in wound closure upon FBL depletion in both DLD-1 and MCF10A(p53DN) cells. Unpaired $t$ test was performed to calculate the $p$ values.

(G) Invasion assays using Boyden chambers (pore size, ~8 μm) to quantify cell migration in DLD-1 and MCF10A(p53DN) cells in control (siLacZ) and FBL-depleted ($N = 3$) cells. Scale bars for DLD-1 (~400 μm) and MCF10A(p53DN) cells (~200 μm).

(H) Quantification of invasion assays for data in Figure 1G showing a significant increase in the number of migrated DLD-1 and MCF10A(p53DN) cells. The data were pooled from $N = 3$ biological replicates.

$p$ values were computed from unpaired Student's $t$ tests in (B), (F), and (G). Error bars indicate SD. *$p < 0.1$, **$p < 0.01$, ***$p < 0.001$, and ****$p < 0.0001$.

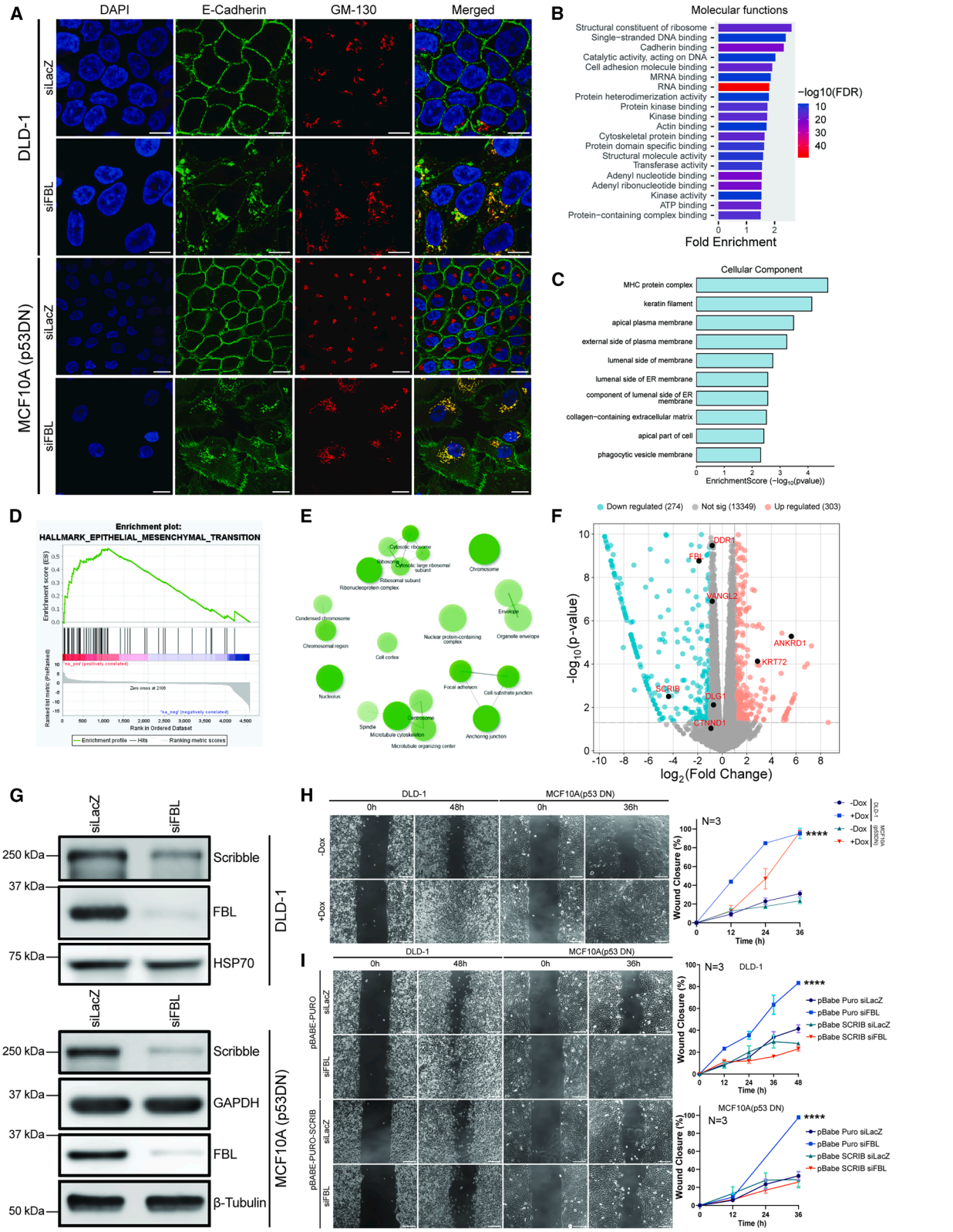


*(legend on next page)*

and S2). Notably, the total protein levels of E-cadherin remained unaltered (Figure S1C(i–iii)). To further ascertain the nature of the internalization of E-cadherin, we co-immunostained E-cadherin with two independent endosomal markers: EEA1 (early endosome antigen 1, an early endosome marker) and Rab11 (a recycling endosome marker).[28,29] Notably, E-cadherin showed a striking increase (∼8-fold) in its colocalization with both early (EEA-1) and recycling (Rab11) endosomes, corroborating the internalization of E-cadherin upon FBL depletion (Figures S4A(i–ii) and S4B(i–ii)). Collectively, these findings underscore an enhanced internalization and trafficking of E-cadherin upon the depletion of FBL.

To assess whether FBL depletion-mediated E-cadherin internalization is due to altered endocytic trafficking, we monitored alterations in global endocytosis using a transferrin uptake assay.[30] We did not detect a significant difference in the extent of transferrin uptake upon FBL depletion (Figure S3A(i–ii)), revealing that E-cadherin internalization is not a manifestation of alterations in overall endocytosis. We further determined if E-cadherin internalization can be rescued upon the inhibition of dynamin (a large GTPase critical for clathrin-mediated endocytosis).[31] We treated DLD-1 cells with Dynasore (an inhibitor of the GTPase domain of dynamin) in an FBL-depleted background. This showed a significant rescue of clathrin-mediated endocytosis of E-cadherin (Figures 1D and S1D(i–ii)),[32–34] suggesting a dynamin-dependent internalization of E-cadherin.

In addition to the adherens junction protein E-cadherin, FBL depletion perturbed the localization of tight junction proteins ZO-1 and occludin (Figures S2C (i–ii) and S3C(i–ii)), revealing a redistribution of key cell-cell adhesion proteins. To assess the effect of E-cadherin internalization on the integrity of tight junctions, we treated cells with EGTA (3 mM for 1 h), which showed internalization of E-cadherin and ZO-1 (Figure S2A).[35] Taken together, these results suggest that internalization of E-cadherin and ZO-1 collectively disrupts cell-cell junctions.

We next asked if the FBL depletion-mediated disruption of cell adhesion impacts cell migration. We performed scratch wound assays on a monolayer of cells to monitor cell migration, while we independently assessed the effect of FBL depletion on cell invasiveness, using the Boyden chamber assay. FBL depletion showed a significant increase in (1) cell migration (∼80% ± 10%) and (2) cell invasion (∼2.65-fold ± 0.3; Figures 1E and 1F). Furthermore, FBL depletion also increased cell invasion through relatively narrow pores (∼8 μm), as monitored by Boyden chamber assays (Figures 1G and 1H(i–ii)).

In summary, FBL maintains cell-cell adhesion by regulating the localization of adherens and tight junction proteins, such as E-cadherin, occludin, and ZO-1, respectively. FBL depletion disrupts cell-cell adhesion, facilitating enhanced cell migration and invasiveness, highlighting a novel and unreported function of FBL in the maintenance of the integrity and morphology of epithelial cells.

## FBL depletion downregulates Scribble expression, enhancing cell migration

We next examined the pattern of E-cadherin internalization upon FBL depletion using immunofluorescence assays (IFAs). Interestingly, the internalized E-cadherin showed distinct co-localization with the Golgi marker GM130, establishing the association of E-cadherin with the Golgi (Figures 2A and S5A(i–iii) and S5B(i–iii)). This striking phenotype of E-cadherin internalization into the Golgi is consistent with the depletion of Scribble, a basolateral cell polarity protein.[36]

To address the molecular underpinnings of FBL function, we performed RNA sequencing (RNA-seq) upon FBL depletion in DLD-1 colorectal cancer cells. Analyses of the RNA-seq datasets using GO (Gene Ontology) enrichment and GSEA (Gene Set Enrichment Analysis)[37] revealed genes that were deregulated in cellular and molecular functions such as (1) structure of ribosome, (2) cell-cell adhesion, (3) apical plasma membrane,

**Figure 2. Depletion of FBL shows a significant decrease in Scribble levels, which promotes cell migration**

(A) Representative images of immunofluorescence assay performed for E-cadherin (green), GM130 (red), and nucleus (DAPI; blue) from DLD-1 and MCF10A(p53DN) cells transfected with siLacZ (control) and siFBL for ∼48 h from $N = 3$ independent biological replicates. The GM130 and E-cadherin panels in siLacZ-transfected cells are from different optical sections of the same confocal image stack. Scale bar, ∼20 μm. Quantification in Figures S5A(i–iii) and S5B(iii).

(B) Bar plot representing the top deregulated molecular functions obtained from Gene Ontology (GO) analysis of RNA-seq data from FBL-depleted DLD-1 cells (∼72 h). Bar height represents the number of genes; FDR cutoff = 0.05.

(C) Bar plot showing the top deregulated cellular components obtained from GO analysis of RNA-seq data. Bar height represents the number of genes; FDR cutoff = 0.05.

(D) Enrichment plot obtained from Gene Set Enrichment Analysis (GSEA) of RNA-seq data showing enrichment of genes involved in epithelial-to-mesenchymal transition (EMT); FDR = 0; normalized enrichment score (NES) = 3.33.

(E) Network analysis of the key dysregulated cellular pathways derived from RNA-seq data upon FBL depletion in DLD-1 cells. Edge cutoff = 0.3.

(F) Volcano plots for differentially expressed genes derived from RNA-seq analysis of cells transfected with siLacZ (control) and siFBL for ∼72 h. Blue, downregulated; orange, upregulated; gray, unchanged. $\text{Log}_2$(fold change cut-off) = 2.0; $-\log_{10}(p$ value) = 2. Data were pooled from $N = 2$ independent biological replicates; siLacZ (control).

(G) Representative western blots showing a decrease for Scribble along with expression levels of FBL in DLD-1 and MCF10A(p53DN) cells transfected with siLacZ (control) and siFBL for ∼48 and ∼36 h, respectively. Loading controls: GAPDH, β-tubulin, and HSP70. Data were pooled from $N = 3$ independent biological replicates. Quantifications shown in Figure S5C(i–ii).

(H) Representative phase-contrast images from scratch wound assays performed independently on DLD-1 and MCF10A(p53DN) cells upon SCRIB depletion using induced expression of shSCRIB, in −Dox and +Dox conditions, obtained from $N = 3$ biological replicates. Two-way ANOVA with Bonferroni correction was used to perform multiple comparisons. Scale bar, ∼100 μm.

(I) Representative images of scratch wound assay of DLD-1 and MCF10A(p53DN) cells transduced with pBabe-Puro and pBabe-SBRIB in siLacZ- and siFBL-transfected backgrounds ($N = 3$). Two-way and one-way ANOVA with Bonferroni correction were used to perform multiple comparisons for DLD-1 and MCF10A, respectively. Scale bar, ∼100 μm.

Error bars indicate SD. $^{*}p < 0.1$, $^{**}p < 0.01$, $^{***}p < 0.001$, and $^{****}p < 0.0001$.

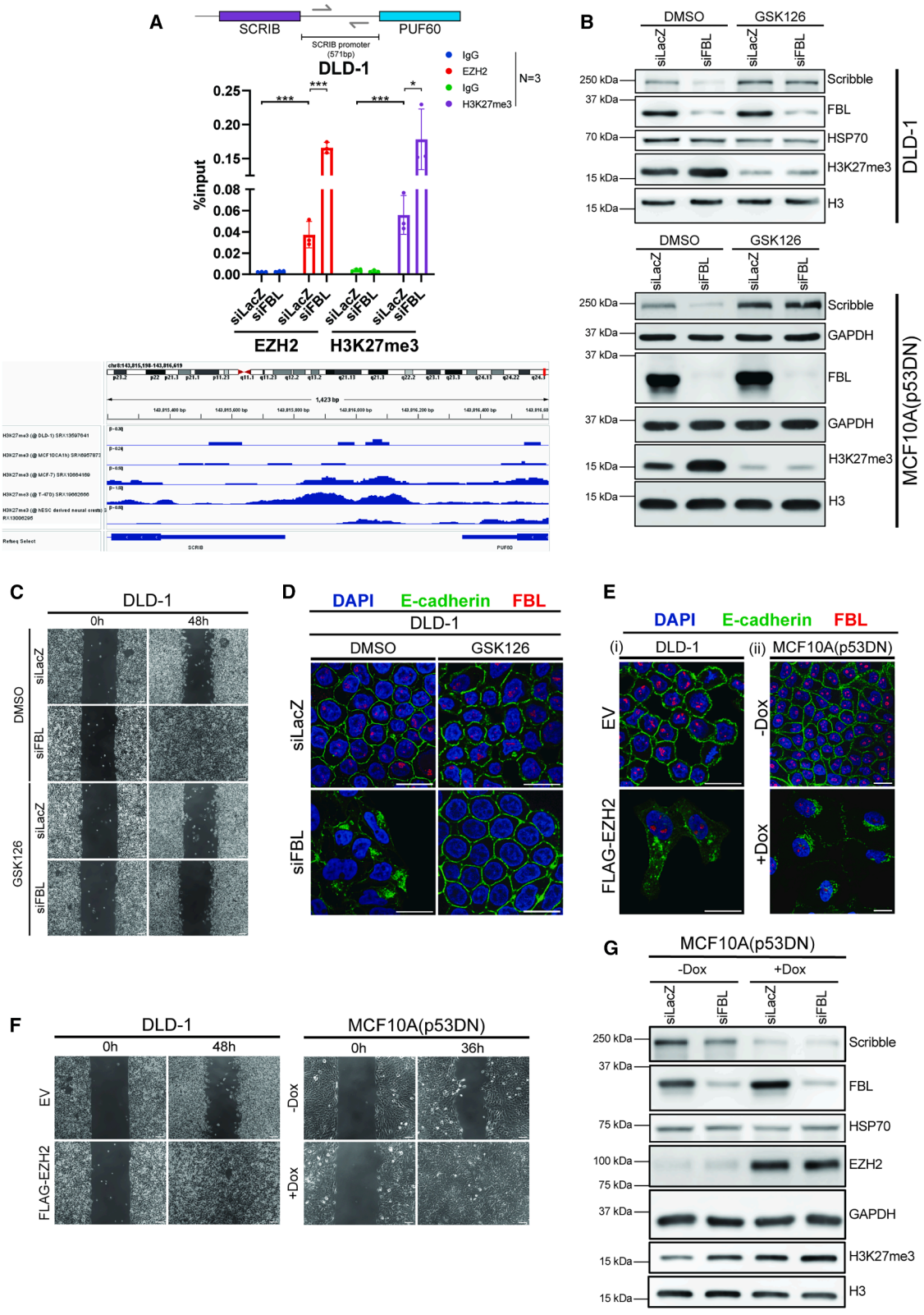


*(legend on next page)*

and (4) EMT, among others (Figures 2B–2E). Notably, Scribble showed a significant downregulation upon FBL depletion (Figure 2F), as corroborated by RT-qPCR (Figure S5D) and immunoblotting (Figures 2G and S5C(i–ii)). Interestingly, Scribble depletion also showed a significant increase in the extent of wound closure (~65% ± 5%), consistent with the role of Scribble depletion in promoting cell migration (Figure 2H).[38] In contrast, overexpression of Scribble in FBL-depleted cells decreased cell migration (Figure 2I). Taken together, these data implicate Scribble as a key molecular determinant of regulating cell migration upon FBL depletion.

## FBL loss increases the occupancy of repressive histone marks (H3K27me3) on the Scribble promoter

We found that Scribble expression was transcriptionally downregulated upon FBL knockdown (Figure S5D). We therefore analyzed the occupancy profiles of histone modifications on the SCRIB promoter in DLD-1 colorectal cancer cells using publicly available data from ChIP-ATLAS.[39] Surprisingly, this analysis showed an enrichment of H3K4me3 (active), H3K27me3 (repressive) histone marks, and H2AK119Ub (repressive mark) upstream of the transcription start site (TSS; −0.5 kb). Similarly, inactive (H3K27me3) histone marks were enriched on the SCRIB promoter in (1) breast epithelial (MCF10A), (2) human embryonic stem cells (hESCs), and (3) breast cancer (MCF-7 and T-47D; Figure 3A).

We next examined the occupancy of H3K27me3 on the SCRIB promoter upon FBL depletion using ChIP-qPCR, since H3K27me3 is indicative of PRC2 occupancy.[40] ChIP-qPCR analyses showed increased enrichment of EZH2 and H3K27me3 on the SCRIB promoter upon FBL depletion (−500 bp from TSS; Figures 3A and S4A), although the total protein levels of EZH2 were unaltered (Figures S4B(i–ii) and S4D). To ascertain the effect of increased EZH2 and H3K27me3 deposition on the SCRIB promoter upon FBL depletion, we treated cells with the EZH2 inhibitor GSK126 (10 μM for 48 h).[41] This showed a significant reduction in the levels of the inactive histone mark H3K27me3 and a concomitant rescue of SCRIB levels even in the FBL-depleted background (Figures 3B and S6B(i–ii)). Remarkably, GSK126-treated cells showed a significant decrease in cell migration as quantified by scratch wound assays (Figures 3C and S7B). We next performed IFAs to monitor the localization of E-cadherin upon inhibition of EZH2 activity. Interestingly, in contrast to FBL depletion, GSK126 treatment showed a significant decrease in the extent of E-cadherin internalization in DLD-1 cells (Figure 3D). To further assess the impact of EZH2 on Scribble regulation, we overexpressed EZH2. Interestingly, EZH2 overexpression led to internalization of E-cadherin into the cytoplasm (Figures 3E and S7A(i–ii)). Furthermore, scratch wound assays showed increased cell migration rates upon EZH2 overexpression (Figures 3F and S7C). Consistent with these observations, immunoblotting revealed that EZH2 overexpression showed a significant decrease in the levels of Scribble (Figures 3G and S6D and S7A(i–ii)).

To determine whether EZH2/H3K27me3 recruitment upon FBL depletion is a general phenomenon or is restricted to specific gene promoters, we selected ten candidate genes showing varied extents of differential deregulation upon FBL depletion from the RNA-seq data and performed ChIP-qPCR to assess the occupancy of EZH2 and H3K27me3 on these genes. We detected increased occupancy of both EZH2 and H3K27me3 on the promoters (−1 kb of TSS) of the downregulated genes ($log_2$FC −3.0 to −7.0; Figures S10C and S10D). In contrast, no significant changes were detected on the promoters of the upregulated genes ($log_2$FC +3.0 to +10.0; Figures S10E and S10F). This indicates that enhanced EZH2 recruitment upon FBL depletion is not limited to the SCRIB promoter. ChIP-Atlas analyses further showed that the downregulated genes were pre-enriched for H3K27me3 (Figures S8A–S8D, S9A, S9C, S9D, and S10A and S10B), indicating the presence of PRC2, suggesting that the relocalized EZH2 was preferentially recruited to the promoters with pre-existing H3K27me3 marks, consistent with a potential epigenetic memory mediated by PRC2.[40]

In summary, FBL depletion downregulates Scribble by increasing EZH2/H3K27me3 occupancy on its promoter. EZH2 inhibition restores Scribble expression, reduces E-cadherin

**Figure 3. FBL depletion increases the occupancy of the inactive histone mark H3K27me3 on the Scribble promoter**

(A) Schematic representation of the SCRIB promoter with primer locations. Bar plot shows significant enrichment of EZH2 and H3K27me3 occupancy on the SCRIB promoter in DLD-1 cells in control (siLacZ) and FBL-depleted (~48 h) cells. Data from $N = 3$ independent biological replicates. Statistical analysis was performed using unpaired $t$ tests.

(B) Immunoblotting performed upon FBL depletion (~48 h) and inhibition of EZH2 (using GSK126) shows rescue of Scribble levels. Loading controls: HSP70, H3, and GAPDH. Data pooled from $N = 3$ independent biological replicates. Quantification in Figure S6B(i–ii).

(C) Representative phase-contrast images of scratch wound assay from DLD-1 cells upon EZH2 inhibition after treatment with GSK126 in siLacZ (control) and siFBL-transfected cells. Data pooled from $N = 3$ independent biological replicates. Scale bar, ~100 μm. Quantification in Figure S7B.

(D) Immunofluorescence assay showing the rescue of E-cadherin localization to the cell border upon the inhibition of EZH2 using GSK126. E-cadherin (green), FBL (red), and nucleus (DAPI; blue) in GSK126-treated cells (10 μm, for 48 h) and control siLacZ and FBL-depleted cells (~48 h). Data were pooled from $N = 3$ independent biological replicates. Scale bar, ~20 μm. Quantification in Figure S7E.

(E) Immunofluorescence analysis displaying E-cadherin (green), FBL (red), and nucleus (DAPI; blue) localization in DLD-1 cells overexpressing either Flag or Flag-EZH2, as well as in EZH2-overexpressing MCF10A(p53DN) cells under a doxycycline (Dox)-inducible promoter. Data were pooled from $N = 3$ independent biological replicates. Scale bar, ~20 μm. Quantification in Figure S6F(i–ii).

(F) Representative phase-contrast images of scratch wound assays of DLD-1 cells transduced with Flag and Flag-EZH2 overexpression constructs and EZH2-overexpressing MCF10A(p53DN) cells under a Dox-inducible promoter. Data were pooled from $N = 3$ independent biological replicates. Scale bar, ~100 μm. Quantification in Figure S7C.

(G) Representative immunoblots showing EZH2 overexpression downregulates Scribble levels in EZH2-overexpressing MCF10A(p53DN) cells under a Dox-inducible promoter, with cells transfected with siLacZ and siFBL (~36 h). Loading controls: HSP70, GAPDH, and H3. Data were pooled from $N = 3$ independent biological replicates.

$^{*}p < 0.1$, $^{**}p < 0.01$, $^{***}p < 0.001$, and $^{****}p < 0.0001$. Quantification in Figure S7A(i–ii).

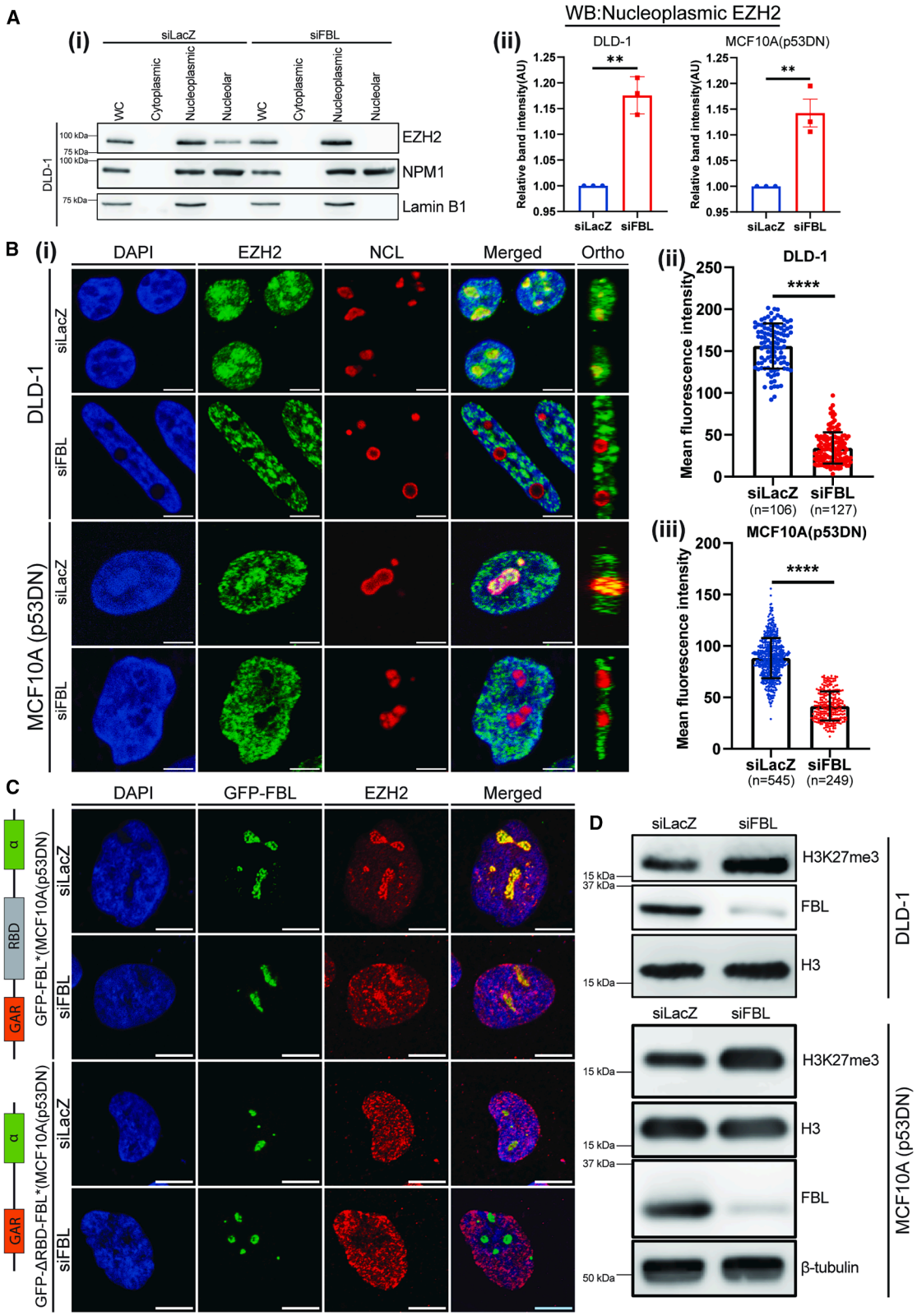


*(legend on next page)*

internalization, and suppresses cell migration. In contrast, EZH2 overexpression directly downregulates SCRIB expression by increased deposition of H3K27me3 on the SCRIB promoter.

## EZH2 translocates from the nucleolus to the nucleoplasm upon FBL depletion

We found that FBL depletion caused a significant increase in the enrichment of EZH2 (∼0.11% ± 0.01%; Figure 3A) on the SCRIB promoter, while the total levels of EZH2 were unaltered. We next asked if FBL depletion impacts the subcellular localization of EZH2, using two independent approaches: (1) immunoblotting to determine total protein levels by subcellular fractionation and (2) immunofluorescence staining at the single-cell level. Interestingly, FBL depletion hardly showed any localization of EZH2 in the nucleolus in both cell lines. This was accompanied by a concomitant and significant increase (∼16% ± 1%) in the nucleoplasmic fraction of EZH2 (Figures 4A(i–ii) and S12E). Furthermore, IFAs showed a significant reduction of EZH2 in the nucleolus (demarcated by nucleolin [NCL]) upon FBL depletion (Figures 4B(i–iii) and S11A(i–ii) and S11B(i–ii); Videos S3 and S4).

FBL has an RNA-binding domain (RBD) that interacts with the CXC domain of EZH2.[42] We therefore generated an FBL mutant with a deletion of the RBD domain to investigate if the abrogation of FBL-EZH2 interaction impacts the relocalization of EZH2 into the nucleoplasm. We expressed an RBD-deleted, siRNA-resistant mutant of FBL tagged with GFP (GFP-ΔRBD FBL) in a background of endogenous FBL depletion, which showed a striking displacement of EZH2 from the nucleolus (∼50% ± 10%; Figures 4C and S13A and S13B; Videos S5, S6, S7, and S8). The disruption of FBL-EZH2 interaction was further validated using co-IP (Figure S12C). Consistent with this finding, the levels of H3K27me3 showed a concomitant increase upon FBL depletion, as monitored by IFA (∼6-fold) and immunoblotting assay (∼60% ± 10%; Figures 4D and S12A, S12B(i–ii), and S12D(i–ii)).

Interestingly, the total levels of EZH2 were unaltered upon FBL depletion. On closer inspection of cells labeled by IFA, nucleolar EZH2 showed a decrease by ∼30% ± 7%, while the amount of nucleoplasmic EZH2 increased by ∼27% ± 4%, further supporting the translocation of EZH2 from the nucleolus to the nucleoplasm (Figure S11C(i–iii)). Taken together, these results reveal that FBL plays a crucial role in sequestering a subpopulation of EZH2 within the nucleolus.

## FBL-mediated nucleolar retention of EZH2 sustains Scribble expression

It is well established that EZH2 interacts with the PRC2 components SUZ12 and EED1.[43–45] Upon FBL depletion, the EZH2 that is released from the nucleolus (henceforth, "nucleolar EZH2") interacts with the nucleoplasmic PRC2 complex. Consistent with the enrichment of H3K27me3 and EZH2 on the SCRIB promoter, we investigated the contribution of nucleolar EZH2 to the downregulation of SCRIB expression. To this end, we utilized BioID2 ChIP-qPCR to tag and monitor nucleolar EZH2 upon FBL knockdown.[46] Cells stably expressing BioID2-FBL (WT) were supplemented with 50 μM biotin. The cells were harvested upon FBL knockdown (for ∼24 h), followed by ChIP. The sonicated chromatin was used for pull-down using streptavidin Dynabeads, followed by ChIP-qPCR analysis. We validated the pull-down of EZH2 using immunoblotting (Figure S14C). Interestingly, the ChIP-qPCR results showed increased occupancy of biotinylated EZH2 on the SCRIB promoter upon FBL depletion (Figures 5A and S15E).

Since we observed that the abrogation of FBL-EZH2 interaction increased nucleoplasmic EZH2, and BioID2 ChIP-qPCR revealed enrichment of the translocated EZH2 on the SCRIB promoter, we determined the impact of abrogating FBL-EZH2 interaction on cell-cell adhesion. We performed IFAs, which revealed a striking internalization of E-cadherin in GFP-ΔRBD FBL(siRes) or vector control (GFP) overexpressing cells, in a background of endogenous FBL depletion (Figures 5B and S14B(i–ii)). Immunoblotting showed a downregulation of Scribble expression due to the loss of FBL-EZH2 interaction (Figures 5C and S14A(i–ii)). Remarkably, the abrogation of FBL-EZH2 interaction also showed an increase in cell migration rates, as quantified from scratch wound assays (Figures 5D and 5E). Taken together, loss of FBL-EZH2 interaction translocates EZH2 from the nucleolus to the nucleoplasm, downregulating Scribble expression, accompanied by the concomitant internalization of E-cadherin and the consequent elongation and loss of

**Figure 4. EZH2 translocates from the nucleolus to the nucleoplasm following fibrillarin depletion**

(A) (i) Representative immunoblots of cell fractions derived from siLacZ- and siFBL-transfected DLD-1 cells (∼48 h), showing whole-cell lysate (WC), cytoplasmic, nuclear, and nucleolar fractions. IB: lamin B1 and nucleophosmin1 (NPM1) serve as nuclear and nucleolar loading controls, respectively. (ii) Quantification of IB (DLD-1 and MCF10A) shows a significant increase in nucleoplasmic EZH2. Data were pooled from $N = 3$ biological replicates. $p$ values were derived from an unpaired $t$ test.

(B) (i) Representative images of immunofluorescence showing a depletion of nucleolar EZH2, with NCL (red) demarcating the nucleolus from the nucleoplasm, in DLD-1 and MCF10A(p53DN) cells transfected with siLacZ and siFBL for ∼48 and ∼36 h, respectively. The nucleus is visualized via DAPI staining. EZH2: green and NCL: red. Data were pooled from $N = 3$ independent biological replicates. Scale bar, ∼20 μm. (ii) Scatterplot (bar overlaid) showing reduction in levels of nucleolar EZH2 upon transfecting DLD-1 cells with siFBL- compared to siLacZ-transfected (control) cells (for ∼48 h). The data were pooled from $n = 233$ nucleoli across $N = 3$ independent biological replicates. $p$ values were pooled using an unpaired $t$ test. (iii) Scatterplot (bar overlaid) showing reduction in levels of nucleolar EZH2 upon transfecting MCF10A(p53DN) cells with siFBL- (for ∼36 h) compared to siLacZ-transfected (control) cells. The data were pooled from $n = 794$ nucleoli across $N = 3$ independent biological replicates. $p$ values were pooled using an unpaired $t$ test.

(C) Representative immunofluorescence images for EZH2 (red) and nucleus (DAPI; blue) from GFP-FBL(siRes)- and ΔRBD-GFP-FBL(siRes)-overexpressing DLD-1 cells transfected with siLacZ and siFBL (for ∼48 h; $n \geq 120$ nucleoli). Data were pooled from $N = 3$ independent biological replicates. Scale bar, ∼20 μm. Quantification of colocalization of EZH2 and GFP is in Figure S11B(ii).

(D) Representative western blots showing a significant increase in H3K27me3 levels in siLacZ- (control) and siFBL-transfected DLD-1 and MCF10A(p53DN) cells for ∼48 and ∼36 h, respectively. Loading control: H3 and β-tubulin in siLacZ- and siFBL-transfected MCF10A(p53DN) cells. Data were pooled from $N = 3$ independent biological replicates. Scale bar, ∼20 μm. Quantification is in Figure S12D(i–ii).

Error bars indicate SD. $^{*}p < 0.1$, $^{**}p < 0.01$, $^{***}p < 0.001$, and $^{****}p < 0.0001$.

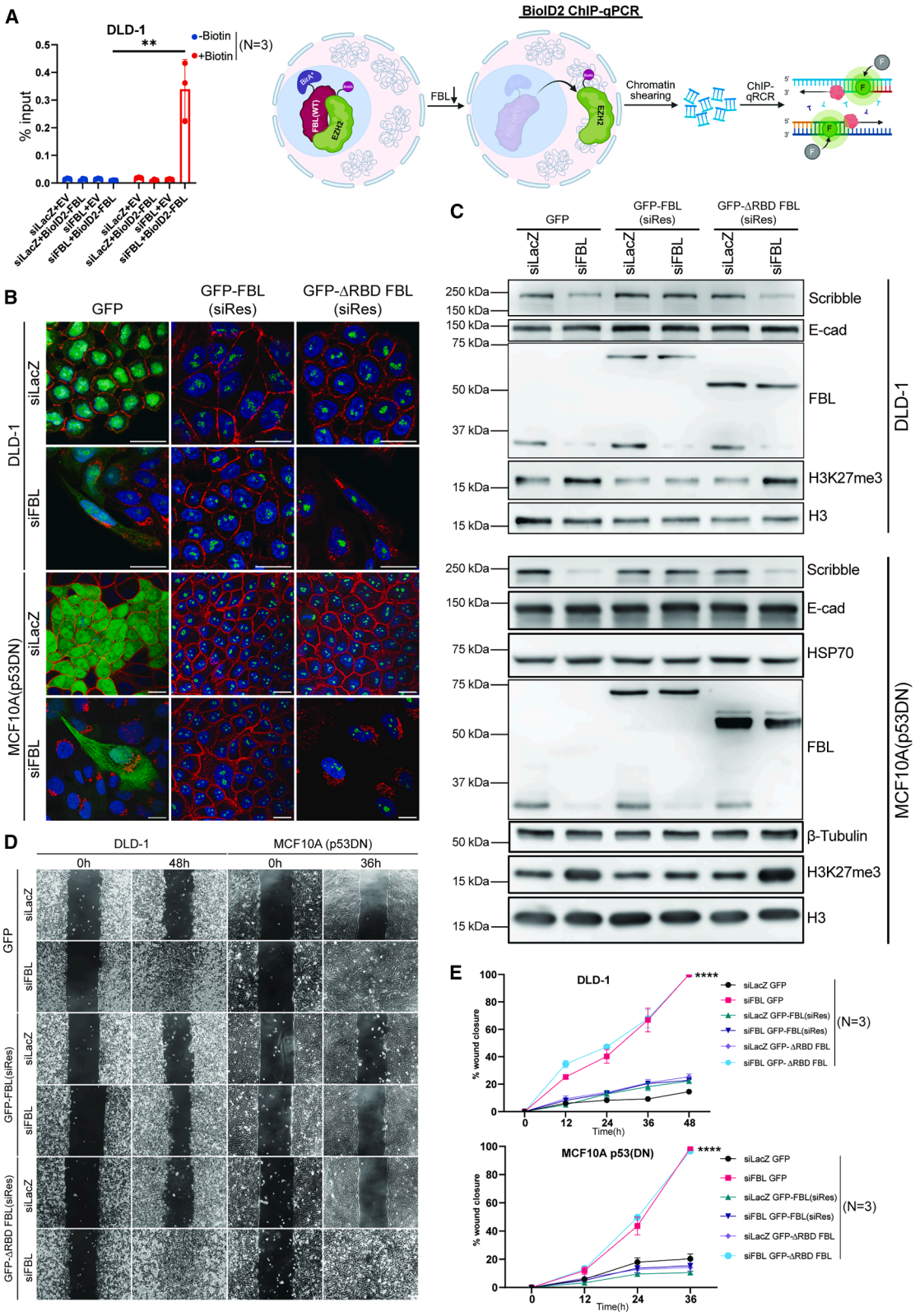


*(legend on next page)*

the cobblestone morphology that define epithelial cells (Figure S15C).

We next performed ChIP-qPCR to examine the occupancy of EZH2 on the SCRIB promoter. Loss of FBL-EZH2 interaction in an endogenous FBL-depleted background showed an increased occupancy of EZH2 on the SCRIB promoter, which downregulates Scribble expression (Figure 5C and S15D). Downregulation of Scribble manifests as mislocalization of E-cadherin and enhanced cell migration. Additionally, we performed a graded overexpression of EZH2 under a doxycycline (Dox)-inducible promoter, which caused an increase in EZH2 levels and downregulation of Scribble (Figures S15A and S15B).

Taken together, the interaction between FBL and EZH2 regulates Scribble expression and cell migration. Disrupting this interaction induces the translocation of nucleolar EZH2 into the nucleoplasm, thereby increasing H3K27me3 deposition on the SCRIB promoter and its consequent downregulation. Collectively, this results in the mislocalization of E-Cadherin, enhancing cell migration, which suggests that the FBL-EZH2 interaction plays a crucial role in the maintenance of the epithelial state of cells.

## FBL depletion induces EMT by downregulating Scribble levels

FBL depletion showed a significant reduction in Scribble levels. Decreased Scribble levels induce EMT in the epithelial breast cell line MCF10A.[47] This transition is facilitated by the inactivation of the Hippo signaling pathway and the subsequent stabilization of TAZ, since TAZ promotes the expression of Snail and FOXC2, which are associated with EMT.[48] Furthermore, Scribble interacts with PHLPP1 to inhibit the phosphorylation or activation of Akt.[49] Activated Akt phosphorylates EZH2 at Ser21, altering the binding affinity of EZH2 for histone H3, resulting in the loss of methylating activity of EZH2 on histone H3.[50]

Since Scribble depletion induces EMT in breast epithelial cells (MCF10A), we examined whether FBL depletion induces EMT in MCF10A(p53DN) cells. Surprisingly, while FBL depletion hardly showed any alteration in the levels of EMT markers at the end of ~36 h, prolonging FBL depletion for ~72 h caused a significant increase in the levels of mesenchymal markers Snail1, Twist1, and Zeb1 (master transcription factors that promote EMT).[51,52] This was accompanied by decreased levels of cell adhesion proteins E-cadherin and occludin (Figures 6A and S19D). Furthermore, a reduction in H3K27me3 levels correlated with Akt activation (Figures 6A and S16A(i)). The levels of E-cadherin (decreased) and vimentin (increased) were further corroborated by IFA and immunoblotting, respectively (Figures 6B and S16E(i–ii)). Scribble levels were relatively lower in FBL-depleted cells (~36-h post-transfection), which, interestingly, recovered upon prolonged FBL depletion (~72 h). ChIP-qPCR showed a significant reduction in the occupancy of EZH2 and H3K27me3 on the SCRIB promoter after ~72 h of FBL depletion (Figure S16D), correlating with global H3K27me3 reduction and recovery of Scribble expression (Figure 6A). IFA revealed that Scribble was predominantly localized in the cytoplasm rather than the cell membrane at ~72 h (Figures 6C and S16B).

Since we previously identified that the interaction between FBL-EZH2 sustains the levels of Scribble, we abrogated FBL-EZH2 interaction by overexpressing GFP-ΔRBD FBL(siRes) in a background of endogenous FBL depletion (~72 h) in MCF10A(p53DN). Remarkably, immunoblotting showed upregulated levels of mesenchymal markers vimentin, Snail, Twist, Zeb1, and TAZ, with a concomitant decrease in the levels of epithelial markers E-cadherin and occludin upon GFP-ΔRBD-FBL(siRes) overexpression in an FBL-depleted background (Figures 6D and S16C(i–ii)). IFAs further showed elevated levels of vimentin and reduced levels of E-cadherin and occludin (Figures 6F and S17A(i–ii)).

Since pAkt was activated upon FBL depletion and Scribble is an antagonist of Akt activation,[49] we examined the role of pAkt in EMT in the context of FBL depletion in MCF10A(p53DN) cells. We inhibited Akt by treating cells with the Akt inhibitor GSK690693[53] at 2 nM for ~72 h. This further curtailed EMT progression, as it decreased Snail, Twist, Zeb1, and vimentin levels and rescued epithelial markers E-cadherin and occludin (Figures 6E and S17C).

Taken together, these studies establish that FBL depletion induces EMT in breast epithelial cells (MCF10A (p53DN)) by collectively (1) disrupting the presence of Scribble at the cell membrane, (2) activating Akt, and (3) reducing EZH2 activity. These events synergistically upregulate Snail, Twist, and Zeb1, while decreasing epithelial markers. However, overexpression of GFP-ΔRBD-FBL(siRes) does not rescue EMT in an endogenous FBL-depleted background, underscoring a requirement for an interaction between FBL-EZH2 for the maintenance of the epithelial state of cells. Furthermore, Akt inhibition rescues

**Figure 5. FBL-mediated nucleolar retention of EZH2 is crucial for maintaining Scribble expression**

(A) Bar plot representing BioID2-ChIP-qPCR enrichment of EZH2 (biotinylated and non-biotinylated) on the SCRIB promoter in DLD-1 and MCF10A(p53DN) cells in siLacZ- and siFBL-transfected cells ($N = 3$) for ~24h. $p$ values derived from an unpaired $t$ test. The schematic represents the steps involved in BioID2-ChIP-qPCR.

(B) Representative images of immunofluorescence for E-cadherin (red) upon overexpression of GFP, GFP-FBL(siRes), and ΔRBD-GFP-FBL(siRes) in DLD-1 and MCF10A(p53DN) cells transfected with siLacZ and siFBL for ~48 and ~36 h respectively. GFP or GFP-tagged proteins are shown in green. Nucleus (blue) stained with DAPI. Data were pooled from $N = 3$ independent biological replicates. Scale bar, ~20 μm. Quantification shown in Figure S14B(i) and (ii).

(C) Representative immunoblots showing Scribble, E-cadherin, FBL, and H3K27me3. Loading controls: HSP70, β-tubulin, H3, and GAPDH from GFP-, GFP-FBL(siRes)-, and ΔRBD-GFP-FBL(siRes)-overexpressing DLD-1 and MCF10A(p53DN) cells transfected with siLacZ and siFBL for ~48 and ~36 h respectively. Data were pooled from $N = 3$ independent biological replicates. Quantification in Figure S12A(i–ii).

(D) Representative phase-contrast images of scratch wound assay performed on DLD-1 and MCF10A(p53DN) cells expressing GFP, GFP-FBL(siRes), and ΔRBD-GFP-FBL(siRes) transfected with siLacZ- and siFBL-transfected cells. Data were pooled from $N = 3$ independent biological replicates.

(E) Quantitative analysis of scratch wound assay from Figure 5D. Two-way ANOVA with Sidak's test was performed to calculate the $p$ value.

Error bars indicate SD. $^{*}p < 0.05$, $^{**}p < 0.01$, and $^{****}p < 0.0001$.

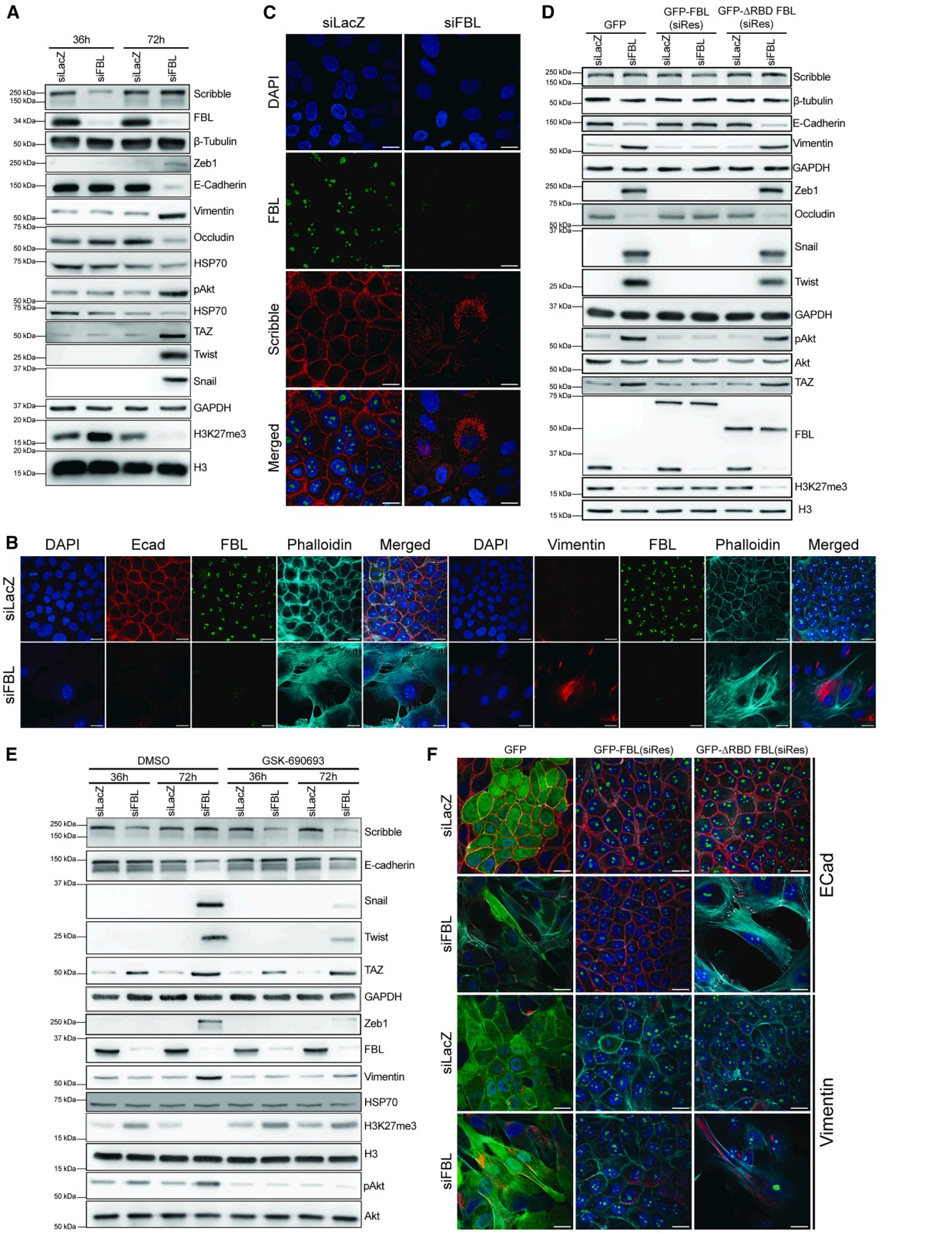


*(legend on next page)*

EMT, highlighting the role of Akt activation in EMT induction upon FBL depletion.

### FBL depletion increases tumorigenicity and lung metastasis

We next investigated the contribution of FBL depletion to tumorigenesis. To this end, we subcutaneously injected FBL-depleted DLD-1 cells (stably expressing shFBL under a Tet-ON inducible promoter) into NOD-SCID mice. FBL depletion was sustained by administering Dox supplemented in drinking water, replaced every ~72 h. Tumor growth was monitored until harvest on day 35 post-injection, which showed a significant increase in tumor growth in FBL-depleted mice (Dox-treated [+Dox] mice, ~40%, compared to control mice [−Dox]; Figure 7B). Consistently, volumes and weights of tumors showed a significant increase upon FBL depletion (+Dox mice; Figure 7C(i–ii)).

To further investigate the crosstalk between FBL and EZH2 in primary cells, the tumors were enzymatically digested using a triple enzyme mix to isolate tumor cells. Notably, FBL depletion upon Dox induction in mice showed a significant decrease (~4-fold) in the localization of EZH2 in the nucleolus, as monitored by its colocalization with NCL, a key marker of the granular component (GC) of the nucleolus (Figures 7D and S20C). Additionally, analysis of tumor lysates revealed a significant decrease in the levels of Scribble and increased H3K27me3 (Figures 7E and S20B), reinforcing that FBL loss decreases Scribble levels, as determined in cultured cells. These findings present a crucial role for FBL depletion in enhancing tumorigenesis.

Since we established that FBL knockdown increases cell migration, we also asked if FBL depletion increases cell invasion and metastasis. We therefore performed tail vein injections of FBL-depleted DLD-1 cells (stably expressing shFBL under a Tet-ON inducible promoter) in immunocompromised NOD-SCID mice. FBL depletion was sustained by administering Dox, supplemented in drinking water, replaced every ~72 h. The mice were sacrificed ~60 days post-injection. We performed a careful visual inspection of the organs, closely examining the lungs, the primary site for metastasis of trapped circulating tumor cells and a known colonization site for DLD-1 upon tail vein injection, making them a preferable organ for assessing metastatic burden.[54] We harvested and processed the lungs for hematoxylin-eosin staining. FBL depletion (+Dox) showed enhanced lung metastasis in mice. Further quantification of metastatic nodules in the lung sections revealed increased metastatic burden upon FBL depletion in +Dox mice (Figures 7F(i–ii) and S20E). This implies that FBL depletion induces the cells to be more invasive and metastatic in nature.

In summary, FBL depletion increases cell invasiveness, as corroborated by xenograft models, which showed increased tumorigenic burden and metastasis, highlighting a novel role for FBL in the regulation of tumorigenesis.

## DISCUSSION

FBL is a nucleolar protein required for post-transcriptional modifications and stability of rRNA. Here, we show that FBL plays a critical role in the maintenance of the integrity of the epithelial cells by regulating cell-cell adhesion. FBL depletion disrupts E-cadherin localization, leading to its internalization via clathrin-mediated endocytosis, compromising the stability of tight junctions. The destabilization of cell-cell adhesion is accompanied by the downregulation of Scribble, a key protein that determines apico-basal cell polarity,[55,56] repressed by increased occupancy of the inactive histone mark (H3K27me3), deposited by EZH2 upon FBL loss. Furthermore, FBL depletion translocates EZH2 from the nucleolus to the nucleoplasm, promoting transcriptional silencing of SCRIB, which enhances cell migration. Prolonged downregulation of Scribble stabilizes TAZ and decreases the deposition of H3K27me3 and SNAI1, ZEB1, and TWIST1 expression, synergistically, contributing to EMT in breast epithelial cells MCF10A(p53DN), as evidenced by the upregulation of mesenchymal markers. Taken together, our findings establish FBL as a crucial regulator of epithelial

**Figure 6. FBL depletion induces EMT by modulating Scribble expression levels**

(A) Representative immunoblots showing Scribble, occludin, E-cadherin, vimentin, Snail, Zeb1, Twist, pAkt, TAZ, FBL, and H3K27me3. Loading controls: 1st HSP70 is the loading control for Zeb1, E-cadherin, vimentin, and occludin, 2nd HSP70 is the loading control for pAkt, β-tubulin, H3, and GAPDH from MCF10A(p53DN) cells transfected with siLacZ and siFBL for 36 and 72h. Data were pooled from $N = 3$ independent biological replicates. Quantification shown in Figure S16A(i–ii).

(B) Representative immunofluorescence images showing FBL (green), E-cadherin (red), F-actin (phalloidin; cyan), and nucleus (DAPI; blue) upon FBL depletion (~72 h) lead to decreased E-cadherin and increased levels of vimentin. Data were pooled from $n = 416$ cells and $N = 3$ independent biological replicates. Quantification shown in Figure S16E(i–ii).

(C) Representative immunofluorescence images showing the internalization of SCRIB transfected with siLacZ and siFBL for 72 h ($n = 211$ cells) show the nucleus via DAPI staining, Scribble (red), and FBL (green). Data were from $N = 3$ independent biological replicates. Scale bar, 20 μm. Quantification is shown in Figure S16B.

(D) Representative immunoblots showing induction of EMT by ~72 h upon abrogating the FBL-EZH2 interaction in GFP-, GFP-FBL(siRes)-, and ΔRBD-GFP-FBL(siRes)-overexpressing MCF10A(p53DN) cells transfected with siLacZ and siFBL. IB: Scribble, occludin, E-cadherin, vimentin, Snail, Zeb1, Twist, pAkt, TAZ, FBL, and H3K27me3 using HSP70, β-tubulin, H3, AKt, and GAPDH as loading controls. Data were from $N = 3$ independent biological replicates. Scale bar, 20 μm. Quantification shown in Figure S16C(i–ii).

(E) Representative immunoblots show rescue of EMT upon the inhibition of Akt. IB: Scribble, E-cadherin, vimentin, Snail, Zeb1, Twist, pAkt, TAZ, FBL, and H3K27me3. Loading controls: HSP70, β-tubulin, H3, AKt, and GAPDH as loading controls from MCF10A(p53DN) cells transfected with siLacZ and siFBL for ~36 and ~72h, respectively, upon treatment with GSK690693 (2 nM) with DMSO (control). Data were pooled from $N = 3$ independent biological replicates. Quantification shown in Figure S17C.

(F) Representative images of immunofluorescence for E-cadherin (red) and vimentin (red), F-actin (phalloidin; cyan), and nucleus (DAPI; blue) for MCF10A(p53DN) cells from GFP-, GFP-FBL(siRes)-, and ΔRBD-GFP-FBL(siRes)-overexpressing MCF10A(p53DN) cells transfected with siLacZ and siFBL for 72h ($N = 3$). Data were pooled from $N = 3$ independent biological replicates. Quantification shown in Figure S17A(i–ii).

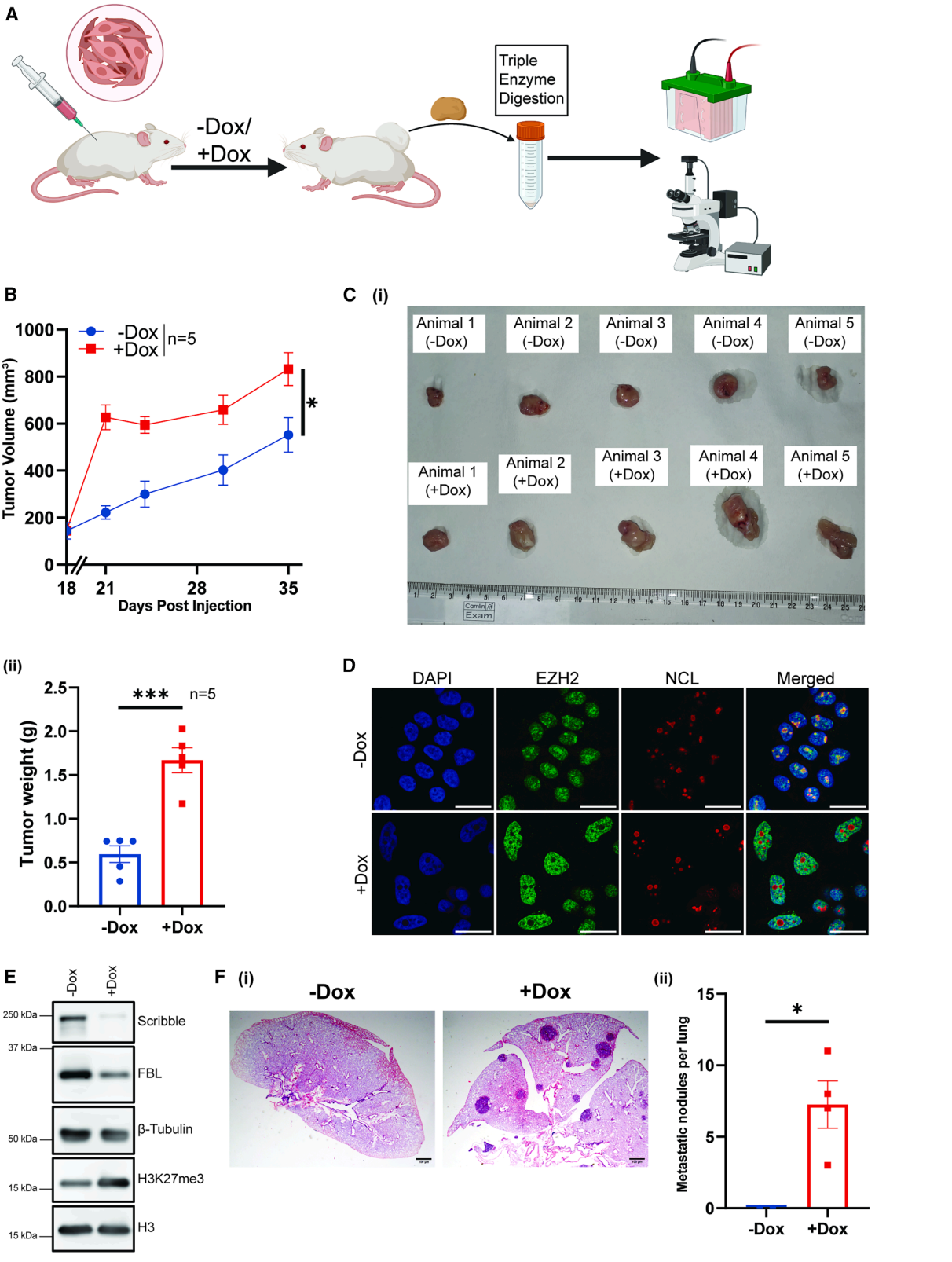


(legend on next page)

homeostasis, as FBL loss drives cell migration and EMT, regulated by Scribble and EZH2 dynamics.

## FBL depletion disrupts cell-cell adhesion and enhances migration

Our study, for the first time, demonstrates that the depletion of FBL profoundly alters cell-cell adhesion in epithelial cells, enhancing cell migration in two independent epithelial cell types: (1) colorectal cancer (DLD-1) and (2) breast epithelial cells (MCF10A(p53DN)). We independently validated the internalization of E-cadherin upon FBL depletion using a proteinase K protection assay (Figure S2E). The generalizability of FBL depletion-mediated E-cadherin internalization was further validated in lung cancer A549 cells (Figure S4C(i-ii)).

While a direct loss of lamins typically manifests as an increase in cell migration in most cancer cells,[57,58] FBL depletion did not show any significant alterations in lamin levels, as determined by RNA-seq analysis.[59] This suggests that FBL depletion promotes cell migration while potentially bypassing nuclear lamins. We surmise that FBL loss reorganizes indirect interactions of LINC complex proteins with cell-cell adhesion molecules, likely creating differential tension on the nuclei of migrating cells.[60]

FBL is required for rRNA biogenesis and modification, and its depletion is likely to impact rates of rRNA and protein synthesis.[22,23] Interestingly, the SUnSET assay did not show a significant difference in protein synthesis rates (Figure S2F).[61] We surmise that (1) the residual levels of FBL post depletion are sufficient for processing nascent 45S rRNA, since FBL depletion does not show a significant effect on 28S and 18S rRNA (Figure S3D), and (2) decreased Scribble on the cell membrane activates the Akt/mTOR/S6K signaling pathway, upregulating global translation,[62] compensating for potential disruptions in protein homeostasis.

## FBL depletion downregulates Scribble expression, leading to cell migration

FBL depletion not only affects E-cadherin localization but also results in its accumulation in the Golgi, as it colocalizes with the Golgi marker GM130 (Figure 2A). E-cadherin has a ubiquitination site at the cytoplasmic domain, which is protected by p120 protein, thereby sustaining the localization and integrity of E-cadherin on the cell membrane. Scribble, a key apical-basal polarity protein, further stabilizes the p120 and E-cadherin interaction at the cell membrane.[36] Decrease in Scribble levels upon FBL depletion led to increased cell elongation, along with concomitant fragmentation of Golgi (Figure 2A), potentially an indirect effect of actin remodeling during cell elongation[63] although a direct role of FBL in modulating Golgi fragmentation and function remains unclear.

It is well established that a multifactorial process maintains the stability of E-cadherin at the cell membrane, such as Discs large homolog 5 (DLG5),[64] CTNND1 (delta-catenin),[65] Epsin3 (EPN3),[66] VANGL planar cell polarity protein 2 (VANGL2),[67] Discoidin domain receptor family member 1 (DDR1),[68] and Scribble (SCRIB).[36] Transcriptome analyses of FBL depletion in DLD-1 cells did not show a significant decrease in the transcript levels of DLG5 and DDR1, otherwise implicated in the internalization of E-cadherin (Figure 2F). Interestingly, RNA sequencing revealed a significant downregulation of Scribble, which regulates E-cadherin trafficking (Figure 2F). Collectively, our study unravels a fundamental mechanistic link between FBL and Scribble in maintaining and regulating the integrity of epithelial cells.

## FBL loss enhances H3K27me3 enrichment and silences SCRIB expression

It is well established that EZH2 occupancy and its histone methyltransferase activity modulate its interactions with PRC2 components EED and SUZ12. Notably, SUZ12 interacts with either EZH1 or EZH2, resulting in a transition of the SET domain (Su(var)3-9, enhancer-of-zeste, and trithorax) from an autoinhibitory to an active configuration, which enhances its methyltransferase activity.[45,69] The SCRIB promoter is potentially bivalent due to the co-occupancy of H3K27me3 and H3K4me3 in differentiated hESCs (5 days post-differentiation; Figure S5D). Such a bivalent state maintains robust expression and dynamic turnover of SCRIB, despite the pre-occupancy of H3K27me3. These findings implicate EZH2 in the regulation of Scribble upon FBL depletion.

## EZH2 translocates to the nucleoplasm and represses Scribble upon FBL depletion

We show that the depletion of FBL relocalizes EZH2 from the nucleolus to the nucleoplasm, which correlates with an

**Figure 7. FBL depletion promotes tumorigenesis**

(A) Schematic representation of xenograft assays performed in NOD/SCID mice showing tumor induction, harvest, and further processing for immunoblotting and immunofluorescence assays.

(B) Quantification of tumor volumes across 35 days in +/− doxycycline (Dox)-administered mice ($n = 5$). Error bars indicate SD; $^{*}p < 0.5$.

(C) (i) Representative images of tumors harvested from mice 35 days post-injection ($n = 5$). (ii) Weight of tumors after harvesting from mice ($n = 5$). Error bars indicate SD. $^{***}p < 0.001$.

(D) Representative images of immunofluorescence for EZH2 and NCL from MCF10A(p53DN) and DLD-1 cells transfected with siLacZ and siFBL ($n \geq 90$) show the nucleus via DAPI staining, EZH2 via green fluorescence, and NCL via red fluorescence. Scale bar, 20 μm, ($N = 3$). Quantification of colocalization analysis of EZH2 and nucleolin (NCL) in Figure 20C.

(E) Representative immunoblots of Scribble, E-cadherin, FBL, and H3K27me3 using β-tubulin and H3 as loading controls from cells harvested from tumors. Quantification in Figure S20B.

(F) (i) Representative hematoxylin and eosin (H&E)-stained lung sections from NOD-SCID mice 60 days after tail vein injection of DLD-1 cells expressing shRNA targeting FBL (shFBL) under the Dox-inducible promoter. Lungs from Dox-administered (+Dox) mice exhibited numerous, well-defined metastatic nodules distributed across the lung parenchyma, whereas shFBL-expressing mice displayed markedly fewer and smaller metastatic lesions. Scale bars, 100 μm. (ii) Quantification of metastatic burden in lungs from NOD-SCID mice following tail vein injection of DLD-1 cells expressing Dox-inducible shFBL. Data are shown as mean ± SEM, with each dot representing each lung sample.

$^{*}p < 0.05$, unpaired *t* test.

increased deposition of H3K27me3 on the SCRIB promoter, repressing Scribble expression.

We examined the generalizability of FBL depletion in two additional colorectal cancer cell lines, HCT116 and SW480. These cell lines showed a decrease in the levels of nucleolar EZH2 (Figures S13C and S13D(i–ii)). EZH2 showed a significant decrease in the nucleoli upon FBL depletion, consistent with observations in DLD-1 and MCF10A(p53DN) (Figure 4B). This further demonstrates that FBL depletion causes relocalization of EZH2 from the nucleoli to the nucleoplasm.

Elevated expression of EZH2 has been implicated in promoting metastasis across various cancer types. In breast cancers, increased EZH2 levels are significantly associated with invasive carcinomas and metastasis.[70] Similarly, in prostate cancer, EZH2 overexpression correlates with advanced stages and metastatic progression. Increased EZH2 expression positively correlates with aggressive forms of bladder cancer, endometrial cancer, and melanoma, where it is linked to enhanced metastatic potential.[71,72] In ovarian cancers, EZH2 enhances metastasis through TGF-β signaling.[73] EZH2 regulates tumor suppressors by transcriptionally silencing adenosylmethionine decarboxylase 1 (AMD-1).[72] Collectively, these findings underscore the critical role of EZH2 in facilitating cancer metastasis across multiple cancer subtypes. Our study unravels Scribble as a key target of EZH2 overexpression.

### FBL depletion induces EMT and enhances tumor growth

FBL depletion induces EMT by downregulating Scribble, stabilizing TAZ, and enhancing Akt activation, which reduces EZH2 activity. In MCF10A(p53DN) cells, FBL loss increased mesenchymal markers and reduced epithelial markers. Scribble levels declined by ∼36 h and partially recovered by ∼72 h but remained cytoplasmic. Using membrane anchoring-deficient Scribble mutants (C4S, C10S, and P305L), we found that cytoplasmic retention alone elevated pAkt (S473), corroborating its sufficiency for Akt activation (Figures S19A, S19B, and S19C).[62] We propose that Snail, which appears by ∼72 h, drives cytoplasmic retention of Scribble, consistent with elevated levels of Snail-high triple-negative breast cancer cells (MDAMB231).[74] Thus, prolonged FBL depletion promotes EMT by sustaining mislocalization of Scribble and activating Akt signaling.

FBL depletion-mediated downregulation of Scribble, the consequent disruption of PTEN proximal to the cell membrane, and decreased levels of PTEN in tumor cells (Figure S20F),[75,76] further function as key targets of FBL-dependent tumorigenesis.[77,78]

Gain-of-function mutations in EZH2, particularly in B cell lymphomas, enhance its methyltransferase activity, leading to aberrant gene repression and oncogenesis. The well-characterized Y641 mutation in the SET domain increases H3K27 trimethylation, promoting malignant transformation.[79] Similarly, the A687V mutation, also in the SET domain, alters substrate specificity and enhances methylation activity, further contributing to lymphoma development.[80] Additionally, the W113C mutation in the SET activation loop stabilizes the active conformation of EZH2, amplifying its catalytic function and driving oncogenesis.[81] Collectively, these studies show that a hyperactive mutation of EZH2 mediates excessive deposition of H3K27me3, playing a critical role in cell proliferation and tumor progression, consistent with our finding that the enhanced deposition of H3K27me3 upon FBL depletion enhances tumorigenesis.

### Future directions

Consistent with elevated levels of FBL and its association with increased chemoresistance and proliferation in cancer cells, therapeutic interventions that modulate FBL expression are key. Among the various approaches for regulating protein levels, proteolysis-targeting chimeras (PROTACs) have emerged as promising therapeutic agents. However, our findings indicate that targeting FBL for degradation via PROTACs may not be a viable therapeutic strategy, as reduced FBL levels can compromise epithelial integrity. A potential therapeutic strategy is to develop small molecule-based stabilizers of the FBL-EZH2 interaction, likely to promote greater retention of EZH2 within the nucleolus rather than the nucleoplasm (Figure 4B). Such stabilizers include small molecules or peptide chimeras with high binding affinity to the FBL-EZH2 interface. Recently, the development of LOCKTACs—compounds that slow dissociation to stabilize natural protein interactions without generating new ones—has opened new avenues in drug design.[82] LOCKTACs function by binding directly within or adjacent to a protein-protein interface or by acting as heterobifunctional molecules that stabilize complexes without directly engaging the interface. Unlike allosteric drugs, which act at distal sites to induce conformational changes, LOCKTACs operate by reinforcing native interactions. To enable intracellular delivery, such stabilizers could be conjugated to cell-penetrating peptides (CPPs), short, positively charged sequences that facilitate membrane translocation via endocytosis or direct penetration.[83] Cyclic peptides generated via click chemistry provide an additional delivery route, offering improved stability and, in some cases, passive cell entry.[84] Delivering these interaction-stabilizing molecules, particularly during early stages of cancer, could preserve epithelial organization and suppress EMT-like phenotypic transitions without perturbing the canonical role of FBL in ribosome biogenesis, thereby preventing metastatic spread. In parallel, enzymatic inhibition of FBL activity also presents a therapeutic opportunity, as disabling its enzymatic function does not significantly affect cell proliferation.[9] Optimized use of FBL enzymatic inhibitors in cancers with elevated FBL levels could reduce rRNA methylation and subsequently limit cap-independent translation of key oncogenes, including IGF1R, MYC, and VEGFA.[8,85] Importantly, previous findings are consistent with ours, which reveal that FBL knockdown does not alter 28S or 18S rRNA levels by more than ∼10% (Figure S3D).[86] Moreover, cells can tolerate substantial reductions in FBL levels (>60%) without compromising ribosome production or viability.[6,9,87] Furthermore, this is consistent with our data, which indicate that when the p53-p21 axis is disabled, FBL depletion does not significantly affect cell viability (Figure S3B). Furthermore, SUnSET assays did not reveal any change in the global protein synthesis rates upon FBL depletion.

### Limitations of the study

The molecular mechanisms by which FBL regulates nucleolar retention of EZH2 and the temporal control of its redistribution to the nucleoplasm are incompletely understood and require

detailed investigation across cancers. Mechanistically, it is crucial to map the epigenomic consequences of EZH2 relocalization to determine its direct and indirect targets and, consequently, the pathways altered upon FBL loss. Complementary to chromatin mapping, focused studies of membrane trafficking are essential to determine the underlying mechanisms by which E-cadherin internalizes but fails to recycle back to the cell membrane, impacting epithelial integrity. Furthermore, the study of tumorigenesis and metastasis needs to be expanded to additional paradigms of cancer progression employing iRFP-labeled[88] cells for *in vivo* imaging for a more comprehensive understanding of the role of FBL in metastasis. Since FBL is involved in rRNA synthesis, the finding that 45S pre-rRNA decreases while mature 18S and 28S levels remain stable implies compensatory homeostasis, which can potentially modulate cell polarity proteins. Consistent with the role of FBL in rRNA methylation, RiboMethSeq[89] would be a useful approach to profile rRNA methylation, and ribosome profiling could elucidate downstream consequences on translation to uncover the effect of modulating nucleolar proteins such as FBL in cancers. Collectively, these studies aim to address the underlying mechanisms by which FBL constrains epithelial plasticity and metastatic progression.

## RESOURCE AVAILABILITY

### Lead contact

Further information and requests for resources and reagents should be directed to and will be fulfilled by the lead contact, Prof. Kundan Sengupta (kunsen@iiserpune.ac.in).

### Materials availability

All unique/stable reagents generated in this study are available from the lead contact without restriction.

### Data and code availability

- RNA-seq data have been deposited at the GEO database with accession ID: GSE289801.
- This paper does not report any original code.

## ACKNOWLEDGMENTS

The authors gratefully acknowledge the Microscopy and FACS facilities and especially Krishnaveni, National Facility for Gene Function in Health and Disease at IISER Pune, for her constant support and technical assistance with the animal experiments. We acknowledge Ayantika Sengupta for her pioneering work on FBL depletion and its role in enhancing cell migration, which laid the foundation for this study and was an integral part of her doctoral thesis. We thank the RNA-sequencing facility of the National Center for Biological Sciences (NCBS), Bangalore, for providing sequencing services. We acknowledge Richa Rikhy, Biology, IISER Pune, and the Biology department for reagents and useful discussions. We thank Jomon Joseph (NCCS, Pune) and Nagaraj Balasubramaniam (IISER, Pune) for reagents. Most illustrations were created using BioRender.com. We gratefully acknowledge funding support from ANRF, Department of Science and Technology (DST), Science and Engineering Research Board (SERB; grant no. CRG/2020/002563), Ministry of Education (grant no. MoE-STARS/STARS-2/2023-0603), Department of Biotechnology (DBT) MedDevice (grant no. BT/PR49745/MED/32/925/2023), Department of Biotechnology (BT/PR52973/MED/30/2535/2024), Intermediate Fellowship of the Wellcome Trust-DBT India Alliance (grant no. 500164/Z/09/Z), and intramural funding from IISER-Pune.

## AUTHOR CONTRIBUTIONS

Conceptualization, S.S. and K.S.; experimental design, S.S. and K.S.; performance of experiments, S.S., A.K.B., and S.M.; data analysis, S.S. and A.K.B.; writing – original draft preparation, S.S.; writing – review and editing, S.S., K.S., A.K.B., and D.N.; visualization, S.S.; supervision, K.S.; project administration, K.S.; funding acquisition, K.S. All authors have read and agreed to the published version of the manuscript.

## DECLARATION OF INTERESTS

The authors declare no competing interests.

## DECLARATION OF GENERATIVE AI AND AI-ASSISTED TECHNOLOGIES IN THE WRITING PROCESS

During the preparation of this work, the author(s) used some portions of the language editing and initial drafting by OpenAI's ChatGPT. All content was subsequently reviewed and verified by the authors. After using this tool/service, the author(s) reviewed and edited the content as needed and take(s) full responsibility for the content of the published article.

## STAR★METHODS

Detailed methods are provided in the online version of this paper and include the following:

- KEY RESOURCES TABLE
- EXPERIMENTAL MODELS AND STUDY PARTICIPANT DETAILS
  - Mice
  - Cell lines
- METHOD DETAILS
  - Cell culture and treatment
  - Generation of constructs
  - siRNA-mediated knockdown
  - Generation and transduction of viral particles
  - RNA sequencing
  - ChIP PCR
  - Chromatin fragmentation
  - Immunoprecipitation
  - Reverse crosslinking and DNA purification
  - PCR amplification and analysis
  - BioID2 ChIP PCR
  - Immunofluorescence assay
  - Western blotting
  - Cell fractionation
  - Proteinase K protection assay
  - Transferrin uptake assay
  - Scratch wound
  - Invasion assay
  - Image analysis
  - Segmentation analysis
  - Subcutaneous xenograft assay in NOD-SCID mice
  - Tail vein injection assay
  - Hematoxylin and eosin (H&E) staining of paraffin-embedded lung and tumor tissues
- QUANTIFICATION AND STATISTICAL ANALYSIS

## SUPPLEMENTAL INFORMATION

Supplemental information can be found online at https://doi.org/10.1016/j.celrep.2025.116608.

Received: May 23, 2025
Revised: October 6, 2025
Accepted: November 4, 2025
Published: November 25, 2025

## REFERENCES


1. Incarnato, D., Anselmi, F., Morandi, E., Neri, F., Maldotti, M., Rapelli, S., Parlato, C., Basile, G., and Oliviero, S. (2017). High-Throughput Single-Base Resolution Mapping of RNA 2′-O-Methylated Residues. Nucleic Acids Res. *45*, 1433–1441. https://doi.org/10.1093/nar/gkw810.
2. Tollervey, D., Lehtonen, H., Carmo-Fonseca, M., and Hurt, E.C. (1991). The Small Nucleolar RNP Protein NOP1 (Fibrillarin) Is Required for Pre-rRNA Processing in Yeast. EMBO J. *10*, 573–583. https://doi.org/10.1002/j.1460-2075.1991.tb07984.x.
3. Watkins, N.J., and Bohnsack, M.T. (2012). The Box C/D and H/ACA snoRNPs: Key Players in the Modification, Processing and the Dynamic Folding of Ribosomal RNA. Wiley Interdiscip. Rev. RNA *3*, 397–414. https://doi.org/10.1002/wrna.117.
4. Kiss-László, Z., Henry, Y., Bachellerie, J.P., Caizergues-Ferrer, M., and Kiss, T. (1996). Site-Specific Ribose Methylation of Preribosomal RNA: A Novel Function for Small Nucleolar RNAs. Cell *85*, 1077–1088. https://doi.org/10.1016/s0092-8674(00)81308-2.
5. Sharma, S., Marchand, V., Motorin, Y., and Lafontaine, D.L.J. (2017). Identification of Sites of 2'-O-Methylation Vulnerability in Human Ribosomal RNAs by Systematic Mapping. Sci. Rep. *7*, 11490. https://doi.org/10.1038/s41598-017-09734-9.
6. Iyer-Bierhoff, A., Krogh, N., Tessarz, P., Ruppert, T., Nielsen, H., and Grummt, I. (2018). SIRT7-Dependent Deacetylation of Fibrillarin Controls Histone H2A Methylation and rRNA Synthesis during the Cell Cycle. Cell Rep. *25*, 2946–2954.e5. https://doi.org/10.1016/j.celrep.2018.11.051.
7. Elliott, B.A., Ho, H.-T., Ranganathan, S.V., Vangaveti, S., Ilkayeva, O., Abou Assi, H., Choi, A.K., Agris, P.F., and Holley, C.L. (2019). Modification of Messenger RNA by 2'-O-Methylation Regulates Gene Expression in Vivo. Nat. Commun. *10*, 3401. https://doi.org/10.1038/s41467-019-11375-7.
8. Marcel, V., Ghayad, S.E., Belin, S., Therizols, G., Morel, A.-P., Solano-Gonzàlez, E., Vendrell, J.A., Hacot, S., Mertani, H.C., Albaret, M.A., et al. (2013). P53 Acts as a Safeguard of Translational Control by Regulating Fibrillarin and rRNA Methylation in Cancer. Cancer Cell *24*, 318–330. https://doi.org/10.1016/j.ccr.2013.08.013.
9. Sun, X., Gao, C., Xu, X., Li, M., Zhao, X., Wang, Y., Wang, Y., Zhang, S., Yan, Z., Liu, X., and Wu, C. (2023). FBL Promotes Cancer Cell Resistance to DNA Damage and BRCA1 Transcription via YBX1. EMBO Rep. *24*, e56230. https://doi.org/10.15252/embr.202256230.
10. Zhi, Y., Guo, Y., Li, S., He, X., Wei, H., Laster, K., Wu, Q., Zhao, D., Xie, J., Ruan, S., et al. (2025). FBL Promotes Hepatocellular Carcinoma Tumorigenesis and Progression by Recruiting YY1 to Enhance CAD Gene Expression. Cell Death Dis. *16*, 348. https://doi.org/10.1038/s41419-025-07684-z.
11. Nguyen Van Long, F., Lardy-Cleaud, A., Carène, D., Rossoni, C., Catez, F., Rollet, P., Pion, N., Monchiet, D., Dolbeau, A., Martin, M., et al. (2022). Low Level of Fibrillarin, a Ribosome Biogenesis Factor, Is a New Independent Marker of Poor Outcome in Breast Cancer. BMC Cancer *22*, 526. https://doi.org/10.1186/s12885-022-09552-x.
12. Takeichi, M. (1991). Cadherin Cell Adhesion Receptors as a Morphogenetic Regulator. Science *251*, 1451–1455. https://doi.org/10.1126/science.2006419.
13. Zaidel-Bar, R. (2013). Cadherin Adhesome at a Glance. J. Cell Sci. *126*, 373–378. https://doi.org/10.1242/jcs.111559.
14. van Roy, F., and Berx, G. (2008). The Cell-Cell Adhesion Molecule E-Cadherin. Cell. Mol. Life Sci. *65*, 3756–3788. https://doi.org/10.1007/s00018-008-8281-1.
15. Lamouille, S., Xu, J., and Derynck, R. (2014). Molecular Mechanisms of Epithelial-Mesenchymal Transition. Nat. Rev. Mol. Cell Biol. *15*, 178–196. https://doi.org/10.1038/nrm3758.
16. Bilder, D., Li, M., and Perrimon, N. (2000). Cooperative Regulation of Cell Polarity and Growth by Drosophila Tumor Suppressors. Science *289*, 113–116. https://doi.org/10.1126/science.289.5476.113.
17. Humbert, P., Russell, S., and Richardson, H. (2003). Scribble and Lgl in Cell Polarity, Cell Proliferation and Cancer. Bioessays *25*, 542–553. https://doi.org/10.1002/bies.10286.
18. Zihni, C., Mills, C., Matter, K., and Balda, M.S. (2016). Tight Junctions: From Simple Barriers to Multifunctional Molecular Gates. Nat. Rev. Mol. Cell Biol. *17*, 564–580. https://doi.org/10.1038/nrm.2016.80.
19. Burute, M., Prioux, M., Blin, G., Truchet, S., Letort, G., Tseng, Q., Bessy, T., Lowell, S., Young, J., Filhol, O., and Théry, M. (2017). Polarity Reversal by Centrosome Repositioning Primes Cell Scattering during Epithelial-to-Mesenchymal Transition. Dev. Cell *40*, 168–184. https://doi.org/10.1016/j.devcel.2016.12.004.
20. Yao, R.-W., Xu, G., Wang, Y., Shan, L., Luan, P.-F., Wang, Y., Wu, M., Yang, L.-Z., Xing, Y.-H., Yang, L., and Chen, L.-L. (2019). Nascent Pre-rRNA Sorting via Phase Separation Drives the Assembly of Dense Fibrillar Components in the Human Nucleolus. Mol. Cell *76*, 767–783.e11. https://doi.org/10.1016/j.molcel.2019.08.014.
21. Bursac, S., Brdovcak, M.C., Donati, G., and Volarevic, S. (2014). Activation of the Tumor Suppressor P53 upon Impairment of Ribosome Biogenesis. Biochim. Biophys. Acta *1842*, 817–830. https://doi.org/10.1016/j.bbadis.2013.08.014.
22. Castillo Duque de Estrada, N.M., Thoms, M., Flemming, D., Hammaren, H.M., Buschauer, R., Ameismeier, M., Baßler, J., Beck, M., Beckmann, R., and Hurt, E. (2023). Structure of Nascent 5S RNPs at the Crossroad between Ribosome Assembly and MDM2-P53 Pathways. Nat. Struct. Mol. Biol. *30*, 1119–1131. https://doi.org/10.1038/s41594-023-01006-7.
23. Scala, F., Brighenti, E., Govoni, M., Imbrogno, E., Fornari, F., Treré, D., Montanaro, L., and Derenzini, M. (2016). Direct Relationship between the Level of P53 Stabilization Induced by rRNA Synthesis-Inhibiting Drugs and the Cell Ribosome Biogenesis Rate. Oncogene *35*, 977–989. https://doi.org/10.1038/onc.2015.147.
24. Yang, K., Yang, J., and Yi, J. (2018). Nucleolar Stress: Hallmarks, Sensing Mechanism and Diseases. Cell Stress *2*, 125–140. https://doi.org/10.15698/cst2018.06.139.
25. Donati, G., Brighenti, E., Vici, M., Mazzini, G., Treré, D., Montanaro, L., and Derenzini, M. (2011). Selective Inhibition of rRNA Transcription Downregulates E2F-1: A New P53-Independent Mechanism Linking Cell Growth to Cell Proliferation. J. Cell Sci. *124*, 3017–3028. https://doi.org/10.1242/jcs.086074.
26. Hahn, W.C., Dessain, S.K., Brooks, M.W., King, J.E., Elenbaas, B., Sabatini, D.M., DeCaprio, J.A., and Weinberg, R.A. (2002). Enumeration of the Simian Virus 40 Early Region Elements Necessary for Human Cell Transformation. Mol. Cell Biol. *22*, 2111–2123. https://doi.org/10.1128/MCB.22.7.2111-2123.2002.
27. Shaulian, E., Zauberman, A., Ginsberg, D., and Oren, M. (1992). Identification of a Minimal Transforming Domain of P53: Negative Dominance through Abrogation of Sequence-Specific DNA Binding. Mol. Cell Biol. *12*, 5581–5592. https://doi.org/10.1128/mcb.12.12.5581-5592.1992.
28. Lock, J.G., and Stow, J.L. (2005). Rab11 in Recycling Endosomes Regulates the Sorting and Basolateral Transport of E-Cadherin. Mol. Biol. Cell *16*, 1744–1755. https://doi.org/10.1091/mbc.E04-10-0867.
29. Mu, F.T., Callaghan, J.M., Steele-Mortimer, O., Stenmark, H., Parton, R.G., Campbell, P.L., McCluskey, J., Yeo, J.P., Tock, E.P., and Toh, B.H. (1995). EEA1, an Early Endosome-Associated Protein. EEA1 Is a Conserved Alpha-Helical Peripheral Membrane Protein Flanked by Cysteine "Fingers" and Contains a Calmodulin-Binding IQ Motif. J. Biol. Chem. *270*, 13503–13511. https://doi.org/10.1074/jbc.270.22.13503.
30. Khurana, H., Baratam, K., Bhattacharyya, S., Srivastava, A., and Pucadyil, T.J. (2023). Mechanistic Analysis of a Novel Membrane-Interacting Variable Loop in the Pleckstrin-Homology Domain Critical for Dynamin Function. Proc. Natl. Acad. Sci. USA *120*, e2215250120. https://doi.org/10.1073/pnas.2215250120.

31. Macia, E., Ehrlich, M., Massol, R., Boucrot, E., Brunner, C., and Kirchhausen, T. (2006). a Cell-Permeable Inhibitor of Dynamin. Dev. Cell *10*, 839–850. https://doi.org/10.1016/j.devcel.2006.04.002.

32. Izumi, G., Sakisaka, T., Baba, T., Tanaka, S., Morimoto, K., and Takai, Y. (2004). Endocytosis of E-Cadherin Regulated by Rac and Cdc42 Small G Proteins through IQGAP1 and Actin Filaments. J. Cell Biol. *166*, 237–248. https://doi.org/10.1083/jcb.200401078.

33. Kon, S., Tanabe, K., Watanabe, T., Sabe, H., and Satake, M. (2008). Clathrin Dependent Endocytosis of E-Cadherin Is Regulated by the Arf6GAP Isoform SMAP1. Exp. Cell Res. *314*, 1415–1428. https://doi.org/10.1016/j.yexcr.2007.11.006.

34. Le, T.L., Yap, A.S., and Stow, J.L. (1999). Recycling of E-Cadherin. J. Cell Biol. *146*, 219–232. https://doi.org/10.1083/jcb.146.1.219.

35. Tria, S., Jimison, L.H., Hama, A., Bongo, M., and Owens, R.M. (2013). Sensing of EGTA Mediated Barrier Tissue Disruption with an Organic Transistor. Biosensors (Basel) *3*, 44–57. https://doi.org/10.3390/bios3010044.

36. Lohia, M., Qin, Y., and Macara, I.G. (2012). The Scribble Polarity Protein Stabilizes E-Cadherin/P120-Catenin Binding and Blocks Retrieval of E-Cadherin to the Golgi. PLoS One *7*, e51130. https://doi.org/10.1371/journal.pone.0051130.

37. Subramanian, A., Tamayo, P., Mootha, V.K., Mukherjee, S., Ebert, B.L., Gillette, M.A., Paulovich, A., Pomeroy, S.L., Golub, T.R., Lander, E.S., and Mesirov, J.P. (2005). Gene Set Enrichment Analysis: A Knowledge-Based Approach for Interpreting Genome-Wide Expression Profiles. Proc. Natl. Acad. Sci. USA *102*, 15545–15550. https://doi.org/10.1073/pnas.0506580102.

38. Qin, Y., Capaldo, C., Gumbiner, B.M., and Macara, I.G. (2005). The Mammalian Scribble Polarity Protein Regulates Epithelial Cell Adhesion and Migration through E-Cadherin. J. Cell Biol. *171*, 1061–1071. https://doi.org/10.1083/jcb.200506094.

39. Oki, S., Ohta, T., Shioi, G., Hatanaka, H., Ogasawara, O., Okuda, Y., Kawaji, H., Nakaki, R., Sese, J., and Meno, C. (2018). ChIP-Atlas: A Data-Mining Suite Powered by Full Integration of Public ChIP-Seq Data. EMBO Rep. *19*, e46255. https://doi.org/10.15252/embr.201846255.

40. Sharma, V., Malgulwar, P.B., Purkait, S., Patil, V., Pathak, P., Agrawal, R., Kulshreshtha, R., Mallick, S., Julka, P.K., Suri, A., et al. (2017). Genome-Wide ChIP-Seq Analysis of EZH2-Mediated H3K27me3 Target Gene Profile Highlights Differences between Low- and High-Grade Astrocytic Tumors. Carcinogenesis *38*, 152–161. https://doi.org/10.1093/carcin/bgw126.

41. McCabe, M.T., Ott, H.M., Ganji, G., Korenchuk, S., Thompson, C., Van Aller, G.S., Liu, Y., Graves, A.P., Della Pietra, A., Diaz, E., et al. (2012). EZH2 Inhibition as a Therapeutic Strategy for Lymphoma with EZH2-Activating Mutations. Nature *492*, 108–112. https://doi.org/10.1038/nature11606.

42. Yi, Y., Li, Y., Meng, Q., Li, Q., Li, F., Lu, B., Shen, J., Fazli, L., Zhao, D., Li, C., et al. (2021). A PRC2-Independent Function for EZH2 in Regulating rRNA 2'-O Methylation and IRES-Dependent Translation. Nat. Cell Biol. *23*, 341–354. https://doi.org/10.1038/s41556-021-00653-6.

43. Cao, R., Wang, L., Wang, H., Xia, L., Erdjument-Bromage, H., Tempst, P., Jones, R.S., and Zhang, Y. (2002). Role of Histone H3 Lysine 27 Methylation in Polycomb-Group Silencing. Science *298*, 1039–1043. https://doi.org/10.1126/science.1076997.

44. Kuzmichev, A., Nishioka, K., Erdjument-Bromage, H., Tempst, P., and Reinberg, D. (2002). Histone Methyltransferase Activity Associated with a Human Multiprotein Complex Containing the Enhancer of Zeste Protein. Genes Dev. *16*, 2893–2905. https://doi.org/10.1101/gad.1035902.

45. Pasini, D., Bracken, A.P., Jensen, M.R., Lazzerini Denchi, E., and Helin, K. (2004). Suz12 Is Essential for Mouse Development and for EZH2 Histone Methyltransferase Activity. EMBO J. *23*, 4061–4071. https://doi.org/10.1038/sj.emboj.7600402.

46. Kim, D.I., Jensen, S.C., Noble, K.A., Kc, B., Roux, K.H., Motamedchaboki, K., and Roux, K.J. (2016). An Improved Smaller Biotin Ligase for BioID Proximity Labeling. Mol. Biol. Cell *27*, 1188–1196. https://doi.org/10.1091/mbc.E15-12-0844.

47. Cordenonsi, M., Zanconato, F., Azzolin, L., Forcato, M., Rosato, A., Frasson, C., Inui, M., Montagner, M., Parenti, A.R., Poletti, A., et al. (2011). The Hippo Transducer TAZ Confers Cancer Stem Cell-Related Traits on Breast Cancer Cells. Cell *147*, 759–772. https://doi.org/10.1016/j.cell.2011.09.048.

48. Lei, Q.-Y., Zhang, H., Zhao, B., Zha, Z.-Y., Bai, F., Pei, X.-H., Zhao, S., Xiong, Y., and Guan, K.-L. (2008). TAZ Promotes Cell Proliferation and Epithelial-Mesenchymal Transition and Is Inhibited by the Hippo Pathway. Mol. Cell Biol. *28*, 2426–2436. https://doi.org/10.1128/MCB.01874-07.

49. Li, X., Yang, H., Liu, J., Schmidt, M.D., and Gao, T. (2011). Scribble-Mediated Membrane Targeting of PHLPP1 Is Required for Its Negative Regulation of Akt. EMBO Rep. *12*, 818–824. https://doi.org/10.1038/embor.2011.106.

50. Cha, T.-L., Zhou, B.P., Xia, W., Wu, Y., Yang, C.-C., Chen, C.-T., Ping, B., Otte, A.P., and Hung, M.-C. (2005). Akt-Mediated Phosphorylation of EZH2 Suppresses Methylation of Lysine 27 in Histone H3. Science *310*, 306–310. https://doi.org/10.1126/science.1118947.

51. Batlle, E., Sancho, E., Francí, C., Domínguez, D., Monfar, M., Baulida, J., and García De Herreros, A. (2000). The Transcription Factor Snail Is a Repressor of E-Cadherin Gene Expression in Epithelial Tumour Cells. Nat. Cell Biol. *2*, 84–89. https://doi.org/10.1038/35000034.

52. Sánchez-Tilló, E., Lázaro, A., Torrent, R., Cuatrecasas, M., Vaquero, E.C., Castells, A., Engel, P., and Postigo, A. (2010). ZEB1 Represses E-Cadherin and Induces an EMT by Recruiting the SWI/SNF Chromatin-Remodeling Protein BRG1. Oncogene *29*, 3490–3500. https://doi.org/10.1038/onc.2010.102.

53. Rhodes, N., Heerding, D.A., Duckett, D.R., Eberwein, D.J., Knick, V.B., Lansing, T.J., McConnell, R.T., Gilmer, T.M., Zhang, S.-Y., Robell, K., et al. (2008). Characterization of an Akt Kinase Inhibitor with Potent Pharmacodynamic and Antitumor Activity. Cancer Res. *68*, 2366–2374. https://doi.org/10.1158/0008-5472.CAN-07-5783.

54. Kato, H., Semba, S., Miskad, U.A., Seo, Y., Kasuga, M., and Yokozaki, H. (2004). High Expression of PRL-3 Promotes Cancer Cell Motility and Liver Metastasis in Human Colorectal Cancer: A Predictive Molecular Marker of Metachronous Liver and Lung Metastases. Clin. Cancer Res. *10*, 7318–7328. https://doi.org/10.1158/1078-0432.CCR-04-0485.

55. Kallay, L.M., McNickle, A., Brennwald, P.J., Hubbard, A.L., and Braiterman, L.T. (2006). Scribble Associates with Two Polarity Proteins, Lgl2 and Vangl2, via Distinct Molecular Domains. J. Cell. Biochem. *99*, 647–664. https://doi.org/10.1002/jcb.20992.

56. Stephens, A.D., Liu, P.Z., Banigan, E.J., Almassalha, L.M., Backman, V., Adam, S.A., Goldman, R.D., and Marko, J.F. (2018). Chromatin Histone Modifications and Rigidity Affect Nuclear Morphology Independent of Lamins. Mol. Biol. Cell *29*, 220–233. https://doi.org/10.1091/mbc.E17-06-0410.

57. Jia, Y., Vong, J.S.-L., Asafova, A., Garvalov, B.K., Caputo, L., Cordero, J., Singh, A., Boettger, T., Günther, S., Fink, L., et al. (2019). Lamin B1 Loss Promotes Lung Cancer Development and Metastasis by Epigenetic Derepression of RET. J. Exp. Med. *216*, 1377–1395. https://doi.org/10.1084/jem.20181394.

58. Zuo, L., Zhao, H., Yang, R., Wang, L., Ma, H., Xu, X., Zhou, P., and Kong, L. (2018). Lamin A/C Might Be Involved in the EMT Signalling Pathway. Gene *663*, 51–64. https://doi.org/10.1016/j.gene.2018.04.040.

59. Amin, M.A., Matsunaga, S., Ma, N., Takata, H., Yokoyama, M., Uchiyama, S., and Fukui, K. (2007). a Nucleolar Protein, Is Required for Normal Nuclear Morphology and Cellular Growth in HeLa Cells. Biochem. Biophys. Res. Commun. *360*, 320–326. https://doi.org/10.1016/j.bbrc.2007.06.092.

60. Uzer, G., Rubin, C.T., and Rubin, J. (2016). Cell Mechanosensitivity Is Enabled by the LINC Nuclear Complex. Curr. Mol. Biol. Rep. *2*, 36–47. https://doi.org/10.1007/s40610-016-0032-8.

61. Schmidt, E.K., Clavarino, G., Ceppi, M., and Pierre, P. (2009). SUnSET, a Nonradioactive Method to Monitor Protein Synthesis. Nat. Methods *6*, 275–277. https://doi.org/10.1038/nmeth.1314.

62. Feigin, M.E., Akshinthala, S.D., Araki, K., Rosenberg, A.Z., Muthuswamy, L.B., Martin, B., Lehmann, B.D., Berman, H.K., Pietenpol, J.A., Cardiff, R.D., and Muthuswamy, S.K. (2014). Mislocalization of the Cell Polarity Protein Scribble Promotes Mammary Tumorigenesis and Is Associated with Basal Breast Cancer. Cancer Res. *74*, 3180–3194. https://doi.org/10.1158/0008-5472.CAN-13-3415.

63. Khuntia, P., Rawal, S., Marwaha, R., and Das, T. (2022). Actin-Driven Golgi Apparatus Dispersal during Collective Migration of Epithelial Cells. Proc. Natl. Acad. Sci. USA *119*, e2204808119. https://doi.org/10.1073/pnas.2204808119.

64. Liu, J., Li, J., Li, P., Wang, Y., Liang, Z., Jiang, Y., Li, J., Feng, C., Wang, R., Chen, H., et al. (2017). Loss of DLG5 Promotes Breast Cancer Malignancy by Inhibiting the Hippo Signaling Pathway. Sci. Rep. *7*, 42125. https://doi.org/10.1038/srep42125.

65. Nanes, B.A., Chiasson-MacKenzie, C., Lowery, A.M., Ishiyama, N., Faundez, V., Ikura, M., Vincent, P.A., and Kowalczyk, A.P. (2012). P120-Catenin Binding Masks an Endocytic Signal Conserved in Classical Cadherins. J. Cell Biol. *199*, 365–380. https://doi.org/10.1083/jcb.201205029.

66. Schiano Lomoriello, I., Giangreco, G., Iavarone, C., Tordonato, C., Caldieri, G., Serio, G., Confalonieri, S., Freddi, S., Bianchi, F., Pirroni, S., et al. (2020). A Self-Sustaining Endocytic-Based Loop Promotes Breast Cancer Plasticity Leading to Aggressiveness and pro-Metastatic Behavior. Nat. Commun. *11*, 3020. https://doi.org/10.1038/s41467-020-16836-y.

67. Nagaoka, T., Inutsuka, A., Begum, K., Bin hafiz, K.M., and Kishi, M. (2014). Vangl2 Regulates E-Cadherin in Epithelial Cells. Sci. Rep. *4*, 6940. https://doi.org/10.1038/srep06940.

68. Chen, H.-R., Yeh, Y.-C., Liu, C.-Y., Wu, Y.-T., Lo, F.-Y., Tang, M.-J., and Wang, Y.-K. (2016). DDR1 Promotes E-Cadherin Stability via Inhibition of Integrin-\beta1-Src Activation-Mediated E-Cadherin Endocytosis. Sci. Rep. *6*, 36336. https://doi.org/10.1038/srep36336.

69. Antonysamy, S., Condon, B., Druzina, Z., Bonanno, J.B., Gheyi, T., Zhang, F., MacEwan, I., Zhang, A., Ashok, S., Rodgers, L., et al. (2013). Structural Context of Disease-Associated Mutations and Putative Mechanism of Autoinhibition Revealed by X-Ray Crystallographic Analysis of the EZH2-SET Domain. PLoS One *8*, e84147. https://doi.org/10.1371/journal.pone.0084147.

70. Alford, S.H., Toy, K., Merajver, S.D., and Kleer, C.G. (2012). Increased Risk for Distant Metastasis in Patients with Familial Early-Stage Breast Cancer and High EZH2 Expression. Breast Cancer Res. Treat. *132*, 429–437. https://doi.org/10.1007/s10549-011-1591-2.

71. Bachmann, I.M., Halvorsen, O.J., Collett, K., Stefansson, I.M., Straume, O., Haukaas, S.A., Salvesen, H.B., Otte, A.P., and Akslen, L.A. (2006). EZH2 Expression Is Associated with High Proliferation Rate and Aggressive Tumor Subgroups in Cutaneous Melanoma and Cancers of the Endometrium, Prostate, and Breast. J. Clin. Oncol. *24*, 268–273. https://doi.org/10.1200/JCO.2005.01.5180.

72. Zingg, D., Debbache, J., Schaefer, S.M., Tuncer, E., Frommel, S.C., Cheng, P., Arenas-Ramirez, N., Haeusel, J., Zhang, Y., Bonalli, M., et al. (2015). The Epigenetic Modifier EZH2 Controls Melanoma Growth and Metastasis through Silencing of Distinct Tumour Suppressors. Nat. Commun. *6*, 6051. https://doi.org/10.1038/ncomms7051.

73. Rao, Z.-Y., Cai, M.-Y., Yang, G.-F., He, L.-R., Mai, S.-J., Hua, W.-F., Liao, Y.-J., Deng, H.-X., Chen, Y.-C., Guan, X.-Y., et al. (2010). EZH2 Supports Ovarian Carcinoma Cell Invasion and/or Metastasis via Regulation of TGF-B1 and Is a Predictor of Outcome in Ovarian Carcinoma Patients. Carcinogenesis *31*, 1576–1583. https://doi.org/10.1093/carcin/bgq150.

74. Olmeda, D., Moreno-Bueno, G., Flores, J.M., Fabra, A., Portillo, F., and Cano, A. (2007). SNAI1 Is Required for Tumor Growth and Lymph Node Metastasis of Human Breast Carcinoma MDA-MB-231 Cells. Cancer Res. *67*, 11721–11731. https://doi.org/10.1158/0008-5472.CAN-07-2318.

75. Jarome, T.J., Perez, G.A., Hauser, R.M., Hatch, K.M., and Lubin, F.D. (2018). EZH2 Methyltransferase Activity Controls Pten Expression and mTOR Signaling during Fear Memory Reconsolidation. J. Neurosci. *38*, 7635–7648. https://doi.org/10.1523/JNEUROSCI.0538-18.2018.

76. Gan, L., Xu, M., Hua, R., Tan, C., Zhang, J., Gong, Y., Wu, Z., Weng, W., Sheng, W., and Guo, W. (2018). The Polycomb Group Protein EZH2 Induces Epithelial–Mesenchymal Transition and Pluripotent Phenotype of Gastric Cancer Cells by Binding to PTEN Promoter. J. Hematol. Oncol. *11*, 9. https://doi.org/10.1186/s13045-017-0547-3.

77. Sun, H., Lesche, R., Li, D.M., Liliental, J., Zhang, H., Gao, J., Gavrilova, N., Mueller, B., Liu, X., and Wu, H. (1999). PTEN Modulates Cell Cycle Progression and Cell Survival by Regulating Phosphatidylinositol 3,4,5,-Trisphosphate and Akt/Protein Kinase B Signaling Pathway. Proc. Natl. Acad. Sci. USA *96*, 6199–6204. https://doi.org/10.1073/pnas.96.11.6199.

78. Nguyen, L.X.T., and Mitchell, B.S. (2013). Akt Activation Enhances Ribosomal RNA Synthesis through Casein Kinase II and TIF-IA. Proc. Natl. Acad. Sci. USA *110*, 20681–20686. https://doi.org/10.1073/pnas.1313097110.

79. Béguelin, W., Teater, M.R., Meydan, C., Phillip, J.M., and Melnick, A. (2019). EZH2 Gain-of-Function Mutations Generate a Lymphoma-Permissive Immune Niche. Blood *134*, 2768. https://doi.org/10.1182/blood-2019-132263.

80. Majer, C.R., Jin, L., Scott, M.P., Knutson, S.K., Kuntz, K.W., Keilhack, H., Smith, J.J., Moyer, M.P., Richon, V.M., Copeland, R.A., and Wigle, T.J. (2012). A687V EZH2 Is a Gain-of-Function Mutation Found in Lymphoma Patients. FEBS Lett. *586*, 3448–3451. https://doi.org/10.1016/j.febslet.2012.07.066.

81. Chu, L., Tan, D., Zhu, M., Qu, Y., Ma, X., Song, B.-L., and Qi, W. (2023). EZH2 W113C Is a Gain-of-Function Mutation in B-Cell Lymphoma Enabling Both PRC2 Methyltransferase Activation and Tazemetostat Resistance. J. Biol. Chem. *299*, 103073. https://doi.org/10.1016/j.jbc.2023.103073.

82. Deshaies, R.J., and Potts, P.R. (2025). Load and Lock: An Emerging Class of Therapeutics That Influence Macromolecular Dissociation. Science *389*, eadx3595. https://doi.org/10.1126/science.adx3595.

83. Madani, F., Lindberg, S., Langel, U., Futaki, S., and Gräslund, A. (2011). Mechanisms of Cellular Uptake of Cell-Penetrating Peptides. J. Biophys. *2011*, 414729. https://doi.org/10.1155/2011/414729.

84. Rezai, T., Yu, B., Millhauser, G.L., Jacobson, M.P., and Lokey, R.S. (2006). Testing the Conformational Hypothesis of Passive Membrane Permeability Using Synthetic Cyclic Peptide Diastereomers. J. Am. Chem. Soc. *128*, 2510–2511. https://doi.org/10.1021/ja0563455.

85. Erales, J., Marchand, V., Panthu, B., Gillot, S., Belin, S., Ghayad, S.E., Garcia, M., Laforêts, F., Marcel, V., Baudin-Baillieu, A., et al. (2017). Evidence for rRNA 2'-O-Methylation Plasticity: Control of Intrinsic Translational Capabilities of Human Ribosomes. Proc. Natl. Acad. Sci. USA *114*, 12934–12939. https://doi.org/10.1073/pnas.1707674114.

86. Ren, X., Hu, B., Song, M., Ding, Z., Dang, Y., Liu, Z., Zhang, W., Ji, Q., Ren, R., Ding, J., et al. (2019). Maintenance of Nucleolar Homeostasis by CBX4 Alleviates Senescence and Osteoarthritis. Cell Rep. *26*, 3643–3656.e7. https://doi.org/10.1016/j.celrep.2019.02.088.

87. Tessarz, P., Santos-Rosa, H., Robson, S.C., Sylvestersen, K.B., Nelson, C.J., Nielsen, M.L., and Kouzarides, T. (2014). Glutamine Methylation in Histone H2A Is an RNA-Polymerase-I-Dedicated Modification. Nature *505*, 564–568. https://doi.org/10.1038/nature12819.

88. Honda, M., Yogosawa, S., Kamada, M., Kamata, Y., Kimura, T., Koike, Y., Harada, T., Takahashi, H., Egawa, S., and Yoshida, K. (2017). A Novel Near-Infrared Fluorescent Protein, iRFP720, Facilitates Transcriptional Profiling of Prostate Cancer Bone Metastasis in Mice. Anticancer Res. *37*, 3009–3013.

89. Marchand, V., Blanloeil-Oillo, F., Helm, M., and Motorin, Y. (2016). Illumina-Based RiboMethSeq Approach for Mapping of 2'-O-Me Residues in RNA. Nucleic Acids Res. *44*, e135. https://doi.org/10.1093/nar/gkw547.

90. Jacobus, A.P., and Gross, J. (2015). Optimal Cloning of PCR Fragments by Homologous Recombination in Escherichia Coli. PLoS One *10*, e0119221. https://doi.org/10.1371/journal.pone.0119221.

91. Gerard, G.F., Collins, S., and Smith, M.D. (2002). Excess dNTPs Minimize RNA Hydrolysis during Reverse Transcription. Biotechniques *33*, 984–990. https://doi.org/10.2144/02335bm03.

92. Tang, D., Chen, M., Huang, X., Zhang, G., Zeng, L., Zhang, G., Wu, S., and Wang, Y. (2023). A Free Online Platform for Data Visualization and Graphing. PLoS One *18*, e0294236. https://doi.org/10.1371/journal.pone.0294236.

93. Ge, S.X., Jung, D., and Yao, R. (2020). A Graphical Gene-Set Enrichment Tool for Animals and Plants. Bioinformatics *36*, 2628–2629. https://doi.org/10.1093/bioinformatics/btz931.

94. Suzuki, K., Bose, P., Leong-Quong, R.Y., Fujita, D.J., and Riabowol, K. (2010). A Two Minute Cell Fractionation Method. BMC Res. Notes *3*, 294. https://doi.org/10.1186/1756-0500-3-294.

95. Liang, Y.M., Wang, X., Ramalingam, R., So, K.Y., Lam, Y.W., and Li, Z.F. (2012). Novel Nucleolar Isolation Method Reveals Rapid Response of Human Nucleolar Proteomes to Serum Stimulation. J. Proteomics *77*, 521–530. https://doi.org/10.1016/j.jprot.2012.09.031.

96. Sen Gupta, A., and Sengupta, K. (2017). Lamin B2 Modulates Nucleolar Morphology, Dynamics, and Function. Mol. Cell Biol. *37*, e00274-17. https://doi.org/10.1128/MCB.00274-17.

97. Ozawa, M., Hoschützky, H., Herrenknecht, K., and Kemler, R. (1990). A Possible New Adhesive Site in the Cell-Adhesion Molecule Uvomorulin. Mech. Dev. *33*, 49–56. https://doi.org/10.1016/0925-4773(90)90134-8.

## STAR★METHODS

### KEY RESOURCES TABLE

| REAGENT or RESOURCE | SOURCE | IDENTIFIER |
|---|---|---|
| Antibodies | | |
| Mouse monoclonal anti-FBL(IB, IFA) | Abcam | Cat#ab4566; RRID:AB_304523 |
| Rabbit polyclonal anti-FBL (IB, IFA) | Abcam | Cat#ab5821; RRID:AB_2105785 |
| Rabbit monoclonal anti-E-cadherin(IB) | Cell Signaling Technology | E-Cadherin (24E10) Rabbit mAb Cat#3195; RRID:AB_2291471 |
| Mouse monoclonal anti-E-cadherin(IB, IFA) | Abcam | Cat#ab1614(HECD-1); RRID:AB_300946 |
| Mouse monoclonal anti-E-cadherin(IB, IFA) | Abcam | Cat#ab11512 (DECMA-1); RRID:AB_298118 |
| Rabbit polyclonal Anti-ZO-1(IFA) | Abcam | Cat#ab59724, RRID:AB_946249 |
| Mouse monoclonal anti-GM130 (IFA) | BD Biosciences | Cat#35/GM130; RRID:AB_398141 |
| Mouse monoclonal anti-Scribble(IB) | SantaCruz | Cat#sc-55543; RRID:AB_2238926 |
| Rabbit monoclonal anti-Scribble(IB, IFA) | Cell Signaling Technology | Scribble Antibody #4475 |
| Mouse monoclonal anti-HSP70(IB) | Abcam | Cat#ab47455; RRID:AB_881520 |
| Mouse monoclonal anti-GAPDH(IB) | SantaCruz | Cat#sc-32233; RRID:AB_627679 |
| Rabbit polyclonal anti-GAPDH(IB) | Merck | Cat#G9545; RRID:AB_796208 |
| Rat monoclonal anti-Beta-tubulin(IB) | Abcam | Cat#[YOL1/34](ab6161); RRID:AB_305329 |
| Mouse monoclonal anti-Beta-tubulin(IB) | DHSB | Cat#E7; RRID:AB_528499 |
| Rabbit polyclonal anti-H3K27me3(IB, IFA) | Merck | Cat#07-449, RRID:AB_310624 |
| Rabbit polyclonal anti-H3(IB) | Abcam | Cat#ab1719; RRID:AB_302613 |
| Rabbit monoclonal anti-EZH2(IB, IFA) | Cell Signaling Technology | Ezh2 (D2C9) XP® Rabbit mAb Cat#5246; RRID:AB_10694683 |
| Rabbit polyclonal anti-EZH2(IB) | Merck | Cat#07-1562 |
| Rabbit polyclonal anti-Zeb1(IB) | Abcam | Cat#ab203829; RRID:AB_2921369 |
| Rabbit polyclonal anti-Vimentin(IB) | Abcam | Cat#ab92547 [EPR3776]; RRID:AB_10562134 |
| Rabbit polyclonal anti-Occludin(IB, IFA) | Abcam | Cat#ab216327 [EPR20992]; RRID:AB_2737295 |
| Rabbit monoclonal anti-pAkt(Ser473)(IB) | Cell Signaling Technology | Cat#9271; RRID:AB_329825 |
| Rabbit monoclonal anti-Akt(IB) | Cell Signaling Technology | Cat#9272; RRID: AB_329827 |
| Rabbit polyclonal anti-TAZ(IB) | Abcam | Cat#ab84927; RRID: AB_1925489 |
| Mouse monoclonal anti-Twist(IB) | Abcam | Cat#ab50887; RRID: AB_883294 |
| Rabbit polyclonal anti-Snail(IB) | Abcam | Cat#ab85931 |
| Rabbit monoclonal anti-Rab11(IFA) | Cell Signaling Technology | Cat#Rab11 (D4F5) XP® Rabbit mAb #5589; RRID: AB_10693925 |
| Mouse monoclonal anti-EEA-1(IFA) | BD Biosciences | Clone 14/EEA1 (RUO); RRID: AB_397830 |
| Mouse monoclonal anti-PTEN(IB) | BD Biosciences | Clone A2B1 (RUO); RRID: AB_1645437 |
| Goat anti-Mouse IgG (H + L) Cross-Adsorbed Secondary Antibody, Alexa Fluor™ 488 | Invitrogen | Cat#A-11029; RRID:AB_2534088 |
| Goat anti-Mouse IgG (H + L) Cross-Adsorbed Secondary Antibody, Alexa Fluor™ 568 | Invitrogen | Cat#A-11004; RRID:AB_2534072 |
| Goat anti-Rabbit IgG (H + L) Cross-Adsorbed Secondary Antibody, Alexa Fluor™ 488 | Invitrogen | Cat#A-11008; RRID: AB_143165 |

(*Continued on next page*)

*Continued*

| REAGENT or RESOURCE | SOURCE | IDENTIFIER |
|---|---|---|
| Goat anti-Rabbit IgG (H + L) Cross-Adsorbed Secondary Antibody, Alexa Fluor™ 568 | Invitrogen | Cat#A-11011; RRID: AB_143157 |
| Peroxidase AffiniPure® Goat Anti-Mouse IgG (H + L) | Jackson ImmunoResearch | Cat#115-035-003; RRID: AB_10015289 |
| Peroxidase AffiniPure® Goat Anti-Rabbit IgG (H + L) | Jackson ImmunoResearch | Cat#111-035-003; RRID: AB_2313567 |
| Goat anti-rat IgG H&L (HRP) | Abcam | Cat#ab97057; RRID: AB_10680316 |
| **Bacterial and virus strains** | | |
| *E.coli* DH5α | Lab generated | N/A |
| **Biological samples** | | |
| N/A | N/A | N/A |
| **Chemicals, peptides, and recombinant proteins** | | |
| Protease inhibitor cocktail complete EDTA-free | Roche | Cat#4693132001 |
| DynaBeads | Invitrogen | Cat#10002D |
| Streptavidin DynaBeads | Invitrogen | Cat#65801D |
| GSK-126 | MedChemExpress | Cat#HY-13470 |
| GSK-690693 | MedChemExpress | Cat#HY-10249 |
| Sodium Deoxycholate | SigmaAldrich | Cat#S1827 |
| Nonidet P-40 | SigmaAldrich | Cat#74385-1L |
| Tris free base | SigmaAldrich | Cat#T1503 |
| Glycine | Thermo Fisher Scientific | Cat#Q24755 |
| NaCl | SigmaAldrich | Cat#S7653 |
| HEPES | SigmaAldrich | Cat#H3375 |
| EDTA | SigmaAldrich | Cat#E9884 |
| DTT | SigmaAldrich | Cat#D0632 |
| Tween 20 | SigmaAldrich | Cat#P9416 |
| SDS | SigmaAldrich | Cat#L3771 |
| BSA | SigmaAldrich | Cat#A7906 |
| MgCl2 | SigmaAldrich | Cat#M1028 |
| DMEM-F12 | Invitrogen | Cat#11330-032 |
| EGF | Peprotech | Cat#AF-100-15 |
| Bovine Insulin | Sigma | Cat#I-1882 |
| Cholera toxin | Sigma | Cat#C-8052 |
| Hydrocortisone | Sigma | Cat#H-0888 |
| Horse Serum | Invitrogen | Cat#16050-122 |
| Pen/Strep | Invitrogen | Cat#15070-063 |
| RPMI-1640 | Invitrogen | Cat#31800-022 |
| Fetal Bovine Serum (Brazil oragin) | Invitrogen | Cat#10270106 |
| Texas Red® Conjugated Human Transferrin | Invitrogen | Cat#T2875; Lot# 1848488 |
| **Critical commercial assays** | | |
| PrimeScript™ 1st strand cDNA Synthesis Kit | Takara | 6110B |
| **Deposited data** | | |
| RNA-sequencing | This paper | GEO: GSE289801 |
| **Experimental models: Cell lines** | | |
| DLD-1 | ATCC | CCL-221 |
| MCF10A | ATCC | CRL-10317 |

(*Continued on next page*)

*Continued*

| REAGENT or RESOURCE | SOURCE | IDENTIFIER |
|---|---|---|
| MCF10A(p53DN) | This paper | N/A |
| A549(p53DN) | This paper | N/A |
| HCT116 | ATCC | CCL-247 |
| SW480 | ATCC | CCL-228 |
| HEK293T | ATCC | CRL-3216 |
| Experimental models: Organisms/strains | | |
| NOD-SCID male/female mice syngeneic | Animal House facility, IISER, Pune, India | N/A |
| Recombinant DNA | | |
| pLKOMCS-GFP | This paper | N/A |
| pLKOMCS-GFP-FBL(siRes) | This paper | N/A |
| pLKOMCS-GFP-ΔRBD FBL(siRes) | This paper | N/A |
| pBabe-SCRIB-Puro | This paper | N/A |
| pBABE-hygro p53 DD | Addgene | Addgene #9058 |
| Tet-pLKO-shFBL-puro | This paper | N/A |
| Tet-pLKO-shSCRIB-puro | This paper | N/A |
| MSCVhygro-F-Ezh2 | Addgene | Addgene #24926 |
| pCW57.1 F-EZH2; FBL-BioID2-HA pBabe-puro | This paper | N/A |
| MSCV Puro SCRIB P305L | This paper | N/A |
| MSCV Puro SCRIB C4S | This paper | N/A |
| MSCV Puro SCRIB C10S | This paper | N/A |
| Software and algorithms | | |
| Graphpad prism V.8.0 | N/A | https://www.graphstats.net/graphpad-prism |
| ImageJ | Schneider et al. | https://imagej.nih.gov/ij/ |
| Galaxy | The Galaxy Community | https://doi.org/10.1093/nar/gkae410 |
| T-scratch | Gebäck et al. (2018) | https://doi.org/10.2144/000113083 |
| Imaris | N/A | RRID:SCR_007370 |

## EXPERIMENTAL MODELS AND STUDY PARTICIPANT DETAILS

### Mice

*In vivo* experiments were carried out using NOD-SCID syngeneic male/female mice at the Animal House Facility of IISER Pune, India, with the approval of Institutional Animal Ethics Committee (IAEC) (IISER_Pune/IAEC/2022_01/01) and all experiments conform to IAEC guidelines. Mice aged six to eight weeks were selected, and their body weights were recorded prior to injections. Each mouse received a subcutaneous injection of ∼7 million DLD-1 cells into a single flank for tumorigenesis studies. On day 35 post-injection, the tumors were excised and processed for subsequent analyses. For tumor infiltration studies each mouse was injected with ∼1 million DLD-1 cells via tail vein injection. On day 60 post-injection, lungs were excised and processed for subsequent analyses.

### Cell lines

DLD-1 colorectal adenocarcinoma cells were maintained in RPMI-1640 supplemented with 10% FBS, L-glutamine, and antibiotics. MCF10A mammary epithelial cells were cultured in DMEM/F-12 with horse serum, EGF, hydrocortisone, cholera toxin, insulin, and antibiotics. HCT116, SW480, and A549 cells were grown in DMEM (Gibco, Brazil) with 10% FBS and antibiotics. All cultures were maintained at 37°C in a humidified incubator with 5% $CO_2$.

## METHOD DETAILS

### Cell culture and treatment

DLD-1 human colorectal adenocarcinoma cells were cultured in RPMI-1640 medium (Gibco) supplemented with 10% fetal bovine serum (FBS) (Invitrogen, 6140-079 Carlsbad, USA), 2 mM L-glutamine (Gibco), and 1% penicillin-streptomycin (100 U/mL penicillin and 100 μg/mL streptomycin), and maintained at 37°C in a humidified incubator with 5% $CO_2$. MCF10A human mammary epithelial cells were cultured in DMEM/F-12 (1:1) medium (Gibco, Thermo Fisher Scientific) supplemented with 5% horse serum

(Sigma-Aldrich), 20 ng/mL epidermal growth factor (EGF) (PeproTech), 0.5 μg/mL hydrocortisone (Sigma-Aldrich), 100 ng/mL cholera toxin (Sigma-Aldrich), 10 μg/mL insulin (Sigma-Aldrich), and 1% penicillin-streptomycin, and maintained under the same conditions. HCT116, SW480, and A549 cells were cultured in DMEM (Gibco, Brazil) supplemented with 10% FBS (Gibco, Brazil) and 1% penicillin-streptomycin, and maintained at 37°C in a humidified incubator with 5% $CO_2$.

### Generation of constructs

FBL CDS was available in the pEGFP-C1-Fibrillarin construct (gift from Sui Huang, Northwestern University). We created an siRNA-resistant GFP-FBL by mutating the seed sequence by PCR amplifying the pEGFP-C1-Fibrillarin construct with partially overlapping mutagenic primers, as described previously.[90] The PCR reaction was subjected to *DpnI* (20 units) digestion for digesting parental plasmid, at 37°C for 3h and was transformed into *E.coli* DH5α. Subsequently the colonies were screened using Sanger sequencing.

The mutated GFP-FBL (siRes) was PCR amplified with BamHI and SalI flanking sites. The PCR reaction was incubated with *DpnI* (20 units) at 37°C for 3h. The amplicon was gel purified using commercially available kits (Qiagen) and 1μg of the purified amplicon was double-digested with *BamHI*(10U) and *SalI*(10U) overnight, at 37°C. The reaction was terminated by heat inactivation at 65°C for 20 min. Subsequently, for ligation reaction, 5μL of the double-digested amplicon was incubated with 30ng of double-digested pLKO-MCS vector (Addgene #185594) and 350U of T4 DNA Ligase, overnight at 16°C. Ultimately, 4μL of the ligation mixture was transformed into *E.coli* DH5α and the colonies were screened using colony PCR and Sanger sequencing. Similarly, FBL(WT) was cloned into MCS-BioID2-HA pBabe-puro (Addgene #120308, gift from Kyle Roux, University of South Dakota) by PCR amplifying FBL from pEGFP-C1-Fibrillarin plasmid and was cloned using BamHI and EcoRI ends. For cloning, Flag-EZH2 into pCW57.1 N-term GFP tTA (Addgene #107551), Flag-EZH2 was amplified from MSCVhygro-F-Ezh2 plasmid (Addgene #24926) with primers flanking NheI and EcoRI sites and was used for digestion and ligation as mentioned previously. Colonies were screened using colony PCR and Sanger sequencing.

SCRIB CDS was obtained from RNA purified from DLD-1. 2μg of the extracted RNA was converted to cDNA using Invitrogen SuperScript II Reverse Transcriptase. The reaction was set up by incubating the following components in a nuclease-free microcentrifuge tube: 1 μL of Oligo(dT)12–18 (500 μg/mL), along with 2μg of total RNA. Then, 2 μL of dNTP Mix (10 mM each) and sterile, distilled water were added to a final volume of 12 μL. Since SCRIB CDS is 4.8kb long, using usual cDNA synthesis protocols would yield fragmented CDS instead of a complete stretch of SCRIB CDS, therefore/We added 4mM (Final concentration) of dNTP mix, as mentioned previously.[91] The mixture was heated to 65°C for 5 min and immediately chilled on ice. After a brief centrifugation, 4 μL of 5X First-Strand Buffer, 2 μL of 0.1 M DTT, and 1 μL of RNaseOUT (40 units/μL) were added. The contents of the tube were gently mixed. The mixture was incubated at 42°C for 2 min. Following this, 1 μL (200 units) of SuperScript II RT was added and mixed gently by pipetting, and the volume was adjusted to 20 μL with Nuclease Free Water. The reaction was incubated at 42°C for the first 40 min, temperature was gradually increased to 55°C for the last 10 min, followed by inactivation through heating at 70°C for 15 min. SCRIB CDS was PCR amplified with BamHI and EcoRI site flanking primers. The amplicon was purified from the gel using commercially available Qiagen kits. Next, 3 μg of the purified amplicon was subjected to double digestion with *BamHI* (20U) and *EcoRI* (20U) overnight at 37°C. Enzyme denaturation at 65°C for 20 min was used to terminate the reaction. For the ligation step, 5 μL of the double-digested amplicon was incubated overnight at 16°C with 30 ng of double-digested pBABE (Plasmid #21836) and 350 U of T4 DNA Ligase. Finally, 4 μL of the ligation mixture was transformed into *E.coli* DH5α, and the resulting colonies were screened using colony PCR and Sanger sequencing.

shSCRIB and shFBL sequences were synthesized as oligos were cloned into Tet-pLKO-puro vector (Addgene #21915). The shRNA oligos were designed and synthesized according to the siRNA sequence. Equimolar amounts of the sense and antisense oligonucleotides were then mixed for phosphorylating the 5′ ends of the oligos, using T4 PNK (10U) in a 10 μL reaction. The reaction was incubated at 37°C for 45 min, and subsequently exposed to 95°C for 5 min, and was gradually cooled to 25°C using step-down PCR. The above reaction conditions simultaneously achieved 5′ end phosphorylation and annealing of the oligonucleotides with overhangs compatible with the restriction sites in the vector. The Tet-pLKO-puro vector was prepared by digesting it with the appropriate restriction enzymes, *AgeI* and *EcoRI*, to linearize it and generate ends compatible with the annealed shRNA insert. The annealed shRNA inserts (5 μL from the PNK reaction) were then ligated into the digested pLKO-Tet-On vector (30ng) using T4 DNA ligase (350U), with the ligation reaction incubated at 16°C overnight. The ligation mixture was subsequently introduced into *E.coli* DH5α. Individual colonies were screened using *XhoI* digestion of extracted plasmid and Sanger sequencing.

FBL(WT) was cloned into MCS-BioID2-HA pBabe-puro (Addgene #120308, gift from Kyle Roux), FBL CDS was amplified from pEGFP-C1-Fibrillarin plasmid and was cloned using BamHI and EcoRI ends. Flag-EZH2 was cloned into pCW57.1 N-term GFP tTA (Addgene #107551) after amplifying the amplicon with NheI and EcoRI ends from the MSCVhygro-F-Ezh2 plasmid (Addgene #24926).

### siRNA-mediated knockdown

siRNA-mediated gene knockdown was carried out using siRNA oligonucleotides (AGGAGAACATGAAGCCGCAdTdT) obtained from Sigma and Dharmacon, USA. DLD-1 and MCF10A(p53DN) cells ($\sim 0.2 \times 10^6$) were seeded in six-well plates 24 h before transfection (till 50–60% confluency is attained). Transfection was performed using RNAiMax transfection reagent (Invitrogen, 13778) in Opti-MEM reduced serum medium (Gibco, 31985), with a final siRNA concentration of 75nM. After 6 h, the transfection medium was replaced with complete RPMI. MCF10A(p53DN) Cells were collected at 36 h and 72 h post-transfection for RNA extraction

or immunofluorescence, or western blot analysis. DLD-1 was incubated for 48- or 72-h post-transfection. siLacZ (CGUACGCGGAAUACUUCGAdTdT) was used as a negative control in RNA interference (RNAi) experiments.

### Generation and transduction of viral particles

Lentiviral transduction was performed by generating lentiviral particles through the co-transfection of HEK293T cells with Lentiviral transfer plasmid constructs, along with second-generation lentiviral packaging plasmids psPAX2 (Addgene #12260) and pMD2.G (Addgene plasmid #12259), in 4:3:1 ratio, with total 20μg DNA being transfected, in a 65% confluent 100 mm dish. Seventy-two hours post-transfection, the viral supernatant was harvested, mixed with Polybrene (12 μg/mL) and used to transduce DLD-1 and MCF10A(p53DN) cells, followed by selection with Puromycin (4 μg/mL, Invitrogen, A1113802) or FACS sorting for fluorophore-tagged cells. To verify the expression of the transduced gene, RT-PCR or immunoblotting was performed. FBL and SCRIB depletion was induced with 1200 ng/mL and 1000 ng/mL Dox, respectively, for 48 h, a condition consistently applied across experiments unless specified otherwise.

Retroviral transduction was carried out by generating retroviral particles through the co-transfection of HEK293T cells with retroviral transfer plasmid constructs, in combination with second-generation lentiviral packaging plasmids pBS-CMV-gagpol (Addgene #35614) and pCAG-VSVG (Addgene #35616), in 4:3:1 ratio, with total 20μg DNA being transfected, in a 65% confluent 100mm dish. Seventy-two hours post-transfection, the viral supernatant was collected, mixed with Polybrene (10 μg/mL) and subsequently used to transduce DLD-1 and MCF10A(p53DN) cells, followed by selection with Puromycin (4 μg/mL, Invitrogen, A1113802) or Hygromycin (50 μg/mL, Invitrogen, 10687010). To confirm the expression of the transduced gene, RT-PCR or immunoblotting was performed.

### RNA sequencing

DLD-1 cells (∼0.6 million) were transfected and incubated for ∼72h. Isolation of total RNA from cells was performed by using a commercially available kit (Qiagen). Library preparation was carried out using the NEBNext Ultra II Directional RNA Library Preparation Kit, following the manufacturer's instructions. Paired-end reads of 51 bp were generated on the Illumina platform. RNA-Seq data submission GEO accession number: GSE289801.

*Data Analyses*: Quality control and preprocessing of raw sequencing reads involved filtering based on quality scores and adapter trimming using FastQC and Trimmomatic, respectively. The processed reads were aligned to the *Homo sapiens* GRCh38 reference genome using the splice-aware aligner HISAT2 on the Galaxy platform. Transcript assembly was performed using StringTie, which also quantified read counts and normalized gene expression levels using the Fragments Per Kilobase of transcript per Million mapped reads (FPKM) metric. Differential expression analysis was conducted with DESeq2, where raw read counts served as input. Genes with a $p$-value below 0.05 were considered significantly differentially expressed between the control and FBL knockdown conditions in DLD-1 cells. Upregulated genes were defined as those with a $\log_2FC > 1$, while downregulated genes had a $\log_2FC < -10$.

To identify differentially regulated pathways, gene ontology and pathway enrichment analyses were performed using Gene Set Enrichment Analysis (GSEA) on the GSEA desktop application, and key enriched gene sets were visualized through enrichment plots. The Gene Ratio corresponds to the Normalized Enrichment Score (NES) obtained from GSEA. Enrichment results are presented as the NES in GSEA. A false discovery rate (FDR) threshold of 0.05 was applied to ensure the inclusion of significantly enriched gene sets. Further details on RNA sequencing analysis are provided in key resources table. The GO (Gene Ontology) analysis of enriched Cellular components, Molecular functions, and Pathway network were performed on SR Plot[92] and ShinyGO,[93] respectively, with FDR = 0.05.

### ChIP PCR

#### *Chromatin crosslinking and cell lysis*

Cells were cultured to approximately 80% confluency and crosslinked with 1% formaldehyde for 10 min at room temperature to preserve protein-DNA interactions. The reaction was quenched by adding glycine to a final concentration of 0.125 M, followed by a 5-min incubation at room temperature. Cells were subsequently washed twice with ice-cold phosphate-buffered saline (PBS, pH 7.4), harvested by scraping, and collected by centrifugation at 1,000 × g for 5 min at 4°C. The supernatant was discarded, and the cell pellet was resuspended in lysis buffer supplemented with protease inhibitors and incubated on ice for 10 min to facilitate nuclear extraction.

### Chromatin fragmentation

Chromatin was sheared by sonication to generate DNA fragments ranging from 200 to 1000 bp. Chromatin shearing was performed using a Covaris focused ultrasonicator. DLD-1 cell lysates were prepared in 130 μL of lysis buffer and transferred to Covaris microTUBEs. Sonication was carried out at 6°C–7°C to prevent overheating. For Covaris M220, samples were processed at 75 W peak incident power, 60% duty factor, and 200 cycles per burst for 30 min, 30 s on 30 s off. Following sonication, samples were centrifuged at 16,000g for 10 min at 4°C, and the supernatant was collected for downstream ChIP assays. Chromatin fragmentation was assessed by agarose gel electrophoresis to confirm a fragment size range of 100–500 bp, and conditions were adjusted as necessary to achieve optimal shearing efficiency.

For MCF10A(p53DN), chromatin was sheared using a Covaris M220 focused ultrasonicator. 130 μL of cell lysate was put in Covaris microTUBEs. Sonication was performed at 75 W peak incident power, 60% duty factor, and 200 cycles per burst for 25 min, 30 s on 30 s off. The sample temperature was maintained at 6°C–7°C using a chiller. Following sonication, samples were centrifuged at

16,000g for 10 min at 4°C, and the supernatant was collected for further processing. DNA fragment size (100–500 bp) was assessed by agarose gel electrophoresis. The extent of shearing was assessed by agarose gel electrophoresis.

### Immunoprecipitation

Sheared chromatin was pre-cleared by incubation with protein A/G Dynabeads for 1 h at 4°C with continuous rotation to reduce nonspecific binding. The pre-cleared chromatin was then incubated overnight at 4°C with an antibody specific to the target protein - 2μg for Histones and 5μg for EZH2, while an IgG control at similar quantities to that of specific antibodies was included to assess nonspecific interactions. The following day, protein A/G Dynabeads were added to captured immune complexes, followed by an additional 1–2 h of incubation at 4°C with rotation. Immunoprecipitates were sequentially washed with low-salt wash buffer (0.1% SDS, 1% Triton X-100, 2 mM EDTA (pH 8.0), 20 mM Tris-HCl (pH 8.0), 150 mM NaCl), high-salt wash buffer (0.1% SDS, 1% Triton X-100, 2 mM EDTA (pH 8.0), 20 mM Tris-HCl (pH 8.0), 500 mM NaCl), LiCl wash buffer (0.25 M LiCl, 1% NP-40, 1% sodium deoxycholate, 1 mM EDTA (pH 8.0), 10 mM Tris-HCl (pH 8.0)), and TE buffer (pH 8.0) to eliminate nonspecific binding.

### Reverse crosslinking and DNA purification

Chromatin complexes were eluted using an elution buffer containing 1% sodium dodecyl sulfate (SDS) and proteinase K (200 μg/mL), followed by incubation at 65°C for 4–6 h to reverse crosslinking. DNA was purified using phenol-chloroform extraction or a commercially available DNA purification kit (Qiagen), followed by ethanol precipitation. The resulting DNA was resuspended in nuclease-free water and stored at −20°C for subsequent analysis.

### PCR amplification and analysis

Purified ChIP-derived DNA (5ng) was subjected to PCR to amplify target genomic regions using specific primer pairs. PCR reactions were performed in a total volume of 10 μL containing template DNA, 2XTB Green Taq DNA polymerase mix (Takara), and gene-specific primers (0.3μM). Thermal cycling parameters were optimized for each target sequence. PCR products were resolved by agarose gel electrophoresis, stained with a nucleic acid dye, and visualized using a gel imaging system. Input DNA, representing a fraction of total chromatin before immunoprecipitation, and IgG controls were included to confirm the enrichment specificity.

### BioID2 ChIP PCR

Cells (~4 million) constitutively expressing FBL(WT)-BirA* and EV were seeded on 100mm dishes and incubated with 50μM Biotin (for at least 16h) before being treated with siLacZ (Control) and siFBL with a final concentration of 75 nM. Cells were harvested 36h after siRNA transfection and were subjected to crosslinking with 1% formaldehyde for 10 min at room temperature to preserve protein-DNA interactions. The crosslinking reaction was terminated by the addition of glycine to a final concentration of 0.125M, followed by incubation at room temperature for 5 min. Cells were subsequently washed twice with ice-cold phosphate-buffered saline (PBS, pH 7.4), detached from the culture surface by scraping, and collected by centrifugation at 1,000 × g for 5 min at 4°C. The resulting cell pellet was resuspended in lysis buffer (50 mM HEPES-KOH pH 7.5, 140 mM NaCl, 1 mM EDTA (pH 8), 1% Triton X-100, 0.1% Sodium Deoxycholate, 0.1% SDS) supplemented with protease inhibitors and incubated on ice for 10 min to facilitate nuclear extraction. To achieve chromatin fragmentation, sonication was performed under optimized conditions to generate DNA fragments within the range of 200–600 bp while maintaining protein-DNA interactions. The efficiency of chromatin shearing was assessed by agarose gel electrophoresis. Fragmented chromatin was incubated with Streptavidin Dynabeads(100μL) at 4°C overnight with continuous rotation to minimize nonspecific binding.

The Dynabeads were isolated using a magnetic stand and subjected to sequential washes. Initially, they were washed twice with a 2% (wt/vol) SDS solution. This was followed by a wash with a buffer containing 0.1% deoxycholate, 1% Triton X-100, 500 mM NaCl, 1 mM EDTA, and 50 mM 4-(2-hydroxyethyl)-1-piperazineethanesulfonic acid (HEPES) at pH 7.5. Subsequently, precipitates were subjected to sequential washes using low-salt wash buffer (0.1% SDS, 1% Triton X-100, 2 mM EDTA (pH 8.0), 20 mM Tris-HCl (pH 8.0), 150 mM NaCl), high-salt wash buffer (0.1% SDS, 1% Triton X-100, 2 mM EDTA (pH 8.0), 20 mM Tris-HCl (pH 8.0), 500 mM NaCl), LiCl wash buffer (0.25 M LiCl, 1% NP-40, 1% sodium deoxycholate, 1 mM EDTA (pH 8.0), 10 mM Tris-HCl (pH 8.0)), and TE buffer (pH 8.0) to eliminate nonspecific binding. Precipitated chromatin was eluted using a buffer containing sodium dodecyl sulfate (SDS) and proteinase K, followed by incubation at 65°C for 4–6 h to reverse protein-DNA crosslinking. DNA was then extracted using a commercial purification kit (Qiagen). The purified DNA was resuspended in nuclease-free water and stored at −20°C for subsequent analysis.

To assess target DNA enrichment, PCR amplification was performed using ChIP-derived DNA (5ng) as a template. Each PCR reaction was conducted in a final volume of 10 μL containing template DNA, 2X TB Green Taq DNA polymerase mix (Takara), and gene-specific primers (0.3μM). PCR conditions were optimized based on the target sequence requirements. Amplified products were resolved by agarose gel electrophoresis, stained with a nucleic acid dye, and visualized using an imaging system. To confirm specificity, input DNA, representing total chromatin prior to immunoprecipitation, was included as an experimental control.

### Immunofluorescence assay

0.2 million cells were cultured on 22 mm × 22 mm coverslips. Cells were subjected to two washes with 1× phosphate-buffered saline (PBS) (pH 7.4) for 5 min each and then fixed using 4% paraformaldehyde (PFA) in 1× PBS (pH 7.4) or for nuclear antigens cells were

pre-permeabilized with CSK buffer (100 mM NaCl, 300 mM Sucrose, 3 mM $MgCl_2$, 10 mM PIPES(pH 7.4), 0.5% Triton X-100) for 4mins on ice prior to PFA fixation. Cells were permeabilized with 0.5% Triton X-100 in PBS for 10 min and blocked with 1% Bovine Serum Albumin (BSA) for 30 min to reduce non-specific binding. The cells were incubated with primary antibodies for 2 h, followed by incubation with secondary antibodies for 60 min. Cells were counterstained with DAPI (0.05 μg/mL solution of 4′,6-diamidino-2-phenylindole (DAPI)) for 2 min at RT, followed by washes with 1X PBS. The cells were mounted using SlowFade Gold Antifade and stored at 4°C. For imaging, Zeiss LSM 710 and Zeiss LSM 780 confocal microscopes (Carl Zeiss, Thornwood, NJ, USA) were utilized, both equipped with a 63× Plan-Apochromat 1.4 NA oil immersion objective. Images were acquired using a zoom factor of 1.0–2.0, with a voxel size of 0.07 μm × 0.07 μm × 0.34μm and a frame resolution of 1912 × 1912 pixels, recorded at a pixel depth of 8-bit per channel. Line averaging was set to 4.0, and imaging was conducted in three/four-channel sequential mode.

## Western blotting

Cell lysates were extracted utilizing Radio Immuno-Precipitation Assay (RIPA) Buffer and protein concentration was estimated with the Bicinchoninic Acid (BCA) Kit (Pierce, 23225). Subsequently, the samples were denatured by heating in 5× Laemmli Buffer before their separation on either a 12.5% or 15% acrylamide-bisacrylamide gel. Following electrophoresis, proteins were transferred onto a pre-activated polyvinylidene difluoride (PVDF) membrane at a constant voltage of 80 V for 180 min. The membrane was then subjected to blocking with 5% non-fat dried milk powder dissolved in 1× Tris-Buffered Saline with Tween 20 (0.1% v/v) (1× TBST). Primary and secondary antibodies were diluted in 0.5% milk in 1× TBST for 120 min and 60 min, respectively. The visualization of protein bands was accomplished using a chemiluminescent substrate (BioRad, Clarity Western ECL Substrate, Cat. no.1705061), with images captured at 10-s incremental exposures using the LAS4000 chemiluminescence system (GE). For molecular weight estimation, Precision Plus Protein Dual Color Standards (250–10kDa, Biorad, Cat. No. 161–0374) were utilized as molecular weight markers. Antibodies have been mentioned in the Supplementary Table.

## Cell fractionation

### *Cytoplasmic and nuclear fraction isolation*

Cytoplasmic and nuclear fractions had been prepared from 10 million cells. The cells were first rinsed with ice-cold phosphate-buffered saline (PBS) adjusted to pH 7.4. They were then detached on ice using a plastic cell scraper and collected into 1.5 mL microcentrifuge tubes containing 1 mL of ice-cold PBS. Brief centrifugation was performed for 10 s at 7500 rpm, after which the supernatant was discarded. The resulting cell pellets were resuspended in 900 μL of ice-cold 0.1% NP-40 in PBS and subjected to five rounds of mixing using a P1000 micropipette. From this lysate, 300 μL had been set aside as the "whole cell lysate". This fraction was mixed with 100μL of 5× Laemmli sample buffer and maintained on ice until sonication. The remaining 600μL was centrifuged for an additional 10 s, allowing for the collection of 300μL of the supernatant as the "cytosolic fraction," which was then combined with 100μL of 5× Laemmli sample buffer and boiled for 1 min. The remaining supernatant was discarded, and the pellet was resuspended in 1 mL of ice-cold 0.1% NP-40 in PBS. Following another centrifugation for 10 s, the supernatant was removed, and the final pellet, approximately 20 μL in volume, was resuspended in 180μL of 1× Laemmli sample buffer, designating this as the "nuclear fraction". Both the nuclear fractions and whole cell lysates containing DNA subsequently underwent sonication using microprobes set to level 2 for two cycles of 5 s each, followed by boiling for an additional minute. Finally, 10μL of whole cell lysate, 10μL of the cytoplasmic fraction, and 5μL of the nuclear fraction were loaded onto an SDS-PAGE gel for electrophoresis and were then transferred onto nitrocellulose membranes for further analysis.[94]

Nucleolar fraction isolation- Nucleolar isolation was performed as mentioned previously [4]. DLD-1 and MCF10A(p53DN) cells (~$10^7$) were thoroughly rinsed and harvested using an ice-cold solution composed of 0.5 mL of 0.5 M sucrose, 3 mM magnesium chloride ($MgCl_2$), and a 1× protease inhibitor cocktail (PIC). The collected cells were subjected to sonication on ice with a Sonics Vibracell, utilizing a protocol of five cycles, each consisting of 10 s of sonication followed by 10 s of rest, set at 50% amplitude. Following sonication, the resulting cell lysate was carefully layered onto 0.7 mL of Solution II, which contained 1.0 M sucrose and 3 mM $MgCl_2$ and was subsequently centrifuged at 1,800 × g for 5 min at 4°C. The supernatant was meticulously removed, and the resulting nucleolar pellet was then resuspended in RIPA buffer for immunoblotting.[95,96]

## Proteinase K protection assay

Proteinase K protection assays were performed to assess the internalization of E-cadherin. DLD-1 cells were transfected with siLacZ (control) or siFBL for ~48 h. Cells were washed twice with ice-cold 1XHBS and incubated on ice with Proteinase K (100 μg/mL, final concentration) in 1XHBS containing 1 mM $CaCl_2$ for 30 min. Triton X-100 (0.5% final concentration) was added to the mentioned wells to permeabilize cells for Proteinase K. Lysates were cleared by centrifugation (14,000 × g, 10 min, 4°C), and equal amounts of protein were subjected to SDS–PAGE followed by immunoblotting for E-cadherin.

To enhance specificity toward the extracellular domain of E-cadherin, we optimized the protocol by using Rat anti-E-cadherin (DECMA-1) monoclonal antibody (during immunoblotting), which binds specifically to the extracellular domain of E-cadherin.[97]

## Transferrin uptake assay

~0.2 million DLD-1 cells were seeded on a coverslip and transfected with siLacZ and siFBL for ~48h. Subsequently, cells were incubated with 50 μg/mL Texas Red-conjugated transferrin (Invitrogen) for 10, 20, and 30 min. For the negative control, siLacZ and siFBL

transfected cells were incubated at 4°C for 30 min. Following incubation with Texas Red-conjugated transferrin, unbound transferrin was removed by thorough acid wash (3X, 2 min each). Cells were fixed with 4% formaldehyde and further processed for confocal imaging after counterstaining with DAPI.

### Scratch wound

Cells were cultured in Roswell Park Memorial Institute (RPMI) 1640 and Dulbecco's Modified Eagle Medium-F12 (DMEM-F12) following transfection with small interfering RNA (siRNA) or subsequent drug treatment. Twelve hours post-transfection, cells were reseeded in 24-well tissue culture plates at a density optimal for establishing a confluent monolayer. After another 12-h incubation, a sterile 200 μL pipette tip was utilized to meticulously create a linear scratch in the center of each well, ensuring the tip was held perpendicular to the substrate. Detached cells were then removed by gently washing the wells twice with phosphate-buffered saline (PBS), after which fresh medium was added. The assay was conducted using 0.5% serum-supplemented RPMI for DLD-1 cells and DMEM-F12 without epidermal growth factor (EGF), and Assay media for MCF10A(p53DN) cells. Following this, the cells were incubated for 48 h, or a modified duration as warranted by the specific cell type being examined. Imaging was carried out under consistent microscopic parameters, with the extent of wound closure or gap distance quantified for further analysis. The formula for measuring wound healing percentage used was-

Wound Closure % = (Initial Wound Area- Current Wound Area) $\times$100.

Where:

Initial Wound Area = the area of the wound at the beginning of observation ($\mu m^2$). Current Wound Area = the area of the wound at a later time (after treatment).

Wound Closure% represents the percentage of wound healing.

### Invasion assay

To assess cell migration, $5X10^4$ cells per well were seeded in the upper chambers of Transwell inserts without a Matrigel coating, using serum-free media. The lower chamber contained 0.6 mL of RPMI or DMEM-F12 with 10% FBS or 5% Horse serum, acting as a chemoattractant. The plate was then incubated at 37°C for 36h hours (after transfection) to allow cell movement. After the incubation period, cells that had traversed to the lower membrane surface were fixed using 4% formaldehyde, and the nuclei were stained using DAPI.

### Image analysis

#### *Colocalization analysis*

Colocalization analysis was performed using the Coloc module in Imaris (Bitplane, Oxford Instruments). Image datasets were imported into Imaris, and individual fluorescence channels were assigned to their respective markers. For analyses restricted to specific subcellular regions, a three-dimensional region of interest (ROI) was defined using the Surpass ROI tool. Colocalization between the two channels of interest was quantified using the Coloc wizard. Intensity thresholds for each channel were determined either automatically using the Costes method or set manually to exclude background signal. Voxels exceeding both thresholds were defined as colocalized, and a colocalization channel mask was generated for visualization. Quantitative colocalization metrics, including Pearson's correlation coefficient (PCC), Manders' overlap coefficients (M1 and M2), colocalized volume, and total number of colocalized voxels, were computed by the software. The resulting colocalization masks were rendered in 3D for qualitative assessment, and numerical data were exported for statistical analysis.

### Segmentation analysis

Segmentation of fluorescence images was performed using the Surfaces module in Imaris. Image datasets were imported into Imaris, and each fluorescence channel was assigned to its corresponding marker. Segmentation was conducted on the channel of interest using either automatic thresholding based on the absolute intensity values or manual adjustment to exclude background signal. A surface creation wizard was used to generate 3D reconstructions, with background subtraction applied to improve object separation. Where necessary, smoothing filters were applied to reduce noise, and the "Split Touching Objects" function was used to separate adjacent structures. The minimum object size was defined to exclude spurious detections. For each segmented object, quantitative parameters including volume, surface area, mean fluorescence intensity, and total voxel count were computed. Segmented surfaces were rendered in 3D for qualitative visualization, and all statistical outputs were exported for further analysis.

### Subcutaneous xenograft assay in NOD-SCID mice

To assess the tumorigenic impact of Fibrillarin (FBL) depletion, subcutaneous xenografts were established in NOD-SCID mice (NOD.CB17-Prkdc$^{scid/NcrCrl}$). All procedures were performed in accordance with institutional ethical guidelines and approved by the Institutional Animal Ethics Committee (IAEC).

DLD-1 cells stably expressing shFBL under a Tet-ON promoter were harvested at ~70–80% confluency, washed with sterile 1X PBS, and resuspended in a 1:1 mixture of 1X PBS at $1 \times 10^7$ cells/mL. A total of $\sim 7 \times 10^6$ cells (100 μL) were injected subcutaneously into the right flank of each mouse using a 26-gauge syringe. FBL knockdown was induced by administering doxycycline (2 mg/mL in drinking water supplemented with 5% sucrose), with water bottles changed every 72 h. Control mice received sucrose water without

doxycycline. Mice were monitored biweekly for tumor growth and general health. The formula for calculating the tumor size is given below-

$$V = (L \times W^2) / 2$$

V = Tumor volume (in cubic millimeters, $mm^3$).
L = Tumor length (the longest dimension of the tumor measured with calipers).
W = Tumor width (the shortest dimension perpendicular to the length).

### Tail vein injection assay

To evaluate the metastatic potential of FBL-depleted cells, experimental lung colonization assays were performed by tail vein injection in NOD-SCID mice. Briefly, DLD-1 cells stably expressing Tet-ON–inducible shFBL were harvested at ~70–80% confluency, washed with sterile PBS, and resuspended at a density of $1 \times 10^7$ cells/mL in ice-cold PBS. A total of $1 \times 10^6$ cells (100 μL) were injected into the lateral tail vein of each mouse using a 29-gauge insulin syringe under brief isoflurane anesthesia. FBL knockdown was induced by doxycycline administration (2 mg/mL in 5% sucrose water, replaced every 72 h), while control animals received sucrose water alone. Mice were monitored for health and body weight throughout the study. After 6–8 weeks, lungs were harvested, fixed in 10% neutral-buffered formalin, paraffin-embedded, and subjected to H&E staining for histological assessment of metastatic burden.

### Hematoxylin and eosin (H&E) staining of paraffin-embedded lung and tumor tissues

Formalin-fixed, paraffin-embedded (FFPE) lung and subcutaneous tumor tissues from NOD-SCID mice were subjected to standard H&E staining to assess tissue morphology and metastatic infiltration. Briefly, tissues were fixed in 10% neutral-buffered formalin (24–48 h, room temperature), dehydrated through graded ethanol, cleared in xylene, and embedded in paraffin. Sections (4–5 μm) were cut using a rotary microtome, floated on a 42°C water bath, mounted on charged slides, and baked at 60°C for 1 h.

For staining, slides were deparaffinized in xylene, rehydrated through graded ethanol, and rinsed in water. Nuclei were stained with Harris or Mayer's hematoxylin (4–5 min), differentiated in 0.3% acid alcohol, blued in 0.1% ammonia water, and rinsed. Cytoplasmic and extracellular components were counterstained with eosin Y (0.5–1%, 1–2 min). Sections were dehydrated through ascending ethanol, cleared in xylene, and mounted with a permanent medium (DPX). Stained slides were imaged under a brightfield microscope.

## QUANTIFICATION AND STATISTICAL ANALYSIS

Statistical significance was assessed using an unpaired Student's *t* test, performed in GraphPad Prism version 8.0. Data are presented as mean ± SE with error bars, and a *p* value $\leq 0.05$ was considered statistically significant. Details of the statistical tests, sample sizes, number of replicates, and definition of error bars are provided in the figure legends.

frontiers | Frontiers in Cell and Developmental Biology

TYPE Review
PUBLISHED 16 December 2022
DOI 10.3389/fcell.2022.1068347



OPEN ACCESS

EDITED BY
Eric C. Schirmer,
University of Edinburgh,
United Kingdom

REVIEWED BY
Susana Gonzalo-Hervas,
Saint Louis University, United States
Fred Dick,
Western University, Canada
Jop Kind,
Hubrecht Institute (KNAW), Netherlands

*CORRESPONDENCE
Kundan Sengupta,
kunsen@iiserpune.ac.in

†These authors have contributed equally to this work

SPECIALTY SECTION
This article was submitted to Nuclear Organization and Dynamics, a section of the journal Frontiers in Cell and Developmental Biology

RECEIVED 12 October 2022
ACCEPTED 05 December 2022
PUBLISHED 16 December 2022

CITATION
Balaji AK, Saha S, Deshpande S, Poola D and Sengupta K (2022), Nuclear envelope, chromatin organizers, histones, and DNA: The many achilles heels exploited across cancers. *Front. Cell Dev. Biol.* 10:1068347. doi: 10.3389/fcell.2022.1068347



# Nuclear envelope, chromatin organizers, histones, and DNA: The many achilles heels exploited across cancers

A. K. Balaji†, Santam Saha†, Shruti Deshpande†, Darshini Poola and Kundan Sengupta*

Chromosome Biology Lab (CBL), Indian Institute of Science Education and Research, Pune, Maharashtra, India

In eukaryotic cells, the genome is organized in the form of chromatin composed of DNA and histones that organize and regulate gene expression. The dysregulation of chromatin remodeling, including the aberrant incorporation of histone variants and their consequent post-translational modifications, is prevalent across cancers. Additionally, nuclear envelope proteins are often deregulated in cancers, which impacts the 3D organization of the genome. Altered nuclear morphology, genome organization, and gene expression are defining features of cancers. With advances in single-cell sequencing, imaging technologies, and high-end data mining approaches, we are now at the forefront of designing appropriate small molecules to selectively inhibit the growth and proliferation of cancer cells in a genome- and epigenome-specific manner. Here, we review recent advances and the emerging significance of aberrations in nuclear envelope proteins, histone variants, and oncohistones in deregulating chromatin organization and gene expression in oncogenesis.

KEYWORDS

**lamins, heterochromatin, genome organization, nuclear envelope, oncohistones, histone variants**

## 1 Introduction

Each chromosome occupies a unique sub-volume in the interphase nucleus, referred to as a chromosome territory (Cremer and Cremer, 2001). A chromosome territory encompasses intra- and inter-chromatin interactions, further fine-tuned by histone modifications. Analyses of chromatin interactions have revealed the organization of chromatin into two distinct compartments—A and B. Compartment A is composed of gene-rich, open chromatin localized toward the nuclear interior. In contrast, compartment B is gene-poor, has a compact conformation, and is localized toward the nuclear periphery. Closer inspection using variants of chromosome conformation capture assays, such as 3C, 4C, and Hi-C, reveals that the 3D genome architecture of a nucleus is intricately organized into Topologically Associating Domains (TADs), where

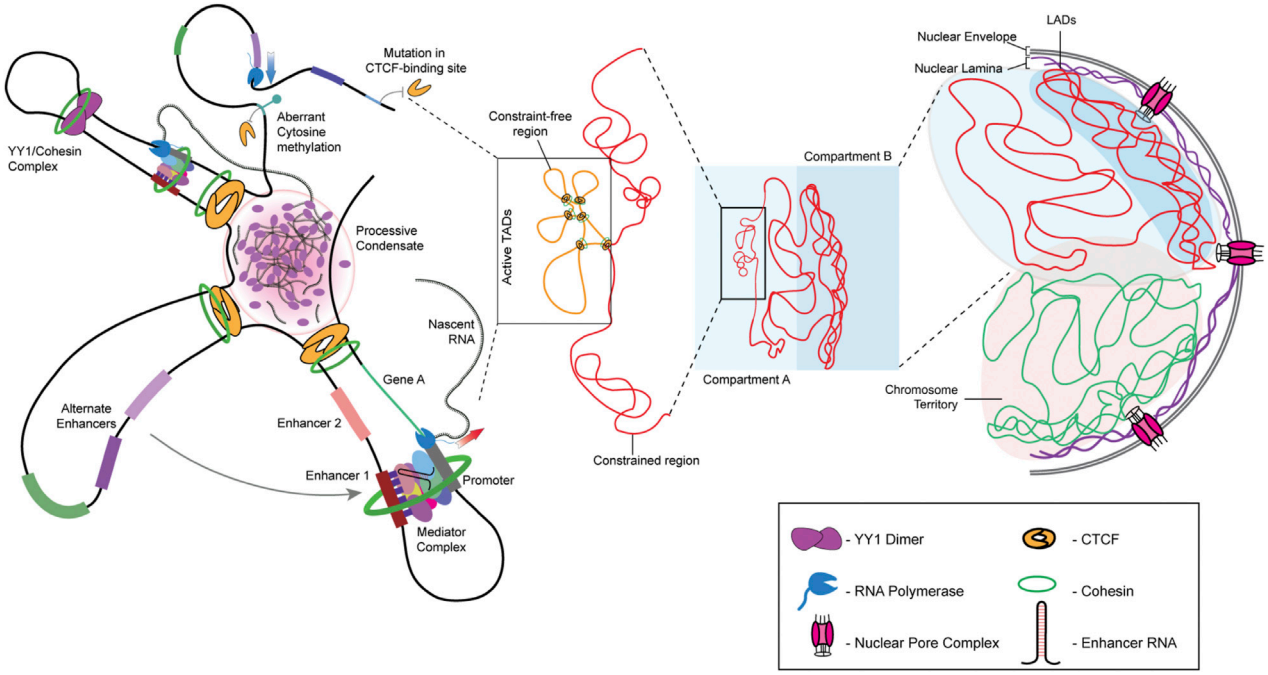


FIGURE 1
Hierarchy of genome organization. The involvement of lamins facilitates LAD organization at the nuclear periphery. Lamins organize the transcriptionally inactive B compartment of the TADs proximal to the nuclear envelope, while the transcriptionally active A compartment is maintained relatively toward the nuclear interior. The promoter-enhancer contacts are maintained by genome organizers such as cohesin, condensin, and CTCF. The presence of multiple such contacts within a TAD allows the formation of splicing condensates.

stretches of chromatin physically interact in a regulated manner to modulate gene expression within the TAD (Figure 1) (Szabo et al., 2019). The loop extrusion model of chromatin organization forms the basis of TAD-mediated genome organization, where chromatin loops are extruded by chromatin organizers and cohesin complexes and are delimited by CCCTC-binding factor (CTCF), another chromatin organizer (Fudenberg et al., 2016; Nuebler et al., 2018). TADs organize looping-in of sequences ~1 Mb (in mammals) apart within close proximity, enabling enhancer-promoter contacts for the spatiotemporal regulation of gene expression (Chetverina et al., 2017). Interestingly, chromatin stretches with the same type of histone modifications show a propensity to interact and compartmentalize in the 3D space of the nucleus, thus revealing CTCF-cohesin-independent chromatin folding mechanisms. For instance, H3K27me3 histone modifications function as a signal for long-range chromatin interactions during hematopoietic stem cell differentiation (Zhang X et al., 2020). Notably, in addition to CTCF, genome organizers such as cohesin and condensin are required for the recruitment of transcription cofactors. Cohesin and CTCF function as boundary elements that collectively maintain genome architecture, which is prudently rigid and guardedly dynamic (Phillips-Cremins et al., 2013). Furthermore, chromatin remodelers alter local chromatin dynamics in response to cell signaling events. The maintenance of TADs is critical since disruption of TAD organization is associated with developmental diseases and cancers (Lupiáñez et al., 2015; Akdemir et al., 2020). In cancers, the aberrant activation of cell signaling pathways relays erratic signals to the nucleus, which alters chromatin organization and transcriptional outputs of the cell. It remains to be examined how chromatin and its organizers respond to aberrant oncogenic signaling in cancer cells.

The double-membraned nucleus functions as the primary protector of the genome. In metazoans, the nucleus not only harbors the genome but also works in tandem with the differentially-compacted chromatin to regulate its tissue-specific spatial and functional organization. The nuclear envelope comprises the nuclear lamina that maintains nuclear integrity and regulates gene expression and is interspersed with Nuclear Pore Complexes (NPCs), whose primary function is to regulate nuclear transport (Lin et al., 2018). Though the chromatin in contact with the nuclear lamina is frequently repressed, NPCs additionally contribute to the regulation of gene expression. Furthermore, owing to the role of NPCs in chromatin organization and function, Nucleoporins (Nups), the class of proteins that comprise the NPC, are also involved in

regulating stemness and cell fate determination (D'Angelo et al., 2012). Interestingly, nucleoporins crosstalk with the chromatin organizer CTCF, which functions as a boundary element between TADs, while facilitating intra-TAD interaction. For instance, the nucleoporins Nup153 and Nup93, along with CTCF, regulate the transcriptional activity of the HOX gene cluster during early development and differentiation (Kadota et al., 2020; Labade et al., 2021).

In metazoans, type V intermediate filament proteins, the lamins, maintain the structural and functional integrity of the nucleus (Aebi et al., 1986; Gruenbaum and Foisner, 2015). The nuclear lamina is predominantly composed of two lamin sub-types—the A-type lamins that include lamins A and C (a spliced variant of lamin A), and the B-type lamins that comprise separately-encoded lamins B1 and B2 (in vertebrates). Each lamin sub-type harbors post-translational modifications (PTMs), exponentially increasing the functional diversity of lamins. Nuclear lamins regulate replication-dependent cell cycle progression, DNA damage repair, genome stability, and 3D organization of the genome (Moir et al., 2000; Bronshtein et al., 2015; Earle et al., 2020). Nuclear lamina interacts with stretches of chromatin that are in proximity to the nuclear periphery, referred to as Lamina-Associated Domains (LADs). LADs are typically repressed, barring exceptions where a subset of euchromatin interacts with lamin B1 and are categorized as euchromatic LADs (eLADs) (Guelen et al., 2008; Pascual-Reguant et al., 2018).

Chromatin in eukaryotes is organized as DNA wrapped around histone octamers, forming nucleosomes. Further, the linker histone H1 is incorporated with the nucleosomes constituting the fundamental units of the chromatin fiber—the chromatosomes (Zhang and Li, 2017). Histones are among the most widely modified proteins, and each modification has the unique ability to regulate gene expression (Turner, 1993; Millán-Zambrano et al., 2022). Actively transcribing genomic regions localized away from the nuclear periphery are often associated with active histone marks such as H3K4me3, H3K9ac, and H3K27ac, deposited by histone remodelers such as KMT2, CBP, and p300, respectively (Ogryzko et al., 1996; Rao and Dou, 2015). On the other hand, histone modifications such as H3K9me2/3, H3K27me3, and H4K20me1 are associated with transcriptional repression. The combination of active and inactive marks fine-tunes transcriptional output (Kimura, 2013; Talbert and Henikoff, 2021). Of note, repressive histone marks such as H3K9me2/3 and H3K27me3, deposited by INM-interacting histone-remodeling complexes such as SUV39H1/2 and the Polycomb Repressor Complex 2 (PRC2) complex, are often enriched on LADs (Shumaker et al., 2006; Cesarini et al., 2015; Harr et al., 2015). These histone-remodeling complexes interact with lamins and maintain the associated chromatin in a state of repression (Marullo et al., 2016; Salvarani et al., 2019; Bianchi et al., 2020; Siegenfeld et al., 2022).

Cancer cells exhibit a remarkable interplay between aberrant genome organization and deregulated transcription. The cancer genome harbors mutations in both coding and non-coding regions, selectively providing tumorigenic cells with a proliferative advantage to outcompete normal cells (Moreno and Basler, 2004; Pon and Marra, 2015; Bailey et al., 2021). For instance, incorporating non-canonical histone variants alters nucleosome stability, often resulting in altered replication and transcription (Bönisch et al., 2012; Henikoff and Smith, 2015; Buschbeck and Hake, 2017). In solid tumors, mutant chromatin remodelers differentially recruit histone modifiers that confer chemoresistance (Drosos et al., 2022). These cancer-associated mutant histones are referred to as oncohistones, which are now emerging as a class of prominent biomarkers of cancers (Bočkaj et al., 2021). In this review, we address the molecular and mechanistic underpinnings of nuclear envelope factors, their crosstalk with chromatin, and their pivotal role in cancer initiation and progression.

## 2 Nuclear envelope and lamins

The nuclear envelope is a crucial barrier between the cytoplasm and the nucleus and functions as a protector of the genome. The nuclear envelope consists of an outer and inner nuclear membrane (ONM and INM, respectively) and NPCs. The INM is lined on the inner side by a protein meshwork referred to as the nuclear lamina, which is composed of type V intermediate filament proteins—the A- and B-type lamins. The A-type lamins, lamin A/C, are produced as two somatic isoforms of prelamin A by alternative mRNA splicing at exon 10 of the LMNA gene (Machiels et al., 1996). Lamin A bears a CaaX motif at its C-terminal end, which is farnesylated, in contrast to lamin C, which does not contain the CaaX motif or undergo farnesylation (Vorburger et al., 1989). Notably, mature lamin A is formed by the loss of farnesylation inside the nucleus. On the other hand, the predominant B-type lamins—lamins B1 and B2 are permanently-farnesylated products of two separate genes—LMNB1 and LMNB2. Lamins interact with chromatin, either directly or through transmembrane proteins of the INM—lamin B receptor (LBR), MAN1, and Emerin (Ye and Worman, 1996; Holaska and Wilson, 2007; Demmerle et al., 2012). Apart from biochemical cues, the nucleus directly perceives mechanical signals through the LINC complex, involving Nesprin and SUN proteins (Figure 2). Nesprins, which extend from the ONM to the perinuclear space, directly interact with cytoskeletal proteins such as vimentin, actin, and microtubules (Ketema et al., 2013; Gimpel et al., 2017; Li et al., 2021). Mechanical cues are subsequently propagated *via* the interaction with the SUN and KASH domain proteins (Starr and Fischer, 2005; Tzur et al., 2006). These lines of evidence suggest that the coordinated functioning of nuclear lamins, nucleoporins, and LINC complex factors is central to the functional organization of the nucleus and the genome.

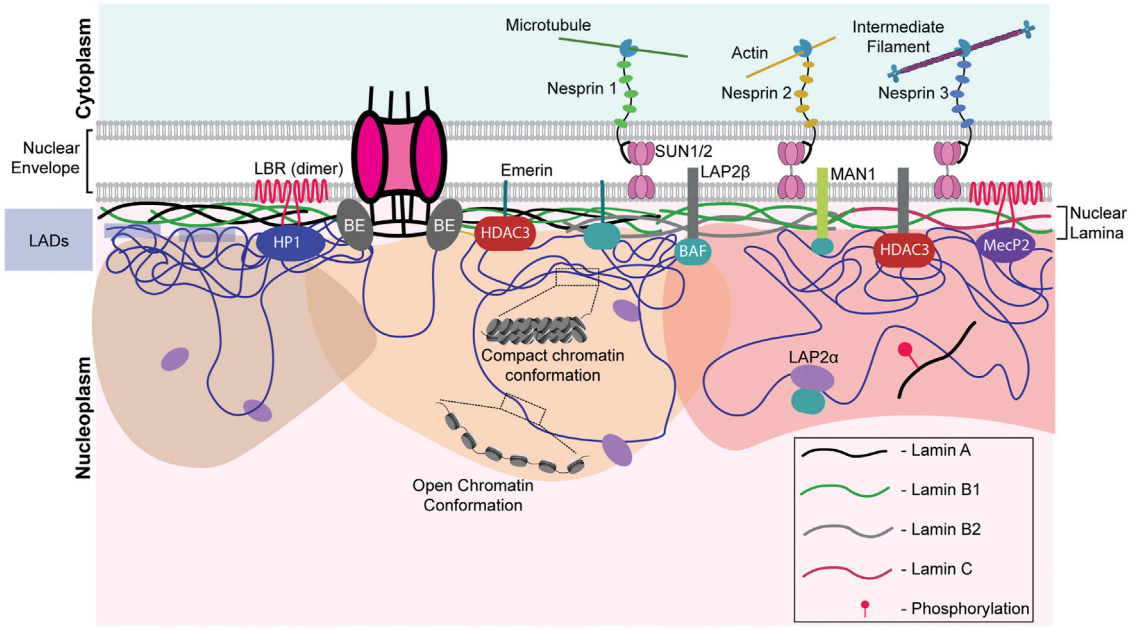


FIGURE 2
Nuclear envelope architecture and its role in genome organization. A schematic model showing the INM proteome involved in maintaining genome organization. Nesprins communicate external mechanical cues to the nucleus *via* the SUN1/2 complex. The regions of the genome contacting the nuclear lamina, the LADs, are maintained in a heterochromatic state. Phosphorylated lamin A binds to active enhancers in the nuclear interior. LAP2α interacts with intra-nuclear lamin A/C and could be regulating its functioning. Chromatin remodelers such as HDACs and sirtuins are often associated with the INM proteins such as emerin, MAN1, LAP2β, lamins, and LBR. NPCs are also associated with chromatin. LAP2α - lamina Associated Peptide 2α, LBR - lamin B receptor, BE - Barrier Element, HP1—Heterochromatin Protein 1, HDAC—histone deacetylase, SUN1/2—Sad1/unc-84 protein-like 1/2 and MeCP2—methyl CpG-binding protein 2.

Aberrations in nuclear morphology, such as invaginations, blebs, and micronuclei, serve as histological markers for grading tumor progression and often correlate with carcinogenesis. For instance, Haematoxylin-Eosin (HE) staining of papillary thyroid carcinoma cells and colon adenocarcinoma revealed enlarged nuclei with irregular morphology compared to normal cells with smaller and spherical nuclei (Fischer, 2020). Furthermore, nearly 90% of solid tumors are characterized by aneuploidy, which predominantly involves deletions and amplifications at the whole chromosomal and sub-chromosomal levels (Holland and Cleveland, 2012). CIN leads to transcriptional imbalances in a cell- and tissue-specific manner (Bakhoum et al., 2018; Benhra et al., 2018). Here, we focus on the mechanisms by which defects in the nuclear envelope manifest themselves, resulting in genomic instability and thereby contributing to cancer progression.

## 2.1 Role of aberrant nuclear envelope factors in cancers

The stability and integrity of LINC complex proteins and nuclear lamins are crucial for maintaining chromatin organization and genome stability, aberrations of which are associated with various cancers (Sur et al., 2014). For instance, immunohistochemistry showed decreased expression of LMNA and LMNB1 in 7/8 primary gastric cancers and 6/8 gastric cancers, respectively (Moss et al., 1999). In addition, nuclear envelope proteins regulate chromosomal stability as they participate in cell cycle progression, chromosome segregation, and nuclear envelope assembly post-mitosis (Dechat et al., 2007; Kuga et al., 2014; Dubińska-Magiera et al., 2019).

Remarkably, nuclear morphology plays a vital role in modulating cell fate in the continuum of cancer progression (Capo-Chichi et al., 2016; Smith et al., 2018; Fischer, 2020). In particular, the loss of emerin and lamin A show aberrations in nuclear morphology, accompanied by an increased aggressiveness of cancer cells (Reis-Sobreiro et al., 2018; Bell et al., 2022). Consistent with this finding, ovarian cancers show decreased emerin and lamin A/C levels, accompanied by a progressive destabilization of the nuclear envelope (Capo-chichi et al., 2011). Lamin A/C-emerin co-depletion alters chromatin mobility, suggestive of their role in the maintenance of genome organization and function (Ranade et al., 2019). Intriguingly, depletion of lamin A/C mislocalized emerin, resulting in altered nuclear morphology and increased invasiveness of DU145 prostate cancer cells (Kong et al., 2012; Reis-Sobreiro et al., 2018).

The nuclear lamina is composed of three lamin sub-types and interacts with the LINC complex genes, and this confers a molecular redundancy on lamin function, which counters abrupt alterations in the lamina—predominantly in response to external cues. For instance, keratinocytes and fibroblasts of the skin derived from lamin A/C-knockout mice showed prolonged expression of LBR as compared to wild-type cells (Solovei et al., 2013). Similar buffering mechanisms were uncovered in EMD- and LMNA-null mice during development. While LAP2α was upregulated in myogenic cells derived from $LMNA^{-/-}$ mice, cells derived from EMD-null mice showed a compensatory increase in lamin A expression (Melcon et al., 2006). However, the mechanistic basis of the transcriptional feedback circuits between lamin A/C and the nuclear envelope factors remains to be examined in greater detail.

The nuclear lamina functions as a docking site for anchoring LADs enriched in heterochromatin. For example, LBR tethers heterochromatin to the nuclear envelope in actively proliferating cancer cells during the early stages of mammalian development, while lamin A/C is a chromatin anchor in differentiated cells (Solovei et al., 2013; Lukášová et al., 2017). It is interesting to note that the loss of both LBR and lamin A/C results in the inversion of chromatin with heterochromatin toward the nuclear interior (Solovei et al., 2013), reiterating the significance of the nuclear lamina in chromatin organization and function. Furthermore, lamin B1 loss significantly increases nuclear bleb formation, while the depletion of lamin A/C shows morphological aberrations such as nuclear atypia, in addition to aneuploidy and CIN (Lammerding et al., 2006; Capo-chichi et al., 2011). Furthermore, destabilization of the nuclear envelope shows enhanced nuclear blebbing and micronuclei formation, which contribute to chromosomal losses and aneuploidy (Capo-Chichi et al., 2016). In addition to A and B-type lamins, peripheral heterochromatin provides additional stiffness, and its deregulation foreseeably weakens the nuclear envelope, contributing to the formation of nuclear blebs (Stephens et al., 2018). In summary, a stable nuclear envelope composition is required for genome organization facilitated by the maintenance of nuclear integrity by reinforcing nuclear stiffness.

Interestingly, the loss of lamin B1 shows CIN and DNA damage by destabilizing key Homologous Recombination (HR) pathway proteins such as Rad51 in U2OS cells (Liu et al., 2015). Correspondingly, A-type lamins regulate HR through transcriptional co-regulation of RAD51 and BRCA1 while modulating Non-Homologous End Joining (NHEJ) through 53BP1 in breast cancer cells (Redwood et al., 2011). Lamin A also regulates DNA damage repair (DDR) *via* its direct interaction with Hsp90—a molecular chaperone involved in protein folding and stability in ovarian cancer cells (Wang et al., 2021). Furthermore, whether the differential stoichiometry of the A and B-type lamins modulates NHEJ or HR pathways to repair damaged DNA in a cell-type- and cancer-specific manner remains an open question.

## 2.2 Role of nucleoporins in genome organization and cancers

Nuclear pore complexes (NPCs) are ~120 nm-wide structures in the nuclear envelope, which mediate selective transport in and out of the nucleus. In vertebrates, NPCs comprise nucleoporins (Nups), a group of ~30 proteins, to form a ~125MDa protein complex (Cronshaw et al., 2002; Cohen et al., 2012). In addition to nuclear transport, the NPCs regulate chromatin interaction and function (Zhou and Panté, 2010; Kadota et al., 2020). Further, Nups are classified into 1) on-pore Nups that are associated with the NPC and 2) off-pore Nups that exist both in the NPC and nucleoplasm. Nups that interact with and regulate essential genes in the genome include Nup93 (on-pore) and Nup153 (off-pore), which interact with super-enhancers, and function as major chromatin regulators (Baumann, 2016; Ibarra et al., 2016). Nup153 and Nup98, present near the nuclear basket of the NPC, communicate with a wide range of poised genes through interactions with CTCF (Pascual-Garcia et al., 2017). Certain on-pore Nups, such as Nup93, interact with and repress HOXA genes which are essential for early development (Labade et al., 2016). In the context of cancer progression, Nup93 facilitates metastasis by enhancing β-catenin import and upregulating EMT target genes, thus inducing epithelial-to-mesenchymal transition (EMT) in breast and hepatocellular cancers (Lin et al., 2022; Nataraj et al., 2022). The on-pore Nup210 interacts with SUN2 to regulate the expression of prometastatic mechanosensitive genes by impeding the spread of heterochromatin (Amin et al., 2021). Intriguingly, a non-canonical extranuclear function of the Nup107-160 complex is to stabilize bipolar spindle arrangement and prevent aneuploidy during each cell division, thus maintaining genome integrity (Orjalo et al., 2006).

Nups contribute to cancer progression by forming fusion proteins. For instance, the off-pore Nup98 is involved in multiple fusion proteins with transcriptional coactivators, histone methyltransferases, helicases, and in some instances, even orphan proteins (Wang et al., 2007; Yassin et al., 2010; Gough et al., 2011). During hematopoietic stem cell differentiation, HoxA7, HoxA9, and HoxA10 levels are upregulated, which progressively decrease as the hematopoietic cells differentiate further into various lineages. The Nup98 fusion protein alters gene expression resulting in Acute Myeloid Leukemia (AML). Intriguingly, in Nup98-NSD1 fusion protein-mediated AML, the fusion protein is recruited to the HoxA7, HoxA9, and HoxA10 gene loci. The FG-repeat (originating from Nup98) of the fusion protein interacts with HAT CBP/p300, leading to overexpression of the aforementioned Hox genes, contributing to AML. Nup98-PHD fusion proteins also promote AML progression *via* a similar mechanism (Wang et al., 2007, 2009). Thus, the aberrant localization and expression of Nups impact genome organization, contributing to oncogenesis. Taken together, the cellular machinery effectively copes with aberrant

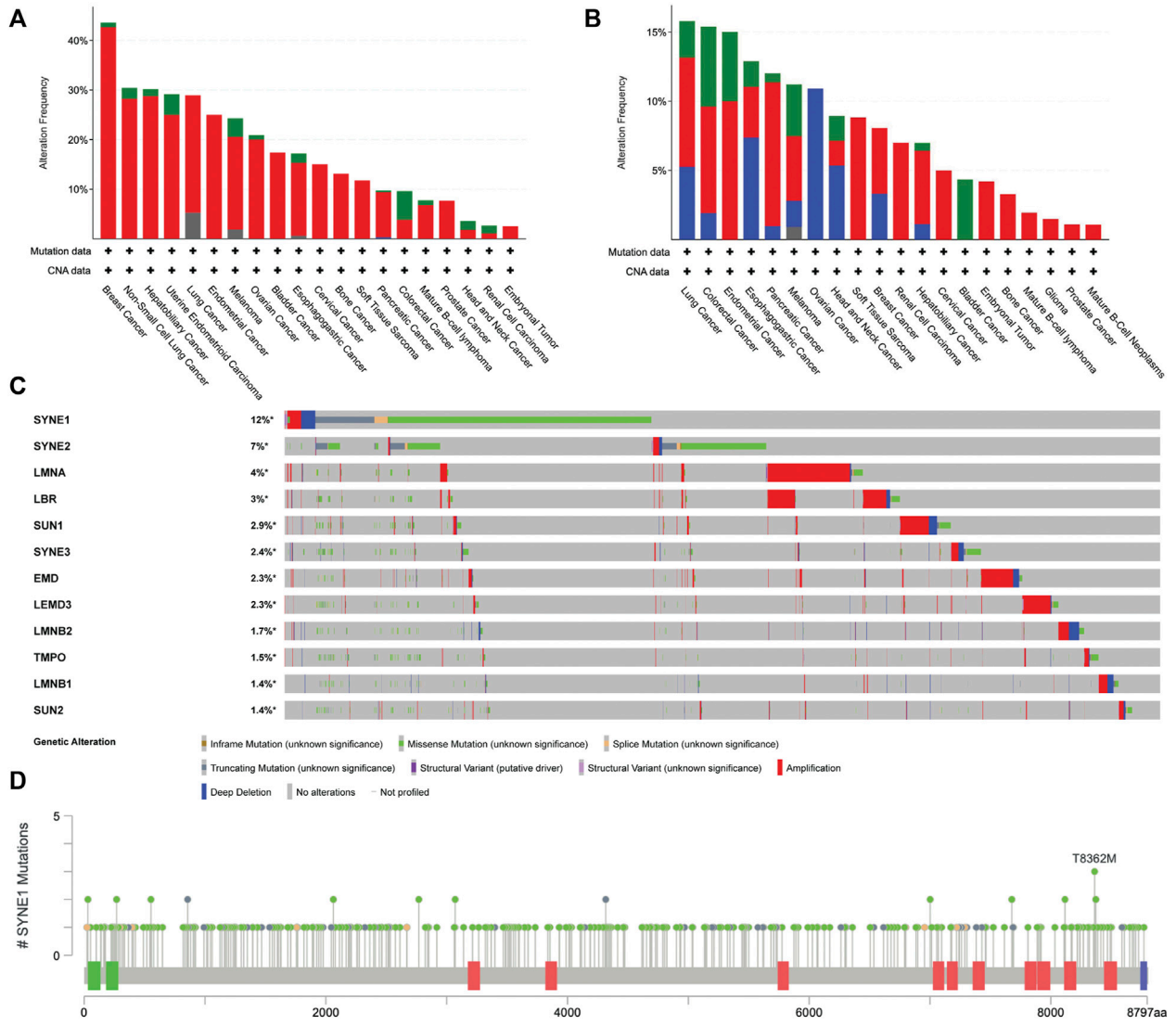


FIGURE 3
Analysis of genetic alterations in nuclear envelope genes in cancer patients using cBioPortal data (ICGC/TCGA Pan-Cancer Analysis of Whole Genomes Consortium 2020) CNAs in **(A)** LMNA **(B)** LMNB (B1 and B2) **(C)** Oncoprint of 10 nuclear envelope genes across 10967 cancer patient samples arranged in descending order based on the frequency of missense mutations **(D)** Localization and frequency of SYNE1 mutations in cancer patients using lollipop plot of cBioPortal (Cerami et al., 2012; Gao et al., 2013).

gene expression—a major target for future therapeutic approaches.

## 2.3 Lamins modulate copy number alterations in cancers

Assessing alterations in chromosome numbers is a key method for cancer diagnostics. Tumorigenesis often involves the progressive acquisition of genetic alterations in specific genes. Copy Number Alterations (CNAs) have been identified and characterized across a wide range of cancer types using high-density single nucleotide polymorphism (SNP) arrays (Chen et al., 2013). Determining therapeutic strategies in the case of deep deletions becomes especially difficult owing to the absence of the gene in the cancer cell genome, with its functional redundancy prepending an added layer of complexity. Teasing apart whether CNAs serve as drivers of cancers or silent passengers of its effects remains an area of active investigation. Here, we review the most recent advances in our understanding of the interplay between CNAs and cancer progression through data curated from cBioportal Figure 3 (Cerami et al., 2012; Gao et al., 2013).

### 2.3.1 Amplifications

It is well established that CIN and aneuploidy involving whole chromosomal and focal amplifications and deletions in the genome are defining features of cancer initiation and progression (Watanabe et al., 2001; Zhou et al., 2002; Kops et al., 2004). Interestingly, genes that encode for lamins are strikingly amplified as compared to the other nuclear envelope genes, implying that the very mechanisms that protect genomic integrity aberrate in cancers. TCGA analyses of nuclear envelope genes across patient samples revealed CNAs of the LMNA-coding sequence in ~13% of cancers. Breast cancer patient samples show the maximum extent of CNAs in LMNA in ~40% of the 211 patient samples (Figure 3A). However, the extent to which gene amplifications in LMNA correlate with changes in its transcript level remains unclear. An intriguing possibility is that transcriptional deregulation of lamin A/C potentially impacts expression levels of B-type lamins or LINC genes as a consequence of copy number amplifications of lamins and the stability of their interacting partners in a cell-type-specific manner.

### 2.3.2 Deletions

Interestingly, the LMNB1 gene shows a significant number of deletions across cancers. It is unique that LMNB1 and LMNB2 genes showed only deep deletions in ovarian cancers (Figures 3B,C). In ovarian cancer cells (HO-8910PM), decreased expression levels of lamin A/C correlate with increased cell migration and poor prognosis (Wang et al., 2019). Moreover, the lamin A:B stoichiometric ratio shows a dominance of A-type lamins in stiffer cartilaginous tissues, while B-type lamins are more prominent in softer tissues such as the brain (Swift et al., 2013). Nevertheless, if lamin A:B stoichiometry does modulate the malignant potential of cancer cells, the extent of complementation and the mechanisms that regulate the altered sub-interactome of the A- and B-type lamins remain to be uncovered.

### 2.3.3 Mutations in nuclear envelope genes—Nesprin (SYNE1)

We examined the status of mutations in genes that encode the nuclear envelope proteins across cancers using cBioPortal. This analysis revealed recurrent mutations in the Nesprin-1 gene—SYNE1 (Figure 3D). Markedly, the SYNE1 gene accumulates the highest number of missense mutations (271), followed by truncating (41) and splice mutations (12). A mutation in exon 33 of the SYNE1 gene modifies a conserved residue in spectrin repeat 11, showing aberrant mitotic phenotypes such as altered distance between the centrosome and the nucleus, potentially contributing to CIN in human hepatoma-derived Huh7 cells (Sur-Erdem et al., 2020). Furthermore, mutation analysis of SYNE1 revealed frequent missense mutations of T8362M across three different cancers—medulloblastoma, pancreatic adenocarcinoma, and ovarian epithelial tumor. However, the physiological significance of these mutations remains to be elucidated. Do mutations in SYNE1 destabilize or hyperactivate mechanochemical signals into the nucleus and chromatin as a consequence of its altered interaction with LINC complex factors and actin? This could further contribute to increased communication with the microenvironment and the consequent proliferation of cancer cells.

## 3 Chromatin organizers in carcinogenesis

The genome is a highly dynamic collection of genes, their regulators, and massive stretches of DNA whose function is yet to be discovered. Maintenance of genome organization involves the concerted function of numerous proteins required for the regulation of chromatin organization and gene expression. The aberrant function of chromatin organizers is associated with cancers (Table 1). Here, we examine the contribution of major chromatin organizers, namely CTCF, cohesins, and condensins, to cancer progression.

## 3.1 CTCF

CCCTC-binding factor (CTCF) is a conserved zinc-finger protein that functions as a chromatin organizer and transcription factor. In association with cohesin, CTCF regulates the organization of gene loci and alternative splicing primed by its sequence-specific binding to CTCF sites. In addition, CTCF functions as an insulator to restrict the expansion of repressive marks (Dixon et al., 2012; Holwerda and de Laat, 2013). The human genome has ~55,000–65,000 CTCF binding sites, amongst which around ~5,000 are highly conserved across species (Yusufzai et al., 2004; Chen et al., 2012; Holwerda and de Laat, 2013), though CTCF occupancy remains tissue- and cancer-specific (Hanssen et al., 2017; Debaugny and Skok, 2020). As per the loop extrusion model for TAD formation, the cohesin complex moves along the chromatin, establishing a loop until it encounters an oriented CTCF dimer. Consequently, further advancement of the cohesin complex is aborted, thus demarcating TAD boundaries enriched in CTCF binding sites (Sanborn et al., 2015; Fudenberg et al., 2016). CTCF also prevents non-specific promoter-enhancer interaction by delimiting the loop size, thus augmenting enhancer-blocking mechanisms (Amankwaa et al., 2022). The Yin Yang 1 (YY1) protein interacts with cohesin and is enriched near enhancer-promoter contact sites, thus assisting CTCF in augmenting enhancer-promoter interaction (Figure 1) (Weintraub et al., 2017).

Aberrant expression or occupancy of CTCF is associated with breast, lung, endometrial, gastrointestinal, prostate, and skin

**TABLE 1 Role of chromatin organizers in cancers.**

| Chromatin organizer | Gene | Cancer | Effect of dysregulation of gene | Reference |
|---|---|---|---|---|
| Cohesin | STAG2 | Glioblastoma | Mutation in STAG2 leads to aneuploidy while its rescue enhances the chromosomal stability | Solomon et al. (2011) |
| | RAD21 | Breast | Overexpression of RAD21 in MDA-MB-231 cells leads to poor prognosis and chemoresistance, while its knockdown reduces chemoresistance | Xu et al. (2011) |
| Condensin | NCAPH | Colorectal | In HCT116, NCAPH depletion decreases cell migration, arrests the cells in G2/M, and enhances apoptosis | Yin et al. (2017) |
| | NCAPG | Liver | NCAPG has a pro-proliferative effect in adenocarcinoma patients | Zhang et al. (2022) |
| | NCAPH | Prostate | Upregulation of NCAPH in prostate cancers promotes cell proliferation and helps in bypassing replication checkpoints, which might hinder cancer progression | Kim et al. (2019) |
| CTCF | | Breast | CTCF and EGR1 reduce cell migration in TNBC cell line MDA-MB-231 by inducing the expression of Nm23-H1 | Wong et al. (2021) |

Mutations in genes that encode for chromatin organizers are implicated in carcinogenesis and impact chromosome organization, stability and transcriptional regulation.

cancers (Eldholm et al., 2014; Kemp et al., 2014; Poulos et al., 2016; Guo et al., 2018; Höflmayer et al., 2020). Of note, multiple mutations map to the DNA-binding zinc finger domain of CTCF across cancers (Bailey et al., 2021). CTCF binding to its target sites is sensitive to their methylation states. For instance, hypermethylation of CTCF binding sites shows a loss of insulation in isocitrate dehydrogenase (IDH) mutant gliomas (Flavahan et al., 2016). This further leads to the ectopic interaction of the IDH enhancer with PDGFRA (platelet-derived growth factor receptor alpha), leading to its constitutive expression and the development of gliomas (Figure 1). However, not all cancer-specific mutations in CTCF affect its binding. For instance, stop codon mutations in its N- and C-terminals, as well as in the zinc finger domain, may exhibit a dominant-negative effect by hindering interactions with functionally important cofactors, thus impeding CTCF function (Debaugny and Skok, 2020).

Analyzing patient data sets from TCGA reveals frequent loss of the CTCF gene in breast and prostate cancer patients, correlating with hypermethylation of CpG islands and hypomethylation of other parts of the genome. CTCF depletion in a prostate cancer cell line, HPECE6/E7, shows hypermethylation of CTCF binding sites, further downregulating respective gene expression (Damaschke et al., 2020). This indicates that CTCF binding to its target sites prevents CpG hypermethylation and safeguards chromatin architecture, not just by organizing the chromatin but also by maintaining it. This study further reveals that drug-induced hypomethylation using 5-aza-2 deoxycytidine (5dAza) rescued chromatin organization, reaffirming the importance of CTCF and its binding sites in cancers. However, 5dAza interacts with a wide range of targets and fails to act precisely on distinct TADs, thus raising the question of specificity in cancer therapies.

CTCF functions as a double-edged sword, acting both as an oncogene as well as a tumor suppressor in a cancer subtype-specific manner. Ovarian cancers exemplify the oncogenic potential of CTCF, where metastatic lesions display elevated CTCF expression. Further, the depletion of CTCF in ovarian cancer cell lines (SKOV3 and A2780) decreased cell migration by consistently downregulating three metastasis-associated genes, including CTBP1, SRC, and SERPINE (Zhao et al., 2017). In contrast, CTCF positively regulates the expression of the metastatic suppressor, Nm23-H1, in breast cancers. Studies in the highly invasive MDA-MB-231 and the less invasive MCF-7 cells show that CTCF-dependent Nm23-H1 levels inversely correlate with cancer aggressiveness (Wong et al., 2021). The mechanism by which CTCF functions in a cancer-specific manner remains poorly understood.

Overall, changes in genome organization due to altered levels or aberrant recruitment of chromatin organizers contribute to cancer progression However, experiments performed in cell culture models need to be complemented with insights from animal models and patient-derived tumor samples. Since adherent cell culture studies are usually performed on a monolayer of cells, these approaches do not mimic the tumor microenvironment, discounting factors such as nutrient accessibility, barrier tissue formation, and variation in drug response, among others. What effects chemotherapeutic agents have on TAD organization and gene expression *in vivo* remains an area of active study. Moreover, it is intriguing that environmental factors, such as diet and social interaction, also impinge on CTCF function and, therefore, chromatin organization and function (Davis et al., 2022; Wang R et al., 2022)—an interesting finding, given that extraneous environmental factors considerably contribute to an increase in the incidence of cancers.

## 3.2 Cohesin

Cohesins are multi-protein complexes essential for mitosis and meiosis, conserved from yeast to humans. The canonical

function of cohesins is to clasp sister chromatids together during the metaphase-to-anaphase transition. Apart from the aforementioned function, cohesin plays a vital role in maintaining inter-TAD and intra-TAD boundaries by looping chromatin in the interphase nucleus, allowing for regulated inter- and intra-TAD interactions (Matthews and Waxman, 2018; Barrington et al., 2019). This promotes enhancer-promoter contacts in a cell type-specific manner.

Through genome-wide sequencing, it is now apparent that cohesin accumulates a number of mutations in the coding region that alter the way it binds the chromatin and promotes aberrant genomic contacts leading to anomalous expression of various genes. Depletion of RAD21, a component of the cohesin complex, promotes enhanced expression of mesenchymal genes such as ITGA5 and TGF-B1 by altering the intrachromosomal chromatin contacts and creating active transcriptional units (Yun et al., 2016). Recent exome sequencing revealed that the STAG2 protein of cohesin is frequently mutated in cancers (Lawrence et al., 2014). It is interesting to note that STAG2 is involved in promoting regulated chromosomal contacts, the depletion of which enhances the loop extrusion and promotes aberrant genomic contacts (Adane et al., 2021; Richart et al., 2021). It remains unclear how the mutated STAG2 functions in cancer, elucidation of which might uncover a new therapeutic candidate. Moreover, the loss of cohesin function in cancers leads to increased replication stress and genomic instability (Leylek et al., 2020; Minchell et al., 2020). We surmise that cohesin mutations enhance genomic instability, facilitate clonal expansion, or enhance tumorigenic potential, eventually leading to cohesin loss of function in the clonal population. However, various lines of evidence suggest that mutations in the cohesin genes contribute to cancer initiation and progression by disrupting chromosome organization and transcriptional regulation (Table 1) (Leeke et al., 2014; Kojic et al., 2018; Antony et al., 2021).

## 3.3 Condensin

Like cohesins, condensins are multi-protein complexes required for chromosome assembly, condensation, and segregation during mitosis and meiosis. While cohesin clasps the sister chromatids together, condensin facilitates mitotic chromosome compaction by uniting the two distant portions of a single chromatid. Condensin isoforms have conserved structural maintenance of chromosome (SMC) proteins, SMC2 and SMC4, but differ in their non-SMC components. Interestingly, decreased condensin expression triggers CIN, consequently driving colorectal cancer progression (Baergen et al., 2019). In addition, mutations in the C-terminal residues R551 and S556 of CAPH2, a condensin II subunit, lead to genomic instability in the human retinal pigment epithelial (RPE1) cell line (Weyburne and Bosco, 2021). Another line of evidence shows the involvement of the condensin complex in maintaining chromosomal stability *via* its recruitment to the pericentromeric regions. The binding of cell cycle regulators pRB and E2F1 to the pericentromeric regions cause replication stress. Studies reveal that these factors recruit condensin II to form a complex in the pericentromeric chromatin, thus regulating replication fidelity and cell ploidy (Coschi et al., 2014). This agrees with an increase in the γH2A.X marker at the pericentromeric region, accompanied by enhanced repeat instability, on depletion of condensin (Samoshkin et al., 2012). However, the precise function of condensin II and the mechanistic basis of its safeguarding function against replicative stress remains to be deciphered.

Apart from chromatin compaction, condensins also play moonlighting roles that include facilitating enhancer RNA transcription and enhancer-promoter looping in condensin-bound ERα (Estrogen Receptor α)-sensitive enhancers in breast cancers by recruiting p300 and RIP140 (Li et al., 2015). Immunoprecipitation of condensins followed by mass spectroscopy or Rapid immunoprecipitation mass spectrometry of endogenous proteins (RIME) during dynamic processes such as cell transformation may reveal other non-canonical functions (Mohammed et al., 2016). Considering the limited number of therapeutic approaches available to combat triple-negative breast cancers (TNBC), it is encouraging that the knockdown of condensin I complex protein NCAPD2 curtailed cell proliferation and invasion. These lines of evidence implicate NCAPD2 expression as a prognostic marker of TNBC patients suggesting a potential therapeutic candidate (Zhang Y et al., 2020). An in-depth biochemical and molecular characterization assumes significance as condensins emerge as potential therapeutic targets for human cancers (Wang et al., 2018).

# 4 Impact of non-canonical histones and oncohistones on chromatin organization in cancers

Non-canonical histone variants occasionally replace canonical histones in the genome, often serving two main purposes. First, histone variants are dynamically incorporated throughout the interphase with the regular nucleosomal turnover of canonical histones to sustain nucleosomal stability. Secondly, additional regulatory domains, interactors, and PTMs in non-canonical histones offer supplementary mechanisms for the control of epigenetic regulation. Since cancers are characterized by large-scale remodeling of their epigenetic landscape, canonical histones in cancers are occasionally interchanged with histone variants (Vardabasso et al., 2015). Structurally, histones are composed of amino- and carboxy-terminal tails and a globular histone fold domain (HFD). Specific mutations in histone genes tend to confer oncogenic

properties to cells, and these mutant histones are referred to as oncohistones (Mohammad and Helin, 2017). Mutations occur both in the tail and globular domains, with different consequences. While tail domain mutants cause a global loss of both active and inactive histone marks, the globular domain destabilizes the nucleosome. Here, we review the functional diversity and regulatory mechanisms involved in genome organization by some non-canonical and oncohistones while discussing the scope for further research in the field.

## 4.1 H3 variants

The histone variant H3.3 functions as a space-filling histone when canonical H3 is evicted from the nucleosome, thus maintaining nucleosomal stability (Ray-Gallet et al., 2011). The incorporation of histone H3.3 facilitates the enrichment of active marks on chromatin associated with dynamic histone turnovers, such as transcriptionally active promoters and enhancers of active genes (Lin et al., 2013; Ha et al., 2014). Contrastingly, histone H3.3 is also incorporated in repeat-rich and repressed telomeres, where H3.3 is incorporated into the nucleosomes and further methylated to H3.3K9me3. The H3.3K9me3 mark is vital for maintaining the integrity of constitutively heterochromatinized telomeres (Udugama et al., 2015). Specific chaperone complexes facilitate the incorporation of the histone H3.3 into different regions in the genome. In the euchromatin, H3.3 is incorporated by the HIRA complex (Shi et al., 2017; Yu et al., 2021; Yang et al., 2022), while DAXX/ATRX complexes incorporate H3.3 in the telomeric and pericentric heterochromatin (Goldberg et al., 2010; Lewis et al., 2010; Heaphy et al., 2011). Of note, DAXX/ATRX is mutated in classes of gliomas, sarcomas, and pancreatic neuroendocrine tumors and is involved in differential H3.3 deposition, thereby deregulating gene expression profiles (Heaphy et al., 2011; Yuen and Knoepfler, 2013; Ren et al., 2018). Deposition of the H3.3 variant in the telomeric regions might potentially contribute to the maintenance of cancer stem cells within tumors by activating embryonic stem cell dynamics and promoting alternative lengthening of telomeres (ALT) (Wong et al., 2009; Gulve et al., 2022). Moreover, the H3.3 recruiter ATRX is also localized to the nuclear periphery with the lamins, suggesting a possible interaction between H3.3, the telomere complex, and lamins, which collectively regulate telomere organization (Pennarun et al., 2021; Teng et al., 2021).

Histone composition in the nucleosome, especially the incorporation of oncohistones, affects the expression of a wide range of genes. For instance, H3/H3.3K27M tail domain mutations accelerate neural stem cell self-renewal by dysregulating neural development genes in diffuse intrinsic pontine gliomas (DIPGs) (Mohammad and Helin, 2017; Larson et al., 2019; Nacev et al., 2019). H3G34V/R and H3.3G34W/L histone tail domain mutations are found in pediatric high-grade gliomas and giant cell tumors of the bone, respectively. Several *in vitro* and *in vivo* studies reveal that both the oncohistones, H3.3K27M and H3.3G34W/L/V/R, reduce H3K27me3 levels, resulting in the aberrant expression of Polycomb-group (PcG)-mediated heterochromatinized genes, though the results are more promising in *in vitro* systems (Mohammad and Helin, 2017). H3.3K27M tumors have enhanced expression of genes associated with neural development, where H3K27me3 loss released bivalent promoters from their poised state (Larson et al., 2019). Likewise, the H3.3K36M mutation, found in 90% of chondroblastomas, shows a parallel trend of decreasing H3K36 di- and tri-methylation, PTMs involved in RNA polymerase elongation (Jha and Strahl, 2014; Fang et al., 2016; Sahu and Lu, 2022). A possible mechanism is reducing methylation levels by the selective sequestration of histone methyltransferases, NSD2, SETD2, and PRC2, creating a dominant negative effect (Figure 4D). Intriguingly, these oncohistones affect multiple histone marks. For instance, the H3.3K36M mutation, despite decreasing H3K36 methylation, increases the deposition of H3K27me3 marks. This leads to the mobilization of the polycomb repressor complex 1 (PRC1) away from its target sites, resulting in aberrations of PcG-regulated heterochromatin and an altered epigenetic profile (Bjerke et al., 2013; Chan et al., 2013; Lu et al., 2016). It remains an open question as to why the tail domain mutants of H3.3 are spatially confined in a hindbrain tissue-specific manner. Surprisingly, the H3.3K27M mutant promotes CIN and induces NHEJ-mediated DNA damage response through the DNA end-processing enzyme Polynucleotide Kinase 3′-Phosphatase (PNKP) (Rondinelli et al., 2022). The rationale underlying the deposition of H3.3 mutants on stalled forks despite the presence of other canonical histones remains unclear. Although oncohistones function as discrete entities, the mechanistic basis underlying their potential regulatory crosstalk would be a tantalizing finding to unravel.

## 4.2 H2A and H2B variants

All histones exist as multiple variants that modulate gene expression, barring histone H4, which has only one variant. Histone H2A and H2B cumulatively have 15 non-canonical histone variants, out of which 11 are H2A variants—H2A.X, H2A.Z.1, H2A.Z.2.1, H2A.Z.2.2, H2A.Bbd, H2A.J, H2A.B, TH2A, H2A.P, macroH2A.1.1, macroH2A.2, and macroH2A1.2, and four are H2B variants—H2BE, H2B.S.M, TH2B, and H2B.W (Oberdoerffer and Miller, 2022), which are often dysregulated in cancers (Figure 4A). γH2A.X, a histone H2A subclass phosphorylated at S139, functions as a molecular beacon that detects DNA damage in the genome (Mah et al., 2010). Of note, the lack of H2A.X causes lethality in mice exposed to γ-irradiation, establishing its importance in

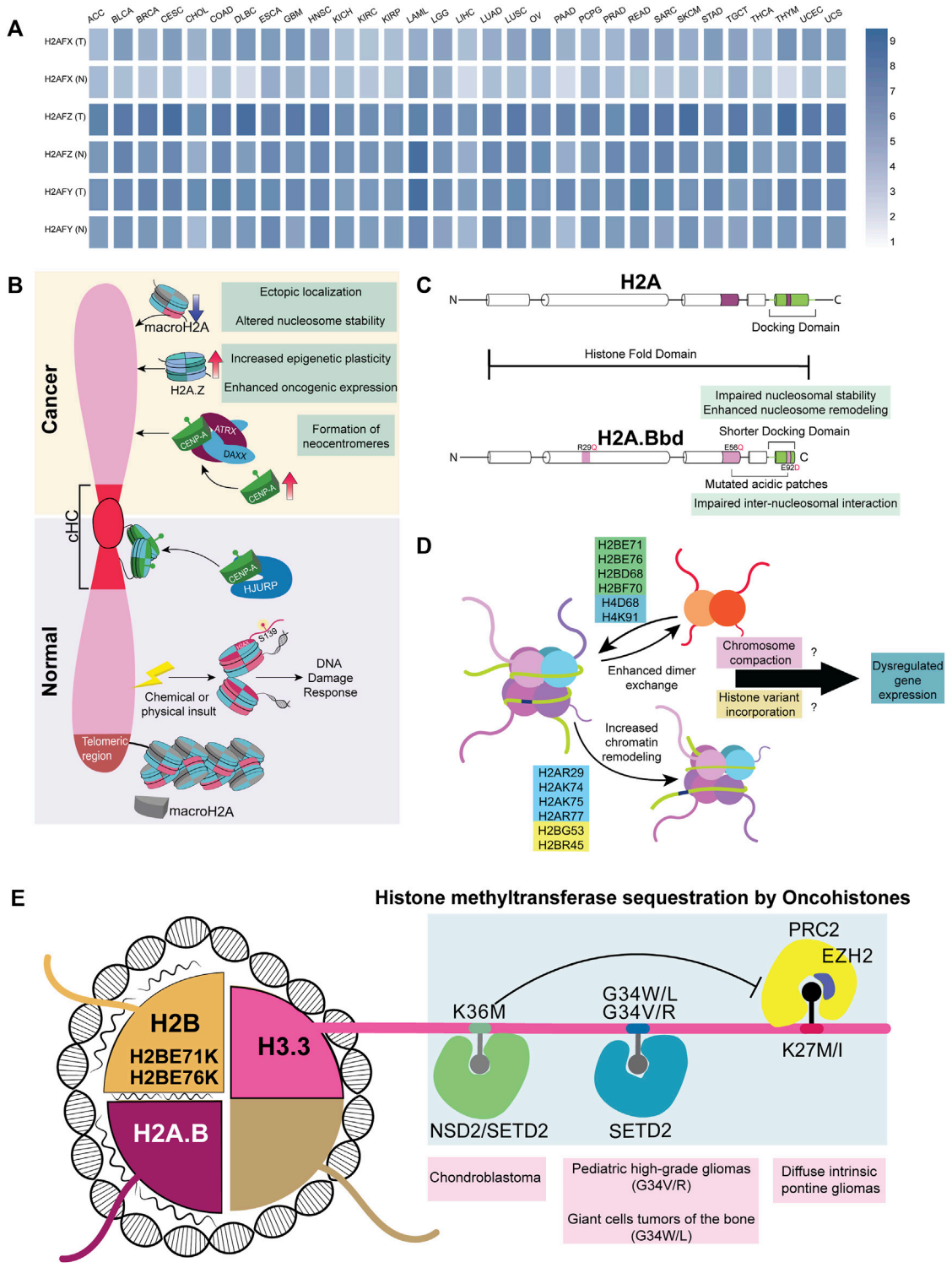


FIGURE 4
Histone variants and mutants in cancer **(A)** A heatmap representing various non-canonical histones across 31 different cancers; data curated from GEPIA2. Genes H2AFX, H2AFZ, and H2AFY code for H2A.X, H2A.Z.1, and macroH2A, respectively **(B)** Difference in the recruitment of non-canonical histones in normal versus cancer cells. cHC—Constitutive heterochromatin **(C)** Comparison between canonical H2A and non-canonical histone H2A.B **(D)** Mutations in the globular domain of core histones (H2B, H2A, and H4) to enhance dimer exchange and chromatin remodeling. This further dysregulates the expression of genes involved in differentiation **(E)** Oncohistones, mutations in the tail and globular domains are found in different cancers. Tail domain mutations sequester histone methyltransferases, while globular domain mutants destabilize the nucleosome, altering the expression of various genes.

maintaining genome stability (Celeste et al., 2002). Surprisingly, H2A.X is also involved in sustaining the self-renewal capacity of pluripotent stem cells (Turinetto et al., 2012). We speculate an H2A.X-dependent mechanism involved in the sustenance and regulation of cancer stem cells (Kim et al., 2012). As the guardian of the genome, the significance of H2A.X in facilitating metastasis was demonstrated when the knockdown of H2A.X induced EMT through the upregulation of transcription factors Twist1, ZEB, and SLUG (mesenchymal markers) in HCT116 colorectal cancer and MCF10A non-tumorigenic breast epithelial cell lines (Weyemi et al., 2016). This strongly suggests alternate functions of H2A.X in various aspects of gene regulation in addition to its role in the DNA damage response machinery.

Both H2A.Z and H3.3 maintain an open conformation of chromatin in nucleosome-depleted regions of the promoter for transcription factors to interact with gene promoters resulting in their transcriptional upregulation (Jin et al., 2009). Consistent with the requirement to transcribe genes, H2A.Z facilitates access to transcribing genomic regions by destabilizing the nucleosome, which is important in regulating stem-cell renewal and differentiation (Buschbeck and Hake, 2017). In cancers, canonical H2A is often replaced by its non-canonical variants H2A.Z.1.1 and H2A.Z.2. Remarkably, these isoforms are upregulated and positively correlate with resistance to chemotherapy in malignant stages of melanoma and pancreatic ductal adenocarcinoma (Vardabasso et al., 2015; Ávila-López et al., 2021). Furthermore, overexpression of H2A.Z correlates with poor prognosis in estrogen receptor-positive breast cancer (Hua et al., 2008). The non-canonical histone variant, macroH2A (mH2A), has a macro-domain and is involved in the inactivation of the X chromosome in mammals (Chadwick et al., 2001). In contrast to other histones, mH2A has a stabilizing effect on the nucleosome and can mediate both gene activation and repression. Notably, the depletion of mH2A dysregulates gene expression in at least nine cancers (Zink and Hake, 2016). However, the recruitment mechanism of mH2A is yet to be completely elucidated.

H2A.Bbd, a member of the short H2A family, is a testis and brain-specific histone variant overexpressed predominantly in Diffuse Large B-cell Lymphomas (DLBCLs) (Chew et al., 2021). Interestingly, H2A.B harbors multiple H2A mutations in its sequence. These include R29Q (DNA binding site mutant) and E92L (acidic-patch mutant) (Figure 4C). Furthermore, H2A.B's truncated C-terminal tail compromises its nucleosomal compaction and, if expressed ectopically, might cause dysregulated gene regulation (González-Romero et al., 2008; Bagert et al., 2021; Chew et al., 2021; Kohestani and Wereszczynski, 2021). From a vantage point, wild-type H2A.B has already evolved into an oncohistone with the ability to promote nucleosomal instability (Bagert et al., 2021). H2B, another histone H2 variant, has the highest number of nucleosome-destabilizing mutations in the globular domain at E71 and E76 (Nacev et al., 2019; Bagert et al., 2021).

Essentially, tail-domain mutants are well-characterized, but not limited to, H3.3. The same is true for globular domain mutations, which are better documented for histone H2 (Nacev et al., 2019). Mutation data shows that 80% of the most frequent mutations in histones occur in their globular domain (Nacev et al., 2019). Many of these mutations in the globular domain enhance chromatin remodeling and histone dimer exchange, which correlates with the altered expression of genes involved in differentiation across patients with different cancers (Bagert et al., 2021). However, the mechanism and contribution of these mutations to cancers remain largely uncharacterized. We surmise that mutations in the globular domain of histones induce nucleosomal instability, which affects chromatin compaction both during mitosis and interphase. Moreover, histones bearing mutations in their globular domains mutant histones can increase the chances of incorporating histone variants, potentially altering gene expression. The temporal preference for the incorporation of histones, both dependent on and independent of replication, adds an additional layer of complexity (Figure 4E). Interestingly, 47% of the missense mutations in histones H2A, H2B, H3, and H4 show a conversion of glutamic acid residues to lysine or glutamine (Nacev et al., 2019), suggestive of 1) altered DNA-histone interactions 2) aberrations in PTM patterns of histones owing to an increase in the number of lysine and glutamine residues. Such a contribution of novel histone PTMs to carcinogenesis remains to be elucidated.

## 4.3 CENP-A

Apart from the role of histones in regulating transcription, histones are essential for modulating DNA damage response, genome organization, and chromosome maintenance. CENP-A, a centromere-specific H3 variant, is necessary and sufficient to ensure the structural and functional organization of the centromere. Heterochromatinization at the centromere is achieved by recruiting RNAi-based DICER machinery and SUV methyltransferases (Peters et al., 2003; Folco et al., 2008). Moreover, heterochromatic regions are associated with the nuclear envelope components, contributing to an additional layer of regulation (Towbin et al., 2012; Solovei et al., 2013; Ebrahimi et al., 2018; Iglesias et al., 2020). For instance, LBR and B-type lamins are involved in the organization of the pericentric heterochromatin in the interphase nucleus (Shimi et al., 2008; Dechat et al., 2010; Lukášová et al., 2018). Centromeres and telomeres are enriched in constitutive heterochromatin marks that frequently localize to the LADs in the genome (Haaf and Schmid, 1991; Weierich et al., 2003; Raz et al., 2008; Bloom, 2014), with a subset of heterochromatic domains clustering

around nucleoli as perinucleolar heterochromatin (Alcobia et al., 2000; Gdula et al., 2013).

The two fundamental functions of CENP-A include 1) centromere formation and maintenance and 2) nucleation of checkpoint assembly proteins involved in chromosomal segregation. The organization of the centromere is dynamic during the various cell cycle stages, contributing to chromatin reorganization. During the early G1 phase, CENP-A molecules form a rosette-like structure nucleated by HJURP, facilitating a 3D ring-like organization during the G1 phase (Figure 4B). During mitosis, this structure is reoriented to form a rod-like pattern (Andronov et al., 2019). Elevated levels of CENP-A form neo-centromeres due to its mislocalization along the chromosomal arms, resulting in the misorientation of microtubule fibers on the kinetochore. This leads to the abnormal segregation of chromosomes, resulting in chromosomal translocations and breakage (Barnhart et al., 2011; Sun et al., 2016). It is now established that CENP-A is recruited to DNA double-strand breaks, and its depletion leads to an impaired DDR (Zeitlin et al., 2009; Lawrence et al., 2015; Stirpe and Heun, 2022). This highlights that CENP-A is recruited to sites other than the centromeric regions, although the exact role of CENP-A in DDR remains to be characterized. The ectopic overexpression of CENP-A increases the tolerance limit to DNA insults and enhances chemoresistance (Lacoste et al., 2014). The mechanism of CENP-A recruitment to DNA breakage sites and the consequent molecular signals required for its residence and dislodgement remains to be elucidated.

## 5 Chromatin organization during senescence

Cellular senescence is a state of dormancy where the cell ceases to divide. Senescence involves shortened telomeres, increased DNA damage, stalled replication, nuclear deformities, mitochondrial dysfunction, and aberrant genome organization (Di Micco et al., 2021). After a somatic cell crosses the Hayflick limit, it reaches replicative senescence because of the end replication problem, i.e., progressive shortening of telomeres with each division cycle due to the inherent inability of DNA polymerases to correctly replicate the cytosine-rich telomere lagging-strand (Hayflick and Moorhead, 1961; Harley et al., 1990). Interestingly, this limit is often bypassed by neoplastic cells, making them immortal (Autexier and Greider, 1996). As aging progresses, the DDR machinery is compromised, predominantly increasing the predisposition to breast, prostate, lung, and colon cancers (Rossi et al., 2007; de Magalhães, 2013). Normally, these functions are tightly regulated, and the activation of oncogenes leads to aberrant replication fork progression, resulting in Oncogene-Induced Senescence (OIS) (Serrano et al., 1997; Di Micco et al., 2006; Rocha et al., 2022). It is noteworthy that cancer cells often evade OIS by altering cellular levels of $p16^{INK4A}$, a cell cycle blocker (McLaughlin-Drubin et al., 2013).

Remarkably, extensive topological changes in chromatin compartmentalization accompany senescence, obfuscating the spatial separation between the A and B compartments. Microscopy and polymer modeling of chromatin reveals that the spatial organization of chromatin compartments is drastically altered in tumor cells. Following this finding, an additional intermediate Compartment I has been proposed that interacts with both A and B compartments in normal tissue and inclines toward the B compartment in cancerous tissue (Johnstone et al., 2020). Cells undergoing OIS show dramatic changes in chromatin architecture, with the formation of Senescence Associated Heterochromatin Foci (SAHF), characteristically enriched with facultative heterochromatic marks such as H3K9me1/2, H3K20me3, along with high-mobility group proteins and non-canonical histones such as mH2A (Narita et al., 2003; Zhang et al., 2007; Nelson et al., 2016). Chromatin polymer modeling suggests that SAHF can mobilize specific loci adjacent to heterochromatic domains in close proximity to each other in the 3D space of the nucleus, enhancing their activity in cell adhesion and cancer-related signaling (Sati et al., 2020). Alongside activating specific genes, the SAHF also affects cell proliferation by epigenetically repressing E2F target genes through the recruitment of pRB and heterochromatin factors (Narita et al., 2003). Moreover, SAHFs are not found in cells going through quiescence (Aird and Zhang, 2013). In agreement with this, the silencing of E2F-responsive elements and the formation of SAHF are characteristic of only irreversibly arrested cells, thus hinting towards an Rb-mediated mechanism for stabilizing the senescent phenotype.

The induction of senescence in cancer cells serves as a traditional therapeutic approach by targeting p53, mTOR, PI3K, and BCL-2 family proteins using senolytic agents (Lee et al., 2010; Muñoz-Espín et al., 2013; Laberge et al., 2015). However, challenges in targeting cancer cells are contributed to by tumor heterogeneity since aged patients have higher numbers of senescent cells, which can lead to fatal off-target effects by senolytic agents (Wang L et al., 2022).

## 6 Perspectives

### 6.1 Effect of lamin mutations on genome organization during cancer progression and senescence

The LADs are parts of chromatin domains that are largely in a state of repression. Surprisingly, the simultaneous loss of all lamin forms in mouse embryonic stem cells did not change the overall TAD structure but reorganized the inter- and intra-TAD interactions, further altering transcriptional

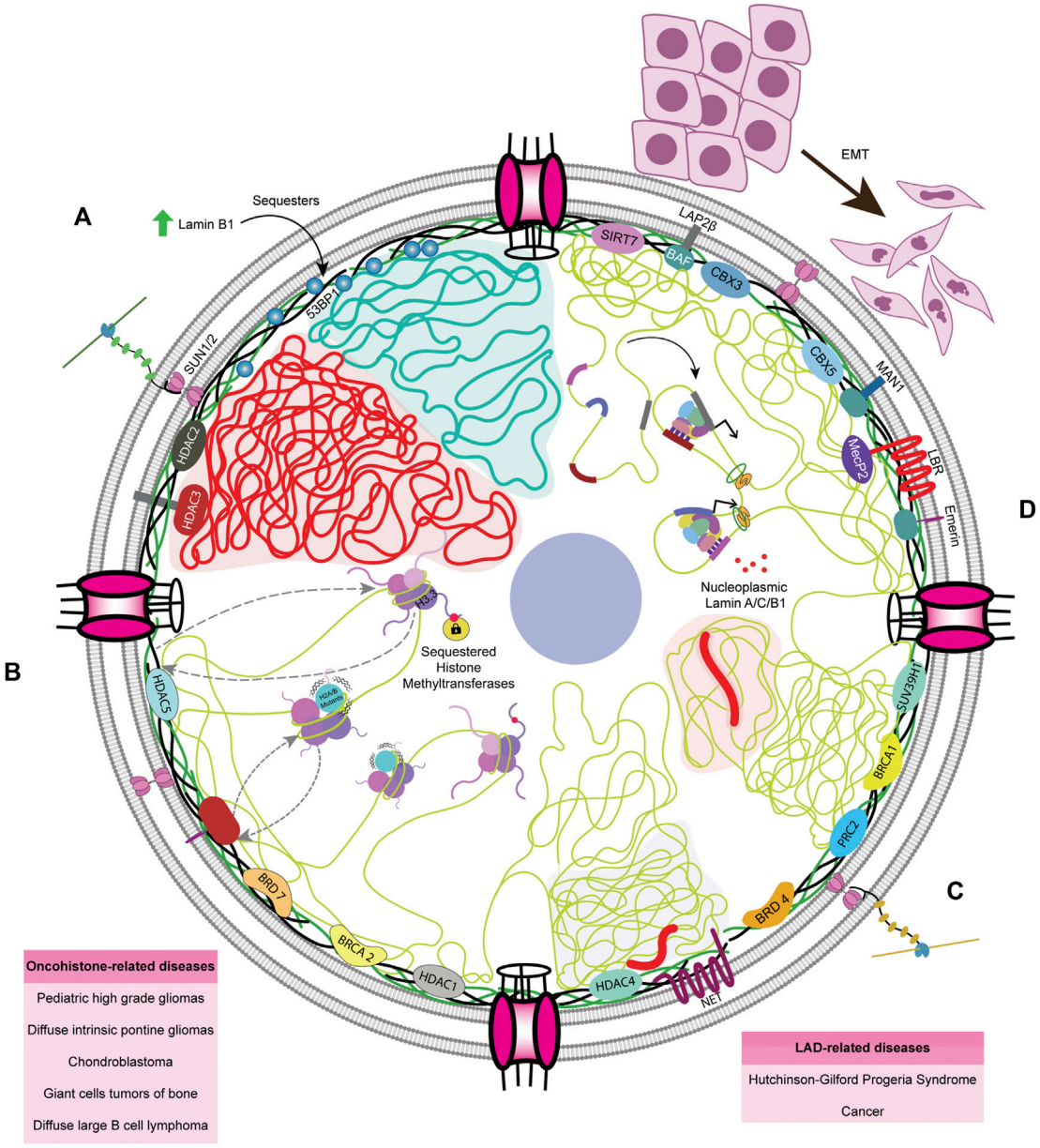


FIGURE 5
Lacunae in the field of genome organization and nuclear envelope **(A)** Lamin B1 is upregulated in most cancers, as per TCGA data, and overexpression of Lamin B1 expression sequesters 53BP1, a major orchestrator of NHEJ pathway. The precise mechanisms as to how cancer cells overcome 53BP1 sequestration is unknown **(B)** Incorporation of both tail and globular domain mutants leads to dysregulated gene expression through various mechanisms, though it remains unclear whether nuclear lamina has any role in either mitigating or worsening it. Globular domain mutations, when associated with the LADs, could be altering the spatial localization of gene loci. **(C)** The nuclear envelope maintains heterochromatin. LADs form a significant portion of the human genome and are regulated by the lamina and its associated complexes, the deregulation of which often leads to HGPS and cancer **(D)** Furthermore, in EMT and cancer progression, phosphorylated lamin A/C and B1 are associated with enhancer sequences, but the role of this association remains to be elucidated.

output (Zheng et al., 2018). It is interesting to note that although lamins are known to organize heterochromatin proximal to the nuclear border, they also modulate the organization of transcriptionally-active euchromatin within the nuclear interior (Pascual-Reguant et al., 2018; Ikegami et al., 2020).

Ovarian cancers harbor homozygous deletion in the LMNB1 gene, while the loss of lamin A/C leads to poor

prognosis and enhanced metastatic potential of cells (Capochichi et al., 2011). In the context of senescence, lamin A/C directly interacts with the telomeric protein TRF2, which facilitates the insertion of 3′ overhangs into telomeric DNA, resulting in T-loop formation that protects the telomere ends and slows cellular senescence in a cell-type specific manner. Mutations in LMNA, like those found in Hutchinson-Gilford progeria syndrome (HGPS), destabilize lamin A/C-TRF2 interaction, further leading to telomere loss and accelerated cellular aging (Wood et al., 2014).

Additionally, TCGA data retrieved from GEPIA2 shows that most of the cancers show upregulated levels of lamin B1. It is known that lamin B1 overexpression sequesters 53BP1, a crucial mediator of the NHEJ pathway (Etourneaud et al., 2021). It remains to be elucidated how a majority of the cancers overexpressing lamin B1 manage to steer the DDR to specific NHEJ pathways (Bouwman et al., 2010) (Figure 5A). Furthermore, lamins repress the activation of mobile transposable elements that trigger chromosomal instability (Andrenacci et al., 2020). During the later stages of cellular aging, the association of lamin with transposable elements declines, coupled with the loss of heterochromatin, leading to aberrant gene expression and type-I interferon response (De Cecco et al., 2019; Cenni et al., 2020). The mechanisms by which chromatin organizers function in cancer cells will facilitate the design of specific small molecule inhibitors.

## 6.2 Interactors of LMNA during cancer progression

Lamin A regulates gene expression by interacting with various chromatin modifiers, the deregulation of which promotes cancers. For instance, lamin A directly interacts with and prevents the proteasomal degradation of SUV39H1, the writer of the H3K9me3 inactive mark (Liu et al., 2013), the dysregulation of which results in HGPS (Figure 5C). Correspondingly, the PcG proteins that deposit the H3K27me3 inactive mark interact with lamins (Cesarini et al., 2015; Marullo et al., 2016). Notably, lamin loss leads to an anomalous distribution of PcG proteins, eventually resulting in dysregulated gene expression and accelerated cancer progression. HDAC2 also plays an active role in heterochromatinization by interacting with LMNA at the nuclear periphery (Mattioli et al., 2018; Santi et al., 2020; Murray-Nerger and Cristea, 2021). However, the molecular mechanisms involving lamin-mediated regulation of inactive H3K9me3 and H3K27me3 and active H3K4me3 marks are yet to be uncovered.

In cancers, chromatin organizers harbor mutations in various domains, resulting in their deregulated activity and altered binding to chromatin or lamins. For instance, sarcomas harbor high-frequency H3.3G34R and H3.3K36M mutations that directly prevent the binding of H3K36me2/3 writer NSD1/2, thus reducing PRC2-H3K36me2 interaction and increasing H3K27me3 levels (Lu et al., 2016). The interaction between SMARCB1 and NSD1 is essential for the deposition of H3K36me2 in the genome, which is a marker for better prognosis in sarcoma. Mutated SMARCB1 is unable to bind to NSD1 but binds to PRC2, leading to an increase in H3K27me3 with poor prognosis in cancer patients (Drosos et al., 2022). Such atypical deposition of inactive histone marks dilutes their occupancy in normally-repressed genes, reorienting the genomic regions localized to the nuclear periphery. As a result, genes typically localized to the nuclear periphery, such as the mesenchymal progenitor genes in the facultative LADs, become de-repressed (Lu et al., 2016). Hence, we surmise a potential crosstalk between the nuclear lamins, chromatin regulators, and oncohistones in the initiation and sustenance of cancer progression.

## 6.3 Crosstalk between the nuclear envelope and oncohistones

The nuclear lamina is primarily associated with inactive histone marks at the nuclear periphery. However, lamins also modulate active euchromatin (Zheng et al., 2018). How the peripheral and nucleoplasmic pools of lamins engage in chromatin dynamics and impinge on the transcriptional regulation mediated by oncohistones such as H3.3K27M/I, H3.3G34W/V/L/R, H3.3K36M, or sH2A is unclear (Figure 5B). In addition, components of the nuclear envelope, namely Nups and LINC complex factors, also participate in chromatin organization. Moreover, lamins are required for chromatin organization, although their potential role in the incorporation of oncohistones by chaperones remains unclear (Figure 5B). The extent of lamin A/C phosphorylation correlates with lamin A/C levels in the DU145 prostate cancer cell line, though this remains to be verified experimentally across cancers (Kong et al., 2012). Phosphorylated lamin A/C and unphosphorylated, probably nucleoplasmic lamin B1, associate with active enhancers and transcribing genes, respectively, which contradicts the conventional function of LADs in gene repression (Guelen et al., 2008; Ikegami et al., 2020). However, the exact role of phosphorylated Lamin A/C in modulating enhancer regions remains an enigma. In addition, the association of lamin B1 with eLADs and higher expression of fibronectin, vimentin, and twist highlight the role of lamin B1 in metastasis (Pascual-Reguant et al., 2018), although its exact purpose of lamin B1 in compartment A remains to be elucidated (Figure 5D). Interestingly, lamin B1 has been shown to localize to the TAD borders of eLADs, opening the possibility of its interaction with border elements such as CTCF and cohesin.

## 7 Conclusion

In summary, it is beyond any doubt that genetic mutations, aberrations in chromatin organization, incorporation of oncohistones, deregulated transcription, and defects in nuclear envelope organization and function collectively deregulate the cellular and molecular processes of cancers. Novel therapeutic targets will be identified by leveraging high-resolution single-cell approaches, such as sc-ChIP-seq, sc-ATAC-seq, and sc-Hi-C, with high-content imaging, including high-resolution FISH. Furthermore, molecular and biochemical assays remain the mainstay for the elucidation of molecular mechanisms. Collectively, these lines of evidence reveal that aberrant genome architecture serves as a precursor and promoter of cancer initiation and progression.

## Author contributions

AKB, SS, SD, DP, and KS wrote the manuscript. SS, SD, and DP prepared the illustrations.

## Funding

We gratefully acknowledge support from Science & Engineering Board (SERB), Grant#CRG/2020/002563 and intramural funding support from IISER-Pune.

## Conflict of interest

The authors declare that the research was conducted in the absence of any commercial or financial relationships that could be construed as a potential conflict of interest.

## Publisher's note

All claims expressed in this article are solely those of the authors and do not necessarily represent those of their affiliated organizations, or those of the publisher, the editors and the reviewers. Any product that may be evaluated in this article, or claim that may be made by its manufacturer, is not guaranteed or endorsed by the publisher.

## References

Adane, B., Alexe, G., Seong, B. K. A., Lu, D., Hwang, E. E., Hnisz, D., et al. (2021). STAG2 loss rewires oncogenic and developmental programs to promote metastasis in Ewing sarcoma. *Cancer Cell* 39, 827–844. e10. doi:10.1016/j.ccell.2021.05.007

Aebi, U., Cohn, J., Buhle, L., and Gerace, L. (1986). The nuclear lamina is a meshwork of intermediate-type filaments. *Nature* 323, 560–564. doi:10.1038/323560a0

Aird, K. M., and Zhang, R. (2013). Detection of senescence-associated heterochromatin foci (SAHF). *Methods Mol. Biol.* 965, 185–196. doi:10.1007/978-1-62703-239-1_12

Akdemir, K. C., Le, V. T., Chandran, S., Li, Y., Verhaak, R. G., Beroukhim, R., et al. (2020). PCAWG Structural Variation Working Group, PCAWG ConsortiumDisruption of chromatin folding domains by somatic genomic rearrangements in human cancer. *Nat. Genet.* 52, 294–305. doi:10.1038/s41588-019-0564-y

Alcobia, I., Dilão, R., and Parreira, L. (2000). Spatial associations of centromeres in the nuclei of hematopoietic cells: Evidence for cell-type-specific organizational patterns. *Blood* 95, 1608–1615. doi:10.1182/blood.V95.5.1608.005k32_1608_1615

Amankwaa, B., Schoborg, T., and Labrador, M. (2022). <i>Drosophila</i> insulator proteins exhibit *in vivo* liquid-liquid phase separation properties. *Life Sci. Alliance* 5, e202201536. doi:10.26508/lsa.202201536

Amin, R., Shukla, A., Zhu, J. J., Kim, S., Wang, P., Tian, S. Z., et al. (2021). Nuclear pore protein NUP210 depletion suppresses metastasis through heterochromatin-mediated disruption of tumor cell mechanical response. *Nat. Commun.* 12, 7216. doi:10.1038/s41467-021-27451-w

Andrenacci, D., Cavaliere, V., and Lattanzi, G. (2020). The role of transposable elements activity in aging and their possible involvement in laminopathic diseases. *Ageing Res. Rev.* 57, 100995. doi:10.1016/j.arr.2019.100995

Andronov, L., Ouararhni, K., Stoll, I., Klaholz, B. P., and Hamiche, A. (2019). CENP-A nucleosome clusters form rosette-like structures around HJURP during G1. *Nat. Commun.* 10, 4436. doi:10.1038/s41467-019-12383-3

Antony, J., Chin, C. V., and Horsfield, J. A. (2021). Cohesin mutations in cancer: Emerging therapeutic targets. *Int. J. Mol. Sci.* 22, 6788. doi:10.3390/ijms22136788

Autexier, C., and Greider, C. W. (1996). Telomerase and cancer: Revisiting the telomere hypothesis. *Trends biochem. Sci.* 21, 387–391. doi:10.1016/S0968-0004(96)10042-6

Ávila-López, P. A., Guerrero, G., Nuñez-Martínez, H. N., Peralta-Alvarez, C. A., Hernández-Montes, G., Álvarez-Hilario, L. G., et al. (2021). H2A.Z overexpression suppresses senescence and chemosensitivity in pancreatic ductal adenocarcinoma. *Oncogene* 40, 2065–2080. doi:10.1038/s41388-021-01664-1

Baergen, A. K., Jeusset, L. M., Lichtensztejn, Z., and McManus, K. J. (2019). Diminished condensin gene expression drives chromosome instability that may contribute to colorectal cancer pathogenesis. *Cancers (Basel)* 11, 1066. doi:10.3390/cancers11081066

Bagert, J. D., Mitchener, M. M., Patriotis, A. L., Dul, B. E., Wojcik, F., Nacev, B. A., et al. (2021). Oncohistone mutations enhance chromatin remodeling and alter cell fates. *Nat. Chem. Biol.* 17, 403–411. doi:10.1038/s41589-021-00738-1

Bailey, C. G., Gupta, S., Metierre, C., Amarasekera, P. M. S., O'Young, P., Kyaw, W., et al. (2021). Structure-function relationships explain CTCF zinc finger mutation phenotypes in cancer. *Cell. Mol. Life Sci.* 78, 7519–7536. doi:10.1007/s00018-021-03946-z

Bakhoum, S. F., Ngo, B., Laughney, A. M., Cavallo, J.-A., Murphy, C. J., Ly, P., et al. (2018). Chromosomal instability drives metastasis through a cytosolic DNA response. *Nature* 553, 467–472. doi:10.1038/nature25432

Barnhart, M. C., Kuich, P. H. J. L., Stellfox, M. E., Ward, J. A., Bassett, E. A., Black, B. E., et al. (2011). HJURP is a CENP-A chromatin assembly factor sufficient to form a functional de novo kinetochore. *J. Cell Biol.* 194, 229–243. doi:10.1083/jcb.201012017

Barrington, C., Georgopoulou, D., Pezic, D., Varsally, W., Herrero, J., and Hadjur, S. (2019). Enhancer accessibility and CTCF occupancy underlie asymmetric TAD architecture and cell type specific genome topology. *Nat. Commun.* 10, 2908. doi:10.1038/s41467-019-10725-9

Baumann, K. (2016). Nuclear organization: NUP-Tial binding to super-enhancers. *Nat. Rev. Mol. Cell Biol.* 17, 738–739. doi:10.1038/nrm.2016.158

Bell, E. S., Shah, P., Zuela-Sopilniak, N., Kim, D., Varlet, A.-A., Morival, J. L. P., et al. (2022). Low lamin A levels enhance confined cell migration and metastatic capacity in breast cancer. *Oncogene* 41, 4211–4230. doi:10.1038/s41388-022-02420-9

Benhra, N., Barrio, L., Muzzopappa, M., and Milán, M. (2018). Chromosomal instability induces cellular invasion in epithelial tissues. *Dev. Cell* 47, 161–174. doi:10.1016/j.devcel.2018.08.021

Bianchi, A., Mozzetta, C., Pegoli, G., Lucini, F., Valsoni, S., Rosti, V., et al. (2020). Dysfunctional polycomb transcriptional repression contributes to lamin A/C-dependent muscular dystrophy. *J. Clin. Invest.* 130, 2408–2421. doi:10.1172/JCI128161

Bjerke, L., Mackay, A., Nandhabalan, M., Burford, A., Jury, A., Popov, S., et al. (2013). Histone H3.3. mutations drive pediatric glioblastoma through upregulation of MYCN. *Cancer Discov.* 3, 512–519. doi:10.1158/2159-8290.CD-12-0426

Bloom, K. S. (2014). Centromeric heterochromatin: The primordial segregation machine. *Annu. Rev. Genet.* 48, 457–484. doi:10.1146/annurev-genet-120213-092033

Bočkaj, I., Martini, T. E. I., de Camargo Magalhães, E. S., Bakker, P. L., Meeuwsen-de Boer, T. G. J., Armandari, I., et al. (2021). The H3.3K27M oncohistone affects replication stress outcome and provokes genomic instability in pediatric glioma. *PLoS Genet.* 17, e1009868. doi:10.1371/journal.pgen.1009868

Bönisch, C., Schneider, K., Pünzeler, S., Wiedemann, S. M., Bielmeier, C., Bocola, M., et al. (2012). H2A.Z.2.2 is an alternatively spliced histone H2A.Z variant that causes severe nucleosome destabilization. *Nucleic Acids Res.* 40, 5951–5964. doi:10.1093/nar/gks267

Bouwman, P., Aly, A., Escandell, J. M., Pieterse, M., Bartkova, J., van der Gulden, H., et al. (2010). 53BP1 loss rescues BRCA1 deficiency and is associated with triple-negative and BRCA-mutated breast cancers. *Nat. Struct. Mol. Biol.* 17, 688–695. doi:10.1038/nsmb.1831

Bronshtein, I., Kepten, E., Kanter, I., Berezin, S., Lindner, M., Redwood, A. B., et al. (2015). Loss of lamin A function increases chromatin dynamics in the nuclear interior. *Nat. Commun.* 6, 8044. doi:10.1038/ncomms9044

Buschbeck, M., and Hake, S. B. (2017). Variants of core histones and their roles in cell fate decisions, development and cancer. *Nat. Rev. Mol. Cell Biol.* 18, 299–314. doi:10.1038/nrm.2016.166

Capo-chichi, C. D., Cai, K. Q., Simpkins, F., Ganjei-Azar, P., Godwin, A. K., and Xu, X.-X. (2011). Nuclear envelope structural defects cause chromosomal numerical instability and aneuploidy in ovarian cancer. *BMC Med.* 9, 28. doi:10.1186/1741-7015-9-28

Capo-Chichi, C. D., Yeasky, T. M., Smith, E. R., and Xu, X.-X. (2016). Nuclear envelope structural defect underlies the main cause of aneuploidy in ovarian carcinogenesis. *BMC Cell Biol.* 17, 37. doi:10.1186/s12860-016-0114-8

Celeste, A., Petersen, S., Romanienko, P. J., Fernandez-Capetillo, O., Chen, H. T., Sedelnikova, O. A., et al. (2002). Genomic instability in mice lacking histone H2AX. *Science* 296, 922–927. doi:10.1126/science.1069398

Cenni, V., Capanni, C., Mattioli, E., Schena, E., Squarzoni, S., Bacalini, M. G., et al. (2020). Lamin A involvement in ageing processes. *Ageing Res. Rev.* 62, 101073. doi:10.1016/j.arr.2020.101073

Cerami, E., Gao, J., Dogrusoz, U., Gross, B. E., Sumer, S. O., Aksoy, B. A., et al. (2012). The cBio cancer genomics portal: An open platform for exploring multidimensional cancer genomics data. *Cancer Discov.* 2, 401–404. doi:10.1158/2159-8290.CD-12-0095

Cesarini, E., Mozzetta, C., Marullo, F., Gregoretti, F., Gargiulo, A., Columbaro, M., et al. (2015). Lamin A/C sustains PcG protein architecture, maintaining transcriptional repression at target genes. *J. Cell Biol.* 211, 533–551. doi:10.1083/jcb.201504035

Chadwick, B. P., Valley, C. M., and Willard, H. F. (2001). Histone variant macroH2A contains two distinct macrochromatin domains capable of directing macroH2A to the inactive X chromosome. *Nucleic Acids Res.* 29, 2699–2705. doi:10.1093/nar/29.13.2699

Chan, K.-M., Fang, D., Gan, H., Hashizume, R., Yu, C., Schroeder, M., et al. (2013). The histone H3.3K27M mutation in pediatric glioma reprograms H3K27 methylation and gene expression. *Genes Dev.* 27, 985–990. doi:10.1101/gad.217778.113

Chen, G. K., Chang, X., Curtis, C., and Wang, K. (2013). Precise inference of copy number alterations in tumor samples from SNP arrays. *Bioinformatics* 29, 2964–2970. doi:10.1093/bioinformatics/btt521

Chen, H., Tian, Y., Shu, W., Bo, X., and Wang, S. (2012). Comprehensive identification and annotation of cell type-specific and ubiquitous CTCF-binding sites in the human genome. *PLoS ONE* 7, e41374. doi:10.1371/journal.pone.0041374

Chetverina, D., Fujioka, M., Erokhin, M., Georgiev, P., Jaynes, J. B., and Schedl, P. (2017). Boundaries of loop domains (insulators): Determinants of chromosome form and function in multicellular eukaryotes. *BioEssays* 39 (3), 1600233. doi:10.1002/bies.201600233

Chew, G.-L., Bleakley, M., Bradley, R. K., Malik, H. S., Henikoff, S., Molaro, A., et al. (2021). Short H2A histone variants are expressed in cancer. *Nat. Commun.* 12, 490. doi:10.1038/s41467-020-20707-x

Cohen, S., Etingov, I., and Panté, N. (2012). Effect of viral infection on the nuclear envelope and nuclear pore complex. *Int. Rev. Cell Mol. Biol.* 299, 117–159. doi:10.1016/B978-0-12-394310-1.00003-5

Coschi, C. H., Ishak, C. A., Gallo, D., Marshall, A., Talluri, S., Wang, J., et al. (2014). Haploinsufficiency of an RB-E2F1-Condensin II complex leads to aberrant replication and aneuploidy. *Cancer Discov.* 4, 840–853. doi:10.1158/2159-8290.CD-14-0215

Cremer, T., and Cremer, C. (2001). Chromosome territories, nuclear architecture and gene regulation in mammalian cells. *Nat. Rev. Genet.* 2, 292–301. doi:10.1038/35066075

Cronshaw, J. M., Krutchinsky, A. N., Zhang, W., Chait, B. T., and Matunis, M. J. (2002). Proteomic analysis of the mammalian nuclear pore complex. *J. Cell Biol.* 158, 915–927. doi:10.1083/jcb.200206106

Damaschke, N. A., Gawdzik, J., Avilla, M., Yang, B., Svaren, J., Roopra, A., et al. (2020). CTCF loss mediates unique DNA hypermethylation landscapes in human cancers. *Clin. Epigenetics* 12, 80. doi:10.1186/s13148-020-00869-7

D'Angelo, M. A., Gomez-Cavazos, J. S., Mei, A., Lackner, D. H., and Hetzer, M. W. (2012). A change in nuclear pore complex composition regulates cell differentiation. *Dev. Cell* 22, 446–458. doi:10.1016/j.devcel.2011.11.021

Davis, L., Rayi, P. R., Getselter, D., Kaphzan, H., and Elliott, E. (2022). CTCF in parvalbumin-expressing neurons regulates motor, anxiety and social behavior and neuronal identity. *Mol. Brain* 15, 30. doi:10.1186/s13041-022-00916-9

De Cecco, M., Ito, T., Petrashen, A. P., Elias, A. E., Skvir, N. J., Criscione, S. W., et al. (2019). L1 drives IFN in senescent cells and promotes age-associated inflammation. *Nature* 566, 73–78. doi:10.1038/s41586-018-0784-9

de Magalhães, J. P. (2013). How ageing processes influence cancer. *Nat. Rev. Cancer* 13, 357–365. doi:10.1038/nrc3497

Debaugny, R. E., and Skok, J. A. (2020). CTCF and CTCFL in cancer. *Curr. Opin. Genet. Dev.* 61, 44–52. doi:10.1016/j.gde.2020.02.021

Dechat, T., Adam, S. A., Taimen, P., Shimi, T., and Goldman, R. D. (2010). Nuclear lamins. *Cold Spring Harb. Perspect. Biol.* 2, a000547. doi:10.1101/cshperspect.a000547

Dechat, T., Shimi, T., Adam, S. A., Rusinol, A. E., Andres, D. A., Spielmann, H. P., et al. (2007). Alterations in mitosis and cell cycle progression caused by a mutant lamin A known to accelerate human aging. *Proc. Natl. Acad. Sci. U. S. A.* 104, 4955–4960. doi:10.1073/pnas.0700854104

Demmerle, J., Koch, A. J., and Holaska, J. M. (2012). The nuclear envelope protein emerin binds directly to histone deacetylase 3 (HDAC3) and activates HDAC3 activity. *J. Biol. Chem.* 287, 22080–22088. doi:10.1074/jbc.M111.325308

Di Micco, R., Fumagalli, M., Cicalese, A., Piccinin, S., Gasparini, P., Luise, C., et al. (2006). Oncogene-induced senescence is a DNA damage response triggered by DNA hyper-replication. *Nature* 444, 638–642. doi:10.1038/nature05327

Di Micco, R., Krizhanovsky, V., Baker, D., and d'Adda di Fagagna, F. (2021). Cellular senescence in ageing: From mechanisms to therapeutic opportunities. *Nat. Rev. Mol. Cell Biol.* 22, 75–95. doi:10.1038/s41580-020-00314-w

Dixon, J. R., Selvaraj, S., Yue, F., Kim, A., Li, Y., Shen, Y., et al. (2012). Topological domains in mammalian genomes identified by analysis of chromatin interactions. *Nature* 485, 376–380. doi:10.1038/nature11082

Drosos, Y., Myers, J. A., Xu, B., Mathias, K. M., Beane, E. C., Radko-Juettner, S., et al. (2022). NSD1 mediates antagonism between SWI/SNF and polycomb complexes and is required for transcriptional activation upon EZH2 inhibition. *Mol. Cell* 82, 2472–2489. e8. doi:10.1016/j.molcel.2022.04.015

Dubińska-Magiera, M., Kozioł, K., Machowska, M., Piekarowicz, K., Filipczak, D., and Rzepecki, R. (2019). Emerin is required for proper nucleus reassembly after mitosis: Implications for new pathogenetic mechanisms for laminopathies detected in EDMD1 patients. *Cells* 8, 1. doi:10.3390/cells8030240

Earle, A. J., Kirby, T. J., Fedorchak, G. R., Isermann, P., Patel, J., Iruvanti, S., et al. (2020). Mutant lamins cause nuclear envelope rupture and DNA damage in skeletal muscle cells. *Nat. Mat.* 19, 464–473. doi:10.1038/s41563-019-0563-5

Ebrahimi, H., Masuda, H., Jain, D., and Cooper, J. P. (2018). Distinct "safe zones" at the nuclear envelope ensure robust replication of heterochromatic chromosome regions. *eLife* 7, e32911. doi:10.7554/eLife.32911

Eldholm, V., Haugen, A., and Zienolddiny, S. (2014). CTCF mediates the TERT enhancer-promoter interactions in lung cancer cells: Identification of a novel enhancer region involved in the regulation of TERT gene. *Int. J. Cancer* 134, 2305–2313. doi:10.1002/ijc.28570

Etourneaud, L., Moussa, A., Rass, E., Genet, D., Willaume, S., Chabance-Okumura, C., et al. (2021). Lamin B1 sequesters 53BP1 to control its recruitment to DNA damage. *Sci. Adv.* 7, eabb3799. doi:10.1126/sciadv.abb3799

Fang, D., Gan, H., Lee, J.-H., Han, J., Wang, Z., Riester, S. M., et al. (2016). The histone H3.3K36M mutation reprograms the epigenome of chondroblastomas. *Science* 352, 1344–1348. doi:10.1126/science.aae0065

Fischer, E. G. (2020). Nuclear morphology and the biology of cancer cells. *Acta Cytol.* 64, 511–519. doi:10.1159/000508780

Flavahan, W. A., Drier, Y., Liau, B. B., Gillespie, S. M., Venteicher, A. S., Stemmer-Rachamimov, A. O., et al. (2016). Insulator dysfunction and oncogene activation in IDH mutant gliomas. *Nature* 529, 110–114. doi:10.1038/nature16490

Folco, H. D., Pidoux, A. L., Urano, T., and Allshire, R. C. (2008). Heterochromatin and RNAi are required to establish CENP-A chromatin at centromeres. *Science* 319, 94–97. doi:10.1126/science.1150944

Fudenberg, G., Imakaev, M., Lu, C., Goloborodko, A., Abdennur, N., and Mirny, L. A. (2016). Formation of chromosomal domains by loop extrusion. *Cell Rep.* 15, 2038–2049. doi:10.1016/j.celrep.2016.04.085

Gao, J., Aksoy, B. A., Dogrusoz, U., Dresdner, G., Gross, B., Sumer, S. O., et al. (2013). Integrative analysis of complex cancer genomics and clinical profiles using the cBioPortal. *Sci. Signal.* 6, pl1. doi:10.1126/scisignal.2004088

Gdula, M. R., Poterlowicz, K., Mardaryev, A. N., Sharov, A. A., Peng, Y., Fessing, M. Y., et al. (2013). Remodeling of three-dimensional organization of the nucleus during terminal keratinocyte differentiation in the epidermis. *J. Invest. Dermatol.* 133, 2191–2201. doi:10.1038/jid.2013.66

Gimpel, P., Lee, Y. L., Sobota, R. M., Calvi, A., Koullourou, V., Patel, R., et al. (2017). Nesprin-1α-Dependent microtubule nucleation from the nuclear envelope via Akap450 is necessary for nuclear positioning in muscle cells. *Curr. Biol.* 27, 2999–3009. doi:10.1016/j.cub.2017.08.031

Goldberg, A. D., Banaszynski, L. A., Noh, K.-M., Lewis, P. W., Elsaesser, S. J., Stadler, S., et al. (2010). Distinct factors control histone variant H3.3 localization at specific genomic regions. *Cell* 140, 678–691. doi:10.1016/j.cell.2010.01.003

González-Romero, R., Méndez, J., Ausió, J., and Eirín-López, J. M. (2008). Quickly evolving histones, nucleosome stability and chromatin folding: All about histone H2A.Bbd. *Gene* 413, 1–7. doi:10.1016/j.gene.2008.02.003

Gough, S. M., Slape, C. I., and Aplan, P. D. (2011). NUP98 gene fusions and hematopoietic malignancies: Common themes and new biologic insights. *Blood* 118, 6247–6257. doi:10.1182/blood-2011-07-328880

Gruenbaum, Y., and Foisner, R. (2015). Lamins: Nuclear intermediate filament proteins with fundamental functions in nuclear mechanics and genome regulation. *Annu. Rev. Biochem.* 84, 131–164. doi:10.1146/annurev-biochem-060614-034115

Guelen, L., Pagie, L., Brasset, E., Meuleman, W., Faza, M. B., Talhout, W., et al. (2008). Domain organization of human chromosomes revealed by mapping of nuclear lamina interactions. *Nature* 453, 948–951. doi:10.1038/nature06947

Gulve, N., Su, C., Deng, Z., Soldan, S. S., Vladimirova, O., Wickramasinghe, J., et al. (2022). DAXX-ATRX regulation of p53 chromatin binding and DNA damage response. *Nat. Commun.* 13, 5033. doi:10.1038/s41467-022-32680-8

Guo, Y. A., Chang, M. M., Huang, W., Ooi, W. F., Xing, M., Tan, P., et al. (2018). Mutation hotspots at CTCF binding sites coupled to chromosomal instability in gastrointestinal cancers. *Nat. Commun.* 9, 1520. doi:10.1038/s41467-018-03828-2

Ha, M., Kraushaar, D. C., and Zhao, K. (2014). Genome-wide analysis of H3.3 dissociation reveals high nucleosome turnover at distal regulatory regions of embryonic stem cells. *Epigenetics Chromatin* 7, 38. doi:10.1186/1756-8935-7-38

Haaf, T., and Schmid, M. (1991). Chromosome topology in mammalian interphase nuclei. *Exp. Cell Res.* 192, 325–332. doi:10.1016/0014-4827(91)90048-y

Hanssen, L. L. P., Kassouf, M. T., Oudelaar, A. M., Biggs, D., Preece, C., Downes, D. J., et al. (2017). Tissue-specific CTCF-cohesin-mediated chromatin architecture delimits enhancer interactions and function *in vivo*. *Nat. Cell Biol.* 19, 952–961. doi:10.1038/ncb3573

Harley, C. B., Futcher, A. B., and Greider, C. W. (1990). Telomeres shorten during ageing of human fibroblasts. *Nature* 345, 458–460. doi:10.1038/345458a0

Harr, J. C., Luperchio, T. R., Wong, X., Cohen, E., Wheelan, S. J., and Reddy, K. L. (2015). Directed targeting of chromatin to the nuclear lamina is mediated by chromatin state and A-type lamins. *J. Cell Biol.* 208, 33–52. doi:10.1083/jcb.201405110

Hayflick, L., and Moorhead, P. S. (1961). The serial cultivation of human diploid cell strains. *Exp. Cell Res.* 25, 585–621. doi:10.1016/0014-4827(61)90192-6

Heaphy, C. M., de Wilde, R. F., Jiao, Y., Klein, A. P., Edil, B. H., Shi, C., et al. (2011). Altered telomeres in tumors with ATRX and DAXX mutations. *Science* 333, 425. doi:10.1126/science.1207313

Henikoff, S., and Smith, M. M. (2015). Histone variants and epigenetics. *Cold Spring Harb. Perspect. Biol.* 7, a019364. doi:10.1101/cshperspect.a019364

Höflmayer, D., Steinhoff, A., Hube-Magg, C., Kluth, M., Simon, R., Burandt, E., et al. (2020). Expression of CCCTC-binding factor (CTCF) is linked to poor prognosis in prostate cancer. *Mol. Oncol.* 14, 129–138. doi:10.1002/1878-0261.12597

Holaska, J. M., and Wilson, K. L. (2007). An emerin "proteome": Purification of distinct emerin-containing complexes from HeLa cells suggests molecular basis for diverse roles including gene regulation, mRNA splicing, signaling, mechanosensing, and nuclear architecture. *Biochemistry* 46, 8897–8908. doi:10.1021/bi602636m

Holland, A. J., and Cleveland, D. W. (2012). Losing balance: The origin and impact of aneuploidy in cancer. *EMBO Rep.* 13, 501–514. doi:10.1038/embor.2012.55

Holwerda, S. J. B., and de Laat, W. (2013). Ctcf: The protein, the binding partners, the binding sites and their chromatin loops. *Philos. Trans. R. Soc. Lond. B Biol. Sci.* 368, 20120369. doi:10.1098/rstb.2012.0369

Hua, S., Kallen, C. B., Dhar, R., Baquero, M. T., Mason, C. E., Russell, B. A., et al. (2008). Genomic analysis of estrogen cascade reveals histone variant H2A.Z associated with breast cancer progression. *Mol. Syst. Biol.* 4, 188. doi:10.1038/msb.2008.25

Ibarra, A., Benner, C., Tyagi, S., Cool, J., and Hetzer, M. W. (2016). Nucleoporin-mediated regulation of cell identity genes. *Genes Dev.* 30, 2253–2258. doi:10.1101/gad.287417.116

Iglesias, N., Paulo, J. A., Tatarakis, A., Wang, X., Edwards, A. L., Bhanu, N. V., et al. (2020). Native chromatin proteomics reveals a role for specific nucleoporins in heterochromatin organization and maintenance. *Mol. Cell* 77, 51–66. e8. doi:10.1016/j.molcel.2019.10.018

Ikegami, K., Secchia, S., Almakki, O., Lieb, J. D., and Moskowitz, I. P. (2020). Phosphorylated lamin A/C in the nuclear interior binds active enhancers associated with abnormal transcription in progeria. *Dev. Cell* 52, 699–713. doi:10.1016/j.devcel.2020.02.011

Jha, D. K., and Strahl, B. D. (2014). An RNA polymerase II-coupled function for histone H3K36 methylation in checkpoint activation and DSB repair. *Nat. Commun.* 5, 3965. doi:10.1038/ncomms4965

Jin, C., Zang, C., Wei, G., Cui, K., Peng, W., Zhao, K., et al. (2009). H3.3/H2A.Z double variant-containing nucleosomes mark "nucleosome-free regions" of active promoters and other regulatory regions. *Nat. Genet.* 41, 941–945. doi:10.1038/ng.409

Johnstone, S. E., Reyes, A., Qi, Y., Adriaens, C., Hegazi, E., Pelka, K., et al. (2020). Large-scale topological changes restrain malignant progression in colorectal cancer. *Cell* 182, 1474–1489. doi:10.1016/j.cell.2020.07.030

Kadota, S., Ou, J., Shi, Y., Lee, J. T., Sun, J., and Yildirim, E. (2020). Nucleoporin 153 links nuclear pore complex to chromatin architecture by mediating CTCF and cohesin binding. *Nat. Commun.* 11, 2606. doi:10.1038/s41467-020-16394-3

Kemp, C. J., Moore, J. M., Moser, R., Bernard, B., Teater, M., Smith, L. E., et al. (2014). CTCF haploinsufficiency destabilizes DNA methylation and predisposes to cancer. *Cell Rep.* 7, 1020–1029. doi:10.1016/j.celrep.2014.04.004

Ketema, M., Kreft, M., Secades, P., Janssen, H., and Sonnenberg, A. (2013). Nesprin-3 connects plectin and vimentin to the nuclear envelope of Sertoli cells but is not required for Sertoli cell function in spermatogenesis. *Mol. Biol. Cell* 24, 2454–2466. doi:10.1091/mbc.E13-02-0100

Kim, J. H., Youn, Y., Kim, K.-T., Jang, G., and Hwang, J.-H. (2019). Non-SMC condensin I complex subunit H mediates mature chromosome condensation and DNA damage in pancreatic cancer cells. *Sci. Rep.* 9, 17889. doi:10.1038/s41598-019-54478-3

Kim, S.-Y., Rhee, J. G., Song, X., Prochownik, E. V., Spitz, D. R., and Lee, Y. J. (2012). Breast cancer stem cell-like cells are more sensitive to ionizing radiation than non-stem cells: Role of ATM. *PLoS ONE* 7, e50423. doi:10.1371/journal.pone.0050423

Kimura, H. (2013). Histone modifications for human epigenome analysis. *J. Hum. Genet.* 58, 439–445. doi:10.1038/jhg.2013.66

Kohestani, H., and Wereszczynski, J. (2021). Effects of H2A.B incorporation on nucleosome structures and dynamics. *Biophys. J.* 120, 1498–1509. doi:10.1016/j.bpj.2021.01.036

Kojic, A., Cuadrado, A., De Koninck, M., Giménez-Llorente, D., Rodríguez-Corsino, M., Gómez-López, G., et al. (2018). Distinct roles of cohesin-SA1 and cohesin-SA2 in 3D chromosome organization. *Nat. Struct. Mol. Biol.* 25, 496–504. doi:10.1038/s41594-018-0070-4

Kong, L., Schäfer, G., Bu, H., Zhang, Y., Zhang, Y., and Klocker, H. (2012). Lamin A/C protein is overexpressed in tissue-invading prostate cancer and promotes prostate cancer cell growth, migration and invasion through the PI3K/AKT/PTEN pathway. *Carcinogenesis* 33, 751–759. doi:10.1093/carcin/bgs022

Kops, G. J. P. L., Foltz, D. R., and Cleveland, D. W. (2004). Lethality to human cancer cells through massive chromosome loss by inhibition of the mitotic checkpoint. *Proc. Natl. Acad. Sci. U. S. A.* 101, 8699–8704. doi:10.1073/pnas.0401142101

Kuga, T., Nie, H., Kazami, T., Satoh, M., Matsushita, K., Nomura, F., et al. (2014). Lamin B2 prevents chromosome instability by ensuring proper mitotic chromosome segregation. *Oncogenesis* 3, e94. doi:10.1038/oncsis.2014.6

Labade, A. S., Karmodiya, K., and Sengupta, K. (2016). HOXA repression is mediated by nucleoporin Nup93 assisted by its interactors Nup188 and Nup205. *Epigenetics Chromatin* 9, 54. doi:10.1186/s13072-016-0106-0

Labade, A. S., Salvi, A., Kar, S., Karmodiya, K., and Sengupta, K. (2021). Nup93 and CTCF modulate spatiotemporal dynamics and function of the HOXA gene locus during differentiation. *J. Cell Sci.* 134, jcs259307. doi:10.1242/jcs.259307

Laberge, R.-M., Sun, Y., Orjalo, A. V., Patil, C. K., Freund, A., Zhou, L., et al. (2015). MTOR regulates the pro-tumorigenic senescence-associated secretory

phenotype by promoting IL1A translation. *Nat. Cell Biol.* 17, 1049–1061. doi:10.1038/ncb3195

Lacoste, N., Woolfe, A., Tachiwana, H., Garea, A. V., Barth, T., Cantaloube, S., et al. (2014). Mislocalization of the centromeric histone variant CenH3/CENP-A in human cells depends on the chaperone DAXX. *Mol. Cell* 53, 631–644. doi:10.1016/j.molcel.2014.01.018

Lammerding, J., Fong, L. G., Ji, J. Y., Reue, K., Stewart, C. L., Young, S. G., et al. (2006). Lamins A and C but not lamin B1 regulate nuclear mechanics. *J. Biol. Chem.* 281, 25768–25780. doi:10.1074/jbc.M513511200

Larson, J. D., Kasper, L. H., Paugh, B. S., Jin, H., Wu, G., Kwon, C.-H., et al. (2019). Histone H3.3 K27M accelerates spontaneous brainstem glioma and drives restricted changes in bivalent gene expression. *Cancer Cell* 35, 140–155. doi:10.1016/j.ccell.2018.11.015

Lawrence, K. S., Chau, T., and Engebrecht, J. (2015). DNA damage response and spindle assembly checkpoint function throughout the cell cycle to ensure genomic integrity. *PLoS Genet.* 11, e1005150. doi:10.1371/journal.pgen.1005150

Lawrence, M. S., Stojanov, P., Mermel, C. H., Robinson, J. T., Garraway, L. A., Golub, T. R., et al. (2014). Discovery and saturation analysis of cancer genes across 21 tumour types. *Nature* 505, 495–501. doi:10.1038/nature12912

Lee, J. J., Lee, J. H., Ko, Y. G., Hong, S. I., and Lee, J. S. (2010). Prevention of premature senescence requires JNK regulation of Bcl-2 and reactive oxygen species. *Oncogene* 29, 561–575. doi:10.1038/onc.2009.355

Leeke, B., Marsman, J., O'Sullivan, J. M., and Horsfield, J. A. (2014). Cohesin mutations in myeloid malignancies: Underlying mechanisms. *Exp. Hematol. Oncol.* 3, 13. doi:10.1186/2162-3619-3-13

Lewis, P. W., Elsaesser, S. J., Noh, K.-M., Stadler, S. C., and Allis, C. D. (2010). Daxx is an H3.3-specific histone chaperone and cooperates with ATRX in replication-independent chromatin assembly at telomeres. *Proc. Natl. Acad. Sci. U. S. A.* 107, 14075–14080. doi:10.1073/pnas.1008850107

Leylek, T. R., Jeusset, L. M., Lichtensztejn, Z., and McManus, K. J. (2020). Reduced expression of genes regulating cohesion induces chromosome instability that may promote cancer and impact patient outcomes. *Sci. Rep.* 10, 592. doi:10.1038/s41598-020-57530-9

Li, W., Hu, Y., Oh, S., Ma, Q., Merkurjev, D., Song, X., et al. (2015). Condensin I and II complexes license full estrogen receptor α-dependent enhancer activation. *Mol. Cell* 59, 188–202. doi:10.1016/j.molcel.2015.06.002

Li, Y.-L., Cheng, X.-N., Lu, T., Shao, M., and Shi, D.-L. (2021). Syne2b/Nesprin-2 is required for actin organization and epithelial integrity during epiboly movement in zebrafish. *Front. Cell Dev. Biol.* 9, 671887. doi:10.3389/fcell.2021.671887

Lin, C.-J., Conti, M., and Ramalho-Santos, M. (2013). Histone variant H3.3 maintains a decondensed chromatin state essential for mouse preimplantation development. *Development* 140, 3624–3634. doi:10.1242/dev.095513

Lin, C.-S., Liang, Y., Su, S.-G., Zheng, Y.-L., Yang, X., Jiang, N., et al. (2022). Nucleoporin 93 mediates β-catenin nuclear import to promote hepatocellular carcinoma progression and metastasis. *Cancer Lett.* 526, 236–247. doi:10.1016/j.canlet.2021.11.001

Lin, D. H., Correia, A. R., Cai, S. W., Huber, F. M., Jette, C. A., and Hoelz, A. (2018). Structural and functional analysis of mRNA export regulation by the nuclear pore complex. *Nat. Commun.* 9, 2319. doi:10.1038/s41467-018-04459-3

Liu, B., Wang, Z., Zhang, L., Ghosh, S., Zheng, H., and Zhou, Z. (2013). Depleting the methyltransferase Suv39h1 improves DNA repair and extends lifespan in a progeria mouse model. *Nat. Commun.* 4, 1868. doi:10.1038/ncomms2885

Liu, N.-A., Sun, J., Kono, K., Horikoshi, Y., Ikura, T., Tong, X., et al. (2015). Regulation of homologous recombinational repair by lamin B1 in radiation-induced DNA damage. *FASEB J.* 29, 2514–2525. doi:10.1096/fj.14-265546

Lu, C., Jain, S. U., Hoelper, D., Bechet, D., Molden, R. C., Ran, L., et al. (2016). Histone H3K36 mutations promote sarcomagenesis through altered histone methylation landscape. *Science* 352, 844–849. doi:10.1126/science.aac7272

Lukášová, E., Kovařík, A., and Kozubek, S. (2018). Consequences of lamin B1 and lamin B receptor downregulation in senescence. *Cells* 7, 1. doi:10.3390/cells7020011

Lukášová, E., Kovarõík, A., Bacõíková, A., Falk, M., and Kozubek, S. (2017). Loss of lamin B receptor is necessary to induce cellular senescence. *Biochem. J.* 474, 281–300. doi:10.1042/BCJ20160459

Lupiáñez, D. G., Kraft, K., Heinrich, V., Krawitz, P., Brancati, F., Klopocki, E., et al. (2015). Disruptions of topological chromatin domains cause pathogenic rewiring of gene-enhancer interactions. *Cell* 161, 1012–1025. doi:10.1016/j.cell.2015.04.004

Machiels, B. M., Zorenc, A. H., Endert, J. M., Kuijpers, H. J., van Eys, G. J., Ramaekers, F. C., et al. (1996). An alternative splicing product of the lamin A/C gene lacks exon 10. *J. Biol. Chem.* 271, 9249–9253. doi:10.1074/jbc.271.16.9249

Mah, L. J., El-Osta, A., and Karagiannis, T. C. (2010). gammaH2AX: a sensitive molecular marker of DNA damage and repair. *Leukemia* 24, 679–686. doi:10.1038/leu.2010.6

Marullo, F., Cesarini, E., Antonelli, L., Gregoretti, F., Oliva, G., and Lanzuolo, C. (2016). Nucleoplasmic Lamin A/C and Polycomb group of proteins: An evolutionarily conserved interplay. *Nucleus* 7, 103–111. doi:10.1080/19491034.2016.1157675

Matthews, B. J., and Waxman, D. J. (2018). Computational prediction of CTCF/cohesin-based intra-TAD loops that insulate chromatin contacts and gene expression in mouse liver. *eLife* 7, e34077. doi:10.7554/eLife.34077

Mattioli, E., Andrenacci, D., Garofalo, C., Prencipe, S., Scotlandi, K., Remondini, D., et al. (2018). Altered modulation of lamin A/C-HDAC2 interaction and p21 expression during oxidative stress response in HGPS. *Aging Cell* 17, e12824. doi:10.1111/acel.12824

McLaughlin-Drubin, M. E., Park, D., and Munger, K. (2013). Tumor suppressor p16INK4A is necessary for survival of cervical carcinoma cell lines. *Proc. Natl. Acad. Sci. U. S. A.* 110, 16175–16180. doi:10.1073/pnas.1310432110

Melcon, G., Kozlov, S., Cutler, D. A., Sullivan, T., Hernandez, L., Zhao, P., et al. (2006). Loss of emerin at the nuclear envelope disrupts the Rb1/E2F and MyoD pathways during muscle regeneration. *Hum. Mol. Genet.* 15, 637–651. doi:10.1093/hmg/ddi479

Millán-Zambrano, G., Burton, A., Bannister, A. J., and Schneider, R. (2022). Histone post-translational modifications - cause and consequence of genome function. *Nat. Rev. Genet.* 23, 563–580. doi:10.1038/s41576-022-00468-7

Minchell, N. E., Keszthelyi, A., and Baxter, J. (2020). Cohesin causes replicative DNA damage by trapping DNA topological stress. *Mol. Cell* 78, 739–751. e8. doi:10.1016/j.molcel.2020.03.013

Mohammad, F., and Helin, K. (2017). Oncohistones: Drivers of pediatric cancers. *Genes Dev.* 31, 2313–2324. doi:10.1101/gad.309013.117

Mohammed, H., Taylor, C., Brown, G. D., Papachristou, E. K., Carroll, J. S., and D'Santos, C. S. (2016). Rapid immunoprecipitation mass spectrometry of endogenous proteins (RIME) for analysis of chromatin complexes. *Nat. Protoc.* 11, 316–326. doi:10.1038/nprot.2016.020

Moir, R. D., Spann, T. P., Herrmann, H., and Goldman, R. D. (2000). Disruption of nuclear lamin organization blocks the elongation phase of DNA replication. *J. Cell Biol.* 149, 1179–1192. doi:10.1083/jcb.149.6.1179

Moreno, E., and Basler, K. (2004). dMyc transforms cells into super-competitors. *Cell* 117, 117–129. doi:10.1016/s0092-8674(04)00262-4

Moss, S. F., Krivosheyev, V., de Souza, A., Chin, K., Gaetz, H. P., Chaudhary, N., et al. (1999). Decreased and aberrant nuclear lamin expression in gastrointestinal tract neoplasms. *Gut* 45, 723–729. doi:10.1136/gut.45.5.723

Muñoz-Espín, D., Cañamero, M., Maraver, A., Gómez-López, G., Contreras, J., Murillo-Cuesta, S., et al. (2013). Programmed cell senescence during mammalian embryonic development. *Cell* 155, 1104–1118. doi:10.1016/j.cell.2013.10.019

Murray-Nerger, L. A., and Cristea, I. M. (2021). Lamin post-translational modifications: Emerging toggles of nuclear organization and function. *Trends biochem. Sci.* 46, 832–847. doi:10.1016/j.tibs.2021.05.007

Nacev, B. A., Feng, L., Bagert, J. D., Lemiesz, A. E., Gao, J., Soshnev, A. A., et al. (2019). The expanding landscape of "oncohistone" mutations in human cancers. *Nature* 567, 473–478. doi:10.1038/s41586-019-1038-1

Narita, M., Nũnez, S., Heard, E., Narita, M., Lin, A. W., Hearn, S. A., et al. (2003). Rb-mediated heterochromatin formation and silencing of E2F target genes during cellular senescence. *Cell* 113, 703–716. doi:10.1016/s0092-8674(03)00401-x

Nataraj, N. B., Noronha, A., Lee, J. S., Ghosh, S., Mohan Raju, H. R., Sekar, A., et al. (2022). Nucleoporin-93 reveals a common feature of aggressive breast cancers: Robust nucleocytoplasmic transport of transcription factors. *Cell Rep.* 38, 110418. doi:10.1016/j.celrep.2022.110418

Nelson, D. M., Jaber-Hijazi, F., Cole, J. J., Robertson, N. A., Pawlikowski, J. S., Norris, K. T., et al. (2016). Mapping H4K20me3 onto the chromatin landscape of senescent cells indicates a function in control of cell senescence and tumor suppression through preservation of genetic and epigenetic stability. *Genome Biol.* 17, 158. doi:10.1186/s13059-016-1017-x

Nuebler, J., Fudenberg, G., Imakaev, M., Abdennur, N., and Mirny, L. A. (2018). Chromatin organization by an interplay of loop extrusion and compartmental segregation. *Proc. Natl. Acad. Sci. U. S. A.* 115, E6697–E6706. doi:10.1073/pnas.1717730115

Oberdoerffer, P., and Miller, K. M. (2022). Histone H2A variants: Diversifying chromatin to ensure genome integrity. *Semin. Cell Dev. Biol.* 135, 59–72. doi:10.1016/j.semcdb.2022.03.011

Ogryzko, V. V., Schiltz, R. L., Russanova, V., Howard, B. H., and Nakatani, Y. (1996). The transcriptional coactivators p300 and CBP are histone acetyltransferases. *Cell* 87, 953–959. doi:10.1016/s0092-8674(00)82001-2

Orjalo, A. V., Arnaoutov, A., Shen, Z., Boyarchuk, Y., Zeitlin, S. G., Fontoura, B., et al. (2006). The Nup107-160 nucleoporin complex is required for correct bipolar spindle assembly. *Mol. Biol. Cell* 17, 3806–3818. doi:10.1091/mbc.E05-11-1061

Pascual-Garcia, P., Debo, B., Aleman, J. R., Talamas, J. A., Lan, Y., Nguyen, N. H., et al. (2017). Metazoan nuclear pores provide a scaffold for poised genes and mediate induced enhancer-promoter contacts. *Mol. Cell* 66, 63–76. doi:10.1016/j.molcel.2017.02.020

Pascual-Reguant, L., Blanco, E., Galan, S., Le Dily, F., Cuartero, Y., Serra-Bardenys, G., et al. (2018). Lamin B1 mapping reveals the existence of dynamic and functional euchromatin lamin B1 domains. *Nat. Commun.* 9, 3420. doi:10.1038/s41467-018-05912-z

Pennarun, G., Picotto, J., Etourneaud, L., Redavid, A.-R., Certain, A., Gauthier, L. R., et al. (2021). Increase in lamin B1 promotes telomere instability by disrupting the shelterin complex in human cells. *Nucleic Acids Res.* 49, 9886–9905. doi:10.1093/nar/gkab761

Peters, A. H. F. M., Kubicek, S., Mechtler, K., O'Sullivan, R. J., Derijck, A. A. H. A., Perez-Burgos, L., et al. (2003). Partitioning and plasticity of repressive histone methylation states in mammalian chromatin. *Mol. Cell* 12, 1577–1589. doi:10.1016/s1097-2765(03)00477-5

Phillips-Cremins, J. E., Sauria, M. E. G., Sanyal, A., Gerasimova, T. I., Lajoie, B. R., Bell, J. S. K., et al. (2013). Architectural protein subclasses shape 3D organization of genomes during lineage commitment. *Cell* 153, 1281–1295. doi:10.1016/j.cell.2013.04.053

Pon, J. R., and Marra, M. A. (2015). Driver and passenger mutations in cancer. *Annu. Rev. Pathol.* 10, 25–50. doi:10.1146/annurev-pathol-012414-040312

Poulos, R. C., Thoms, J. A. I., Guan, Y. F., Unnikrishnan, A., Pimanda, J. E., and Wong, J. W. H. (2016). Functional mutations form at CTCF-cohesin binding sites in melanoma due to uneven nucleotide excision repair across the motif. *Cell Rep.* 17, 2865–2872. doi:10.1016/j.celrep.2016.11.055

Ranade, D., Pradhan, R., Jayakrishnan, M., Hegde, S., and Sengupta, K. (2019). Lamin A/C and Emerin depletion impacts chromatin organization and dynamics in the interphase nucleus. *BMC Mol. Cell Biol.* 20, 11. doi:10.1186/s12860-019-0192-5

Rao, R. C., and Dou, Y. (2015). Hijacked in cancer: The KMT2 (MLL) family of methyltransferases. *Nat. Rev. Cancer* 15, 334–346. doi:10.1038/nrc3929

Ray-Gallet, D., Woolfe, A., Vassias, I., Pellentz, C., Lacoste, N., Puri, A., et al. (2011). Dynamics of histone H3 deposition *in vivo* reveal a nucleosome gap-filling mechanism for H3.3 to maintain chromatin integrity. *Mol. Cell* 44, 928–941. doi:10.1016/j.molcel.2011.12.006

Raz, V., Vermolen, B. J., Garini, Y., Onderwater, J. J. M., Mommaas-Kienhuis, M. A., Koster, A. J., et al. (2008). The nuclear lamina promotes telomere aggregation and centromere peripheral localization during senescence of human mesenchymal stem cells. *J. Cell Sci.* 121, 4018–4028. doi:10.1242/jcs.034876

Redwood, A. B., Perkins, S. M., Vanderwaal, R. P., Feng, Z., Biehl, K. J., Gonzalez-Suarez, I., et al. (2011). A dual role for A-type lamins in DNA double-strand break repair. *Cell Cycle* 10, 2549–2560. doi:10.4161/cc.10.15.16531

Reis-Sobreiro, M., Chen, J.-F., Novitskaya, T., You, S., Morley, S., Steadman, K., et al. (2018). Emerin deregulation links nuclear shape instability to metastatic potential. *Cancer Res.* 78, 6086–6097. doi:10.1158/0008-5472.CAN-18-0608

Ren, X., Tu, C., Tang, Z., Ma, R., and Li, Z. (2018). Alternative lengthening of telomeres phenotype and loss of ATRX expression in sarcomas. *Oncol. Lett.* 15, 7489–7496. doi:10.3892/ol.2018.8318

Richart, L., Lapi, E., Pancaldi, V., Cuenca-Ardura, M., Pau, E. C.-S., Madrid-Mencía, M., et al. (2021). STAG2 loss-of-function affects short-range genomic contacts and modulates the basal-luminal transcriptional program of bladder cancer cells. *Nucleic Acids Res.* 49, 11005–11021. doi:10.1093/nar/gkab864

Rocha, A., Dalgarno, A., and Neretti, N. (2022). The functional impact of nuclear reorganization in cellular senescence. *Brief. Funct. Genomics* 21, 24–34. doi:10.1093/bfgp/elab012

Rondinelli, B., Giacomini, G., Piquet, S., Chevallier, O., Dabin, J., Bai, S.-K., et al. (2022). Aberrant DNA repair is a vulnerability in histone H3.3-mutant brain tumors. *BioRxiv* 1, 1. doi:10.1101/2022.09.29.510093

Rossi, D. J., Bryder, D., Seita, J., Nussenzweig, A., Hoeijmakers, J., and Weissman, I. L. (2007). Deficiencies in DNA damage repair limit the function of haematopoietic stem cells with age. *Nature* 447, 725–729. doi:10.1038/nature05862

Sahu, V., and Lu, C. (2022). Oncohistones: Hijacking the histone code. *Annu. Rev. Cancer Biol.* 6, 293–312. doi:10.1146/annurev-cancerbio-070120-102521

Salvarani, N., Crasto, S., Miragoli, M., Bertero, A., Paulis, M., Kunderfranco, P., et al. (2019). The K219T-Lamin mutation induces conduction defects through epigenetic inhibition of SCN5A in human cardiac laminopathy. *Nat. Commun.* 10, 2267. doi:10.1038/s41467-019-09929-w

Samoshkin, A., Dulev, S., Loukinov, D., Rosenfeld, J. A., and Strunnikov, A. V. (2012). Condensin dysfunction in human cells induces nonrandom chromosomal breaks in anaphase, with distinct patterns for both unique and repeated genomic regions. *Chromosoma* 121, 191–199. doi:10.1007/s00412-011-0353-6

Sanborn, A. L., Rao, S. S. P., Huang, S.-C., Durand, N. C., Huntley, M. H., Jewett, A. I., et al. (2015). Chromatin extrusion explains key features of loop and domain formation in wild-type and engineered genomes. *Proc. Natl. Acad. Sci. U. S. A.* 112, E6456–E6465. doi:10.1073/pnas.1518552112

Santi, S., Cenni, V., Capanni, C., Lattanzi, G., and Mattioli, E. (2020). PCAF involvement in lamin A/C-HDAC2 interplay during the early phase of muscle differentiation. *Cells* 9, 1. doi:10.3390/cells9071735

Sati, S., Bonev, B., Szabo, Q., Jost, D., Bensadoun, P., Serra, F., et al. (2020). 4D genome rewiring during oncogene-induced and replicative senescence. *Mol. Cell* 78, 522–538. doi:10.1016/j.molcel.2020.03.007

Serrano, M., Lin, A. W., McCurrach, M. E., Beach, D., and Lowe, S. W. (1997). Oncogenic ras provokes premature cell senescence associated with accumulation of p53 and p16INK4a. *Cell* 88, 593–602. doi:10.1016/s0092-8674(00)81902-9

Shi, L., Wen, H., and Shi, X. (2017). The histone variant H3.3 in transcriptional regulation and human disease. *J. Mol. Biol.* 429, 1934–1945. doi:10.1016/j.jmb.2016.11.019

Shimi, T., Pfleghaar, K., Kojima, S., Pack, C.-G., Solovei, I., Goldman, A. E., et al. (2008). The A- and B-type nuclear lamin networks: Microdomains involved in chromatin organization and transcription. *Genes Dev.* 22, 3409–3421. doi:10.1101/gad.1735208

Shumaker, D. K., Dechat, T., Kohlmaier, A., Adam, S. A., Bozovsky, M. R., Erdos, M. R., et al. (2006). Mutant nuclear lamin A leads to progressive alterations of epigenetic control in premature aging. *Proc. Natl. Acad. Sci. U. S. A.* 103, 8703–8708. doi:10.1073/pnas.0602569103

Siegenfeld, A. P., Roseman, S. A., Roh, H., Lue, N. Z., Wagen, C. C., Zhou, E., et al. (2022). Polycomb-lamina antagonism partitions heterochromatin at the nuclear periphery. *Nat. Commun.* 13, 4199. doi:10.1038/s41467-022-31857-5

Smith, E. R., Capo-Chichi, C. D., and Xu, X.-X. (2018). Defective nuclear lamina in aneuploidy and carcinogenesis. *Front. Oncol.* 8, 529. doi:10.3389/fonc.2018.00529

Solomon, D. A., Kim, T., Diaz-Martinez, L. A., Fair, J., Elkahloun, A. G., Harris, B. T., et al. (2011). Mutational inactivation of STAG2 causes aneuploidy in human cancer. *Science* 333, 1039–1043. doi:10.1126/science.1203619

Solovei, I., Wang, A. S., Thanisch, K., Schmidt, C. S., Krebs, S., Zwerger, M., et al. (2013). LBR and lamin A/C sequentially tether peripheral heterochromatin and inversely regulate differentiation. *Cell* 152, 584–598. doi:10.1016/j.cell.2013.01.009

Starr, D. A., and Fischer, J. A. (2005). KASH 'n karry: The KASH domain family of cargo-specific cytoskeletal adaptor proteins. *Bioessays* 27, 1136–1146. doi:10.1002/bies.20312

Stephens, A. D., Liu, P. Z., Banigan, E. J., Almassalha, L. M., Backman, V., Adam, S. A., et al. (2018). Chromatin histone modifications and rigidity affect nuclear morphology independent of lamins. *Mol. Biol. Cell* 29, 220–233. doi:10.1091/mbc.E17-06-0410

Stirpe, A., and Heun, P. (2022). The ins and outs of CENP-A: Chromatin dynamics of the centromere-specific histone. *Semin. Cell Dev. Biol.* 135, 24–34. doi:10.1016/j.semcdb.2022.04.003

Sun, X., Clermont, P.-L., Jiao, W., Helgason, C. D., Gout, P. W., Wang, Y., et al. (2016). Elevated expression of the centromere protein-A(CENP-A)-encoding gene as a prognostic and predictive biomarker in human cancers. *Int. J. Cancer* 139, 899–907. doi:10.1002/ijc.30133

Sur, I., Neumann, S., and Noegel, A. A. (2014). Nesprin-1 role in DNA damage response. *Nucleus* 5, 173–191. doi:10.4161/nucl.29023

Sur-Erdem, I., Hussain, M. S., Asif, M., Pınarbası, N., Aksu, A. C., and Noegel, A. A. (2020). Nesprin-1 impact on tumorigenic cell phenotypes. *Mol. Biol. Rep.* 47, 921–934. doi:10.1007/s11033-019-05184-w

Swift, J., Ivanovska, I. L., Buxboim, A., Harada, T., Dingal, P. C. D. P., Pinter, J., et al. (2013). Nuclear lamin-A scales with tissue stiffness and enhances matrix-directed differentiation. *Science* 341, 1240104. doi:10.1126/science.1240104

Szabo, Q., Bantignies, F., and Cavalli, G. (2019). Principles of genome folding into topologically associating domains. *Sci. Adv.* 5, eaaw1668. doi:10.1126/sciadv.aaw1668

Talbert, P. B., and Henikoff, S. (2021). Histone variants at a glance. *J. Cell Sci.* 134, jcs244749. doi:10.1242/jcs.244749

Teng, Y.-C., Sundaresan, A., O'Hara, R., Gant, V. U., Li, M., Martire, S., et al. (2021). ATRX promotes heterochromatin formation to protect cells from G-quadruplex DNA-mediated stress. *Nat. Commun.* 12, 3887. doi:10.1038/s41467-021-24206-5

Towbin, B. D., González-Aguilera, C., Sack, R., Gaidatzis, D., Kalck, V., Meister, P., et al. (2012). Step-wise methylation of histone H3K9 positions heterochromatin at the nuclear periphery. *Cell* 150, 934–947. doi:10.1016/j.cell.2012.06.051

Turinetto, V., Orlando, L., Sanchez-Ripoll, Y., Kumpfmueller, B., Storm, M. P., Porcedda, P., et al. (2012). High basal γH2AX levels sustain self-renewal of mouse embryonic and induced pluripotent stem cells. *Stem Cells* 30, 1414–1423. doi:10.1002/stem.1133

Turner, B. M. (1993). *Decoding the nucleosome minireview*: Cell Press. 75 (1), 5–8. doi:10.1016/S0092-8674(05)80078-9

Tzur, Y. B., Wilson, K. L., and Gruenbaum, Y. (2006). SUN-Domain proteins: "Velcro" that links the nucleoskeleton to the cytoskeleton. *Nat. Rev. Mol. Cell Biol.* 7, 782–788. doi:10.1038/nrm2003

Udugama, M., M Chang, F. T., Chan, F. L., Tang, M. C., Pickett, H. A., R McGhie, J. D., et al. (2015). Histone variant H3.3 provides the heterochromatic H3 lysine 9 tri-methylation mark at telomeres. *Nucleic Acids Res.* 43, 10227–10237. doi:10.1093/nar/gkv847

Vardabasso, C., Gaspar-Maia, A., Hasson, D., Pünzeler, S., Valle-Garcia, D., Straub, T., et al. (2015). Histone variant H2A.Z.2 mediates proliferation and drug sensitivity of malignant melanoma. *Mol. Cell* 59, 75–88. doi:10.1016/j.molcel.2015.05.009

Vorburger, K., Kitten, G. T., and Nigg, E. A. (1989). Modification of nuclear lamin proteins by a mevalonic acid derivative occurs in reticulocyte lysates and requires the cysteine residue of the C-terminal CXXM motif. *EMBO J.* 8, 4007–4013. doi:10.1002/j.1460-2075.1989.tb08583.x

Wang, G. G., Cai, L., Pasillas, M. P., and Kamps, M. P. (2007). NUP98-NSD1 links H3K36 methylation to Hox-A gene activation and leukaemogenesis. *Nat. Cell Biol.* 9, 804–812. doi:10.1038/ncb1608

Wang, G. G., Song, J., Wang, Z., Dormann, H. L., Casadio, F., Li, H., et al. (2009). Haematopoietic malignancies caused by dysregulation of a chromatin-binding PHD finger. *Nature* 459, 847–851. doi:10.1038/nature08036

Wang, L., Lankhorst, L., and Bernards, R. (2022). Exploiting senescence for the treatment of cancer. *Nat. Rev. Cancer* 22, 340–355. doi:10.1038/s41568-022-00450-9

Wang, R.-R., Qiu, X., Pan, R., Fu, H., Zhang, Z., Wang, Q., et al. (2022). Dietary intervention preserves β cell function in mice through CTCF-mediated transcriptional reprogramming. *J. Exp. Med.* 219, e20211779. doi:10.1084/jem.20211779

Wang, X., Hughes, A. C., Brandão, H. B., Walker, B., Lierz, C., Cochran, J. C., et al. (2018). *In vivo* evidence for ATPase-dependent DNA translocation by the Bacillus subtilis SMC condensin complex. *Mol. Cell* 71, 841–847. e5. doi:10.1016/j.molcel.2018.07.006

Wang, Y., Chen, Q., Wu, D., Chen, Q., Gong, G., He, L., et al. (2021). Lamin-A interacting protein Hsp90 is required for DNA damage repair and chemoresistance of ovarian cancer cells. *Cell Death Dis.* 12, 786. doi:10.1038/s41419-021-04074-z

Wang, Y., Jiang, J., He, L., Gong, G., and Wu, X. (2019). Effect of lamin-A expression on migration and nuclear stability of ovarian cancer cells. *Gynecol. Oncol.* 152, 166–176. doi:10.1016/j.ygyno.2018.10.030

Watanabe, T., Wu, T. T., Catalano, P. J., Ueki, T., Satriano, R., Haller, D. G., et al. (2001). Molecular predictors of survival after adjuvant chemotherapy for colon cancer. *N. Engl. J. Med.* 344, 1196–1206. doi:10.1056/NEJM200104193441603

Weierich, C., Brero, A., Stein, S., von Hase, J., Cremer, C., Cremer, T., et al. (2003). Three-dimensional arrangements of centromeres and telomeres in nuclei of human and murine lymphocytes. *Chromosome Res.* 11, 485–502. doi:10.1023/a:1025016828544

Weintraub, A. S., Li, C. H., Zamudio, A. V., Sigova, A. A., Hannett, N. M., Day, D. S., et al. (2017). YY1 is a structural regulator of enhancer-promoter loops. *Cell* 171, 1573–1588. doi:10.1016/j.cell.2017.11.008

Weyburne, E., and Bosco, G. (2021). Cancer-associated mutations in the condensin II subunit CAPH2 cause genomic instability through telomere dysfunction and anaphase chromosome bridges. *J. Cell. Physiol.* 236, 3579–3598. doi:10.1002/jcp.30113

Weyemi, U., Redon, C. E., Sethi, T. K., Burrell, A. S., Jailwala, P., Kasoji, M., et al. (2016). Twist1 and Slug mediate H2AX-regulated epithelial-mesenchymal transition in breast cells. *Cell Cycle* 15, 2398–2404. doi:10.1080/15384101.2016.1198864

Wong, K. M., Song, J., and Wong, Y. H. (2021). CTCF and EGR1 suppress breast cancer cell migration through transcriptional control of Nm23-H1. *Sci. Rep.* 11, 491. doi:10.1038/s41598-020-79869-9

Wong, L. H., Ren, H., Williams, E., McGhie, J., Ahn, S., Sim, M., et al. (2009). Histone H3.3 incorporation provides a unique and functionally essential telomeric chromatin in embryonic stem cells. *Genome Res.* 19, 404–414. doi:10.1101/gr.084947.108

Wood, A. M., Rendtlew Danielsen, J. M., Lucas, C. A., Rice, E. L., Scalzo, D., Shimi, T., et al. (2014). TRF2 and lamin A/C interact to facilitate the functional organization of chromosome ends. *Nat. Commun.* 5, 5467. doi:10.1038/ncomms6467

Xu, H., Yan, M., Patra, J., Natrajan, R., Yan, Y., Swagemakers, S., et al. (2011). Enhanced RAD21 cohesin expression confers poor prognosis and resistance to chemotherapy in high grade luminal, basal and HER2 breast cancers. *Breast Cancer Res.* 13, R9. doi:10.1186/bcr2814

Yang, Y., Zhang, L., Xiong, C., Chen, J., Wang, L., Wen, Z., et al. (2022). HIRA complex presets transcriptional potential through coordinating depositions of the histone variants H3.3 and H2A.Z on the poised genes in mESCs. *Nucleic Acids Res.* 50, 191–206. doi:10.1093/nar/gkab1221

Yassin, E. R., Abdul-Nabi, A. M., Takeda, A., and Yaseen, N. R. (2010). Effects of the NUP98-DDX10 oncogene on primary human CD34+ cells: Role of a conserved helicase motif. *Leukemia* 24, 1001–1011. doi:10.1038/leu.2010.42

Ye, Q., and Worman, H. J. (1996). Interaction between an integral protein of the nuclear envelope inner membrane and human chromodomain proteins homologous to Drosophila HP1. *J. Biol. Chem.* 271, 14653–14656. doi:10.1074/jbc.271.25.14653

Yin, L., Jiang, L.-P., Shen, Q.-S., Xiong, Q.-X., Zhuo, X., Zhang, L.-L., et al. (2017). NCAPH plays important roles in human colon cancer. *Cell Death Dis.* 8, e2680. doi:10.1038/cddis.2017.88

Yu, G., Zhang, Y., Gupta, V., Zhang, J., MacCarthy, T., Duan, Z., et al. (2021). The role of HIRA-dependent H3.3 deposition and its modifications in the somatic hypermutation of immunoglobulin variable regions. *Proc. Natl. Acad. Sci. U. S. A.* 118, e2114743118. doi:10.1073/pnas.2114743118

Yuen, B. T. K., and Knoepfler, P. S. (2013). Histone H3.3 mutations: A variant path to cancer. *Cancer Cell* 24, 567–574. doi:10.1016/j.ccr.2013.09.015

Yun, J., Song, S.-H., Kim, H.-P., Han, S.-W., Yi, E. C., and Kim, T.-Y. (2016). Dynamic cohesin-mediated chromatin architecture controls epithelial-mesenchymal plasticity in cancer. *EMBO Rep.* 17, 1343–1359. doi:10.15252/embr.201541852

Yusufzai, T. M., Tagami, H., Nakatani, Y., and Felsenfeld, G. (2004). CTCF tethers an insulator to subnuclear sites, suggesting shared insulator mechanisms across species. *Mol. Cell* 13, 291–298. doi:10.1016/s1097-2765(04)00029-2

Zeitlin, S. G., Baker, N. M., Chapados, B. R., Soutoglou, E., Wang, J. Y. J., Berns, M. W., et al. (2009). Double-strand DNA breaks recruit the centromeric histone CENP-A. *Proc. Natl. Acad. Sci. U. S. A.* 106, 15762–15767. doi:10.1073/pnas.0908233106

Zhang, H., and Li, T. (2017). Effects of spermidine and ATP on stabilities of chromatosomes and histone H1-depleted chromatosomes. *Bioorg. Med. Chem. Lett.* 27, 1149–1153. doi:10.1016/j.bmcl.2017.01.072

Zhang, R., Ai, J., Wang, J., Sun, C., Lu, H., He, A., et al. (2022). NCAPG promotes the proliferation of hepatocellular carcinoma through the CKII-dependent regulation of PTEN. *J. Transl. Med.* 20, 325. doi:10.1186/s12967-022-03519-z

Zhang, R., Chen, W., and Adams, P. D. (2007). Molecular dissection of formation of senescence-associated heterochromatin foci. *Mol. Cell. Biol.* 27, 2343–2358. doi:10.1128/MCB.02019-06

Zhang, X., Jeong, M., Huang, X., Wang, X. Q., Wang, X., Zhou, W., et al. (2020). Large DNA methylation nadirs anchor chromatin loops maintaining hematopoietic stem cell identity. *Mol. Cell* 78, 506–521. doi:10.1016/j.molcel.2020.04.018

Zhang, Y., Liu, F., Zhang, C., Ren, M., Kuang, M., Xiao, T., et al. (2020). Non-SMC condensin I complex subunit D2 is a prognostic factor in triple-negative breast cancer for the ability to promote cell cycle and enhance invasion. *Am. J. Pathol.* 190, 37–47. doi:10.1016/j.ajpath.2019.09.014

Zhao, L., Yang, Y., Yin, S., Yang, T., Luo, J., Xie, R., et al. (2017). CTCF promotes epithelial ovarian cancer metastasis by broadly controlling the expression of metastasis-associated genes. *Oncotarget* 8, 62217–62230. doi:10.18632/oncotarget.19216

Zheng, X., Hu, J., Yue, S., Kristiani, L., Kim, M., Sauria, M., et al. (2018). Lamins organize the global three-dimensional genome from the nuclear periphery. *Mol. Cell* 71, 802–815. doi:10.1016/j.molcel.2018.05.017

Zhou, L., and Panté, N. (2010). The nucleoporin Nup153 maintains nuclear envelope architecture and is required for cell migration in tumor cells. *FEBS Lett.* 584, 3013–3020. doi:10.1016/j.febslet.2010.05.038

Zhou, W., Goodman, S. N., Galizia, G., Lieto, E., Ferraraccio, F., Pignatelli, C., et al. (2002). Counting alleles to predict recurrence of early-stage colorectal cancers. *Lancet* 359, 219–225. doi:10.1016/S0140-6736(02)07448-2

Zink, L.-M., and Hake, S. B. (2016). Histone variants: Nuclear function and disease. *Curr. Opin. Genet. Dev.* 37, 82–89. doi:10.1016/j.gde.2015.12.002